Porphyrin-Based Molecular Wires



He Zhu

St. Anne's College

University of Oxford

A thesis submitted for the degree of

Doctor of Philosophy

Trinity 2024

Acknowledgements

First of all, I would like to express my thanks to my supervisor, Prof. Harry L. Anderson, for accommodating me in his group for the past three and half years. His inspiring ideas, patient supervision and guidance have been essential for my DPhil study. I am truly grateful for having had the opportunity to learn from such a passionate chemist.

I would like to thank my collaborators, Dr Edmund Leary (IMDEA Nanoscience Institute, Spain), Guanzhao Wen, Dr. Wenhao Zheng, Prof. Hai I. Wang and Prof. Mischa Bonn (Max Planck Institute for Polymer Research, Germany). I have been very lucky to learn such advanced techniques from various areas and have insightful discussions on the projects with them.

I would also like to thank all the former and current members of the group, who makes the group a cheerful and fun place to work: Andrew, Arnau, Bobby, Connor, Edward, Henrik, Iago, Igor, Jack, Jake, James, Jeff, Jieren, Josh, Junfu, Kate, Kavita, Keith, Marcin, Owen, Prakhar, Qiang, Sara, Sebastian, Théa, Toby, Virginia, Wenjun, Wojtek and Yueze. In particular, I would like to thank Prof. Qiang Chen and Dr. Jieren Deng, who I have been working closely with, for their insightful discussions throughout my DPhil, especially back to when I started in Oxford during the COVID-19 pandemic. I would also like to express my appreciation to Arnau, Jake and Josh for educating me with a wide knowledge of western culture both in and out of the lab. Another special thanks go to Dr. Jieren Deng, Joshua L. Field, Dr. Henrik Gotfredsen, Dr. Connor Patrick, Dr. Arnau Rubio, Prof. Hai I. Wang and Guanzhao Wen for proofreading parts of this thesis.

My final, but sincerest thanks must go to my family, especially to my parents and my best friend and partner, Connor, for their unconditional love and support; my time in Oxford would not be possible without any of you. Thank you for the constant support, trust, and encouragement during either happy or hard times.

Abstract

This thesis presents an exploration of new opportunities offered by employing porphyrins as functional units in molecular electronic tasks, with a focus on their conducting behavior.

Chapter 1 reviews the charge-transport characteristics of organic oligomeric structures (including hydrocarbon chains and porphyrin-based structures) evaluated as molecular wire candidates, with a focus on their single-molecule conductance behavior.

Chapter 2 proposes a design of molecular geometric switch consisting of porphyrin and paraquat as main functioning units, aiming at creating two hysteretic conductance states in a single molecule to serve as a memory device. A conceptual porphyrin-paraquat conjugate was synthesized for single-molecule conductance study using the STM-BJ technique. While the preliminary conductance results showed that the interaction between porphyrin and paraquat can induce a change in the single-molecule conductance, the switching within one molecule could not be detected.

Chapter 3 presents a theoretical and synthetic exploration of a one-dimensionally extended fully fused anthracene-porphyrin hetero-oligomer structure. The successful preparation of short anthracene-porphyrin nanoribbons offers a scaffold as a new molecular wire candidate, reminiscent of a heteroatom-doped GNR. The extension of the structure was investigated on a bisanthracene-linked porphyrin system but has yet to be synthetically realized.

Chapter 4 studies the intrinsic charge carrier character of triply fused porphyrin oligomers using noncontact optical-pump THz probe spectroscopy. With a series of polydisperse Ni(II) porphyrin nanoribbons, we demonstrated the strong length-dependent charge carrier mobility in this system. In extremely long and deformation-free ribbons, our results indicate that they are expected to have some of the highest intrinsic carrier mobilities among the known GNRs.

Supplement to Statement of Authorship

The work presented in my thesis involve collaborative work with scientists from different fields.

Chapter 2 details the synthesis towards a porphyrin-paraquat conjugate as a molecular memory device. STM break-junction measurements and data analysis were carried out by Dr. Edmund Leary and Lydia Abellan (IMDEA Nanoscience Institute, Spain). The synthesis of compounds **P-2** and **P-Q3** were performed by Prof. Qiang Chen.

Chapter 3 details the synthesis towards fully fused porphyrin-anthracene hetero-oligomers. The computational studies of infinite polymers were carried out by the author in collaboration with Dr. Igor Rončević. Dr. Kirsten E. Christensen determined the crystal structure of **AP2a**. Prakhar Gupta determined the crystal structure of **3.18c**.

Chapter 4 details the synthesis of a series of polydisperse Ni(II) porphyrin nanoribbons and their photoconductivity measured by optical-pump THz probe spectroscopy. THz experiments and data analysis were carried out by Guanzhao Wen and Dr. Wenhao Zheng, under the supervision of Prof. Hai I. Wang and Prof. Mischa Bonn (Max Planck Institute for Polymer Research, Germany).

Contents

List of Publications xi

List of Abbreviations xiii

1 Introduction 1

1.1 Molecular Electronics ... 2

1.2 Charge Transport Through Molecular Wires ... 3

1.2.1 Molecular Junctions ... 3

1.2.2 Charge Transport Mechanism of Molecular Wires ... 5

1.3 Molecular Bridges as Molecular Wires ... 7

1.3.1 Saturated Hydrocarbon Chains ... 8

1.3.2 π-Conjugated Hydrocarbon Chains ... 8

1.3.2.1 Oligoynes and Cumulenes ... 8

1.3.2.2 Oligoenes and Oligomethines ... 11

1.3.2.3 Aromatic Ring-Dominated Chains ... 13

1.4 Porphyrins as Building Blocks for Molecular Wires ... 17

1.4.1 Porphyrins ... 17

1.4.2 π-Bridged Porphyrin Oligomers as Molecular Wires ... 19

1.4.3 Triply Fused Porphyrin Oligomers as Molecular Wires ... 22

1.5 Prospectus ... 24

1.6 References ... 26

2 Porphyrin-Paraquat Conjugate for Molecular Memory Devices 31

2.1 Introduction ... 32

2.1.1 Molecular Switches for Memory Devices ... 32

2.1.2 Porphyrin and Paraquat Unit ... 35

2.1.3 Project Aim ... 36

2.2 Molecular Design and Synthetic Approaches ... 38

2.2.1 Choice of Anchoring Group ... 38

2.2.2 Synthesis of Porphyrin-Paraquat Conjugate **P-Q1** and Control Molecules 39
2.2.2.1 Synthesis of a Porphyrin-Based Molecular Backbone 40
2.2.2.2 Fabrication of Paraquat Arm with SMe-Terminal 41
2.2.2.3 Purification of **P-Q1** 44
2.3 Single-Molecule Conductance of **P-Q1** and Control Molecules 47
2.3.1 STM-BJ Experiment 47
2.3.2 STM-BJ Measurement on **P-Q1** and Control Molecules 48
2.4 Conclusions 52
2.5 References 53
2.6 Experimental 56

3 Anthracene-Porphyrin Nanoribbons **89**
3.1 Introduction 90
3.1.1 π-Extension of Porphyrins 90
3.1.2 Anthracene-Fused Porphyrins 92
3.1.3 Project Aim 93
3.2 Synthesis of Anthracene-Fused Porphyrins Dimers and Trimer 94
3.2.1 Computational Study of Infinite Polymers 94
3.2.2 Molecular Design and Synthetic Approaches 95
3.2.3 X-ray Crystal Structure, Optoelectronic Properties and Metal Exchange Feasibility 98
3.3 Extending Anthracene-Porphyrin Hybrid System 102
3.3.1 Preparation of a Bisanthracene-Fused Porphyrin Dimer 102
3.3.2 Development of Different Solubilizing Groups 105
3.3.3 Stability of Hexyl-Enlarged Solubilizing Group 111
3.4 Conclusions 113
3.5 References 115
3.6 Experimental 118

4 Synthesis of Polydisperse Porphyrin Nanoribbons **225**
4.1 Introduction ... 226
4.1.1 Terahertz Time-Domain Spectroscopy ... 227
4.1.2 THz Response of Charge-Carriers ... 229
4.1.3 THz Properties of Carbon-Based Materials ... 232
4.1.4 Project Aim ... 235
4.2 Synthesis of Polydisperse Porphyrin Nanoribbons ... 236
4.2.1 Synthesis of Zn(II) Porphyrin Nanoribbons ... 237
4.2.2 Synthesis of Ni(II) Porphyrin Nanoribbons ... 241
4.2.3 Length Characterization of Porphyrin Nanoribbons ... 248
4.3 Photoconductivity of Ni(II) Porphyrin Nanoribbons from Terahertz Spectroscopy ... 251
4.4 Conclusions ... 253
4.5 References ... 255
4.6 Experimental ... 259

List of Publications

1 H. Zhu, Q. Chen, I. Rončević, K. E. Christensen and H. L. Anderson, *Angew. Chem. Int. Ed.*, 2023, **62**, e202307035.

2 J.-R. Deng, M. T. González, H. Zhu, H. L. Anderson and E. Leary, *J. Am. Chem. Soc.*, 2024, **146**, 3651–3659.

3 S. M. Kopp, H. Gotfredsen, J. Hergenhahn, A. Rodríguez-rubio, J.-R. Deng, H. Zhu, W. Stawski and H. L. Anderson, *ChemRxiv*, 2024, DOI: 10.26434/chemrxiv-2024-wg9xj.

List of Abbreviations

Abbreviations

Ar	Aryl
BLA	Bond Length Alternation
Bpin	Pinacolborane
BiPy	2,2'-Bipyridine
Bu	Butyl
CCDC	Cambridge Crystallographic Data Centre
CNT	Carbon Nanotube
COD	1,5-Cyclooctadiene
COSY	Homonuclear Correlation Spectroscopy
CVD	Chemical Vapor Deposition
DIPA	Diisopropylamine
DDQ	2,3-Dichloro-5,6-dicyano-1,4-benzoquinone
DFT	Density Functional Theory
DMF	*N*,*N*-Dimethylformamide
DMSO	Dimethylsulfoxide
DS	Drude-Smith
equiv.	Equivalents
ESI	Electrospray Ionization
Fc	Ferrocene
GNR	Graphene Nanoribbon
GPC	Gel Permeation Chromatography
Hex	Hexyl
HMBC	Heteronuclear Multiple Bond Correlation Spectroscopy
HRMS	High-Resolution Mass Spectrometry
HSQC	Heteronuclear Single Quantum Correlation Spectroscopy
MALDI	Matrix-Assisted Laser Desorption/Ionization
MCBJ	Mechanically Controlled Break Junctions
MIR	Mid-wavelength Infrared
MS	Mass Spectrometry
NBS	*N*-Bromosuccinimide
NIR	Near-Infrared
NMR	Nuclear Magnetic Resonance
NOESY	Nuclear Overhauser Effect Spectroscopy
PAH	Polycyclic Aromatic Hydrocarbons
PF_6^-	Hexafluorophosphate
PIFA	(Bis(trifluoroacetoxy)iodo)benzene
SEC	Size Exclusion Chromatography
STM	Scanning Tunneling Microscopy
STM-BJ	Scanning Tunneling Microscopy Break Junctions
TBAF	Tetrabutylammonium fluoride
TD-DFT	Time-Dependent Density Functional Theory
TEA	Triethylamine
TFA	Trifluoroacetic acid
TfOH	Trifluoromethanesulfonic acid
TI	Topological Insulators
THF	Tetrahydrofuran
THS	Tri-*n*-hexylsilyl
THz	Terahertz
TMS	Trimethylsilyl
TLC	Thin Layer Chromatography
UV–vis	Ultraviolet–visible
VASP	Vienna *Ab initio* Simulation Package

1

Introduction

Contents

1.1 Molecular Electronics 2

1.2 Charge Transport Through Molecular Wires 3

1.2.1 Molecular Junctions 3

1.2.2 Charge Transport Mechanism of Molecular Wires 5

1.3 Molecular Bridges as Molecular Wires 7

1.3.1 Saturated Hydrocarbon Chains 8

1.3.2 π-Conjugated Hydrocarbon Chains 8

1.3.2.1 Oligoynes and Cumulenes 8

1.3.2.2 Oligoenes and Oligomethines 11

1.3.2.3 Aromatic Ring-Dominated Chains 13

1.4 Porphyrins as Building Blocks for Molecular Wires 17

1.4.1 Porphyrins 17

1.4.2 π-Bridged Porphyrin Oligomers as Molecular Wires 19

1.4.3 Triply Fused Porphyrin Oligomers as Molecular Wires 22

1.5 Prospectus 24

1.6 References 26

Chapter 1 - Introduction

1.1 Molecular Electronics

The exponential increase in the number of electronic components in a single chip (the transistor count) was first highlighted by Gordon Moore back in the 1960s.[1] This can be mostly attributed to the aggressive downscaling of the feature size in silicon-based transistors, benefiting from advancements in fabrication process that progressed from micrometer-scale precision to sub-5 nanometer over the past few decades.[2] However, the reduction in the size of transistors has recently slowed down due to the inherent limitations in top-down lithographic techniques, combined with issues in cost and energy efficiency.[3] To continuously access cheaper and more energy-efficient microprocessors, while enhancing the component density and performance, the subject of exploring alternative approaches to sustainably develop the electronic technology industry persists.

By means of bottom-up design, molecules can be purposefully engineered with atomic-scale precision, with tailored functionality. Such a vision of utilizing molecular components for electronic applications, initially sketched out in pioneering theoretical work by Aviram and Ratner back in 1974, has evolved into the contemporary field of molecular electronics.[4] Molecular electronics ultimately refer to the use of individual molecules as the active elements to accomplish tasks such as wiring, rectification or switching in electronic circuitry.[5] The diversity in chemical design and ease in bulk preparation of identical molecules provide a prospectus for a highly flexible and low-cost manufacturing towards miniaturized electronic devices.[6] While promising, for the moment this is unlikely to replace the role of silicon-based transistors in today's information society. Before practical molecular integrated circuits can become a reality, there are many challenges that must first be overcome. For example, the mass production of single-molecule devices, the practical implementation compatibility with existing electronic devices, or the control on the environmental effects and fluctuations on device performance are all important factors.

The desire to realize molecular electronics necessitates the technological development of practical experimental platforms, to characterize and manipulate electron transport through individual molecules, meanwhile build a thorough understanding of the relationship between

chemical structures and the corresponding transport mechanism. In fact, the recognition of molecular electronics nowadays extends beyond the goal of miniaturizing devices; it also provides an ideal platform for investigating the quantum mechanical features at the single-molecule level.

This chapter aims to give an overview of the charge-transport characteristics of organic structures that have been evaluated as molecular wire candidates. To narrow the scope of the discussion, the following content focuses on their single-molecule conductance behavior, with a primary focus on break-junction experiments. Section 1.2 provides a general introduction to molecular junctions and charge transport mechanisms through molecular wires. We review the charge transport studies with exemplified molecular wire structures in Section 1.3 and primarily focus on porphyrin-based molecular wires in Section 1.4, to understand how their structure-property relationships governing their conducting behavior.

1.2 Charge Transport Through Molecular Wires

1.2.1 Molecular Junctions

The fundamental function of electronic devices can be intuitively reflected by their conductance through direct electrical measurements. For example: conducting wires require the flow of the current with a minimal, ideally zero, loss of energy due to resistance over long distances; diodes for rectification require asymmetric conductance allowing a high current flow from one direction and being resistive in the reverse; and memory devices require stable, recognizable high contrast switching between their on and off conductance states (a more detailed discussion can be found in Chapter 2). In a similar vein, the functionality of molecules as electronic components can be assessed through their molecular conductance behavior. This first requires experimental testbeds for conductance measurements at the molecular level.

The first direct conductance measurement through molecules was reported in 1971 by Mann *et al.*, where monolayers of fatty acids were sandwiched between metal electrodes.[7] This was the first time that molecule-level samples were sandwiched between metal electrodes, revealing the conductivity decay through the organic monolayer with layer thickness. The first experiment resembling the transport through single molecules was not achieved until 1996, when single-molecule conductance of a 1,4-bis(phenylethynyl)benzene-based molecular wire

was measured through scanning tunneling microscopy (STM).[8] Since then, more efficient methods such as scanning tunneling microscope break junctions (STM-BJ, discussed in Chapter 2), mechanically controlled break junctions (MCBJ), and conductive atomic force microscopy have emerged to characterize single-molecule conductance.[9–13]

These techniques are based on platforms termed "molecular junctions". Molecular junctions involve three aspects: the molecular bridge, the electrode, and the anchoring group. (Figure 1.1).[14] Bringing molecules into contact with a metallic electrode leads to the formation of a molecule–electrode interface.[15] As an individual molecule is positioned in between two metal electrodes, it in turn forms a single-molecule junction, where the conductance of one molecule can be measured. In a single-molecule junction, the molecular orbital of the bridging molecule overlaps with the continuous band of energy levels on the metal electrodes, in a way that is heavily affected by both the electronic character of molecular bridge and the chemistry of anchoring group. Efficient electron transport occurs when the electrode Fermi level (E_F) and molecular energy level are well-aligned, which allows electrons to tunnel or hop through the molecule backbone with minimal resistance (further details for the charge transport mechanism can be found in Section 1.2.2). Single-molecule conductance studies have largely contributed to the fundamental understanding of inherent electron-transport phenomena of materials at molecular level.

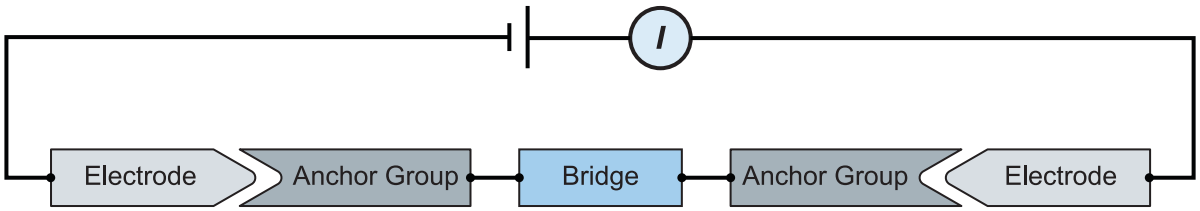


Figure 1.1: A schematic representation of a molecular junction. When a single molecule is bridging between two electrodes, it becomes a single-molecule junction.[14]

Molecular wires are basic electrical components which function as the connections in nanocircuits, linking one electronic element to another. Serving as the conduits for transporting electrons, it is necessary to ensure high efficiency for electron transmission through molecular wires.[6] Thus, conductance studies on molecular wires are particularly suited for evaluating their functional performance, as well as a basis for developing required techniques for the realization of molecular electronics.

1.2.2 Charge Transport Mechanism of Molecular Wires

Based on the movement of electrons along the molecular backbone, charge transport processes through molecular wires involve two primary mechanisms: coherent tunneling and incoherent hopping.[16] Over short distances (generally describing distances less than 4 nm), electron transport through molecular junctions mainly relies on the metal-to-metal coherent off resonant tunneling phenomenon, where electrons cross the molecular bridge in a single step without charge localization (Figure 1.2a).[17]

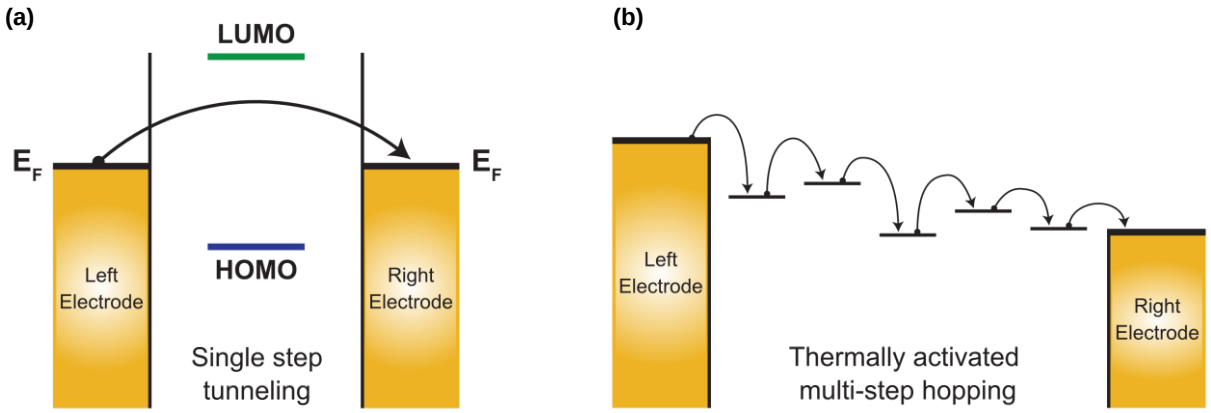


Figure 1.2: Schematic energy diagram for (a) single step tunneling and (b) multi-step hopping through a molecular wire between electrodes. Reproduced with perimission[17]

The coherent nature of tunneling implies that the wavefunction of the electron can be transmitted through the potential barrier without significant distortion. An energy mismatch (ΔE) commonly exists between the electrode Fermi level (E_F) and closest molecular energy level. The molecule acts as a potential barrier that the electron must tunnel through, with a height of ΔE and a width corresponding to the length of the molecule, L (Figure 1.3).[18] In this situation, the probability of electron transmission T from one contact to the other can be described as:

$$T = T_{LC} \cdot T_{RC} \cdot T_{mol} \tag{1.1}$$

$$T_{mol} = e^{-\beta_T L} \tag{1.2}$$

$$\beta_T = \frac{4\pi}{h}\sqrt{2m_e \Delta E} \tag{1.3}$$

where T_{LC} and T_{RC} give the transmission efficiency across the left and right contacts, respectively, T_{mol} reflects the electron transmission through the molecule, β_T is a decay constant for tunneling transmission across the molecular barrier, h is Planck's constant, and m_e is the effective mass of an electron.[19,20]

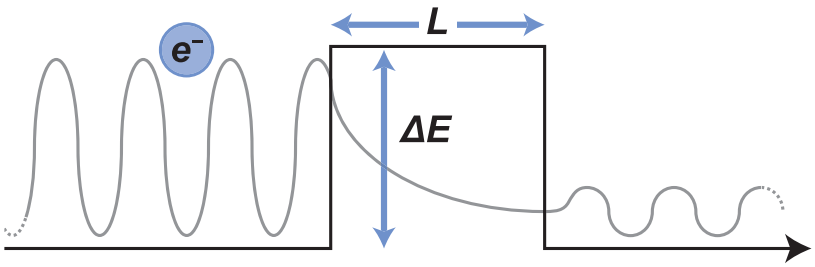


Figure 1.3: Demonstration of an electron tunneling through a potential barrier with a height of ΔE and a width corresponding to the length of the molecule, L.[18]

The conductance G of a molecular junction is related to the probability of electron transmission $T(E)$ (as a function of energy, influenced by factors such as the alignment of molecular orbitals with E_F and orbital hybridization) through the Landauer formula:

$$G = G_0 \int T(E) \tag{1.4}$$

where the G_0 is the conductance quantum and is defined as $G_0 = 2e^2/h = 77.5$ μS (e is the charge of an electron).[21,22] Therefore, the measured molecular conductance G (resistance $R = 1/G$) through this transport mechanism is expected to decrease (increase) exponentially with L, which can be described by the following empirical model:

$$G = G_C e^{-\beta L} \tag{1.5}$$

$$R = R_C e^{\beta L} \tag{1.6}$$

where G_C/R_C is the respective contact conductance/resistance prefactor of the molecular junction, while β is the respective conductance/resistance attenuation factor, extracted from fitting an exponential to experimental conductance (resistance) values, given in units of inverse length.[17] In the case of short-distance tunneling, the charge transport of different molecular backbones can be evaluated by comparing the β values (typically 1–5 nm^{-1} for organic conjugated systems, as also exemplified in Section 1.3).[23–25] In oligomeric molecular backbones, β values also depend on the electronic coupling strength between each repeat unit, which essentially refers to the bridging nature and the degree of conjugation in molecular structures. The model describing the influence from the nature of bridge between repeating units to β value derived by Engelkes *et al.* as follows:

$$\beta = \frac{2}{L_i} \ln\left(\frac{E_i - E_F}{\gamma_{i,i+1}}\right) \tag{1.7}$$

where L_i is the length of each individual unit, E_i is the site energy of each repeating unit and $\gamma_{i,i+1}$ is the electronic coupling energy between the neighboring units.[20]

As molecular wires become longer, environmental factors such as defects, impurities or vibrations become more prominent. These factors can disrupt the electron wavefunction, thereby introducing phase-breaking processes that strongly suppress the rate of tunneling.[26] Instead, electrons can be injected into the frontier orbitals of molecules and transport along the system through an incoherent hopping mechanism (Figure 1.2b).[17,27] The hopping process of electrons are in general thermally activated, allowing them to overcome the potential barriers between localized states within the molecule and then hop along.[28,29] The transition from tunneling to hopping experimentally can be observed as a weaker length-dependent conductance with a much lower apparent β value as the molecular structure becomes longer. The junction resistance R for the hopping mechanism increases linearly along with the molecular length L, following the equation:

$$R = R_C + \alpha L = R_C + \alpha_\infty L e^{(\frac{E_a}{k_B T})} \tag{1.8}$$

where R_C is the contact resistance, α is a molecular specific parameter with units of resistance per unit length, k_B is the Boltzmann constant, and E_a is the activation energy required to reach the transition state for electron hopping through the wire molecule.

1.3 Molecular Bridges as Molecular Wires

Though all three aspects in the molecular junctions exert strong impacts on measured molecular conductance, from the perspective of synthetic organic chemistry, molecular bridges are deemed to hold the greatest potential for manipulation. Theoretically, a molecular bridge can be created from any chemically reasonable, wire-shaped structure that can be prepared by attaching two anchoring groups to build contact with electrodes.[14] This section reviews several typical examples of oligomeric molecular backbones that have been investigated as candidates for molecular wires in the single-molecule break-junction experiments. We discuss their single-molecule conductance, their charge transport performance over distances and their contribution towards furthering our understanding of the factors affecting single-molecule conductance.

1.3.1 Saturated Hydrocarbon Chains

Saturated hydrocarbon chains refer to the systems of alkane consisting of sp^3 C–C backbones. Due to their saturated nature, these molecules lack vacant carbon *p*-orbitals for π-bonds formation, resulting in a large energy gap between their highest occupied molecular orbitals (HOMO) and lowest unoccupied molecular orbitals (LUMO). Alkanes typically exhibit high β values (8.5 nm^{-1} with a bias of 0.1 V) where the conduction is mediated by tunneling mechanism, indicating their very limited charge transport ability over distances.[9,10] However, the studies on saturated alkanes have made significant contributions to advance the fundamental experimental testbeds in the field. For instance, the powerful STM-BJ technique was demonstrated for the first time on single-molecule conductance measurements with hexanedithiol, octanedithiol and decanedithiol these alkane-based structures.[9]

1.3.2 π-Conjugated Hydrocarbon Chains

Compared to saturated hydrocarbons, conjugated hydrocarbon chains are equipped with π-systems, which means that the electrons can delocalize through strongly conjugated molecular orbitals, tending to facilitate the charge transport over the molecule. Two types of oligomeric structures with conjugated hydrocarbon backbones attract the most attention as molecular wires: double/triple C–C bond-dominated chains and aromatic ring-dominated chain.

1.3.2.1 Oligoynes and Cumulenes

Conceptually, the simplest π-conjugated organic molecules are linear, *sp*-hybridized all-carbon wires, where the electrons delocalize almost cylindrically along a one-dimensional, rigid-rod, length-persistent chain.[30] Based on the bonding patterns, they can be divided into two distinct groups: alternating single and triple C–C bond to give oligoynes, or equalized C–C double bonds to give cumulenes (Figure 1.4). The bond length alternating nature of oligoynes makes them predicted to be semiconducting when infinitely long, while cumulenes, with much more subtle bond length alternation, are predicted to have a metallic electronic structure (*i.e.*, no band gap).[31,32]

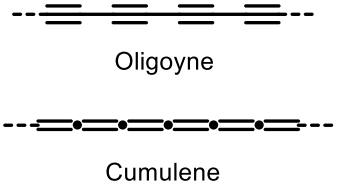
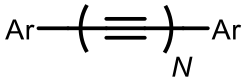


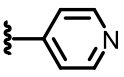
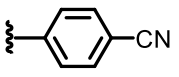
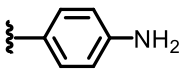
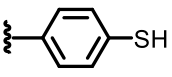
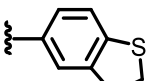
Figure 1.4: Structures of oligoyne and cumulene.

Wang *et al.* first conducted single-molecule conductance measurement on oligoynes with pyridyl **PY** (Table 1.1) end-capped mono- (N = 1), di- (N =

2), and tetrayne-based ($N = 4$) molecular wires through single-molecule junctions under solvent-free conditions, where β value was determined at 0.6 nm^{-1} through tunneling transport mechanism (with a bias of 0.1 V).[33] Subsequently, the electrical conductance studies of these molecules and the analogous with different anchoring groups (Table 1.1) in solution by Moreno-García *et al.* provided a more detailed insight into oligoyne-based molecular wires.[34] Using both the STM-BJ and MCBJ methods, it was found that their β values constantly vary with the type of the anchoring group. This suggests that for oligoyne-based wires, the anchoring group dominates the molecule–electrode coupling (*i.e.*, the molecular energy level involved in the electron transport) in the single-molecule junction.[35] It was noted that the **PY** series exhibits a distinct a difference in β values when measured in dry or in-solution samples. This could be explained by the "solvent-induced gating" effect revealed by Milan *et al.* in 2016, wherein the electrostatic interactions between the solvent molecules and oligoyne backbones strongly impact on the efficiency of the electron transmission through molecular bridge.[36]

Table 1.1: Molecular structures of oligoyne and the anchoring groups used in the single-molecule conductance studies.[33,34]



Anchor (Ar)	 **PY**	 **CN**	 **NH_2**	 **SH**	 **BT**
β (nm^{-1})	0.6 or 3.1	1.7	2.5	3.2	2.9

The fabrication of cumulenic structures in single-molecule junctions was only achieved recently, due to their generally low stability. Single-molecule conductance of cumulenes were first explored by Xu *et al.* on a series of [*N*]cumulenes ($N = 1$ (alkene), 2 (allene), 3 and 5, Figure 1.5), where *N* is the number of consecutive C=C bonds in the cumulene core, combined with a theoretical investigation on [4]cumulene.[37] STM-BJ experiments under solvent-free conditions (with a bias of 0.2 V) showed that [3]- and [5]cumulenes have essentially the same conductance, which is slightly higher than that of alkene and 50 times higher than that of allene. While the steric interactions between the terminal aryl groups in alkene account for its minor reduction in conductance, the much smaller conductance observed on allene is attributed to its largely twisted geometry. This aligns with the prediction from early theoretical studies, where the conductance of cumulenes should present an oscillatory manner with *N* due to the orbital orientations, taking higher conductance for odd-numbered [*N*]cumulenes than even-

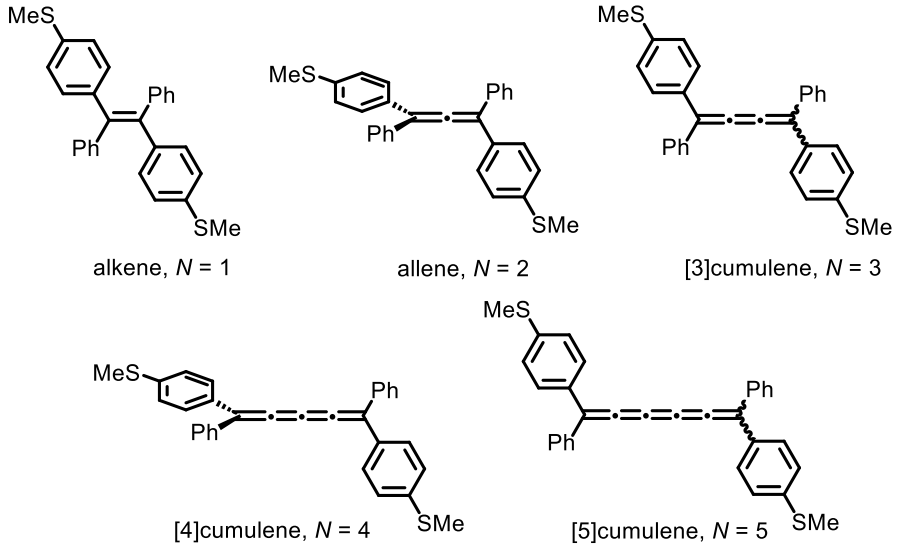


Figure 1.5: Structures of [*N*]cumulenes in single-molecule conductance study (*N* = 1–5, *N* represents the number of C–C double bonds in the structure).[37]

numbered homologous.[38] The DFT-calculated frontier molecular orbitals also reveal that HOMO and LUMO of [3]- and [5]cumulene form extended π-conjugated transport paths throughout the entire backbones including the terminal 4-thioanisole groups. However, such paths do not exist in the even-numbered allene and [4]cumulene structures due to their 90° twisted geometry, leading to a much lower electronic transmission.

Furthermore, the non-decaying conductance obtained from [3]- to longer [5]cumulene indicates their novel length-independent conducting behavior, attributed to the strongly decreased HOMO–LUMO gap as the π-extension with the increasing length. In another study, Zang *et al.* carried out a single-molecule conductance investigation of [3]-, [5]-, [7]cumulene in different solutions, where negative β values were consistently observed (Figure 1.6).[39] This suggests that the conductance of cumulenes increases with length and confirms that this highly conductive property is inherent to cumulenes, and unrelated to the measurement environment.

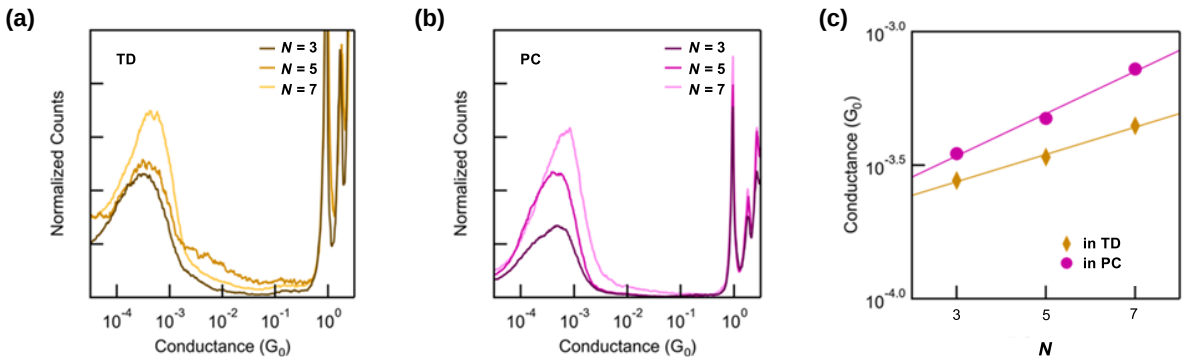


Figure 1.6: (a) and (b) 1D conductance histograms of [3]-, [5]-, [7]cumulene at 0.1 V in tetradecane (TD, nonpolar) and propylene carbonate (PC, polar). (c) Conductance determined from Gaussian fits to histogram peaks from (a) and (b) as a function of *N* along with a linear fit. Reprinted with permission from Zang *et al.*, *Nano Lett.*, 2020, **20**, 8415–8419. Copyright 2020 American Chemical Society.[39]

However, it should be noted that [9]cumulenes remain the longest derivatives that have been experimentally isolated and characterized to date.[40] The challenging accessibility and their poor stability of long cumulenes presents obvious restrictions for their use in practice.

1.3.2.2 Oligoenes and Oligomethines

Oligoenes are characterized by an array of even-numbered of sp^2 hybridized carbon atoms with alternating double and single C–C bonds along the π-system (Figure 1.7). The extended conjugation through these linear molecules leads to a nearly planar arrangement of their structure. STM-BJ experiments on oligoenes with different sulfur-based anchoring groups between gold electrodes have been performed by Meisner *et al.*[41] They proved that, while the linkage to the electrode of oligoenes would impact on the electron tunneling paths, causing high or low conductance states, the intrinsic length-dependence of the molecular backbone through coherent tunneling mechanism would not significantly alter, giving a constant β value at 2.2 nm^{-1} (under a constant bias voltage ranging from 0.2 to 0.75V).

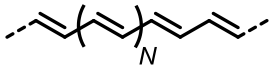


Figure 1.7: Structure of oligoene.

Structurally alike the oligoenes, oligomethines also consist of a linear array of alternating double and single C–C bonds, but contain an odd number of carbon atoms.[42] Symmetric oligomethines (such as in cyanine dyes) can be represented as a hybrid of two resonance structures (Figure 1.8), suggesting that they have near-uniform π-bond orders. Accordingly, this increased π-electron delocalization manifests structurally as a minor degree of bond length alternation in the oligomethine backbone, which renders their unique conducting performance, as discussed below.[43]

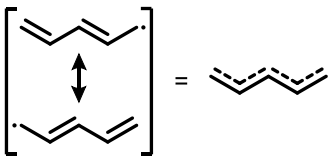


Figure 1.8: Resonance structures of an oligomethine radical, suggesting that oligomethine systems have near-uniform π-bond orders.

The single-molecule conductance study on **Cy3**$^+$, **Cy5**$^+$ and **Cy7**$^+$ (where the number corresponds to the number of carbon atoms present in between two nitrogen-containing heterocyclic rings, Figure 1.9) performed by Gunasekaran *et al.* using the STM-BJ technique suggested that, the conductance of this series of short cyanine dyes exhibit relatively small length-dependence.[44] The sign of β displayed an interesting variance through the choice of solvent (with a bias of 0.09 V, β = 0.4 nm^{-1} in 1-nonanol, β = 1.4 nm^{-1} in 1,2,4-trichlorobenzene (TCB) and β = −0.8 nm^{-1} in propylene carbonate (PC)). This can be explained by the shifts in

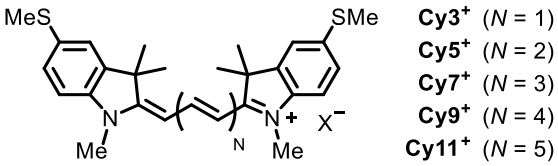


Figure 1.9: Structures of the cyanine dyes investigated by STM-BJ studies.[44,46]

E_F, caused by the solvent and molecules adsorbed on the electrodes, induce the energy level realignment with the molecular orbitals.[45] Excluding such effects, in a solvent-free STM-BJ study Xu *et al.* observed a small increase in the conductance from **Cy3**$^+$, **Cy5**$^+$ to **Cy7**$^+$ (*i.e.*, a negative β).[46] Moreover, the increase trend of conductance is accentuated at higher bias due to their small HOMO–LUMO gaps, where a very negative β value at -1.6 nm^{-1} was recorded at 0.9 V (Figure 1.10). These results highlight the interesting reversed conductance decay of the cumulene series.

However, after reaching a certain length threshold, oligomethines are expected to undergo a Peierls distortion, where the symmetry of the oligomeric backbone breaks and thereby increases the bond-length alternation, resembling an oligoene.[43] Such a symmetry breaking process of oligomethines was first demonstrated as a single-molecule conductance transition in the same work reported by Xu *et al.*[46] X-ray single crystal structures of **Cy7**$^+$, **Cy9**$^+$ to **Cy11**$^+$ reveal that the cationic cyanines with PF_6^- counterions exhibited pronounced bond-length alternation compared to the short derivatives. Correspondingly, a marked decrease in conductance was observed from **Cy7**$^+$, **Cy9**$^+$ to **Cy11**$^+$, which matches the theoretically predicted molecular-length threshold for this transition (Figure 1.10). While oligomethines hold the promise as candidates for molecular wire applications, long-range transport may be challenging for them due to this Peierls distortion. This work highlights the valuable insight that single-molecule conductance study could unveil, serving as an excellent platform for monitoring physical and chemical phenomena at molecular level.

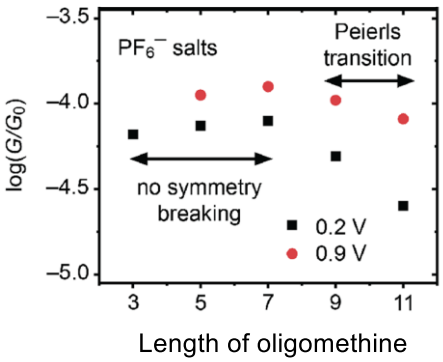
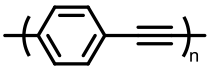
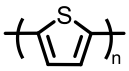
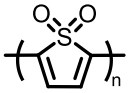


Figure 1.10: Conductance as a function of length for **Cy3**$^+$–**Cy11**$^+$. Black squares are the conductance at 0.2 V, Red circles are the conductance at 0.9 V. The counterion of cyanine dyes is PF_6^-. Reprinted with permission from Xu *et al.*, *J. Am. Chem. Soc.*, 2021, **143**, 20472–20481. Copyright 2021 American Chemical Society.[46]

1.3.2.3 Aromatic Ring-Dominated Chains

Compared to the linear carbon chains, aromatic rings, such as benzene or thiophene units, are more chemically stable structures than noncyclic analogues due to the delocalization of electron within the ring. Linking them together with a C–C single bond, vinylene or acetylene form "oligoarylene" molecular backbones. Extensive research efforts have been devoted to developing their synthetic methodology and examining their conductance behavior. Representative oligomeric structures in this category and corresponding β values studied through single-molecule junctions are summarized in Table 1.2.[29,47–51] While the ease of synthesis could lead to a variety of long oligoarylenic scaffolds extending over nanometers, these molecules generally suffer from inefficient charge transport over long distances. The exponential decay makes them too resistive for single-molecule conductance measurements when they become longer than 3–4 nm.

Table 1.2: β values of representative oligoarylenic structures when the conductance is in the region dominated by coherent-tunneling mechanism.

Backbone	Structure	β (nm^{-1})	Ref
oligophenylene		4.3	[47]
Oligo(phenylene-ethynylene) (OPEs)		2, 3.4	[29,48]
Oligothiophene		1.6, 4.0	[49,50]
Oligothiophene dioxide		2.0	[51]

It recently has been shown that one-dimensional topological insulators (1D TIs) could yield molecular wires with radical characters where the conductance increases with the molecular length. One example is based on oligophenylene bis(triarylamines) (Figure 1.11a).[52] In this study, Li *et al.* studied a series of oligophenylene bis(triarylamines) wires **Bn**, with n = 1–4 *p*-phenylene bridging units, using the STM-BJ technique, in which the bis(triarylamines) units could be chemically oxidized to yield stable mono- and di-radical cations. The conductance of **Bn** in neutral states was found to decrease with an increasing number of phenylene units and show a decay constant β = 3.7 nm^{-1} (with a bias of 0.05V), consistent with other reported oligophenylene-based wires. In stark contrast, the conductance of doubly

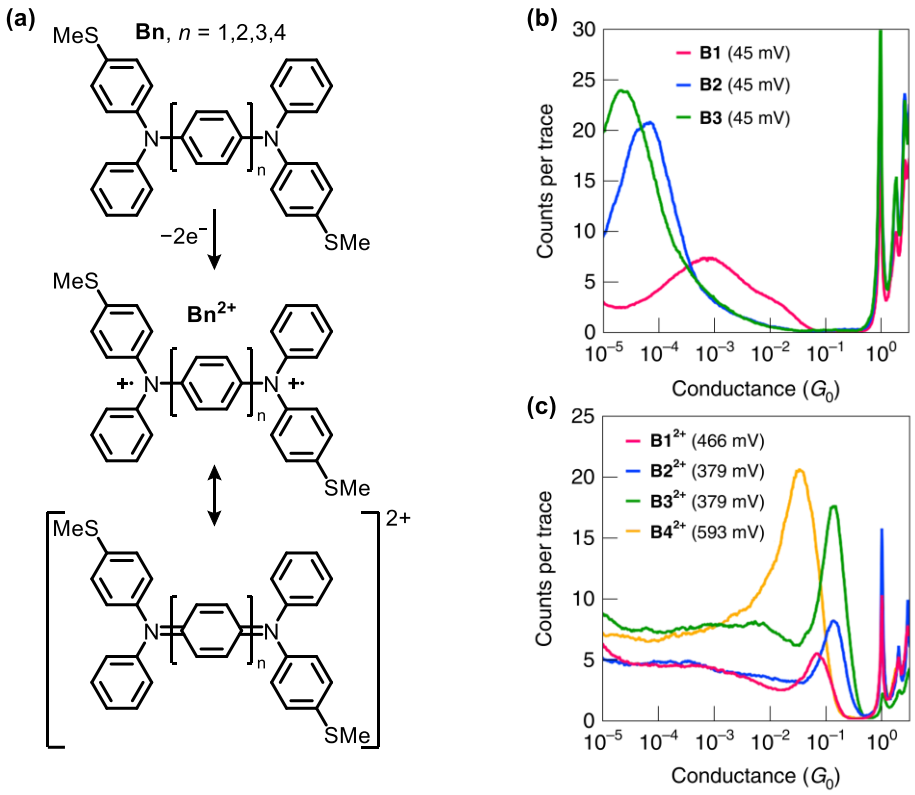


Figure 1.11: (a) Chemical structures of oligophenylene bis(triarylamines)-based molecular wires **Bn** and their doubly oxidized diradical cation version. (b) and (c) 1D conductance histograms of neutral **Bn** and diradical cation $\mathbf{Bn}^{2+}$. Reproduced with permission.[52]

oxidized $\mathbf{Bn}^{2+}$ is remarkably higher than those of corresponding neutral species (*e.g.*, the conductance of $\mathbf{B3}^{2+}$ is 0.13 G_0, achieving ~5000 times higher than that of **B3**). A negative β (−0.07 nm^{-1}) was obtained from $\mathbf{B1}^{2+}$ to $\mathbf{B3}^{2+}$ (red, blue and green traces in Figure 1.11c), whereas the conductance of $\mathbf{B4}^{2+}$ decreases (yellow trace in Figure 1.11c). The DFT calculations reveal that for $\mathbf{Bn}^{2+}$, at a short chain limit where two radical states remain overlap, their coupling weakens as the chain grows longer and the increased di-radical character of the molecule leads to a narrower HOMO–LUMO gap. This leads to the reversed conductance decay from $n = 1$ to 3. However, if the chain becomes longer than the limit where the two radical states are decoupled, this will result in reduced electron density in the middle of the chain. Accordingly, the conductance will start to fall along with increasing length. This chain-length limit, where the middle of the chain becomes poorly conducting while the terminal radical states remain highly conductive, can be regarded as typical 1D topological insulator behavior. The small decrease in conductance observed for $\mathbf{B4}^{2+}$ indicates that this radical delocalization does not extend beyond ~1.4 nm (three phenylene units).

To overcome this length limit, a new strategy that uses a series of 1D TIs as repeating units has been demonstrated by the same group, to achieve high conductance through longer wires.[53] Oligo[*n*]emeraldines (**OE**[*n*]), constituted by phenylene units and secondary amine linkages, can be oxidized to a multiradical form (topological **OE**[*n*], t-**OE**[*n*]) by applying positive bias. In this case, every two secondary amines with one phenylene in the middle form a short 1D TI unit so that the paired radical states in each TI are spatially close and electronically coupled (Figure 1.12). The radicals in such structures are stabilized by the presence of nitrogen units and the resonance energy of phenylenes. Conductance studies using the STM-BJ technique on the t-**OE**[*n*] series (n = 2–7) suggested that these molecules clearly possess increasing conductance along with length, but the increase is not exponentially linear. Instead, the conductance–length relation was found following an attenuated reversed conductance decay correlating to the number of TI units, n:

$$G(L) = Ae^{-\alpha/n} \tag{1.9}$$

where α is the attenuation factor. Following this, the rate of increase in conductance decreases with an increasing n. Up to the longest example reported in this study (n = 7), the reversed conductance decay persists, confirming that this phenomenon has been observed for molecular backbones of almost 5 nm in length.

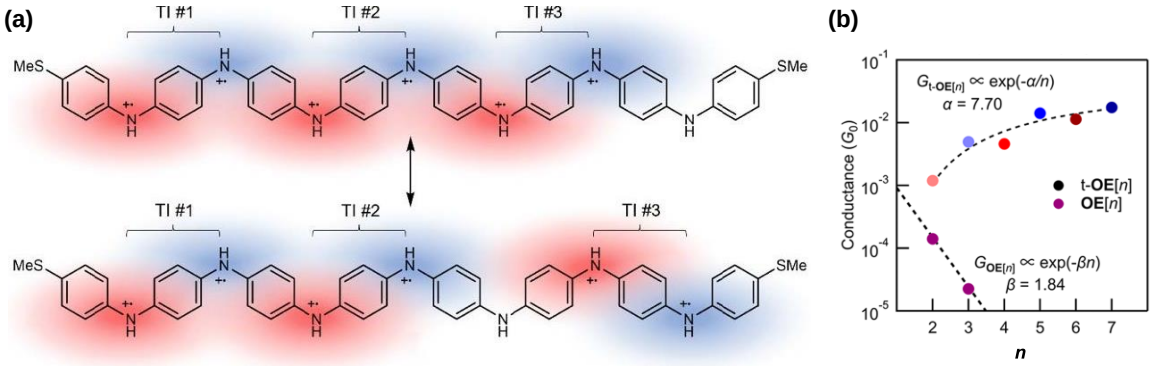


Figure 1.12: (a) Structures of t-**OE**[7]; a pair of red and blue region indicates the location of one TI unit. (b) Measured conductance of the t-**OE**[*n*] chains against n, showing an attenuated reversed conductance decay trend. In contrast, the measured conductance for neutral **OE**[2] and **OE**[3] chains (purple) show an exponential conductance decay phenomenon. Reprinted with permission from Li *et al.*, *J. Am. Chem. Soc.*, 2023, **145**, 2492–2498. Copyright 2023 American Chemical Society.[53]

The one-dimensional systems made from fused aromatic rings, such as graphene nanoribbons (GNRs), open up a number of additional possibilities for aromatic ring-dominated systems. GNRs promise to function as key components in nanoscale electronic devices. For example, their non-zero band gaps, arising from quantum confinement effects, impart them

with promising semiconducting properties.[54] The electronic properties of GNRs critically depend on the ribbon width, length, edge structure and heteroatom-doping.[55] In recent years, "bottom-up" synthetic approach has enabled the preparation of atomically precise GNRs. This allows chemical control over producing homogeneous GNRs and assess their intrinsic conductivity through noncontact methods, such as terahertz (THz) time-domain spectroscopy (a detailed discussion can be found in Chapter 4).[56–58]

Conductance measurement of individual GNRs were first performed in pioneering work by Koch *et al.* through STM pulling experiment (Figure 1.13).[59] Using an STM tip, one end of a GNR, precisely synthesized through on-surface annealing, is lifted off the gold substrate, and then the conductance is measured *in situ* in this lifting geometry. These experiments revealed the electronic behavior of GNRs in molecular junctions.[60–62] For example, it was observed that the decay constant β shows a bias-dependence and, under high bias where with the molecular orbital level better aligns with E_F, the conductance decay with length diminishes. However, GNR in such experiments always adopts a bending geometry, which induces the conductance decay while complexes the theoretical model for analyzing such charge transport paths. Together with the restriction on requiring a low temperature and ultrahigh-vacuum set-up, expanding the abilities to study the conductance of *ex situ*-synthesized GNRs under ambient conditions would be highly desirable.

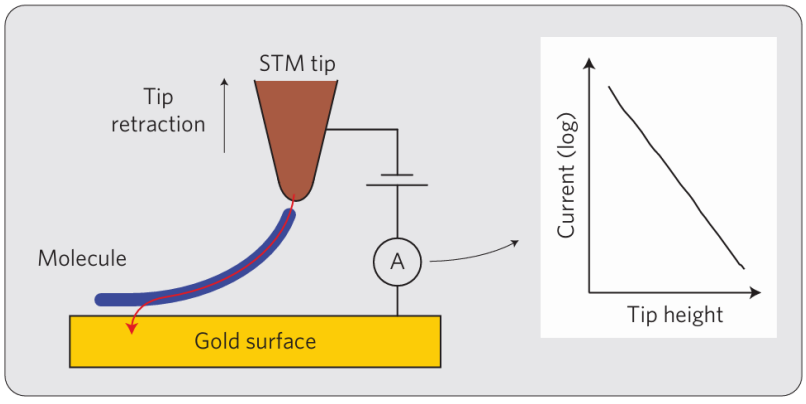


Figure 1.13: Schematic of STM pulling experiment (red arrow indicates the current path). A characteristic current signal during the pulling process is shown in the right panel. Reprint with permission.[59]

An effective method of synthesizing N-doped GNRs with 30 linearly-fused ring backbone (7.7 nm in length) through an iterative approach was reported by Cortizo-Lacalle *et al.* in 2018.[63] By means of doubling the length of building block, this method was able to afford even longer ribbons, up to 60-ring backbone (14.9 nm in length) as the longest molecular

GNR.[64] Very recently, this group of molecules with 6, 16 and 26 fused-ring backbones has been successfully fabricated into single-molecule junctions using diamino anchoring groups, allowing study of their charge transport via STM-BJ conductance measurements (Figure 1.14).[65] This work demonstrates that the 26-ring GNR can mediate a long-range tunneling charge transport (beyond 5 nm) and overall, this series of GNRs is characterized with a shallow length decay (β = 0.68 nm^{-1}). The computational study indicates that this decay correlates with the number of conducting channels involved in the process and its distribution within the molecule.

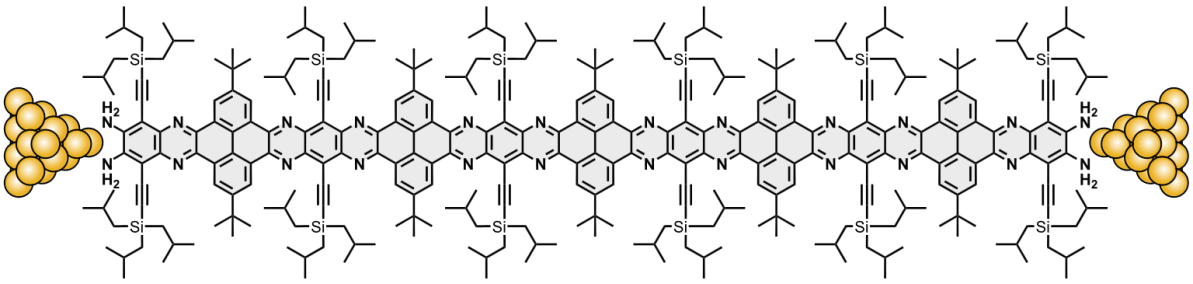


Figure 1.14: Schematic diagram showing the molecular GNR junctions with a 26 linearly-fused ring backbone.[65] Reproduced from original publication.

To briefly summarize, linear molecular wires of cumulenes, oligomethines and 1D TI-based oligoarylenes could offer a higher efficiency of electron transport owing to their length-independent conductance or, in some cases, reversed conductance decay, compared to oligoynes, oligoenes and many other oligoarylenes. Despite these advantages, when it comes to long-range conductive applications, challenges arise with the growing molecular length, particularly in terms of the rapidly decreasing chemical stability and sensitivity to changes in the environment. Conductance studies of molecular GNR junctions shine light on their capability of long-range electron transport. Although, nanoscale charge transport for many other types of GNRs through single-molecule conductance measurements is yet to be explored.

1.4 Porphyrins as Building Blocks for Molecular Wires

1.4.1 Porphyrins

Porphyrins are a family of cyclic molecules comprising four pyrroles bridged by methines with a widespread presence in natural systems.[66–68] Chemically, their parent structure is porphine, where the entire periphery of the macrocycle is substituted by hydrogen atoms, together with an uncoordinated central cavity (also known as a free-base porphyrin). The structure and two standard labelling conventions (IUPAC and common nomenclature using α, β and *meso* to

label different carbon atoms) of atom positions for a free-base porphyrin are shown in Figure 1.15a. Porphyrins have a delocalized electronic system of 26 π-electrons, 18 of which form a conjugated pathway around the cyclic system, thereby making porphyrins aromatic following Hückel's rule of aromaticity (Figure 1.15b). The central cavity of a porphyrin readily coordinates the majority of metal ions in the periodic table, where the porphyrin behaves as a square planar tetradentate ligand (Figure 1.15c).[69–72] Depending on the size of the metal ion and the degree of interaction with porphyrin electrons, the choice of metal can significantly alter the electronic and photophysical properties of the porphyrin.

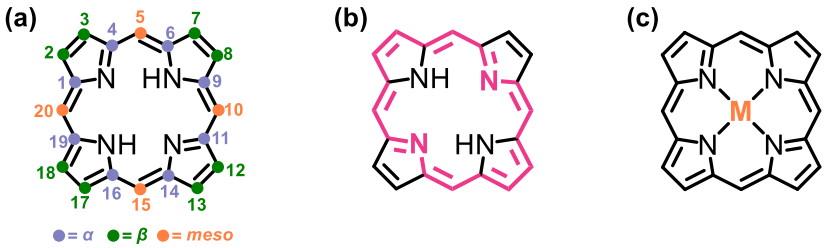


Figure 1.15: (a) General structure of a free-base porphyrin (porphine) numbered by IUPAC or common nomenclature. (b) The pink indicates one of the 18 π-electron conjugated pathways rendering porphyrins aromatic. (c) Representation of the metal ion coordination in porphyrin.

The *β* and *meso*-positions of the porphyrin framework are also readily functionalized, either through peripheral modification with other substituents (further details can be found in Chapter 3) or oligomerization with a variety of linkers. In particular, through inter-porphyrin connections, the electronic communication can be extended to adjacent porphyrin units to create π-conjugated porphyrin oligomers. These oligomers, starting from a large-sized monomeric unit (~7 Å), are ready to extend the molecular lengths towards a few nanometers, while still retaining their structural robustness and high stability. For these reasons, conjugated porphyrin oligomers are particularly suitable to be considered for long-range charge transport. The use of π-conjugated porphyrin oligomers as molecular wire candidates and their corresponding single-molecule conductance behavior are discussed in the following section.

1.4.2 π-Bridged Porphyrin Oligomers as Molecular Wires

The extent of the inter-porphyrin electronic coupling highly depends on the type of the linker and bridging positions. The varied degree of overall conjugation through the oligomeric porphyrin backbones (*i.e.*, the strength of electronic coupling between adjacent porphyrins) is reflected in their absorption spectra. A typical absorption spectrum of a porphyrin monomer consists of two transitions (Figure 1.16): one strong transition to the second excited state ($S_0 \rightarrow S_2$) at approximate 400 nm (the Soret or B band) and a weak one to the first excited state ($S_0 \rightarrow S_1$) at around 550 nm (the Q band).[73] The electronic coupling extending between porphyrin units would be reflected as a bathochromic shift of the Q band.

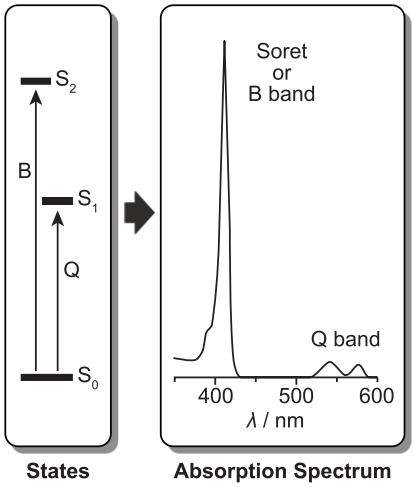


Figure 1.16: Demonstration of a typical porphyrin monomer absorption spectrum and the corresponding electron transitions processes.[73]

Meso-linkages (*i.e.*, single bond or phenylene-linker, Figure 1.17) result in strongly twisted porphyrin oligomer conformations, therefore they only induce weak inter-porphyrin interactions. Their maximum absorption peaks, relative to porphyrin monomers, barely shift as the chain grows.[74] Therefore, these structures are considered non-conjugated porphyrin oligomers. Bridging porphyrin units with unsaturated linkers at the *meso*-positions (*e.g.*, 1,3-butadiyne and ethyne, Figure 1.17) gives rise to π-bridged porphyrin oligomers exhibiting moderate electronic coupling. The extended π-conjugation can be attributed to their relatively co-planar conformations, which is evidenced by the progressive bathochromic shift of their Q

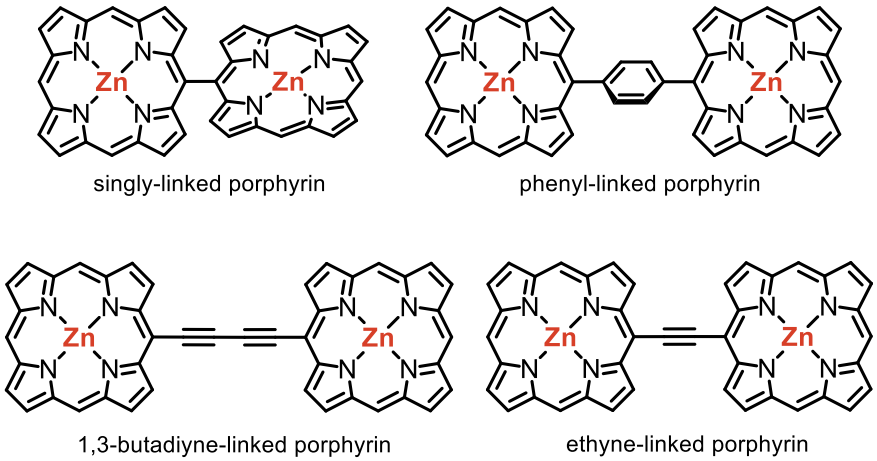


Figure 1.17: Structures of *meso–meso* singly linked, phenyl-linked, 1,3-butadiyne-linked and ethyne-linked porphyrin oligomers.

bands. This is exemplified in Figure 1.18, which demonstrates a series of the UV–vis–NIR absorption spectra of *meso–meso* 1,3-butadiyne-linked (from this point referred to as butadiyne-linked) Zn(II) porphyrin oligomers.[75] Both *meso–meso* ethyne-linked (from this point referred to as ethyne-linked) and butadiyne-linked porphyrin oligomers have been considered as promising molecular wires. The DFT calculations estimate that both series of one-dimensional infinite porphyrin oligomers have a small band gap of ~1 eV, indicating their effective extension of the conjugation throughout the system.[76] The charge transport characteristics of both series up to their corresponding trimer have been evaluated by single-molecule conductance study, as discussed below.

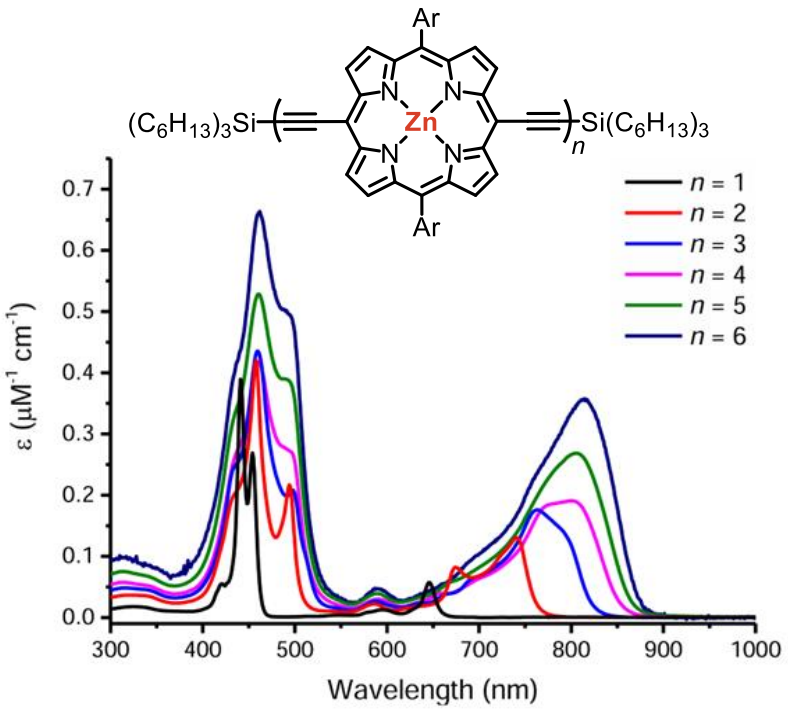


Figure 1.18: UV–vis–NIR absorption spectra of porphyrin-based molecular wires with 1,3-butadiyne linkages (measured in CH_2Cl_2/1% pyridine). Here shown: porphyrin monomer to hexamer (n = 1–6), Ar = 3,5-bis(*t*-butyl)phenyl.[75]

The STM-BJ study of ethyne-linked porphyrin oligomers reported by Li *et al.* investigated their junction-resistance (R = 1/G) dependence with length.[77] Up to the trimer (~4 nm molecular length), all molecules show a high- and low-conductance state due to the variant contact within the junction. The β value determined from either high- or low-conductance states corresponds to 0.34 nm^{-1} (with a bias of 0.1 V). The low length-dependence confirms that the ethyne linker creates effective inter-porphyrin electronic coupling in the oligomeric backbones, leading to a reasonable efficiency for charge transport at nanometer-scale.

Detailed investigations have been devoted to the butadiyne-linked series. For the first time, Sedghi *et al.* "wired" butadiyne-linked porphyrin oligomers (monomer to trimer) between metal electrodes at the single-molecule level using a non-contact variant of the STM-BJ method, called the STM-based $I(s)$ technique.[78–80] With the presence of aryl-thioacetate terminal groups, the absolute wire distance for the trimer was extended to over 5 nm. The charge transport through these junctions is mediated by a coherent-tunneling mechanism with a low β value (0.4 nm^{-1} at 0.6 V), experimentally and theoretically supported by a variable-temperature STM study.[81] In addition, a recent STM-BJ measurement by Leary *et al.* reported that their conductance also displays a bias-voltage dependence (Figure 1.19a).[25] The conductance of each molecule increases with the applied voltage, meanwhile the increasing magnitude becomes more obvious as the number of porphyrin units increases (Figure 1.19b). This can also be interpreted as the length dependence of their conductance (β value) decreases as bias-voltage increases: β = 2.0 nm^{-1} at 0 V, β = 1.4 nm^{-1} at 0.7 V, reaching β = 0.9 nm^{-1} at 0.9 V. Despite the small variation in the obtained β values between studies with different techniques, the low attenuation of butadiyne-linked porphyrin oligomers remains inherent. The theoretical model based on Equation (1.7) suggests that, if a constant electronic coupling γ exists between butadiyne-bridge porphyrin units, this bias-voltage dependent trend of β can be rationalized by a shift of E_F: tuning the applied bias shifts E_F closer to the site energy (smaller ΔE), in turn it

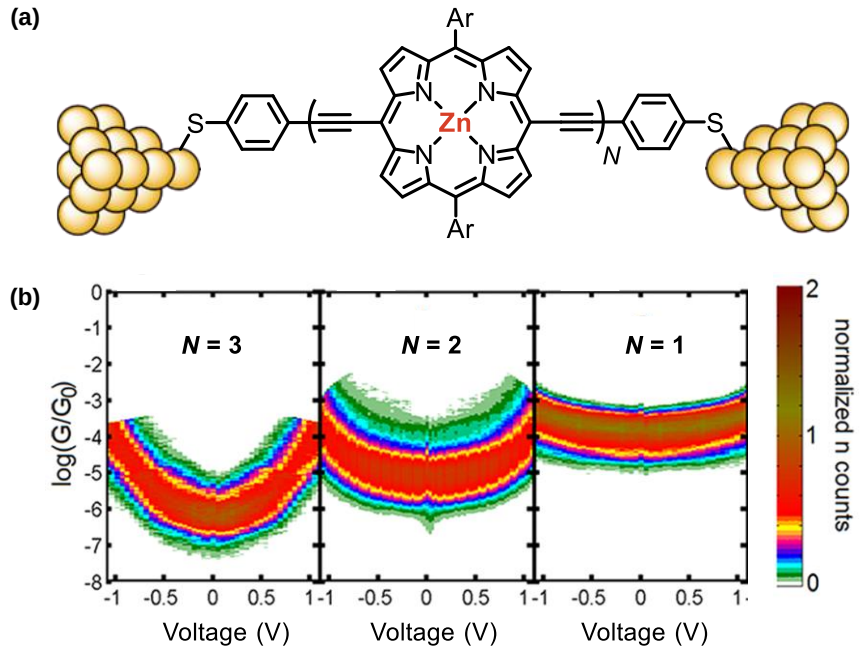


Figure 1.19: (a) Schematic diagram showing a connection of butadiyne-linked porphyrin oligomers (N = 1–3) to two gold electrodes. (b) log(G/G_0)–bias-voltage 2D histograms of butadiyne-linked porphyrin oligomers generated from all current–voltage traces recorded for each junction.[25] Reproduced from original publication.

leads to a decrease in β value. Such a behavior was also observed in *meso–meso*, β–β, β–β triply-linked porphyrin ribbons (discussed in the next section). Though this was the first time that the bias-voltage dependence of the β value was experimentally observed, it is reasonable to anticipate its intrinsic existence in any chain of repeating units.

1.4.3 Triply Fused Porphyrin Oligomers as Molecular Wires

Strong inter-porphyrin electronic communication has been found when directly connecting porphyrin units together via *meso–meso*, β–β, β–β linkages to form the triply-linked porphyrin oligomers, termed porphyrin ribbons (Figure 1.20). This linking type forces the porphyrin rings into a co-planar geometry, which facilitates π-electron delocalization throughout the entire molecule, rendering dramatic reductions in their HOMO–LUMO gaps with increasing length. The porphyrin ribbons exhibit some of the smallest HOMO–LUMO gaps for any neutral organic compounds, as evidenced by their UV–vis–NIR absorption spectra (Figure 1.20, where the fused porphyrin dodecamer shows a ~0.4 eV optical gap).[74] Theoretically, a metallic behavior (*i.e.*, no band gap) is predicted for one-dimensional infinite porphyrin ribbons.[76] Synthetically, porphyrin ribbons are readily prepared from corresponding *meso–meso* singly-linked porphyrin oligomer precursors, treated under oxidative cyclodehydrogenation conditions (see further details in Chapter 4). Their one-dimensional extendibility and unusual optoelectronic features position them as intriguing subjects in charge transport studies as molecular wires.

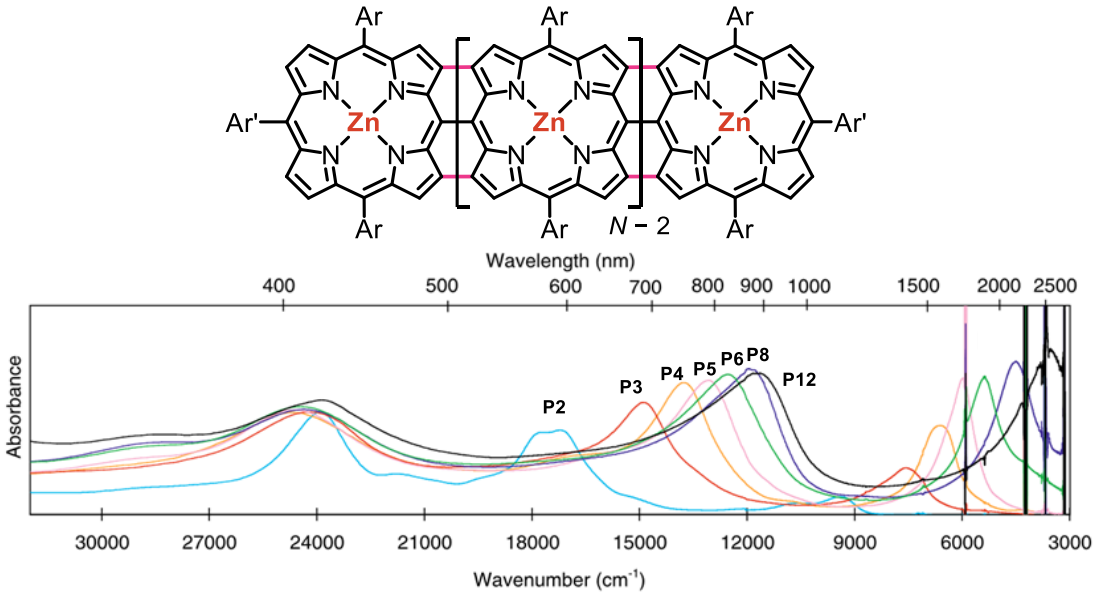


Figure 1.20: (top) Structure of porphyrin ribbons. (bottom) Normalized absorption spectra of porphyrin ribbons (N = 2–6, 8, 12; Ar = 3,5-bis(*t*-butyl)phenyl; Ar'= phenyl).[74] Reproduced from original publication.

Embedding porphyrin ribbons into single-molecule junctions was first achieved in a comparative study that systematically investigated the β value of three types of porphyrin-based molecular wires from monomer to trimer using the STM-based $I(s)$ technique.[82] Under a constant applied bias voltage of 0.6 V, porphyrin ribbons were recorded with a β value of 0.19 nm^{-1}, exhibiting at least a two-fold smaller decay factor in comparison to the corresponding butadiyne-linked series (β = 0.42 nm^{-1}) and *meso–meso* singly-linked series (β = 1.1 nm^{-1}). In STM-BJ measurement carried by Leary *et al.* the bias-voltage dependence of β value was also observed.[25] It was determined that β = 0 nm^{-1} at 0 V, which indicates that length dependence of porphyrin ribbons conductance is vanishing. As the applied bias increases to 0.7 V, β decreases to a negative value (−1.5 nm^{-1}), suggesting a reversed conductance decay at high bias. The theoretical study reveals that the absence or reversal of conductance decay arises from the large decrease in the HOMO–LUMO gap along the fused series. This results in the significant reduction in the effective energy barrier ΔE for the tunneling transport, compensating the attenuating tendency for electrical conductance with increasing length.[83]

In addition, porphyrin ribbons can exhibit bias-induced charging in two-terminal single-molecule junctions under high bias voltage, which switches the molecular bridge between a low (uncharged) and a high (charged) conductance state.[84] These two states display a conductance difference of more than two orders of magnitude. In general, the charging phenomena is more likely to happen under higher bias in longer porphyrin ribbons with a smaller HOMO–LUMO gap. For example, for a fused Zn(II) porphyrin trimer, it was found that, when sweeping the applied bias between ± 0.8 V only < 20% of the traces indicating the molecular charging, but this charging predominantly occurs when extending the bias range to ± 1.2 V. In contrast, the monomer is barely recorded with any charging behavior even under high bias.

The same trend was observed in a very recent study on a series of fused Ni(II) porphyrins from monomer up to octamer with a molecular length of 7.1 nm.[85] The highest conductance of charged fused porphyrin octamer was found able to reach 1 G_0, attributed to a near-perfect alignment of molecular frontier orbital (HOMO in this case) with E_F. It was also found that the charged state could survive in the order of seconds, where the charged molecule exhibits a nonlinear current-bias voltage hysteretic response (*i.e.*, it stays at a high-conducting

state even when the bias is swept back to the low bias region). The theoretical investigation indicates that the conductance boost and switching, and the hysteresis behavior can be rationalized with a two-channel mechanism: a coherent tunneling channel, which is usually associated with the alignment of E_F and a delocalized frontier orbital, determines the measured conductance; and a hopping channel (through a localized molecular orbital) acts as an *in situ* gate, altering the aforementioned alignment. This mechanism can also account for the absence of charging properties in monomers, where the hopping process becomes inaccessible as the consequence of its large HOMO–LUMO gap.

To summarize, single-molecule conductance measurements of conjugated porphyrin oligomers have demonstrated their low length-dependent conductance attenuation with the coherent tunneling as the dominant charge transport mechanism. They exhibit robust chemical stability in single-molecule junctions, which have already been established over 5 nm range and with the potential to be extended even longer. Together with their high-conductance feature, conjugated porphyrin oligomers (especially the porphyrin ribbon family) are considered as promising candidates for highly conductive molecule wires facilitating long-range charge transport. Furthermore, these intriguing conducting properties cannot be attained by a single porphyrin monomer alone. This highlights the importance of investigating the electrical properties of porphyrin-based materials beyond one porphyrin unit, or in conjunction with other non-porphyrin moieties.

1.5 Prospectus

This thesis explores new opportunities offered by employing porphyrins as functional units in molecular electronic tasks, with a focus on their conducting performance. In Chapter 2, we propose a molecular switch design comprising of porphyrin and paraquat units, aiming at creating two conductance states in a single molecule through geometric switching. Exploring the single-molecule conductance behavior of this conjugate could provide insights into the core principles and additional requirements necessary to achieve the targeted memory functionality of this project. In Chapter 3, we study the synthetic accessibility of periphery-modified porphyrins towards one-dimensionally π-extended fully fused anthracene-porphyrin hetero-oligomers, reminiscent of a heteroatom-doped graphene nanoribbon. This offers a new molecular scaffold suitable for molecular wire applications. In Chapter 4, with a series of

polydisperse porphyrin nanoribbons, the intrinsic charge carrier behavior and its length-dependence of porphyrin nanoribbons is studied using non-contact THz time-domain spectroscopy. This work evaluates the potential of long porphyrin nanoribbons as future optoelectronics compared to graphene nanoribbons. All these studies would help to build our understanding of the conducting behavior of porphyrin-based molecules, thereby broadening our perspective on utilizing porphyrin in molecular-scale electronics.

1.6 References

1 G. E. Moore, *Electronics*, 1965, **38**, 114–116.

2 International Roadmap for Devices and Systems, https://irds.ieee.org/, (accessed 7 March 2024).

3 E. Lörtscher, *Nat. Nanotechnol.*, 2013, **8**, 381–384.

4 A. Aviram and M. A. Ratner, *Chem. Phys. Lett.*, 1974, **29**, 277–283.

5 D. Xiang, X. Wang, C. Jia, T. Lee and X. Guo, *Chem. Rev.*, 2016, **116**, 4318–4440.

6 D. M. Guldi, H. Nishihara and L. Venkataraman, *Chem. Soc. Rev.*, 2015, **44**, 842–844.

7 B. Mann and H. Kuhn, *J. Appl. Phys.*, 1971, **42**, 4398–4405.

8 L. A. Bumm, J. J. Arnold, M. T. Cygan, T. D. Dunbar, T. P. Burgin, L. Jones, D. L. Allara, J. M. Tour and P. S. Weiss, *Science*, 1996, **271**, 1705–1707.

9 B. Xu and N. J. Tao, *Science*, 2003, **301**, 1221–1223.

10 X. Li, J. He, J. Hihath, B. Xu, S. M. Lindsay and N. Tao, *J. Am. Chem. Soc.*, 2006, **128**, 2135–2141.

11 M. A. Reed, C. Zhou, C. J. Muller, T. P. Burgin and J. M. Tour, *Science*, 1997, **278**, 252–254.

12 C. Zhou, M. R. Deshpande, M. A. Reed, L. Jones and J. M. Tour, *Appl. Phys. Lett.*, 1997, **71**, 611–613.

13 D. J. Wold and C. D. Frisbie, *J. Am. Chem. Soc.*, 2001, **123**, 5549–5556.

14 T. A. Su, M. Neupane, M. L. Steigerwald, L. Venkataraman and C. Nuckolls, *Nat. Rev. Mater.*, 2016, **1**, 16002.

15 H. B. Akkerman and B. de Boer, *J. Phys.: Condens. Matter*, 2008, **20**, 013001.

16 S. H. Choi, B. Kim and C. D. Frisbie, *Science*, 2008, **320**, 1482–1486.

17 K. H. Khoo, Y. Chen, S. Li and S. Y. Quek, *Phys. Chem. Chem. Phys.*, 2015, **17**, 77–96.

18 F. Trixler, *Curr. Org. Chem.*, 2013, **17**, 1758–1770.

19 A. Salomon, D. Cahen, S. Lindsay, J. Tomfohr, V. B. Engelkes and C. D. Frisbie, *Adv. Mater.*, 2003, **15**, 1881–1890.

20 V. B. Engelkes, J. M. Beebe and C. D. Frisbie, *J. Am. Chem. Soc.*, 2004, **126**, 14287–14296.

21 A. Nitzan, *Annu. Rev. Phys. Chem.*, 2001, **52**, 681–750.

22 C. J. Lambert, *Chem. Soc. Rev.*, 2015, **44**, 875–888.

23 J. He, F. Chen, J. Li, O. F. Sankey, Y. Terazono, C. Herrero, D. Gust, T. A. Moore, A. L. Moore and S. M. Lindsay, *J. Am. Chem. Soc.*, 2005, **127**, 1384–1385.

24 W. Chen, J. R. Widawsky, H. Vázquez, S. T. Schneebeli, M. S. Hybertsen, R. Breslow and L. Venkataraman, *J. Am. Chem. Soc.*, 2011, **133**, 17160–17163.

25 E. Leary, B. Limburg, A. Alanazy, S. Sangtarash, I. Grace, K. Swada, L. J. Esdaile, M. Noori, M. T. González, G. Rubio-Bollinger, H. Sadeghi, A. Hodgson, N. Agraït, S. J. Higgins, C. J. Lambert, H. L. Anderson and R. J. Nichols, *J. Am. Chem. Soc.*, 2018, **140**, 12877–12883.

26 L. Luo, S. H. Choi and C. D. Frisbie, *Chem. Mater.*, 2011, **23**, 631–645.

27 C. Joachim and M. A. Ratner, *Proc. Natl. Acad. Sci.*, 2005, **102**, 8801–8808.

28 D. Segal, A. Nitzan, W. B. Davis, M. R. Wasielewski and M. A. Ratner, *J. Phys. Chem. B*, 2000, **104**, 3817–3829.

29 Q. Lu, K. Liu, H. Zhang, Z. Du, X. Wang and F. Wang, *ACS Nano*, 2009, **3**, 3861–3868.

30 F. Banhart, *Beilstein J. Nanotechnol.*, 2015, **6**, 559–569.

31 W. A. Chalifoux and R. R. Tykwinski, *Nat. Chem.*, 2010, **2**, 967–971.

32 M. H. Garner, W. Bro-Jørgensen, P. D. Pedersen and G. C. Solomon, *J. Phys. Chem. C*, 2018, **122**, 26777–26789.

33 C. Wang, A. S. Batsanov, M. R. Bryce, S. Martín, R. J. Nichols, S. J. Higgins, V. M. García-Suárez and C. J. Lambert, *J. Am. Chem. Soc.*, 2009, **131**, 15647–15654.

34 P. Moreno-García, M. Gulcur, D. Z. Manrique, T. Pope, W. Hong, V. Kaliginedi, C. Huang, A. S. Batsanov, M. R. Bryce, C. Lambert and T. Wandlowski, *J. Am. Chem. Soc.*, 2013, **135**, 12228–12240.

35 M. R. Bryce, *J. Mater. Chem. C*, 2021, **9**, 10524–10546.

36 D. C. Milan, O. A. Al-Owaedi, M.-C. Oerthel, S. Marqués-González, R. J. Brooke, M. R. Bryce, P. Cea, J. Ferrer, S. J. Higgins, C. J. Lambert, P. J. Low, D. Z. Manrique, S. Martin, R. J. Nichols, W. Schwarzacher and V. M. García-Suárez, *J. Phys. Chem. C*, 2016, **120**, 15666–15674.

37 W. Xu, E. Leary, S. Hou, S. Sangtarash, M. T. González, G. Rubio-Bollinger, Q. Wu, H. Sadeghi, L. Tejerina, K. E. Christensen, N. Agraït, S. J. Higgins, C. J. Lambert, R. J. Nichols and H. L. Anderson, *Angew. Chem. Int. Ed.*, 2019, **58**, 8378–8382.

38 N. D. Lang and P. Avouris, *Phys. Rev. Lett.*, 1998, **81**, 3515–3518.

39 Y. Zang, T. Fu, Q. Zou, F. Ng, H. Li, M. L. Steigerwald, C. Nuckolls and L. Venkataraman, *Nano Lett.*, 2020, **20**, 8415–8419.

40 D. Wendinger and R. R. Tykwinski, *Acc. Chem. Res.*, 2017, **50**, 1468–1479.

41 J. S. Meisner, M. Kamenetska, M. Krikorian, M. L. Steigerwald, L. Venkataraman and C. Nuckolls, *Nano Lett.*, 2011, **11**, 1575–1579.

42 S. Dähne, *Science*, 1978, **199**, 1163–1167.

43 L. M. Tolbert and X. Zhao, *J. Am. Chem. Soc.*, 1997, **119**, 3253–3258.

44 S. Gunasekaran, D. Hernangómez-Pérez, I. Davydenko, S. Marder, F. Evers and L. Venkataraman, *Nano Lett.*, 2018, **18**, 6387–6391.

45 B. Choi, B. Capozzi, S. Ahn, A. Turkiewicz, G. Lovat, C. Nuckolls, M. L. Steigerwald, L.

Venkataraman and X. Roy, *Chem. Sci.*, 2016, **7**, 2701–2705.

46 W. Xu, E. Leary, S. Sangtarash, M. Jirasek, M. T. González, K. E. Christensen, L. Abellán Vicente, N. Agraït, S. J. Higgins, R. J. Nichols, C. J. Lambert and H. L. Anderson, *J. Am. Chem. Soc.*, 2021, **143**, 20472–20481.

47 L. Venkataraman, J. E. Klare, C. Nuckolls, M. S. Hybertsen and M. L. Steigerwald, *Nature*, 2006, **442**, 904–907.

48 V. Kaliginedi, P. Moreno-García, H. Valkenier, W. Hong, V. M. García-Suárez, P. Buiter, J. L. H. Otten, J. C. Hummelen, C. J. Lambert and T. Wandlowski, *J. Am. Chem. Soc.*, 2012, **134**, 5262–5275.

49 R. Yamada, H. Kumazawa, T. Noutoshi, S. Tanaka and H. Tada, *Nano Lett.*, 2008, **8**, 1237–1240.

50 B. Capozzi, E. J. Dell, T. C. Berkelbach, D. R. Reichman, L. Venkataraman and L. M. Campos, *J. Am. Chem. Soc.*, 2014, **136**, 10486–10492.

51 E. J. Dell, B. Capozzi, J. Xia, L. Venkataraman and L. M. Campos, *Nat. Chem.*, 2015, **7**, 209–214.

52 L. Li, J. Z. Low, J. Wilhelm, G. Liao, S. Gunasekaran, C. R. Prindle, R. L. Starr, D. Golze, C. Nuckolls, M. L. Steigerwald, F. Evers, L. M. Campos, X. Yin and L. Venkataraman, *Nat. Chem.*, 2022, **14**, 1061–1067.

53 L. Li, S. Louie, A. M. Evans, E. Meirzadeh, C. Nuckolls and L. Venkataraman, *J. Am. Chem. Soc.*, 2023, **145**, 2492–2498.

54 Y.-W. Son, M. L. Cohen and S. G. Louie, *Phys. Rev. Lett.*, 2006, **97**, 216803.

55 K. Nakada, M. Fujita, G. Dresselhaus and M. S. Dresselhaus, *Phys. Rev. B*, 1996, **54**, 17954–17961.

56 L. Dössel, L. Gherghel, X. Feng and K. Müllen, *Angew. Chem. Int. Ed.*, 2011, **50**, 2540–2543.

57 M. G. Schwab, A. Narita, Y. Hernandez, T. Balandina, K. S. Mali, S. De Feyter, X. Feng and K. Müllen, *J. Am. Chem. Soc.*, 2012, **134**, 18169–18172.

58 R. S. K. Houtsma, J. de la Rie and M. Stöhr, *Chem. Soc. Rev.*, 2021, **50**, 6541–6568.

59 M. Koch, F. Ample, C. Joachim and L. Grill, *Nat. Nanotechnol.*, 2012, **7**, 713–717.

60 P. H. Jacobse, A. Kimouche, T. Gebraad, M. M. Ervasti, J. M. Thijssen, P. Liljeroth and I. Swart, *Nat. Commun.*, 2017, **8**, 119.

61 P. H. Jacobse, M. J. J. Mangnus, S. J. M. Zevenhuizen and I. Swart, *ACS Nano*, 2018, **12**, 7048–7056.

62 J. Lawrence, P. Brandimarte, A. Berdonces-Layunta, M. S. G. Mohammed, A. Grewal, C. C. Leon, D. Sánchez-Portal and D. G. de Oteyza, *ACS Nano*, 2020, **14**, 4499–4508.

63 D. Cortizo-Lacalle, J. P. Mora-Fuentes, K. Strutyński, A. Saeki, M. Melle-Franco and A. Mateo-Alonso, *Angew. Chem. Int. Ed.*, 2018, **57**, 703–708.

64 F. Hernández-Culebras, M. Melle-Franco and A. Mateo-Alonso, *Angew. Chem. Int. Ed.*,

2022, **61**, e202205018.

65 M. Marongiu, T. Ha, S. Gil-Guerrero, K. Garg, M. Mandado, M. Melle-Franco, I. Diez-Perez and A. Mateo-Alonso, *J. Am. Chem. Soc.*, 2024, **146**, 3963–3973.

66 R. Willstätter, *J. Am. Chem. Soc.*, 1915, **37**, 323–345.

67 G. McDermott, S. M. Prince, A. A. Freer, A. M. Hawthornthwaite-Lawless, M. Z. Papiz, R. J. Cogdell and N. W. Isaacs, *Nature*, 1995, **374**, 517–521.

68 L. R. Milgrom, *The Colours of Life: An Introduction to the Chemistry of Porphyrins and Related Compounds*, Oxford university press, 1997.

69 K. Kadish, K. M. Smith and R. Guilard, *The Porphyrin Handbook (Volume 3)*, Academic Press, 2000.

70 S. Cotton, *Lanthanide and Actinide Chemistry*, Wiley-WCH, 2006.

71 L. Cuesta and J. L. Sessler, *Chem. Soc. Rev.*, 2009, **38**, 2716.

72 C.-P. Wong, R. F. Venteicher and W. D. Horrocks, *J. Am. Chem. Soc.*, 1974, **96**, 7149–7150.

73 H. L. Anderson, *Chem. Commun.*, 1999, 2323–2330.

74 A. Tsuda and A. Osuka, *Science*, 2001, **293**, 79–82.

75 P. N. Taylor, J. Huuskonen, R. T. Aplin, H. L. Anderson, J. Huuskonen, G. Rumbles and E. Williams, *Chem. Commun.*, 1998, 909–910.

76 V. Posligua, A. Aziz, R. Haver, M. D. Peeks, H. L. Anderson and R. Grau-Crespo, *J. Phys. Chem. C*, 2018, **122**, 23790–23798.

77 Z. Li, T.-H. Park, J. Rawson, M. J. Therien and E. Borguet, *Nano Lett.*, 2012, **12**, 2722–2727.

78 G. Sedghi, K. Sawada, L. J. Esdaile, M. Hoffmann, H. L. Anderson, D. Bethell, W. Haiss, S. J. Higgins and R. J. Nichols, *J. Am. Chem. Soc.*, 2008, **130**, 8582–8583.

79 W. Haiss, H. van Zalinge, S. J. Higgins, D. Bethell, H. Höbenreich, D. J. Schiffrin and R. J. Nichols, *J. Am. Chem. Soc.*, 2003, **125**, 15294–15295.

80 W. Haiss, H. van Zalinge, H. Höbenreich, D. Bethell, D. J. Schiffrin, S. J. Higgins and R. J. Nichols, *Langmuir*, 2004, **20**, 7694–7702.

81 G. Sedghi, V. M. García-Suárez, L. J. Esdaile, H. L. Anderson, C. J. Lambert, S. Martín, D. Bethell, S. J. Higgins, M. Elliott, N. Bennett, J. E. Macdonald and R. J. Nichols, *Nat. Nanotechnol.*, 2011, **6**, 517–523.

82 G. Sedghi, L. J. Esdaile, H. L. Anderson, S. Martin, D. Bethell, S. J. Higgins and R. J. Nichols, *Adv. Mater.*, 2012, **24**, 653–657.

83 N. Algethami, H. Sadeghi, S. Sangtarash and C. J. Lambert, *Nano Lett.*, 2018, **18**, 4482–4486.

84 E. Leary, G. Kastlunger, B. Limburg, L. Rincón-García, J. Hurtado-Gallego, M. T. González, G. R. Bollinger, N. Agrait, S. J. Higgins, H. L. Anderson, R. Stadler and R. J.

Nichols, *Nanoscale Horiz.*, 2021, **6**, 49–58.

85 J.-R. Deng, M. T. González, H. Zhu, H. L. Anderson and E. Leary, *J. Am. Chem. Soc.*, 2024, **146**, 3651–3659.

2

Porphyrin-Paraquat Conjugate for Molecular Memory Devices

Contents

2.1 Introduction 32

2.1.1 Molecular Switches for Memory Devices 32

2.1.2 Porphyrin and Paraquat Unit 35

2.1.3 Project Aim 36

2.2 Molecular Design and Synthetic Approaches 38

2.2.1 Choice of Anchoring Group 38

2.2.2 Synthesis of Porphyrin-Paraquat Conjugate **P-Q1** and Control Molecules 39

2.2.2.1 Synthesis of a Porphyrin-Based Molecular Backbone 40

2.2.2.2 Fabrication of Paraquat Arm with SMe-Terminal 41

2.2.2.3 Purification of **P-Q1** 44

2.3 Single-Molecule Conductance of **P-Q1** and Control Molecules 47

2.3.1 STM-BJ Experiment 47

2.3.2 STM-BJ Measurement on **P-Q1** and Control Molecules 48

2.4 Conclusions 52

2.5 References 53

2.6 Experimental 56

Chapter 2 - Porphyrin-Paraquat Conjugate for Molecular Memory Devices

2.1 Introduction

2.1.1 Molecular Switches for Memory Devices

In Chapter 1, we discussed how the fundamental conducting behavior of single-molecule junctions can be altered with molecular structures. Strategic design for bridging molecules can be used to address more specific applications. Electrical switching, a fundamental feature required by memory storage technologies, is one of the many functionalities that could offer by single-molecule devices, promising both cost-efficiency and high data density. In terms of performance, an ideal molecular switch is required to change its conductance between at least two stable states (termed on/off states) with a high contrast (high on/off ratio, typically in the order of 10^2–10^3).[1] More specifically for memory applications, the molecule should be able to perform the write, erase (*i.e.*, can access and transition in between any of the conductance states) and read (*i.e.,* reasonably persistent in each state during the conductance measurement, known as hysteresis) processes.[2] Additional practical factors, such as the reproducibility, endurance (*i.e.*, the number of on/off cycles the device can perform), scalability of the device, data retention time (*i.e.*, the stability of each conductance state), the refresh rate (*i.e.*, switching speed between states) and power consumption (*i.e.*, required energy to switch), should all be taken into account for a molecular memory device design before they can become commercialized.[3–6] With regard to a single molecule, the primary challenge lies in finely balancing the stability and switchability of each molecular state, such that there is neither quick, spontaneous thermal relaxation between on and off states nor excessive stability of a state that would otherwise lead to slow switching speeds.[7]

The switchability of a molecule usually originates from two intrinsic mechanisms: transitioning between structural isomers (geometric switches) or altering between different charging states (redox switches).[8] In general, geometric switches require the existence of two structural isomers with distinct conducting pathways. Examples of geometric switching mechanisms, such as the well-known *cis–trans* (photo)isomerization in the family of azobenzene molecules and photoisomerization-controlled formation/breaking of chemical

bonds in the diarylethene-based molecules, are shown in Figure 2.1.[9–13] However, the changes in molecular length during geometric switching limits their implementation in molecular junctions, where the electrodes remain stationary with a fixed distance (controlled switching of diarylethene-based molecular junctions was demonstrated only recently).[13,14]

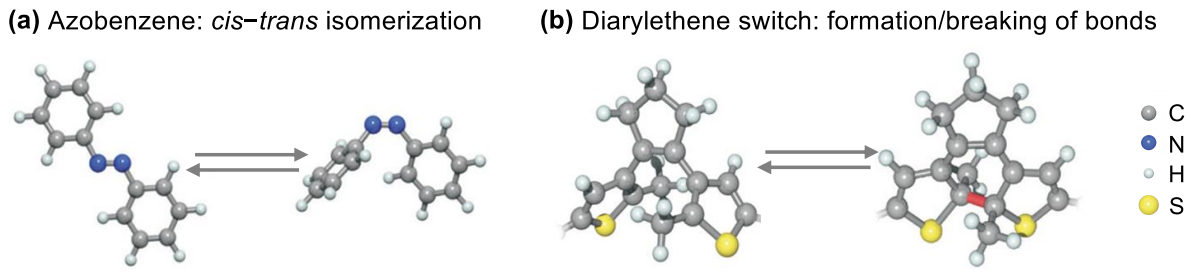


Figure 2.1: Examples of different geometric switching mechanisms: (a) *cis–trans* isomerization of azobenzene; and (b) photoisomerization of diarylethene molecules with differing conjugation. Reproduced with permission.[8]

The switching mechanism of redox switches relies on changes in conductivity as the molecular energy level shifts between different redox states. While not the focus of this thesis, many examples reported the molecular switches based on an active molecular layer using two-terminal devices, have demonstrated that this mechanism could offer robust resistive memory elements with large on/off ratios.[4,15–24] In a single-molecule conductance experiment, electrochemically gated charging is typically employed to study the redox-induced switching. A three-terminal set-up with a scanning tunneling microscope (STM) tip is utilized to control the redox states of the molecule while simultaneously recording the changes in molecular conductance (Figure 2.2).[25–28] On the other hand, the gated nature means only one state can be accessed under a certain gating potential, which requires the molecule to possess a long-lived charging state to show the needed hysteresis for memory devices.

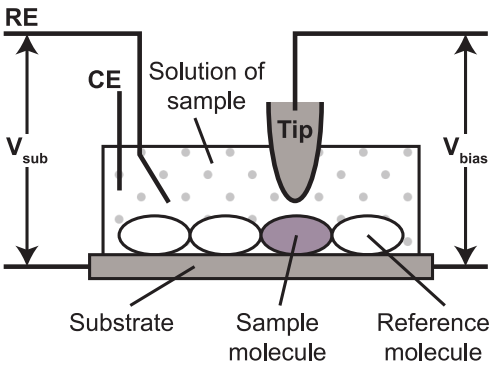


Figure 2.2: Schematic of a typical three-terminal electrochemically gated set-up for a single-molecule redox-induced switching experiment. RE and CE represent the reference and counter electrodes, respectively. V_{sub} and V_{bias} are the substrate potential (with respect to the reference electrode) and the tip-substrate bias voltage, respectively, which are controlled independently. Reproduced with permission.[25]

While both mechanisms have been widely employed to produce molecular switches from solution-phase chemistry, such switchability is hard to retain when the molecules are bound to electrodes in solid-phase junctions. Due to the change of local contact environment (*e.g.,* molecular orbital hybridization with electrodes), it is common to observe that they suffer from small on/off ratios (<10), low reproducibility and low stability.[29]

A special group of molecular switches is formed by mechanically interlocked molecules, such as catenanes and rotaxanes, which exploit the non-covalent interactions between molecular components in complexes to impose a profound effect on the molecular conductance.[31] In these structures, the ring component can reversibly move along the axle between two or multiple stations through non-covalent interactions (*e.g.*, hydrophobic interactions, hydrogen bonding or π-π interactions), giving rise to different translational isomers as the on/off individual states. The transition between states involves an electrically driven redox process (as [2]rotaxane $\mathbf{R}^{4+}$ exemplified in Figure 2.3) involving a number of steps:[30] 1) in the ground-state co-conformation (GSCC), the electron-deficient blue ring preferentially locates near the electron-richer green station (*i.e.*, tetrathiafulvalene); 2) by controlling the applied bias on the electrode to positively charge the green station, now the favored electronic interaction is between the blue ring and the red station (*i.e.*, 1,5-dioxynaphthalene), allowing the molecule to undergo an isomerization to the metastable state

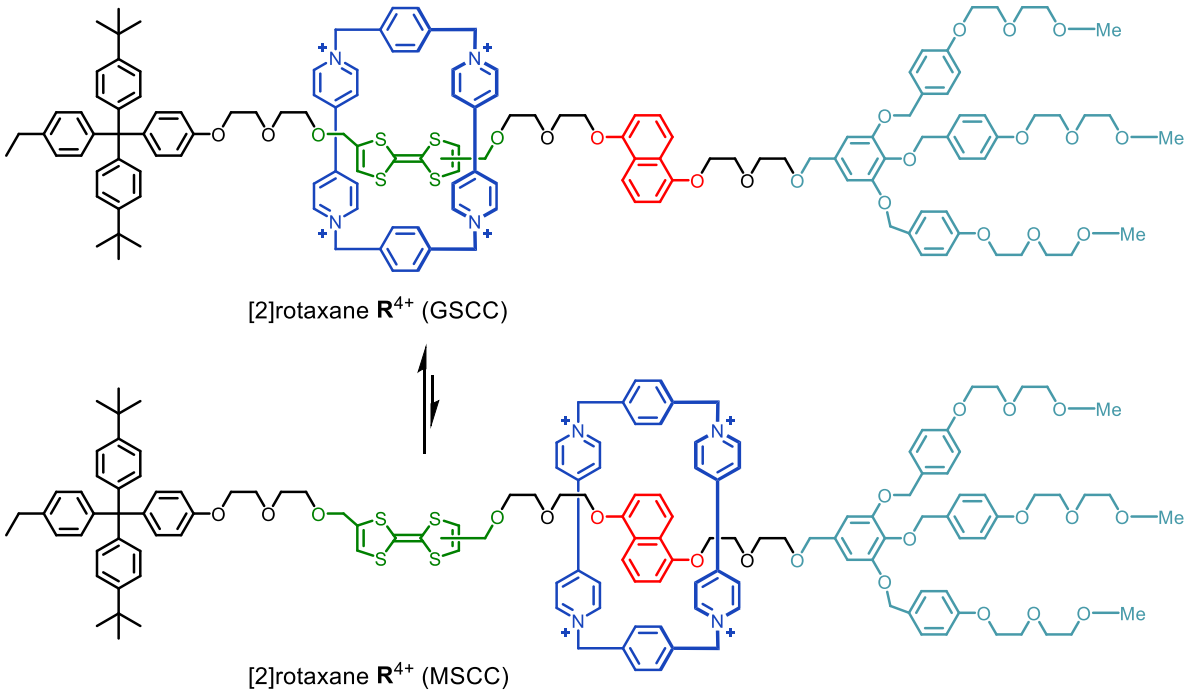


Figure 2.3: Example of mechanically interlocked molecule [2]rotaxane $\mathbf{R}^{4+}$ with its two translational isomers as a redox and geometric switch.[30]

co-conformation (MSCC); 3) after removing the applied bias, the weak π-π interaction between blue ring and red station impedes the instant relaxation to GSCC state and thus gives desired hysteresis. Therefore, these switchable rotaxanes and catenanes can be considered as both redox and geometric switches. Significant attention has been devoted to studying the conductance behavior of molecules in this group, either through single-molecule junctions or fabricated as monolayers in molecular switch tunnel junctions.[31,32] The tunable lifetime for individual states, high on/off ratio and good reproducibility presented by these mechanically interlocked molecules highlight the advantage of utilizing non-covalent interactions in engineering the molecular switches, especially memory elements.

2.1.2 Porphyrin and Paraquat Unit

For decades, both porphyrins and paraquat units have been investigated as the redox active elements for constructing molecular switches, especially in electrochemically gated experiments.[25,26] In the following section, their individual characteristics will be briefly discussed. In the solid-state device, the self-assembled monolayers of porphyrin monomers typically feature two cationic states at low potentials (< 1 V vs. Ag/Ag^+), capable of storing charge for extended periods (up to minutes) in the absence of an applied voltage and repeating for over 10^{10} cycles.[33] Introducing another redox-active moiety onto porphyrins (*e.g.,* ferrocene, another porphyrin unit or ligands through metal coordination) enables access to additional redox states for multibit storage applications.[34–36] The paraquat unit possesses three oxidation states: the dicationic ground state $\mathbf{Q}^{2+}$, the radical cation state $\mathbf{Q}^{\bullet+}$ (Figure 2.4) and the fully reduced neutral form $\mathbf{Q}^0$. Single-molecule study of paraquat using the STM-based $I(s)$ technique has proven the redox-state dependence of its conductance.[26] In an assembled solid-phase device fabricated with a pre-organized $\mathbf{Q}^{2+}$ single-layer as the active element, a high conductance state was detected, created by forming a stable dimer complex $[\mathbf{Q}^{\bullet+}]_2$ through π-π stacking and pairing of electron spins of each $\mathbf{Q}^{\bullet+}$. Compared to the less conductive ground state $\mathbf{Q}^{2+}$, the pairing of spins together with the migration of counterions of paraquat in the solid-state tunnel junctions led to a high on/off ratio (6.7×10^3) with low drive voltage (< 1 V).[7]

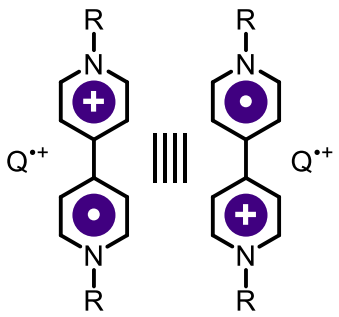


Figure 2.4: The radical cation state $\mathbf{Q}^{\bullet+}$ of paraquat.

In addition, the electron-deficient paraquat moiety has been widely incorporated in constructing mechanically interlocked molecular switches (as mentioned in Figure 2.3), harnessing non-covalent interactions with suitable electron-rich counterparts to induce molecular motion. Such non-covalent forces have also been demonstrated with porphyrins. By using a strapped porphyrin-based macrocycle as the electron donor, the porphyrin site effectively accommodates the paraquat dication guests via π-π stacking and attractive van der Waals interactions (Figure 2.5).[37,38] It is reasonable to anticipate that if a geometric isomer that brings the paraquat unit out of contact with the porphyrin can be created, a new design of molecular switch with two distinct energy states may become available.

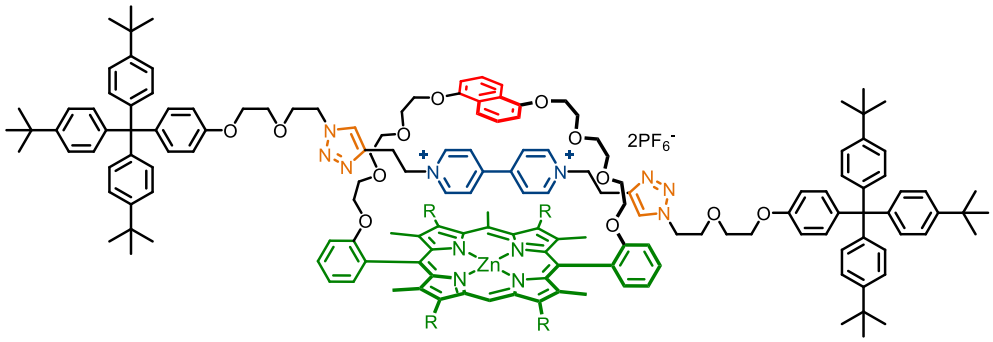


Figure 2.5: Example structure of porphyrin-paraquat rotaxane synthesized through the effective host of porphyrin to the paraquat dication.[38]

2.1.3 Project Aim

In this chapter, we propose an innovative molecular design towards molecular memory devices, consisting of a porphyrin-based conjugated backbone (Figure 2.6, highlighted in green) and a covalently linked paraquat-based 'arm' (highlighted in orange). The geometric switching mechanism for this memory device is designed to be electrically driven. Theoretically, without applying any voltage, the paraquat dication would preferentially be located near the porphyrin site (ground state) due to their attractive electronic interactions. The charged nature of paraquat gives it a high sensitivity to the direction of the applied electric field, which can either align with or oppose the direction of paraquat in the ground state. In the latter case, when the applied voltage reaches a threshold that can overcome the interaction between two attractive molecular counterparts, a geometric change in the paraquat unit would occur due to the electronic attraction from the electrode. The extent of movement that can be reached by the paraquat unit is restricted by the length of the alkyl chain linking it to the molecular backbone, therefore this process should be reversible between cycles. We expect that the different relative positions of

the porphyrin and the paraquat units will result in a change in molecular conductance. Considering the abundance of redox states in porphyrin and paraquat, it is also rational to predict the possibility of observing multi-state behavior. Moreover, a thiomethyl terminal group (SMe, highlighted in blue) is positioned at the terminus of the paraquat 'arm' to create a weak, reversible connection to gold electrodes. This aims to prevent an instant relaxation of the paraquat unit after the removal of the applied voltage, thereby inducing hysteresis to each state.

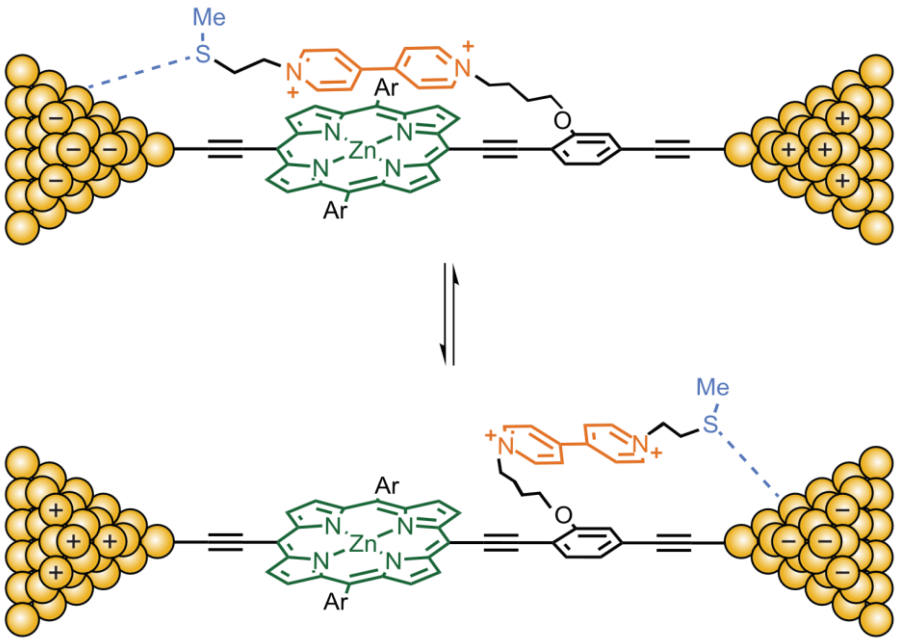


Figure 2.6: Demonstration of the geometric switching of designed porphyrin-paraquat conjugate in the single-molecule junction under opposite electric fields.

In this work, we plan to explore the synthesis of such a porphyrin-paraquat conjugate consisting of the aforementioned three main components, and then evaluate its conductance behavior as a memory element using the STM break-junction (STM-BJ) technique. Wiring the molecule into circuits to make a device typically involves the formation of molecule-electrode contact. This requires an optimal choice of anchoring group to bind two termini of individual molecules to the electrodes (discussed in the next section). To better comprehend the impact arising from the paraquat and the SMe subunits on the overall conductance, two control molecules are also designed for STM-BJ studies.

2.2 Molecular Design and Synthetic Approaches

2.2.1 Choice of Anchoring Group

Anchoring groups are placed at the termini of molecular bridge to bind the molecule to the electrodes. In a single-molecule junction, the chemistry of the anchoring groups (*e.g.,* binding strength with electrodes, local orientational geometry etc.) has a strong impact on the efficiency of electron transport.[39] While the molecule behaves as the functional unit for electronic tasks, the effect of anchoring groups is primarily reflected by the magnitude of the measured conductance *G* and its reproducibility. A robust and effective molecule-electrode contact would give a high signal-to-noise ratio (*i.e.*, high conductance) with low fluctuation in conductance from junction to junction (*i.e.*, uniform binding geometry), thus reflecting the intrinsic molecular conducting behavior.

Here the discussion is mainly restricted to using gold as the electrode material. The contact between the anchoring group and the electrode can be classified as non-covalent or covalent connections. Anchoring groups based on such as pyridines, amines, thioethers and nitriles form weaker non-covalent contacts with gold electrodes by means of donor-acceptor coordination.[40–43] A covalent linkage to the gold electrode generally creates a more effective pathway for electrons to travel through (stronger molecule-electrode electronic coupling) and thus normally give a higher measured conductance. Gold–sulfur covalent linkages (Au–S contact) are readily formed from thiols, and are one of the most frequently used chemical anchoring groups in break-junction experiments.[44] In comparison, a direct covalent linkage between gold and carbon (Au–C contact), formed from such as diazonium salts, organotin, or trimethylsilyl (TMS) anchoring groups, has been reported to be capable of achieving a higher measured conductance compared to a Au–S contact for the same molecular bridges.[45–48] Our recent work on porphyrin-based single-molecule junctions have demonstrated that TMS-protected acetylenes could effectively form direct Au–C linkages to electrodes without requiring any external activation (*i.e.*, cleave TMS groups with tetrabutylammonium fluoride), giving a highly conductive single-molecule junction (~10^{-2} G_0).[49] Therefore, considering the synthetic accessibility and chemical stability, TMS-protected acetylenes were chosen as the anchoring group for the synthesis of porphyrin-paraquat conjugate in this work.

2.2.2 Synthesis of Porphyrin-Paraquat Conjugate P-Q1 and Control Molecules

To integrate all of the aforementioned concepts into one molecule, porphyrin-paraquat conjugate **P-Q1** was designed as the target structure for this single-molecule conductance study, together with its control molecules **P-Q2** and **P-1** (Figure 2.7). All three molecules possess the same conjugated Zn(II) 5,15-bis(3,5-bis(*tert*-butyl)phenyl)porphyrin-based molecular backbone. **P-Q2**, with the absence of the SMe group, and **P-1**, with the absence of both the paraquat and the SMe units, could provide insights into the functionality of each component, verifying whether they function as expected under an applied bias. Based on the DFT optimized geometry of **P-Q2** (Figure 2.8), a chain comprising of four carbon atoms should provide enough

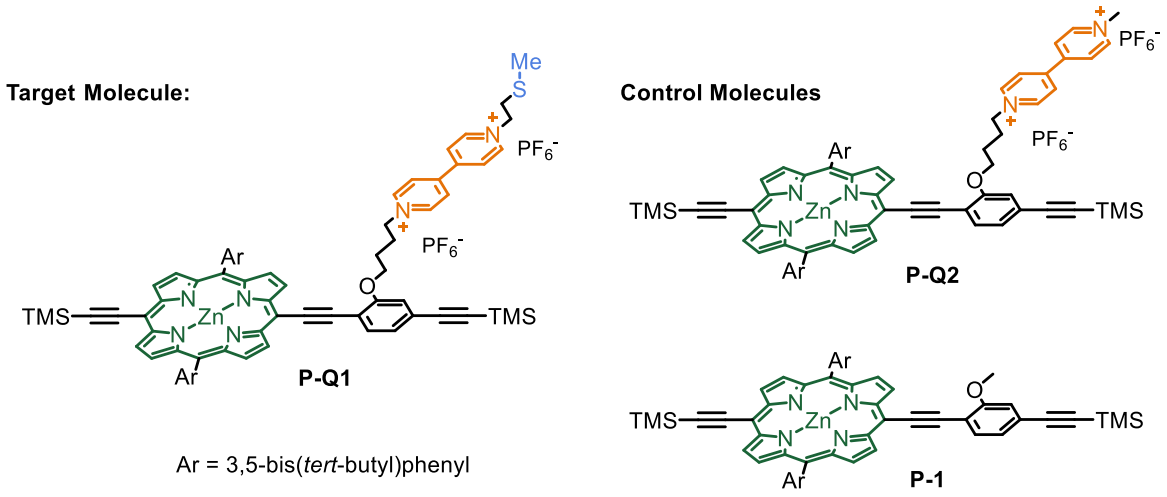


Figure 2.7: Structures of memory molecule **P-Q1** and two control molecules **P-Q2** and **P-1** for the single-molecule conductance study.

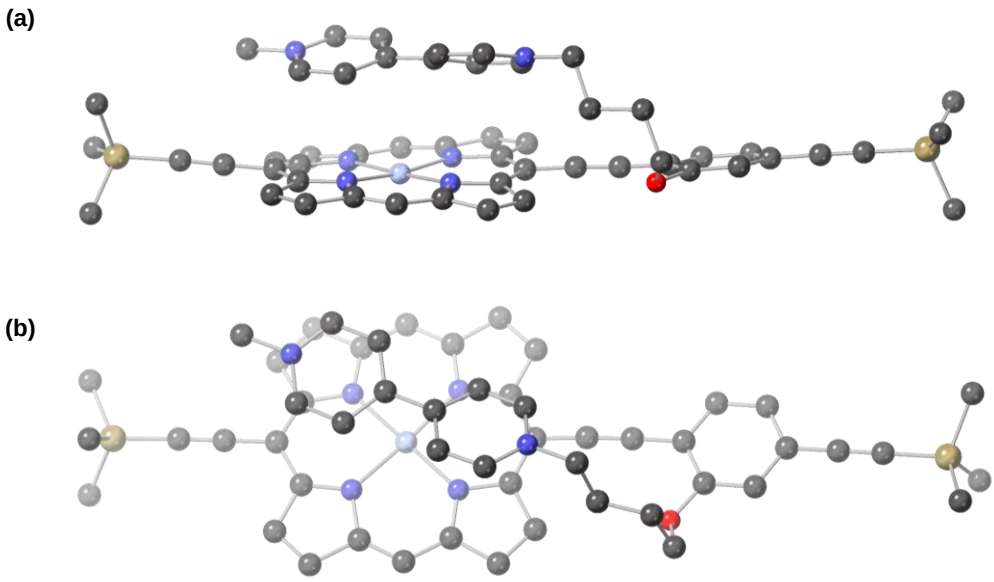
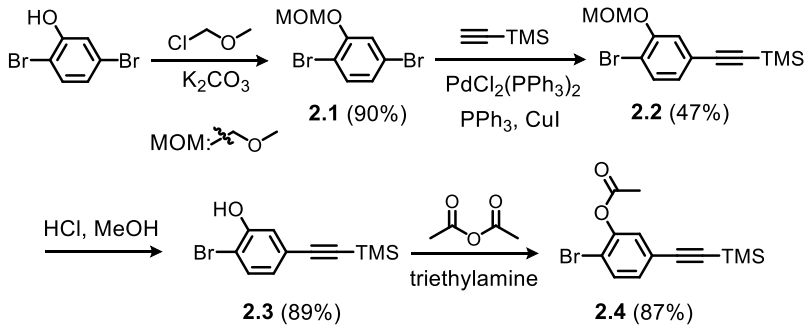


Figure 2.8: (a) Side view and (b) top view of optimized structure of porphyrin-paraquat conjugate **P-Q2**. Optimization made at the B3LYP/6-31G(d) level of theory. The side aryl groups of porphyrin and protons were omitted for clarity.

distance for the paraquat arm to reach and stack with the porphyrin in the ground state. As such, a $(CH_2)_4$ chain was chosen here to link the paraquat unit and the backbone together.

2.2.2.1 Synthesis of a Porphyrin-Based Molecular Backbone

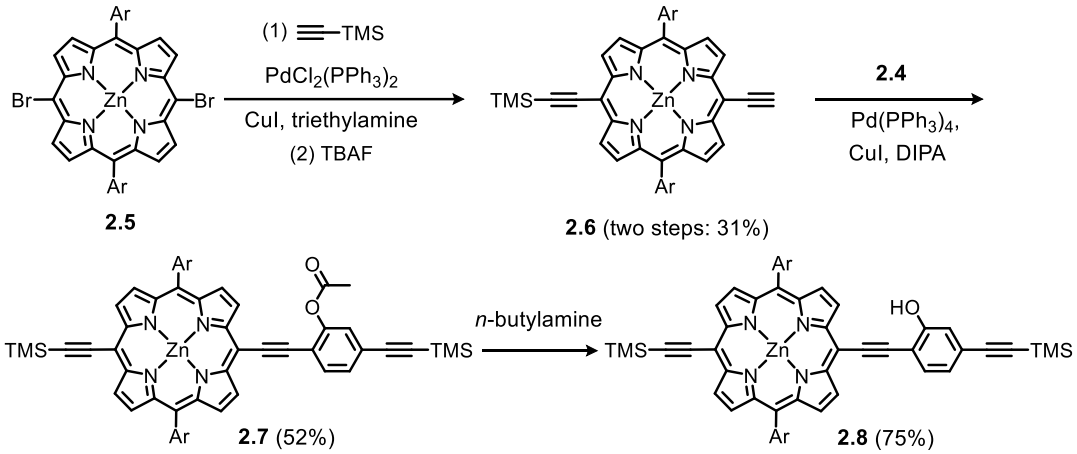
The synthetic route was designed so that during the synthesis of **P-Q1**, both control molecules can be readily prepared from its intermediates. To simplify the synthesis, an asymmetric phenol side chain (**2.3**) bearing a bromide and a TMS-acetylene group was first prepared (Scheme 2.1). A porphyrin moiety can easily be incorporated at a later stage with **2.3** via a Sonogashira coupling through the bromide handle. Synthesis of **2.3** started from 2,5-dibromophenol. The methoxymethyl (MOM) group was chosen because it can be cleaved under orthogonal (acidic) conditions to TMS, making it an ideal candidate to protect the phenolic hydroxyl group and preserve the TMS group. An S_N2 substitution on 2,5-dibromophenol with MOM-chloride afforded the MOM-protected dibromophenol **2.1** in 90% yield. The electron donation from MOM-group leaves the *meta*-bromide as the more reactive site for Sonogashira coupling, which yielded **2.2** as the only TMS-acetylene mono-coupled product in 47% yield, with the remainder being unreacted starting material or di-coupled species. The MOM group in **2.2** was then removed with high efficiency when treated with hydrochloric acid, to yield **2.3**, leaving TMS group unaffected.



Scheme 2.1: Synthesis of acetate protected asymmetric phenol-based side chain **2.4**.

Meanwhile, mono-TMS terminated porphyrin **2.6** was prepared following a reported procedure, and obtained in an overall 31% yield after two steps (Scheme 2.2).[50] The target molecular backbone **2.8** could be prepared through a Sonogashira coupling between **2.2** or **2.3** with porphyrin **2.6**. However, trial reactions with neither **2.2** (possibly due to the increased steric hindrance or the deactivation by MOM group) nor **2.3** (where the phenol was deprotonated under the coupling conditions) provided the desired product. Therefore, an

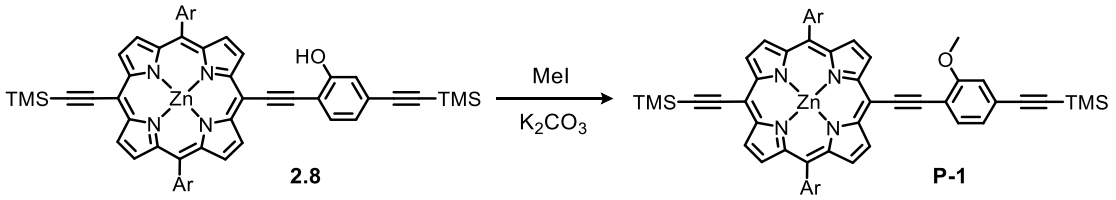
additional acetate protection of phenolic group was performed, giving **2.4** in 87% yield (Scheme 2.1). Sonogashira coupling between **2.4** and **2.6** successfully afforded the TMS-acetylene terminated molecular backbone **2.7** in 52% yield. By treating **2.7** with dilute *n*-butylamine solution in THF (5%, v/v) at room temperature, the acetate group was removed to give phenol-porphyrin **2.8** in 75% yield. While the TMS-group retained its stability in these mildly basic conditions, the MOM-protecting step is still considered necessary to preserve the selectivity in the Sonogashira coupling towards the formation of **2.2**.



Scheme 2.2: Synthesis of TMS-acetylene terminated porphyrin molecular backbone **2.8**.

2.2.2.2 Fabrication of Paraquat Arm with SMe-Terminal

With phenol-porphyrin **2.8** in hand, the control molecule **P-1** was formed quantitatively through a nucleophilic substitution on hydroxyl group with iodomethane in the presence of potassium carbonate in dry DMF, so as to avoid the deprotection of TMS groups (Scheme 2.3).



Scheme 2.3: Synthesis of control molecule **P-1**.

Investigations were then made into fabricating the covalently linked paraquat 'arm'. The main obstacle encountered here was to determine the correct order of connecting the paraquat and SMe groups onto the porphyrin backbone. As shown in Figure 2.9, three different points can be used to link these three components together, and thus three synthetic routes were considered: 1) stepwise substitution on hydroxyl group on the phenol at Point 3 and on 4,4'-bipyridine at Points 1 and 2 (Scheme 2.4, *Route 1*); 2) nucleophilic attack at Point 2 using SMe-

substituted bipyridine (Scheme 2.5, *Route 2*); and 3) substitution on hydroxyl group of **2.8** at Point 3 using the whole paraquat-SMe 'arm' (Scheme 2.6, *Route 3*).

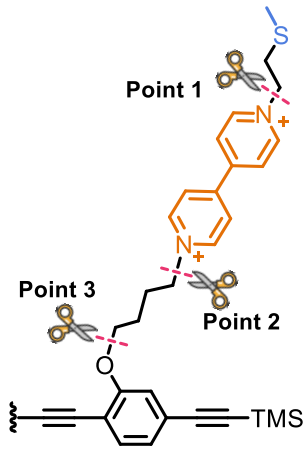
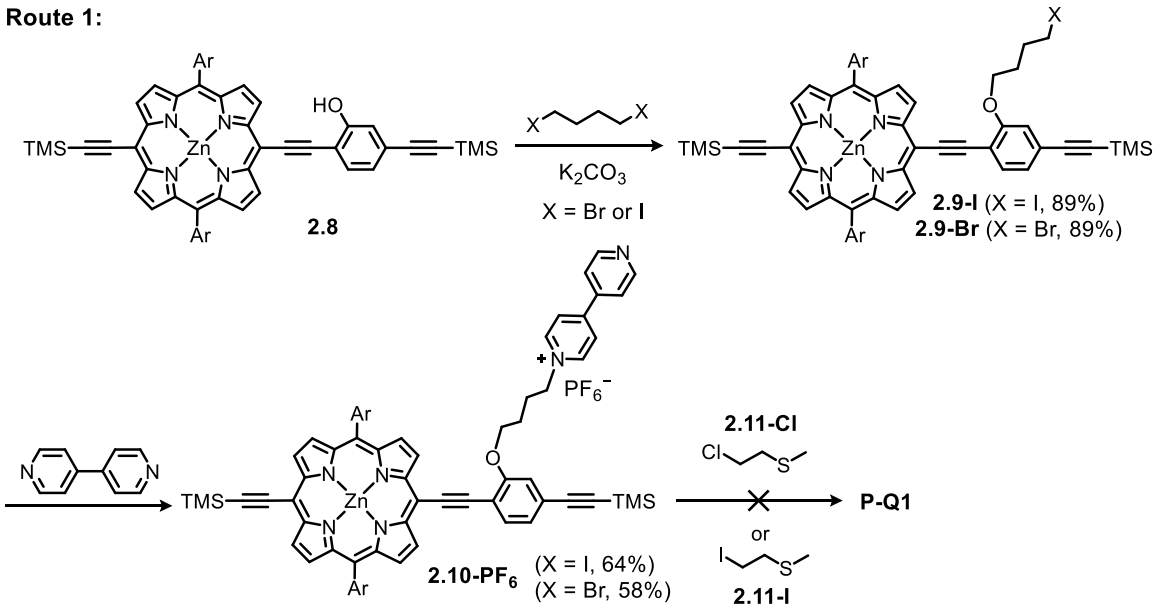


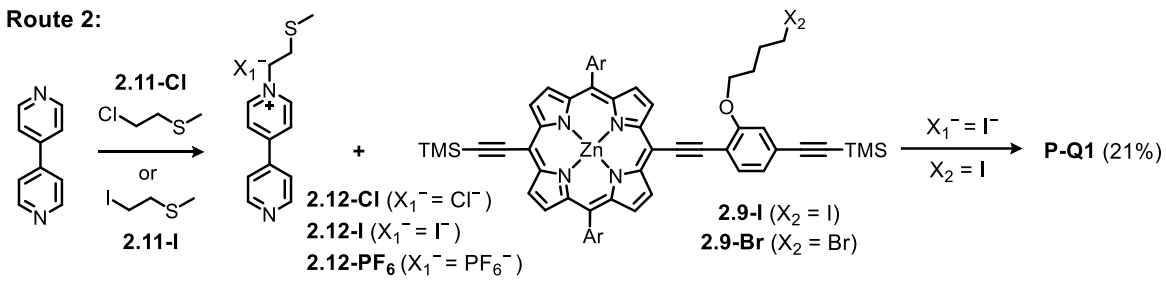
Figure 2.9: Demonstration of three linking points can be utilized to construct the paraquat 'arm'.

Route 1: By treating **2.8** with a corresponding 1,4-dihalobutane, both **2.9-I** and **2.9-Br** (Scheme 2.4) were obtained quantitatively. Terminal halide in **2.9** was subsequently substituted by 4,4'-bipyridine to form bipyridinium-porphyrin **2.10** with its respective halide counterion. However, the purification of **2.10** was only achieved after exchanging the counterion to hexafluorophosphate (PF_6^-). **P-Q2** was successfully prepared by treating **2.10-PF$_6$** with a large excess of iodomethane. The addition of the terminal SMe group on **P-Q1** was attempted using the commercially available (2-chloroethyl)(methyl)sulfane **2.11-Cl**, or the equivalent iodo compound **2.11-I** (which is readily prepared through a halide exchange from **2.11-Cl** with sodium iodide). However, after multiple attempts using either **2.11-Cl** or **2.11-I**, there was no evidence that the target **P-Q1** was formed by this route. Only the decomposition of **2.10-PF$_6$** was observed.



Scheme 2.4: *Route 1* – unsuccessful synthesis towards **P-Q1**.

Route 2: A test reaction between **2.11-Cl** and 4,4'-bipyridine successfully yielded the 1-(2-(methylthio)ethyl)-4,4'-bipyridinium chloride salt **2.12-Cl** (Scheme 2.5). Therefore, we



Scheme 2.5: *Route 2* – successful synthesis of **P-Q1**.

instead chose to explore an alternative route, that constructs the paraquat 'arm' by a one-step substitution at Point 2 (Figure 2.9). It was found that the counterion in **2.12** salt (X_1^-) and the halide group on the butyl chain (X_2) both significantly affect the reaction outcomes (conditions summarized in Table 2.1). When X_1^- = Cl^-, no **P-Q1** was formed, regardless of whether X_2 = Br or I, or through changing reaction solvents, or elevating the reaction temperature (entries **1**–**3**). Instead, it was observed that the large excess of free chloride ions presents in the mixture led to a halide exchange with X_2. This in turn caused X_2 to become a worse leaving group and thus reduced its reactivity. This ultimately impeded the formation of **P-Q1**. In this case, it was considered necessary to replace X_1^- with other unreactive counterions (*e.g.*, iodide or PF_6^-).

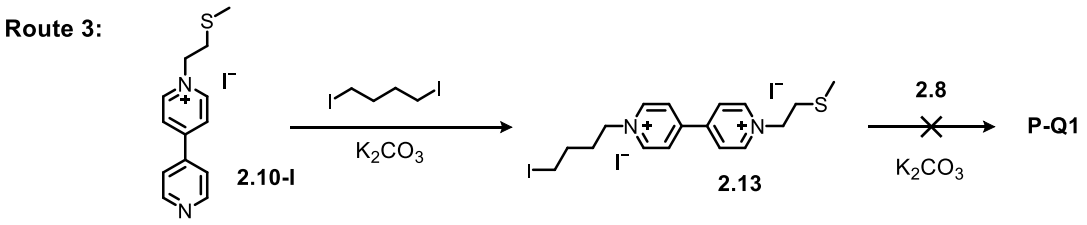
Table 2.1: List of nucleophilic substitution conditions on halobutyl in **2.9** with **2.12** (step 2 in Scheme 2.5) and their respective outcomes.

Entry	X_1^-	X_2	Solvents	Temperature	Results
1	Cl^-	Br	toluene/ acetonitrile	80 °C	Halide exchange
2	Cl^-	I	toluene/ acetonitrile	80 °C	Halide exchange
3	Cl^-	I	toluene/ DMSO	150 °C	Halide exchange
4	PF_6^-	I	toluene/ acetonitrile	80 °C	TMS-deprotection
5	I^-	I	toluene/ acetonitrile	80 °C	**P-Q1** in 21%

Treating **2.12-Cl** with a saturated KPF_6 aqueous solution cleanly prepared **2.12-PF_6**, which precipitated from the reaction mixture. However, employing PF_6^- as the counterion appears to negatively affect the stability of the TMS group. It was observed that the TMS group would deprotect at temperatures above 60 °C, presumably due to the presence of free fluoride ions from decomposed PF_6^- (Table 2.1, entry **4**).[51] **2.12-I** was successfully synthesized in 86%

yield from **2.11-I** and 4,4'-bipyridine. By ensuring that both X_1^- and X_2 = I, this excluded any competing ion exchange reaction that would prevent the formation of **P-Q1**. Fortunately, by reacting a mixture of **2.9-I** and **2.12-I** in a toluene/acetonitrile mixture at 80 °C for 4 days, **P-Q1** was successfully formed in 21% yield (entry **5**). The identity of **P-Q1** was confirmed by MALDI-TOF MS analysis.

Route 3: A direct one-step nucleophilic substitution of phenol-porphyrin **2.8** at Point 3 (Figure 2.9) was also investigated. The bipyridinium dication **2.13** was only formed when using the more electrophilic diiodobutane due to its charged nature giving it reduced nucleophilicity (Scheme 2.6). Unfortunately, this salt suffered from low stability. This, coupled with the fact that there are multiple reactive positions in **2.13**, led to the formation of a complex mixture with unidentified products, which ultimately rendered this route unsuccessful.



Scheme 2.6: *Route 3* – unsuccessful synthesis towards **P-Q1**.

2.2.2.3 Purification of P-Q1

Route 2 was found to be as a viable approach to access **P-Q1**, yet its isolation from residual charged species **2.12** remained problematic. The crude **P-Q1**, with iodide as the counterion, exhibited high polarity, making it challenging to purify by silica chromatography, despite using a high polarity eluent (dichloromethane/methanol, 4:1). It was also found that **P-Q1** appeared to decompose when loaded onto a size-exclusion column. One approach is to exchange iodide with the bulkier PF_6^- counterion, which would make **P-Q1** less polar and help its affinity for an organic environment. Such an ion exchange was achieved by washing the product with an excess of KPF_6 solution through a silica gel column. To aid the efficiency of the purification, the crude mixture was first washed with toluene to precipitate the majority of the **2.12** salt. A slow, long silica column using 1% KPF_6 solutions was conducted afterwards. The column started using a KPF_6 solution (in dichloromethane with 5–10% acetone), and the salt **2.12** was first eluted while **P-Q1** remained at the top of the column. Increasing the solvent polarity of KPF_6

solution to a mixture of methanol/acetone/dichloromethane (5:20:75) eluted clean **P-Q1**. However, **P-Q1** was found to be unstable when exposed to an overly concentrated KPF_6 solution. Therefore, heated rotary evaporation of the eluent was avoided and instead the solvent was removed by blowing the sample with a moderate flow of nitrogen. Once the majority of solvent had been removed, any residual solvent was then removed by placing the sample under vacuum for 10 min. The sample was then redissolved in dichloromethane, filtered (to remove the remaining KPF_6 salts from the product) and then dried again. Following this procedure, only a minor amount of decomposed **P-Q1** was observed. The purity of the sample was confirmed by ^{1}H NMR spectroscopy recorded in acetone-d_6 (Figure 2.10 and Figure 2.11).

The number of peaks and their integrals in the ^{1}H NMR spectrum of **P-Q1** are in good agreement with its structure. Four different 2H doublets between 7.2–9.2 ppm are observed and correspond to protons in the paraquat unit (highlighted by blue dots in Figure 2.10). These resonances are more shielded compared to those in **2.13** (highlighted by yellow dots), which indicates the effective interaction between the porphyrin and the paraquat units. Peaks at 2.79, 2.76, 2.21, 2.05 and 1.90 ppm correspond to resonances from NMR solvent (highlighted in grey in Figure 2.11).[52] The singlet peak at 2.12 ppm (highlighted in green in Figure 2.11) corresponds to the protons of the terminal SMe group.

However, it was noted that there were two small doublets resonating at 9.8 and 9.6 ppm (highlighted by pink dots, Figure 2.12a), which correspond to impurities present in the sample

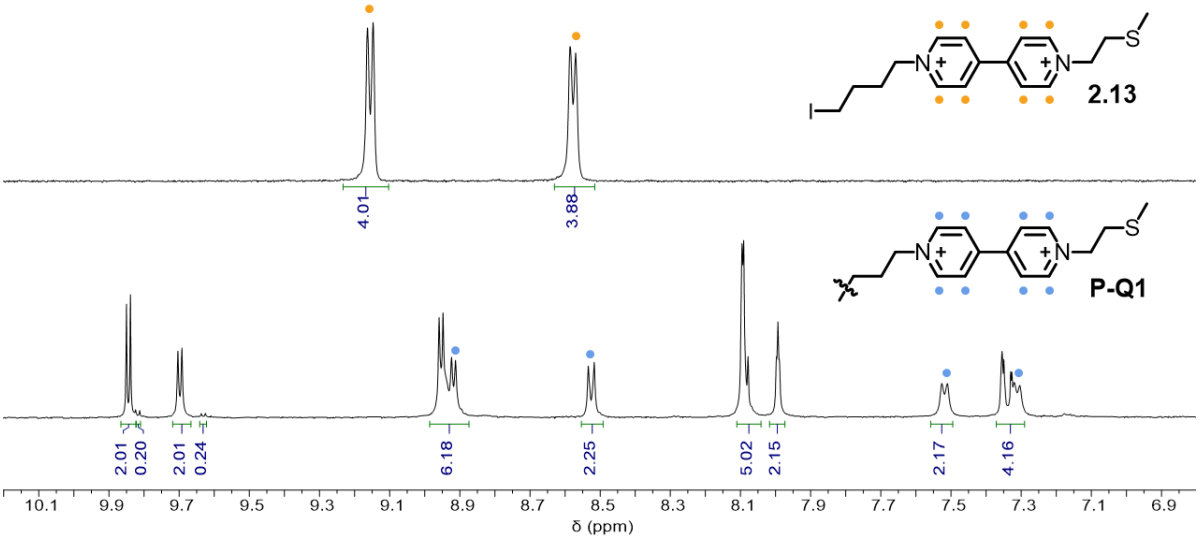


Figure 2.10: Partial ^{1}H NMR (400 MHz) spectra of **2.13** (top) and **P-Q1** (bottom) in acetone-d_6 at 298 K. Blue dots highlight the peaks for four different proton environments in the paraquat unit in **P-Q1**, where the paraquat resonances are more shielded compared to those in **2.13** (highlighted by orange dots).

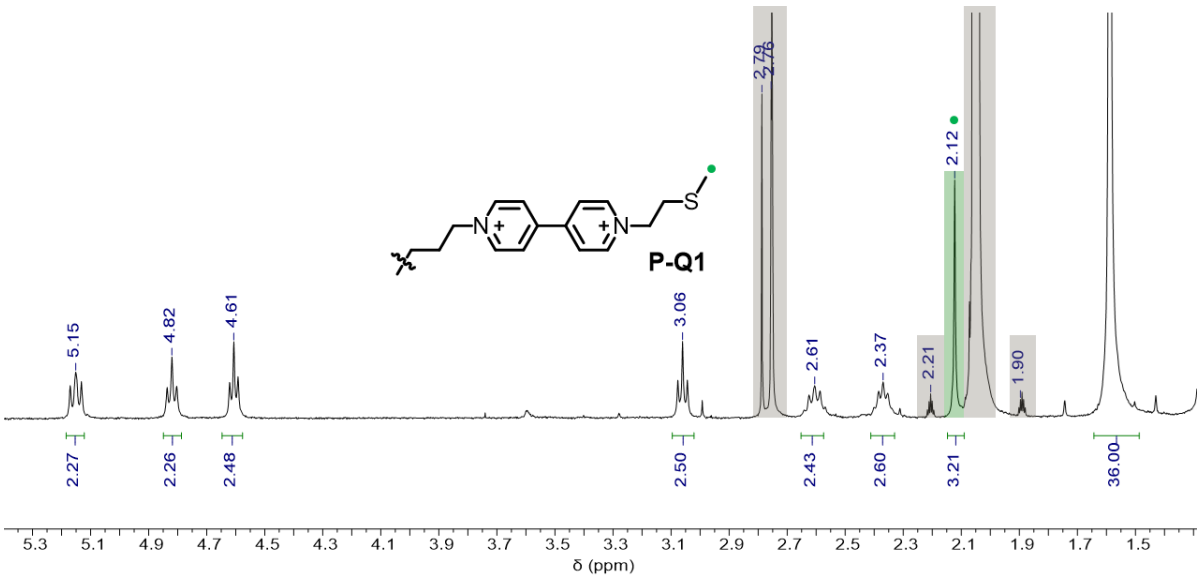


Figure 2.11: Partial ^{1}H NMR (400 MHz) spectrum of **P-Q1** (acetone-d_6, 298 K). Regions highlighted in grey are peaks from the acetone-d_6 solvent and the peak highlighted in green corresponds to the protons of the terminal SMe group.

(quantities estimated to be approximately 10% based on ^{1}H NMR). It was also observed that the integral of the TMS peak at 0.64 ppm (attached to porphyrin) was about 10% smaller than the TMS peak at 0.30 ppm (adjacent to the phenoxy group, both resonances for the two TMS groups are highlighted in pink in Figure 2.12b).

Combining this with the data from MALDI-TOF MS analysis, the impurity is suspected to be a TMS deprotected by-product, possibly caused by either bipyridinium salts during the substitution reaction or by the excess of KPF_6 salt during the purification. Due to the small quantity of the impurities, the proton peak corresponding to the free acetylene proton was not observed. Considering that in the single-molecule conductance studies, the TMS groups will be

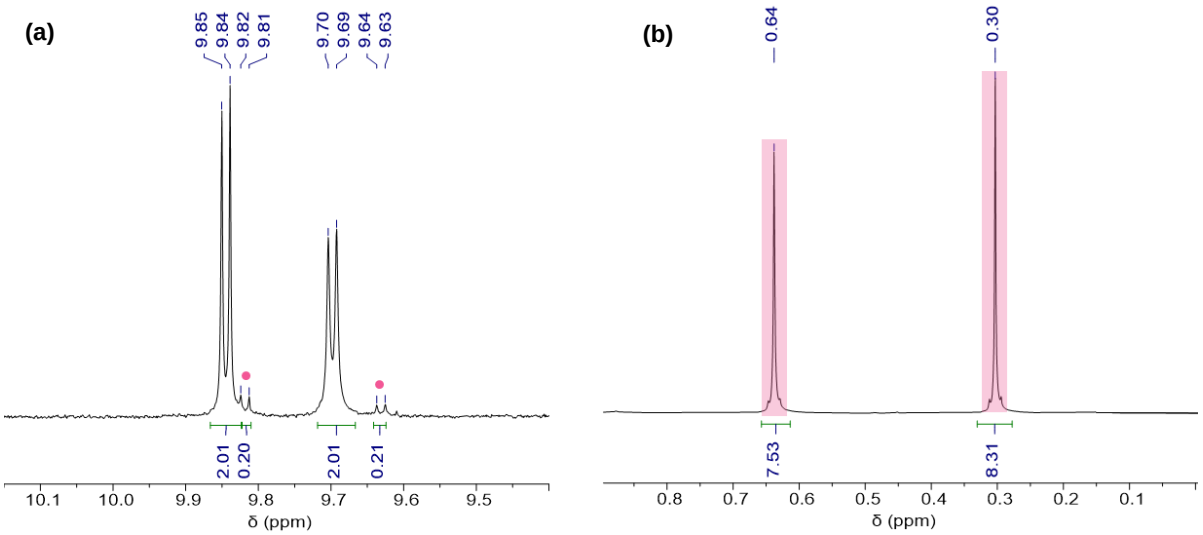


Figure 2.12: Partial ^{1}H NMR (400 MHz) spectra of **P-Q1** in (a) 9.5–10.1 ppm and (b) 0.1–0.8 ppm (acetone-d_6, 298 K). Pink dots highlight the presence of the small quantity of impurities in the **P-Q1** sample and regions highlighted in pink correspond to signals from both terminal TMS groups.

deprotected when attached to the gold surface, the sample was deemed sufficiently pure to commence the single-molecule conductance experiments.

2.3 Single-Molecule Conductance of P-Q1 and Control Molecules

2.3.1 STM-BJ Experiment

STM-BJ experiments were conducted based on the repeated formation and breaking of single-molecule junctions between a conductive STM tip and substrate. The inert nature of the gold substrates upon exposure to air makes it a suitable material as the molecule contacts in these experiments. Here we adopted a solvent-free STM-BJ set-up: molecules are deposited onto the gold substrate by dipping the substrate into a solution of the molecule under study, where the molecule is then adsorbed through anchoring group when the sample is dry.[53] A typical STM-BJ cycle includes the following four steps, as shown in Figure 2.13: (a) the tip approaching the substrate with adsorbed molecules, (b) contact of the tip with substrate to form metal–metal and metal–molecule contacts, (c) pulling, breaking the metal–metal contact and forming the single-molecule junction and (d) breaking the single-molecule junction.[54]

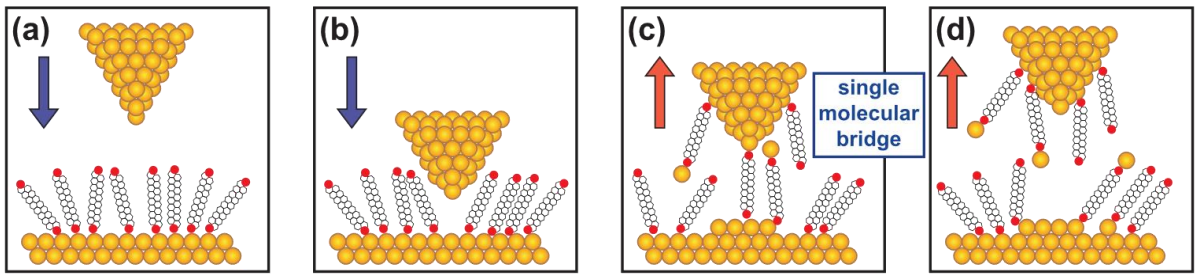


Figure 2.13: Schematic of a close-open cycle in STM-BJ experiments: (a) approaching, (b) formation of contacts, (c) pulling and formation of the single-molecule junction, and (d) breaking the single-molecule junction. Reprinted with permission from Li *et al.*, *J. Am. Chem. Soc.*, 2008, **130**, 318–326. Copyright 2008 American Chemical Society.[54]

Initially, the STM tip is fixed over the molecular sample. When the break-junction experiment starts, the tip is then moved vertically towards the substrate until a sufficient contact (*i.e.*, the measured conductance is higher than the conductance quantum G_0) between the tip and the surface (*i.e.*, metal–metal contact) is reached. Afterwards, the tip is withdrawn at a set speed and the measured conductance is plotted as a function of the distance travelled by the tip z to give the measured conductance traces. The conductance features G_0 when a single-atom contact between electrodes is made.[55] At this point, withdrawing the tip further ruptures the metal–metal contact and a nanogap in the region of 0.4–0.6 nm is suddenly generated. Such a

nanogap is able to trap a target molecule to form a single-molecule junction. If not, tunneling transport through the measurement medium (*i.e.*, air, in this example) direct from electrode to electrode takes place (tunneling-only trace). Upon withdrawing the tip further, when the junction ruptures the measured conductance sharply drops to the noise level of instrument. This whole process constitutes one close-open cycle.

When a molecule is present between the electrodes, the formation of single-molecule junction results in a plateau in the measured conductance trace upon further separation of electrodes (exemplified in Figure 2.14). The presence of such a plateau in the trace implies that the charge transport is through a relatively constant pathway provided by the molecule. In the molecular junctions, the plateau commonly contain sudden jumps either up or down due to the changes in the local geometry of the contact, such as stress, conformational change, or addition of other molecules to the junction.[39] Therefore, the above process is normally repeated many times, in order to build a statistical model from thousands of single-molecule junctions. Plotting the obtained traces into one (1D) and two-dimensional (2D) histograms of the conductance can better summarize the data and interpret general molecular conducting behavior.

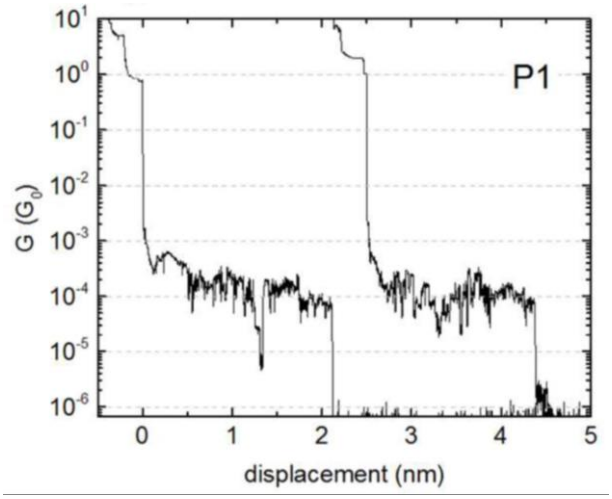


Figure 2.14: Examples of individual conductance traces with plateaus for a reported Zn(II) porphyrin monomer (P1) measured with bias of 0.2 V.[56] Reproduced from original publication.

2.3.2 STM-BJ Measurement on P-Q1 and Control Molecules

Due to time constraints, only the single-molecule conductance measurement of **P-Q1** under low-bias was performed using the STM-BJ method described above.[56] STM-BJ measurements for control molecules **P-1** and **P-Q2** are ongoing. In this experiment, **P-Q1** molecules were adsorbed by immersing a 1 × 1 cm^2 flame-annealed gold substrate in a dichloromethane

solution (2.0 mL) with 0.5 mg of **P-Q1** for 1 h. The substrate was then briefly dried under a mild flow of nitrogen. The relatively low concentration and controlled immersion time were chosen to target a low coverage on the gold substrate, which in turn favors single-molecule events. We performed thousands of close-open cycles on this sample and focused on the opening process (step (c) and (d) in Figure 2.13) of the measurement. After removing the tunneling-only traces through clustering analysis (which groups the traces based on the shape and conductance value), a total of 1571 traces containing plateaus were acquired, with an overall junction formation percentage of 9.3%.

As shown in the 1D and 2D histograms for **P-Q1** in Figure 2.15, the cluster of plateaus is classified into three different patterns: high conductance (log G/G_0 = −5.0 to −2.0) with short

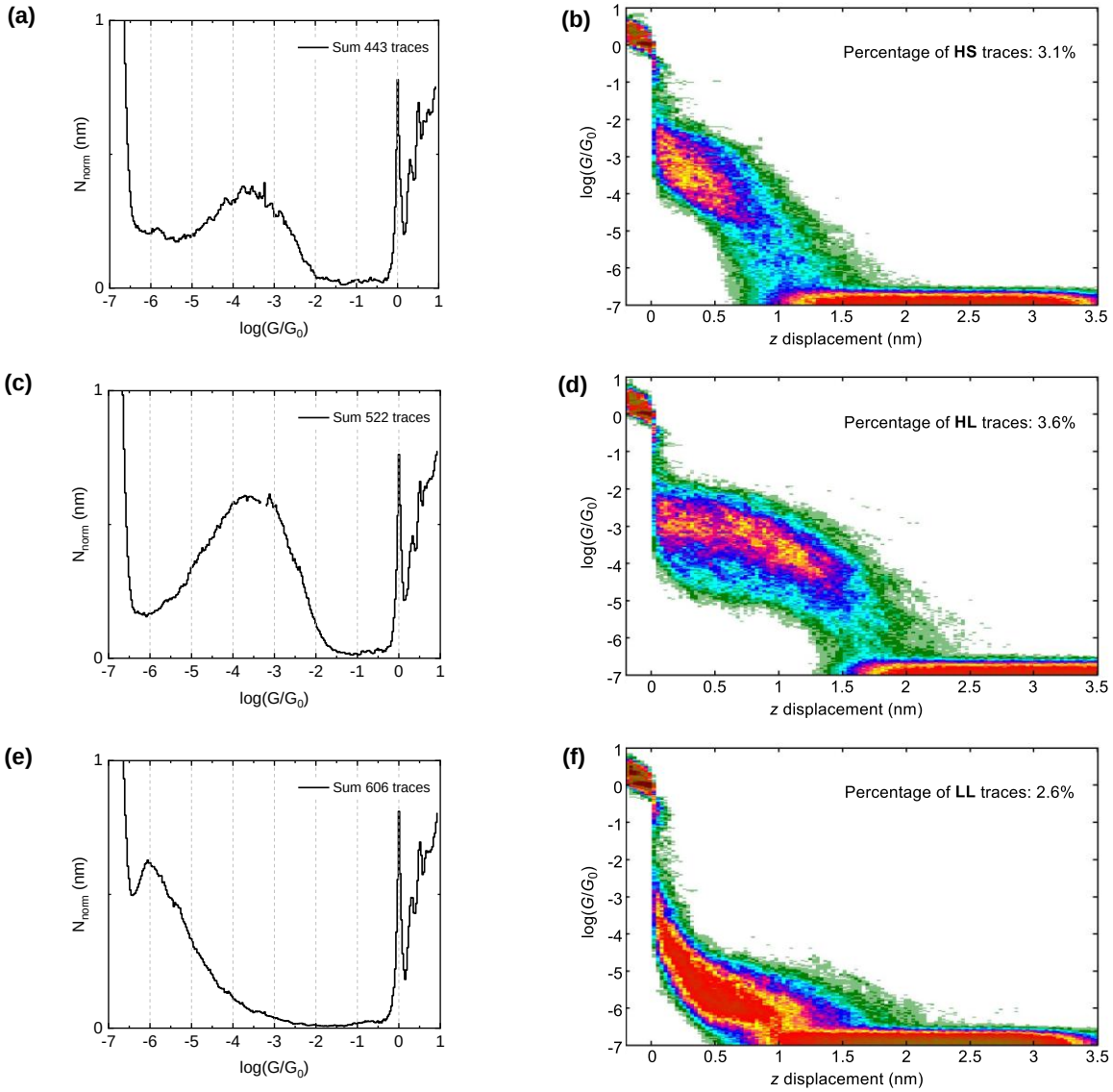


Figure 2.15: Three different patterns of 1D (a, c, e) and 2D (b, d, f) histograms for plateau-containing conductance traces for **P-Q1** (measured with a bias of 0.22 V, **HS**: high G, short z; **HL**: high G, long z; **LL**: low G, long z). Inserts depict the number of traces with plateaus and percentage of junction formation in each pattern.

plateau-lengths of 1.0–1.5 nm (**HS** state); high conductance (log G/G_0 = −5.0 to −2.0) with long plateau-lengths of 1.5–2.0 nm (**HL** state); and low conductance (log G/G_0 = −6.5 to −4.0) with long plateau-lengths of 1.5–2.0 nm (**LL** state). The corresponding example G–z traces can be seen in Figure 2.16 (**HS** state, black trace; **HL** state, red trace; **LL** state, blue trace).

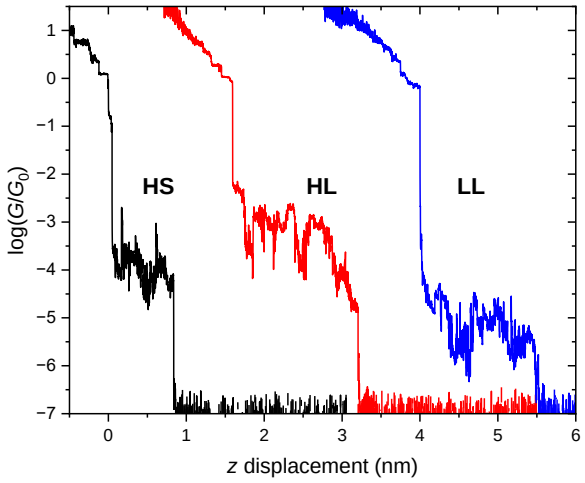


Figure 2.16: Example G–z traces for **P-Q1** with a bias of 0.22 V for three observed plateau patterns (**HS**: high G, short z; **HL**: high G, long z; **LL**: low G, long z).

After subtracting the jumping distance travelled by the gold electrodes when the molecular junction breaks (typically between 0.4–0.6 nm), the plateau-length shown in **HL** and **LL** states matched well with the estimated molecular length of the porphyrin-based backbone (1.8 nm). **HS** traces may result from the molecules that are not fully stretched in between two electrodes. As shown in the 1D histograms in Figure 2.15c and e, both **HL** and **LL** states cover a broad range (2.5 to 3 orders of magnitude) of conductance. The peak conductance of the **HL** state (10^{-2} G_0) is about 2 orders of magnitude higher than that of the **LL** state (10^{-4} G_0). Such a difference is suspected to arise from the geometric change of the paraquat subunit being in or out of contact with porphyrin. However, this is not comparable with the STM-BJ results obtained from **P-2** and **P-Q3** (Figure 2.17, prepared in a parallel work conducted by Prof. Qiang Chen). The measurements on these two molecules indicate that, with SMe as the anchoring group, the molecular conductance reduces in ~2 orders of magnitude, compared to using the TMS-protected acetylenes in **P-Q1**. The incorporation of paraquat in **P-Q3** (peak conductance of 10^{-5} G_0) increases the molecular conductance for about ~0.5 orders of magnitude compared to that of **P-2** (peak conductance of $10^{-5.5}$ G_0). While this confirms that the interaction between

paraquat and porphyrin is able to induce a change in conductance, the change would not be as large as the 100 on/off ratio recorded for **P-Q1**.

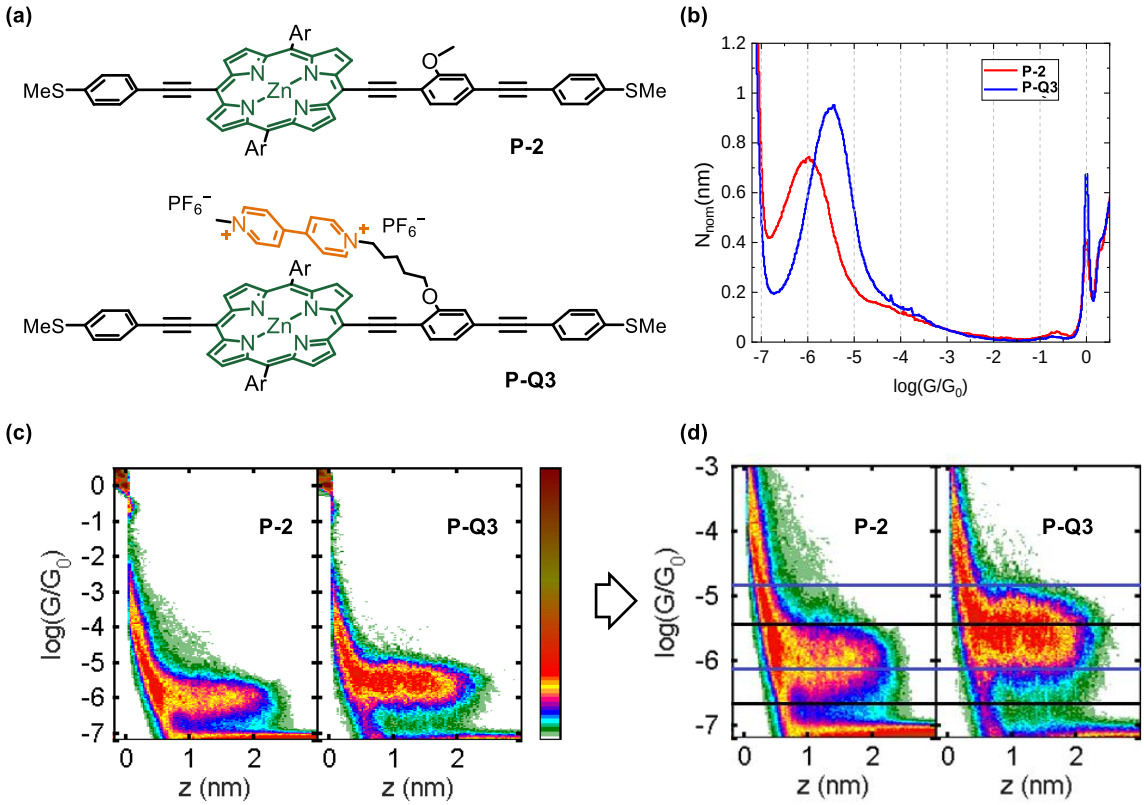


Figure 2.17: (a) Structures of **P-2** and **P-Q3** studied using the STM-BJ technique. Comparison of (b) 1D, (c) 2D and (d) partial zoomed-in 2D histograms for plateau-containing conductance traces for **P-2** and **P-Q3** (measured with a bias of 0.20 V).

Another explanation for the phenomenon of **HL** and **LL** states could be that, instead of forming a Au-acetylene contact from the TMS group, SMe at the end of paraquat 'arm' behaves like a weak anchoring group interacting with electrodes. Therefore, in this case, the broad conductance peaks shown in 1D histogram in each pattern may display a sum of two different conductance states caused by different geometric positions of paraquat. Nevertheless, with only the results from the low-bias conductance measurements of **P-Q1**, there is no definitive proof for the occurrence of geometric switching of the paraquat unit in the system during the measurements. Further studies based on the $\log(G/G_0)$–V measurements, in which the applied bias is swept from negative to positive (*i.e.*, reversing the direction of the electric field), could provide more insight into the electric field-dependence of the conducting behavior for **P-Q1**.

2.4 Conclusions

In this chapter, we have designed and successfully synthesized a porphyrin-paraquat conjugate with a proposed use in molecular memory applications. We documented the attempts towards building the porphyrin-based molecular backbone and the stepwise incorporation of paraquat-based 'arm'. TMS-acetylene anchoring groups were chosen to form strong electrode-molecule contacts in single-molecule junctions but complicated the synthesis and purification due to its ease of cleavage. These were further complicated by the involvement of counterions from the highly polar paraquat dication. By cautiously selecting reagents and the substitution order for each component, the target memory molecule **P-Q1** and its control molecules **P-Q2** and **P-1** for single-molecule conductance study were successfully synthesized and isolated. All three compounds were well-characterized by NMR, UV–vis absorption spectroscopy, and mass spectrometry.

STM-BJ experiments show that **P-Q1** successfully formed single-molecule junctions with gold electrodes. However, in the low-bias conductance study, resulting conductance traces displayed three distinct patterns, each covering a wide range of conductance value. These results indicate that the conducting behavior of **P-Q1** is complex to interpret, which may be caused by the freedom of the paraquat unit, and the interaction between the SMe unit with electrodes forming another conductive pathway. Further STM-BJ experiments on the control molecules are currently underway and we anticipate that these will help shed some light on the understanding of the results observed so far.

2.5 References

1 S. Kumar, M. Merelli, W. Danowski, P. Rudolf, B. L. Feringa and R. C. Chiechi, *Adv. Mater.*, 2019, **31**, 1–6.

2 J. C. Scott and L. D. Bozano, *Adv. Mater.*, 2007, **19**, 1452–1463.

3 W. Lin, S. Liu, T. Gong, Q. Zhao and W. Huang, *Adv. Mater.*, 2014, **26**, 570–606.

4 S. Goswami, A. J. Matula, S. P. Rath, S. Hedström, S. Saha, M. Annamalai, D. Sengupta, A. Patra, S. Ghosh, H. Jani, S. Sarkar, M. R. Motapothula, C. A. Nijhuis, J. Martin, S. Goswami, V. S. Batista and T. Venkatesan, *Nat. Mater.*, 2017, **16**, 1216–1224.

5 B. Cho, S. Song, Y. Ji, T. Kim and T. Lee, *Adv. Funct. Mater.*, 2011, **21**, 2806–2829.

6 R. Gupta, P. Jash and P. C. Mondal, *J. Mater. Chem. C*, 2021, **9**, 11497–11516.

7 Y. Han, C. Nickle, Z. Zhang, H. P. A. G. Astier, T. J. Duffin, D. Qi, Z. Wang, E. del Barco, D. Thompson and C. A. Nijhuis, *Nat. Mater.*, 2020, **19**, 843–848.

8 S. Jan van der Molen and P. Liljeroth, *J. Phys.: Condens. Matter*, 2010, **22**, 133001.

9 M. Alemani, M. V. Peters, S. Hecht, K.-H. Rieder, F. Moresco and L. Grill, *J. Am. Chem. Soc.*, 2006, **128**, 14446–14447.

10 B.-Y. Choi, S.-J. Kahng, S. Kim, H. Kim, H. W. Kim, Y. J. Song, J. Ihm and Y. Kuk, *Phys. Rev. Lett.*, 2006, **96**, 156106.

11 M. J. Comstock, N. Levy, A. Kirakosian, J. Cho, F. Lauterwasser, J. H. Harvey, D. A. Strubbe, J. M. J. Fréchet, D. Trauner, S. G. Louie and M. F. Crommie, *Phys. Rev. Lett.*, 2007, **99**, 038301.

12 M. Irie, *Chem. Rev.*, 2000, **100**, 1685–1716.

13 C. Jia, A. Migliore, N. Xin, S. Huang, J. Wang, Q. Yang, S. Wang, H. Chen, D. Wang, B. Feng, Z. Liu, G. Zhang, D.-H. Qu, H. Tian, M. A. Ratner, H. Q. Xu, A. Nitzan and X. Guo, *Science*, 2016, **352**, 1443–1445.

14 T. A. Su, M. Neupane, M. L. Steigerwald, L. Venkataraman and C. Nuckolls, *Nat. Rev. Mater.*, 2016, **1**, 16002.

15 M. Russew and S. Hecht, *Adv. Mater.*, 2010, **22**, 3348–3360.

16 A. Bandyopadhyay, S. Sahu and M. Higuchi, *J. Am. Chem. Soc.*, 2011, **133**, 1168–1171.

17 C. Simão, M. Mas-Torrent, N. Crivillers, V. Lloveras, J. M. Artés, P. Gorostiza, J. Veciana and C. Rovira, *Nat. Chem.*, 2011, **3**, 359–364.

18 S. Erbas-Cakmak, D. A. Leigh, C. T. McTernan and A. L. Nussbaumer, *Chem. Rev.*, 2015, **115**, 10081–10206.

19 S. Jan van der Molen, J. Liao, T. Kudernac, J. S. Agustsson, L. Bernard, M. Calame, B. J. van Wees, B. L. Feringa and C. Schönenberger, *Nano Lett.*, 2009, **9**, 76–80.

20 S. Grunder, R. Huber, V. Horhoiu, M. T. González, C. Schönenberger, M. Calame and M. Mayor, *J. Org. Chem.*, 2007, **72**, 8337–8344.

21 A. C. Aragonès, D. Aravena, J. I. Cerdá, Z. Acís-Castillo, H. Li, J. A. Real, F. Sanz, J. Hihath, E. Ruiz and I. Díez-Pérez, *Nano Lett.*, 2016, **16**, 218–226.

22 L. Bogani and W. Wernsdorfer, *Nat. Mater.*, 2008, **7**, 179–186.

23 S. Goswami, R. Pramanick, A. Patra, S. P. Rath, M. Foltin, A. Ariando, D. Thompson, T. Venkatesan, S. Goswami and R. S. Williams, *Nature*, 2021, **597**, 51–56.

24 B. Hu, C. Wang, J. Wang, J. Gao, K. Wang, J. Wu, G. Zhang, W. Cheng, B. Venkateswarlu, M. Wang, P. S. Lee and Q. Zhang, *Chem. Sci.*, 2014, **5**, 3404–3408.

25 N. J. Tao, *Phys. Rev. Lett.*, 1996, **76**, 4066–4069.

26 W. Haiss, H. van Zalinge, S. J. Higgins, D. Bethell, H. Höbenreich, D. J. Schiffrin and R. J. Nichols, *J. Am. Chem. Soc.*, 2003, **125**, 15294–15295.

27 Z. Li, B. Han, G. Meszaros, I. Pobelov, T. Wandlowski, A. Błaszczyk and M. Mayor, *Faraday Discuss.*, 2006, **131**, 121–143.

28 E. A. Osorio, K. O'Neill, N. Stuhr-Hansen, O. F. Nielsen, T. Bjørnholm and H. S. J. van der Zant, *Adv. Mater.*, 2007, **19**, 281–285.

29 J. Lee, H. Chang, S. Kim, G. S. Bang and H. Lee, *Angew. Chem. Int. Ed.*, 2009, **48**, 8501–8504.

30 J. O. Jeppesen, J. Perkins, J. Becher and J. F. Stoddart, *Angew. Chem. Int. Ed.*, 2001, **40**, 1216–1221.

31 H. Chen and J. Fraser Stoddart, *Nat. Rev. Mater.*, 2021, **6**, 804–828.

32 A. Coskun, J. M. Spruell, G. Barin, W. R. Dichtel, A. H. Flood, Y. Y. Botros and J. F. Stoddart, *Chem. Soc. Rev.*, 2012, **41**, 4827.

33 J. S. Lindsey and D. F. Bocian, *Acc. Chem. Res.*, 2011, **44**, 638–650.

34 Q. Li, G. Mathur, S. Gowda, S. Surthi, Q. Zhao, L. Yu, J. S. Lindsey, D. F. Bocian and V. Misra, *Adv. Mater.*, 2004, **16**, 133–137.

35 C. Clausen, D. T. Gryko, A. A. Yasseri, J. R. Diers, D. F. Bocian, W. G. Kuhr and J. S. Lindsey, *J. Org. Chem.*, 2000, **65**, 7371–7378.

36 K.-H. Schweikart, V. L. Malinovskii, J. R. Diers, A. A. Yasseri, D. F. Bocian, W. G. Kuhr and J. S. Lindsey, *J. Mater. Chem.*, 2002, **12**, 808–828.

37 M. J. Gunter, T. P. Jeynes, M. R. Johnston, P. Turner and Z. Chen, *J. Chem. Soc. Perkin Trans.*, 1998, 1945–1958.

38 V. Raymont, H. Wilson, M. Pfrunder, J. C. McMurtrie and K. M. Mullen, *New J. Chem.*, 2013, **37**, 893–900.

39 E. Leary, A. La Rosa, M. T. González, G. Rubio-Bollinger, N. Agraït and N. Martín, *Chem. Soc. Rev.*, 2015, **44**, 920–942.

40 M. Kamenetska, S. Y. Quek, A. C. Whalley, M. L. Steigerwald, H. J. Choi, S. G. Louie, C. Nuckolls, M. S. Hybertsen, J. B. Neaton and L. Venkataraman, *J. Am. Chem. Soc.*, 2010, **132**, 6817–6821.

41 M. Kamenetska, M. Koentopp, A. C. Whalley, Y. S. Park, M. L. Steigerwald, C. Nuckolls, M. S. Hybertsen and L. Venkataraman, *Phys. Rev. Lett.*, 2009, **102**, 126803.

42 P. Moreno-García, M. Gulcur, D. Z. Manrique, T. Pope, W. Hong, V. Kaliginedi, C. Huang, A. S. Batsanov, M. R. Bryce, C. Lambert and T. Wandlowski, *J. Am. Chem. Soc.*, 2013, **135**, 12228–12240.

43 A. Mishchenko, L. A. Zotti, D. Vonlanthen, M. Bürkle, F. Pauly, J. C. Cuevas, M. Mayor and T. Wandlowski, *J. Am. Chem. Soc.*, 2011, **133**, 184–187.

44 M. A. Reed, C. Zhou, C. J. Muller, T. P. Burgin and J. M. Tour, *Science*, 1997, **278**, 252–254.

45 T. Hines, I. Díez-Pérez, H. Nakamura, T. Shimazaki, Y. Asai and N. Tao, *J. Am. Chem. Soc.*, 2013, **135**, 3319–3322.

46 Z.-L. Cheng, R. Skouta, H. Vazquez, J. R. Widawsky, S. Schneebeli, W. Chen, M. S. Hybertsen, R. Breslow and L. Venkataraman, *Nat. Nanotechnol.*, 2011, **6**, 353–357.

47 D. Millar, L. Venkataraman and L. H. Doerrer, *J. Phys. Chem. C*, 2007, **111**, 17635–17639.

48 W. Hong, H. Li, S.-X. Liu, Y. Fu, J. Li, V. Kaliginedi, S. Decurtins and T. Wandlowski, *J. Am. Chem. Soc.*, 2012, **134**, 19425–19431.

49 J.-R. Deng, M. T. González, H. Zhu, H. L. Anderson and E. Leary, *J. Am. Chem. Soc.*, 2024, **146**, 3651–3659.

50 C. Roche, Q. Luo, G. Gil-Ramírez, H. W. Jiang, D. R. Kohn, Y. Xiong, A. L. Thompson and H. L. Anderson, *J. Org. Chem.*, 2017, **82**, 7446–7462.

51 M. G. Freire, C. M. S. S. Neves, I. M. Marrucho, J. A. P. Coutinho and A. M. Fernandes, *J. Phys. Chem. A*, 2010, **114**, 3744–3749.

52 G. R. Fulmer, A. J. M. Miller, N. H. Sherden, H. E. Gottlieb, A. Nudelman, B. M. Stoltz, J. E. Bercaw and K. I. Goldberg, *Organometallics*, 2010, **29**, 2176–2179.

53 M. T. González, E. Leary, R. García, P. Verma, M. Á. Herranz, G. Rubio-Bollinger, N. Martín and N. Agraït, *J. Phys. Chem. C*, 2011, **115**, 17973–17978.

54 C. Li, I. Pobelov, T. Wandlowski, A. Bagrets, A. Arnold and F. Evers, *J. Am. Chem. Soc.*, 2008, **130**, 318–326.

55 C. Huang, A. V. Rudnev, W. Hong and T. Wandlowski, *Chem. Soc. Rev.*, 2015, **44**, 889–901.

56 E. Leary, B. Limburg, A. Alanazy, S. Sangtarash, I. Grace, K. Swada, L. J. Esdaile, M. Noori, M. T. González, G. Rubio-Bollinger, H. Sadeghi, A. Hodgson, N. Agraït, S. J. Higgins, C. J. Lambert, H. L. Anderson and R. J. Nichols, *J. Am. Chem. Soc.*, 2018, **140**, 12877–12883.

2.6 Experimental

Contents

General Methods 57

Synthesis of Known Compounds 58

Dipyrromethane (DPM) 58

Zn(II) 5,15-bis(3,5-bis(*tert*-butyl)phenyl)porphyrin 59

Zn(II) 5,15-dibromo-10,20-bis(3,5-bis(*tert*-butyl)phenyl)porphyrin **2.5** 60

Zn(II) 5,15-bis(TMS-acetylene)-10,20-bis(3,5-bis(*tert*-butyl)phenyl)porphyrin 60

Zn(II) 5,15-bisacetylene-TMS-monodeprotected porphyrin **2.6** 61

(2-Iodoethyl)(methyl)sulfane **2.11-I** 62

Synthesis of Novel Compound 63

MOM-protected dibromophenol **2.1** 63

MOM-protected 2-bromo-5-(TMS-acetylene)phenol **2.2** 63

2-Bromo-5-(TMS-acetylene)phenol **2.3** 64

Acetate-protected 2-bromo-5-(TMS-acetylene)phenol **2.4** 65

Acetate-protected bis(TMS-acetylene)-terminated phenol-porphyrin **2.7** 65

Bis(TMS-acetylene)-terminated phenol-porphyrin **2.8** 66

Bis(TMS-acetylene)-terminated phenoxymethyl-porphyrin **P-1** 67

Bis(TMS-acetylene)-terminated phenoxy(Iodobutyl)-porphyrin **2.9-I** 68

Mono-charged 4,4'-bipyridinium-porphyrin **2.10-PF_6** 69

Porphyrin-Paraquat Conjugate **P-Q2** 70

1-(2-(Methylthio)ethyl)-4,4'-bipyridinium **2.12-I** 71

Porphyrin-Paraquat Conjugate **P-Q1** 72

Selected NMR Spectra 74

Selected UV–vis–NIR Absorption Spectra 84

Selected Mass Spectra 85

References 87

General Methods

Commercially available reagents from Alfa Aesar, Fluorochem, Merck, Strem Chemicals and TCI were used as received. Reactions, unless otherwise stated, were performed in oven-dried glassware under an argon atmosphere. Anhydrous acetonitrile, dichloromethane, dimethylformamide (DMF), toluene, tetrahydrofuran (THF), dimethyl sulfoxide (DMSO) and triethylamine were purified by an MBraun MN-SPS-5 Bench-Top under nitrogen atmosphere (H_2O content < 20 ppm as determined by Karl-Fischer titration). All other solvents used for extraction or column chromatography (silica gel: SiO_2, 60 Å, 40–63 μm) are in HPLC grade. Thin layer chromatography (TLC) was carried out on aluminum-backed silica gel 60 F254 plates (Merck) and visualized under UV irradiation either at 254 or 365 nm. Petroleum ether (pet. ether) boiling point range of 40–60 °C was used for chromatography. Size-exclusion chromatography was carried out using Bio-Rad Bio-Beads S-X1 (1% cross linked, 40–80 μm bead size). Evaporation of solvents was performed at 20–50 °C and 5–1010 mbar. Reported yields refer to pure compounds dried under high vacuum (< 0.1 mbar).

^{1}H and ^{13}C nuclear magnetic resonance (NMR) spectra were recorded on a Bruker AVIII HD 400, AVIII HD 500 and Avance NEO 600 (broadband helium cryoprobe) spectrometers at 400 MHz, 500 MHz, 600 MHz (^{1}H) and 101 MHz, 126 MHz and 151 MHz (^{13}C), respectively at 298 K unless otherwise stated. ^{1}H NMR chemical shifts are reported in ppm to the nearest 0.01 ppm relative to $SiMe_4$ (δ = 0) and coupling constants (J) are in Hertz. ^{1}H NMR spectra have been referenced internally to the residual solvent protons of the deuterated solvent using the reported values (δ = 5.32 for dichloromethane-d_2, 7.26 for chloroform-d, 3.31 for methanol-d_4, 2.05 for acetone-d_6). Multiplicities are reported in accordance with the following: s = singlet; br s = broad singlet; d = doublet; dd = doublet of doublet; t = triplet and m = multiplet. ^{13}C chemical shifts are reported in ppm to the nearest 0.1 ppm relative to $SiMe_4$ (δ = 0) and have been referenced internally with respect to the residual carbons in the solvents (δ = 53.8 for dichloromethane-d_2, 77.2 for chloroform-d, 49.0 for methanol-d_4, 206.3 and 29.8 for acetone-d_6). ^{1}H assignments were made using 2D NMR methods (COSY, NOESY, HSQC, HMBC).

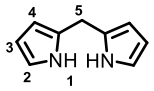
MALDI-TOF MS spectra were measured using Bruker MALDI Autoflex Speed spectrometer utilizing *trans*-2-[3-(4-*tert*-butylphenyl-2-methyl-2-propenylidene]-

malononitrile (DCTB) as matrix. High resolution ESI mass spectrometry (HR-MS) measurements were performed by the mass spectrometry service at the University of Oxford on a Waters GTC classic.

UV−vis spectra were recorded in solution at 298 K with a Perkin-Elmer Lambda 20 spectrometer with temperature control by a PTP-1 Peltier unit using Infrasil® Quartz 1 cm cuvettes.

Synthesis of Known Compounds

Dipyrromethane (DPM)

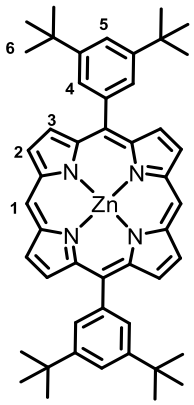


Pyrrole (100 mL, 1.4 mol) and formaldehyde (33% w/w solution in water, 5.4 mL, 60 mmol) were added into a 500 mL round-bottom flask and solution was degassed by bubbling with argon for 20 min. Trifluoroacetic acid (0.54 mL, 3.1 mmol) was subsequently added dropwise into the mixture with vigorous stirring. After 5 min, dichloromethane (100 mL) was added into the mixture, immediately followed by the addition of saturated Na_2CO_3 aqueous solution (100 mL). The organic phase was extracted and washed with saturated Na_2CO_3 aqueous solution (80 mL × 2) and water (100 mL), then dried over Na_2SO_4. The solvent and excess pyrrole were removed under reduced pressure and residue oil was distilled by a Kugelrohr apparatus (195−200 °C, 0.60 mbar). Dipyrromethane (4.5 g, 51%) was yielded as a light-yellow solid.

^{1}**H NMR** (400 MHz, $CDCl_3$, 298 K) δ_H 7.77 (br s, 2H, *H1*), 6.64 (m, 2H, *H2*), 6.16 (m, 2H, *H3*), 6.06 (m, 2H, *H4*), 3.96 (s, 2H, *H5*).

Analytical data as in lit.[1]

Zn(II) 5,15-bis(3,5-bis(*tert*-butyl)phenyl)porphyrin

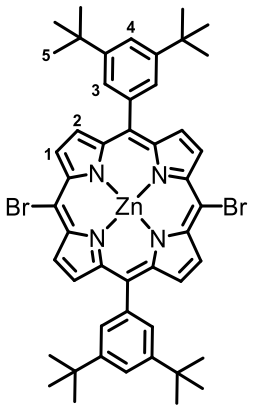


3,5-Di-*tert*-butylbenzaldehyde (1.4 g, 2.0 equiv., 6.5 mmol,) and dipyrromethane (0.94 g, 2.0 equiv., 6.5 mmol) were added into a 2.0 L round-bottom flask followed by the addition of dichloromethane (1.25 L). The solution was degassed by bubbling with argon for 20 min before the addition of trifluoroacetic acid (0.32 mL, 1.3 equiv., 4.2 mmol). The mixture was stirred in the dark for 3 h and DDQ (1.9 g, 2.6 equiv., 8.2 mmol) was then added. The mixture was left stirring at room temperature for another 30 min. Subsequently the reaction was quenched by the addition of triethylamine (6.3 mL). The solution was concentrated under reduced pressure and purified by a short silica plug (dichloromethane). The product was redissolved in chloroform (150 mL). A solution of $Zn(OAc)_2{\cdot}2H_2O$ (1.6 g, 2.2 equiv., 7.2 mmol) in methanol (15 mL) was added and the mixture was stirred at 40 °C for 1 h. The reaction was monitored by TLC (pet. ether/dichloromethane, v/v, 9:1) and the resulting solution was concentrated under reduced pressure, purified through a short silica plug (pet. ether/dichloromethane, v/v, 4:1). Zn(II) 5,15-bis(3,5-bis(*tert*-butyl)phenyl)porphyrin (0.99 g, 41%) was yielded as a red-purple solid after recrystallization by layer addition (dichloromethane/methanol) at 4 °C overnight.

^{1}**H NMR** (400 MHz, $CDCl_3$, 298 K) δ_H 10.34 (s, 2H, *H1*), 9.46 (d, *J* = 4.5 Hz, 4H, *H2*), 9.21 (d, *J* = 4.4 Hz, 4H, *H3*), 8.15 (d, *J* = 1.8 Hz, 4H, *H4*), 7.85 (s, 2H, *H5*), 1.58 (s, 36H, *H6*).

Analytical data as in lit.[2]

Zn(II) 5,15-dibromo-10,20-bis(3,5-bis(*tert*-butyl)phenyl)porphyrin 2.5

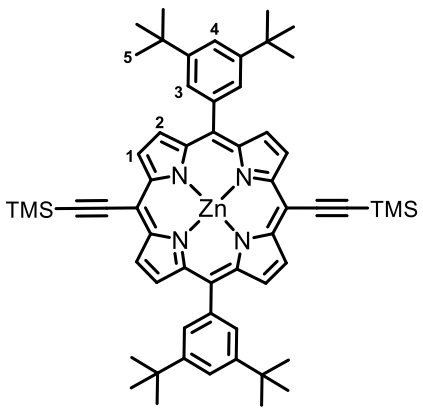


Zn(II) 5,15-bis(3,5-bis(*tert*-butyl)phenyl)porphyrin (2.2 g, 2.9 mmol) was added into a 500 mL round-bottom flask followed by the addition of dichloromethane (250 mL) and pyridine (2.5 mL). The solution was cooled to 0 °C using an ice-bath and, while being stirred, a solution of *N*-bromosuccinimide (1.1 g, 2.1 equiv., 6.2 mmol) in chloroform (50 mL) was added dropwise. The reaction proceeded at 0 °C for 15 min with stirring. Subsequently, acetone (20 mL) was added to quench the excess of *N*-bromosuccinimide. The resulting solution was concentrated under reduced pressure and the crude product was recrystallized by layer addition of dichloromethane/methanol at 4 °C overnight. Zn(II) 5,15-dibromo-10,20-bis(3,5-bis(*tert*-butyl)phenyl) porphyrin **2.5** (2.4 g, 89%) was yielded as a dark purple solid.

^{1}**H NMR** (400 MHz, $CDCl_3$, 298 K) δ_H 9.64 (d, *J* = 4.6 Hz, 4H, *H1*), 8.89 (d, *J* = 4.6 Hz, 4H, *H2*), 7.97 (d, *J* = 1.8 Hz, 4H, *H3*), 7.79 (t, *J* = 1.8 Hz, 2H, *H4*), 1.53 (s, 36H, *H5*).

Analytical data as in lit.[2]

Zn(II) 5,15-bis(TMS-acetylene)-10,20-bis(3,5-bis(*tert*-butyl)phenyl)porphyrin

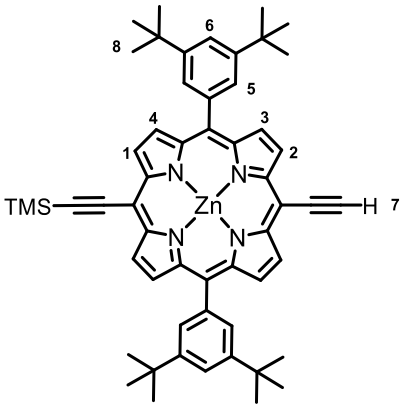


Porphyrin **2.5** (32 mg, 35 μmol), $PdCl_2(PPh_3)_2$ (2.5 mg, 0.10 equiv., 3.5 μmol) and copper(I) iodide (0.67 mg, 0.10 equiv., 3.5 μmol) were added into a 10 mL Schlenk tube and it was evacuated and backfilled with argon for three times. Anhydrous THF (1.3 mL) and triethylamine (0.33 mL) were added using a syringe and the solution was degassed by three freeze-pump-thaw cycles followed by the addition of ethynyltrimethylsilane (0.20 mL, 4 equiv., 0.14 mmol). The reaction proceeded at 45 °C for 20 h with stirring. EtOAc (10 mL) was added to the cooled reaction mixture and the combined organic extracts washed with water (10 mL × 2) and dried over Na_2SO_4 before the solvent was removed under reduced pressure. The residue was purified through silica chromatography (pet. ether/dichloromethane v/v, gradient elution from 10:0 to 4:1). Zn(II) 5,15-bis(TMS-acetylene)-10,20-bis(3,5-bis(*tert*-butyl)phenyl)porphyrin (32 mg, 96%) was yielded as a blue-green solid.

^{1}H NMR (400 MHz, $CDCl_3$, 298 K) δ_H 9.72 (d, J = 4.6 Hz, 4H, *H1*), 8.97 (d, J = 4.6 Hz, 4H, *H2*), 8.05 (d, J = 1.8 Hz, 4H, *H3*), 7.83 (t, J = 1.8 Hz, 2H, *H4*), 1.56 (s, 36H, *H5*), 0.60 (s, 18H, H_{TMS}).

Analytical data as in lit.[3]

Zn(II) 5,15-bisacetylene-TMS-monodeprotected porphyrin 2.6



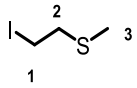
Tetra-*n*-butylammonium fluoride (TBAF, 0.10 mL, 1.0 M solution in THF, 0.1 mmol) was diluted in chloroform (10 mL). Zn(II) 5,15-bis(TMS-acetylene)-10,20-bis(3,5-bis(*tert*-butyl)phenyl)porphyrin (32 mg, 35 μmol) was added to a 20 mL round-bottom flask with chloroform (5 mL). The diluted TBAF solution (0.6 mL) was added using a syringe under argon and the reaction proceeded at room temperature for 30 min with stirring and is monitored by TLC until an ideal statistical mixture was observed. The mixture was immediately passed through a silica plug with chloroform eluent to quench the reaction. The resulting solution was

concentrated under reduced pressure and the crude material was purified through silica chromatography (cyclohexane/pyridine/EtOAc, v/v, gradient elution from 50:1:1 to 50:3:3). Porphyrin **2.6** (9.6 mg, 32%) was yielded as a green solid.

^{1}H NMR (400 MHz, $CDCl_3$, 298 K) δ_H 9.67 (2 overlap d, *J* = 4.4 Hz, 4H, *H1*, *H1*), 8.93 (d, *J* = 4.6 Hz, 2H, *H3*), 8.91 (d, *J* = 4.6 Hz, 2H, *H4*), 8.01 (d, *J* = 1.8 Hz, 4H, *H5*), 7.80 (t, *J* = 1.8 Hz, 2H, *H6*), 4.14 (s, 1H, *H7*), 1.55 (s, 36H, *H8*), 0.59 (s, 9H, H_{TMS}).

Analytical data as in lit.[4]

(2-Iodoethyl)(methyl)sulfane 2.11-I



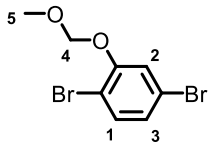
NaI (21 g, 3.0 equiv., 81mmol) was added into a 100 mL round-bottom flask and it was evacuated and backfilled with argon for three times. (2-Chloroethyl)(methyl)sulfane (2.7 mL, 20 μmol) and anhydrous acetone (30 mL, dried over 3 Å molecular sieves) were added using a syringe and the reaction proceeded at 50 °C for 20 h with stirring. The excess NaI was removed by filtration and diethyl ether (50 mL) was added to the cooled reaction mixture. The organic phase was extracted and washed with water (30 mL × 2) and 1M sodium thiosulfate solution (30 mL), then dried over Na_2SO_4. The resulting solution was concentrated under reduced pressure. (2-Iodoethyl)(methyl)sulfane **2.11-I** (2.25 g, 41%) was yielded as a yellow oil.

^{1}H NMR (400 MHz, $CDCl_3$, 298 K) δ_H 3.32 – 3.26 (m, 2H, *H1*), 2.97 – 2.91 (m, 2H, *H2*), 2.14 (s, 3H, *H3*).

Analytical data as in lit.[5]

Synthesis of Novel Compound

MOM-protected dibromophenol 2.1



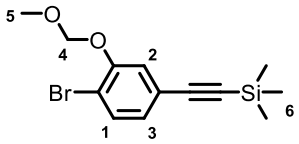
2,5-Dibromophenol (2.5 g, 9.9 mmol) and K_2CO_3 (5.5 g, 40 mmol) were added into a 100 mL round-bottom flask followed by the addition of DMF (30 mL). The reaction mixture was cooled to 0 °C using an ice bath and, while being stirred, chloro(methoxy)methane (1.1 mL, 1.5 equiv., 15 mmol) was added dropwise. The reaction proceeded at room temperature for 20 h with stirring and was quenched by dropwise addition of water (10 mL). Diethyl ether (30 mL) was added to the reaction mixture and the organic phase was extracted and washed with water (30 mL × 2) and dried over Na_2SO_4. The resulting solution was concentrated under reduced pressure and the crude material was purified through silica chromatography (pet. ether/EtOAc v/v, 10:1). MOM-protected dibromophenol **2.1** (2.7 g, 90%) was yielded as a colorless oil.

^{1}H NMR (400 MHz, $CDCl_3$, 298 K) δ_H 7.39 (d, *J* = 8.4 Hz, 1H, *H1*), 7.30 (d, *J* = 2.2 Hz, 1H, *H2*), 7.02 (dd, *J* = 8.4, 2.2 Hz, 1H, *H3*), 5.23 (s, 2H, *H4*), 3.52 (s, 3H, *H4*).

^{13}C NMR (101 MHz, $CDCl_3$, 298 K) δ_C 154.5, 134.2, 126.2, 121.6, 119.5, 111.7, 95.3, 56.6.

HR MS: *m/z* = 297.082 $[M+H]^+$ ($C_8H_8Br_2O_2$, MH^+ requires 296.894).

MOM-protected 2-bromo-5-(TMS-acetylene)phenol 2.2



MOM-protected dibromophenol **2.1** (1.0 g, 3.38 mmol), $PdCl_2(PPh_3)_2$ (71 mg, 0.03 equiv., 0.10 mmol), PPh_3 (53 mg, 0.06 equiv., 0.2 mmol) and copper(I) iodide (24 mg, 0.04 equiv., 0.13 mmol) were added into a 20 mL Schlenk tube and it was evacuated and backfilled with argon for three times. Anhydrous toluene (6.8 mL) and triethylamine (3.4 mL) were added using a syringe and the solution was degassed by three freeze-pump-thaw cycles followed by the

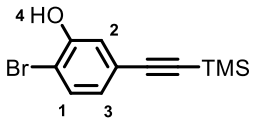
addition of ethynyltrimethylsilane (0.56 mL, 1.2 equiv., 4.1 mmol). The reaction proceeded at 40 °C for 22 h with stirring and was quenched by dropwise addition of water (8 mL). EtOAc (20 mL) was added to the cooled reaction mixture and the organic phase was extracted and washed with water (10 mL × 2) and dried over Na_2SO_4. The resulting solution was concentrated under reduced pressure and the crude material was purified through silica chromatography (pet. ether/dichloromethane v/v, 25:1, TLC with diethyl ether/ pet. ether, v/v, 1:50) to yield MOM-protected 2-bromo-5-(TMS-acetylene)phenol **2.2** (0.48 g, 47%) as a colorless oil.

^{1}H NMR (400 MHz, $CDCl_3$, 298 K) δ_H 7.46 (d, *J* = 8.2 Hz, 1H, *H1*), 7.23 (d, *J* = 1.8 Hz, 1H, *H2*), 6.99 (dd, *J* = 8.2, 1.8 Hz, 1H, *H3*), 5.25 (s, 2H, *H4*), 3.52 (s, 3H, *H5*), 0.24 (s, 9H, H_{TMS} (*H6*)).

^{13}C NMR (101 MHz, $CDCl_3$, 298 K) δ_C 153.5, 133.3, 126.7, 123.5, 119.1, 113.7, 104.0, 95.3, 95.1, 56.5.

HR MS: *m/z* = 334.989 $[M+Na]^+$ ($C_{13}H_{17}BrO_2Si$, MNa^+ requires 334.989).

2-Bromo-5-(TMS-acetylene)phenol 2.3

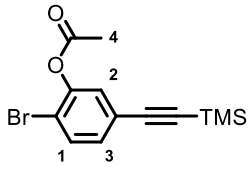


MOM-protected 2-bromo-5-(TMS-acetylene)phenol **2.2** (30 mg, 0.10 mmol) was added into a 50 mL round-bottom flask followed by the addition of dichloromethane (0.50 mL) and methanol (3.0 mL). Hydrochloric acid (0.11 mL, 10 M, 1.1 mmol) was added dropwise and the reaction proceeded at 35 °C for 20 h with stirring. Dichloromethane (5.0 mL) was added to the cooled reaction mixture and the organic phase was extracted and washed with saturated $NaHCO_3$ aqueous solution (10 mL) and water (10 mL × 2), and then dried over Na_2SO_4. The resulting solution was concentrated under reduced pressure and the crude material was purified through silica chromatography (pet. ether/dichloromethane, v/v, 7:1). 2-Bromo-5-(TMS-acetylene)phenol **2.3** (23 mg, 89%) was yielded as a light-yellow solid.

^{1}H NMR (400 MHz, $CDCl_3$, 298 K) δ_H 7.38 (d, *J* = 8.3 Hz, 1H, *H1*), 7.11 (d, *J* = 1.9 Hz, 1H, *H2*), 6.91 (dd, *J* = 8.3, 1.9 Hz, 1H, *H3*), 5.46 (s, 1H, *H4*), 0.24 (s, 9H, H_{TMS}).

HR MS: *m/z* = 267.992 $[M+H]^+$ ($C_{13}H_{15}BrO_2Si$, MH^+ requires 267.972).

Acetate-protected 2-bromo-5-(TMS-acetylene)phenol 2.4



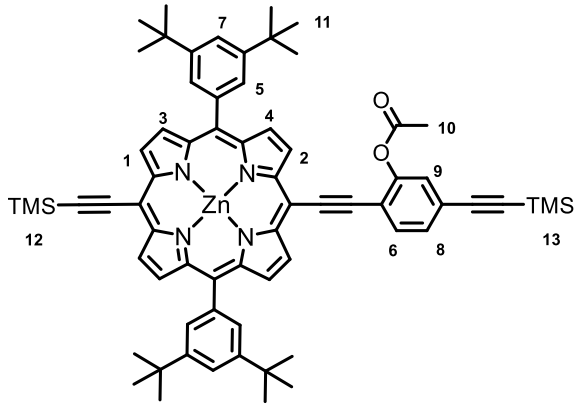
2-Bromo-5-(TMS-acetylene)phenol **2.3** (0.32 g, 1.2 mmol) was added into a 15 mL round-bottom flask containing dichloromethane (3.0 mL). Triethylamine (0.43 mL, 3.5 mmol) and acetic anhydride (0.13 mL, 1.4 mmol) were added using a syringe and the reaction proceeded at room temperature for 12 h. EtOAc (5.0 mL) was added to the reaction mixture and the organic phase was extracted and washed with brine (20 mL) and water (20 mL × 2) and dried over Na_2SO_4. The resulting solution was concentrated under reduced pressure and the crude material was purified through silica chromatography (pet. ether/dichloromethane v/v, 5:1). Acetate-protected 2-bromo-5-(TMS-acetylene)phenol **2.4** (0.32 g, 87%) was yielded a light-yellow oil.

^{1}H NMR (400 MHz, $CDCl_3$, 298 K) δ_H 7.52 (d, J = 8.2 Hz, 1H, *H1*), 7.22 (d, J = 1.8 Hz, 1H, *H2*), 7.19 (dd, J = 8.2, 1.9 Hz, 1H, *H3*), 2.34 (s, 3H, *H4*), 0.23 (s, 9H, H_{TMS}).

^{13}C NMR (101 MHz, $CDCl_3$, 298 K) δ_C 168.3, 148.1, 133.3, 130.7, 127.2, 124.0, 117.0, 103.0, 96.6, 29.9, 20.9.

HR MS: m/z = 311.2348 $[M+H]^+$ ($C_{13}H_{15}BrO_2Si$, MH^+ requires 311.0097).

Acetate-protected bis(TMS-acetylene)-terminated phenol-porphyrin 2.7



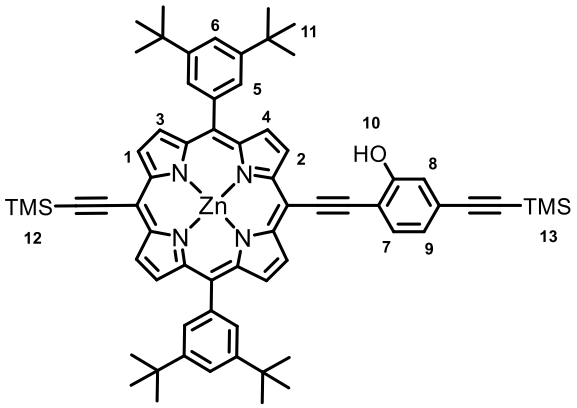
Porphyrin **2.6** (0.10 g, 0.12 mmol) and acetate-protected 2-bromo-5-(TMS-acetylene)phenol **2.4** (0.28 g, 7.5 equiv., 0.90 mmol) were added into a 25 mL Schlenk tube and it was evacuated

and backfilled with argon for three times. Anhydrous THF (5.4 mL) and diisopropylamine (DIPA, 3.6 mL) were added using a syringe and the solution was degassed by three freeze-pump-thaw cycles followed by the addition of copper(I) iodide (6.9 mg, 0.30 equiv., 36 μmol) and $Pd(PPh_3)_4$ (28 mg, 0.20 equiv., 24 μmol). The reaction proceeded at 60 °C for 24 h with stirring and was quenched by dropwise addition of water (8.0 mL). EtOAc (20 mL) was added to the cooled reaction mixture and the organic phase was extracted and washed with water (30 mL × 2) and dried over Na_2SO_4. The resulting solution was concentrated under reduced pressure and the crude material was purified through silica chromatography (pet. ether/dichloromethane v/v, 4:1). Porphyrin **2.7** (69 mg, 52%) was yielded as a blue-green solid.

^{1}H NMR (400 MHz, $CDCl_3$, 298 K) δ_H 9.74 (d, *J* = 4.6 Hz, 2H, *H1*), 9.72 (d, *J* = 4.6 Hz, 2H, *H2*), 9.00 (d, *J* = 4.6 Hz, 2H, *H3*), 8.97 (d, *J* = 4.6 Hz, 2H, *H4*), 8.07 (d, *J* = 1.8 Hz, 4H, *H5*), 7.97 (d, *J* = 8.0 Hz, 1H, *H6*), 7.84 (t, *J* = 1.8 Hz, 2H, *H7*), 7.52 (dd, *J* = 8.0, 1.6 Hz, 1H, *H8*), 7.45 (d, *J* = 1.5 Hz, 1H, *H9*), 2.54 (s, 3H, *H10*), 1.57 (s, 36H, *H11*), 0.61 (s, 9H, *H12*), 0.31 (s, 9H, *H13*).

MALDI-TOF: *m/z* = 1098.257 ($C_{68}H_{74}N_4O_2Si_2Zn$, M^+ requires 1098.464).

Bis(TMS-acetylene)-terminated phenol-porphyrin 2.8



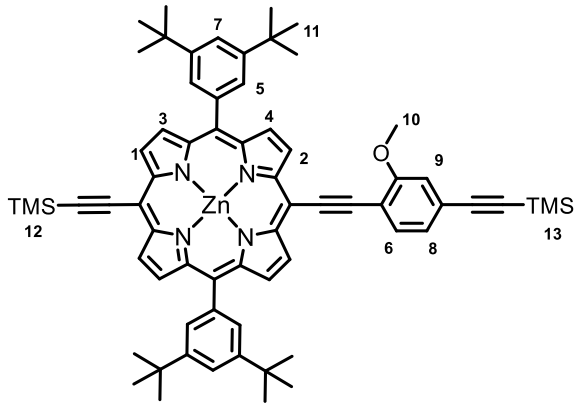
Porphyrin **2.7** (48 mg, 44 μmol) was added to a 100 mL round-bottom flask containing anhydrous THF (40 mL). Butylamine (2.0 mL, 5% v/v in THF) was added using a syringe and the reaction proceeded at room temperature for 20 min. The resulting solution was diluted with dichloromethane (40 mL) and neutralized with dilute hydrochloric acid (2.0 mL). The organic phase was extracted and washed twice with brine (20 mL) and water (30 mL × 2) and dried over Na_2SO_4. The resulting solution was concentrated under reduced pressure and the residue was

purified through a silica column chromatography (dichloromethane). Porphyrin **2.8** (35 mg, 75%) was yielded as a green solid.

^{1}H NMR (400 MHz, $CDCl_3$, 298 K) δ_H 9.62 (2 overlap d, *J* = 4.6 Hz, 4H, *H1*, *H2*), 8.91 (d, *J* = 4.6 Hz, 2H, *H3*), 8.88 (d, *J* = 4.6 Hz, 2H, *H4*), 7.97 (d, *J* = 1.8 Hz, 4H, *H5*), 7.75 (t, *J* = 1.8 Hz, 2H, *H6*), 7.73 (d, *J* = 7.9 Hz, 1H, *H7*), 7.15 (dd, *J* = 7.9, 1.5 Hz, 1H, *H9*), 3.12(s, 1H, *H10*) 1.49 (s, 36H, *H11*), 0.53 (s, 9H, *H12*), 0.24 (s, 9H, *H13*).

MALDI-TOF: *m/z* = 1057.008 ($C_{66}H_{72}N_4OSi_2Zn$, M^+ requires 1056.454).

Bis(TMS-acetylene)-terminated phenoxymethyl-porphyrin P-1



Porphyrin **2.8** (5.0 mg, 4.7 μmol) and K_2CO_3 (36 mg, 55 equiv., 0.26 mmol) were added into a 25 mL Schlenk tube and it was evacuated and backfilled with argon for three times. Anhydrous DMF (3.0 mL) and iodomethane (15 μL, 50 equiv., 0.24 mmol) were added using a syringe and the reaction proceeded at room temperature for 5 h with stirring. EtOAc (30 mL) was added to the reaction mixture and the excess K_2CO_3 was removed by filtration. The organic phase was extracted and washed with water (30 mL × 2), then dried over Na_2SO_4. The resulting solution was concentrated under reduced pressure and the crude material was purified through silica chromatography (pet. ether/EtOAc v/v, 30:1). Control molecule **P-1** (4.9 mg, 97%) was yielded as a green solid.

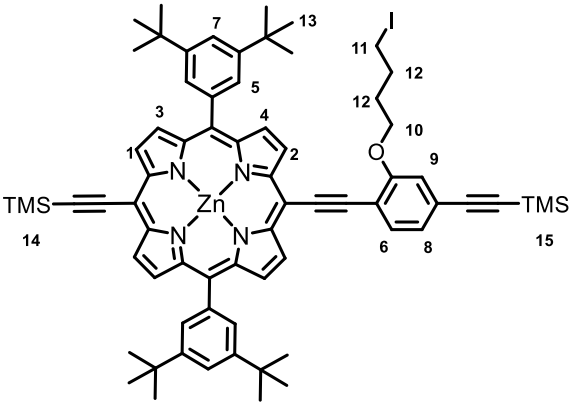
^{1}H NMR (400 MHz, $CDCl_3$, 298 K) δ_H 9.87 (d, *J* = 4.6 Hz, 2H, *H1*), 9.70 (d, *J* = 4.5 Hz, 2H, *H2*), 8.99 (d, *J* = 4.6 Hz, 2H, *H3*), 8.96 (d, *J* = 4.6 Hz, 2H, *H4*), 8.07 (d, *J* = 1.8 Hz, 4H, *H5*), 7.86 (d, *J* = 7.8 Hz, 1H, *H6*), 7.83 (t, *J* = 1.8 Hz, 2H, *H7*), 7.24 (dd, *J* = 7.8, 1.4 Hz, 1H, *H8*), 7.17 (d, *J* = 1.4 Hz, 1H, *H9*), 4.21 (s, 3H, *H10*), 1.57 (s, 36H, *H11*), 0.60 (s, 9H, *H12*), 0.32 (s, 9H, *H13*).

^{13}C NMR (126 MHz, $CDCl_3$, 298 K) δ_C 160.3, 152.4, 152.1, 150.7, 150.6, 148.9, 141.3, 133.2, 133.2, 132.7, 131.3, 131.2, 129.9, 124.9, 124.4, 121.2, 114.2, 102.2, 101.9, 96.4, 56.4, 35.2, 31.9, 29.9, 22.9, 14.3, 1.2.

MALDI-TOF: *m/z* = 1070.343 ($C_{67}H_{74}N_4OSi_2Zn$, M^+ requires 1070.469).

UV–vis (dichloromethane) λ_{max} (ε / 10^4 $M^{-1}cm^{-1}$): 468 (19.4), 616 (0.62), 676 (3.05) nm.

Bis(TMS-acetylene)-terminated phenoxy(Iodobutyl)-porphyrin 2.9-I



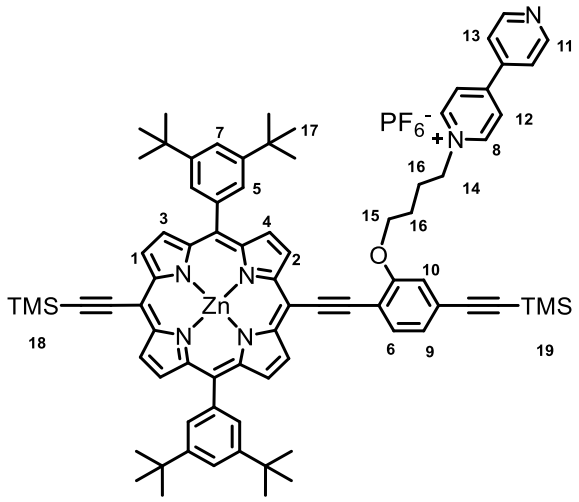
Porphyrin **2.8** (15 mg,14 μmol) and K_2CO_3 (0.11 g, 55 equiv., 0.78 mmol) were added into a 25 mL Schlenk tube and it was evacuated and backfilled with argon for three times. Anhydrous DMF (5.0 mL) and 1,4-dibromobutane (93 μL, 50 equiv., 0.71 mmol) were added using a syringe and the reaction proceeded at room temperature for 5 h with stirring. EtOAc (30 mL) was added to the reaction mixture and the excess K_2CO_3 was removed by filtration. The organic phase was extracted and washed with water (30 mL × 2), then dried over Na_2SO_4. The resulting solution was concentrated under reduced pressure and the crude material was purified through silica chromatography (pet. ether/EtOAc v/v, 30:1). Porphyrin **2.9-I** (10 mg, 89%) was yielded as a green solid.

^{1}H NMR (400 MHz, $CDCl_3$, 298 K) δ_H δ 9.88 (d, *J* = 4.6 Hz, 2H, *H1*), 9.70 (d, *J* = 4.6 Hz, 2H, *H2*), 9.00 (d, *J* = 4.5 Hz, 2H, *H3*), 8.96 (d, *J* = 4.6 Hz, 2H, *H4*), 8.06 (d, *J* = 1.8 Hz, 4H, *H5*), 7.89 (d, *J* = 7.8 Hz, 1H, *H6*), 7.83 (t, *J* = 1.8 Hz, 2H, *H7*), 7.25 (dd, *J* = 7.8, 1.4 Hz, 1H, *H8*), 7.16 (d, *J* = 1.5 Hz, 1H, *H9*), 4.34 (t, *J* = 5.9 Hz, 2H, *H10*), 3.28 (t, *J* = 6.4 Hz, 2H, *H11*), 2.41 – 2.23 (m, 4H, *H12*), 1.56 (s, 36H, *H13*), 0.60 (s, 9H, *H14*), 0.32 (s, 9H, *H15*).

^{13}C NMR (126 MHz, $CDCl_3$, 298 K) δ_C 159.4, 152.3, 151.9, 150.6, 150.5, 148.8, 141.1, 133.2, 132.9, 132.8, 131.1, 131.1, 129.8, 124.8, 124.3, 124.1, 121.1, 114.9, 67.9, 35.1, 33.4, 31.8, 29.7, 29.4, 28.2, 1.0.

MALDI-TOF: *m/z* = 1239.107 ($C_{70}H_{79}IN_4OSi_2Zn$, M^+ requires 1238.413).

Mono-charged 4,4'-bipyridinium-porphyrin 2.10-PF_6



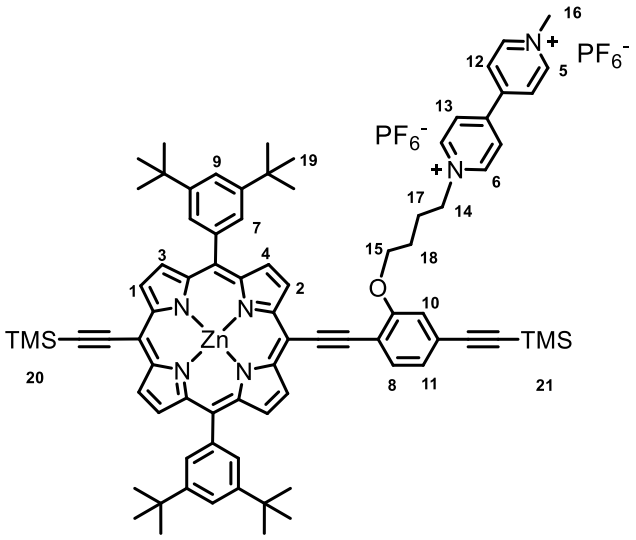
Porphyrin **2.9-I** (10 mg, 8.4 μmol) and 4,4'-bipyridine (0.13 g, 100 equiv., 0.84 mmol) were added into a 25 mL Schlenk tube and it was evacuated and backfilled with argon for three times. Anhydrous acetonitrile (2.0 mL) and toluene (1.0 mL) were added using a syringe and the reaction proceeded at 100 °C for 24 h with stirring. EtOAc (10 mL) was added to the cooled reaction mixture and the combined organic extracts washed with water (10 mL × 2) and dried over Na_2SO_4 before the solvent was removed under reduced pressure. The residue was purified through silica chromatography with 1% KPF_6 solution (dichloromethane/methanol, v/v, 20:1). Mono-charged 4,4'-bipyridinium-porphyrin **2.10-PF_6** (6.2 mg, 58%) was yielded as a green solid.

^{1}H NMR (400 MHz, MeOD, 298 K) δ_H 9.72 (d, *J* = 4.6 Hz, 2H, *H1*), 9.66 (d, *J* = 4.6 Hz, 2H, *H2*), 8.90 (d, *J* = 4.5 Hz, 2H, *H3*), 8.88 (d, *J* = 4.6 Hz, 2H, *H4*), 7.87 (d, *J* = 1.8 Hz, 4H, *H5*), 7.84 (d, *J* = 7.8 Hz, 1H, *H6*), 7.80 (t, *J* = 1.8 Hz, 2H, *H7*), 7.54 – 7.48 (m, 2H, *H8*), 7.27 (dd, *J* = 7.8, 1.3 Hz, 1H, *H9*), 7.20 (d, *J* = 1.5 Hz, 1H, *H10*), 7.18 – 7.13 (m, 2H, *H11*), 5.11 (d, *J* = 6.0 Hz, 2H, *H12*), 4.77 – 4.73 (m, 2H, *H13*), 4.40 – 4.32 (m, 4H, *H14*, *H15*), 2.03 (m, 4H, *H16*), 1.50 (s, 36H, *H17*), 0.59 (s, 9H, *H18*), 0.28 (s, 9H, *H19*).

^{13}C NMR (151 MHz, MeOD, 298 K) δ_C 152.5, 151.1, 150.7, 150.2, 149.0, 148.9, 142.6, 141.0, 133.2, 132.9, 132.5, 131.5, 130.6, 129.6, 125.1, 124.2, 122.7, 121.3, 119.5, 115.5, 77.7, 77.5, 77.2, 68.5, 61.2, 34.9, 31.4, 29.1, 25.5.

MALDI-TOF: *m/z* = 1267.852 ($C_{80}H_{87}N_6OSi_2Zn^+$, M requires 1267.577).

Porphyrin-Paraquat Conjugate P-Q2



Mono-charged 4,4'-bipyridinium-porphyrin **2.10-PF$_6$** (14 mg, 11 μmol) was added to a 10 mL Schlenk tube and it was evacuated and backfilled with argon for three times. Anhydrous acetonitrile (0.90 mL), toluene (0.30 mL) and iodomethane (0.33 mL, 500 equiv., 5.4 mmol) were added using a syringe and the reaction proceeded at 80 °C for 3 h with stirring. EtOAc (10 mL) was added to the reaction mixture and the organic phase was extracted and washed with water (10 mL × 2), then dried over Na_2SO_4. The resulting solution was concentrated under reduced pressure and the crude material was purified through silica chromatography using 1% KPF_6 solution (dichloromethane/methanol, v/v, 20:1). Porphyrin-paraquat conjugate **P-Q2** (10 mg, 76%) was yielded as a green solid.

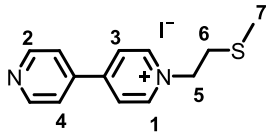
^{1}H NMR (400 MHz, acetone-d_6, 298 K) δ_H 9.58 (d, *J* = 4.5 Hz, 2H, *H1*), 9.49 (d, *J* = 4.6 Hz, 2H, *H2*), 8.75 (d, *J* = 4.5 Hz, 2H, *H3*), 8.70 (d, *J* = 4.6 Hz, 2H, *H4*), 8.45 (m, 2H, *H5*), 8.09 (d, *J* = 6.2 Hz, 2H, *H6*), 7.95 (d, *J* = 1.8 Hz, 4H, *H7*), 7.90 (d, *J* = 7.8 Hz, 1H, *H8*), 7.82 (t, *J* = 1.8 Hz, 2H, *H9*), 7.22 (d, *J* = 1.4 Hz, 1H, *H10*), 7.18 (dd, *J* = 7.8, 1.4 Hz, 1H, *H11*), 7.08 (m, 2H, *H12*), 6.91 (m, 2H, *H13*), 4.94 (dd, *J* = 9.0, 6.7 Hz, 2H, *H14*), 4.45 (t, *J* = 5.5 Hz, 2H, *H15*), 4.16 (s, 3H, *H16*),

2.43 (m, 2H, *H17*), 2.25 – 2.17 (m, 2H, *H18*), 1.44 (s, 36H, *H19*), 0.49 (s, 9H, *H20*), 0.17 (s, 9H, *H21*).

MALDI-TOF: *m/z* = 1282.494 ($C_{81}H_{90}N_6OSi_2Zn^+$, M requires 1282.600).

UV–vis (dichloromethane) λ_{max} (ε / 10^4 $M^{-1}cm^{-1}$): 477 (18.4), 662 (1.15), 712 (2.98) nm.

1-(2-(Methylthio)ethyl)-4,4'-bipyridinium 2.12-I

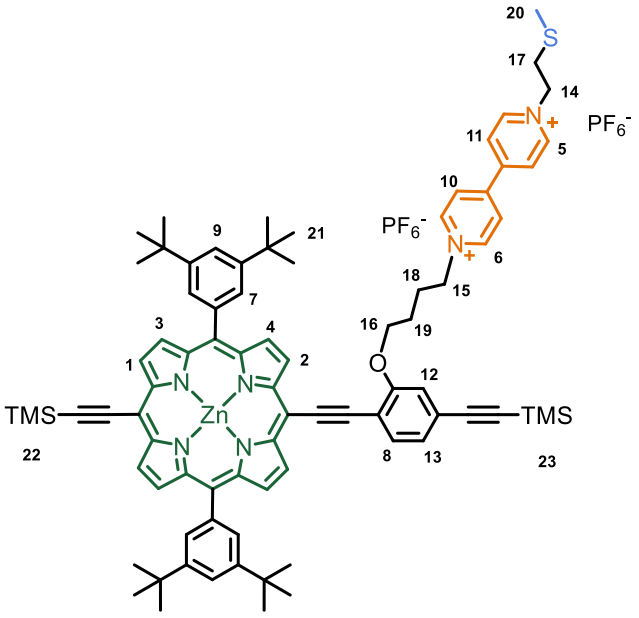


(2-Iodoethyl)(methyl)sulfane **2.11-I** (2.0 g, 9.9 μmol) and 4,4'bipyridine (6.2 g, 4.0 equiv., 40 mmol) were added into a Schlenk tube and it was evacuated and backfilled with argon for three times. Anhydrous acetone (8.0 mL, dried over 3 Å molecular sieves) was added using a syringe and the reaction proceeded at room temperature for 20 h with stirring. The reaction was monitored by TLC and after the completion, toluene (20 mL) was added to precipitate the product. 1-(2-(Methylthio)ethyl)-4,4'-bipyridinium **2.12-I** (2.0 g, 86%) was yielded as a light-yellow solid after filtration.

^{1}H NMR (400 MHz, MeOD, 298 K) δ_H 9.13 (d, *J* = 7.0 Hz, 2H, *H1*), 8.86 – 8.82 (m, 2H, *H2*), 8.55 (d, *J* = 6.9 Hz, 2H, *H3*), 8.02 – 7.96 (m, 2H, *H4*), 4.89 (t, *J* = 6.5 Hz, 2H, *H5*), 3.19 (t, *J* = 6.4 Hz, 2H, *H6*), 2.20 (s, 3H, *H7*).

HR MS: *m/z* = 231.0943[M] ($C_{13}H_{15}N_2S^+$, M requires 231.0950).

Porphyrin-Paraquat Conjugate P-Q1



Porphyrin **2.9-I** (28 mg, 23 μmol) and 1-(2-(methylthio)ethyl)-4,4'-bipyridinium **2.12-I** (0.52 g, 100 equiv., 2.3 mmol) were added into a 25 mL Schlenk tube and it was evacuated and backfilled with argon for three times. Anhydrous acetonitrile (1.6 mL) and toluene (0.8 mL) were added using a syringe and the reaction proceeded at 80 °C for 4 days with stirring. After the mixture cooled down to room temperature, the excess bipyridinium salt was removed by filtration washing with toluene and the solvent was removed by blowing nitrogen flow. The residue was purified through a slow silica column chromatography eluting with 1% KPF_6 solution (dichloromethane/acetone, v/v, gradient elution from 20:1 to 10:1, then change the solvent to a mixture of methanol/acetone/dichloromethane, v/v, 5:20:75). The recrystallized porphyrin-paraquat conjugate **P-Q1** (6.5 mg, 21%) from dichloromethane/pentane was yielded as a green solid.

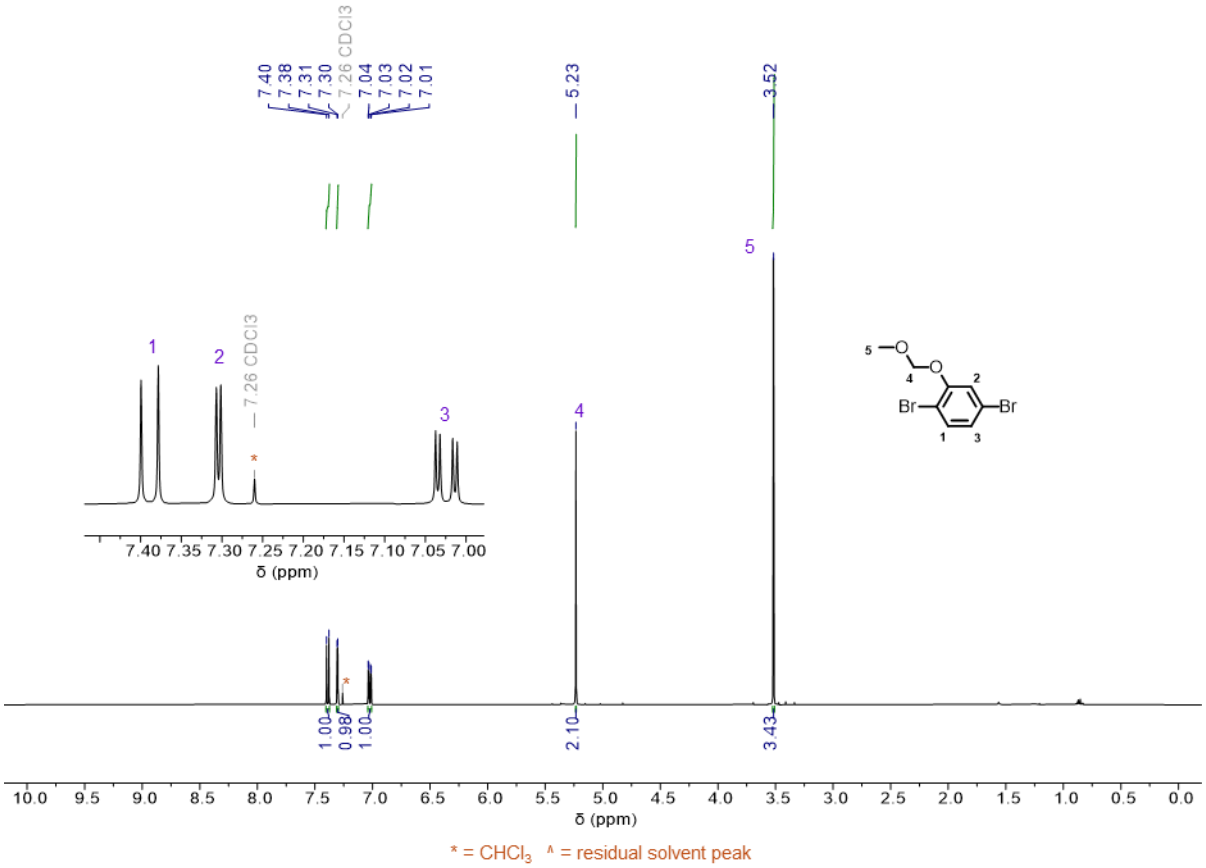
^{1}H NMR (600 MHz, acetone-d_6, 298 K) δ_H 9.84 (d, J = 4.6 Hz, 2H, *H1*), 9.70 (d, J = 4.6 Hz, 2H, *H2*), 8.95 (d, J = 4.5 Hz, 4H, *H3*, *H4*), 8.92 (d, J = 4.6 Hz, 2H, *H5*), 8.53 (d, J = 6.5 Hz, 2H, *H6*), 8.09 (d, J = 2.0 Hz, 4H, *H7*), 8.08 (d, J = 7.8 Hz 1H, *H8*), 7.99 (t, J = 1.8 Hz, 2H, *H9*), 7.52 (d, J = 6.3 Hz, 2H, *H10*), 7.35 (d, J = 1.4 Hz 1H, *H12*), 7.34 (dd, J = 7.8, 1.4 Hz 1H, *H13*), 7.31 (d, J = 6.4 Hz, 2H, *H11*), 5.18 – 5.12 (m, 2H, *H14*), 4.82 (t, J = 6.6 Hz, 2H, *H15*), 4.61 (t, J = 5.8 Hz, 2H, *H16*), 3.06 (t, J = 6.6 Hz, 2H, *H17*), 2.64 – 2.57 (m, 2H, *H18*), 2.40 – 2.34 (m, 2H, *H19*), 2.12 (s, 3H, *H20*), 1.59 (s, 36H, *H21*), 0.64 (s, 8H, *H22*), 0.30 (s, 9H, *H23*).

^{13}C NMR (151 MHz, acetone-d_6, 298 K) δ_C 159.6, 152.0, 151.5, 150.5, 150.3, 149.0, 147.8, 144.8, 141.3, 133.1, 132.9, 131.0, 129.6, 129.6, 125.6, 125.0, 124.9, 124.5, 124.2, 121.4, 115.5, 114.4, 104.7, 101.2, 100.5, 96.0, 68.3, 61.9, 60.2, 34.8, 34.4, 31.1, 29.6, 29.4, 25.7, 14.2

MALDI-TOF: m/z = 1342.516 ($C_{83}H_{94}N_6OSSi_2Zn^{2+}$, M^{2+} requires 1342.603).

UV–vis (dichloromethane) λ_{max} (ε / 10^4 $M^{-1}cm^{-1}$): 469 (19.3), 610 (0.71), 670 (1.96) nm.

Selected NMR Spectra



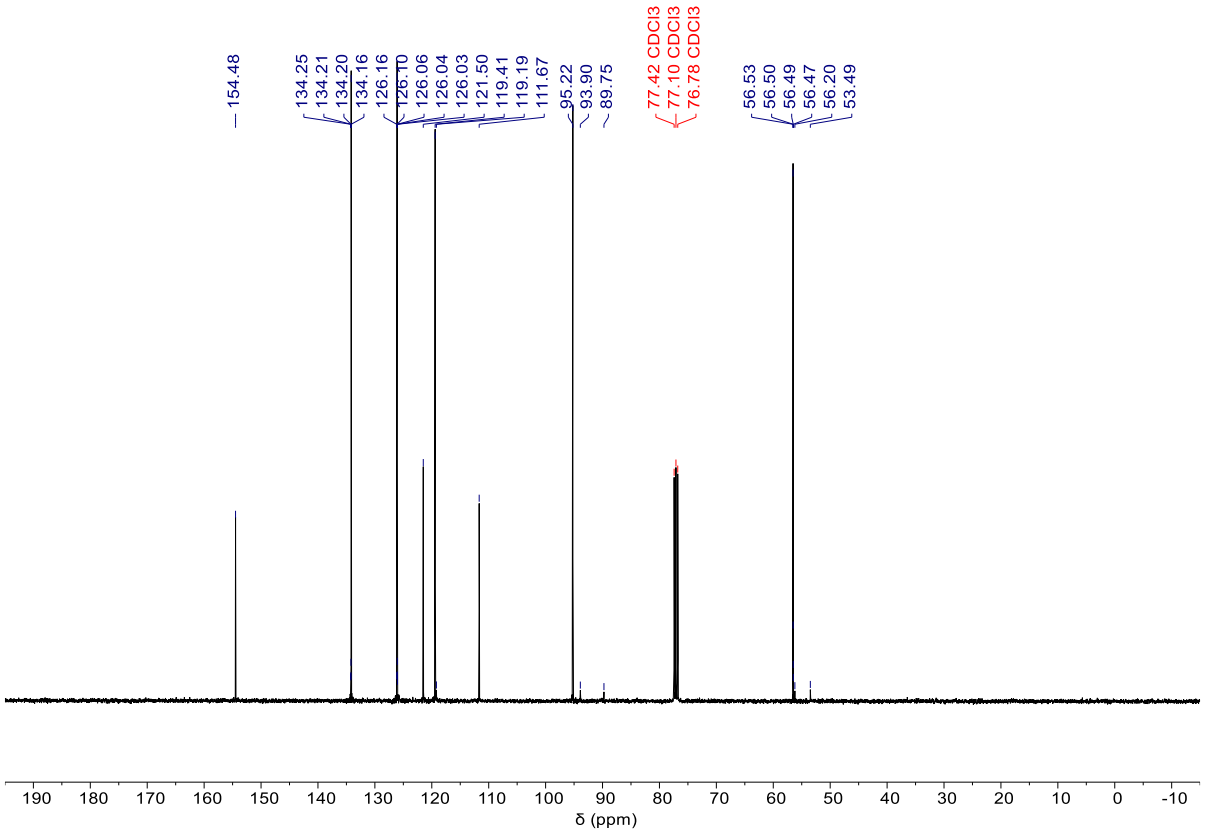


Figure S2.1: (top) ^{1}H NMR (400 MHz) and (bottom) ^{13}C NMR (101 MHz) spectra of **2.1** ($CDCl_3$, 298 K).

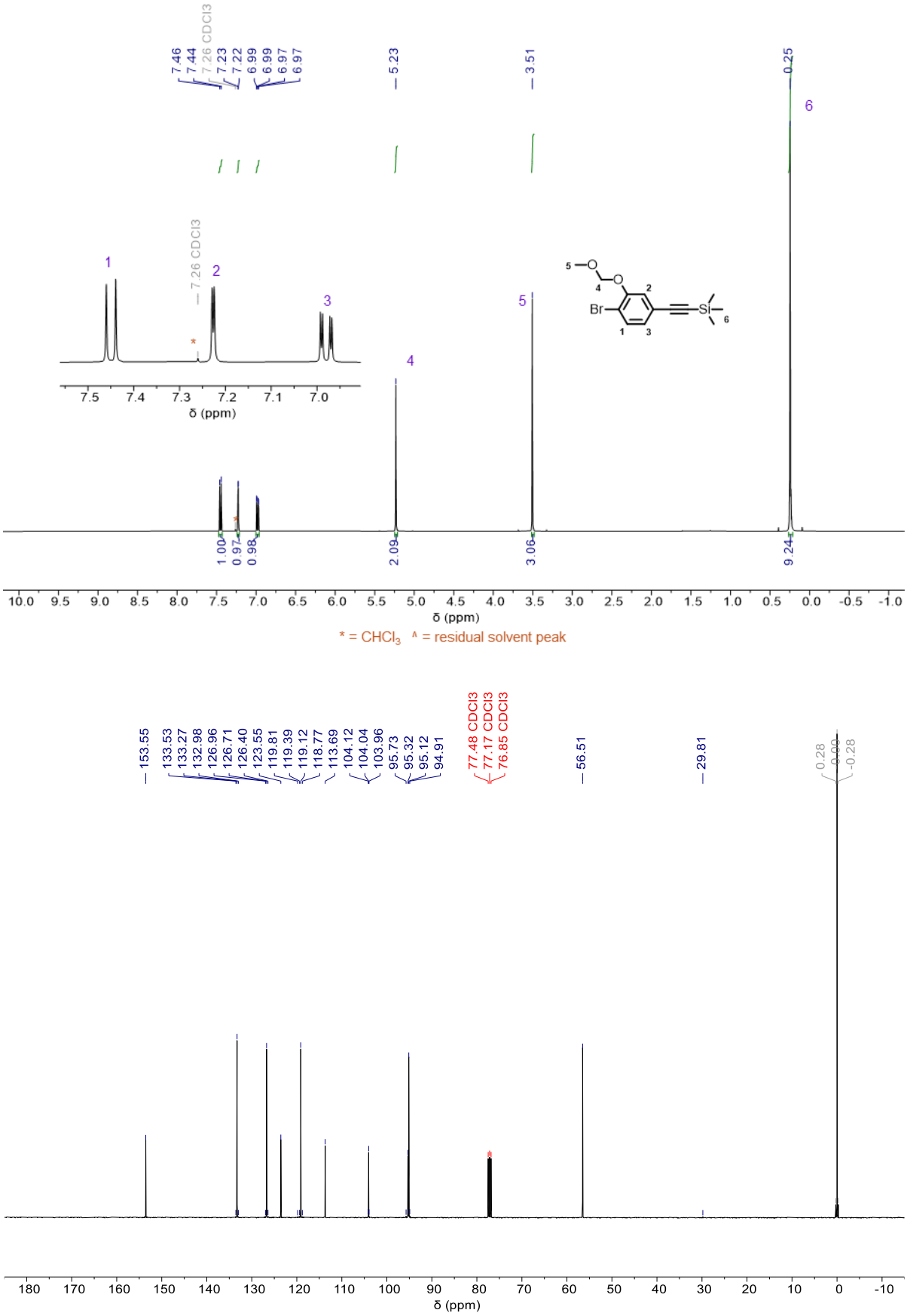


Figure S2.2: (top) ^{1}H NMR (400 MHz) and (bottom) ^{13}C NMR (101 MHz) spectra of **2.2** ($CDCl_3$, 298 K).

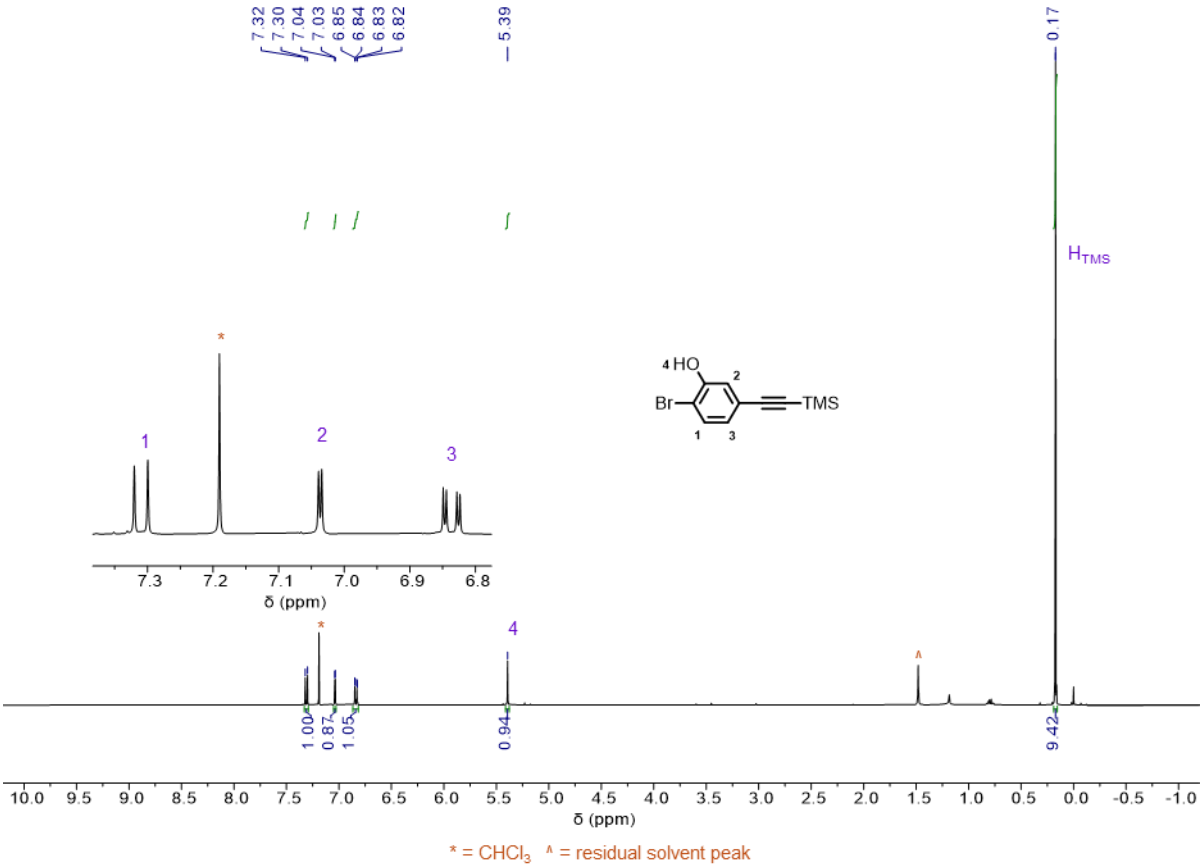


Figure S2.3: ^{1}H NMR (400 MHz) spectrum of **2.3** ($CDCl_3$, 298 K).

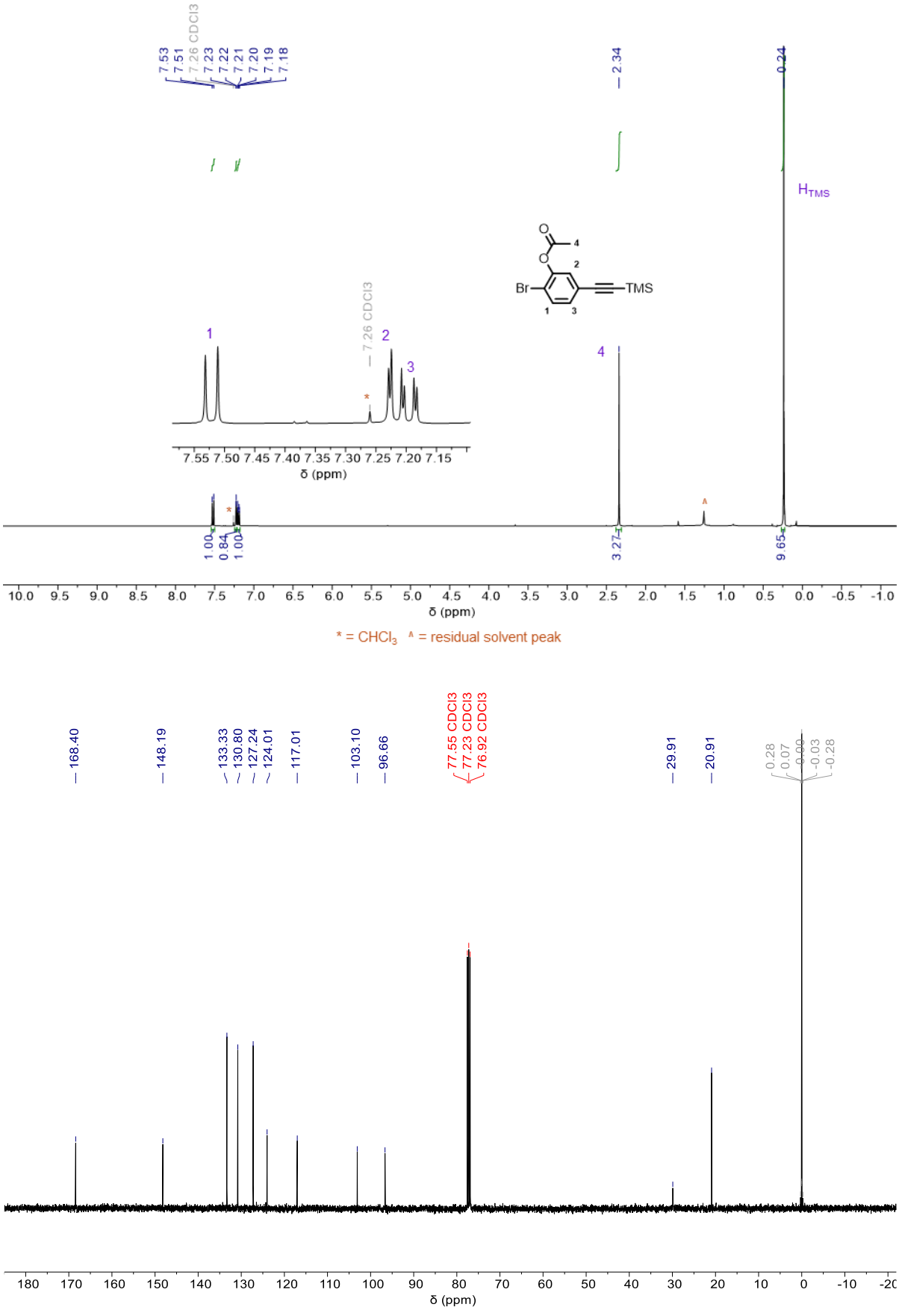


Figure S2.4: (top) ^{1}H NMR (400 MHz) and (bottom) ^{13}C NMR (101 MHz) spectra of **2.4** ($CDCl_3$, 298 K).

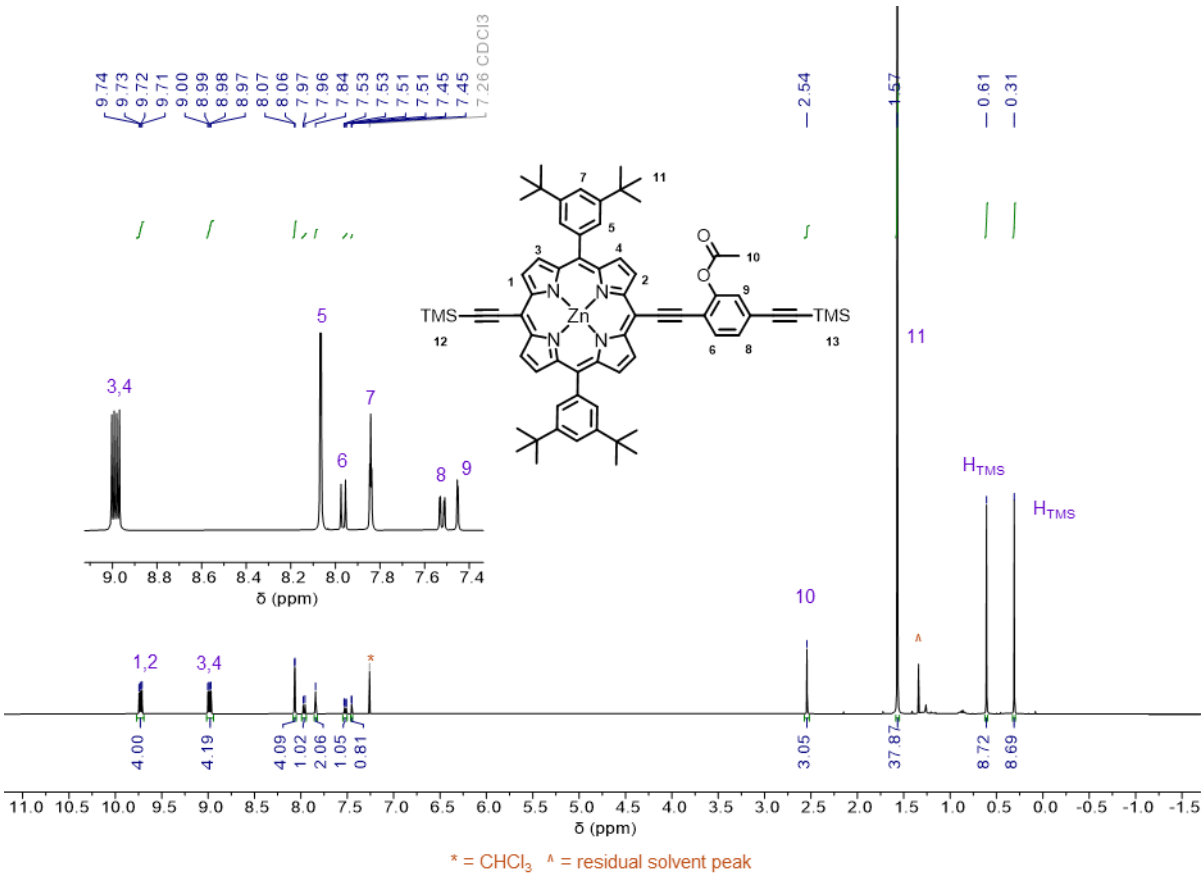


Figure S2.5: ^{1}H NMR (400 MHz) spectrum of porphyrin **2.7** ($CDCl_3$, 298 K).

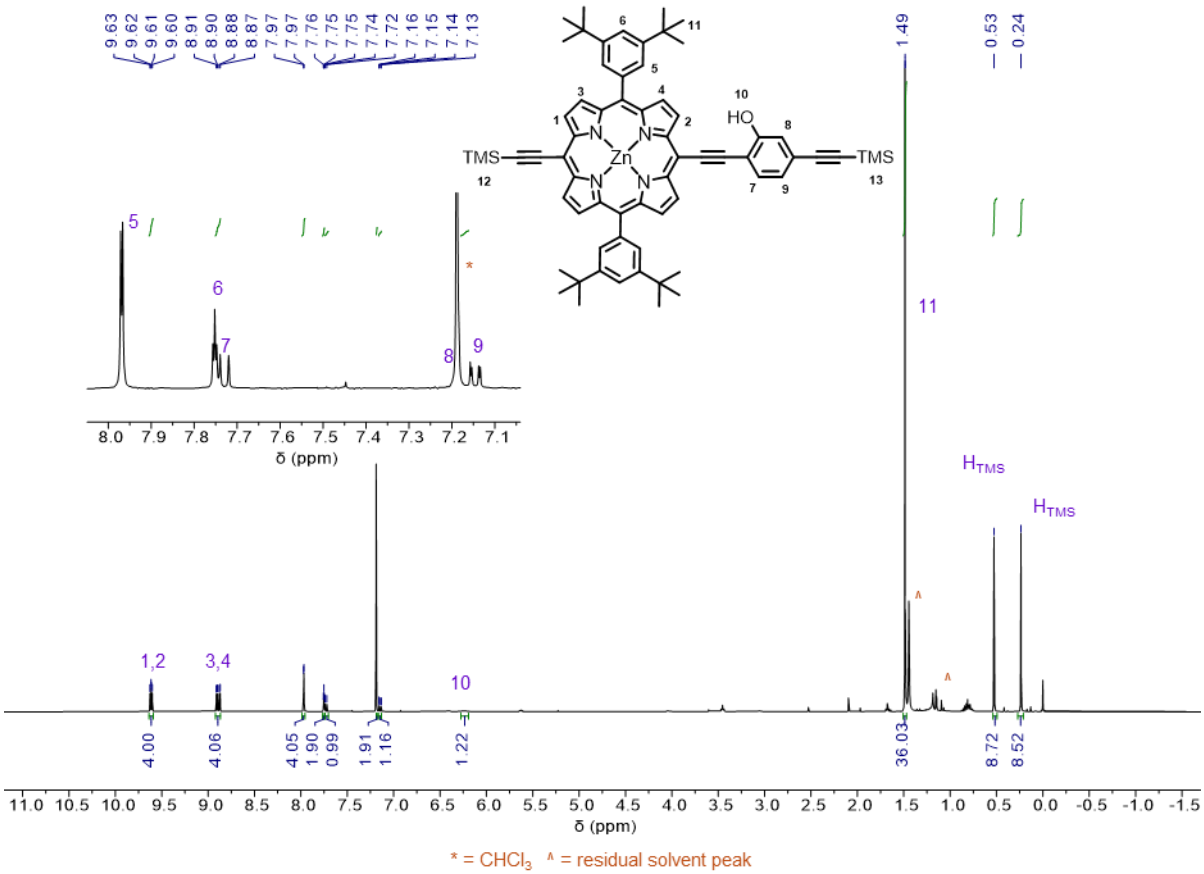


Figure S2.6: ^{1}H NMR (400 MHz) spectrum of porphyrin **2.8** ($CDCl_3$, 298 K).

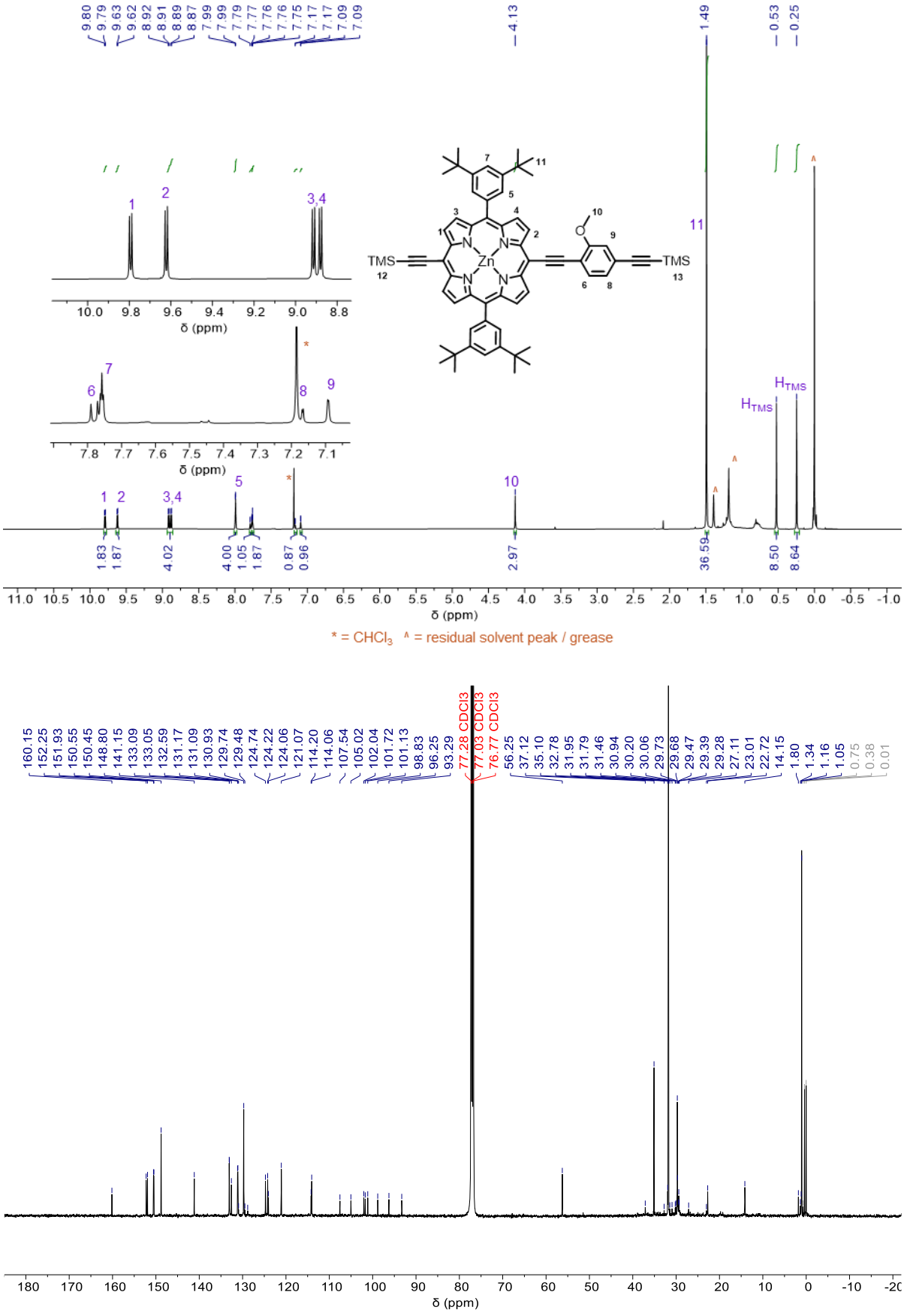


Figure S2.7: (top) ^{1}H NMR (400 MHz) and (bottom) ^{13}C NMR (126 MHz) spectra of porphyrin **P-1** ($CDCl_3$, 298 K).

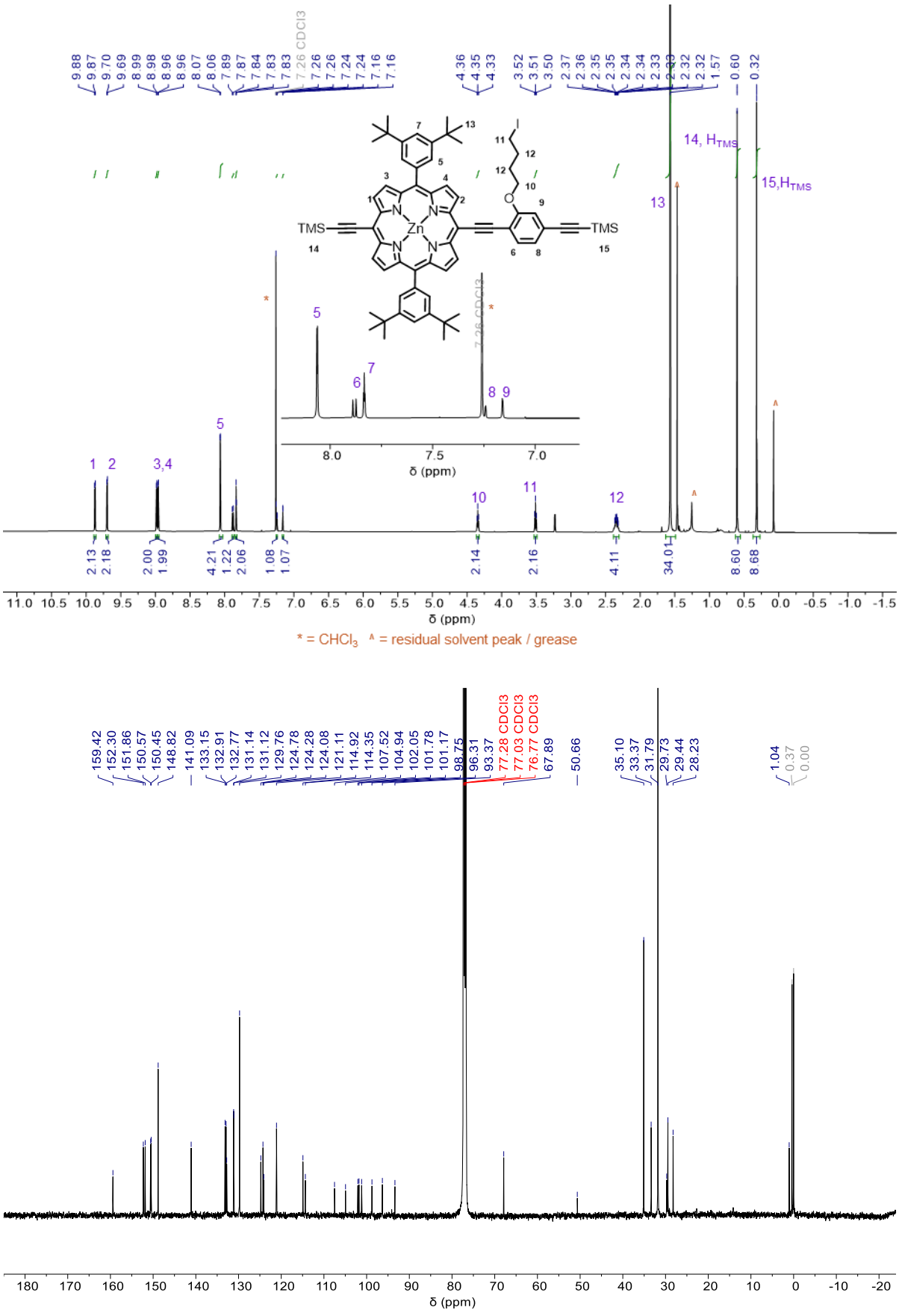


Figure S2.8: (top) ^{1}H NMR (400 MHz) and (bottom) ^{13}C NMR (126 MHz) spectra of porphyrin **2.9-I** ($CDCl_3$, 298 K).

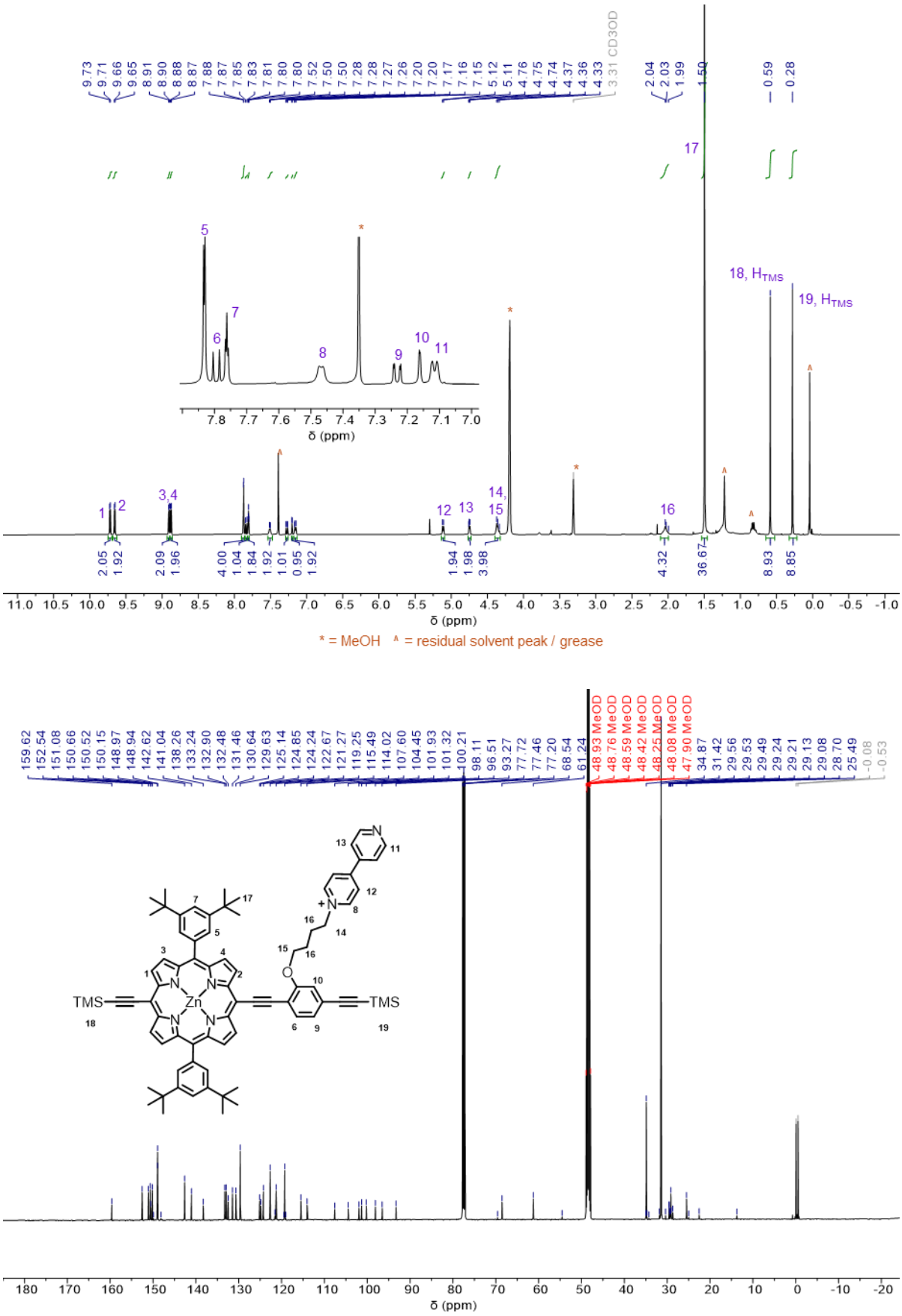


Figure S2.9: (top) ^{1}H NMR (400 MHz) and (bottom) ^{13}C NMR (151 MHz) spectra of porphyrin **2.10-PF$_6$** (MeOD, 298 K).

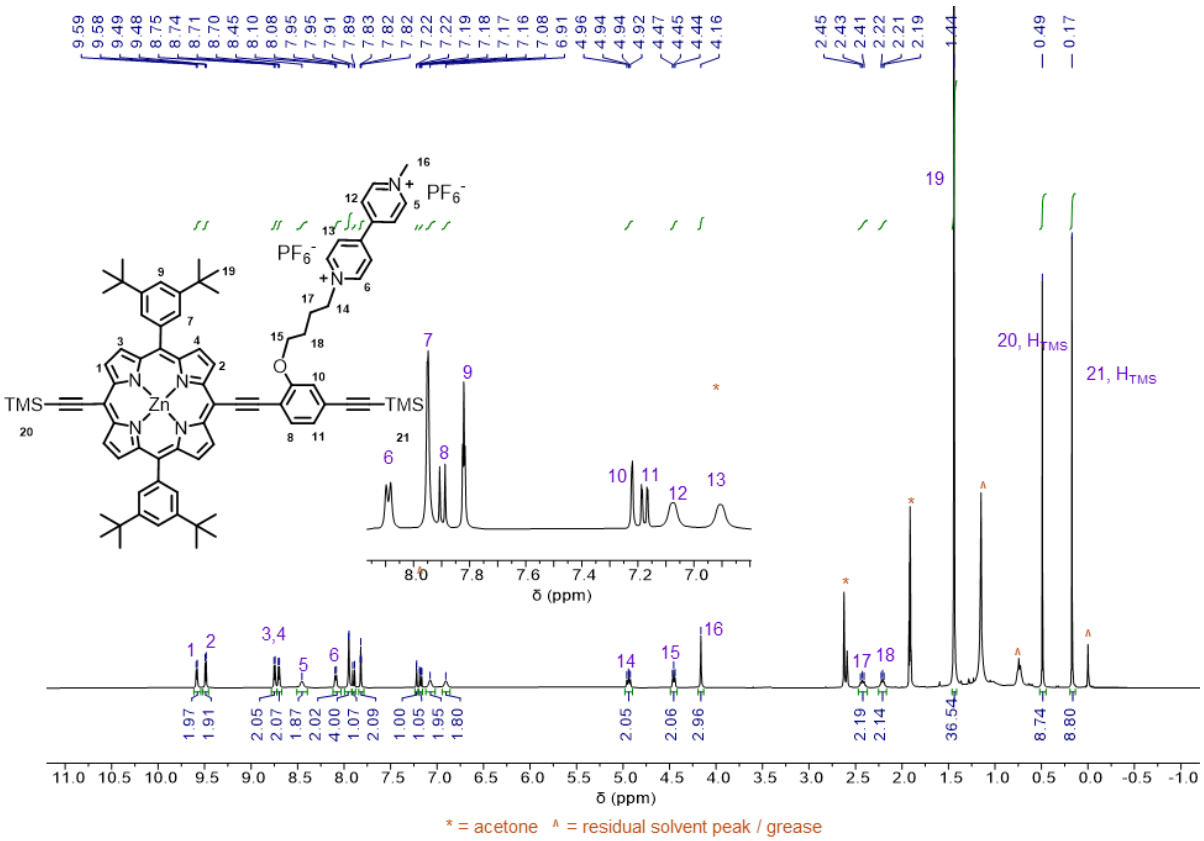


Figure S2.10: ^{1}H NMR (400 MHz) spectrum of porphyrin-paraquat conjugate **P-Q2** (acetone-d_6, 298 K).

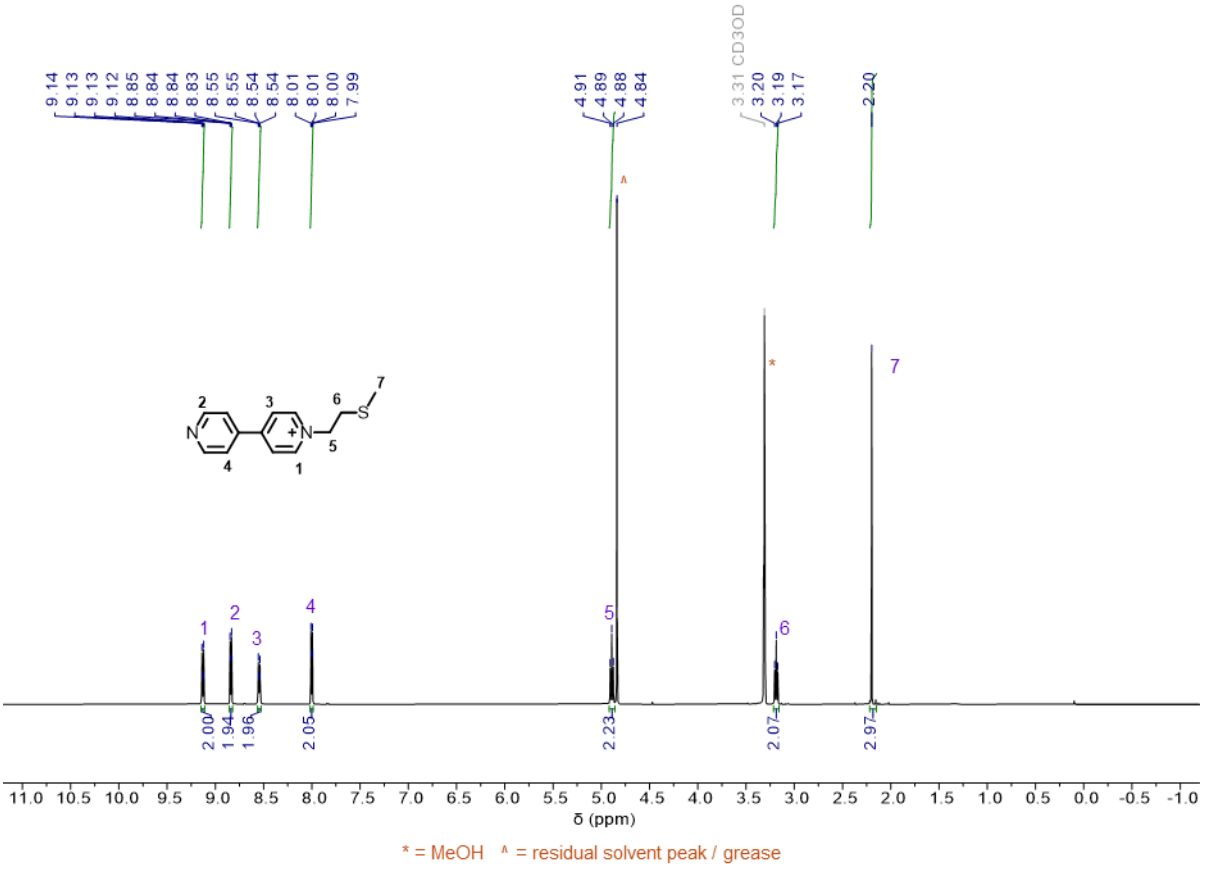


Figure S2.11: ^{1}H NMR (400 MHz) spectrum of **2.12-I** (acetone-d_6, 298 K).

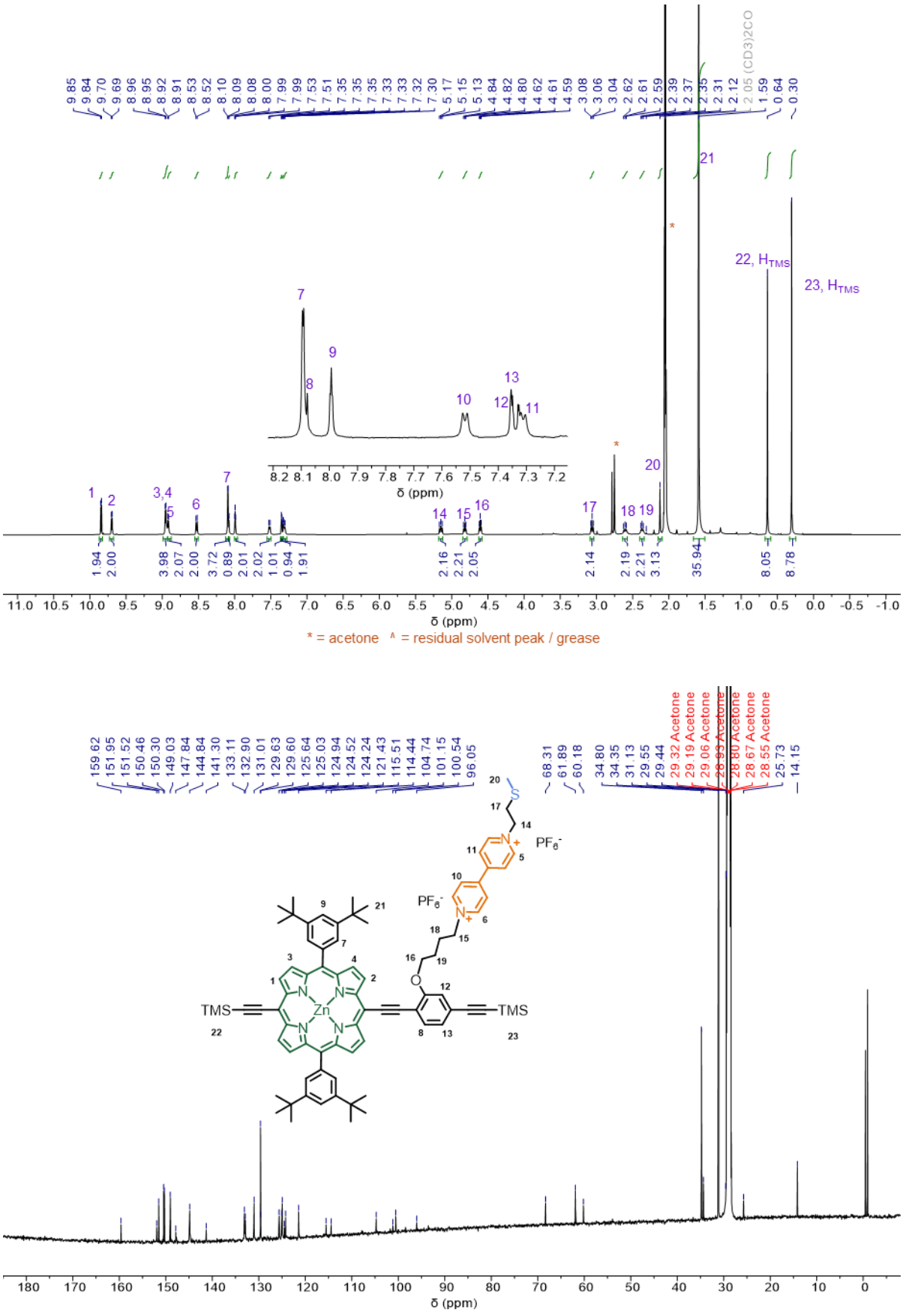


Figure S2.12: (top) ^{1}H NMR (600 MHz) and (bottom) ^{13}C NMR (151 MHz) spectra of porphyrin-paraquat conjugate **P-Q1** (acetone-d_6, 298 K).

Selected UV–vis–NIR Absorption Spectra

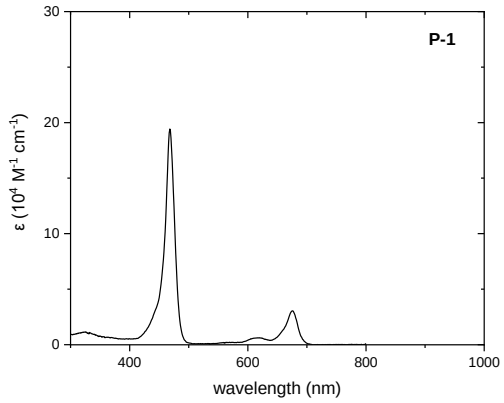


Figure S2.13: UV–vis absorption spectrum of **P-1** in dichloromethane (298 K).

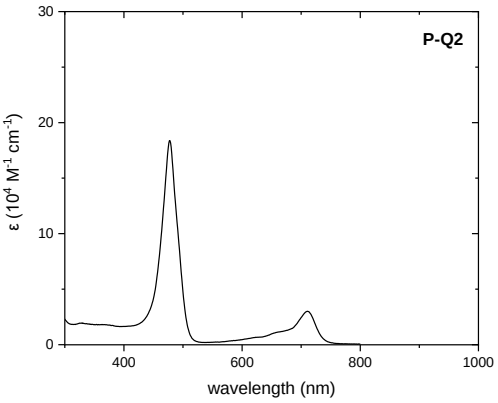


Figure S2.14: UV–vis absorption spectrum of **P-Q2** in dichloromethane (298 K).

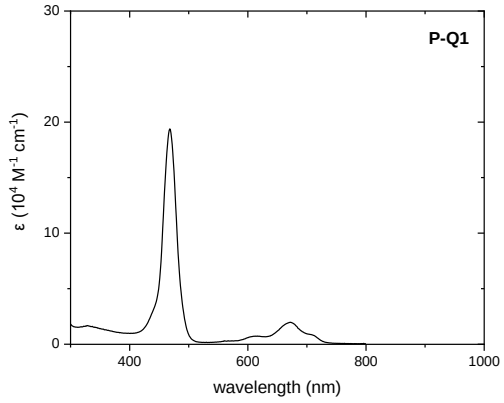
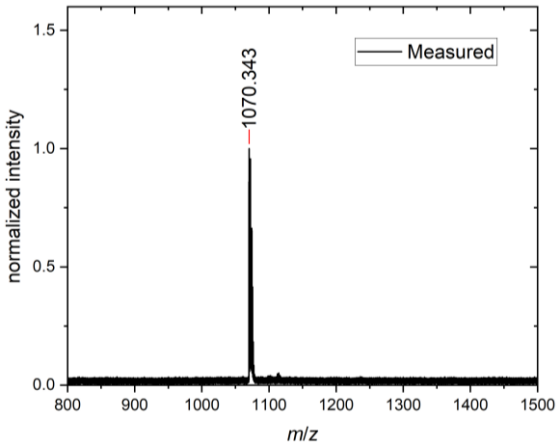
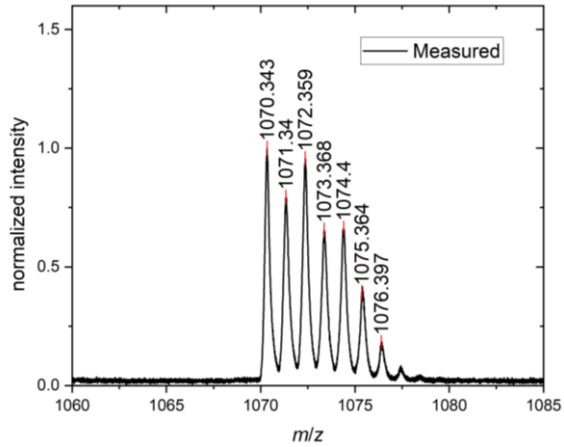


Figure S2.15: UV–vis absorption spectrum of **P-Q1** in dichloromethane (298 K).

Selected Mass Spectra





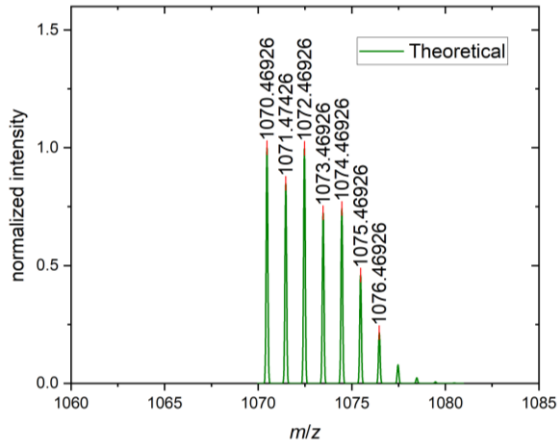
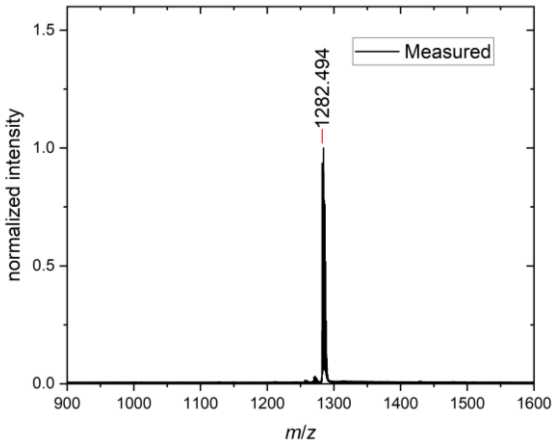
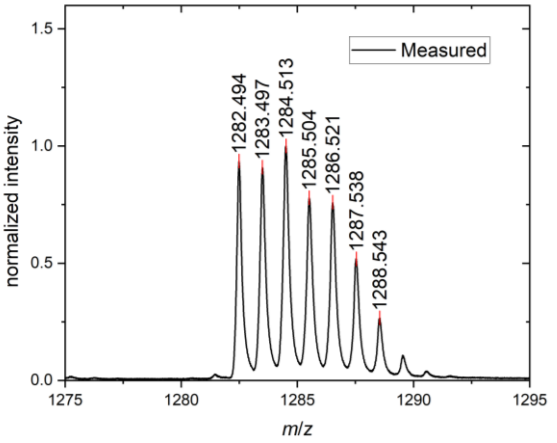


Figure S2.16: MALDI-TOF MS spectrum of **P-1**.





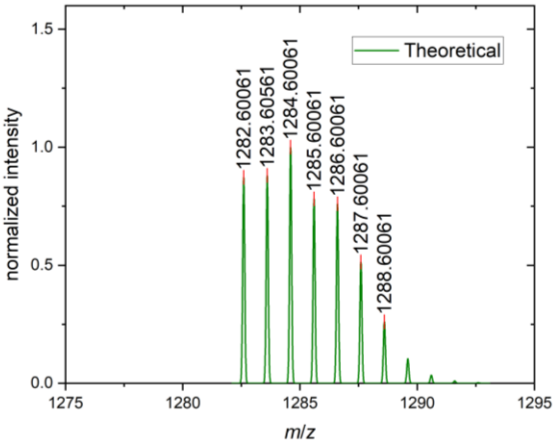


Figure S2.17: MALDI-TOF MS spectrum of **P-Q2**.

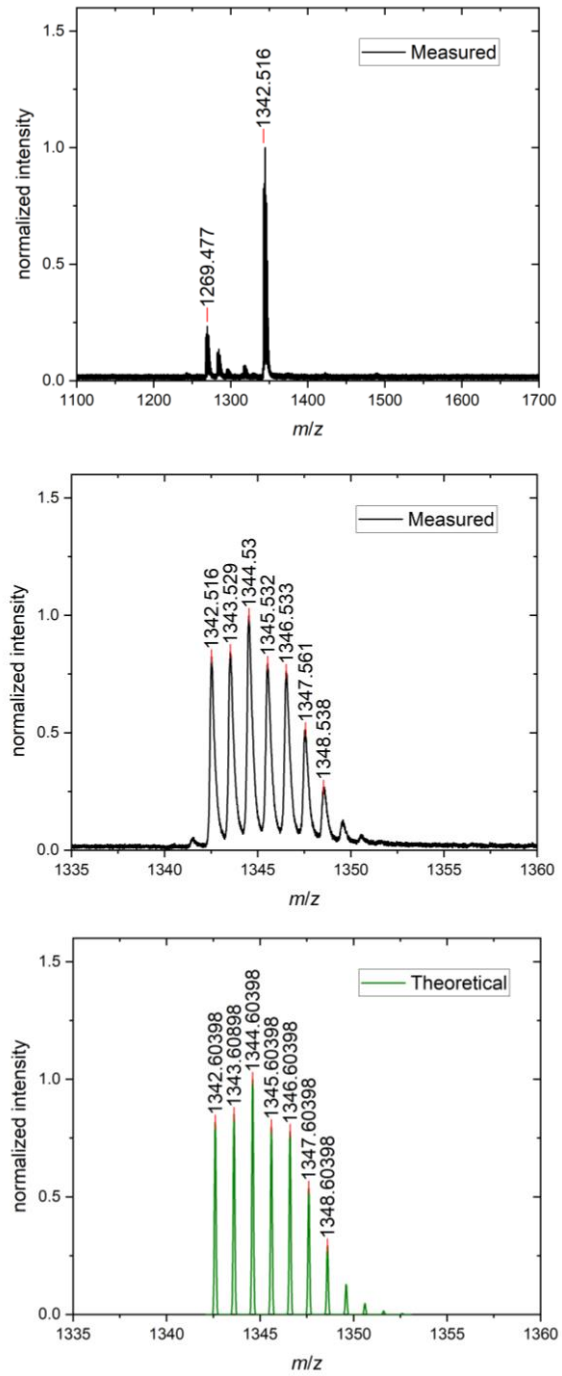


Figure S2.18: MALDI-TOF MS spectrum of **P-Q1**.

References

1 G. Garcia, D. Naud-Martin, D. Carrez, A. Croisy and P. Maillard, *Tetrahedron*, 2011, **67**, 4924–4932.

2 M. J. Langton, J. D. Matichak, A. L. Thompson and H. L. Anderson, *Chem. Sci.*, 2011, **2**, 1897.

3 M. J. Plater, S. Aiken and G. Bourhill, *Tetrahedron*, 2002, **58**, 2405–2413.

4 C. Roche, Q. Luo, G. Gil-Ramírez, H. W. Jiang, D. R. Kohn, Y. Xiong, A. L. Thompson and H. L. Anderson, *J. Org. Chem.*, 2017, **82**, 7446–7462.

5 D. E. Sunko, B. Juršić and M. Ladika, *J. Org. Chem.*, 1987, **52**, 2299–2301.

3

Anthracene-Porphyrin Nanoribbons

Contents

3.1 Introduction 90

3.1.1 π-Extension of Porphyrins 90

3.1.2 Anthracene-Fused Porphyrins 92

3.1.3 Project Aim 93

3.2 Synthesis of Anthracene-Fused Porphyrins Dimers and Trimer 94

3.2.1 Computational Study of Infinite Polymers 94

3.2.2 Molecular Design and Synthetic Approaches 95

3.2.3 X-ray Crystal Structure, Optoelectronic Properties and Metal Exchange Feasibility 98

3.3 Extending Anthracene-Porphyrin Hybrid System 102

3.3.1 Preparation of a Bisanthracene-Fused Porphyrin Dimer 102

3.3.2 Development of Different Solubilizing Groups 105

3.3.3 Stability of Hexyl-Enlarged Solubilizing Group 111

3.4 Conclusions 113

3.5 References 115

3.6 Experimental 118

Parts of the work in this chapter were published in:

H. Zhu, Q. Chen, I. Rončević, K. E. Christensen and H. L. Anderson, *Angew. Chem. Int. Ed.*, 2023, **62**, e202307035. (also in *ChemRxiv*, 2023, DOI: 10.26434/chemrxiv-2023-zl7ck).

Chapter 3 - Anthracene-Porphyrin Nanoribbons

3.1 Introduction

One-dimensional nanostructures, such as nanoribbons or nanotubes, crafted from small π-conjugated molecular building blocks are emerging candidates for organic semiconductors. These materials allow for precisely tuning the electronic band structure and optical properties of semiconductors at the molecular level, with synthetic control over their size, structure and composition.[1] Porphyrins, with high chemical versatility and structural robustness, are one class of intriguing aromatic building units in this field of research.[2–4] Over the past decades, the fine-tuning of their optoelectronic properties has been demonstrated with dozens of examples, through effective perturbations of their electronic structures by peripheral substitution, ligand coordination, or exchange of the central metal ion.[5–7] Together with their markedly improved synthetic accessibility, porphyrins have been extensively considered in the applications such as sensing, light harvesting and molecular optoelectronics.[8–12]

3.1.1 π-Extension of Porphyrins

Assembling porphyrins into oligomers through diverse chemical linkages or conjugatively modifying the periphery of porphyrins with aromatic segments are effective strategies for expanding the π-conjugated system of porphyrins. From a structural viewpoint, the π-extension of porphyrins are classified into (a) *meso*-linked porphyrin oligomers, (b) *β*, *β* fusion type, (c) *meso, β* fusion type, (d) *meso*-aryl (Ar), *β* fusion type, and (e) *β*, *meso, β* fusion type (Figure 3.1).[5]

For porphyrin oligomers, the type of linker between individual units is the decisive factor impacting the extent of inter-porphyrin coupling and structural rigidity.[5] As discussed in

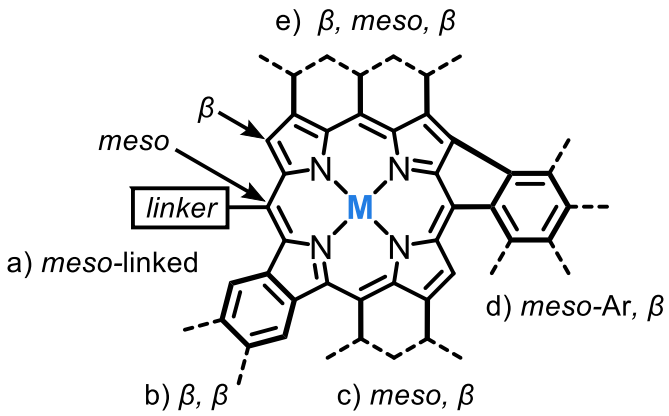


Figure 3.1: The π-extension types of porphyrin. Reproduced with permission.[5]

Chapter 1, triply linked porphyrin oligomers exhibit highly delocalized π-conjugation within the whole molecule, leading to extremely strong inter-porphyrin interactions, evidenced by their remarkable bathochromic shift of the Q band as the number of porphyrin units increases.[12] Their one-dimensional extended configurations and high single-molecule conductance over long distances with low attenuation make them attractive candidates for the construction of molecular wires.[13–16]

Pioneering work by Cammidge *et al.* documented the intramolecular cyclization between porphyrin and naphthalene, which unintentionally gave the first observation of the effective π-extension of the porphyrin core using polycyclic aromatic hydrocarbons (PAHs).[17] Since then, fusing PAHs or aromatic heterocycles directly onto the porphyrin periphery has been demonstrated as an effective means of expanding the π-conjugated electronic network of porphyrins to generate the so-called π-extended porphyrins. Through intramolecular ring-closure reactions, porphyrin and the aromatic segments are covalently connected. This enforces the formation of a combined coplanar conformation, assuring the enhanced electronic interactions between the porphyrin and the fused aromatic segment. A variety of aromatic units have been used to extend porphyrin π-systems, including anthracene, pyrene, azulene and other polycyclic aromatics. [5,18–23] These enlarged conjugated systems have emerged as appealing subjects in fields spanning from nonlinear optical materials to photodynamic therapy due to their intriguing optoelectronic feature.[24–27]

Structurally hybridizing porphyrin oligomers with PAHs will afford a ribbon-like scaffold reminiscent of heteroatom-doped graphene nanoribbons (GNRs). The copolymers are expected to preserve the conjugation throughout the entire molecule meanwhile PAHs act as a novel linker to vary the electronic communication between each porphyrin. While the potential of π-extending a single porphyrin unit has been extensively explored, the synthesis of nanostructures combining these two prominent materials to form alternating porphyrin-PAH hetero-oligomers remains scarce. To date, only *N*-annulated-perylene has been successfully fused in between two porphyrins to form a dimer through solution-based synthesis (Figure 3.2).[26] Examples such as porphyrin dimers (linked by up to four fused

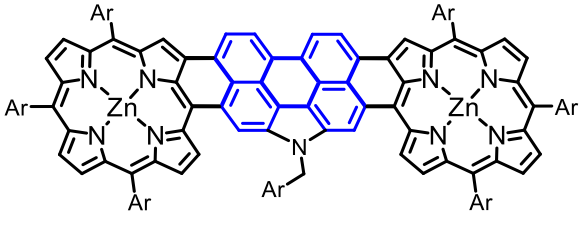


Figure 3.2: Structure of *N*-annulated-perylene-fused porphyrin dimer (Ar: 3,5-di(*t*-butyl)phenyl).[26]

anthracenes, Figure 3.3) and a porphyrin polymer (incorporating narrow benzenoid and non-benzenoid nanographene as spacers) have emerged recently, from on-surface synthesis.[28,29] Nevertheless, on-surface annealing methodology limits the investigation of their macroscopic properties and the access to their bulk synthesis is essential for practical applications.

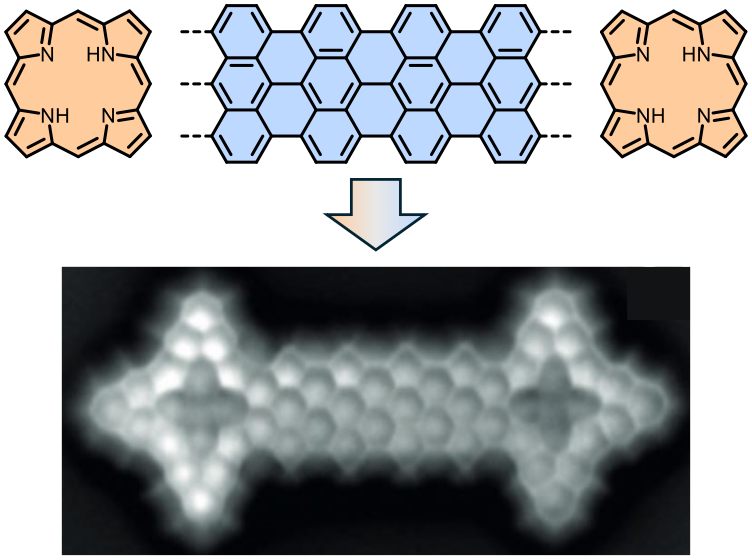


Figure 3.3: On-surface synthesized porphyrin-anthracene hybrid nanoribbon and the bond-resolved AFM image. Reproduced with permission.[28]

3.1.2 Anthracene-Fused Porphyrins

Anthracene stands out among the choices of PAH substituents to extend the porphyrin π-structure owing to its structural compatibility with the porphyrin periphery. As shown in Figure 3.4, the zigzag edge of the anthracene geometrically fit the *meso*- and *β*-positions of porphyrin, with an average size difference of 0.03 Å in between two units (based on the crystal structure data of 12 porphyrins).[30,31,40,41,32–39] In earlier work, Davis *et al.* has demonstrated that the introduction of anthracene onto porphyrin can cause a significant narrowing of the energy gaps.[18–20] Compared to porphyrin monomers, the bathochromic shift of the Q band in absorption spectra caused by mono-anthracenyl π-extension is 0.86 eV (from 525 nm to 828 nm in chloroform),

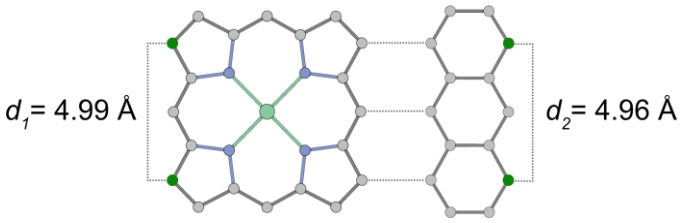


Figure 3.4: Comparison of porphyrin and anthracene crystal geometries and sizes based on the crystal structure data of twelve porphyrins. (All selected porphyrins are 5,15-proton-10,20-aryl substituted, with Ni(II), Zn(II) and Cu(II) as central coordinated metal ions).[30,31,40,41,32–39]

1.09 eV (from 525 nm to 973 nm in chloroform) by bis-anthracenyl and more dramatically 1.37 eV (from 553 nm to 1417 nm in toluene) by tetra-anthracenyl (Figure 3.5). However, it was found that in order to promote the oxidative fusion with porphyrin, the anthracene unit was essential to equipped with an electron-donating ether substituent *para* to the point of fusion. This requirement made it impossible to fuse an anthracene bridge between two porphyrins. This impasse has now been overcome by using the improved Scholl reaction conditions pioneered by Rathore and co-workers in combination with Ni(II) metalation of the porphyrins, so that they are not demetallated by the strongly acidic condition.[42–44]

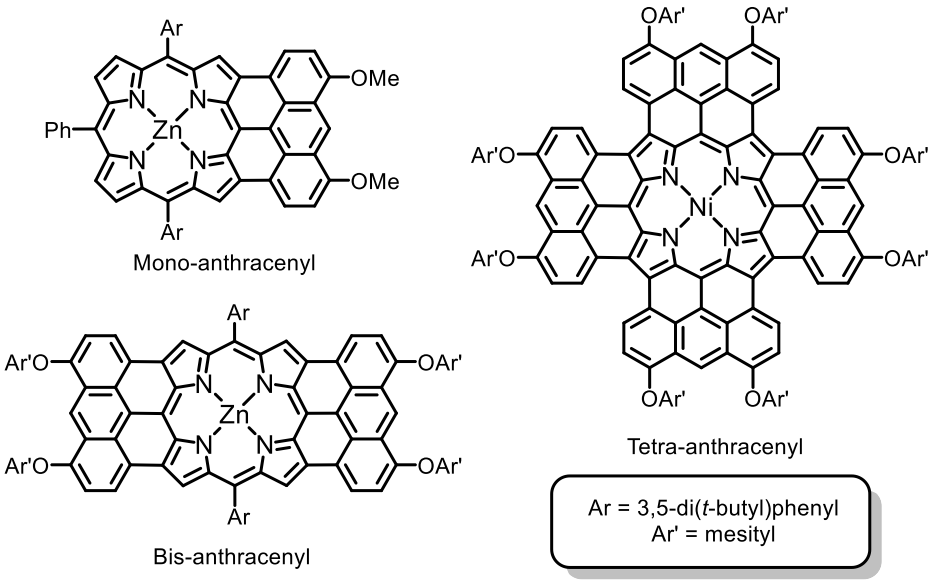


Figure 3.5: Structures of previously reported mono-anthracenyl, bis-anthracenyl and tetra-anthracenyl fused porphyrins.[18–20]

3.1.3 Project Aim

Using anthracene as repeating units and one-dimensionally extended the π-system forms the armchair GNR with 7-atom width, termed as **7-AGNR** (Figure 3.6). In conjunction with porphyrin ribbons (**P*N***) by fusing anthracene as the linker, this project aims to understand the extent to which the optoelectronic features would be altered by forming their hetero-oligomers (**AP*N***, Figure 3.6). In this chapter, we first theoretically investigate the properties of an infinite fully fused polymer structure consisting of alternating porphyrin and anthracene units, as the hybrid between **7-AGNR** and **P*N***. We then demonstrate the synthetic accessibility to short oligomers (dimer and trimer) to model this anthracene-fused porphyrin nanoribbon system. Considering strong oxidation conditions required in the final cyclodehydrogenation reactions,

Ni(II) porphyrins are selected here to build the target molecules. To further extend the structure, an exploration of the side aryl group design is conducted, for which the ideal option is meant to enhance the solubility while also being stable under fusion reaction conditions.

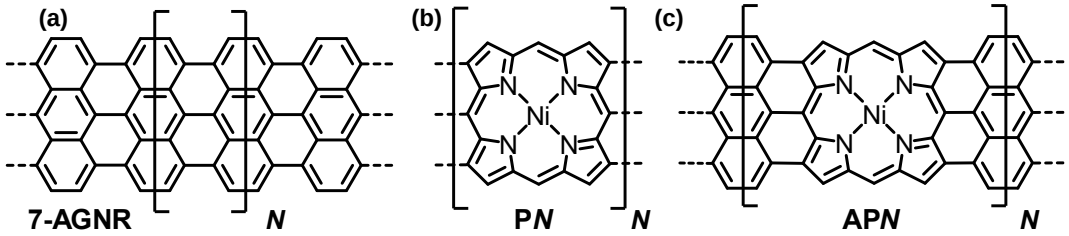


Figure 3.6: Infinite polymer structures of (a) **7-AGNR**, (b) **P*N*** and (c) **AP*N***.

3.2 Synthesis of Anthracene-Fused Porphyrins Dimers and Trimer

3.2.1 Computational Study of Infinite Polymers

In order to evaluate how the electronic structure of this anthracene-fused porphyrin nanoribbon differs from its parent molecules, a theoretical comparison of **AP*N***, **7-AGNR** and **P*N***, with Ni(II) coordinated in every porphyrin, was performed. The calculation followed a similar procedure as published by Grau-Crespo which studied the band structure of infinite Zn(II) coordinated porphyrin ribbons.[45] The geometry optimizations was performed using a dispersion-corrected Perdew–Burke–Ernzerhof functional (PBE-D2) with total energy converged to 0.01 meV.[46,47] This was followed by a single-point calculation using a short-range screened hybrid function developed by Heyd, Scuseria, and Ernzerhof (HSE06), which has 25% exact exchange in the short range and 0% in the long range.[48] Band structures and density of states were obtained by interpolating the HSE06 band energies using Boltztrap2, which was also used to compute the charge transport properties.[49] Band energies are reported with respect to the vacuum reference.

The theoretical band gap of **7-AGNR** is E_g = 2.03 eV, which is in good agreement with experimental data.[50,51] For an infinitely long **P*N*** strand, the calculated band gap is E_g = 0.34 eV, where the presence of the Ni(II) cation in **P*N*** significantly increases the band gap, compared with the corresponding Zn(II) complex.[45] The calculated band gap for the hybrid **AP*N*** is E_g = 0.45 eV, which is almost as narrow as that of **P*N***. The band structure calculations summarized in Figure 3.7 indicate that the effective masses of the charge carriers in the

conduction band and valence band, m_{CB} and m_{VB}, for **APN** and **PN** are exceptionally low, implying that these polymers should exhibit higher charge-carrier mobilities than **7-AGNR** (the relation between effective mass and charge carrier mobility will be discussed in Chapter 4). Therefore, we can expect **APN** as a structure to offer new options for organic semiconductors.

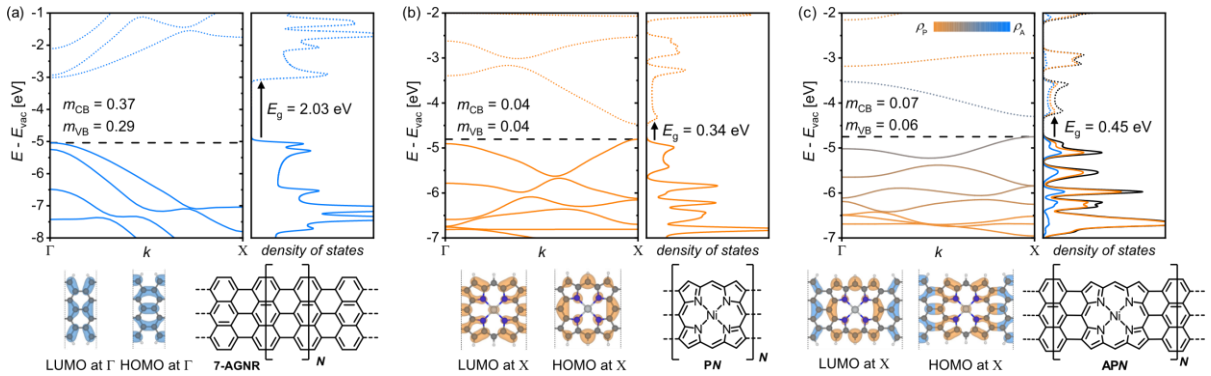


Figure 3.7: Band structures, density of states, and frontier orbitals plots of (a) **7-AGNR**, (b) ***PN*** and (c) ***APN***. The band gap (E_g), valence and conductance band, and effective mass (m_{CB} and m_{VB}) are shown; energies are reported relative to the vacuum reference. The color scale in the case of ***APN*** represents for the proportion of electron density on anthracene (blue) or porphyrin (orange); occupied and unoccupied levels are shown by solid and dotted lines, respectively.

3.2.2 Molecular Design and Synthetic Approaches

Fully fused anthracene-linked porphyrin dimers and trimer (Figure 3.8) were targeted as model structures of ***APN***. An important feature of the porphyrin design is to use *meso*-aryl solubilizing substituents with *ortho*-methyl groups (*e.g.*, mesityl or 2,6-dimethyl-4-dodecylphenyl in Figure 3.8) to prevent accidental oxidative fusion of the aryl group with the *β*-position of porphyrin (*i.e.*, to prevent the formation of a 5-membered ring).

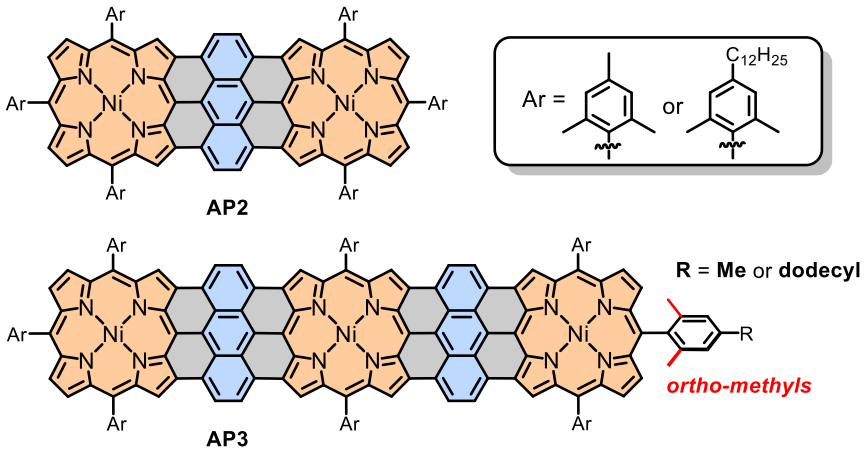
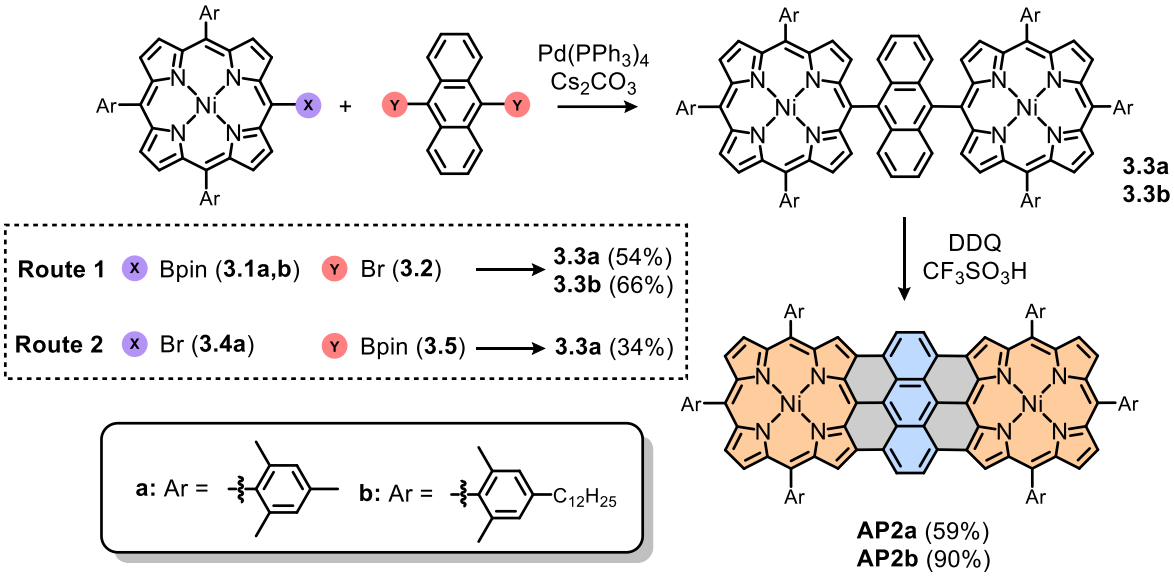


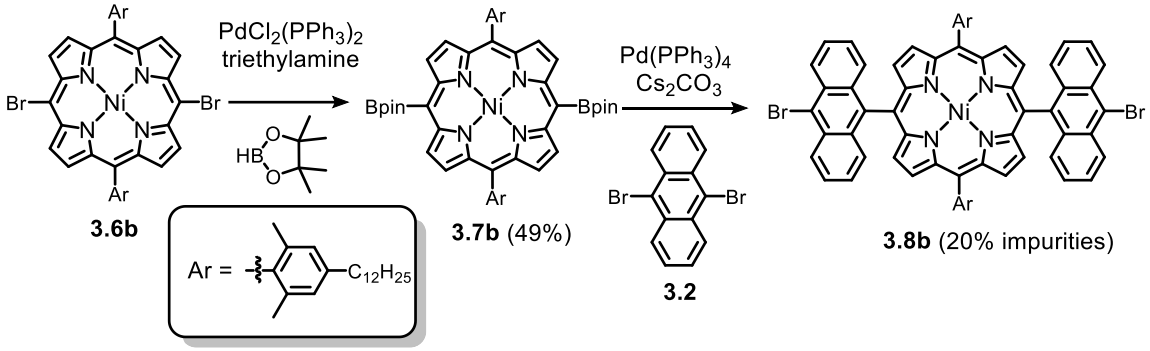
Figure 3.8: Structure of fully fused anthracene-linked porphyrin dimers and trimer as model structures of ***APN***.

Synthesis of the anthracene-fused porphyrin dimers **AP2a** and **AP2b** (with mesityl and 2,6-dimethyl-4-dodecylphenyl aryl groups, respectively, Scheme 3.1, *Route 1*) started with a Suzuki-Miyaura coupling of the porphyrin boronate ester **3.1a**,**b** with 9,10-dibromoanthracene **3.2** to give **3.3a**,**b** in 54% and 66% yield, respectively. Swapping the boron and bromine functional groups in the coupling partners for this reaction (*i.e.*, attempting to synthesize **3.3a** from the bromoporphyrin **3.4a** and the anthracene diboronic acid **3.5**, Scheme 3.1, *Route 2*) was less successful, only yielding 34% of **3.3a**. This is due to the reduced stability of the boronate ester when attached to anthracene, together with the formation of an inseparable bisanthracene-linked porphyrin dimer by-product. Oxidative cyclodehydrogenation of **3.3a** and **3.3b** with 2,3-dichloro-5,6-dicyano-1,4-benzoquinone (DDQ) and trifluoromethanesulfonic acid (CF_3SO_3H, TfOH) in dichloromethane (1:100, v/v) gave the fully fused dimers **AP2a** (59%) and **AP2b** (90%).[23] The mesityl-substituted dimer **AP2a** is only soluble enough for NMR characterization in CS_2/CD_2Cl_2, whereas **AP2b** dissolves well in solvents such as dichloromethane and toluene. ^{1}H and ^{13}C NMR spectra of **AP2a** and **AP2b** recorded in the CS_2/CD_2Cl_2 (2:1, v/v) are well resolved and display the expected pattern of resonances.



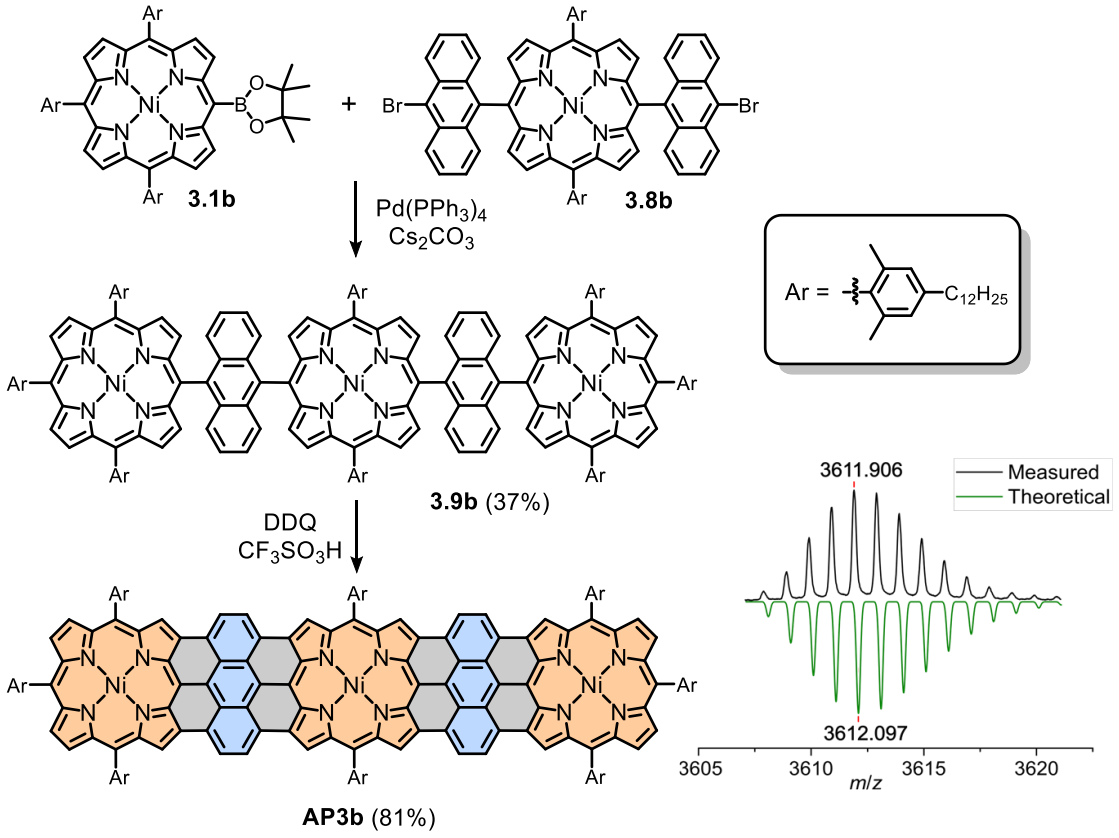
Scheme 3.1: Synthesis of **AP2a** and **AP2b**.

The fully fused anthracene-linked porphyrin trimer could only be prepared by employing the more soluble 2,6-dimethyl-4-dodecylphenyl-substituted porphyrins (Scheme 3.2), since the cyclodehydrogenated product of the mesityl substituted derivative was highly insoluble.



Scheme 3.2: Synthesis of bisanthracenyl-porphyrin linker **3.8b**.

Dipinacolborate ester porphyrin **3.7b**, obtained from the borylation of dibromoporphyrin **3.6b**, was first subjected to **3.2**, which led to the formation of bisanthracenyl-porphyrin **3.8b** with 20 mol% inseparable monoanthracenyl-porphyrin impurities (based on ^{1}H NMR). Suzuki-Miyaura coupling of **3.1b** with **3.8b** gave the pure singly linked precursor **3.9b** in 37% yield (Scheme 3.3). Ring closure to **AP3b** was realized under the same Scholl reaction conditions in 81% yield. The well resolved MALDI-TOF mass spectrum of **AP3b** shows the expected molecular ion (Scheme 3.3, insert) and demonstrates that 16 H atoms are removed in the oxidative cyclodehydrogenation step. The ^{1}H NMR spectrum of the fused trimer **AP3b** (measured in CD_2Cl_2/CS_2, Figure S3.15) is consistent with the structure,



Scheme 3.3: Synthesis of **AP3b**. (Inset: experimental and calculated isotope patterns for the molecular ion of **AP3b** from MALDI-TOF MS analysis.)

although some peaks are poorly resolved, and this compound was not soluble enough to record its ^{13}C NMR spectrum.

3.2.3 X-ray Crystal Structure, Optoelectronic Properties and Metal Exchange Feasibility

The structure of **AP2a** was confirmed by X-ray single-crystal diffraction analysis of crystals grown by slow diffusion of ethanol vapor into a solution of **AP2a** in CD_2Cl_2/CS_2 (Figure 3.9). The central 24-atom coronene core of the dimer is essentially flat (root-mean-square deviation 0.039 Å), but the porphyrins bend away from this plane generating an S-shaped geometry. The nonplanar conformation of the porphyrin units (root-mean-square deviation of 24-atom core: 0.23 Å) is similar to that in many tetrasubstituted Ni(II) porphyrin, and is attributed to the small radius of the Ni(II) cation.[7] The molecular unit has a C_2 symmetry axis and the asymmetric unit contains one porphyrin and half the anthracene core. Molecules of **AP2a** pack into infinite linear strands with the mesityl group of one molecule making C–H/π-interactions with the next molecule in the chain (H···π distances: 2.63–3.35 Å; Figure 3.10).

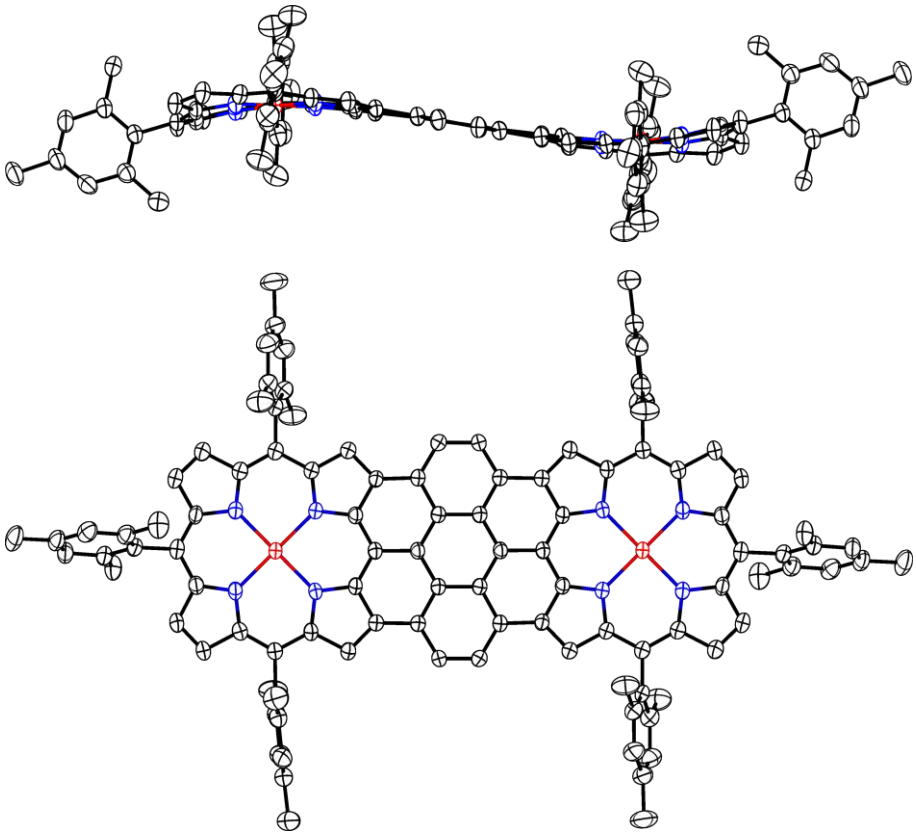


Figure 3.9: Side view (top) and front view (bottom) X-ray single-crystal structure of **AP2a**. Hydrogen atoms omitted for clarity. Thermal ellipsoids plotted at the 50% level.

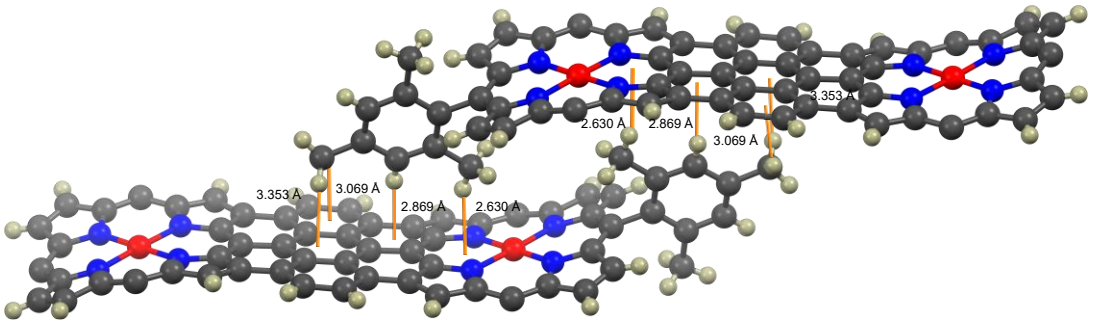


Figure 3.10: Partial X-ray crystallographic structure of **AP2b** highlighting C–H/π interactions in between two closely packed molecules. The distance is measured from hydrogen atom (from the molecule nearby) to the calculated mean plane of central 24-atom coronene core.

In order to evaluate the effect of the anthracene units on the electronic properties of these nanoribbons, we synthesized the directly edge-fused porphyrin dimer **P2b** and trimer **P3b** (Figure 3.11), and compared their UV–vis–NIR absorption spectra with those of **AP2b** and **AP3b** (Figure 3.12; dimers in red; trimers in blue). All spectra were recorded in toluene-d_8 since most solvents have a vibrational overtone NIR absorption band (*e.g.*, at 1160 nm for dichloromethane and 1670 nm for toluene) that overlap with Q bands of **AP2b** and **AP3b**, resulting in an undesired distortion of the spectra. The absorption spectra of **P2b** and **P3b** display typical features for porphyrin ribbons, with Q bands at 874 nm and 1157 nm, respectively.[52,53] The incorporation of an anthracene bridge in **AP2b** results in a sharp intense absorption band at 1188 nm (optical gap 1.04 eV). The absorption maximum of **AP3b** shows a further red-shift to 1642 nm (optical gap 0.76 eV). Thus, **AP2b** and **AP3b** both exhibit strongly red-shifted absorption spectra, compared with their counterparts without anthracene units, **P2b** and **P3b**, respectively. The absorption spectra of **AP2b** and **AP3b** are in good agreement with the calculated transitions from time-dependent DFT (TD-DFT) calculations using the B3LYP functional (Figure 3.13).

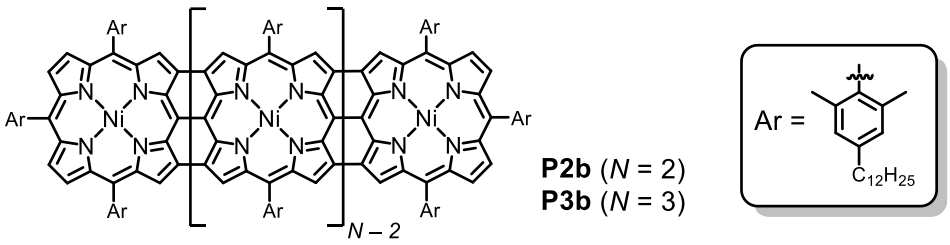


Figure 3.11: Structures of fused porphyrin dimer **P2b** and trimer **P3b**, which were synthesized for comparison with **AP2b** and **AP3b**.

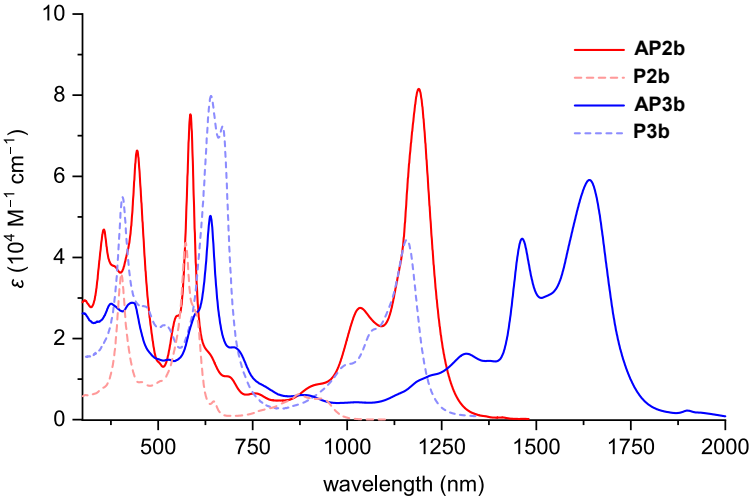


Figure 3.12: UV–vis–NIR absorption spectra of **AP2b** and **AP3b** in comparison with the corresponding directly edge-fused porphyrin dimer **P2b** and trimer **P3b** (measured in toluene-d_8 at room temperature).

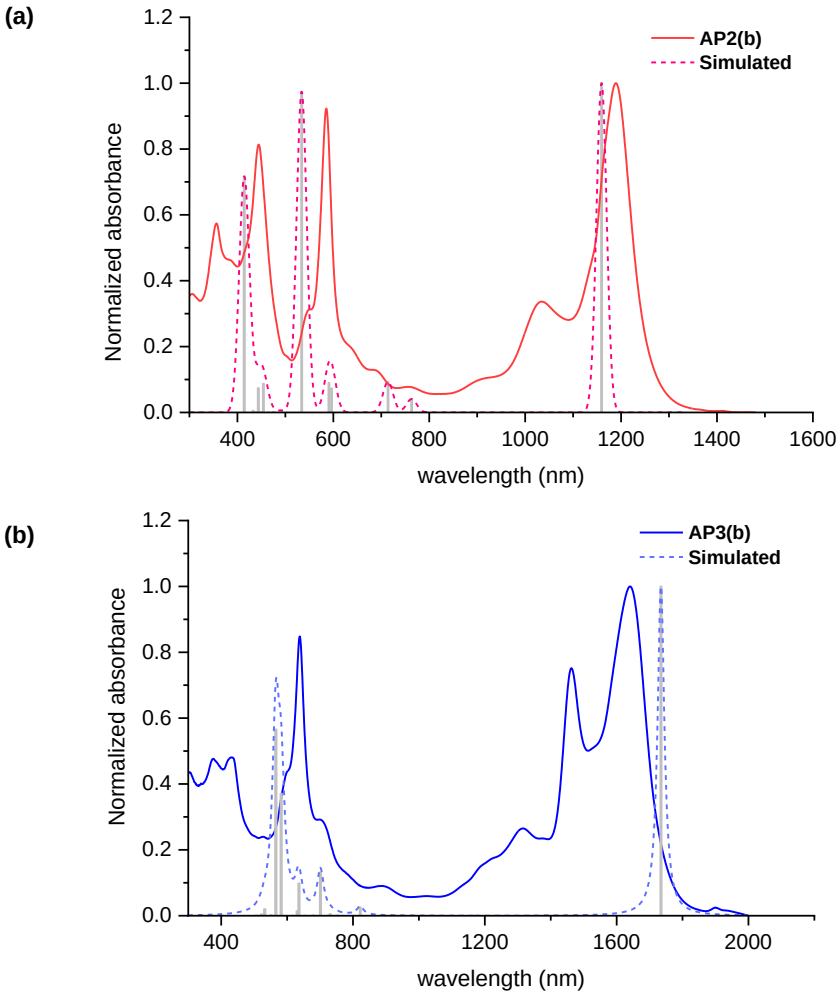


Figure 3.13: Simulated UV–vis–NIR absorption spectra (dashed line) and calculated oscillator strength (grey bars) of (a) **AP2b** (red) and (b) **AP3b** (blue) comparing with experimental spectra measured in toluene-d_8 at 298 K. Simulated absorption spectra assuming a Gaussian line-shape for each transition (line broadening FWHM: 55 nm for **AP2b** and 90 nm for **AP3b**). Calculated at the B3LYP/6-31G level of energy for the first 50 states with toluene as the solvent environment.

Besides, the close absorption maximum of **AP2b** with that of **P3b**, and **AP3b** with reported directly fused Zn(II) porphyrin pentamer (λ_{max} = ~1600 nm) indicate that the fusion

of one anthracene as linker into porphyrin ribbons could induce the similar extent of optical energy gap change as the fusion of an additional porphyrin unit.[54]

Square-wave and cyclic voltammetry were used to compare the redox potentials of dimers **AP2b** and **P2b** (Figure 3.14). The first oxidation and reduction potentials of **AP2b** are at 0.07 and –0.78 V, respectively (vs. Fc/Fc^+), corresponding to an electrochemical gap of 0.85 eV. When compared to **P2b** (E_{ox} 0.26 V, E_{red} −1.14 V; E_g 1.40 eV), it is clear that fusing the bridging anthracene into the center of the dimer makes it easier to oxidize and reduce, due to a narrower HOMO–LUMO gap.

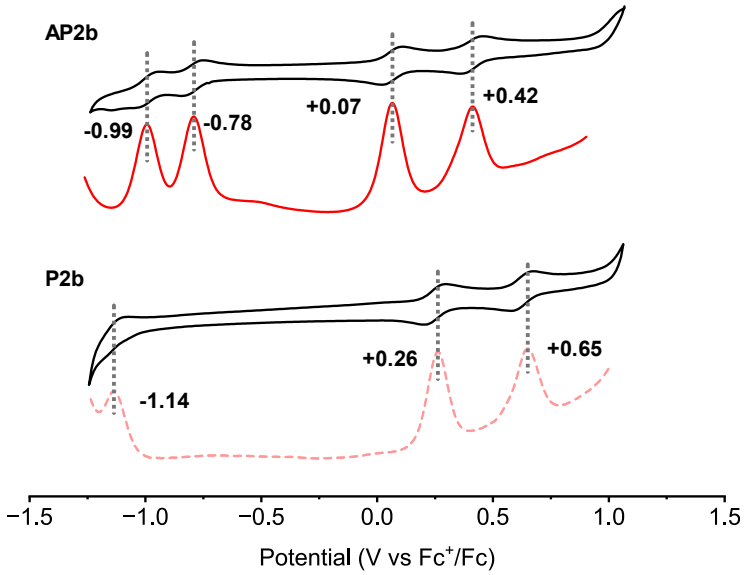
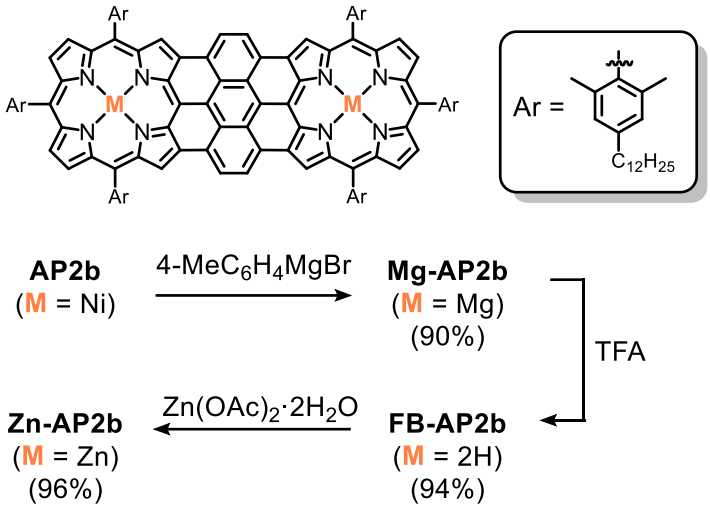


Figure 3.14: Square-wave and cyclic voltammograms of **AP2b** and **P2b** in dichloromethane with 0.1 M Bu_4NPF_6 as the electrolyte; potentials relative to internal ferrocene (Fc/Fc^+ at 0 V).

The coordination chemistry of porphyrins provides an opportunity to tune their electronic, photophysical, magnetic and catalytic behavior by varying the metal ion. We, therefore, investigated whether the coordinated Ni(II) ion in the anthracene-porphyrin nanoribbons could be exchanged for other metals. Many Ni(II) porphyrins can be demetallated by sulfuric acid in trifluoroacetic acid (TFA), but we found **AP2b** to be inert to these strongly acidic conditions. Another approach to remove Ni(II) ion from porphyrins is to use a Grignard reagent such as *p*-tolylmagnesium bromide, which exchanges Ni(II) for Mg(II).[55] We found that treatment of **AP2b** with excess *p*-tolylmagnesium bromide at 80 °C affords the anthracene-fused Mg(II) porphyrin dimer (**Mg-AP2b**, Scheme 3.4) in 90% yield. This magnesium complex is readily demetallated with TFA to give the free-base **FB-AP2** in 94% yield, which can coordinate other metals, such as in a reaction with zinc acetate, affording **Zn-AP2** in 96% yield.

The successful exchange of the coordination metal of porphyrins in this fused hybrid dimer showcases its molecular engineering flexibility. This provides a way to introduce paramagnetic spin centers or catalytic sites, creating a platform to investigate their other properties such as spintronic and magnetic behaviors.[56–59]



Scheme 3.4: Metal exchange from **AP2b** to prepare the Mg(II) (**Mg-AP2b**), free-base (**FB-AP2b**) and Zn(II) (**Zn-AP2b**) porphyrin dimers.

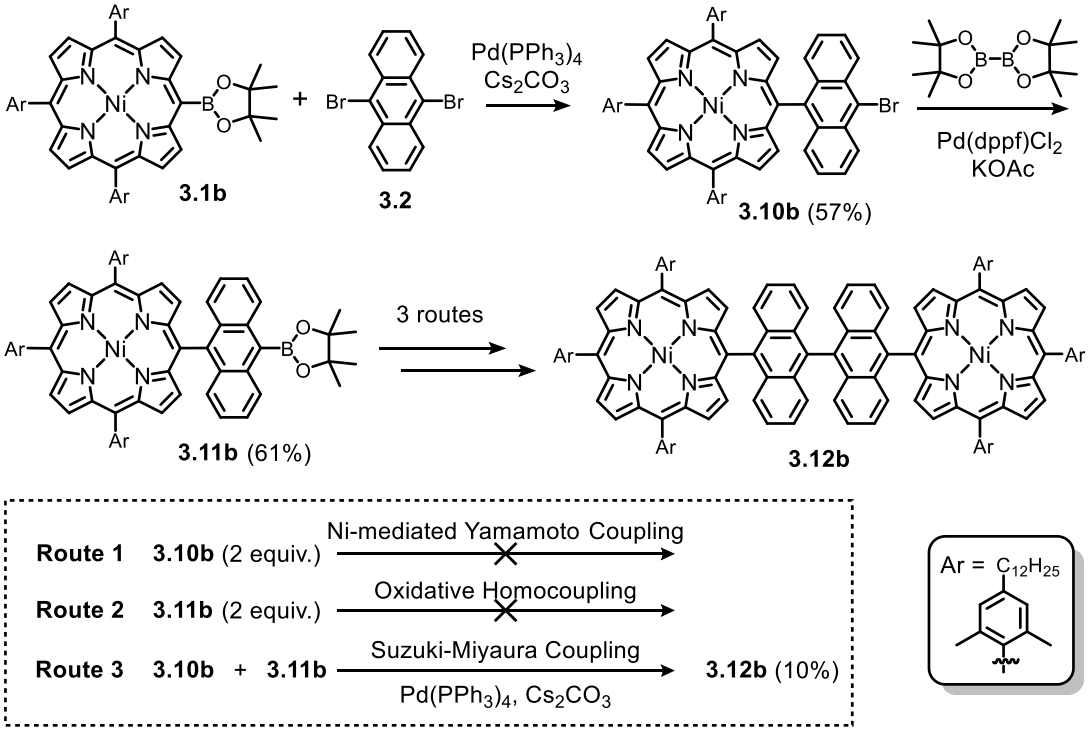
3.3 Extending Anthracene-Porphyrin Hybrid System

3.3.1 Preparation of a Bisanthracene-Fused Porphyrin Dimer

The study of anthracene-fused porphyrin oligomers **AP*N*** has demonstrated that anthracene bridges are capable of introducing the effective one-dimensional π-extension to the porphyrin ribbons. Following this study, we next move our focus onto using a bisanthracene as the linker. It is selected not only because it is a structural expansion compared to anthracene, but also due to its unusual open-shell diradical character.[60] Here, we investigate the synthesis of a bisanthracene-linked porphyrin dimer (by embedding the bisanthracene unit between two porphyrin units) to assess if porphyrin can stabilize the bisanthracene diradical singlet ground state and give rise to a further π-extended structure.

During the synthetic exploration towards **3.3b** (Scheme 3.1), a small amount of monoanthracenyl-porphyrin functionalized with one bromide (**3.10b**, Scheme 3.5) was obtained as a side-product from the two-fold Suzuki-Miyaura coupling. By treating **3.1b** with excessive **3.2**, the yield of **3.10b** can be improved to 57% (Scheme 3.5). A subsequent borylation

of **3.10b** provided a reasonable yield of **3.11b** (61%). Similar to previous results, swapping the boron and bromine functional groups on porphyrin and anthracene, respectively, in this Suzuki-Miyaura coupling led to a lower yield of **3.11b**. With both **3.10b** and **3.11b** in hand, investigations were then made into preparing the singly-linked bisanthracene-porphyrin dimer **3.12b** (Scheme 3.5). The synthesis of **3.12b** was explored through three methods: 1) Yamamoto homocoupling of **3.10b**; 2) oxidative homocoupling of a boronate ester using **3.11b**; and 3) a one-step Suzuki-Miyaura coupling between **3.10b** and **3.11b**.

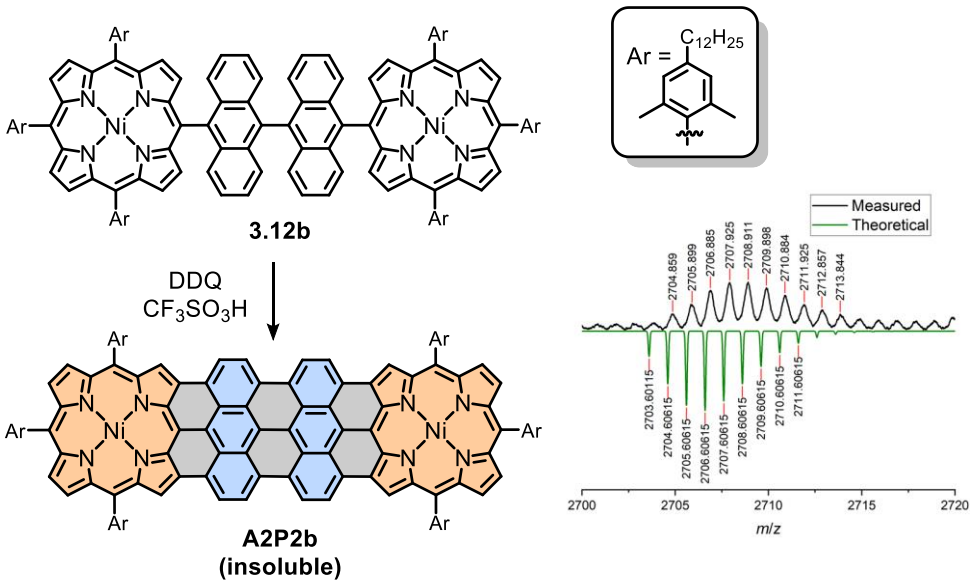


Scheme 3.5: Synthesis of singly-linked bisanthracene-porphyrin dimer **3.12b** using 2,6-dimethyl-4-dodecylphenyl-substituted porphyrins.

Yamamoto dimerization of **3.10b** was tested by treating the substrate with $Ni(COD)_2$ in either DMF or THF. However, after reacting overnight, only a very minor amount of **3.12b** was isolated from the reaction mixture, and instead, debrominated **3.10b** was found to be the main product. Later attempts at re-bromination with *N*-bromosuccinimide or $CuBr_2$ ultimately proved unsuccessful. Similar results were obtained from the trial Pd-mediated oxidative homocoupling reactions on **3.11b** where significant deborylation was observed (conditions: (i) $PdCl_2(PPh_3)_2$, KF, $B(OH)_3$, THF/H_2O, 50 °C; and (ii) $Pd(OAc)_2$, 1,3-Bis(diphenylphosphino)propane, DMSO/toluene, 70 °C).[61,62]

In the Suzuki-Miyaura cross-coupling reaction, **3.10b** and **3.11b** were treated with $Pd(PPh_3)_4$ and Cs_2CO_3 in toluene/DMF (4:1) (Scheme 3.5), where **3.12b** was isolated in 10% yield after reacting overnight. Though the efficiency of the coupling reaction was not as high as desired, it provided enough material in the first place to examine the feasibility of the final fusion step.

The oxidative cyclodehydrogenation of **3.12b** proceeded under Scholl reaction conditions with DDQ/TfOH as the respective oxidant and acid (Scheme 3.6). The progress of fusion was monitored by MALDI-ToF MS analysis. Note that, due to poor calibration of the instrument, the experimentally recorded mass of **3.12b** (m/z = 2716.867) deviated by 1.17 mass-to-charge ratio from the simulated value (m/z = 2715.695). Comparably, under identical conditions, after reacting for 2 h, MALDI-ToF MS recorded the experimental mass of the fused product at m/z = 2704.859, which shows a 1.26 mass-to-charge ratio difference from the theoretical result (m/z = 2703.601). The mass spectra of the fused product obtained from **3.12b** and the calculated isotopic pattern for **A2P2b** are compared in Scheme 3.6 (insert). The mass-to-charge ratio difference between the starting material and the obtained product (12.008) matched the number of hydrogen atoms required to be removed for a complete fusion. Hence, this confirms the successful formation of **A2P2b**.



Scheme 3.6: Fusion of **3.12b** towards **A2P2b**. (insert: experimental recorded isotope patterns for the fused product of **3.12b** from MALDI-ToF MS and the calculated isotope patterns for the molecular ion of **A2P2b.**

Unfortunately, as suspected, the solubility of the fused product was significantly reduced. This poor solubility necessitated a higher laser power to detect **A2P2b** to acquire mass

spectrum, but this emphasized the presence of negligible quantities of more soluble impurities in the starting material (Figure 3.15). After reacting overnight, the product precipitated out from the solution and the signal corresponding to **A2P2b** could not be detected via MALDI-ToF mass spectrometry anymore.

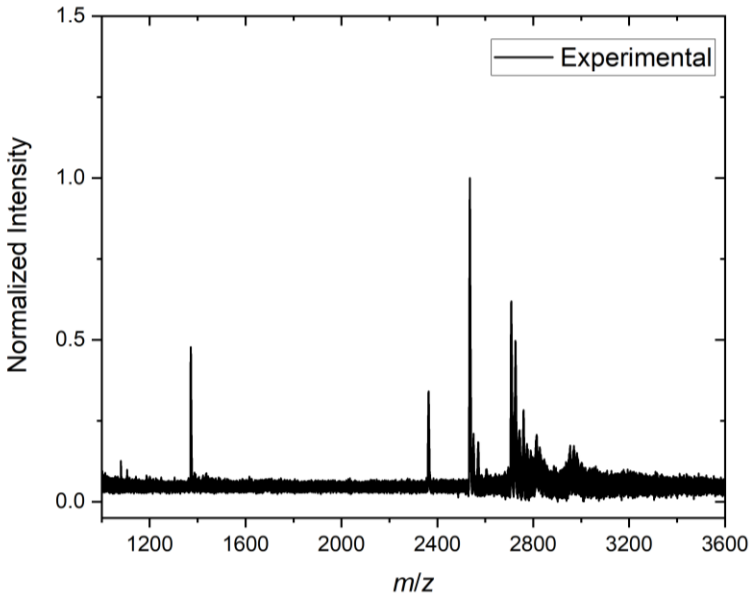


Figure 3.15: Zoomed-out MALDI-TOF MS spectrum of the fused product of **3.12b**.

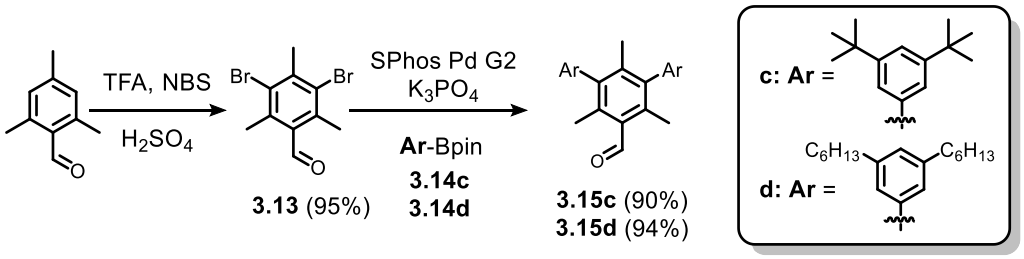
The unsuccessful isolation of bisanthracene-fused porphyrin dimer could be attributed to two potential factors: 1) instability of the fused bisanthracene-linker situated between the two porphyrins (*e.g.*, formation of a biradical open-shell system); or 2) even if the bisanthracene-linked porphyrin dimer could be fully fused under current conditions, the 2,6-dimethyl-4-dodecylphenyl side aryl groups may not be sufficient to solubilize the fused compound. In the former case, though introducing bulky substituents (*e.g.*, *tert*-butyl group) onto anthracene can effectively block the reactive sites, this approach would lead to significant steric hindrance between porphyrin and anthracene, thereby impeding complete fusion.[63–65] Therefore, the second factor, which is more likely to be addressed by incorporating enhanced solubilizing groups in the molecule, is examined here, to determine whether the solubility is the main restriction causing the failure in isolating the final product.

3.3.2 Development of Different Solubilizing Groups

To fulfill the same requirement for avoiding the accidental oxidative fusion of the porphyrin *β*-position and aryl group, the designs of new aryl group were derived from the original mesityl

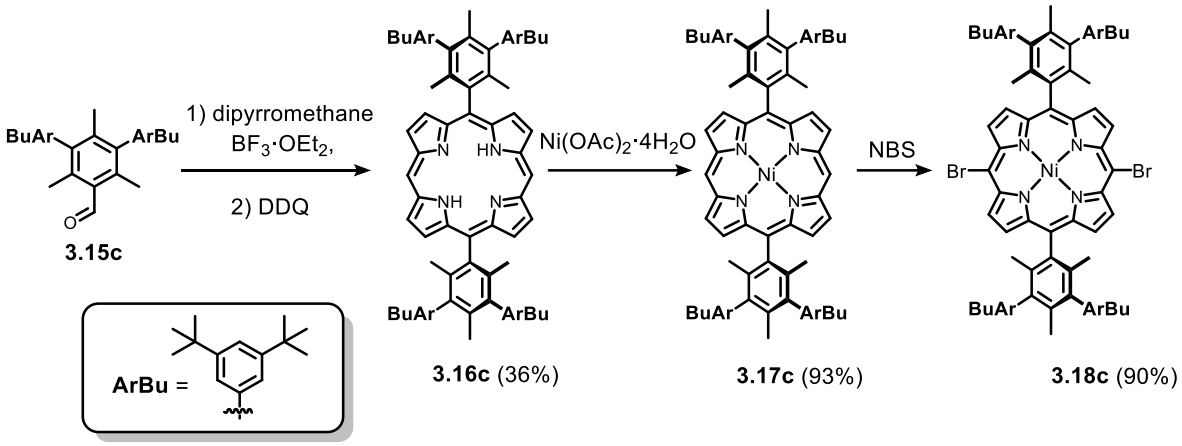
structure, which contains methyl groups on the *ortho*- and *para*-positions. Additionally adding bulky groups (to enhance the rigidity of the aryl group) or long alkyl chains (to improve the solubility in organic solvents) onto the *meta*-positions were considered as the methods to modify the side aryl groups of the porphyrin.

Two aryl groups were chosen here: 3,5-di-*tert*-butylphenyl, **ArBu**, and 3,5-dihexylphenyl, **ArHex**. The syntheses of porphyrins with extended side aryl groups started with preparing the corresponding aryl aldehyde. Brominating the *meta*-positions of 2,4,6-trimethylbenzaldehyde effectively yielded 3,5-dibromo-2,4,6-trimethylbenzaldehyde **3.13** in 95% (Scheme 3.7).[66] 1-Bpin-3,5-di-*tert*-butylbenzene **3.14c** and 1-Bpin-3,5-dihexylbenzene **3.14d** were quantitatively prepared from borylating their corresponding, commercially available bromo-precursors. A subsequent two-fold Suzuki-Miyaura cross-coupling between **3.13** and **3.14c**, **d** afforded the targeted aryl aldehyde **3.15c** and **3.15d** in 90% and 94% yield, respectively.



Scheme 3.7: Synthesis of 3,5-diaryl-2,4,6-trimethylbenzaldehyde **3.15c** and **3.15d**. (Ar: 3,5-di-*tert*-butylphenyl or 3,5-dihexylphenyl; SPhos Pd G2: chloro(2-dicyclohexylphosphino-2′,6′-dimethoxy-1,1′-biphenyl)[2-(2′-amino-1,1′-biphenyl)]palladium(II)).

The porphyrin synthesis was first examined with aryl aldehyde **3.15c**. With this new bulky aldehyde, free-base porphyrin **3.16c** was afforded in 36% yield by the condensation of **3.15c** with dipyrrolemethane (Scheme 3.8). As a result of incorporating the less polar **ArBu** groups, **3.16c** was found to be poorly soluble in DMF. To obtain Ni(II) porphyrin **3.17c**, the metallation was then carried out in a mixture of *m*-xylene/DMF (1:1) overnight, followed by a quantitative bromination to give dibromoporphyrin **3.18c**. The structure of **3.18c** was revealed by X-ray single-crystal diffraction analysis of crystals grown by slow diffusion of methanol vapor into its solution in dichloromethane. Compared with the mesityl-substituted porphyrins, the width of the substituent perpendicular to the mean plane of porphyrin increased to over 11 Å (Figure 3.16).



Scheme 3.8: Synthesis of dibromoporphyrin **3.18c** with **ArBu** as the side aryl group.

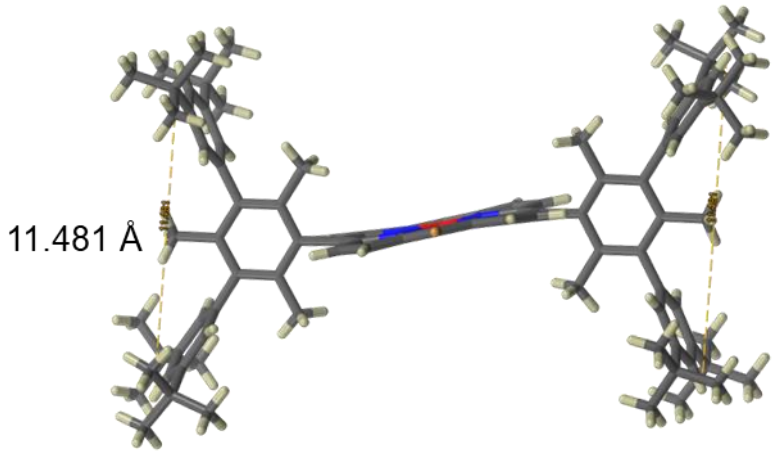
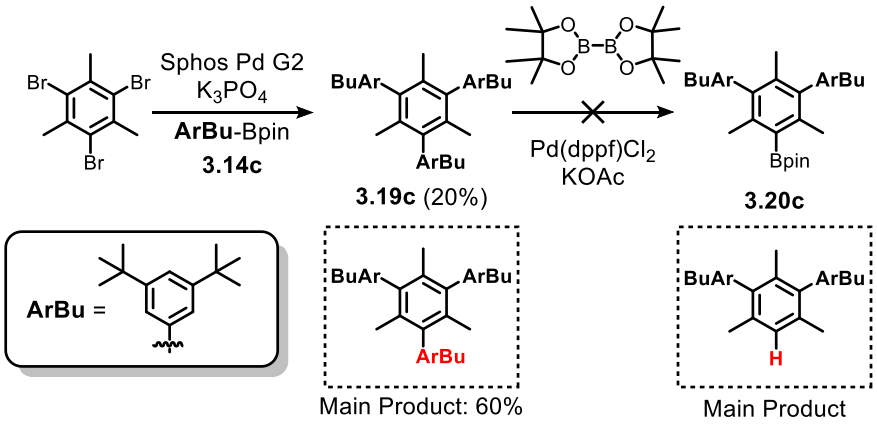


Figure 3.16: Side view of X-ray single-crystal structure of dibromoporphyrin **3.18c**.

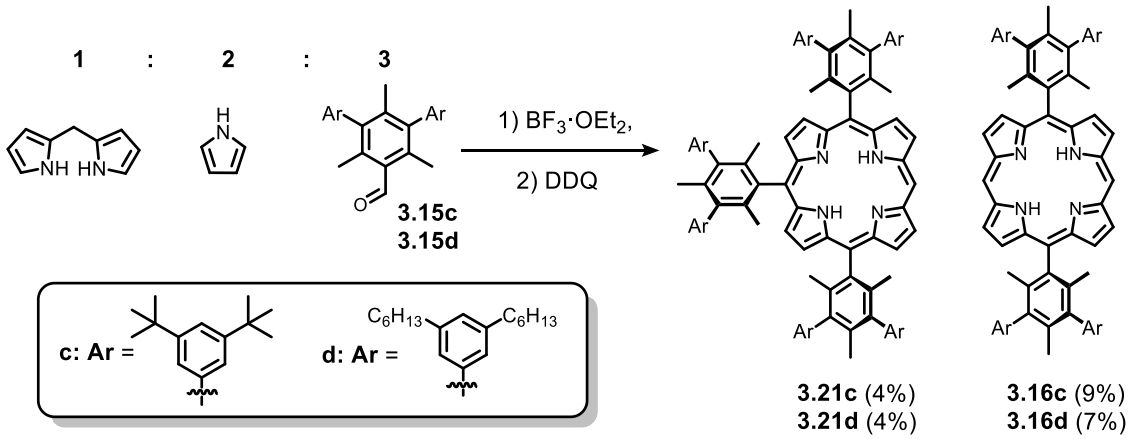
To obtain only the bisanthracene-fused porphyrin dimer in the final step (*i.e.*, no intermolecular fusion), it was necessary to prepare a triaryl-substituted porphyrin building block to cap the terminal of the structure. The synthesis of this molecule can be approached through two methods: 1) a one-fold Suzuki-Miyaura coupling of 5,15-dibromo-10,20-bisarylporphyrin with an aryl boronate ester, as demonstrated before; or 2) a condensation of the aryl aldehyde with pyrrole/dipyrromethane in 3:2:1 molar ratio. An aryl boronate ester **3.20c** (Scheme 3.9) was required for the first method. We attempted to prepare **3.20c** from a two-fold Suzuki-Miyaura reaction on 1,3,5-tribromo-2,4,6-trimethylbenzene with **3.14c**. However, despite subjecting only a stoichiometric amount of **3.14c** (2.1 equiv.) to the reaction, the dominant product was the three-fold coupled compound (1,3,5-tribromo-2,4,6-trimethylbenzene, 60%), with only 20% two-fold product **3.19c** isolated. Further reducing the amount of **3.14c** failed to improve the two-fold coupling selectivity. Moreover, significant debromination of **3.19c** occurred in the following borylation step, leading to the absence of targeted **3.20c** in the final isolation. This can be rationalized by the electron-donation from



Scheme 3.9: Unsuccessful synthetic route towards **3.20c**.

ArBu, leaving the bromo-sites in its *meta*-positions more reactive. While this accelerates the oxidative addition in the catalytic cycle, the reductive elimination is not efficient enough, resulting in debromination being the dominant reaction pathway.

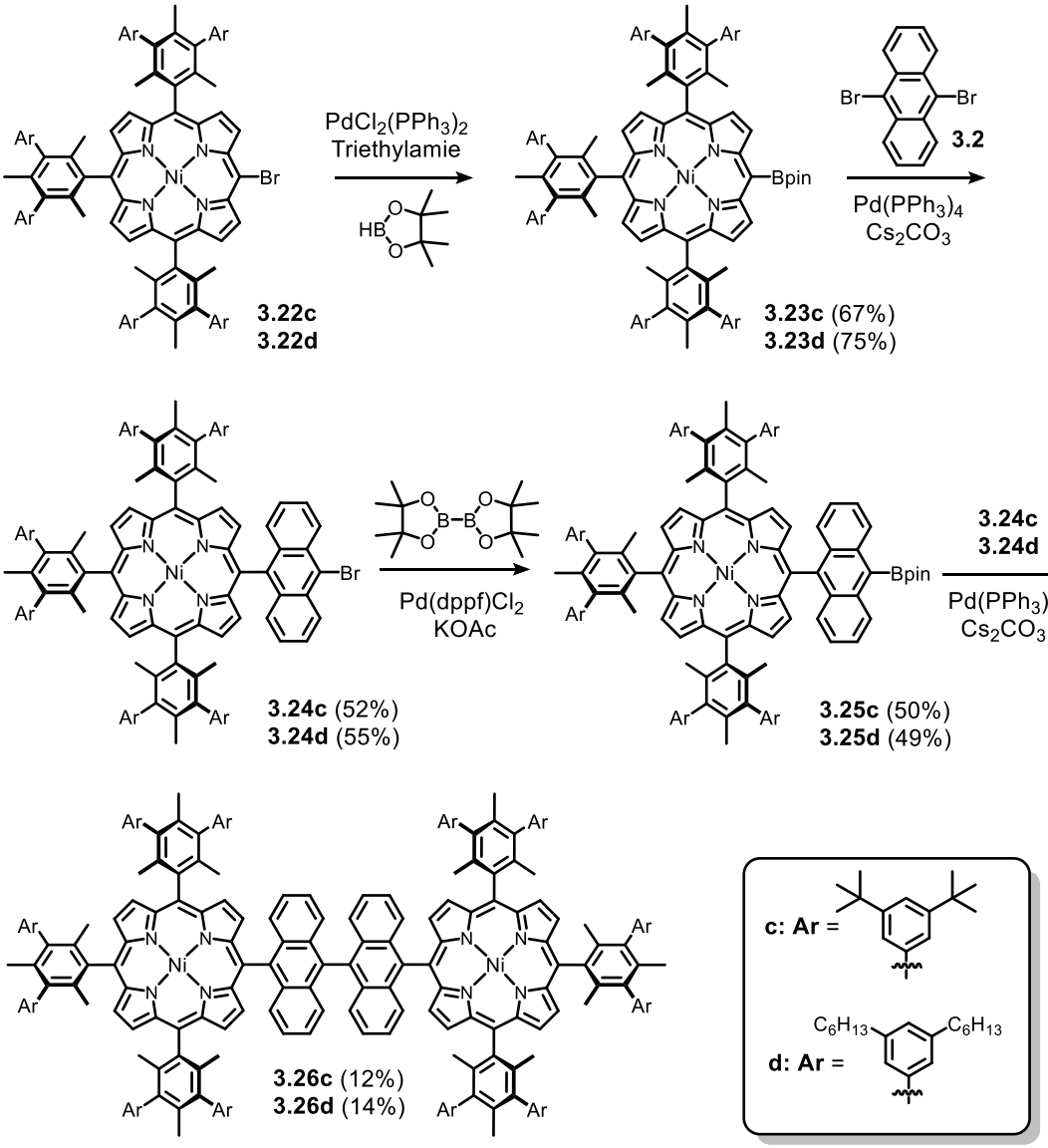
Considering the simplicity of scaling up the synthesis of aldehyde, the second route by directly condensing **3.15c**, **d** with pyrrole and dipyrromethane was explored (Scheme 3.10). This route afforded triaryl free-base porphyrin **3.21c** (4%) and **3.21d** (4%), together with the formation of bisaryl porphyrin **3.16c** (9%) and **3.16d** (7%). These yields are about half compared to that of trimesityl porphyrin **3.1a** over two steps. The separation of triaryl- and bisaryl-substituted porphyrins was achieved though size-exclusion chromatography. After a quantitative metallation and bromination, triaryl-substituted porphyrin building block **3.22c** and **3.22d** were successfully constructed (Scheme 3.11).



Scheme 3.10: Synthesis of 5,10,15-triaryl substituted porphyrins **3.21c** and **3.21d**.

The synthesis towards two singly-linked bisanthracene-porphyrin dimers **3.26c**, **d** started with a Suzuki-Miyaura coupling of porphyrin boronate **3.23c**, **d** with a large excess of **3.2** (30 equiv.) to give **3.24c**, **d** in 52% and 65% yield, respectively (Scheme 3.11). Through the

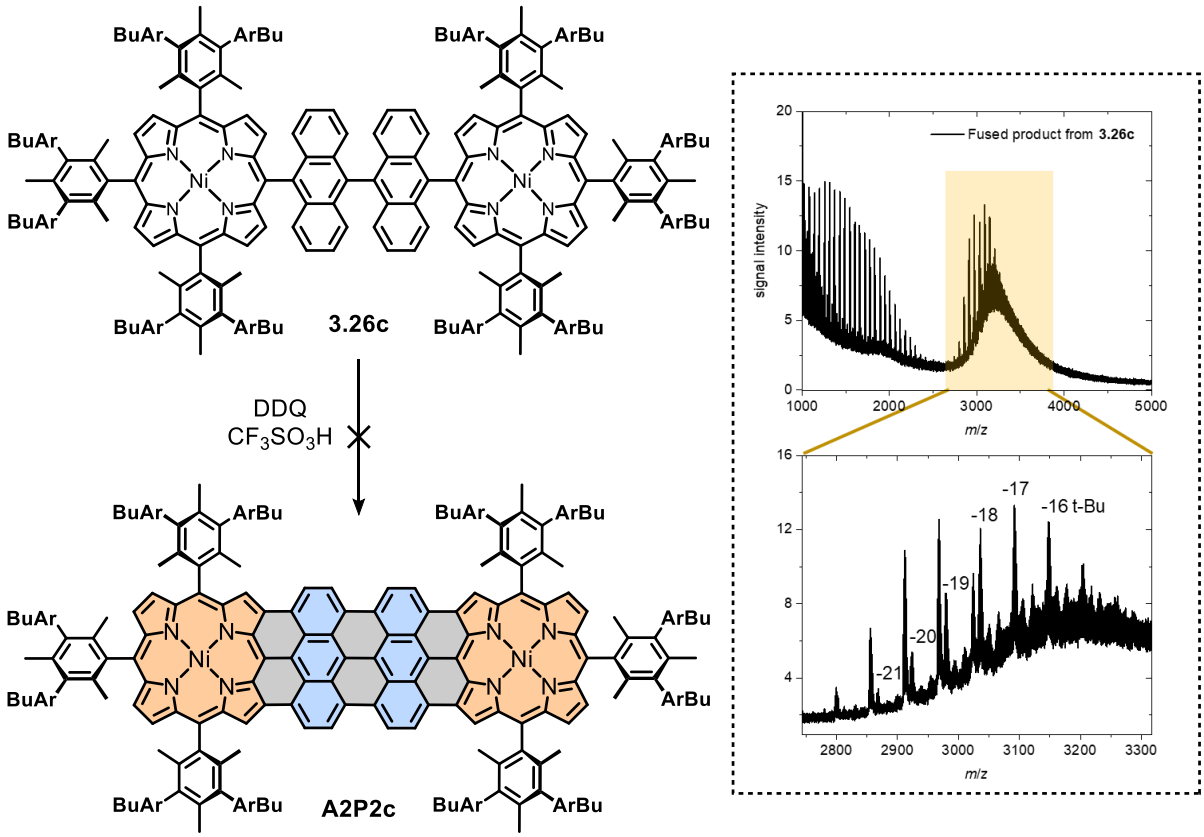
investigation towards **3.12b** (Scheme 3.5), we learned that borylating the bromo-functionalized anthracene more efficiently yields the boronate ester-functionalized monoanthracenyl-porphyrins. Therefore, both **3.24c**, **d** were borylated to provide **3.25c**, **d**. In the following Suzuki-Miyaura reaction, with a 1:1 input ratio of **3.24c**, **d** and **3.25c**, **d** reacting overnight, the coupled product **3.26c**, **d** were obtained in 12% and 14%, respectively.



Scheme 3.11: Synthesis of singly-linked bisanthracene-porphyrin dimer **3.26c** and **3.26d**.

The final oxidative cyclodehydrogenation reactions were tested on both **3.26c**, **d** under the same fusion conditions. Unfortunately, neither of them provided positive results. In the reaction of **3.26c** (Scheme 3.12), insoluble black solids started to precipitate out from the solution after 2 h. MALDI-ToF MS analysis confirmed that all the starting material was consumed, but there was no evidence for the formation of fully fused product. Instead, the mass

spectrum of the reaction mixture revealed an evenly spaced mass pattern around the $m/z = 3000$ range (Scheme 3.12, insert). This represented approximately a 1000 mass-to-charge ratio difference from the expected fused product ($m/z = 4036.45$). The mass difference between each peak corresponds to one *tert*-butyl group. Each peak can be assigned to a mass approximating to the fused product with a certain number (ranging from 16 to 22) of *tert*-butyl groups being removed. Because of the complex spectrum, determining the completion of fusion was challenging, especially for such a small number of removed protons in cyclodehydrogenation compared to the whole molecular mass.



Scheme 3.12: Failed fusion of bisanthracene-linked porphyrin dimer. (Inset: experimental mass spectrum of resulted reaction mixture from **3.26c** from MALDI-TOF MS, indicating the removal of *t*-Bu groups.)

The loss of *tert*-butyls from the porphyrin aryl groups can be rationalized in the following way: under strong acidic conditions, these *tert*-butyls will be protonated and form a stable tertiary carbon cation center, readily cleaving off from the phenyl group. Despite this observation, the fusion reaction was continued to assess whether the reaction could achieve the complete removal of all *tert*-butyl groups. However, after reacting overnight, the product fully precipitated out from the solution and no signal was detected from MALDI-TOF MS analysis. The cleavage of *tert*-butyl groups was also confirmed by a test reaction on **ArBu**-porphyrin

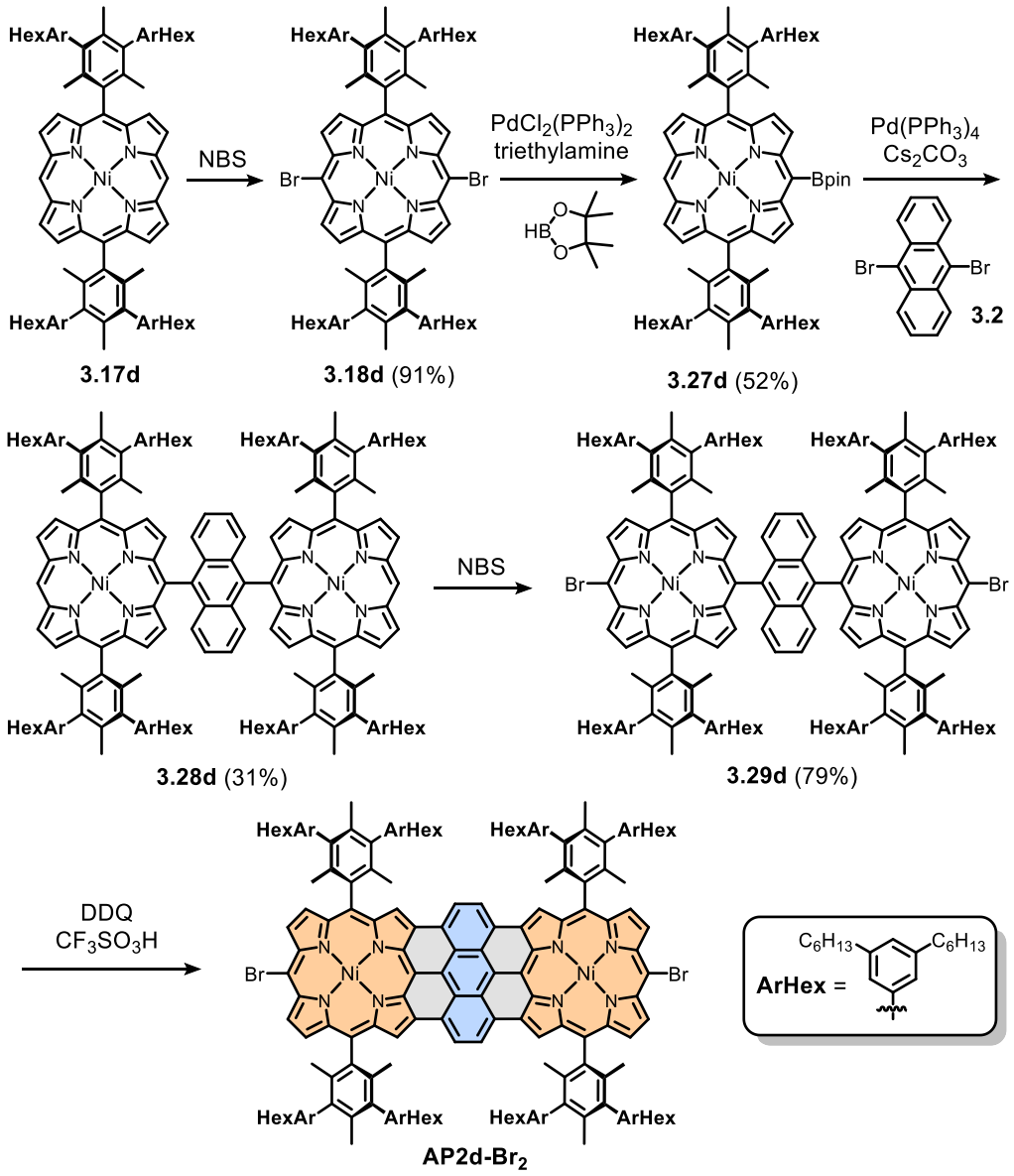
monomer **3.22c** (Scheme 3.11) by treating it under the same fusion conditions. These suggest that the *tert*-butyl group in this specific aryl design is not compatible with the strongly acidic fusion conditions.

The product resulting from attempted fusion of **3.26d** failed to provide any useful insight into the fusion process (after reacting for 2 h) based on the MALDI-ToF analysis. Therefore, there was no evidence either confirming the actual formation of the fused **A2P2d** or establishing that **ArHex** is not sufficient to solubilize the final product. The outcome appears to be worse than the result obtained from **3.12b (**with 2,6-dimethyl-4-dodecylphenyl side aryl groups). Considering the same monitoring interval for all three samples, this observation can be rationalized in that: for **3.26c**, the desired fusion reaction occurs parallel with the cleavage of the *tert*-butyl groups, thus they were in competition with each other. Therefore, the partially fused, but more soluble intermediate originating from **3.26c** was detected by MALDI-ToF MS. For **3.26d**, in comparison to **3.12b**, the additional **ArHex** group functions as an electron donating group, which in turn accelerates the formation of the arenium ion intermediate and the subsequent electrophilic attack process in Scholl reaction. This ultimately means that the fusion occurs at a faster rate, and the loss of signal in MALDI-ToF MS could be resulting from either: 1) insufficient solubility of fused product, causing it to precipitate from the reaction mixture before the MS measurement; or 2) the degradation of the unstable fused product occurring before measuring its mass spectrum. Nevertheless, these results imply that using **ArHex** is not a viable approach to isolate bisanthracene-fused porphyrin dimer.

3.3.3 Stability of Hexyl-Enlarged Solubilizing Group

To investigate the stability of **ArHex** under Scholl fusion conditions, and whether the incorporation of **ArHex** has any positive impact on solubilizing the fused species, a trial fusion reaction was conducted using a singly-linked anthracene-porphyrin dimer without the terminal aryl group **3.29d** (prepared following the synthetic route shown in Scheme 3.13). This anthracene-porphyrin dimer (without terminal aryl groups on the porphyrins) was synthesized using 2,6-dimethyl-4-dodecylphenyl-substituted porphyrins as well. However, the fusion result from that compound suggested that, though the completely fused compound could be detected by MALDI-ToF MS, once it precipitates from the solution, its redissolution in any solvent

became challenging due to the strong aggregation. With **3.29d**, it was found that the fusion gave the fully fused product **AP2d-Br$_2$** and no obvious side reaction (*i.e.*, no debromination or side-group cleavage) was observed. Additionally, the product is soluble enough to be purified via silica chromatography (eluting with toluene), which was a significant enhancement compared to the result obtained when applying 2,6-dimethyl-4-dodecylphenyl-substituted porphyrins.



Scheme 3.13: Synthesis of bisanthracene-linked porphyrin dimer **AP2d-Br$_2$**.

It is encouraging to observe that both bromo-functional sites and **ArHex** could withstand strong fusion conditions, and that the resulting product remains soluble. At the time of writing, the synthesis of **AP2d-Br$_2$** is undergoing scale-up so that further investigations can be made. These results highlight a modular approach to preserve the functionalizing sites on anthracene-porphyrin hybrid nanoribbons, for instance, for attachment of anchoring group

(*e.g.*, thiomethyl (SMe), thioacetate (SAc), or TMS-acetylenes) at the termini, to form conducting single-molecule junctions (Figure 3.17). With the previously established synthetic route towards the anthracene-fused porphyrin trimer, utilizing this enlarged **ArHex** group could potentially provide more extended molecular structures that are sufficiently soluble. This will allow for the investigation into their single-molecule conductance using the scanning tunneling microscope break-junctions (STM-BJ) technique and to evaluate their applicability as molecular wire candidates.

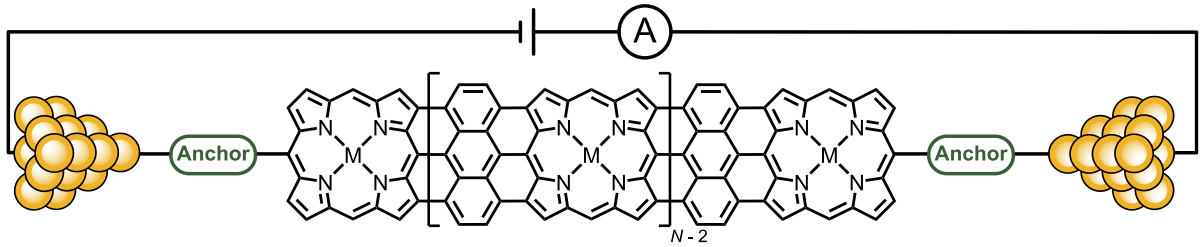


Figure 3.17: Proposed structure of the single-molecule charge transport study on anthracene-porphyrin nanoribbons using the STM-BJ technique (Proposed anchoring group: thiomethyl (SMe), thioacetate (SAc) or TMS-acetylene groups).

3.4 Conclusions

A new series of fully fused anthracene-linked porphyrin oligomers (dimers and trimer) have been prepared through solution-phase synthesis. These are the first examples serving as model structures for one-dimensionally extended anthracene-porphyrin hetero-polymers. X-ray crystallography illustrates that fusion of the anthracene-linked porphyrin dimer creates a regular planar coronene in the middle with terminal porphyrins distorting from that plane. The fusion of anthracene into porphyrin ribbons effectively reduced the HOMO–LUMO energy gap. The optical characterization results further demonstrate that, at short oligomer lengths, when anthracene is incorporated into porphyrin ribbons, it can induce a change in the optical energy gap comparable to that caused by one porphyrin unit. These results render the anthracene-porphyrin nanoribbon a competitive subject to porphyrin ribbons in the study of molecular wires. Multi-metal systems are accessible due to their metal exchange flexibility which can be employed later to engineer their magnetic and catalytic properties.

This chapter also documents attempts towards building increasingly extended anthracene-porphyrin hybrid systems. We have successfully incorporated two bulky side aryl groups onto porphyrins and obtained singly-linked bisanthracene-porphyrin dimers. However, owing to the harsh conditions required in the fusion step, the significantly reduced solubility

and unknown instability of the fused product, the targeted bisanthracene-fused porphyrin dimer remained inaccessible. A promising result from this exploration is that with the help of the **ArHex** group, a bromo-functionalized fused anthracene-porphyrin dimer becomes purifiable and stable under exposure to air and light. These observations suggest that **ArHex**, to some extent, enhances the solubility of the fused product. This molecule could potentially serve as the precursor for the fabrication of anchoring groups, suitable for studying its single-molecule conductance using the STM-BJ technique.

3.5 References

1 F. S. Kim, G. Ren and S. A. Jenekhe, *Chem. Mater.*, 2011, **23**, 682–732.

2 Z. Liu, A. A. Yasseri, J. S. Lindsey and D. F. Bocian, *Science*, 2003, **302**, 1543–1545.

3 J. S. Lindsey, *Acc. Chem. Res.*, 2010, **43**, 300–311.

4 H. L. Anderson, *Chem. Commun.*, 1999, 2323–2330.

5 H. Mori, T. Tanaka and A. Osuka, *J. Mater. Chem. C*, 2013, **1**, 2500.

6 J. P. Lewtak and D. T. Gryko, *Chem. Commun.*, 2012, **48**, 10069–10086.

7 C. J. Kingsbury and M. O. Senge, *Coord. Chem. Rev.*, 2021, **431**, 213760.

8 D. Monti, S. Nardis, M. Stefanelli, R. Paolesse, C. Di Natale and A. D'Amico, *J. Sensors*, 2009, **2009**, 1–10.

9 M. Urbani, M. Grätzel, M. K. Nazeeruddin and T. Torres, *Chem. Rev.*, 2014, **114**, 12330–12396.

10 M. Jurow, A. E. Schuckman, J. D. Batteas and C. M. Drain, *Coord. Chem. Rev.*, 2010, **254**, 2297–2310.

11 M. H. Sayyad, M. Saleem, K. S. Karimov, M. Yaseen, M. Ali, K. Y. Cheong and A. F. Mohd Noor, *Appl. Phys. A*, 2010, **98**, 103–109.

12 N. Aratani, D. Kim and A. Osuka, *Chem. Asian J.*, 2009, **4**, 1172–1182.

13 A. Tsuda and A. Osuka, *Science*, 2001, **293**, 79–82.

14 T. Ikeda, N. Aratani and A. Osuka, *Chem. Asian J.*, 2009, **4**, 1248–1256.

15 G. Sedghi, L. J. Esdaile, H. L. Anderson, S. Martin, D. Bethell, S. J. Higgins and R. J. Nichols, *Adv. Mater.*, 2012, **24**, 653–657.

16 E. Leary, B. Limburg, A. Alanazy, S. Sangtarash, I. Grace, K. Swada, L. J. Esdaile, M. Noori, M. T. González, G. Rubio-Bollinger, H. Sadeghi, A. Hodgson, N. Agraït, S. J. Higgins, C. J. Lambert, H. L. Anderson and R. J. Nichols, *J. Am. Chem. Soc.*, 2018, **140**, 12877–12883.

17 A. N. Cammidge, P. J. Scaife, G. Berber and D. L. Hughes, *Org. Lett.*, 2005, **7**, 3413–3416.

18 N. K. S. Davis, M. Pawlicki and H. L. Anderson, *Org. Lett.*, 2008, **10**, 3945–3947.

19 N. K. S. Davis, A. L. Thompson and H. L. Anderson, *Org. Lett.*, 2010, **12**, 2124–2127.

20 N. K. S. Davis, A. L. Thompson and H. L. Anderson, *J. Am. Chem. Soc.*, 2011, **133**, 30–31.

21 O. Yamane, K. Sugiura, H. Miyasaka, K. Nakamura, T. Fujimoto, K. Nakamura, T. Kaneda, Y. Sakata and M. Yamashita, *Chem. Lett.*, 2004, **33**, 40–41.

22 K. Kurotobi, K. S. Kim, S. B. Noh, D. Kim and A. Osuka, *Angew. Chem. Int. Ed.*, 2006, **45**, 3944–3947.

23 Q. Chen, L. Brambilla, L. Daukiya, K. S. Mali, S. De Feyter, M. Tommasini, K. Müllen

and A. Narita, *Angew. Chem. Int. Ed.*, 2018, **130**, 11403–11407.

24 R. W. Boyle and D. Dolphin, *Photochem. Photobiol.*, 1996, **64**, 469–485.

25 C. Jiao, N. Zu, K.-W. Huang, P. Wang and J. Wu, *Org. Lett.*, 2011, **13**, 3652–3655.

26 C. Jiao, K.-W. Huang, Z. Guan, Q.-H. Xu and J. Wu, *Org. Lett.*, 2010, **12**, 4046–4049.

27 C. Jiao and J. Wu, *Synlett*, 2012, **2012**, 171–184.

28 L. M. Mateo, Q. Sun, S. Liu, J. J. Bergkamp, K. Eimre, C. A. Pignedoli, P. Ruffieux, S. Decurtins, G. Bottari, R. Fasel and T. Torres, *Angew. Chem. Int. Ed.*, 2020, **132**, 1350–1355.

29 J. Deyerling, M. Pörtner, L. Đorđević, A. Riss, D. Bonifazi and W. Auwärter, *J. Phys. Chem. C*, 2022, **126**, 8467–8476.

30 P. J. Dandliker, F. Diederich, M. Gross, C. B. Knobler, A. Louati and E. M. Sanford, *Angew. Chem. Int. Ed.*, 1994, **33**, 1739–1742.

31 M.-C. Kuo, H.-F. Chen, J.-J. Shyue, D. M. Bassani and K.-T. Wong, *Chem. Commun.*, 2012, **48**, 8051.

32 A. Tsuda, T. Nakamura, S. Sakamoto, K. Yamaguchi and A. Osuka, *Angew. Chem. Int. Ed.*, 2002, **41**, 2817–2821.

33 J. Jiang and D. K. P. Ng, *Acc. Chem. Res.*, 2009, **42**, 79–88.

34 S. Matsunaga, N. Endo and W. Mori, *Chem. Lett.*, 2017, **46**, 937–939.

35 C. A. S. P and P. Thilagar, *Dalton Trans.*, 2016, **45**, 4688–4696.

36 P. Şen, C. Hirel, C. Andraud, C. Aronica, Y. Bretonnière, A. Mohammed, H. Ågren, B. Minaev, V. Minaeva, G. Baryshnikov, H.-H. Lee, J. Duboisset and M. Lindgren, *Materials (Basel).*, 2010, **3**, 4446–4475.

37 T. Ikeda, A. Tsuda, N. Aratani and A. Osuka, *Chem. Lett.*, 2006, **35**, 946–947.

38 M. V. Volostnykh, M. A. Mikhaylov, A. A. Sinelshchikova, G. A. Kirakosyan, A. G. Martynov, M. S. Grigoriev, D. A. Piryazev, A. Y. Tsivadze, M. N. Sokolov and Y. G. Gorbunova, *Dalton Trans.*, 2019, **48**, 1835–1842.

39 M. O. Senge, *Acta Crystallogr. Sect. E Struct. Rep. Online*, 2012, **68**, m1191–m1192.

40 Y. Matano, T. Shibano, H. Nakano, Y. Kimura and H. Imahori, *Inorg. Chem.*, 2012, **51**, 12879–12890.

41 X.-S. Wang, L. Meng, Q. Cheng, C. Kim, L. Wojtas, M. Chrzanowski, Y.-S. Chen, X. P. Zhang and S. Ma, *J. Am. Chem. Soc.*, 2011, **133**, 16322–16325.

42 P. Zhang, C. Yu, Y. Yin, J. Droste, S. Klabunde, M. R. Hansen and Y. Mai, *Chem. Eur. J.*, 2020, **26**, 16497–16503.

43 L. Zhai, R. Shukla and R. Rathore, *Org. Lett.*, 2009, **11**, 3474–3477.

44 L. Zhai, R. Shukla, S. H. Wadumethrige and R. Rathore, *J. Org. Chem.*, 2010, **75**, 4748–4760.

45 V. Posligua, A. Aziz, R. Haver, M. D. Peeks, H. L. Anderson and R. Grau-Crespo, *J. Phys. Chem. C*, 2018, **122**, 23790–23798.

46 J. P. Perdew, K. Burke and M. Ernzerhof, *Phys. Rev. Lett.*, 1996, **77**, 3865–3868.

47 A. Allouche, *J. Comput. Chem.*, 2012, **32**, 174–182.

48 J. Heyd, G. E. Scuseria and M. Ernzerhof, *J. Chem. Phys.*, 2003, **118**, 8207–8215.

49 G. K. H. Madsen, J. Carrete and M. J. Verstraete, *Comput. Phys. Commun.*, 2018, **231**, 140–145.

50 P. Ruffieux, J. Cai, N. C. Plumb, L. Patthey, D. Prezzi, A. Ferretti, E. Molinari, X. Feng, K. Müllen, C. A. Pignedoli and R. Fasel, *ACS Nano*, 2012, **6**, 6930–6935.

51 S. Linden, D. Zhong, A. Timmer, N. Aghdassi, J. H. Franke, H. Zhang, X. Feng, K. Müllen, H. Fuchs, L. Chi and H. Zacharias, *Phys. Rev. Lett.*, 2012, **108**, 216801.

52 A. Tsuda, H. Furuta and A. Osuka, *J. Am. Chem. Soc.*, 2001, **123**, 10304–10321.

53 P. D. Kilmer, *Journal.*, 2010, **11**, 369–373.

54 D. Kim and A. Osuka, *J. Phys. Chem. A*, 2003, **107**, 8791–8816.

55 K. Murakami, Y. Yamamoto, H. Yorimitsu and A. Osuka, *Chem. Eur. J.*, 2013, **19**, 9123–9126.

56 K. L. Cunningham, K. M. McNett, R. A. Pierce, K. A. Davis, H. H. Harris, D. M. Falck and D. R. McMillin, *Inorg. Chem.*, 1997, **36**, 608–613.

57 I. Pozo, Z. Huang, F. Lombardi, D. I. Alexandropoulos, F. Kong, M. Slota, I. Tkach, M. Bennati, J.-R. Deng, W. Stawski, P. N. Horton, S. J. Coles, W. K. Myers, L. Bogani and H. L. Anderson, *Chem*, 2024, **10**, 299–316.

58 J. M. Van Raden, D. I. Alexandropoulos, M. Slota, S. Sopp, T. Matsuno, A. L. Thompson, H. Isobe, H. L. Anderson and L. Bogani, *J. Am. Chem. Soc.*, 2022, **144**, 8693–8706.

59 T. Pei, J. O. Thomas, S. Sopp, M.-Y. Tsang, N. Dotti, J. Baugh, N. F. Chilton, S. Cardona-Serra, A. Gaita-Ariño, H. L. Anderson and L. Bogani, *Nat. Commun.*, 2022, **13**, 4506.

60 S. Das and J. Wu, *Phys. Sci. Rev.*, 2017, **2**, 1–23.

61 E. R. Darzi, B. M. White, L. K. Loventhal, L. N. Zakharov and R. Jasti, *J. Am. Chem. Soc.*, 2017, **139**, 3106–3114.

62 H. Hata, H. Shinokubo and A. Osuka, *J. Am. Chem. Soc.*, 2005, **127**, 8264–8265.

63 A. Konishi, Y. Hirao, M. Nakano, A. Shimizu, E. Botek, B. Champagne, D. Shiomi, K. Sato, T. Takui, K. Matsumoto, H. Kurata and T. Kubo, *J. Am. Chem. Soc.*, 2010, **132**, 11021–11023.

64 A. Konishi, Y. Hirao, K. Matsumoto, H. Kurata, R. Kishi, Y. Shigeta, M. Nakano, K. Tokunaga, K. Kamada and T. Kubo, *J. Am. Chem. Soc.*, 2013, **135**, 1430–1437.

65 W. Zeng and J. Wu, *Chem*, 2021, **7**, 358–386.

66 J. N. Moorthy, P. Mal, R. Natarajan and P. Venugopalan, *J. Org. Chem.*, 2001, **66**, 7013–7019.

3.6 Experimental

Contents

General Methods 120

Synthesis of Known Compounds 121

9,10-BisBpinanthracene **3.5** 121

5,15-Bismesitylporphyrin 122

Ni(II) 5,15-bismesitylporphyrin 123

Ni(II) 5,15-dibromo-10,20-bismesitylporphyrin 123

Ni(II) 5-bromo-10,15,20-trimesitylporphyrin **3.4a** 124

4-Bromo-2,6-dimethylbenzaldehyde 125

4-Dodecyl-2,6-dimethylbenzaldehyde 126

5,15-Bis(2,6-dimethyl-4-dodecylphenyl)porphyrin 127

Ni(II) 5,15-bis(2,6-dimethyl-4-dodecylphenyl)porphyrin 128

Ni(II) 5,15-dibromo-10,20-bis(2,6-dimethyl-4-dodecylphenyl)porphyrin **3.6b** 128

2-Bromo-5-dodecyl-1,3-dimethylbenzene 129

2,6-Dimethyl-4-dodecylphenylboronic acid pinacol ester 130

3,5-Dibromo-2,4,6-trimethylbenzaldehyde **3.13** 130

1-Bpin-3,5-di-*tert*-butylbenzene **3.14c** 131

Synthesis of Novel Compounds 132

Ni(II) 5-Bpin-10,15,20-trimesityl-porphyrin **3.1a** 132

Anthracene-linked porphyrin dimer **3.3a** 133

Meso-singly-linked porphyrin dimer ***s*-P2a** 134

Ni(II) 5-bromo-10,15,20-tri(2,6-dimethyl-4-dodecylphenyl)porphyrin **3.4b** 135

Ni(II) 5-Bpin-10,15,20-tri(2,6-dimethyl-4-dodecylphenyl)porphyrin **3.1b** 136

Anthracene-linked porphyrin dimer **3.3b** 137

Meso-singly-linked porphyrin dimer ***s*-P2b** 138

Fused anthracene-linked porphyrin dimer **AP2a** 138

Fused mesityl porphyrin dimer **P2a** 140

Fused anthracene-linked porphyrin dimer **AP2b** 141

Fused dodecyl porphyrin dimer **P2b** 142

Ni(II) 5,15-diBpin-10,20-bis(2,6-dimethyl-4-dodecylphenyl)porphyrin **3.7b** 143

Bisanthracenyl-porphyrin **3.8b** 144

Anthracene-linked porphyrin trimer **3.9b** 145

Fused anthracene-linked porphyrin trimer **AP3b** 146
Singly-linked dodecyl porphyrin trimer ***s*-P3b** 147
Fused dodecyl porphyrin trimer **P3b** 148
Fused anthracene-linked Mg(II) porphyrin dimer **Mg-AP2b** 149
Fused anthracene-linked free-base porphyrin dimer **FB-AP2b** 150
Fused anthracene-linked Zn(II) porphyrin dimer **Zn-AP2b** 151
Bromo-functionalized monoanthracenyl-porphyrin **3.10b** 152
Boronate ester-functionalized monoanthracenyl-porphyrin **3.11b** 153
Singly-linked bisanthracene-porphyrin dimer **3.12b** 154
1-Bpin-3,5-dihexyl benzene **3.14d** 155
Tetra-*tert*-butyl aldehyde **3.15c** 155
Tetra-hexyl aldehyde **3.15d** 156
5,15-Bis(tetra-*tert*-butylphenyl)porphyrin **3.16c** 157
5,10,15-Tri(tetra-*tert*-butylphenyl)-porphyrin **3.21c** 158
5,15-Bis(tetra-hexylphenyl)porphyrin **3.16d** 159
5,10,15-Tri(tetra-hexylphenyl)porphyrin **3.21d** 160
Ni(II) 5-bromo-10,15,20-tri(tetra-*tert*-butyl)porphyrin **3.22c** 160
Ni(II) 5-bromo-10,15,20-tri(tetra-hexyl)porphyrin **3.22d** 161
Ni(II) 5-Bpin-10,15,20-tri(tetra-*tert*-butyl)porphyrin **3.23c** 162
Ni(II) 5-Bpin-10,15,20-tri(tetra-hexyl)porphyrin **3.23d** 163
Bromo-functionalized monoanthracenyl-porphyrin **3.24c** 164
Bromo-functionalized monoanthracenyl-porphyrin **3.24d** 165
Boronate ester-functionalized monoanthracenyl-porphyrin **3.25c** 166
Boronate ester-functionalized monoanthracenyl-porphyrin **3.25d** 167
Singly-linked bisanthracene-porphyrin dimer **3.26c** 168
Singly-linked bisanthracene-porphyrin dimer **3.26d** 169
Singly-linked anthracenyl-dibromoporphyrin dimer **3.27d** 169
Band Structure Calculation 172
Selected NMR Spectra 176
Selected UV–vis–NIR Absorption Spectra 208
Selected Mass Spectra 211
References 223

General Methods

Commercially available reagents from Alfa Aesar, Fluorochem, Merck, Strem Chemicals and TCI were used as received. Reactions, unless otherwise stated, were performed in oven-dried glassware under an argon atmosphere. Anhydrous dichloromethane, dimethylformamide (DMF), toluene, tetrahydrofuran (THF), 1,4-dioxane, *m*-xylene, dimethyl sulfoxide (DMSO) and triethylamine were purified by an MBraun MN-SPS-5 Bench-Top under nitrogen atmosphere (H_2O content < 20 ppm as determined by Karl-Fischer titration). All other solvents used for extraction or column chromatography (silica gel: SiO_2, 60 Å, 40–63 μm) are in HPLC grade. Thin layer chromatography (TLC) was carried out on aluminum-backed silica gel 60 F254 plates (Merck) and visualized under UV irradiation either at 254 or 365 nm. Petroleum ether (pet. ether) boiling point range of 40–60 °C was used for chromatography. Size-exclusion chromatography was carried out using Bio-Rad Bio-Beads S-X1 (1% cross linked, 40–80 μm bead size). Evaporation of solvents was performed at 20–50 °C and 5–1010 mbar. Reported yields refer to pure compounds dried under high vacuum (< 0.1 mbar).

^{1}H and ^{13}C nuclear magnetic resonance (NMR) spectra were recorded on a Bruker AVIII HD 400, AVIII HD 500, Avance NEO 600 (broadband helium cryoprobe) and AVIII 700 (1H/13C/15N TCI cryoprobe) spectrometers at 400 MHz, 500 MHz, 600 MHz, 700 MHz (^{1}H) and 101 MHz, 126 MHz, 151 MHz and 175 MHz (^{13}C), respectively at 298 K unless otherwise stated. ^{1}H NMR chemical shifts are reported in ppm to the nearest 0.01 ppm relative to $SiMe_4$ ($\delta = 0$) and coupling constants (J) are in Hertz. ^{1}H NMR spectra have been referenced internally to the residual solvent protons of the deuterated solvent using the reported values (δ = 5.32 for dichloromethane-d_2, 7.26 for chloroform-d, 2.08, 6.97, 7.01 and 7.09 for toluene-d_8). Multiplicities are reported in accordance with the following: s = singlet; d = doublet; dd = doublet of doublet; t = triplet; dt = doublet of triplet and m = multiplet. ^{13}C chemical shifts are reported in ppm to the nearest 0.1 ppm relative to $SiMe_4$ (δ = 0) and have been referenced internally with respect to the residual carbons in the solvents (δ = 53.8 for dichloromethane-d_2, 77.2 for chloroform-d, 137.5, 128.9, 128.0, 125.1 and 20.4 for toluene-d_8). ^{1}H assignments were made using 2D NMR methods (COSY, NOESY, HSQC, HMBC).

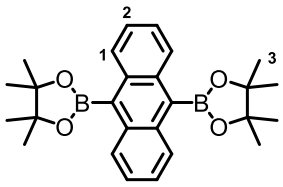
MALDI-TOF MS spectra were measured using Bruker MALDI Autoflex Speed spectrometer utilizing *trans*-2-[3-(4-*tert*-butylphenyl-2-methyl-2-propenylidene]-

malononitrile (DCTB) as matrix. High resolution ESI mass spectrometry (HR-MS) measurements were performed by the mass spectrometry service at the University of Oxford on a Waters GTC classic.

UV−vis−NIR spectra were recorded in solution at 298 K with a Perkin-Elmer Lambda 20 spectrometer with temperature control by a PTP-1 Peltier unit or a JASCO V-770 spectrometer using Infrasil® Quartz 1 cm cuvettes.

Synthesis of Known Compounds

9,10-BisBpinanthracene 3.5

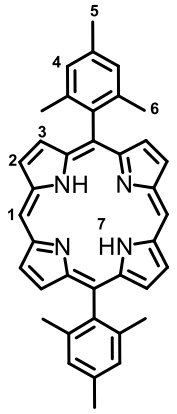


9,10-Dibromoanthracene **3.2** (0.50 g, 1.5 mmol), $Pd(dppf)Cl_2$ (0.24 g, 0.20 equiv., 0.30 mmol), bis(pinacolate)-diboron (1.5 g, 4.0 equiv., 5.9 mmol) and potassium acetate (1.7 g, 12 equiv., 18 mmol) were added into a 100 mL two-neck round-bottom flask and it was evacuated and backfilled with argon for three times. Anhydrous DMF (45 mL) was added using a syringe and the suspension was degassed by three freeze-pump-thaw cycles. The reaction proceeded under 80 °C for 24 h with stirring and monitored by TLC (pet. ether/EtOAc, v/v, 4:1). The reaction was diluted with EtOAc (50 mL) and the organic phase was extracted and washed twice with water (60 mL × 3) and dried over Na_2SO_4. The resulting solution was concentrated under reduced pressure and the residue was purified by silica column chromatography (pet. ether/EtOAc, v/v, 30:1). 9,10-BisBpinanthracene **3.5** (0.59 g, 92%) was yielded as a white solid.

^{1}**H NMR** (400 MHz, $CDCl_3$, 298 K) δ_H 8.26 (dd, J = 6.7, 3.3 Hz, 4H, *H1*), 7.37 (dd, J = 6.7, 3.3 Hz, 4H, *H2*), 1.50 (s, 24H, *H3*).

Analytical data as in lit.[1]

5,15-Bismesitylporphyrin

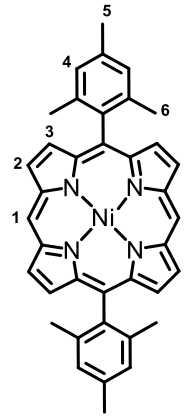


2,4,6-Trimethylbenzaldehyde (0.50 g, 2.0 equiv., 3.4 mmol) and dipyrromethane (0.49 g, 2.0 equiv., 3.4 mmol) were added into a 1.0 L round-bottom flask which contains dichloromethane (500 mL) and ethanol (2.6 mL). The solution was degassed by argon bubbling for 20 min before the addition of boron trifluoride etherate ($BF_3{\cdot}OEt_2$, 0.28 mL, 1.3 equiv., 2.2 mmol). The mixture was stirred in the dark for 3 h and DDQ (1.2 g, 3.0 equiv., 5.1 mmol) was then added. The mixture was left stirring under room temperature for another 30 min. Subsequently the reaction was quenched by the addition of triethylamine (4.5 mL). The solution was concentrated under reduced pressure and purified by a short silica plug (pet. ether/dichloromethane, v/v, 10:1). 5,15-Bismesitylporphyrin (0.28 g, 30%) was yielded as a red-purple solid after recrystallization by layer addition (dichloromethane/methanol) at 4 °C overnight.

^{1}**H NMR** (400 MHz, $CDCl_3$, 298 K) δ_H 10.23 (s, 2H, *H1*), 9.34 (d, *J* = 4.6 Hz, 4H, *H2*), 8.90 (d, *J* = 4.6 Hz, 4H, *H3*), 7.35 (s, 4H, *H4*), 2.68 (s, 6H, *H5*), 1.87 (s, 12H, *H6*), –3.02(s, 2H, *H7*).

Analytical data as in lit.[2]

Ni(II) 5,15-bismesitylporphyrin

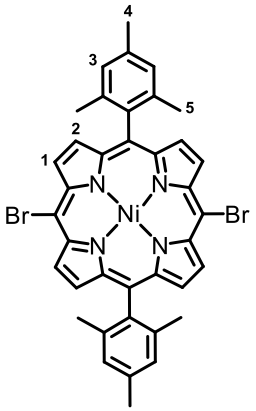


5,15-Bismesitylporphyrin (0.20 g, 0.37 mmol) and $Ni(OAc)_2{\cdot}4H_2O$ (0.27 g, 3.0 equiv., 1.10 mmol) was added into a 50 mL Schlenk tube and the tube was backfilled with argon for three times. Anhydrous DMF (20 mL) was added using a syringe and the suspension was stirred at 140 °C for 2 h. After the reaction was completed, the mixture was cooled to room temperature, followed by the addition of methanol (70 mL) and purple crystals precipitated out of the solution. The mixture was filtered, washed with methanol (30 mL × 2) and dried under vacuum to yield Ni(II) 5,15-bismesitylporphyrin (0.19 g, 88%) as a purple solid.

^{1}**H NMR** (400 MHz, $CDCl_3$, 298 K) δ_H 9.90 (s, 2H, *H1*), 9.15 (d, *J* = 4.7 Hz, 4H, *H2*), 8.78 (d, *J* = 4.7 Hz, 4H, *H3*), 7.26 (s, 4H, *H4*), 2.62 (s, 6H, *H5*), 1.80 (s, 12H, *H6*).

Analytical data as in lit.[3]

Ni(II) 5,15-dibromo-10,20-bismesitylporphyrin



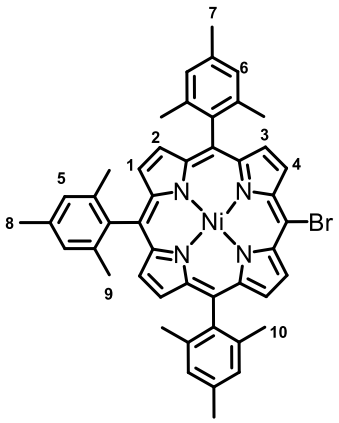
Ni(II) 5,15-bismesitylporphyrin (0.69 g, 1.2 mmol) was added into a 500 mL round-bottom flask followed by the addition of dichloromethane (300 mL) and pyridine (3.0 mL). The solution

was cooled to 0 °C using an ice-bath and, while being stirred, a solution of *N*-bromosuccinimide (0.43 g, 2.1 equiv., 2.4 mmol) in chloroform (60 mL) was added dropwise. The reaction was conducted at 0 °C for 15 min. Subsequently, acetone (20 mL) was added to quench the excess of *N*-bromosuccinimide. The resulting solution was concentrated under reduced pressure and the crude product was recrystallized by layer addition of dichloromethane/methanol. Ni(II) 5,15-dibromo-10,20-bismesitylporphyrin (0.85 g, 98%) was yielded as a dark purple solid.

^{1}**H NMR** (400 MHz, $CDCl_3$, 298 K) δ_H 9.43 (d, *J* = 4.9 Hz, 4H, *H1*), 8.58 (d, *J* = 5.0 Hz, 4H, *H2*), 7.22 (s, 4H, *H3*), 2.58 (s, 6H, *H4*), 1.79 (s, 12H, *H5*).

Analytical data as in lit.[4]

Ni(II) 5-bromo-10,15,20-trimesitylporphyrin 3.4a



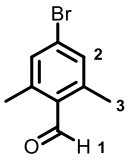
Ni(II) 5,15-dibromodimesityl-10,20-bismesityldibromoporphyrin (0.50 g, 0.66 mmol) and mesitylboronic acid (0.11 g, 1.1 equiv., 0.69 mmol), $Pd(PPh_3)_4$ (76 mg, 0.10 equiv., 66 μmol) and Cs_2CO_3 (6.4 g, 30 equiv., 20 mmol) were added to a two-neck round bottom flask (100 mL) and it was evacuated and backfilled with argon for three times. Anhydrous DMF (5.0 mL) and toluene (30 mL) were added under argon using a syringe and the suspension was degassed by three freeze-pump-thaw cycles. The reaction proceeded at 80 °C for 12 h with stirring and monitored by TLC (pet. ether/dichloromethane, v/v, 4:1). The reaction mixture was diluted with EtOAc (50 mL) and the organic phase was extracted and washed with water (60 mL × 2) and dried over Na_2SO_4. The resulting solution was concentrated under reduced pressure and passed through silica column chromatography (pet. ether/dichloromethane, v/v, 9:1). The second fraction (0.35 g) was collected and based on NMR, 14 mol% of debrominated starting material was mixed with the product. The crude product was dissolved in

dichloromethane (40 mL) and pyridine (0.40 mL). The solution was cooled to 0° C by ice bath, followed by the dropwise addition of a dichloromethane (8.0 mL) solution of *N*-bromosuccinimide (10 mg, 1.2 equiv., 56 μmol). The mixture was left stirring for 30 min and quenched by acetone (5.0 mL). The solvent was removed under reduced pressure and the residue was purified through silica column chromatography (pet. ether/dichloromethane, v/v, 9:1). Ni(II) 5-bromo-10,15,20-trimesitylporphyrin **3.4a** (0.28 g, 52%) as yielded as a purple-red solid.

^{1}**H NMR** (400 MHz, $CDCl_3$, 298 K) δ_H 9.48 (d, J = 4.9 Hz, 2H, *H4*), 8.62 (d, J = 4.9 Hz, 2H, *H3*), 8.50 (s, 4H, *H1*, *H2*), 7.23 – 7.20 (m, 4H, *H6*), 7.18 (s, 2H, *H5*), 2.58 (s, 6H, *H7*), 2.55 (s, 3H, *H8*), 1.81 (s, 18H, *H9*, *H10*).

Analytical data as in lit.[5]

4-Bromo-2,6-dimethylbenzaldehyde

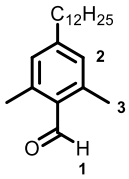


5-Bromo-2-iodo-1,3-dimethylbenzene (8.0 g, 26 mmol) was added into a 250 mL two-neck round-bottom flask and it was evacuated and backfilled with argon three times. Anhydrous THF (72 mL) was added using a syringe and the solution was cooled to −15 °C. *i*-PrMgCl (36 mL, 1.3 M, 1.8 equiv., 46 mmol) was added dropwise and the reaction proceeded at −15 °C and after 2 h of stirring, DMF (4.4 mL, 2.2 equiv., 57 mmol) was added. The mixture was stirred at room temperature for another 1 h and quenched with 1M HCl (20 mL). The reaction mixture was diluted with EtOAc (100 mL) and the organic phase was extracted and washed with water (60 mL × 2) and dried over Na_2SO_4. The resulting solution was concentrated under reduced pressure and the residue was purified through silica column chromatography (pet. ether/EtOAc, v/v, 30:1). 4-Bromo-2,6-dimethylbenzaldehyde (5.4 g, 98%) was yielded as a white solid.

^{1}**H NMR** (400 MHz, $CDCl_3$, 298 K) δ_H 10.47 (s, 1H, *H1*), 7.19 (d, J = 0.9 Hz, 2H, *H2*), 2.51 (s, 6H, *H3*).

Analytical data as in lit.[6]

4-Dodecyl-2,6-dimethylbenzaldehyde

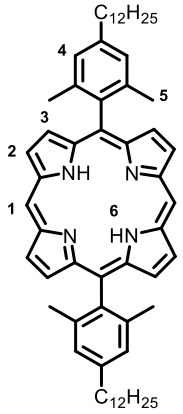


9-BBN (56 mL, 0.50 M in THF, 2.0 equiv., 28 mmol) and dodec-1-ene (6.3 mL, 2.0 equiv., 28 mmol) were added into a 50 mL Schlenk tube and the solution was degassed by three freeze-pump-thaw cycles. The reaction was stirred at room temperature for 12 h. 4-Bromo-2,6-dimethylbenzaldehyde (3.0 g, 14 mmol), $Pd(PPh_3)_4$ (0.81 g, 0.05 equiv., 0.70 mmol), NaOH (3.9 g, 2.0 equiv., 28 mmol), THF (24 mL) and water (4.8 mL) were added under argon and the suspension was degassed by three freeze-pump-thaw cycles again. The reaction mixture was refluxed under argon for another 12 h and monitored by TLC in (pet. ether/EtOAc, v/v, 20:1). The reaction mixture was diluted with EtOAc (20 mL) and the organic phase was extracted and washed with water (20 mL × 2) and dried over Na_2SO_4. The resulting solution was concentrated under reduced pressure and the residue was purified through silica column chromatography (pet. ether/EtOAc, v/v, 99:1). 4-Dodecyl-2,6-dimethylbenzaldehyde (4.0 g, 94%) was yielded as a white solid.

^{1}**H NMR** (400 MHz, $CDCl_3$, 298 K) δ_H 10.57 (s, 1H, *H1*), 6.90 (s, 2H, *H2*), 2.59 (s, 6H, *H3*), 2.58 – 2.50 (m, 2H, $H_{dodecyl}$), 1.74 – 1.51 (m, 2H, $H_{dodecyl}$), 1.39 – 1.12 (m, 22H, $H_{dodecyl}$), 1.01 – 0.49 (m, 3H, $H_{dodecyl}$).

Analytical data as in lit.[7]

5,15-Bis(2,6-dimethyl-4-dodecylphenyl)porphyrin

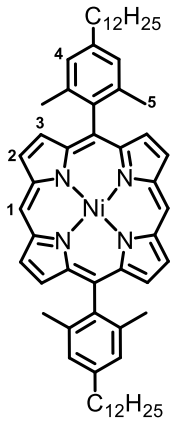


4-Dodecyl-2,6-dimethylbenzaldehyde (1.5 g, 2.0 equiv., 5.1 mmol) and dipyrromethane (0.74 g, 2.0 equiv., 5.1 mmol) were added into a 1.0 L round-bottom flask followed by the addition of dichloromethane (750 mL) and ethanol (3.8 mL). The mixture was degassed by with argon bubbling for 20 min before the addition of boron trifluoride etherate ($BF_3{\cdot}OEt_2$, 0.42 mL, 1.3 equiv., 3.4 mmol). The mixture was stirred in the dark for 3 h and DDQ (1.7 g, 3.0 equiv., 7.6 mmol) was then added. The mixture was stirred at room temperature for another 30 min. Subsequently, the reaction was quenched by the addition of triethylamine (7.5 mL). The solution was concentrated under reduced pressure and purified by a short silica plug (pet. ether/dichloromethane, v/v, 1:1). 5,15-Bis(2,6-dimethyl-4-dodecylphenyl)porphyrin (1.1 g, 49%) was yielded as a red-purple solid after the recrystallization by layer addition (dichloromethane/methanol) at 4 °C overnight.

^{1}**H NMR** (400 MHz, $CDCl_3$, 298 K) δ_H 10.23 (s, 2H, *H1*), 9.34 (d, *J* = 4.5 Hz, 4H, *H2*), 8.90 (d, *J* = 4.6 Hz, 4H, *H3*), 7.33 (s, 4H, *H4*), 2.95 – 2.88 (m, 4H, $H_{dodecyl}$), 2.00 – 1.90 (m, 4H, $H_{dodecyl}$), 1.87 (s, 12H, *H5*), 1.66 – 1.25 (m, 42H, $H_{dodecyl}$), 0.97 – 0.88 (m, 6H, $H_{dodecyl}$), –3.05 (s, 2H, *H6*).

Analytical data as in lit.[7]

Ni(II) 5,15-bis(2,6-dimethyl-4-dodecylphenyl)porphyrin

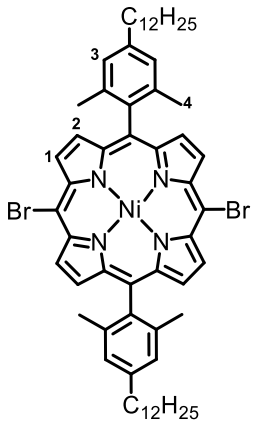


5,15-Bis(2,6-dimethyl-4-dodecylphenyl)porphyrin (0.75 g, 0.88 mmol) and $Ni(OAc)_2{\cdot}4H_2O$ (1.6 g, 3.0 equiv., 2.6 mmol) were added into a 250 mL round-bottom flask and it was evacuated and backfilled with argon for three times. Anhydrous DMF (75 mL) was added using a syringe and the suspension was stirred at 140 °C for 2 h. After the reaction was completed, the mixture was cooled to room temperature, followed by the addition of methanol (70 mL) and purple crystals precipitated out of the solution. The mixture was filtered and washed with methanol (30 mL × 2). Ni(II) 5,15-bis(2,6-dimethyl-4-dodecylphenyl)porphyrin (0.77 g, 96%) was yielded as a purple solid.

^{1}**H NMR** (400 MHz, $CDCl_3$, 298 K) δ_H 9.91 (s, 2H, *H1*), 9.15 (d, *J* = 4.7 Hz, 4H, *H2*), 8.79 (d, *J* = 4.7 Hz, 4H, *H3*), 7.25 (s, 4H, *H4*), 2.86 (t, *J* = 7.8 Hz, 4H, $H_{dodecyl}$), 1.91 (m, 4H, $H_{dodecyl}$), 1.81 (s, 12H, *H5*), 1.62 – 1.27 (m, 41H, $H_{dodecyl}$), 0.97 – 0.87 (m, 6H, $H_{dodecyl}$).

Analytical data as in lit.[7]

Ni(II) 5,15-dibromo-10,20-bis(2,6-dimethyl-4-dodecylphenyl)porphyrin 3.6b

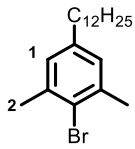


Ni(II) 5,15-bis(2,6-dimethyl-4-dodecylphenyl)porphyrin (0.28 g, 0.31 mmol, 1.0 equiv.) was added into a 250 mL round-bottom flask followed by the addition of dichloromethane (150 mL) and pyridine (1.5 mL). The reaction mixture was cooled to 0 °C using an ice bath and, while being stirred, a solution of *N*-bromosuccinimide (0.12 g, 0.66 mmol, 2.1 equiv.) in chloroform (30 mL) was added dropwise. The reaction was conducted at 0 °C for 15 min. Subsequently, acetone (10 mL) was added to quench the excess *N*-bromosuccinimide. The resulting mixture was concentrated under reduced pressure and purified by a silica plug (pet. ether/dichloromethane, v/v, 20:1) to yield Ni(II) 5,15-dibromo-10,20-bis(2,6-dimethyl-4-dodecylphenyl)porphyrin 3.6b (0.30 g, 91%) as a red-purple solid.

^{1}**H NMR** (400 MHz, $CDCl_3$, 298 K) δ_H 9.43 (d, J = 5.0 Hz, 4H, *H1*), 8.58 (d, J = 5.0 Hz, 4H, *H2*), 7.21 (s, 4H, *H3*), 2.87 – 2.78 (m, 4H, $H_{dodecyl}$), 1.92 – 1.83 (m, 4H, $H_{dodecyl}$), 1.80 (s, 12H, *H4*), 1.58 – 1.25 (m, 41H, $H_{dodecyl}$), 0.95 – 0.87 (m, 6H, $H_{dodecyl}$).

Analytical data as in lit.[7]

2-Bromo-5-dodecyl-1,3-dimethylbenzene

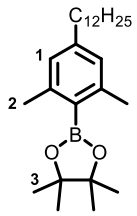


9-BBN (18 mL, 0.50 M in THF, 1.8 equiv., 9.2 mmol) and dodec-1-ene (1.2 mL, 1.1 equiv., 5.4 mmol) were added into a 50 mL Schlenk tube and the solution was degassed by three freeze-pump-thaw cycles. The reaction was stirred at room temperature for 12 h. 2-Bromo-5-iodo-1,3-dimethylbenzene (1.6 g, 5.1 mmol), $Pd(PPh_3)_4$ (0.3 g, 0.05 equiv., 0.26 mmol), K_2CO_3 (1.4 g, 2.0 equiv., 10 mmol), THF (12 mL) and water (2.4 mL) were added under argon and the suspension was degassed by three freeze-pump-thaw cycles again. The reaction was refluxed under argon for another 12 h and monitored by TLC (pet. ether/EtOAc, v/v, 20:1). The reaction mixture was diluted with EtOAc (20 mL) and the organic phase was extracted and washed with water (20 mL × 2) and dried over Na_2SO_4. The resulting solution was concentrated under reduced pressure and the residue was purified through silica column chromatography (pet. ether/EtOAc, v/v, 99:1). 2-Bromo-5-dodecyl-1,3-dimethylbenzene (1.8 g, 98%) was yielded as a colorless oil.

^{1}H NMR (400 MHz, $CDCl_3$, 298 K) δ_H 6.91 (s, 2H, *H1*), 2.52 (d, *J* = 7.5 Hz, 2H, $H_{dodecyl}$), 2.41 (s, 6H, *H2*), 1.60 (t, *J* = 7.6 Hz, 2H, $H_{dodecyl}$), 1.29 (s, 22H, $H_{dodecyl}$), 0.92 (t, *J* = 6.8 Hz, 3H, $H_{dodecyl}$).

Analytical data as in lit.[7]

2,6-Dimethyl-4-dodecylphenylboronic acid pinacol ester

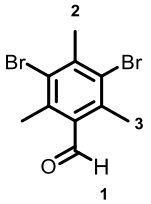


2-Bromo-5-dodecyl-1,3-dimethylbenzene (0.33 g, 0.93 mmol), $Pd(dppf)Cl_2$ (66 mg, 0.10 equiv., 93 μmol), bis(pinacolate)-diboron (0.47 g, 2.0 equiv., 1.9 mmol) and KOAc (0.55 g, 6.0 equiv., 5.6 mmol) were added into a 10 mL Schlenk tube and it was evacuated and backfilled with argon for three times. Anhydrous 1,4-dioxane (3.0 mL) was added using a syringe and the suspension was degassed by three freeze-pump-thaw cycles. The reaction mixture was stirred at 100 °C for 24 h and monitored by TLC (pet. ether/EtOAc, v/v, 10:1). The reaction mixture was diluted with EtOAc (50 mL) and the organic phase was extracted and washed with water (60 mL × 2) and dried over Na_2SO_4. The resulting solution was concentrated under reduced pressure and the residue was purified through silica column chromatography (pet. ether/EtOAc, v/v, 30:1). 2-(4-Dodecyl-2,6-dimethylphenyl)-4,4,5,5-tetramethyl-1,3,2-dioxaborolane (0.26 g, 70%) as yielded as a light-yellow oil.

^{1}H NMR (400 MHz, $CDCl_3$, 298 K) δ_H 6.79 (s, 2H, *H1*), 2.50 (t, *J* = 7.5 Hz, 2H, $H_{dodecyl}$), 2.40 (s, 6H, *H2*), 1.61 – 1.52 (m, 2H, $H_{dodecyl}$), 1.39 (s, 12H, *H3*), 1.28 (s, 19H, $H_{dodecyl}$), 0.94 – 0.87 (m, 3H, $H_{dodecyl}$).

Analytical data as in lit.[7]

3,5-Dibromo-2,4,6-trimethylbenzaldehyde 3.13

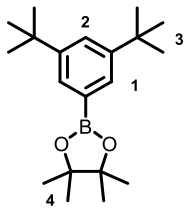


2,4,6-Trimethylbenzaldehyde (1.0 g, 1.0 mL, 6.8 mmol) was dissolved in TFA (3.7 mL, 7.0 equiv., 47.5 mmol) followed by the dropwise addition of concentrated sulfuric acid (7.3 mL, 20 equiv., 0.14 mol). *N*-Bromosuccinimide (2.7 g, 2.2 equiv., 15 mmol) was added and the reaction proceeded at room temperature open to the atmosphere for 18 h with vigorous stirring. The solution turned brown, and the excess sulfuric acid was neutralized using 2M NaOH solution (50 mL) cooled by an ice bath. The reaction mixture was diluted with EtOAc (100 mL) and the organic phase was extracted and washed with water (200 mL × 2) and dried over Na_2SO_4. The resulting solution was concentrated under reduced pressure and the residue was purified through a silica column chromatography (pet. ether/EtOAc, v/v, 10:1). 3,5-Dibrom-2,4,6-trimethylbenzaldehyde **3.13** (1.9 g, 93%) was yielded as a white solid.

^{1}H NMR (400 MHz, $CDCl_3$, 298 K) δ_H 10.47 (s, 1H, *H1*), 2.74 (s, 3H, *H2*), 2.57 (s, 6H, *H3*).

Analytical data as in lit.[8]

1-Bpin-3,5-di-*tert*-butylbenzene 3.14c



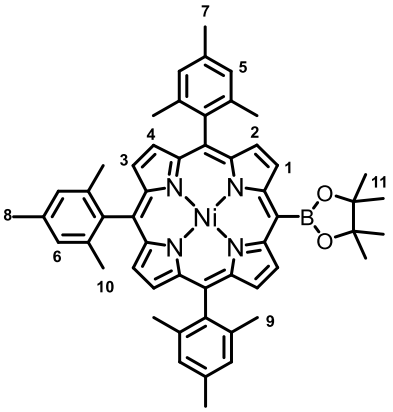
1-Bromo-3,5-di-*tert*-butylbenzene (3.5 g, 13 mmol), $Pd(dppf)Cl_2$ (0.48 g, 0.05 equiv., 0.65 mmol), bis(pinacolate)-diboron (4.3 g, 1.3 equiv., 17 mmol) and potassium acetate (3.9 g, 3.0 equiv., 40 mmol) were added to a 150 mL two-neck round-bottom flask and it was evacuated and backfilled with argon three times. Anhydrous DMSO (65 mL) was added under argon using a syringe and the suspension was degassed by three freeze-pump-thaw cycles. The reaction proceeded at 80 °C for 20 h with stirring and monitored by TLC (pet. ether/EtOAc, v/v, 15:1). The reaction mixture was diluted with EtOAc (50 mL) and the organic phase was extracted and washed twice with water (100 mL × 2) and dried over Na_2SO_4. The resulting solution was concentrated under reduced pressure and the residue was purified through a silica column chromatography (pet. ether/EtOAc, v/v, 30:1). 1-Bpin-3,5-di-*tert*-butylbenzene **3.14c** (3.8 g, 92%) was yielded as a white solid after recrystallization by layer addition (dichloromethane/methanol) at 4 °C overnight.

^{1}H NMR (400 MHz, $CDCl_3$, 298 K) δ_H 7.67 (d, *J* = 2.0 Hz, 2H, *H1*), 7.55 (t, *J* = 2.0 Hz, 1H, *H2*), 1.35 (s, 18H, *H3*), 1.34 (s, 12H, *H4*).

Analytical data as in lit.[9]

Synthesis of Novel Compounds

Ni(II) 5-Bpin-10,15,20-trimesityl-porphyrin 3.1a



Porphyrin **3.4a** (18 mg, 23 μmol) and $PdCl_2(PPh_3)_2$ (1.6 mg, 0.10 equiv., 2.3 μmol) were added into a 10 mL Schlenk tube and it was evacuated and backfilled with argon for three times. Anhydrous THF (1.2 mL), toluene (1.2 mL) and triethylamine (0.26 mL, 75 equiv., 1.7 mmol) were added using a syringe and the solution was degassed by three freeze-pump-thaw cycles followed by the addition of 4,4,5,5-tetramethyl-1,3,2-dioxaborolane (0.12 mL, 36 equiv., 0.81 mmol). The reaction proceeded at 68 °C for 16 h and the excess of pinacolborane was quenched by dropwise addition of water (2.0 mL). EtOAc (10 mL) was added to the cooled reaction mixture and the organic phase was extracted and washed with water (10 mL × 2) and dried over Na_2SO_4. The resulting solution was concentrated under reduced pressure and the crude material was purified through silica chromatography (pet. ether/EtOAc v/v, gradient elution from 10:0 to 10:3) to yield porphyrin **3.1a** (14 mg, 71%) as a purple solid.

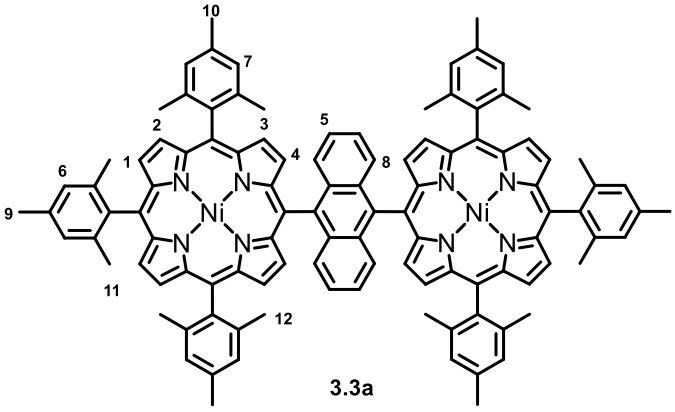
^{1}H NMR (400 MHz, $CDCl_3$, 298 K) δ_H 9.68 (d, *J* = 4.9 Hz, 2H, *H1*), 8.67 (d, *J* = 4.9 Hz, 2H, *H2*), 8.57 – 8.48 (m, 4H, *H3*, *H4*), 7.21 (s, 4H, *H5*), 7.19 (s, 2H, *H6*), 2.58 (s, 6H, *H7*), 2.56 (s, 3H, *H8*), 1.82 (2 overlap s, 18H, *H9*, *H10*), 1.72 (s, 12H, *H11*).

^{13}C NMR (151 MHz, $CDCl_3$, 298 K) δ_C 147.0, 142.9, 142.1, 141.8, 139.3, 139.2, 137.7, 137.7, 137.6, 137.4, 133.9, 132.0, 131.7, 130.97, 127.8, 127.8, 118.3, 117.0, 85.0, 25.4, 21.6, 21.6, 21.5, 1.2.

MALDI-TOF MS: m/z = 845.328 ($C_{53}H_{53}BN_4NiO_2$, M^+ requires 845.365).

UV–vis (dichloromethane) λ_{max} (ε / 10^4 $M^{-1}cm^{-1}$): 411 (17.7), 530 (1.16) nm.

Anthracene-linked porphyrin dimer 3.3a



3.3a

Porphyrin **3.1a** (14 mg, 2.5 equiv., 16 μmol), 9,10-dibromoanthracene **3.2** (2.2 mg, 6.5 μmol), $Pd(PPh_3)_4$, (2.3 mg, 0.3 equiv., 2.0 μmol) and Cs_2CO_3 (5.3 mg, 2.5 equiv., 16 mmol) were combined in a 10 mL Schlenk tube and it was evacuated and backfilled with argon for three times. In another 25 mL Schlenk tube, anhydrous DMF (0.6 mL) and toluene (2.4 mL) were degassed by three freeze-pump-thaw cycles. The mixed solvent was added into the solid mixture and the reaction proceeded at 110 °C for 12 h with stirring and monitored by TLC in pet. ether/dichloromethane (4:1, v/v). EtOAc (10 mL) was added to the cooled reaction mixture and the combined organic extracts washed with water (10 mL × 2) and dried over Na_2SO_4 before the solvent was removed under reduced pressure. The residue was purified through silica chromatography (pet. ether/dichloromethane v/v, gradient elution from 10:0 to 4:1). Singly-linked porphyrin-anthracene dimer **3.3a** (5.7 mg, 54%) was isolated as a red solid and *meso*-singly-linked porphyrin dimer ***s*-P2a** (1.6 mg, 17%) as a reds solid as a side product.

^{1}H NMR (400 MHz, $CDCl_3$, 298 K) δ_H 8.63 – 8.59 (m, 8H, *H1*, *H2*), 8.58 (d, J = 4.8 Hz, 4H, *H3*), 8.51 (d, J = 4.9 Hz, 4H, *H4*), 7.35 – 7.29 (dd, J = 6.9, 3.3 Hz, 4H, *H5*), 7.25 (s, 4H, *H6*), 7.22 (s,

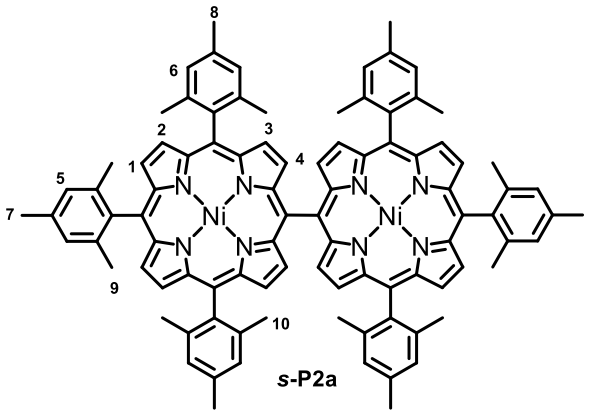
8H, *H7*), 7.00 (dd, *J* = 7.1, 3.2 Hz, 4H, *H8*), 2.60 (s, 6H, *H9*), 2.58 (s, 12H, *H10*), 1.90 (s, 12H, *H11*), 1.89 (s, 24H, *H12*).

^{13}C NMR (151 MHz, $CDCl_3$, 298 K) δ_C 144.2, 143.1, 142.8, 142.6, 139.1, 139.1, 137.7, 137.5, 137.4, 136.5, 133.8, 132.3, 131.7, 131.4, 131.3, 128.6, 127.8, 127.7, 125.3, 117.6, 117.5, 114.2, 29.7, 21.5, 21.4.

MALDI-TOF MS: *m/z* = 1614.709 ($C_{108}H_{90}N_8Ni_2$, M^+ requires 1614.600).

UV–vis (dichloromethane) λ_{max} (ε / 10^4 $M^{-1}cm^{-1}$): 415 (27.1), 429 (27.6), 529 (3.86) nm.

***Meso*-singly-linked porphyrin dimer *s*-P2a**



Synthetic procedure as described above.

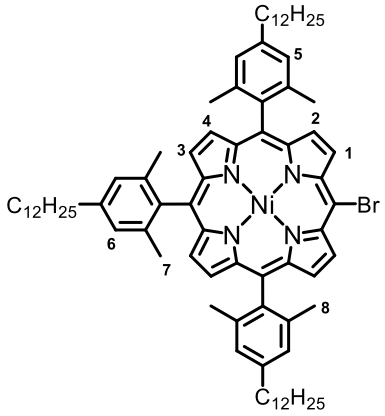
^{1}H NMR (400 MHz, $CDCl_3$, 298 K) δ_H 8.64 – 8.57 (m, 8H, *H1*, *H2*), 8.34 (d, *J* = 4.9 Hz, 4H, *H3*), 8.00 (d, *J* = 4.9 Hz, 4H, *H4*), 7.25 (s, 4H, *H5*), 7.14 (s, 8H, *H6*), 2.60 (s, 6H, *H7*), 2.49 (s, 12H, *H8*), 1.90 (s, 12H, *H9*), 1.84 (s, 24H, *H10*).

^{13}C NMR (151 MHz, $CDCl_3$, 298 K) δ_C 147.5, 143.4, 142.9, 142.6, 139.3, 139.2, 137.8, 137.7, 137.6, 134.3, 131.5, 131.2, 130.9, 127.9, 127.8, 118.3, 118.0, 116.3, 21.7, 21.7, 21.6, 21.5.

MALDI-TOF MS: *m/z* = 1438.029 ($C_{94}H_{82}N_8Ni_2$, M^+ requires 1438.537).

UV–vis (dichloromethane) λ_{max} (ε / 10^4 $M^{-1}cm^{-1}$): 413 (9.56), 446 (11.4), 536 (2.81) nm.

Ni(II) 5-bromo-10,15,20-tri(2,6-dimethyl-4-dodecylphenyl)porphyrin 3.4b



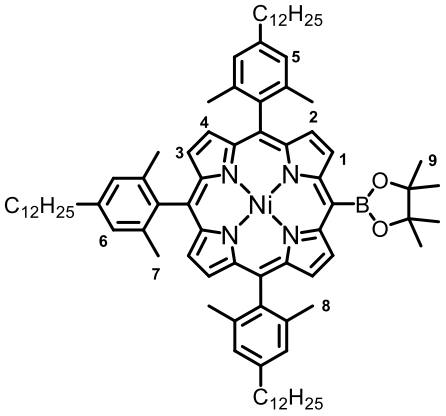
Ni(II) 5,15-bis(2,6-dimethyl-4-dodecylphenyl)-10,20-porphyrin **3.6b** (0.28 g, 1.2 equiv., 0.26 μmol), 2-(4-dodecyl-2,6-dimethylphenyl)-4,4,5,5-tetramethyl-1,3,2-dioxaborolane (92 mg, 0.23 mmol), $Pd(PPh_3)_4$ (80 mg, 0.30 equiv., 69 μmol) and Cs_2CO_3 (0.23 g, 3.0 equiv., 0.69 mmol) were added to a 20 mL Schlenk tube and it was backfilled with argon for three times. Anhydrous DMF (2.0 mL) and toluene (10 mL) were added under argon using a syringe and the suspension was degassed by three freeze-pump-thaw cycles. The reaction proceeded at 100 °C for 12 h with stirring and monitored by TLC (pet. ether/dichloromethane v/v, 10:1). The reaction mixture was diluted with EtOAc (30 mL) and the organic phase was extracted and washed with water (30 mL × 2) and dried over Na_2SO_4. The resulting solution was concentrated under reduced pressure and the residue was purified through silica column chromatography (pet. ether/dichloromethane, v/v, 20:1). The second fraction was collected and purified through size-exclusion chromatography (Bio-Rad S-X1, toluene) and porphyrin **3.4b** (83 mg, 29%) yielded as a purple-red solid.

^{1}H NMR (400 MHz, $CDCl_3$, 298 K) δ_H 9.49 (d, J = 4.9 Hz, 2H, *H1*), 8.64 (d, J = 4.9 Hz, 2H, *H2*), 8.52 (s, 4H, *H3*, *H4*), 7.22 (s, 4H, *H5*), 7.19 (s, 2H, *H6*), 2.88 – 2.78 (m, 6H, $H_{dodecyl}$), 1.84 (m, 24H, *H7*, *H8*, $H_{dodecyl}$), 1.59 – 1.24 (m, 61H, $H_{dodecyl}$), 0.91 (m, 9H, $H_{dodecyl}$).

^{13}C NMR (151 MHz, $CDCl_3$, 298 K) δ_C 143.1, 139.5, 138.0, 131.9, 130.2, 127.3, 117.6, 104.7, 36.3, 32.2, 31.9, 30.0, 29.9, 29.9, 29.9, 29.6, 22.9, 21.9, 14.3.

MALDI-TOF MS: m/z = 1261.108 ($C_{80}H_{107}BrN_4Ni$, M^+ requires 1260.703).

Ni(II) 5-Bpin-10,15,20-tri(2,6-dimethyl-4-dodecylphenyl)porphyrin 3.1b



Porphyrin **3.4b** (33 mg, 26 μmol), $PdCl_2(PPh_3)_2$ (1.8 mg, 0.1 equiv., 2.6 μmol) were added into a 15 mL Schlenk tube and it was evacuated and backfilled with argon for three times. Anhydrous THF (1.2 mL), toluene (1.2 mL) and triethylamine (0.27 mL, 75 equiv., 2.0 mmol) were added using a syringe and the solution was degassed by three freeze-pump-thaw cycles followed by the addition of 4,4,5,5-tetramethyl-1,3,2-dioxaborolane (68 μL, 18 equiv., 0.47 mmol). The reaction proceeded at 68 °C for 5 h and the excess of pinacolborane was quenched by dropwise addition of water (4.0 mL). EtOAc (10 mL) was added to the cooled reaction mixture and the organic extract was washed with water (10 mL × 2) and dried over Na_2SO_4. The resulting solution was concentrated under reduced pressure and the crude material was purified through silica chromatography (pet. ether/EtOAc v/v, gradient elution from 10:0 to 10:1) to yield porphyrin **3.1b** (24 mg, 70%) as a purple solid.

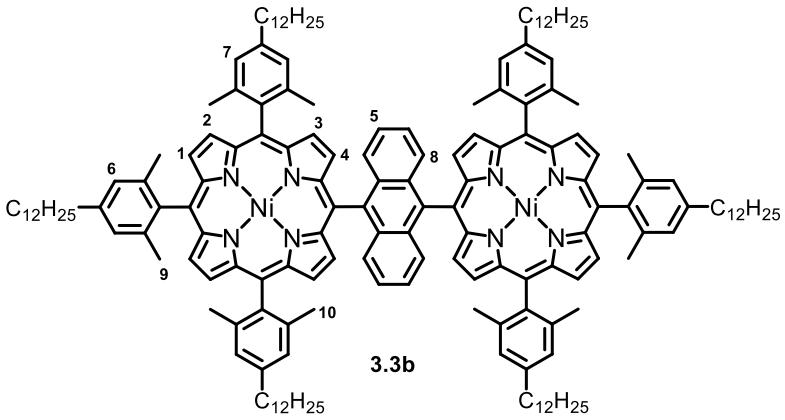
^{1}H NMR (400 MHz, $CDCl_3$, 298 K) δ_H 9.70 (d, *J* = 4.9 Hz, 2H, *H1*), 8.68 (d, *J* = 4.9 Hz, 2H, *H2*), 8.55 (d, *J* = 4.8 Hz, 2H, *H3*), 8.52 (d, *J* = 4.8 Hz, 2H, *H4*), 7.21 (s, 4H, *H5*), 7.19 (s, 2H, *H6*), 2.82 (q, *J* = 8.2 Hz, 6H, $H_{dodecyl}$), 1.84 (m, 24H, $H_{dodecyl}$, *H7*, *H8*), 1.73 (s, 12H, *H9*), 1.60 – 1.22 (m, 54H, $H_{dodecyl}$), 0.91 (m, 9H, $H_{dodecyl}$).

^{13}C NMR (101 MHz, $CDCl_3$, 298 K) δ_C 145.8, 141.8, 141.7, 141.6, 140.9, 140.7, 137.9, 137.9, 136.4, 132.4, 130.8, 130.5, 129.8, 125.9, 117.3, 115.9, 83.8, 83.8, 35.0, 34.9, 30.9, 30.9, 30.7, 30.6, 28.8, 28.7, 28.7, 28.7, 28.7, 28.7, 28.6, 28.6, 28.4, 28.4, 24.4, 21.7, 20.5, 20.5, 13.1.

MALDI-TOF MS: *m/z* = 1307.344 ($C_{86}H_{119}BN_4NiO_2$, M^+ requires 1037.881).

UV–vis (dichloromethane) λ_{max} (ε / 10^4 $M^{-1}cm^{-1}$): 412 (20.3), 530 (1.12) nm.

Anthracene-linked porphyrin dimer 3.3b



3.3b

Porphyrin **3.1b** (83 mg, 2.5 equiv., 64 μmol), 9,10-dibromoanthracene (8.5 mg, 25 μmol), $Pd(PPh_3)_4$ (8.8 mg, 0.3 equiv., 7.6 μmol) and Cs_2CO_3 (21 mg, 2.5 equiv., 64 μmol) were added to a 40 mL Schlenk tube and it was evacuated and backfilled with argon for three times. Anhydrous DMF (3.0 mL) and toluene (12 mL) were added under argon using a syringe and the suspension was degassed by three freeze-pump-thaw cycles. The reaction proceeded at 80 °C for 12 h with stirring and monitored by TLC in pet. ether/dichloromethane (4:1, v/v). The reaction mixture was diluted with EtOAc (20 mL) and the organic phase was extracted and washed with water (20 mL × 2) and dried over Na_2SO_4. The resulting solution was concentrated under reduced pressure and the residue was purified through a silica column chromatography (pet. ether/EtOAc, v/v, 10:1). Singly-linked porphyrin-anthracene dimer **3.3b** (40 mg, 66%) was isolated as a red solid and *meso*-singly-linked porphyrin dimer ***s*-P2b** (3.3 mg, 6%) obtained as a red solid as a side product.

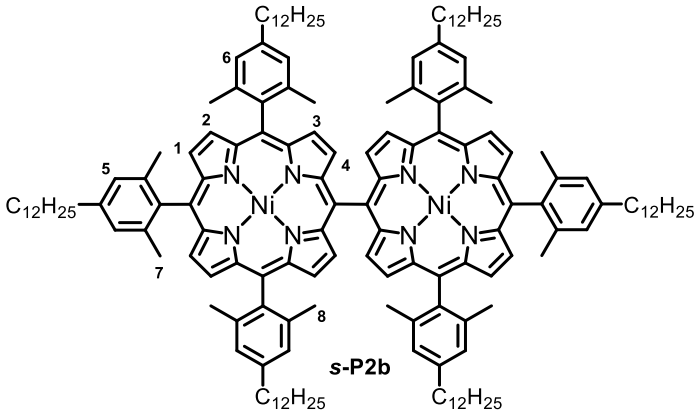
^{1}H NMR (500 MHz, $CDCl_3$, 298 K) δ_H 8.62 (m, 8H, *H1*, *H2*), 8.59 (d, *J* = 4.8 Hz, 4H, *H3*), 8.52 (d, *J* = 4.9 Hz, 4H, *H4*), 7.33 (dd, *J* = 7.1, 3.3 Hz, 4H, *H5*), 7.25 (s, 4H, *H6*), 7.22 (s, 8H, *H7*), 7.01 (dd, *J* = 7.2, 3.2 Hz, 4H, *H8*), 2.84 (m, 12H, $H_{dodecyl}$), 1.92 (s, 12H, *H9*), 1.91 (s, 24H, *H10*), 1.49 – 1.26 (m, 114H, $H_{dodecyl}$), 0.90 (t, *J* = 6.9 Hz, 18H, $H_{dodecyl}$).

^{13}C NMR (126 MHz, $CDCl_3$, 298 K) δ_C 144.2, 143.1, 142.8, 142.8, 142.8, 142.6, 139.0, 139.0, 137.6, 137.6, 136.5, 133.9, 132.3, 131.7, 131.5, 131.4, 128.7, 127.1, 127.0, 125.2, 117.7, 117.6, 114.2, 36.0, 36.0, 32.0, 31.7, 31.7, 29.8, 29.8, 29.8, 29.8, 29.7, 29.7, 29.7, 29.7, 29.4, 29.4, 22.7, 21.6, 14.2.

MALDI-TOF MS: *m/z* = 2539.651 ($C_{174}H_{222}N_8Ni_2$, M^+ requires 2539.632).

UV–vis (dichloromethane) λ_{max} (ε / 10^4 $M^{-1}cm^{-1}$): 412 (25.8), 426 (25.9), 526 (3.70) nm.

Meso-singly-linked porphyrin dimer *s*-P2b



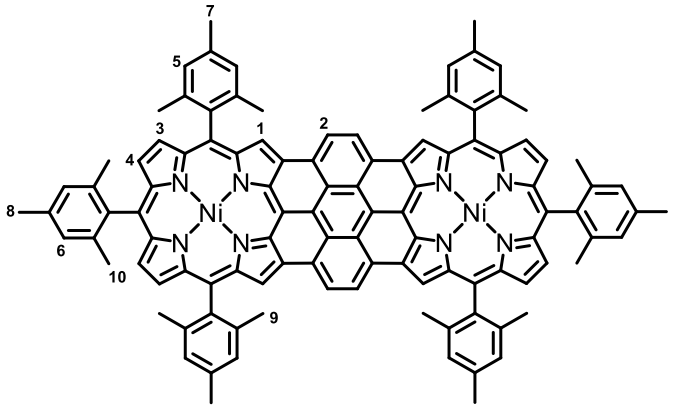
Synthetic procedure as described above.

^{1}H NMR (500 MHz, $CDCl_3$, 298 K) δ_H 8.65 – 8.59 (m, 8H, *H1*, *H2*), 8.36 (d, *J* = 4.9 Hz, 4H, *H3*), 8.02 (d, *J* = 5.0 Hz, 4H, *H4*), 7.25 (s, 4H, *H5*), 7.14 (s, 8H, *H6*), 2.86 (t, *J* = 7.8 Hz, 4H, $H_{dodecyl}$), 2.75 (t, *J* = 7.7 Hz, 8H, $H_{dodecyl}$), 1.92 (s, 12H, H^7), 1.86 (s, 24H, *H8*), 1.78 (t, *J* = 7.6 Hz, 12H, $H_{dodecyl}$), 1.52 – 1.19 (m, 108H, $H_{dodecyl}$), 0.94 – 0.89 (m, 6H, $H_{dodecyl}$), 0.85 (t, *J* = 6.8 Hz, 12H, $H_{dodecyl}$).

^{13}C NMR (126 MHz, $CDCl_3$, 298 K) δ_C 147.5, 143.4, 142.9, 142.8, 142.5, 139.2, 139.0, 137.9, 137.8, 134.2, 131.5, 131.2, 130.9, 127.2, 127.1, 118.3, 118.0, 116.3, 36.2, 36.1, 32.1, 32.1, 31.8, 31.7, 29.9, 29.9, 29.9, 29.8, 29.8, 29.8, 29.7, 29.6, 29.5, 22.9, 22.8, 21.8, 21.7, 14.3, 14.3.

MALDI-TOF MS: *m/z* = 2363.489 ($C_{160}H_{214}N_8Ni_2$, M^+ requires 2363.570).

Fused anthracene-linked porphyrin dimer AP2a



Anthracenyl-porphyrin dimer **3.3a** (7.3 mg, 4.5 μmol) and 2,3-dichloro-5,6-dicyano-1,4-benzoquinone (15 mg, 15 equiv., 68 μmol) were added into a 15 mL Schlenk tube and the tube was evacuated and backfilled with argon for three times. Degassed dichloromethane (8.0 mL) was added to the mixture under argon followed by the addition of TfOH (80 μL). The reaction proceeded at room temperature for 2 h with stirring and monitored by aluminum oxide TLC in pet. ether/dichloromethane (4:1). After the reaction was completed, the mixture was quenched by triethylamine (5.0 mL) and methanol (10 mL) was added to precipitate out the fused product. The collected solid was further purified via aluminum oxide chromatography (pet. ether/dichloromethane, v/v, 4:1) to yield anthracene-fused porphyrin dimer **AP2a** (4.3 mg, 59%) as a black solid.

^{1}H NMR (600 MHz, CD_2Cl_2/CS_2 (2:1, v/v), 298 K) δ_H 7.70 (s, 4H, *H1*), 7.65 (s, 4H, *H2*), 7.63 (d, *J* = 4.8 Hz, 4H, *H3*), 7.58 (d, *J* = 4.7 Hz, 4H, *H4*), 7.15 (s, 8H, *H5*), 7.10 (s, 4H, *H6*), 2.55 (s, 12H, *H7*), 2.49 (s, 6H, *H8*), 2.02 (s, 24H, *H9*), 1.95 (s, 12H, *H10*).

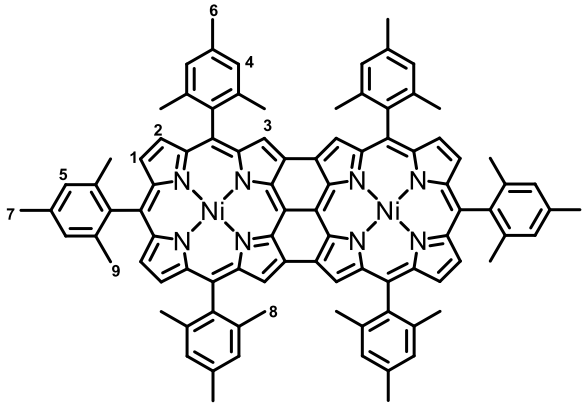
^{13}C NMR (151 MHz, CD_2Cl_2/CS_2 (2:1, v/v), 298 K) δ_C 146.8, 146.2, 144.9, 143.5, 138.7, 138.7, 138.1, 138.0, 136.7, 136.6, 136.0, 132.3, 131.7, 131.0, 130.6, 128.4, 128.4, 127.4, 127.2, 123.1, 122.8, 120.9, 111.5, 30.4, 21.8, 21.4, 21.2.

MALDI-TOF MS: *m/z* = 1606.648 ($C_{108}H_{82}N_8Ni_2$, M^+ requires 1606.537).

UV–vis–NIR (toluene-d_8) λ_{max} (ε / 10^4 $M^{-1}cm^{-1}$): 356 (4.00), 446 (6.23), 588 (7.30), 1026 (2.59), 1188 (8.85) nm.

Single Crystal Data: $C_{110}H_{86}Cl_4N_8Ni_2$, Mr =1779.18. 150 K – orthorhombic, P b c a, *a* = 18.1093(5) Å, b = 16.4169(4) Å, *c* = 28.9379(10) Å, *V* = 8603.2(4) Å^3, Data/restraints/parameters – 9007/ 0/ 559, R_{int} = 0.096, Final R_1 = 0.0831, wR_2 = 0.2362 (I>2σ(*I*)).

Fused mesityl porphyrin dimer P2a



Meso-singly-linked porphyrin dimer ***s*-P2a** (2.2 mg, 1.5 μmol) was added into a 15 mL Schlenk tube and the tube was evacuated and backfilled with argon for three times. Dry 1,2-dichloroethane (4.0 mL) was added to the tube under argon. Under vigorous stirring, a suspension of $AuCl_3$ (0.9 mg, 2.0 equiv., 3.0 μmol) and AgOTf (3.9 mg, 10 equiv., 15 μmol) in dry 1,2-dichloroethane (2.0 mL) was added dropwise to the tube and the reaction mixture was stirred for 2 h at room temperature. The reaction was quenched by the addition of triethylamine (1.0 mL) and the residue purified through a silica gel plug eluting with dichloromethane. After removal of solvent under reduced pressure, fused mesityl porphyrin dimer **P2a** (2.0 mg, 90%) was yielded as a purple-red solid.

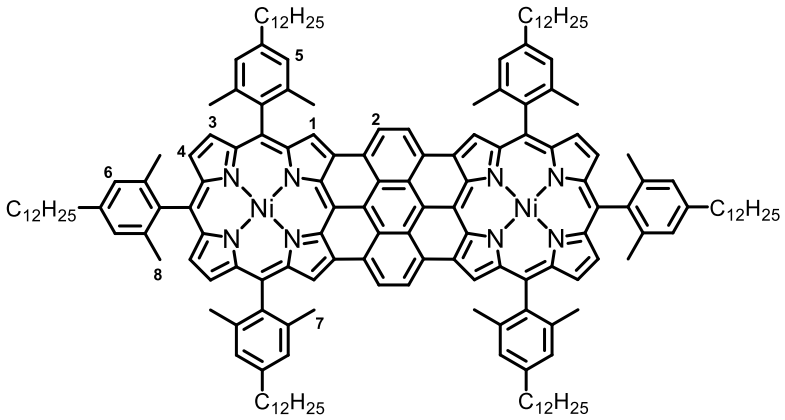
^{1}H NMR (400 MHz, $CDCl_3$, 298 K) δ_H 7.50 (s, 8H, *H1*, *H2*), 7.17 (s, 4H, *H3*), 7.09 (s, 8H, *H4*), 7.06 (s, 4H, *H5*), 2.49 (s, 12H, *H6*), 2.46 (s, 6H, *H7*), 1.97 (s, 24H, *H8*), 1.91 (s, 12H, *H9*).

^{13}C NMR (151 MHz, $CDCl_3$, 298 K) δ_C 146.4, 145.8, 144.5, 143.1, 138.3, 138.3, 137.7, 137.7, 136.3, 136.2, 135.6, 131.9, 131.3, 130.6, 130.2, 128.0, 128.0, 127.0, 126.8, 122.7, 122.4, 120.5, 111.1, 30.0, 21.4, 21.3, 21.0, 20.8.

MALDI-TOF MS: *m/z* = 1433.992 ($C_{94}H_{78}N_8Ni_2$, M^+ requires 1434.506).

UV–vis–NIR (toluene-d_8) λ_{max} (ε / 10^4 $M^{-1}cm^{-1}$): 405 (3.49), 576 (4.06), 874 (0.53), 941 (0.51) nm.

Fused anthracene-linked porphyrin dimer AP2b



Anthracenyl-porphyrin dimer **3.3b** (5.8 mg, 2.3 μmol) and 2,3-dichloro-5,6-dicyano-1,4-benzoquinone (7.8 mg, 15 equiv., 34 μmol) were added into a 15 mL Schlenk tube and the tube was evacuated and backfilled with argon three times. Degassed dichloromethane (4.0 mL) was added to the mixture under argon followed by the addition of TfOH (40 μL). The reaction proceeded in the dark at room temperature for 18 h with stirring and monitored by TLC in toluene. After the reaction was completed, the mixture was quenched by triethylamine (0.3 mL) and methanol (20 mL) was added to precipitate out the fused product. The residue was purified through a short silica gel plug eluting with toluene. Fused anthracenyl-porphyrin dimer **AP2b** (5.2 mg, 90%) was yielded as a black solid.

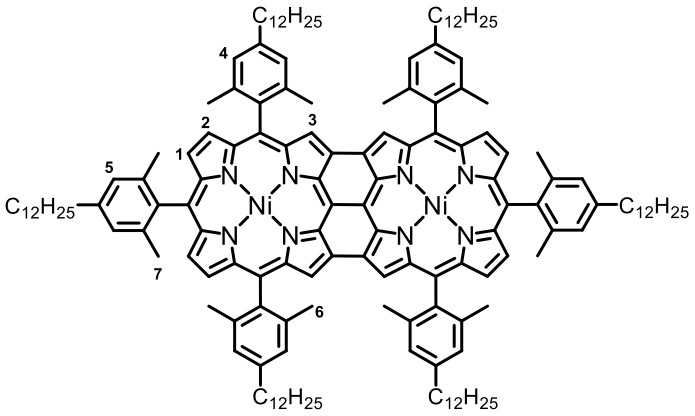
^{1}H NMR (600 MHz, CD_2Cl_2/CS_2 (2:1, v/v), 298 K) δ_H 7.71 (s, 4H, *H1*), 7.66 (s, 4H, *H2*), 7.62 (d, *J* = 4.8 Hz, 4H, *H3*), 7.58 (d, *J* = 4.8 Hz, 4H, *H4*), 7.15 (s, 8H, *H5*), 7.09 (s, 4H, *H6*), 2.80 – 2.77 (m, 8H, $H_{dodecyl}$), 2.75 – 2.72 (m, 4H, $H_{dodecyl}$), 2.02 (s, 24H, *H7*), 1.95 (s, 12H, *H8*), 1.85 – 1.77 (m, 12H, $H_{dodecyl}$), 1.54 – 1.31 (m, 108H, $H_{dodecyl}$), 0.95 – 0.92 (m, 24H, $H_{dodecyl}$).

^{13}C NMR (151 MHz, CD_2Cl_2/CS_2 (2:1, v/v), 298 K) δ_C 146.4, 145.8, 144.5, 143.1, 142.8, 138.2, 136.4, 135.6, 131.3, 130.7, 130.2, 126.9, 122.9, 122.40, 37.3, 36.2, 36.1, 33.0, 32.2, 31.8, 30.4, 30.2, 29.5, 27.3, 23.0, 22.7, 21.1, 20.9, 14.2.

MALDI-TOF MS: *m/z* = 2531.542 ($C_{174}H_{214}N_8Ni_2$, M^+ requires 2531.565).

UV–vis–NIR (toluene-d_8) λ_{max} (ε / 10^4 $M^{-1}cm^{-1}$): 358 (4.66), 586 (7.52), 1032 (2.75), 1190 (8.15) nm.

Fused dodecyl porphyrin dimer P2b



Porphyrin dimer ***s*-P2b** (15 mg, 6.5 μmol) was added into a 25 mL Schlenk tube and it was evacuated and backfilled with argon for three times. Dry 1,2-dichloroethane (6.0 mL) was added to the tube under argon. Under vigorous stirring, a suspension of $AuCl_3$ (3.9 mg, 2.0 equiv., 13 μmol) and AgOTf (17 mg, 10 equiv., 65 μmol) in dry 1,2-dichloroethane (3.6 mL) was added dropwise to the tube and stirred for 2 h at room temperature. The reaction was quenched by the addition of triethylamine (1.5 mL) and the residue was purified through a silica gel plug with dichloromethane. Fused dodecyl porphyrin dimer **P2b** (13 mg, 83%) was yielded as a purple-red solid.

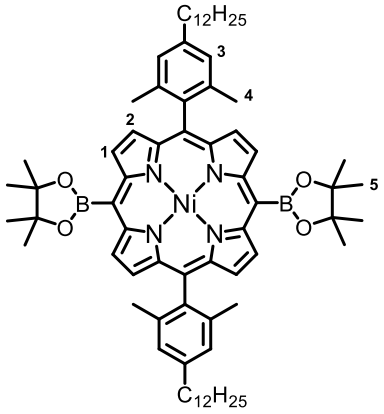
^{1}H NMR (400 MHz, $CDCl_3$, 298 K) δ_H 7.49 (m, 8H, *H1*, *H2*), 7.20 (s, 4H, *H3*), 7.08 (s, 8H, *H4*), 7.05 (s, 4H, *H5*), 2.71 (m, 12H, $H_{dodecyl}$), 1.98 (s, 24H, *H6*), 1.92 (s, 12H, *H7*), 1.75 (m, 12H, $H_{dodecyl}$), 1.51 – 1.28 (m, 108H, $H_{dodecyl}$) 0.90 (t, J = 6.5 Hz, 18H, $H_{dodecyl}$).

^{13}C NMR (126 MHz, $CDCl_3$, 298 K) δ_C 147.5, 143.4, 142.9, 142.8, 142.5, 139.2, 139.0, 137.9, 137.8, 134.2, 131.5, 131.2, 130.9, 127.2, 127.1, 118.3, 118.0, 116.3, 36.2, 36.1, 32.1, 32.1, 31.8, 31.7, 29.9, 29.9, 29.9, 29.8, 29.8, 29.8, 29.7, 29.6, 29.5, 22.9, 22.8, 21.8, 21.7, 14.3, 14.3.

MALDI-TOF MS: m/z = 2359.534 ($C_{160}H_{210}N_8Ni_2$, M^+ requires 2359.539).

UV–vis–NIR (toluene-d_8) λ_{max} (ε / 10^4 $M^{-1}cm^{-1}$): 403 (3.57), 572 (4.35), 874 (0.63), 938 (0.51) nm.

Ni(II) 5,15-diBpin-10,20-bis(2,6-dimethyl-4-dodecylphenyl)porphyrin 3.7b



Porphyrin **3.6b** (0.30 g, 0.28 mmol), $PdCl_2(PPh_3)_2$ (39 mg, 0.2 equiv., 56 μmol) were added into a 100 mL two-neck round-bottom flask and it was evacuated and backfilled with argon three times. Anhydrous THF (26 mL), toluene (26 mL) and triethylamine (5.9 mL, 150 equiv., 42 mmol) were added using a syringe and the solution was degassed by three freeze-pump-thaw cycles followed by the addition of 4,4,5,5-tetramethyl-1,3,2-dioxaborolane (1.5 mL, 36 equiv., 10 mmol). The reaction proceeded at 68 °C for 5 h and the excess of pinacolborane was quenched by dropwise addition of water (10 mL). EtOAc (30 mL) was added to the cooled reaction mixture and the organic extract was washed with water (60 mL × 2) and dried over Na_2SO_4. The resulting solution was concentrated under reduced pressure and the crude material was purified through silica chromatography (pet. ether/EtOAc v/v, gradient elution from 100:3 to 100:20). Porphyrin **3.7b** (0.16 g, 49%) was yielded as a purple solid.

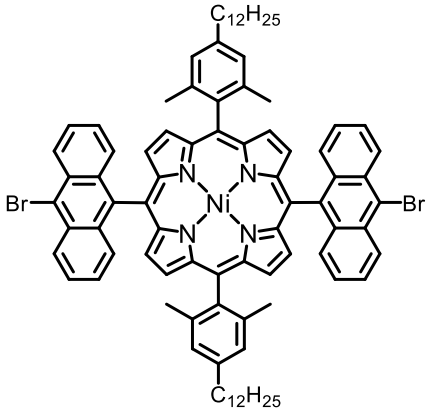
^{1}H NMR (400 MHz, $CDCl_3$, 298 K) δ_H 9.72 (d, J = 4.8 Hz, 4H, *H1*), 8.68 (d, J = 4.9 Hz, 4H, *H2*), 7.22 (s, 4H, *H3*), 2.85 (t, J = 7.7 Hz, 4H, $H_{dodecyl}$), 1.93 – 1.85 (m, 4H, $H_{dodecyl}$), 1.83 (s, 12H, *H4*), 1.72 (s, 24H, *H5*), 1.61 – 1.27 (m, 36H, $H_{dodecyl}$), 0.96 – 0.90 (m, 6H, $H_{dodecyl}$).

^{13}C NMR (101 MHz, $CDCl_3$, 298 K) δ_C 145.8, 142.7, 142.1, 139.0, 137.5, 134.2, 131.6, 127.0, 116.9, 84.9, 36.10, 32.0, 31.8, 29.8, 29.8, 29.8, 29.7, 29.7, 29.5, 25.2, 22.8, 21.50, 14.19.

MALDI-TOF MS: m/z = 1160.673 ($C_{72}H_{98}B_2N_4NiO_4$, M^+ requires 1160.720).

UV–vis (dichloromethane) λ_{max} (ε / 10^4 $M^{-1}cm^{-1}$): 411 (19.2), 531 (1.04), 575 (0.85) nm.

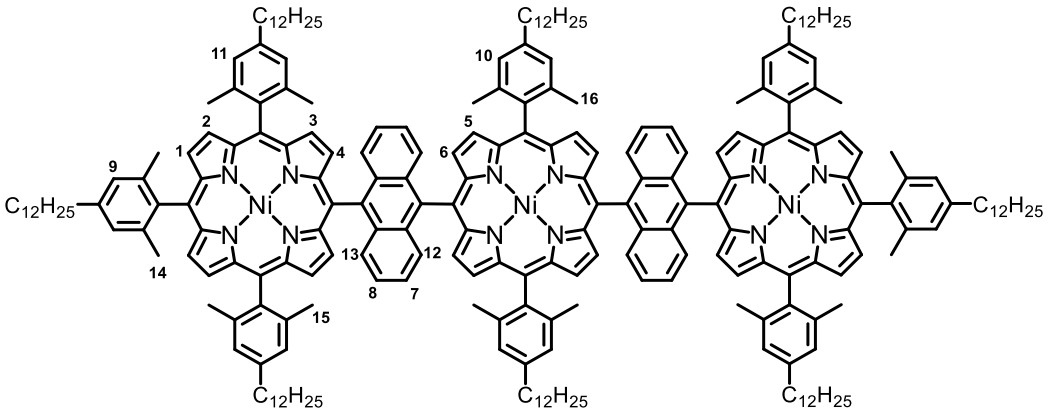
Bisanthracenyl-porphyrin 3.8b



Porphyrin **3.7b** (74 mg, 63 cmol), 9,10-dibromoanthracene (1.1 g, 50 equiv., 3.2 mmol), $Pd(PPh_3)_4$ (44 mg, 0.6 equiv., 38 μmol) and Cs_2CO_3 (0.21 g, 10 equiv., 0.63 mmol) was added to a 50 mL Schlenk tube and it was evacuated and backfilled with argon for three times. Anhydrous DMF (4.5 mL) and toluene (18 mL) were added under argon using a syringe and the suspension was degassed by three freeze-pump-thaw cycles. The reaction proceeded at 80 °C for 12 h with stirring and monitored by TLC in pet. ether/dichloromethane (4:1, v/v). The reaction mixture was diluted with EtOAc (30 mL) and the organic phase was extracted and washed with water (30 mL × 2) and dried over Na_2SO_4. The resulting solution was concentrated under reduced pressure and the residue was purified through silica column chromatography (pet. ether/dichloromethane v/v, 10:1). The second fraction was collected and purified through size-exclusion chromatography (Bio-Rad S-X1, toluene), crude bisanthracenyl-porphyrin **3.8b** (19 mg, 21%) was obtained as a red solid, which was used directly for the next step without further purification.

MALDI-TOF MS: m/z = 1418.441 ($C_{88}H_{90}Br_2N_4Ni$, M^+ requires 1418.489).

Anthracene-linked porphyrin trimer 3.9b



Porphyrin **3.1b** (43 mg, 3.2 equiv., 33 μmol), crude bisanthracenyl-porphyrin **3.8b** (19 mg, 10 μmol), $Pd(PPh_3)_4$ (4.5 mg, 0.4 equiv., 3.9 μmol) and Cs_2CO_3 (11 mg, 3.1 equiv., 33 μmol) were added to a 20 mL Schlenk tube and it was evacuated and backfilled with argon for three times. Anhydrous DMF (1.2 mL) and toluene (4.8 mL) were added under argon using a syringe and the suspension was degassed by three freeze-pump-thaw cycles. The reaction proceeded at 110 °C for 12 h with stirring and monitored by TLC in pet. ether/dichloromethane (3:1, v/v). The reaction mixture was diluted with EtOAc (30 mL) and the organic phase was extracted and washed with water (30 mL × 2) and dried over Na_2SO_4. The resulting solution was concentrated under reduced pressure and the residue was purified through silica column chromatography (pet. ether/EtOAc, v/v, 10:1). Then the third fraction was purified through size-exclusion chromatography (Bio-Rad S-X1, toluene). Singly-linked anthracenyl-porphyrin trimer **3.9b** (18 mg, 37%) was yielded as a red solid.

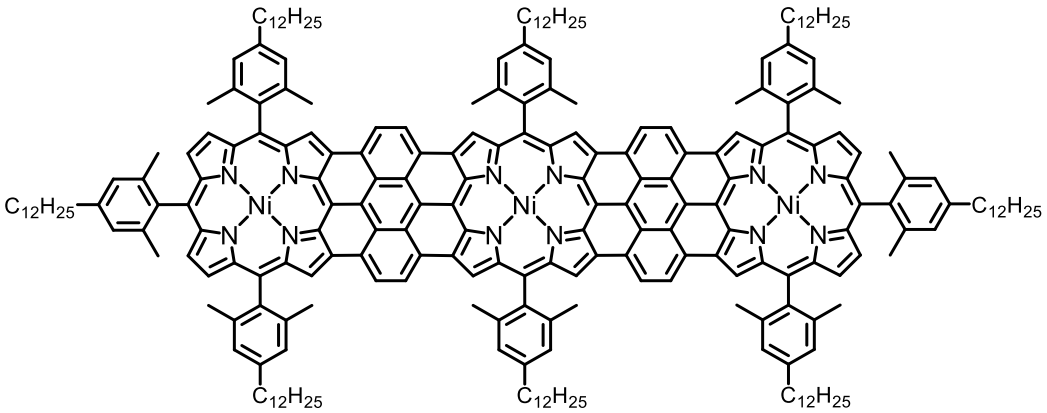
^{1}H NMR (600 MHz, CD_2Cl_2, 298 K) δ_H 8.66 (d, *J* = 4.7 Hz, 4H, *H5*), 8.63 – 8.60 (m, 16H, *H1*, *H2*, *H3*, *H6*), 8.56 (d, *J* = 4.7 Hz, 4H, *H4*), 7.40 – 7.32 (m, 8H, *H7*, *H8*), 7.27 – 7.24 (m, 16H, *H9*, *H10*, *H11*), 7.08 – 7.01 (m, 8H, *H11*, *H12*), 2.84 (m, 16H, $H_{dodecyl}$), 1.96 (s, 12H, *H14*), 1.91 (s, 36H, *H15*, *H16*), 1.86 (m, 16H, $H_{dodecyl}$), 1.49 – 1.27 (m, 144H, $H_{dodecyl}$), 0.92 – 0.86 (m, 24H, $H_{dodecyl}$).

^{13}C NMR (151 MHz, CD_2Cl_2, 298 K) δ_C 144.2, 144.1, 143.2, 143.1, 143.0, 143.0, 142.7, 142.6, 138.9, 137.4, 137.3, 137.2, 136.6, 136.3, 134.0, 132.8, 132.4, 132.0, 131.8, 131.6, 131.5, 128.6, 128.5, 127.2, 127.2, 125.4, 125.4, 118.2, 117.7, 117.7, 114.7, 114.0, 36.0, 32.0, 32.0, 31.8, 31.7, 31.7, 29.8, 29.8, 29.8, 29.8, 29.7, 29.7, 29.7, 29.7, 29.5, 29.5, 22.8, 21.4, 21.3, 21.3, 14.0.

MALDI-TOF MS: *m/z* = 3624.403 ($C_{248}H_{304}N_{12}Ni_3$, M^+ requires 3624.222).

UV–vis (dichloromethane) λ_{max} (ε / 10^4 $M^{-1}cm^{-1}$): 413 (42.3), 438 (43.5), 530 (7.61) nm.

Fused anthracene-linked porphyrin trimer AP3b

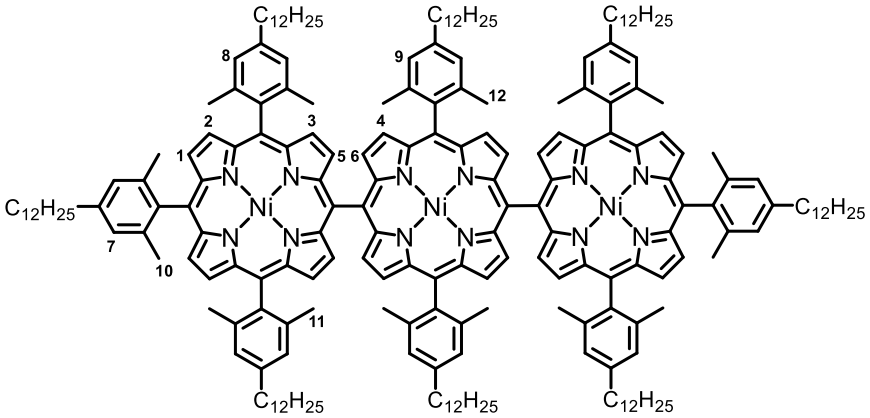


Singly-linked anthracenyl-porphyrin trimer **3.9b** (5.2 mg, 1.4 μmol) and 2,3-dichloro-5,6-dicyano-1,4-benzoquinone (7.8 mg, 24 equiv., 34 μmol) were added into 15 mL Schlenk tube and the tube was backfilled with argon for three times. Degassed dichloromethane (5.0 mL) was added to the mixture under argon followed by the addition of TfOH (50 μL). The reaction proceeded in the dark at room temperature for 18 h with stirring and monitored by TLC in toluene. After the reaction was completed, the mixture was quenched by triethylamine (0.4 mL) and methanol (20 mL) was added to precipitate out the fused product. The residue was purified through a short silica gel plug eluting with toluene. Fused anthracenyl-porphyrin trimer **AP3b** (4.2 mg, 81%) was yielded as a black solid.

MALDI-TOF MS: *m/z* = 3607.898 ($C_{248}H_{288}N_{12}Ni_3$, M^+ requires 3608.096).

UV–vis–NIR (toluene-d_8) λ_{max} (ε / 10^4 $M^{-1}cm^{-1}$): 377 (2.86), 436 (2.88), 639 (5.02), 1317 (1.63), 1463 (4.46), 1640 (5.91) nm.

Singly-linked dodecyl porphyrin trimer *s*-P3b



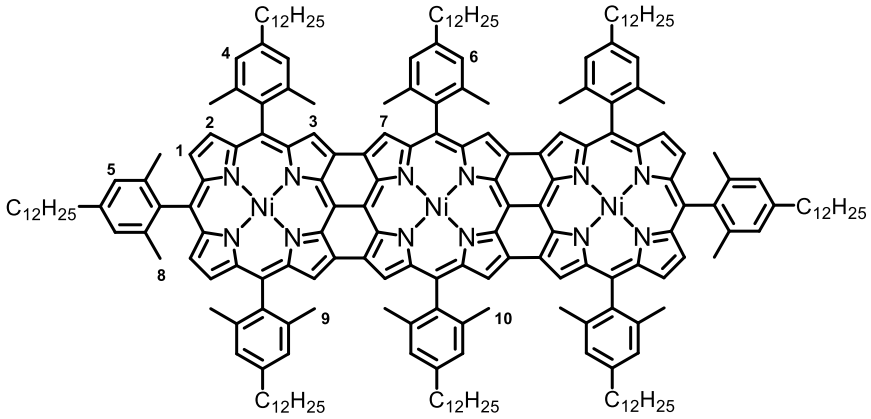
Porphyrin **3.1b** (16 mg, 2.7 equiv., 12 μmol), porphyrin **3.7b** (4.8 mg, 4.5 μmol), $Pd(PPh_3)_4$ (1.6 mg, 0.3 equiv., 1.4 μmol) and Cs_2CO_3 (3.7 mg, 2.5 equiv., 11 μmol) were added to a 15 mL Schlenk tube and it was evacuated and backfilled with argon for three times. Anhydrous DMF (0.4 mL) and toluene (1.6 mL) were added under argon using a syringe and the suspension was degassed by three freeze-pump-thaw cycles. The reaction proceeded at 80 °C for 12 h with stirring and monitored by TLC (pet. ether/dichloromethane, v/v, 4:1). The reaction mixture was diluted with EtOAc (15 mL) and the organic phase was extracted and washed with water (15 mL × 2) and dried over Na_2SO_4. The resulting solution was concentrated under reduced pressure and the residue was purified through a silica plug (pet. ether/dichloromethane, v/v, 1:1) and size-exclusion chromatography (Bio-Rad S-X1, toluene). Singly-linked dodecyl porphyrin trimer ***s*-P3b** (9.6 mg, 65%) was yielded as a red solid.

^{1}H NMR (400 MHz, $CDCl_3$, 298 K) δ_H 8.65 – 8.58 (m, 8H, *H1*, *H2*), 8.40 (m, 8H, *H3*, *H4*), 8.09 (m, 8H, *H5*, *H6*), 7.24 (s, 4H, *H7*), 7.14 (s, 8H, *H8*), 7.06 (s, 4H, *H9*), 2.85 (t, J = 7.8 Hz, 4H, $H_{dodecyl}$), 2.75 (t, J = 7.8 Hz, 8H, $H_{dodecyl}$), 2.66 (t, J = 7.7 Hz, 4H, $H_{dodecyl}$), 1.92 (s, 12H, *H10*), 1.87 (s, 36H, *H11*, *H12*), 1.41 – 1.16 (m, 142H, $H_{dodecyl}$), 0.91 (d, J = 6.7 Hz, 6H, $H_{dodecyl}$), 0.85 (q, J = 6.8 Hz, 12H, $H_{dodecyl}$), 0.81 – 0.75 (m, 6H, $H_{dodecyl}$).

^{13}C NMR (151 MHz, $CDCl_3$, 298 K) δ_C 147.5, 147.4, 143.4, 143.1, 142.9, 142.9, 142.9, 142.8, 142.6, 139.2, 139.1, 139.0, 137.9, 137.8, 137.7, 134.5, 134.3, 131.5, 131.2, 131.0, 130.9, 127.2, 127.1, 127.1, 119.4, 118.4, 118.1, 117.1, 116.2, 36.2, 36.1, 36.0, 32.1, 32.1, 32.0, 31.8, 31.7, 31.6, 29.9, 29.9, 29.9, 29.8, 29.8, 29.8, 29.8, 29.7, 29.7, 29.7, 29.6, 29.5, 29.4, 22.9, 22.8, 22.8, 21.8, 21.8, 14.3, 14.3, 14.2, 14.2, 1.2.

MALDI-TOF MS: *m/z* = 3271.873 ($C_{220}H_{288}N_{12}Ni_3$, M^+ requires 3272.097).

Fused dodecyl porphyrin trimer P3b



Singly-linked dodecyl porphyrin trimer ***s*-P3b** (5.2 mg, 1.6 μmol) was added into a 15 mL Schlenk tube and the tube was evacuated and backfilled with argon for three times. Dry 1,2-dichloroethane (2.0 mL) was added to the tube under argon. Under vigorous stirring, a suspension of $AuCl_3$ (1.9 mg, 4.0 equiv., 6.4 μmol) and AgOTf (8.2 mg, 20 equiv., 32 μmol) in dry 1,2-dichloroethane (1.2 mL) was added to the tube dropwise and stirred for 2 h at room temperature. The reaction was quenched by the addition of triethylamine (1.0 mL) and the residue purified through a silica gel plug with dichloromethane. Fused dodecyl porphyrin trimer **P3b** (4.8 mg, 92%) was yielded as black-green solid.

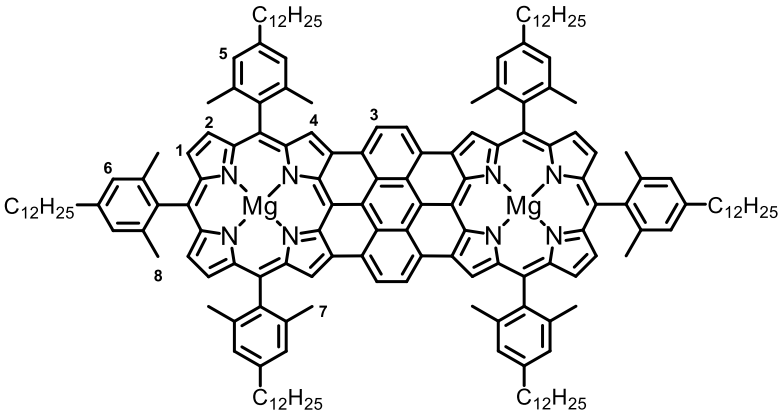
^{1}H NMR (400 MHz, $CDCl_3$, 298 K) δ_H 7.52 (d, *J* = 4.9 Hz, 4H, *H1*), 7.49 (d, *J* = 4.9 Hz, 4H, *H2*), 7.14 (s, 4H, *H3*), 7.06 – 7.04 (two s, 16H, *H4*, *H5*, *H6*), 6.57 (s, 4H, *H7*), 3.10 (m, 4H, $H_{dodecyl}$), 2.74 – 2.67 (m, 16H, $H_{dodecyl}$), 2.14 (s, 12H, *H8*), 1.92 (s, 24H, *H9*), 1.89 (s, 12H, *H10*), 1.75 (d, *J* = 8.7 Hz, 20H, $H_{dodecyl}$), 1.47 – 1.26 (m, 136H, $H_{dodecyl}$), 0.88 (s, 24H, $H_{dodecyl}$).

^{13}C NMR (151 MHz, $CDCl_3$, 298 K) δ_C 148.4, 147.4, 146.4, 145.7, 145.6, 145.0, 142.9, 138.4, 138.4, 138.0, 136.5, 136.4, 135.4, 134.2, 134.1, 130.6, 130.2, 127.2, 127.1, 125.5, 124.7, 122.0, 116.1, 53.6, 46.0, 36.1, 36.0, 36.0, 32.2, 32.1, 32.1, 31.6, 31.6, 31.6, 30.0, 30.0, 29.9, 29.9, 29.9, 29.9, 29.9, 29.8, 29.8, 29.7, 29.7, 29.7, 29.6, 29.6, 29.5, 22.9, 22.9, 22.8, 21.4, 21.3, 21.1, 14.3, 14.3, 14.3, 8.8, 1.2.

MALDI-TOF MS: *m/z* = 3263.928 ($C_{220}H_{280}N_{12}Ni_3$, M^+ requires 3264.034).

UV–vis–NIR (toluene-d_8) λ_{max} (ε / 10^4 $M^{-1}cm^{-1}$): 408 (5.43), 640 (7.98), 671 (7.23), 1157 (4.43) nm.

Fused anthracene-linked Mg(II) porphyrin dimer Mg-AP2b



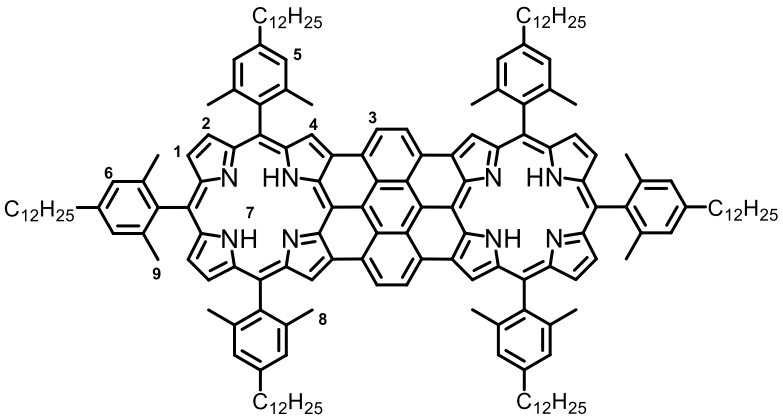
AP2b (3.3 mg, 1.3 μmol) was added into a 10 mL Schlenk tube which was evacuated and backfilled with argon for three times. Dry toluene (2.1 mL) was added to the tube under argon followed by the addition of *p*-tolylmagnesium bromide (0.1 mL, 1 M in THF, 80 equiv.). The reaction proceeded at 85 °C for 16 h. The reaction was quenched by water and the organic phase was extracted by toluene (5 mL × 3) and dried over Na_2SO_4. The resulting solution was concentrated under reduced pressure and the residue was purified through silica plug using toluene as the eluent solvent. **Mg-AP2b** (2.9 mg, 90%) was yielded as a black-green solid.

^{1}H NMR (400 MHz, toluene-d_8, 298 K) δ_H 7.56 (q, J = 4.6 Hz, 12H, *H1*, *H2*, *H3* or *H4*), 7.19 (s, 8H, *H5*), 7.08 (p, J = 1.1 Hz, 57H, H_{tol} and *H6*), 6.79 (s, 4H, *H3* or *H4*), 2.79 (t, J = 7.9 Hz, 12H, $H_{dodecyl}$), 2.70 (t, J = 7.8 Hz, 6H, $H_{dodecyl}$), 2.18 (s, 24H, *H7*), 2.01 (s, 12H, *H8*), 1.85 (q, J = 7.6 Hz, 12H, $H_{dodecyl}$), 1.76 (d, J = 8.9 Hz, 8H, $H_{dodecyl}$), 0.96 – 0.92 (m, 18H, $H_{dodecyl}$).

MALDI-TOF MS: m/z = 2463.661($C_{174}H_{214}Mg_2N_8$, M^+ requires 2463.669).

UV–vis–NIR (dichloromethane) λ_{max} (ε / 10^4 $M^{-1}cm^{-1}$): 473 (3.65), 620 (3.66), 1203 (1.14), 1411 (2.66) nm.

Fused anthracene-linked free-base porphyrin dimer FB-AP2b

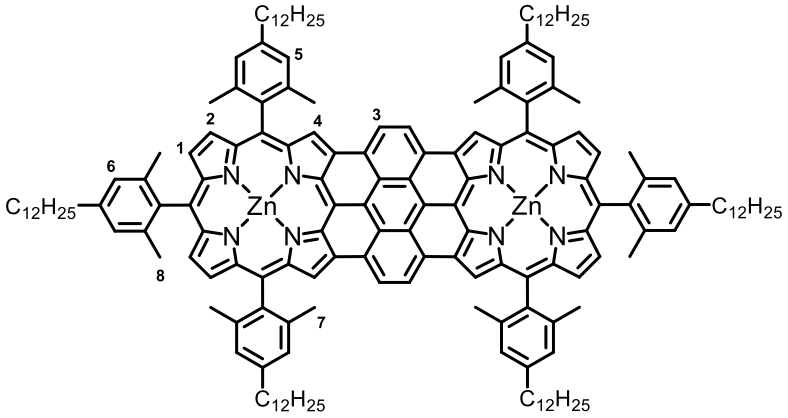


Mg-AP2b (2.9 mg, 1.2 μmol) was added into a 50 mL round-bottom flask. Toluene (5.0 mL) was added, followed by addition of TFA (0.5 mL). The mixture was stirred at room temperature for 30 min. The solution was neutralized by sodium bicarbonate solution (2.0 M, 10 mL). The organic phase was extracted by toluene (5 mL × 3) and dried over Na_2SO_4. The resulting solution was concentrated under reduced pressure and the residue was purified through silica plug using toluene as the eluent solvent. **FB-AP2b** (2.6 mg, 94%) was yielded as a black-green solid.

^{1}H NMR (400 MHz, toluene-d_8, 298 K) δ_H 7.61 (s, 4H, *H3* or *H4*), 7.57 – 7.48 (m, 8H, *H1*, *H2*), 7.18 (s, 8H, *H5*), 7.07 (s, 4H, *H6*), 6.80 (s, 4H, *H3* or *H4*), 5.20 (s, 4H, *H7*), 2.78 (t, J = 7.8 Hz, 9H, $H_{dodecyl}$), 2.69 (t, J = 7.8 Hz, 5H, $H_{dodecyl}$), 2.17 (s, 24H, *H8*), 1.96 (s, 12H, *H9*), 1.86 (t, J = 7.1 Hz, 9H, $H_{dodecyl}$), 1.78 (t, J = 7.4 Hz, 6H, $H_{dodecyl}$), 1.57 – 1.26 (m, 160H, $H_{dodecyl}$), 0.98 – 0.92 (m, 18H, $H_{dodecyl}$).

MALDI-TOF MS: m/z = 2419.634 ($C_{174}H_{218}N_8$, M^+ requires 2419.730).

Fused anthracene-linked Zn(II) porphyrin dimer Zn-AP2b



FB-AP2b (2.6 mg, 1.1 μmol) was added into a 25 mL round bottom flask followed by the addition of dichloromethane (5 mL). $Zn(OAc)_2{\cdot}2H_2O$ (0.7 mg, 3.0 equiv., 3.2 μmol) in methanol (0.5 mL) was added to the reaction flask and the reaction was proceeded at 35 °C for 16 h. The reaction was quenched by water and the organic phase was extracted by toluene (15 mL × 3) and dried over Na_2SO_4. The resulting solution was concentrated under reduced pressure and the residue was purified through silica plug using toluene as the eluent solvent. **Zn-AP2b** (2.6 mg, 96%) was yielded as a black-green solid.

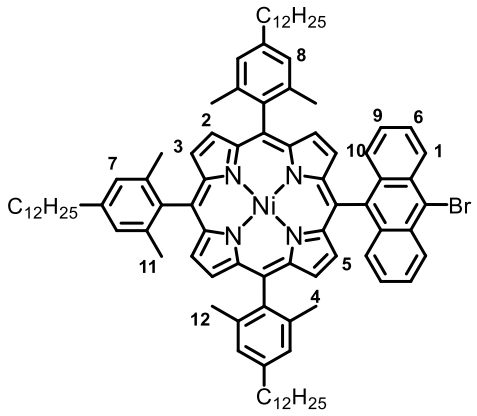
^{1}H NMR (600 MHz, CD_2Cl_2/CS_2 (2:1, v/v), 298 K) δ_H 7.50 (m, 8H, *H1*, *H2*), 7.47 (s, 4H, *H3*), 7.46 (s, 4H, *H4*), 7.14 (s, 8H, *H5*), 7.10 (s, 4H, *H6*), 2.81 – 2.77 (m, 8H, $H_{dodecyl}$), 2.76 – 2.73 (m, 4H, $H_{dodecyl}$), 2.05 (s, 24H, *H7*), 1.99 (s, 12H, *H8*), 1.87 – 1.82 (m, 8H, $H_{dodecyl}$), 1.78 (d, J = 7.7 Hz, 4H, $H_{dodecyl}$), 1.57– 1.31 (m, 108H, $H_{dodecyl}$), 0.94 – 0.91 (m, 18H, $H_{dodecyl}$).

^{13}C NMR (151 MHz, CD_2Cl_2/CS_2 (2:1, v/v), 298 K) δ_C 153.7, 152.8, 151.9, 151.2, 142.9, 142.9, 138.6, 137.9, 137.8, 136.6, 132.7, 131.1, 130.6, 128.5, 128.2, 127.6, 127.6, 125.4, 122.2, 36.6, 36.5, 32.6, 32.6, 32.3, 32.2, 30.5, 30.4, 30.4, 30.4, 30.4, 30.3, 30.3, 30.1, 30.1, 23.5, 23.5, 21.7, 21.4, 14.7, 14.6.

MALDI-TOF MS: m/z = 2543.488 ($C_{108}H_{84}N_8Zn_2$, M^+ requires 2543.557).

UV–vis–NIR (dichloromethane) λ_{max} (ε / 10^4 $M^{-1}cm^{-1}$): 462 (7.44), 608 (8.37), 1123 (2.52), 1039 (6.97) nm.

Bromo-functionalized monoanthracenyl-porphyrin 3.10b

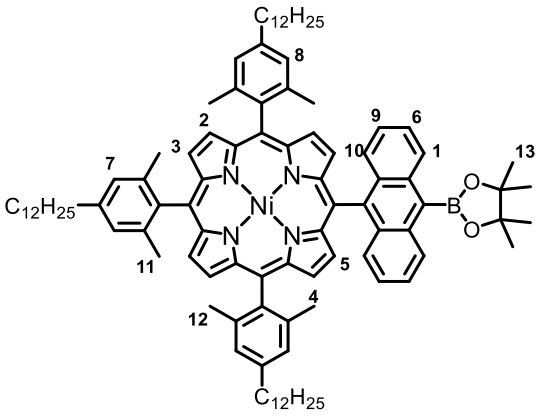


Porphyrin **3.1b** (17 mg, 13 μmol), 9,10-dibromoanthracene **3.2** (21 mg, 5.0 equiv., 63 μmol), $Pd(PPh_3)_4$ (4.4 mg, 0.30 equiv., 3.8 μmol) and Cs_2CO_3 (10 mg, 2.5 equiv., 32 μmol) were added to a 10 mL Schlenk tube and it was evacuated and backfilled with argon for three times. Anhydrous DMF (0.75 mL) and toluene (3.0 mL) were added under argon using a syringe and the suspension was degassed by three freeze-pump-thaw cycles. The reaction proceeded at 80 °C for 12 h with stirring and monitored by TLC (pet. ether/dichloromethane, v/v, 4:1). The reaction mixture was diluted with EtOAc (20 mL) and the organic phase was extracted and washed with water (20 mL × 2) and dried over Na_2SO_4. The resulting solution was concentrated under reduced pressure and the residue was purified through a silica column chromatography (pet. ether/EtOAc, v/v, 10:1). Bromo-functionalized monoanthracenyl-porphyrin **3.10b** (10 mg, 57%) was yielded as a red solid.

^{1}H NMR (400 MHz, $CDCl_3$, 298 K) δ_H 8.82 – 8.75 (m, 2H, *H1*), 8.57 (2 overlap d, *J* = 4.9 Hz, 4H, *H2*, *H3*), 8.41 (d, *J* = 4.9 Hz, 2H, *H4*), 8.09 (d, *J* = 4.9 Hz, 2H, *H5*), 7.56 (ddd, *J* = 9.0, 6.1, 1.5 Hz, 2H, *H6*), 7.21 (s, 2H, *H7*), 7.15 (s, 4H, *H8*), 7.13 – 7.05 (m, 4H, *H9*, *H10*), 2.80 (2 overlap t, *J* = 7.7 Hz, 6H, $H_{dodecyl}$), 1.87 (s, 6H, *H11*), 1.83 (s, 14H, *H12*), 1.44 – 1.23 (m, 68H, $H_{dodecyl}$), 0.91 – 0.86 (m, 9H, $H_{dodecyl}$).

MALDI-TOF MS: *m/z* = 1436.804 ($C_{94}H_{115}BrN_4Ni$, M^+ requires 1436.766).

Boronate ester-functionalized monoanthracenyl-porphyrin 3.11b

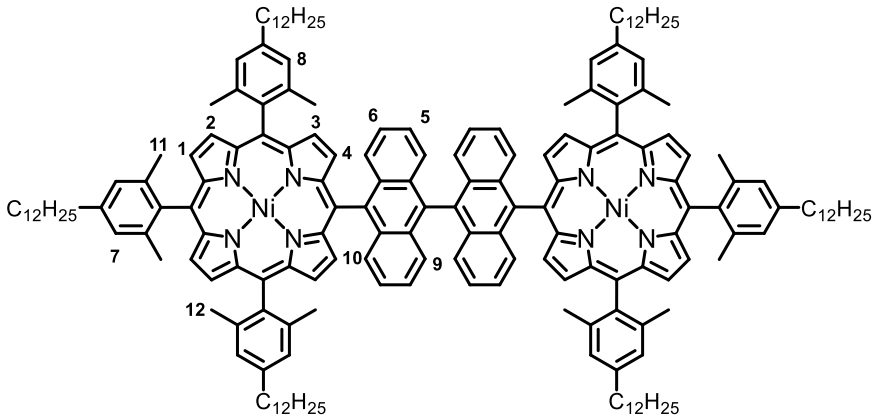


Bromo-functionalized monoanthracenyl-porphyrin **3.10b** (6.9 mg, 4.8 μmol), Pd(dppf)Cl_2 (0.5 mg, 0.15 equiv., 0.70 μmol), bis(pinacolate)diboron (3.7 mg, 3.0 equiv., 14 μmol) and potassium acetate (4.2 mg, 9.0 equiv., 43.1 μmol) were added to a 10 mL Schlenk tube and it was evacuated and backfilled with argon for three times. Anhydrous DMF (5.0 mL) was added under argon using a syringe and the suspension was degassed by three freeze-pump-thaw cycles. The reaction proceeded at 60 °C for 5 h with stirring and monitored by TLC (pet. ether/dichloromethane, v/v, 3:1). The reaction mixture was diluted with EtOAc (20 mL) and the organic phase was extracted and washed with water (20 mL × 2) and dried over Na_2SO_4. The resulting solution was concentrated under reduced pressure and the residue was purified through a silica column chromatography TLC (pet. ether/EtOAc, v/v, 4:1). Boronate ester-functionalized monoanthracenyl-porphyrin **3.11b** (4.4 mg, 61%) was yielded as a red solid.

^{1}H NMR (400 MHz, $CDCl_3$, 298 K) δ_H 8.60 – 8.53 (m, 6H, *H1*, *H2*, *H3*), 8.38 (d, *J* = 5.0 Hz, 2H, *H4*), 8.07 (d, *J* = 4.9 Hz, 2H, *H5*), 7.44 (ddd, *J* = 8.9, 6.3, 1.4 Hz, 2H, *H6*), 7.21 (s, 2H, *H7*), 7.15 (s, 4H, *H8*), 7.09 – 7.04 (m, 2H, *H9*), 7.00 (ddd, *J* = 8.9, 6.2, 1.1 Hz, 2H, *H10*), 2.80 (2 overlap t, *J* = 7.8 Hz, 6H, $H_{dodecyl}$), 1.86 (s, 6H, *H11*), 1.82 (s, 12H, *H12*), 1.72 (s, 12H, *H13*), 0.91 – 0.86 (m, 9H, $H_{dodecyl}$).

MALDI-TOF MS: *m/z* = 1485.561 ($C_{100}H_{127}BN_4NiO_2$, M^+ requires 1484.941).

Singly-linked bisanthracene-porphyrin dimer 3.12b

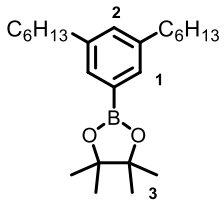


Bromo-functionalized monoanthracenyl-porphyrin **3.10b** (5.3 mg, 1.2 equiv., 3.6 μmol), boronate ester-functionalized monoanthracenyl-porphyrin **3.11b** (4.4 mg, 2.9 μmol), $Pd(PPh_3)_4$ (0.5 mg, 0.15 equiv., 0.4 μmol) and Cs_2CO_3 (1.4 mg, 1.5 equiv., 4.4 μmol) were added to a 10 mL Schlenk tube and it was evacuated and backfilled with argon for three times. Anhydrous DMF (0.3 mL) and toluene (1.2 mL) were added under argon using a syringe and the suspension was degassed by three freeze-pump-thaw cycles. The reaction proceeded at 70 °C for 18 h with stirring and monitored by TLC (pet. ether/dichloromethane, v/v, 4:1). The reaction mixture was diluted with EtOAc (10 mL) and the organic phase was extracted and washed with water (15 mL × 2) and dried over Na_2SO_4. The resulting solution was concentrated under reduced pressure and the residue was purified through a silica column chromatography (pet. ether/dichloromethane, v/v, 4:1). Singly-linked bisanthracene-porphyrin dimer **3.12b** (0.8 mg, 10%) was yielded as a red solid.

^{1}H NMR (400 MHz, CD_2Cl_2, 298 K) δ_H 8.63 – 8.54 (m, 12H, *H1*, *H2*, *H3*), 8.50 (d, J = 4.9 Hz, 4H, *H4*), 7.73 – 7.69 (d, J = 4.9 Hz, 4H, *H5*), 7.35 – 7.29 (m, 8H, *H6*, *H9*), 7.26 (s, 4H, *H7*), 7.23 (s, 8H, *H8*), 7.19 – 7.11 (m, 4H, *H10*), 2.82 (2 overlap t, J = 7.8 Hz, 12H, $H_{dodecyl}$), 1.90 (2 overlap s, 36H, *H11*, *H12*), 1.26 (s, 109H, $H_{dodecyl}$), 0.88 – 0.82 (m, 18H, $H_{dodecyl}$).

MALDI-TOF MS: m/z = 2715.768 ($C_{188}H_{230}N_8Ni_2$, M^+ requires 2715.695).

1-Bpin-3,5-dihexyl benzene 3.14d



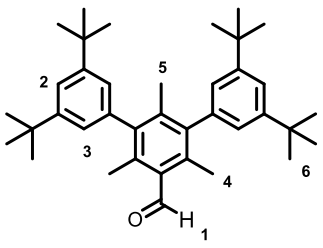
1-Bromo-3,5-dihexylbenzene (1.6 g, 4.8 mmol), Pd(dppf)Cl_2 (0.18 g, 0.05 equiv., 0.24 mmol), bis(pinacolate)diboron (1.6 g, 1.3 equiv., 6.2 mmol) and potassium acetate (1.5 g, 3.0 equiv., 15 mmol) were added to a 100 mL two-neck round bottom flask and it was evacuated and backfilled with argon for three times. Anhydrous DMSO (32 mL) was added under argon using a syringe and the suspension was degassed by three freeze-pump-thaw cycles. The reaction proceeded at 80 °C for 20 h with stirring and monitored by TLC (pet. ether/EtOAc, v/v, 15:1). The reaction mixture was diluted with EtOAc (30 mL) and the organic phase was extracted and washed with water (100 mL × 2) and dried over Na_2SO_4. The resulting solution was concentrated under reduced pressure and the residue was purified through a silica column chromatography (pet. ether/EtOAc, v/v, 10:1). 1-Bpin-3,5-dihexyl benzene **3.14d** (1.5 g, 82%) was yielded as a white solid after recrystallization by layer addition (dichloromethane/methanol) at 4 °C overnight.

^{1}**H NMR** (400 MHz, $CDCl_3$, 298K) δ_H 7.49 (d, *J* = 1.7 Hz, 2H, *H1*), 7.13 (t, *J* = 1.8 Hz, 1H, *H2*), 2.66 – 2.57 (m, 4H, H_{hexyl}), 1.70 – 1.60 (m, 4H, H_{hexyl}), 1.38 (s, 12H, *H3*), 1.34 (m, 12H, H_{hexyl}), 0.95 – 0.89 (m, 6H, H_{hexyl}).

^{13}**C NMR** (101 MHz, $CDCl_3$, 298K) δ_C 142.2, 132.2, 131.7, 83.6, 36.0, 31.8, 31.8, 29.2, 24.9, 22.7, 14.2.

HR MS: *m/z* = 372.323 $[M+H]^+$ ($C_{24}H_{41}BO_2$, MH^+ requires 372.320).

Tetra-*tert*-butyl aldehyde 3.15c

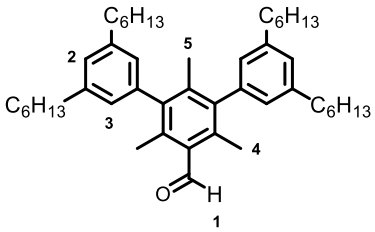


1-Bpin-3,5-di-*tert*-butylbenzene **3.14c** (0.3 g, 2.5 equiv., 0.95 mmol), 3,5-dibrom-2,4,6-trimethylbenzaldehyde **3.13** (0.12 g, 0.38 mmol) and SPhos G2 Pd (27 mg, 0.1 equiv., 38 μmol) were mixed in a two-neck round bottom flask and it was evacuated and backfilled with argon three times before the addition of anhydrous DMSO (76 mL). A 2M solution of K_3PO_4 (3.2 g, 40 equiv., 15 mmol) in water (7.6 mL) was sparged for at least 1 h. The reaction solution was heated to 80 °C and the degassed K_3PO_4 solution was added into the mixture. The reaction proceeded at 80 °C for 2 h with stirring and monitored by TLC (pet. ether/EtOAc, v/v, 10:1) until all the starting materials have been consumed, at which point the solution was allowed to cool to room temperature. The crude reaction solution was concentrated and diluted with EtOAc (30 mL). The organic phase was extracted and washed with water (100 mL × 2) and dried over Na_2SO_4. The residue was purified through a silica column chromatography (pet. ether/EtOAc, v/v, 10:1). Tetra-*tert*-butyl aldehyde **3.15c** (0.18 g, 90%) was yielded as a white solid.

^{1}H NMR (400 MHz, $CDCl_3$, 298 K) δ_H 10.70 (s, 1H, *H1*), 7.37 (t, *J* = 1.8 Hz, 2H, *H2*), 6.99 (d, *J* = 1.8 Hz, 4H, *H3*), 2.26 (s, 6H, *H4*), 1.70 (s, 3H, *H5*), 1.33 (s, 36H, *H6*)

HR MS: *m/z* = 524.400 $[M+H]^+$ ($C_{38}H_{52}O$, MH^+ requires 524.402).

Tetra-hexyl aldehyde 3.15d



1-Bpin-3,5-dihexyl benzene **3.14d** (1.5 g, 2.5 equiv., 4.1 mmol), 3,5-dibrom-2,4,6-trimethylbenzaldehyde **3.13** (0.5 g, 1.6 mmol) and SPhos G2 Pd (0.12 g, 0.1 equiv., 0.16 mmol) were mixed in a 500 mL two-neck round bottom flask and it was evacuated and backfilled with argon for three times before the addition of anhydrous DMSO (0.32 L). A 2M solution of K_3PO_4 (14 g, 40 equiv., 65 mmol) in water (32 mL) was sparged for at least 1 h. The reaction solution was heated to 80 °C and the degassed K_3PO_4 solution was added into the mixture. The reaction proceeded at 80 °C for 2 h with stirring and monitored by TLC (pet. ether/EtOAc, v/v, 10:1) until all the starting materials have been consumed at which point the solution was allowed to

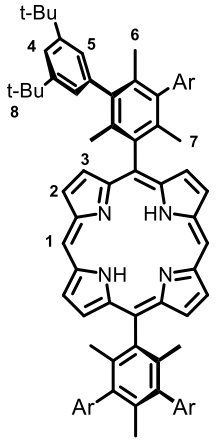
cool to room temperature. The crude reaction solution was concentrated and diluted with EtOAc (30 mL). The organic phase was extracted and washed twice with water (100 mL × 2) and dried over Na_2SO_4. The residue was purified through a silica column chromatography (pet. ether/EtOAc, v/v, 10:1). Tetra-hexyl aldehyde **3.15d** (0.98 g, 94%) was yielded as a white solid.

^{1}H NMR (400 MHz, $CDCl_3$, 298 K) δ_H 10.70 (s, 1H, *H1*), 6.98 (t, *J* = 1.7 Hz, 2H, *H2*), 6.77 (d, *J* = 1.6 Hz, 4H, *H3*), 2.61 (t, *J* = 7.6 Hz, 8H, H_{hexyl}), 2.27 (s, 6H, *H4*), 1.71 (s, 3H, *H5*), 1.66 – 1.58 (m, 9H, H_{hexyl}), 1.30 (h, *J* = 4.9 Hz, 24H, H_{hexyl}), 0.90 – 0.85 (m, 13H, H_{hexyl}).

^{13}C NMR (101 MHz, $CDCl_3$, 298K) δ_C 195.4, 143.1, 143.0, 142.9, 141.8, 140.5, 140.1, 136.9, 131.7, 127.1, 127.0, 126.6, 126.5, 35.9, 31.7, 31.4, 28.9, 24.9, 22.6, 20.4, 18.3, 17.7, 14.1.

HR MS: *m/z* = 636.524 $[M+H]^+$ ($C_{46}H_{68}O$, MH^+ requires 636.527).

5,15-Bis(tetra-*tert*-butylphenyl)porphyrin 3.16c



3.16c

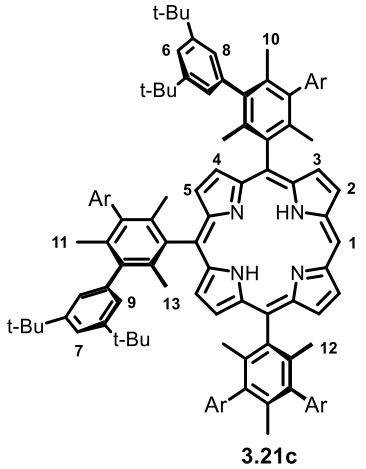
Tetra-*tert*-butyl aldehyde **3.15c** (1.2 g, 3.0 equiv., 2.3 mmol), dipyrromethane (0.11 g, 0.77 mmol) and pyrrole (0.1 g, 2.0 equiv., 1.5 mmol) were added into a 500 mL round-bottom flask which contains dichloromethane (400 mL) and ethanol (2.0 mL). The mixture was degassed by bubbling with argon for 20 min before the addition of boron trifluoride etherate ($BF_3{\cdot}OEt_2$, 0.19 mL, 2.0 equiv., 1.5 mmol). The mixture was left in the dark stirring for 3 h and DDQ (0.78 g, 4.5 equiv., 3.4 mmol) was then added. The mixture was left stirring at room temperature for another 30 min and subsequently neutralized by triethylamine (4.0 mL). After passing through a silica plug eluted with dichloromethane, the solvent was removed under reduced pressure and the residue was purified through silica column chromatography (pet.

ether/dichloromethane, v/v, 3:1). Following purification by size-exclusion chromatography (Bio-Rad S-X1, toluene), 5,15-bis(tetra-*tert*-butyl)porphyrin **3.16c** (85 mg, 9%) and 5,10,15-tri(tetra-*tert*-butyl)porphyrin **3.21c** (60 mg, 4%) were yielded as red-purple solids after recrystallization by layer addition (dichloromethane/methanol) at 4 °C overnight.

^{1}H NMR (400 MHz, $CDCl_3$, 298 K) δ_H 10.25 (s, 2H, *H1*), 9.41 (d, *J* = 4.5 Hz, 4H, *H2*), 9.17 (d, *J* = 4.6 Hz, 4H, *H3*), 7.37 (t, *J* = 1.9 Hz, 4H, *H4*), 7.35 (d, *J* = 1.8 Hz, 8H, *H5*), 2.05 (s, 6H, *H6*), 1.57 (s, 12H, *H7*), 1.40 (s, 72H, *H8*), –2.95 (s, 2H, H_N).

MALDI-TOF MS: *m/z* = 1299.215 ($C_{94}H_{114}N_4$, M^+ requires 1299.204).

5,10,15-Tri(tetra-*tert*-butylphenyl)-porphyrin 3.21c



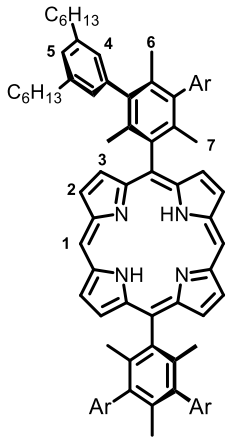
3.21c

Synthetic procedure as described above.

^{1}H NMR (400 MHz, $CDCl_3$, 298 K) δ_H 10.09 (s, 1H, *H1*), 9.32 (d, *J* = 4.6 Hz, 2H, *H2*), 9.06 (d, *J* = 4.6 Hz, 2H, *H3*), 9.03 – 8.98 (m, 4H, *H4*, *H5*), 7.35 (2t, *J* = 1.9 Hz, 6H, *H6*, *H7*), 7.31 (2d, *J* = 1.9 Hz, 12H, *H8*, *H9*), 2.02 (2s 9H, *H10*, *H11*), 1.57 (s, 12H, *H12*), 1.54 (s, 6H, *H13*), 1.40 – 1.36 (m, 115H, $H_{t\text{-}Bu}$), –2.67 (s, 2H, H_N).

MALDI-TOF MS: *m/z* = 1793.839 ($C_{131}H_{164}N_4$, M^+ requires 1793.296).

5,15-Bis(tetra-hexylphenyl)porphyrin 3.16d



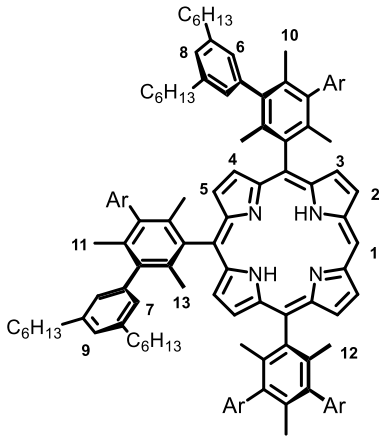
3.16d

Tetra-hexyl aldehyde **3.15d** (1.4 g, 3.0 equiv., 2.2 mmol) and dipyrromethane (0.1 g, 0.72 mmol) and pyrrole (96 mg, 2.0 equiv., 1.4 mmol) were added into a 250 mL round-bottom flask which contains dichloromethane (180 mL) and ethanol (0.9 mL). The mixture was degassed by bubbling with argon for 20 min before the addition of boron trifluoride etherate ($BF_3{\cdot}OEt_2$, 0.18 mL, 2.0 equiv., 1.4 mmol). The mixture was left in the dark stirring for 3 h and DDQ (0.73 mg, 4.5 equiv., 3.2 mmol) was then added. The mixture was left stirring under room temperature for another 30 min and subsequently neutralized by triethylamine (1.8 mL). After passing through a silica plug eluted with dichloromethane, the solvent was removed under reduced pressure and the residue was purified through silica column chromatography using (pet. ether/dichloromethane, v/v, 3:1) as the eluent system. After purification through size-exclusion chromatography (Bio-Rad S-X1, toluene), 5,15-bis(tetra-hexyl)porphyrin **3.16d** (75 mg, 7%) and 5,10,15-tri(tetra-hexyl)porphyrin **3.21d** (58 mg, 4%) were yielded as red-purple solids.

^{1}H NMR (400 MHz, $CDCl_3$, 298 K) δ_H 10.23 (s, 2H, *H1*), 9.38 (d, *J* = 4.5 Hz, 4H, *H2*), 9.09 (d, *J* = 4.5 Hz, 4H, *H3*), 7.12 (d, *J* = 1.6 Hz, 8H, *H4*), 6.96 (d, *J* = 1.7 Hz, 4H, *H5*), 2.66 (t, *J* = 7.7 Hz, 16H, H_{hexyl}), 2.06 (s, 6H, *H6*), 1.72 – 1.61 (m, 18H, H_{hexyl}), 1.55 (s, 12H, *H7*), 1.28 (m, 61H, H_{hexyl}), 0.88 – 0.79 (m, 27H, H_{hexyl}), –2.98 (s, 2H, H_N).

MALDI-TOF MS: *m/z* = 1523.253 ($C_{110}H_{146}N_4$, M^+ requires 1523.155)

5,10,15-Tri(tetra-hexylphenyl)porphyrin 3.21d



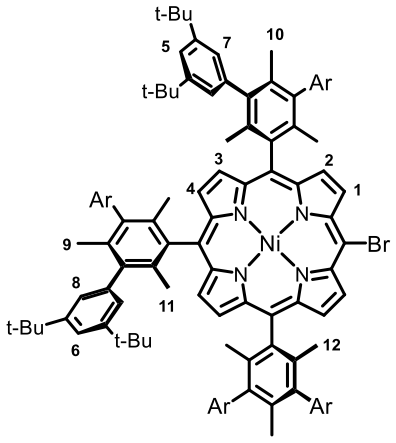
3.21d

Synthetic procedure as described above.

^{1}H NMR (400 MHz, $CDCl_3$, 298 K) δ_H 10.07 (s, 1H, *H1*), 9.29 (d, *J* = 4.6 Hz, 2H, *H2*), 8.99 (d, *J* = 4.6 Hz, 2H, *H3*), 8.92 (m, 4H, *H4*, *H5*), 7.10 – 7.07 (2d, *J* = 1.9 Hz, 12H, *H6*, *H7*), 6.94 (2t, *J* = 1.9 Hz, 6H, *H8*, *H9*), 2.68 – 2.60 (m, 24H, H_{hexyl}), 2.03 (2s, 9H, *H10*, *H11*), 1.65 (t, *J* = 7.5 Hz, 24H, H_{hexyl}), 1.54 (2s, 24H, *H12*, *H13*), 1.39 – 1.21 (m, 81H, H_{hexyl}), 0.85 – 0.79 (m, 37H, H_{hexyl}), –2.71 (s, 2H, H_N).

MALDI-TOF MS: *m/z* = 2130.869 ($C_{155}H_{212}N_4$, M^+ requires 2131.429).

Ni(II) 5-bromo-10,15,20-tri(tetra-*tert*-butyl)porphyrin 3.22c



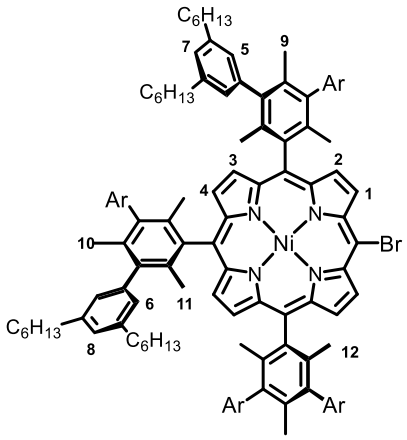
5,10,15-Tri(tetra-*tert*-butyl)porphyrin **3.21c** (30 mg, 17 μmol) and $Ni(OAc)_2{\cdot}4H_2O$ (41 mg, 4.0 equiv., 68 μmol) were added into a 50 mL round-bottom flask and it was backfilled with argon for three times. Anhydrous DMF (10 mL) and *m*-xylene (10 mL) were added using a syringe and the suspension was stirred at 140 °C overnight. After the reaction was completed,

the mixture was cooled to room temperature. The resulting solution was concentrated under reduced pressure and the residue was filtrated through a silica plug eluted using dichloromethane. Ni(II) 5,10,15-tri(tetra-*tert*-butyl)porphyrin crude (30 mg, 16 μmol) was yielded as purple solid and added into a 50 mL round bottom flask which contains dichloromethane (6 mL) and pyridine (0.06 mL). The solution was cooled to 0 °C using an ice bath, followed by the dropwise addition of a solution of *N*-bromosuccinimide (3.8 mg, 1.3 equiv., 21 μmol) in dichloromethane (1.2 mL). The mixture was left stirring for 30 min and quenched by acetone (3.0 mL). The resulting solution was concentrated under reduced pressure and the crude product recrystallized by layer addition of dichloromethane/methanol. Ni(II) 5-bromo-10,15,20-tri(tetra-*tert*-butyl)porphyrin **3.22c** (31 mg, 99%) was yielded as a dark purple solid.

^{1}H NMR (400 MHz, $CDCl_3$, 298 K) δ_H 9.52 (d, *J* = 5.0 Hz, 2H, *H1*), 8.86 (d, *J* = 4.9 Hz, 2H, *H2*), 8.82 (d, *J* = 0.9 Hz, 4H, *H3*, *H4*), 7.34 (2d, *J* = 1.9 Hz, 6H, *H5*, *H6*), 7.26 – 7.21 (m, 12H, *H7*, *H8*), 1.96 (s, 6H, *H10*), 1.93 (s, 3H, *H9*), 1.52 (2s, 18H, *H11*, *H12*), 1.37 – 1.34 (m, 108H, $H_{t\text{-}Bu}$).

MALDI-TOF MS: *m/z* = 1931.546 ($C_{131}H_{161}BrN_4Ni$, M^+ requires 1930.354).

Ni(II) 5-bromo-10,15,20-tri(tetra-hexyl)porphyrin 3.22d



5,10,15-Tri(tetra-hexyl)porphyrin **3.21d** (25 mg, 12 μmol) and $Ni(OAc)_2{\cdot}4H_2O$ (22 mg, 4.0 equiv., 35 μmol) were added into a 25 mL round-bottom flask and it was backfilled with argon for three times. Anhydrous DMF (4 mL) and *m*-xylene (4 mL) were added using a syringe and the suspension was stirred at 140 °C overnight. After the reaction was completed, the mixture was cooled to room temperature. The resulting solution was concentrated and the residue was filtrated through a silica plug using DCM as the eluent system. Ni(II)

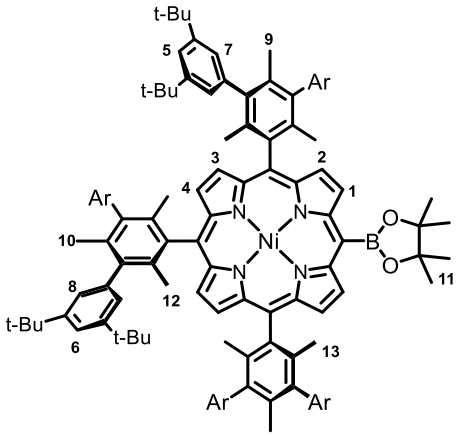
5,10,15-tri(tetra-hexyl)porphyrin crude (25 mg) was yielded as purple solid. Ni(II) porphyrin (15 mg, 6.9 μmol) was added into a 25 mL round bottom flask which contains dichloromethane (5.0 mL) and pyridine (0.05 mL). The solution was cooled to 0 °C by ice bath, followed by the dropwise addition of a solution of *N*-bromosuccinimide (1.6 mg, 1.3 equiv., 8.9 μmol) in dichloromethane (1.0 mL). The mixture was left stirring for 30 min and quenched by acetone (3.0 mL). The resulting solution was concentrated under reduced pressure and the crude product recrystallized by layer addition of dichloromethane/methanol. Ni(II) 5-bromo-10,15,20-tri(tetra-hexyl)porphyrin **3.22d** (14 mg, 90%) was yielded as a dark purple solid.

^{1}H NMR (400 MHz, $CDCl_3$, 298 K) δ_H 9.53 (d, *J* = 4.9 Hz, 2H, *H1*), 8.82 (d, *J* = 4.9 Hz, 2H, *H2*), 8.75 (s, 4H, *H3*, *H4*), 7.06 – 7.01 (m, 12H, *H5*, *H6*), 6.95 (m, 6H, *H7*, *H8*), 2.64 (m, 24H, H_{hexyl}), 1.98 (s, 6H, *H9*), 1.96 (s, 3H, *H10*), 1.68 – 1.61 (m, 24H, H_{hexyl}), 1.51 (s, 6H, *H11*), 1.50 (s, 12H, *H12*), 1.37 – 1.23 (m, 90H, H_{hexyl}), 0.86 – 0.81 (m, 41H, H_{hexyl}).

^{13}C NMR (101 MHz, $CDCl_3$, 298K) δ_C 143.4, 143.3, 143.1, 142.9, 142.8, 142.8, 142.5, 141.9, 141.9, 139.89, 139.9, 137.5, 135.8, 135.8, 134.1, 133.0, 132.3, 132.0, 132.0, 127.1, 127.0, 127.0, 126.6, 126.6, 119.2, 119.1, 101.9, 36.0, 35.9, 35.9, 31.7, 31.7, 31.6, 31.5, 29.7, 29.0, 22.6, 22.6, 20.3, 20.3, 19.7, 14.1, 14.0, 14.0.

MALDI-TOF MS: *m/z* = 2267.588 ($C_{155}H_{209}BrN_4Ni$, M^+ requires 2267.002).

Ni(II) 5-Bpin-10,15,20-tri(tetra-*tert*-butyl)porphyrin 3.23c



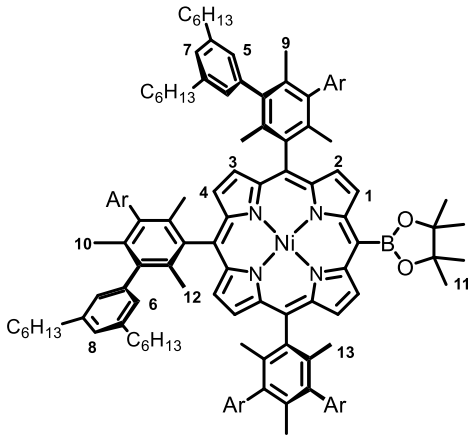
Ni(II) 5-bromo-10,15,20-tri(tetra-*tert*-butyl)porphyrin **3.22c** (22 mg, 11 μmol), $PdCl_2(PPh_3)_2$ (1.6 mg, 0.2 equiv., 2.3 μmol) were added into a 15 mL Schlenk tube and it was evacuated and backfilled with argon for three times. Anhydrous THF (0.7 mL), toluene (0.7 mL) and

triethylamine (0.16 mL, 100 equiv., 1.1 mmol) were added using a syringe and the solution was degassed by three freeze-pump-thaw cycles followed by the addition of 4,4,5,5-tetramethyl-1,3,2-dioxaborolane (0.13 mL, 75 equiv., 0.86 mmol). The reaction proceeded at 68 °C for 5 h and the excess of pinacolborane was neutralized by dropwise added water (4.0 mL). EtOAc (5.0 mL) was added to the cooled reaction mixture and the organic extract was washed with water (10 mL × 2) and dried over Na_2SO_4. The resulting solution was concentrated under reduced pressure and the crude material was purified through silica chromatography (pet. ether/EtOAc, v/v, gradient elution from 100:0 to 100:20) to yield Ni(II) 5-Bpin-10,15,20-tri(tetra-*tert*-butyl)porphyrin **3.23c** (15 mg, 67%) as a purple solid.

^{1}H NMR (400 MHz, $CDCl_3$, 298 K) δ_H 9.73 (d, J = 4.9 Hz, 2H, *H1*), 8.90 (d, J = 4.9 Hz, 2H, *H2*), 8.87 – 8.83 (m, 4H, *H3*, *H4*), 7.33 (t, J = 1.9 Hz, 6H, *H5*, *H6*), 7.26 – 7.22 (m, 12H, *H7*, *H8*), 1.96 (s, 6H, *H10*), 1.94 (s, 3H, *H9*), 1.74 (s, 12H, *H11*), 1.53 (s, 6H, *H12*), 1.51 (s, 12H, *H13*), 1.37 – 1.34 (m, 108H, $H_{t\text{-}Bu}$).

MALDI-TOF MS: m/z = 1978.673 ($C_{137}H_{173}BN_4NiO_2$, M^+ requires 1977.420).

Ni(II) 5-Bpin-10,15,20-tri(tetra-hexyl)porphyrin 3.23d



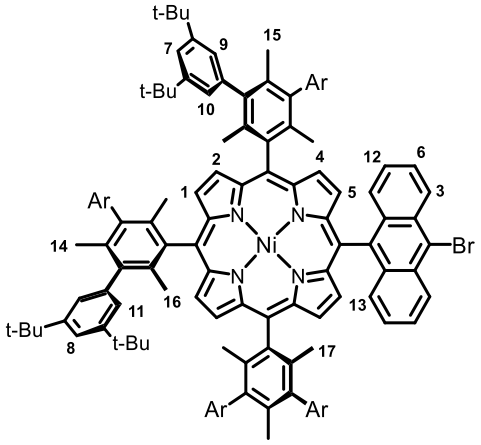
Ni(II) 5-bromo-10,15,20-tri(tetra-hexyl)porphyrin **3.22d** (15 mg, 6.6 μmol), $PdCl_2(PPh_3)_2$ (0.93 mg, 0.2 equiv., 1.3 μmol) were added into a 10 mL Schlenk tube and it was flushed with argon for three times. Anhydrous THF (0.4 mL), toluene (0.4 mL) and triethylamine (0.9 mL, 100 equiv., 0.66 mmol) were added using a syringe and the solution was degassed by three freeze-pump-thaw cycles followed by the addition of 4,4,5,5-tetramethyl-1,3,2-dioxaborolane (0.07 mL, 75 equiv., 0.50 mmol). The reaction proceeded at 68 °C for 5 h and the excess of

pinacolborane was neutralized by dropwise added water (4.0 mL). EtOAc (5.0 mL) was added to the cooled reaction mixture and the organic extract was washed with water (10 mL × 2) and dried over Na_2SO_4. The resulting solution was concentrated under reduced pressure and the crude material was purified through silica chromatography (pet. ether/EtOAc, v/v, gradient elution from 10:0 to 10:2) to yield Ni(II) 5-Bpin-10,15,20-tri(tetra-hexyl)porphyrin **3.23d** (12 mg, 75%) as a purple solid.

^{1}H NMR (400 MHz, $CDCl_3$, 298 K) δ_H 9.73 (d, *J* = 4.9 Hz, 2H, *H1*), 8.86 (d, *J* = 4.9 Hz, 2H, *H2*), 8.80 – 8.74 (m, 4H, *H3*, *H4*), 7.04 – 7.01 (m, 12H, *H5*, *H6*), 6.93 (2t, *J* = 1.9 Hz, 6H, *H7*, *H8*), 2.62 (m, 24H, H_{hexyl}), 1.96 (s, 6H, *H9*), 1.95 (s, 3H, *H10*), 1.74 (s, 12H, *H11*), 1.68 – 1.59 (m, 26H, H_{hexyl}), 1.50 (s, 6H, *H12*), 1.49 (s, 12H, *H13*), 1.37 – 1.18 (m, 88H, H_{hexyl}), 0.86 – 0.79 (m, 38H, H_{hexyl}).

MALDI-TOF MS: *m/z* = 2310.916 ($C_{161}H_{221}BN_4NiO_2$, M^+ requires 2311.676).

Bromo-functionalized monoanthracenyl-porphyrin 3.24c



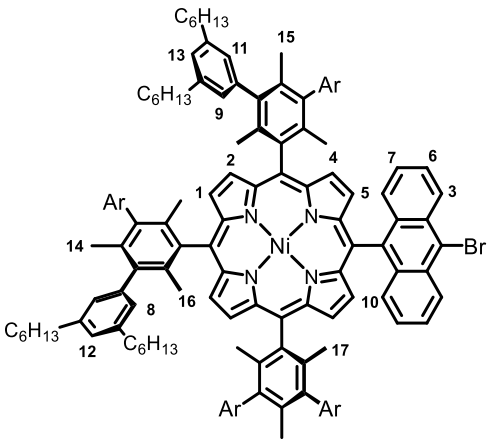
Ni(II) 5-Bpin-10,15,20-tri(tetra-*tert*-butyl)porphyrin **3.23c** (12 mg, 6.0 μmol), 9,10-dibromoanthracene **3.2** (60 mg, 30 equiv., 0.18 mmol), $Pd(PPh_3)_4$ (2.1 mg, 0.3 equiv., 1.8 μmol) and Cs_2CO_3 (4.9 mg, 2.5 equiv., 15 μmol) were added to a 15 mL Schlenk tube and it was evacuated and backfilled with argon for three times. Anhydrous DMF (0.75 mL) and toluene (3 mL) were added under argon using a syringe and the suspension was degassed by three freeze-pump-thaw cycles. The reaction proceeded at 110 °C for 3 h with stirring and monitored by TLC in pet. ether/dichloromethane (4:1, v/v). The reaction mixture was diluted with EtOAc (10 mL) and the organic phase was extracted and washed with water (10 mL × 2)

and dried over Na_2SO_4. The resulting solution was concentrated under reduced pressure and the residue was purified through a silica column chromatography (pet. ether/EtOAc, v/v, 10:1). Bromo-functionalized monoanthracenyl-porphyrin **3.24c** (6.5 mg, 52%) was isolated as a red solid.

^{1}H NMR (400 MHz, $CDCl_3$, 298 K) δ_H 8.92 – 8.86 (m, 4H, *H1*, *H2*), 8.81 – 8.77 (m, 2H, *H3*), 8.65 (d, *J* = 4.9 Hz, 2H, *H4*), 8.13 (d, *J* = 4.9 Hz, 2H, *H5*), 7.56 (ddd, *J* = 9.0, 6.4, 1.3 Hz, 2H, *H6*), 7.37 – 7.30 (m, 10H, *H7*, *H8*, *H9*), 7.23 (t, *J* = 1.6 Hz, 4H, *H11*), 7.16 (t, *J* = 1.6 Hz, 4H, *H10*), 7.15 – 7.12 (m, 2H, *H12*), 7.06 (m, 2H, *H13*), 1.97 (s, 3H, *H14*), 1.90 (s, 6H, *H15*), 1.58 (s, 6H, *H16*), 1.52 (s, 12H, *H17*), 1.37 (s, 36H, $H_{t\text{-}Bu}$), 1.35 (s, 36H, $H_{t\text{-}Bu}$), 1.30 (s, 36H, $H_{t\text{-}Bu}$).

MALDI-TOF MS: *m/z* = 2104.332 ($C_{145}H_{169}BrN_4Ni$, M^+ requires 2103.188).

Bromo-functionalized monoanthracenyl-porphyrin 3.24d



Ni(II) 5-Bpin-10,15,20-tri(tetra-hexyl)porphyrin **3.23d** (12 mg, 5.0 μmol), 9,10-dibromoanthracene (50 mg, 30 equiv., 0.15 mmol), $Pd(PPh_3)_4$ (1.7 mg, 0.3 equiv., 1.5 μmol) and Cs_2CO_3 (4.1 mg, 2.5 equiv., 12 μmol) were added to a 15 mL Schlenk tube and it was evacuated and backfilled with argon for three times. Anhydrous DMF (0.88 mL) and toluene (3.5 mL) were added under argon using a syringe and the suspension was degassed by three freeze-pump-thaw cycles. The reaction proceeded at 110 °C for 3 h with stirring and monitored by TLC in pet. ether/dichloromethane (4:1, v/v). The reaction mixture was diluted with EtOAc (10 mL) and the organic phase was extracted and washed twice with water (10 mL × 2) and dried over Na_2SO_4. The resulting solution was concentrated under reduced pressure and the residue was purified through a silica column chromatography (pet. ether/EtOAc, v/v,

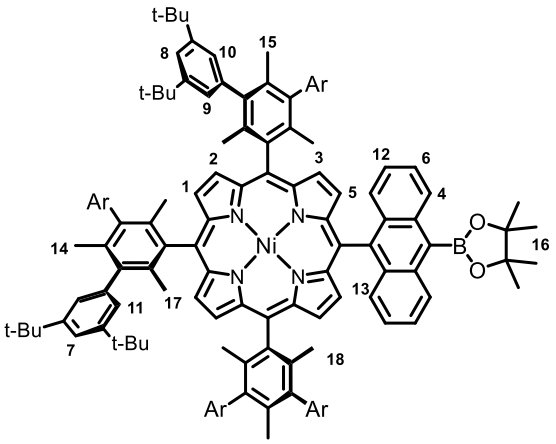
10:1). Bromo-functionalized monoanthracenyl-porphyrin **3.24d** (6.7 mg, 55%) was isolated as a red solid.

^{1}H NMR (400 MHz, $CDCl_3$, 298 K) δ_H 8.84 – 8.81 (m, 4H, *H1*, *H2*), 8.79 (dt, *J* = 9.1, 0.9 Hz, 2H, *H3*), 8.59 (d, *J* = 4.9 Hz, 2H, *H4*), 8.12 (d, *J* = 4.9 Hz, 2H, *H5*), 7.56 (ddd, *J* = 9.1, 6.2, 1.3 Hz, 2H, *H6*), 7.07 (dt, *J* = 9.0, 1.0 Hz, 2H, *H7*), 7.06 – 7.00 (m, 10H, *H9*, *H10*, *H13*), 6.95 (t, *J* = 1.6 Hz, 2H, *H12*), 6.93 (d, *J* = 1.6 Hz, 4H, *H11*), 6.91 (d, *J* = 1.7 Hz, 4H, *H8*), 2.62 (2 overlap t, *J* = 6.6 Hz, 17H, H_{hexyl}), 2.56 (t, *J* = 7.7 Hz, 8H, H_{hexyl}), 1.98 (s, 3H, *H14*), 1.92 (s, 6H, *H15*), 1.64 (m, 18H, H_{hexyl}), 1.56 (s, 6H, *H16*), 1.49 (s, 12H, *H17*), 1.37 – 1.17 (m, 82H, H_{hexyl}), 0.78 – 0.75 (m, 36H, H_{hexyl}).

^{13}C NMR (101 MHz, $CDCl_3$, 298K) δ_C 144.1, 143.6, 143.2, 143.1, 143.0, 142.8, 142.1, 142.1, 140.0, 139.9, 138.1, 138.0, 136.4, 136.0, 136.0, 135.4, 134.1, 134.0, 131.9, 131.8, 131.7, 131.5, 130.0, 129.4, 127.8, 127.2, 127.2, 127.1, 127.0, 126.7, 126.7, 126.1, 124.2, 119.5, 119.2, 36.1, 36.1, 36.1, 31.8, 31.8, 31.7, 31.7, 31.7, 29.9, 29.1, 29.1, 22.8, 22.7, 20.5, 20.5, 19.9, 19.8, 14.2, 14.1.

MALDI-TOF MS: *m/z* = 2443.262 ($C_{169}H_{217}BrN_4Ni$, M^+ requires 2443.220).

Boronate ester-functionalized monoanthracenyl-porphyrin 3.25c



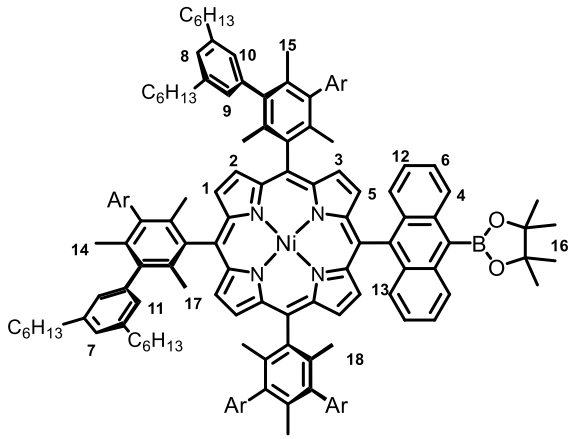
Bromo-functionalized monoanthracenyl-porphyrin **3.24c** (6.5 mg, 3.1 μmol), $Pd(dppf)Cl_2$ (0.4 mg, 0.15 equiv., 0.5 μmol), bis(pinacolate)diboron (2.4 mg, 3.0 equiv., 9.3 μmol) and potassium acetate (2.7 mg, 9.0 equiv., 28 μmol) were added to a 10 mL Schlenk tube and it was evacuated and backfilled with argon for three times. Anhydrous DMF (2.0 mL) was added under argon using a syringe and the suspension was degassed by three freeze-pump-thaw cycles. The reaction proceeded at 60 °C for 5 h with stirring and monitored by TLC in pet.

ether/dichloromethane (3:1). The reaction mixture was diluted with EtOAc (5.0 mL) and the organic phase was extracted and washed with water (10 mL × 2) and dried over Na_2SO_4. The resulting solution was concentrated under reduced pressure and the residue was purified through a silica column chromatography (pet. ether/EtOAc, v/v, 4:1). Boronate ester-functionalized monoanthracenyl-porphyrin **3.25c** (3.4 mg, 50%) was yielded as a red solid.

^{1}H NMR (400 MHz, $CDCl_3$, 298 K) δ_H 8.88 (m, 4H, *H1*, *H2*), 8.62 (d, *J* = 4.9 Hz, 2H, *H3*), 8.59 (d, *J* = 8.8 Hz, 2H, *H4*), 8.11 (d, *J* = 4.9 Hz, 2H, *H5*), 7.46 – 7.41 (m, 2H, *H6*), 7.34 (t, *J* = 1.8 Hz, 2H, *H7*), 7.30 (t, *J* = 1.9 Hz, 4H, *H8*), 7.22 (t, *J* = 1.6 Hz, 4H, *H11*), 7.17 (t, *J* = 1.7 Hz, 4H, *H10*), 7.09 (d, *J* = 8.7 Hz, 2H, *H12*), 7.02 – 6.97 (m, 2H, *H13*), 1.97 (s, 3H, *H14*), 1.90 (s, 6H, *H15*), 1.73 (s, 12H, *H16*), 1.58 (s, 6H, *H17*), 1.51 (s, 12H, *H18*), 1.36 (s, 36H, $H_{t\text{-}Bu}$), 1.35 (s, 36H, $H_{t\text{-}Bu}$), 1.30 (s, 36H, $H_{t\text{-}Bu}$).

MALDI-TOF MS: *m/z* = 2151.619 ($C_{151}H_{181}BN_4NiO_2$, M^+ requires 2151.363).

Boronate ester-functionalized monoanthracenyl-porphyrin 3.25d



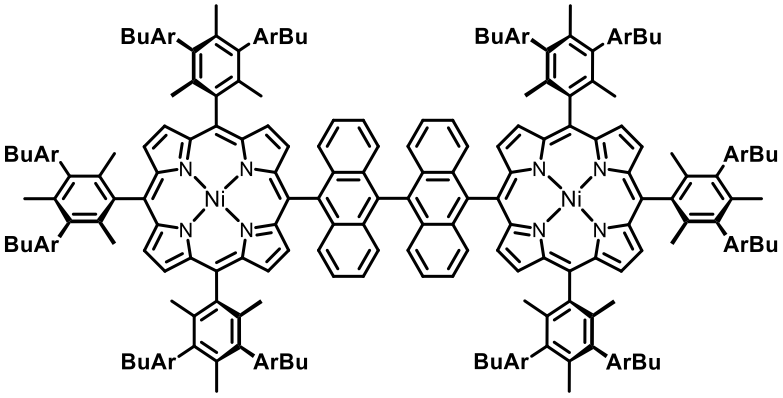
Bromo-functionalized monoanthracenyl-porphyrin **3.24d** (5.1 mg, 2.1 μmol), $Pd(dppf)Cl_2$ (0.3 mg, 0.15 equiv., 0.3 μmol), bis(pinacolate)diboron (1.6 mg, 3.0 equiv., 6.3 μmol) and potassium acetate (1.8 mg, 9.0 equiv., 19 μmol) were added to a 10 mL Schlenk tube and it was evacuated and backfilled with argon for three times. Anhydrous DMF (2.0 mL) and toluene (0.2 mL) were added under argon using a syringe and the suspension was degassed by three freeze-pump-thaw cycles. The reaction proceeded at 60 °C for 5 h with stirring and monitored by TLC in pet. ether/dichloromethane (3:1). The reaction mixture was diluted with EtOAc (5 mL) and the organic phase was extracted and washed with water (10 mL × 2) and dried over Na_2SO_4. The resulting solution was concentrated under reduced pressure and the residue was

purified through a silica column chromatography (pet. ether/EtOAc, v/v, 4:1). Boronate ester-functionalized monoanthracenyl-porphyrin **3.25d** (2.6 mg, 49%) was yielded as a red solid.

^{1}H NMR (400 MHz, $CDCl_3$, 298 K) δ_H 8.77 – 8.72 (m, 4H, *H1*, *H2*), 8.53 – 8.48 (m, 4H, *H3*, *H4*), 8.03 (d, *J* = 4.9 Hz, 2H, *H5*), 7.39 – 7.33 (m, 2H, *H6*), 6.98 (t, *J* = 1.6 Hz, 4H, *H8*), 6.95 – 6.93 (m, 4H, *H7*, *H12*), 6.88 (t, *J* = 1.8 Hz, 8H, *H9*, *H11*), 6.83 (t, *J* = 1.6 Hz, 4H, *H10*), 2.58 – 2.47 (m, 24H, H_{hexyl}), 1.91 (s, 3H, *H14*), 1.84 (s, 6H, *H15*), 1.66 (s, 12H, *H16*), 1.55 (m, 23H, H_{hexyl}), 1.47 (s, 6H, *H17*), 1.42 (s, 12H, *H18*), 0.76 – 0.67 (m, 35H, H_{hexyl}).

MALDI-TOF MS: *m/z* = 2490.478 ($C_{175}H_{229}BN_4NiO_2$, M^+ requires 2490.286).

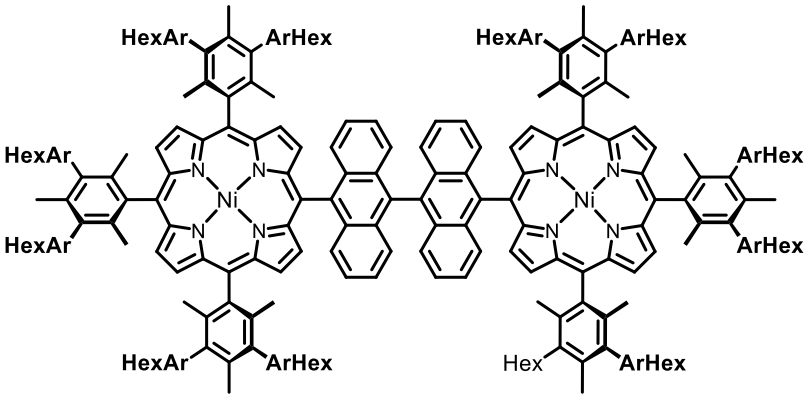
Singly-linked bisanthracene-porphyrin dimer 3.26c



Bromo-functionalized monoanthracenyl-porphyrin **3.24c** (3.9 mg, 1.9 equiv., 1.9 μmol), boronate ester-functionalized monoanthracenyl-porphyrin **3.24c** (2.6 mg, 1.0 μmol), $Pd(PPh_3)_4$ (0.36 mg, 0.2 equiv., 0.3 μmol) and Cs_2CO_3 (1.0 mg, 2.0 equiv., 3.1 μmol) were added to a 10 mL Schlenk tube and it was evacuated and backfilled with argon for three times. Anhydrous DMF (0.3 mL) and toluene (1.2 mL) were added under argon using a syringe and the suspension was degassed by three freeze-pump-thaw cycles. The reaction proceeded at 70 °C for 18 h with stirring and monitored by TLC (pet. ether/dichloromethane, v/v, 3:1). The reaction mixture was diluted with EtOAc (10 mL) and the organic phase was extracted and washed with water (15 mL × 2) and dried over Na_2SO_4. The resulting solution was concentrated under reduced pressure and the residue was purified through a silica column chromatography (pet. ether/dichloromethane, v/v, 4:1). Singly-linked bisanthracene-porphyrin dimer **3.26c** (0.78 mg, 12%) was yielded as a red solid.

MALDI-TOF MS: *m/z* = 4050.178 ($C_{290}H_{338}N_8Ni_2$, M^+ requires 4048.540).

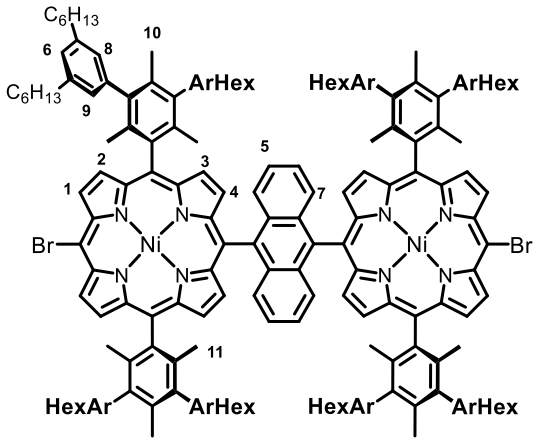
Singly-linked bisanthracene-porphyrin dimer 3.26d



Bromo-functionalized monoanthracenyl-porphyrin **3.24d** (3.3 mg, 1.3 equiv., 1.4 μmol), boronate ester-functionalized monoanthracenyl-porphyrin **3.25d** (3.3 mg, 1.4 μmol), $Pd(PPh_3)_4$ (0.24 mg, 0.2 equiv., 0.21 μmol) and Cs_2CO_3 (0.67 mg, 2 equiv., 2.1 μmol) were added to a 10 mL Schlenk tube and it was evacuated and backfilled with argon for three times. Anhydrous DMF (0.25 mL) and toluene (1.0 mL) were added under argon using a syringe and the suspension was degassed by three freeze-pump-thaw cycles. The reaction proceeded at 70 °C for 18 h with stirring and monitored by TLC (pet. ether/dichloromethane, v/v, 4:1). The reaction mixture was diluted with EtOAc (10 mL) and the organic phase was extracted and washed with water (15 mL × 2) and dried over Na_2SO_4. The resulting solution was concentrated under reduced pressure and the residue was purified through a silica column chromatography (pet. ether/dichloromethane, v/v, 4:1). Singly-linked bisanthracene-porphyrin dimer **3.26d** (0.7 mg, 14%) was yielded as a red solid.

MALDI-TOF MS: *m/z* = 4723.518 ($C_{338}H_{434}N_8Ni_2$, M^+ requires 4721.291).

Singly-linked anthracenyl-dibromoporphyrin dimer 3.27d



Porphyrin **3.16d** (0.37 g, 0.24 mmol, 1 equiv.) and $Ni(OAc)_2{\cdot}4H_2O$ (0.45 g, 0.72 mmol, 3 equiv.) were added into a 100 mL round-bottom flask followed by the addition of DMF (20 mL) and *m*-xylene (20 mL). The mixture was stirred at 140 °C overnight and the reaction was monitored by TLC (pet. ether/dichloromethane, v/v, 4:1). The resulting solution was concentrated under reduced pressure and purified through a short silica plug (pet. ether/dichloromethane, v/v, 1:1) to yield Ni(II) 5,15-bis(tetra-hexylphenyl)porphyrin **3.17d** (0.35 g, 91%) was yielded as a red-purple solid.

Porphyrin **3.17d** (78 mg, 49 μmol, 1.0 equiv.) was added into a 100 mL round-bottom flask followed by the addition of dichloromethane (50 mL) with pyridine (0.5 mL). It was cooled to 0 °C in an ice bath and to the stirred mixture, a solution of *N*-bromosuccinimide (19 mg, 0.11 mmol, 2.2 equiv.) in dichloromethane (10 mL) was added dropwise. The reaction was conducted at 0 °C for 15 min. Subsequently, acetone (1.0 mL) was added to quench the excess *N*-bromosuccinimide. The resulting mixture was concentrated under reduced pressure and purified by a silica plug (pet. ether/dichloromethane, v/v, 1:1) to yield Ni(II) 5,15-dibromo-10,20-bis(tetra-hexylphenyl)porphyrin **3.18d** (78 mg, 91%).

Porphyrin **3.18d** (53 mg, 31 μmol), $PdCl_2(PPh_3)_2$ (4.3 mg, 0.2 equiv., 6.1 μmol) were added into a 20 mL two-neck Schlenk tube and it was evacuated and backfilled with argon for three times. Anhydrous THF (1.9 mL), toluene (1.9 mL) and triethylamine (0.43 mL, 100 equiv., 3.1 mmol) were added using a syringe and the solution was degassed by three freeze-pump-thaw cycles followed by the addition of 4,4,5,5-tetramethyl-1,3,2-dioxaborolane (0.33 mL, 75 equiv., 2.3 mmol). The reaction proceeded at 68 °C for 5 h and the excess of pinacolborane was quenched by dropwise addition of water (2.0 mL). EtOAc (10 mL) was added to the cooled reaction mixture and the organic extract was washed with water (10 mL × 2) and dried over Na_2SO_4. The resulting solution was concentrated under reduced pressure and the crude material was purified through silica chromatography (pet. ether/EtOAc v/v, gradient elution from 100:3 to 100:20). Ni(II) 5,15-diBpin-10,20-bis(tetra-hexylphenyl)porphyrin (25 mg, 45%) was yielded as a purple solid and Ni(II) 5-Bpin-10,20-bis(tetra-hexylphenyl)porphyrin (27 mg, 52%) **3.27d** was yielded as a purple side product.

Porphyrin **3.27d** (27 mg, 2.5 equiv., 16 μmol), 9,10-dibromoanthracene **3.2** (2.1 mg, 6.3 μmol), $Pd(PPh_3)_4$ (2.2 mg, 0.3 equiv., 1.9 μmol) and Cs_2CO_3 (5.2 mg, 2.5 equiv., 16 μmol)

were added to a 20 mL Schlenk tube and it was evacuated and backfilled with argon for three times. Anhydrous DMF (0.75 mL) and toluene (3 mL) were added under argon using a syringe and the suspension was degassed by three freeze-pump-thaw cycles. The reaction proceeded at 80 °C for 12 h with stirring and monitored by TLC in pet. ether/dichloromethane (4:1, v/v). The reaction mixture was diluted with EtOAc (10 mL) and the organic phase was extracted and washed with water (10 mL × 2) and dried over Na_2SO_4. The resulting solution was concentrated under reduced pressure and the residue was purified through a silica column chromatography (pet. ether/EtOAc, v/v, 10:1). Singly-linked anthracenyl-porphyrin dimer **3.28d** (6.5 mg, 31%) was isolated as a red solid.

Singly-linked anthracenyl-porphyrin dimer **3.28d** (6.5 mg, 2.0 μmol, 1.0 equiv.) was added into a 25 mL round-bottom flask followed by the addition of dichloromethane (10 mL) with pyridine (0.1 mL). It was cooled to 0 °C in an ice bath and to the stirred mixture, a solution of *N*-bromosuccinimide (1.0 mg, 5.8 μmol, 3.0 equiv.) in dichloromethane (2.0 mL) was added dropwise. The reaction was conducted at 0 °C for 15 min. Subsequently, acetone (1.0 mL) was added to quench the excess *N*-bromosuccinimide. The resulting mixture was concentrated under reduced pressure and purified by a silica plug (pet. ether/dichloromethane, v/v, 1:1) to yield singly-linked anthracenyl-dibromoporphyrin dimer **3.29d** (5.4 mg, 79%).

^{1}H NMR (700 MHz, CD_2Cl_2, 298 K) δ_H 9.62 (d, J = 4.8 Hz, 4H, *H1*), 8.90 (d, J = 4.8 Hz, 4H, *H2*), 8.76 (d, J = 4.7 Hz, 4H, *H3*), 8.54 (d, J = 4.7 Hz, 4H, *H4*), 7.26 (dd, J = 7.1, 3.3 Hz, 4H, *H5*), 7.07 (s, 8H, *H6*), 7.01 (s, 8H, *H7*), 6.99 (dd, J = 7.5, 3.0 Hz, 4H, *H8*), 6.97 (t, J = 0.8 Hz, 8H, *H9*), 2.66 (t, J = 7.7 Hz, 16H, H_{hexyl}), 2.61 (t, J = 7.7 Hz, 16H, H_{hexyl}), 1.69 – 1.58 (m, 44H, H_{hexyl}), 1.56 (s, 24H, *H10*), 1.52 (s, 48H, *H11*), 1.38 – 1.19 (m, 186H, H_{hexyl}), 0.84 (d, J = 7.2 Hz, 24H, H_{hexyl}), 0.77 (t, J = 7.1 Hz, 24H, H_{hexyl}).

^{13}C NMR (176 MHz, CD_2Cl_2, 298 K) δ_C 144.5, 143.7, 143.1, 143.0, 142.5, 141.8, 140.1, 137.1, 136.1, 135.6, 134.2, 133.8, 133.4, 132.8, 132.5, 128.3, 127.0 126.9, 126.7, 125.4, 119.7, 114.8, 53.8, 35.9, 35.9, 31.9, 31.7, 31.67, 31.6, 31.5, 29.7, 29.4, 28.9, 28.8, 27.1, 22.7, 22.6, 22.5, 20.0, 19.4, 13.9, 13.8, 13.8.

MALDI-TOF MS: m/z = 3490.602 ($C_{234}H_{292}Br_2N_8Ni_2$, M^+ requires 3488.017).

Band Structure Calculation

The simulation cells were prepared by placing the polymer tape in the *xy* plane, with a 12 Å wide vacuum region in the *z* direction. For the anthracene-bridged Ni(II) porphyrin ribbons (**AP*N***), we used a 10×1×1 reciprocal space mesh; for fused Ni(II) porphyrin polymers (**P*N***) we used a 14×1×1 mesh, and for anthracene-based graphene nanoribbons (**7-AGNR**) we used a 22×1×1 mesh. All calculations were done using the Vienna *Ab initio* Simulation Package (VASP) code using the default PBE PAW potentials and a plane-wave kinetic energy cutoff of 520 eV.[10–12]

Geometries were optimized using PBE-D2. Both the unit cell parameters and atoms were allowed to relax. To minimize errors due to Pulay stress, the unit cell volume was constrained to a constant value during optimizations. To obtain accurate electronic structures, we carried out single-point calculations using the HSE06 short-range screened hybrid functional.[48] In these runs, electronic energies were converged to 0.001 meV. Band structures were obtained by interpolating HSE06 results using Boltztrap2.[13] All band energies are reported with respect to the vacuum reference, which was determined using VASPKIT.[14]

Ni-P*N* optimized geometry (POSCAR):

```
 1.00000000000000
   8.3332184354927747    0.0000000000000000   -0.0000000000000000
   0.0000000000000000   20.0323208955272811    0.0000000000000000
  -0.0000000000000000    0.0000000000000000   11.8989272468669469
 C   N   H   Ni
 20   4   6   1
Direct
  0.0873862326627865  0.5000000000000000  0.5000000000000000
  0.9126137743372104  0.5000000000000000  0.5000000000000000
  0.1705084338036026  0.4396213989898927  0.5000000000000000
  0.8294915661963974  0.5603785710101049  0.5000000000000000
  0.8294915661963974  0.4396213989898927  0.5000000000000000
  0.1705084338036026  0.5603785710101049  0.5000000000000000
  0.0860699662238518  0.3768083778715521  0.5000000000000000
  0.9139300407761451  0.6231916221284479  0.5000000000000000
  0.9139300407761451  0.3768083778715521  0.5000000000000000
  0.0860699662238518  0.6231916221284479  0.5000000000000000
  0.2028533896287311  0.3282259730767751  0.5000000000000000
  0.7971465953712640  0.6717740569232274  0.5000000000000000
  0.7971465953712640  0.3282259730767751  0.5000000000000000
```

0.2028533896287311 0.6717740569232274 0.5000000000000000
0.3538190080413472 0.3621881490386161 0.5000000000000000
0.6461809919586528 0.6378118509613839 0.5000000000000000
0.6461809919586528 0.3621881490386161 0.5000000000000000
0.3538190080413472 0.6378118509613839 0.5000000000000000
0.5000000000000000 0.3296992038855243 0.5000000000000000
0.5000000000000000 0.6703007961144757 0.5000000000000000
0.3340044166216211 0.4311129372830277 0.5000000000000000
0.6659955833783717 0.5688870327169696 0.5000000000000000
0.6659955833783717 0.4311129372830277 0.5000000000000000
0.3340044166216211 0.5688870327169696 0.5000000000000000
0.1894803831419338 0.2742591630679805 0.5000000000000000
0.8105195868580637 0.7257408369320193 0.5000000000000000
0.8105195868580637 0.2742591630679805 0.5000000000000000
0.1894803831419338 0.7257408369320193 0.5000000000000000
0.5000000000000000 0.2752970900950859 0.5000000000000000
0.5000000000000000 0.7247029099049141 0.5000000000000000
0.5000000000000000 0.5000000000000000 0.5000000000000000

Ni-AP*N* optimized geometry (POSCAR):

1.00000000000000
12.6057119012702241 0.0000000000000000 -0.0000000000000000
0.0000000000000000 19.9346780644507895 0.0000000000000000
0.0000000000000000 0.0000000000000000 11.4936952236801169
C N H Ni
34 4 10 1
Direct
0.8860908369522390 0.5000000000000000 0.5000000000000000
0.1139091630477611 0.5000000000000000 0.5000000000000000
0.2271799674563502 0.5000000000000000 0.5000000000000000
0.7728200325436499 0.5000000000000000 0.5000000000000000
0.9432943582842641 0.5622688719646913 0.5000000000000000
0.0567056417157357 0.4377311280353018 0.5000000000000000
0.0567056417157357 0.5622688719646913 0.5000000000000000
0.9432943582842641 0.4377311280353018 0.5000000000000000
0.8874652216150004 0.6246595895281630 0.5000000000000000
0.1125347783849997 0.3753404104718369 0.5000000000000000
0.1125347783849997 0.6246595895281630 0.5000000000000000
0.8874652216150004 0.3753404104718369 0.5000000000000000
0.9450437631816616 0.6851506675340180 0.5000000000000000
0.0549562368183311 0.3148493324659821 0.5000000000000000
0.0549562368183311 0.6851506675340180 0.5000000000000000
0.9450437631816616 0.3148493324659821 0.5000000000000000
0.2828090756547429 0.4392316687085181 0.5000000000000000
0.7171909243452572 0.5607683012914794 0.5000000000000000

0.7171909243452572 0.4392316687085181 0.5000000000000000
0.2828090756547429 0.5607683012914794 0.5000000000000000
0.2264618638321240 0.3767149833724529 0.5000000000000000
0.7735381361678760 0.6232849866275443 0.5000000000000000
0.7735381361678760 0.3767149833724529 0.5000000000000000
0.2264618638321240 0.6232849866275443 0.5000000000000000
0.3038416515885703 0.3273824863896473 0.5000000000000000
0.6961583484114369 0.6726175436103554 0.5000000000000000
0.6961583484114369 0.3273824863896473 0.5000000000000000
0.3038416515885703 0.6726175436103554 0.5000000000000000
0.4031742505480570 0.3611917357754625 0.5000000000000000
0.5968257494519357 0.6388082642245374 0.5000000000000000
0.5968257494519357 0.3611917357754625 0.5000000000000000
0.4031742505480570 0.6388082642245374 0.5000000000000000
0.5000000000000000 0.3287145293120510 0.5000000000000000
0.5000000000000000 0.6712854706879489 0.5000000000000000
0.3902525192329730 0.4307930838343033 0.5000000000000000
0.6097474807670268 0.5692068861656944 0.5000000000000000
0.6097474807670268 0.4307930838343033 0.5000000000000000
0.3902525192329730 0.5692068861656944 0.5000000000000000
0.9017907872889842 0.7325700188019214 0.5000000000000000
0.0982092127110087 0.2674299811980786 0.5000000000000000
0.0982092127110087 0.7325700188019214 0.5000000000000000
0.9017907872889842 0.2674299811980786 0.5000000000000000
0.2948268424567575 0.2731644765689261 0.5000000000000000
0.7051731575432424 0.7268355234310742 0.5000000000000000
0.7051731575432424 0.2731644765689261 0.5000000000000000
0.2948268424567575 0.7268355234310742 0.5000000000000000
0.5000000000000000 0.2740190378466463 0.5000000000000000
0.5000000000000000 0.7259809621533538 0.5000000000000000
0.5000000000000000 0.5000000000000000 0.5000000000000000

7-AGNR optimized geometry (POSCAR):

1.00000000000000
4.3042208168134506 0.0000000000000000 0.0000000000000000
0.0000000000000000 19.9793875396563791 0.0000000000000000
0.0000000000000000 0.0000000000000000 10.3842410096927917
C H
14 4

Direct
0.1669443068275796 0.4380399870108694 0.5000000000000000
0.8330556931724205 0.5619600129891306 0.5000000000000000
0.8330556931724205 0.4380399870108694 0.5000000000000000
0.1669443068275796 0.5619600129891306 0.5000000000000000
0.3325650631157031 0.3764302449045125 0.5000000000000000

0.6674349368842969 0.6235697850954900 0.5000000000000000
0.6674349368842969 0.3764302449045125 0.5000000000000000
0.3325650631157031 0.6235697850954900 0.5000000000000000
0.1592874970431955 0.3160518129109266 0.5000000000000000
0.8407125029568044 0.6839481870890735 0.5000000000000000
0.8407125029568044 0.3160518129109266 0.5000000000000000
0.1592874970431955 0.6839481870890735 0.5000000000000000
0.3346058269080325 0.5000000000000000 0.5000000000000000
0.6653941730919675 0.5000000000000000 0.5000000000000000
0.2782478668306834 0.2680149795439714 0.5000000000000000
0.7217521331693166 0.7319849904560262 0.5000000000000000
0.7217521331693166 0.2680149795439714 0.5000000000000000
0.2782478668306834 0.7319849904560262 0.5000000000000000

Selected NMR Spectra

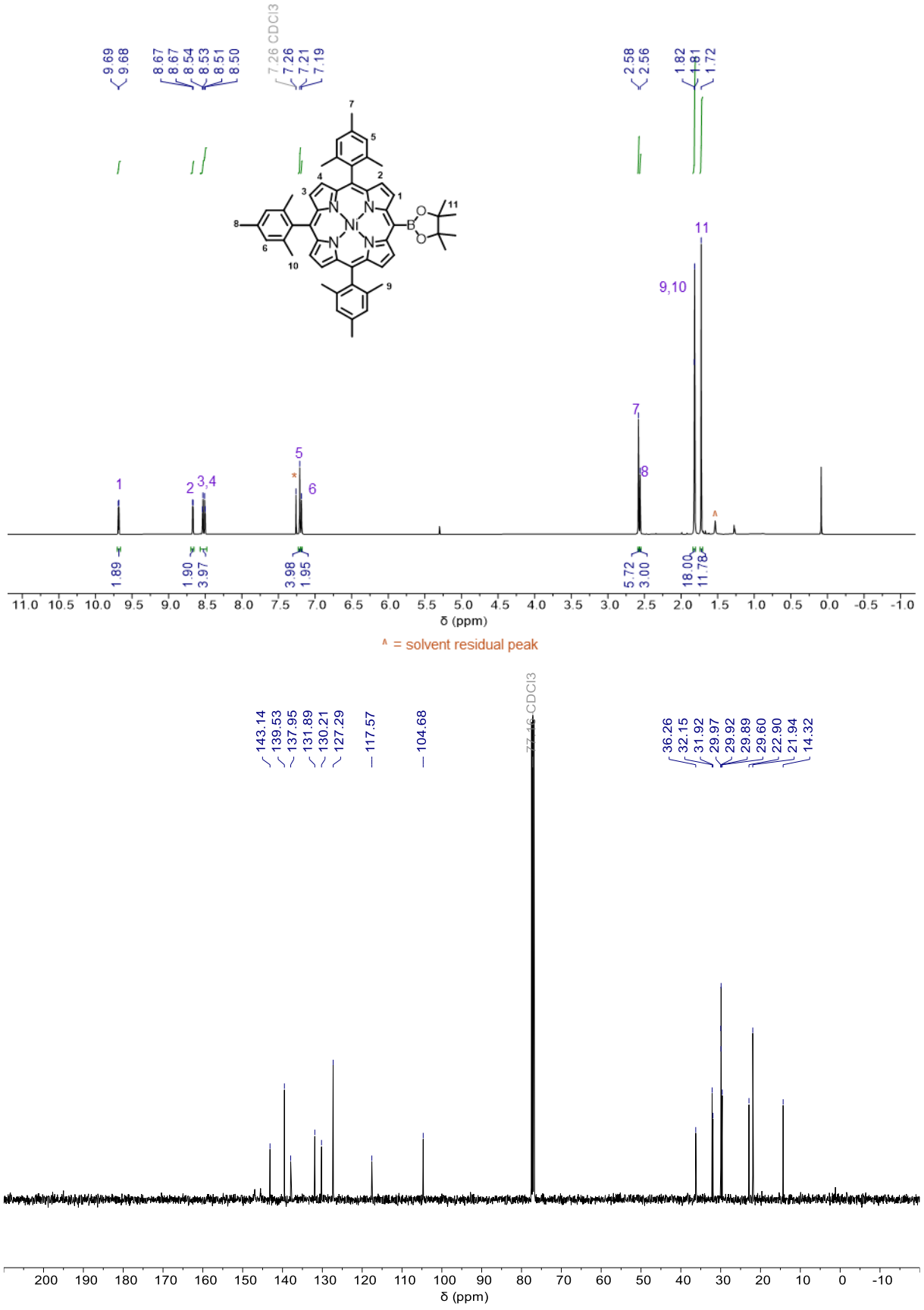


Figure S3.1: (top) ^{1}H NMR (400 MHz) and (bottom) ^{13}C NMR (151 MHz) spectra of porphyrin **3.1a** ($CDCl_3$, 298 K).

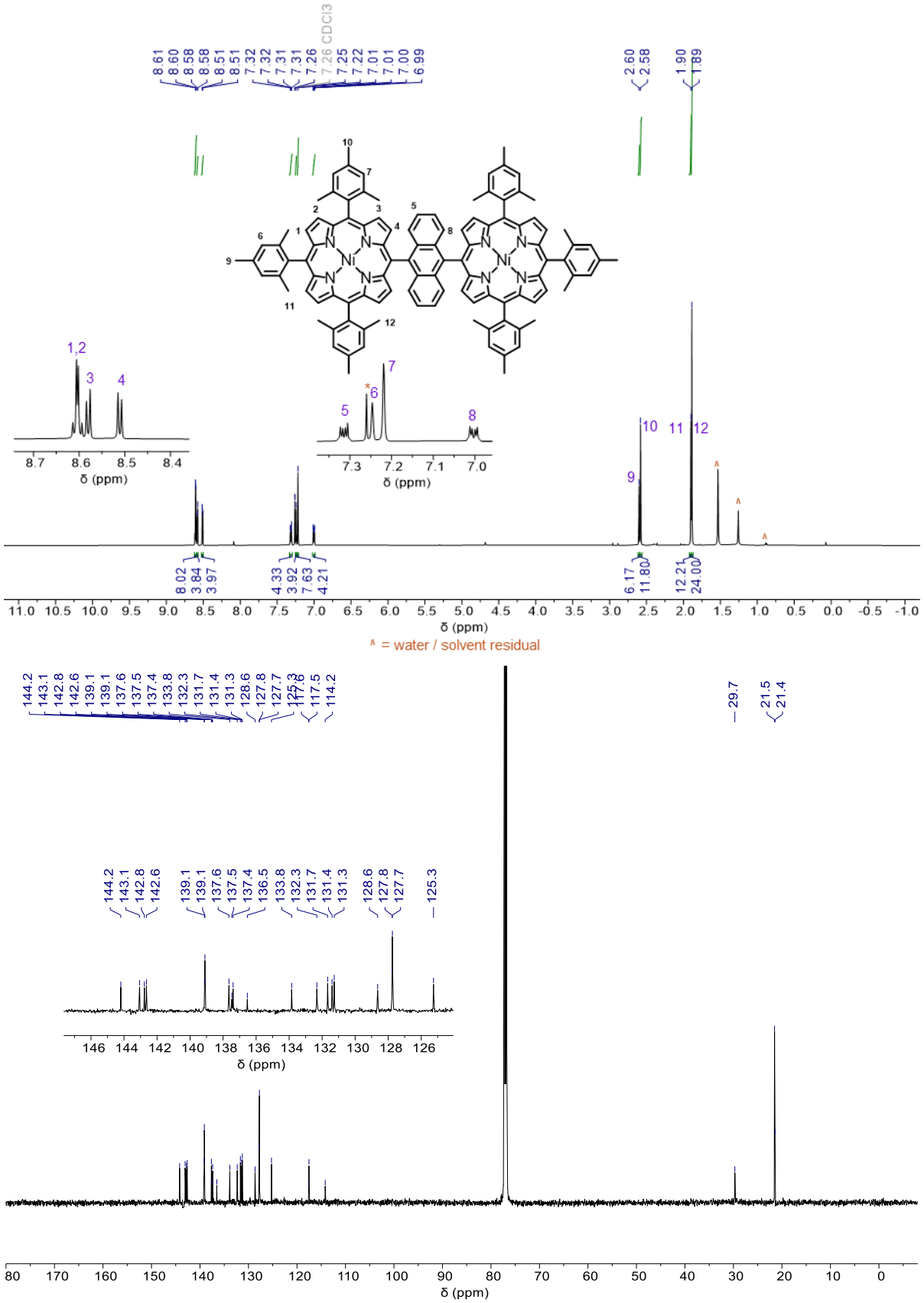


Figure S3.2: (top) ^{1}H NMR (400 MHz) and (bottom) ^{13}C NMR (151 MHz) spectra of porphyrin dimer **3.3a** ($CDCl_3$, 298 K).

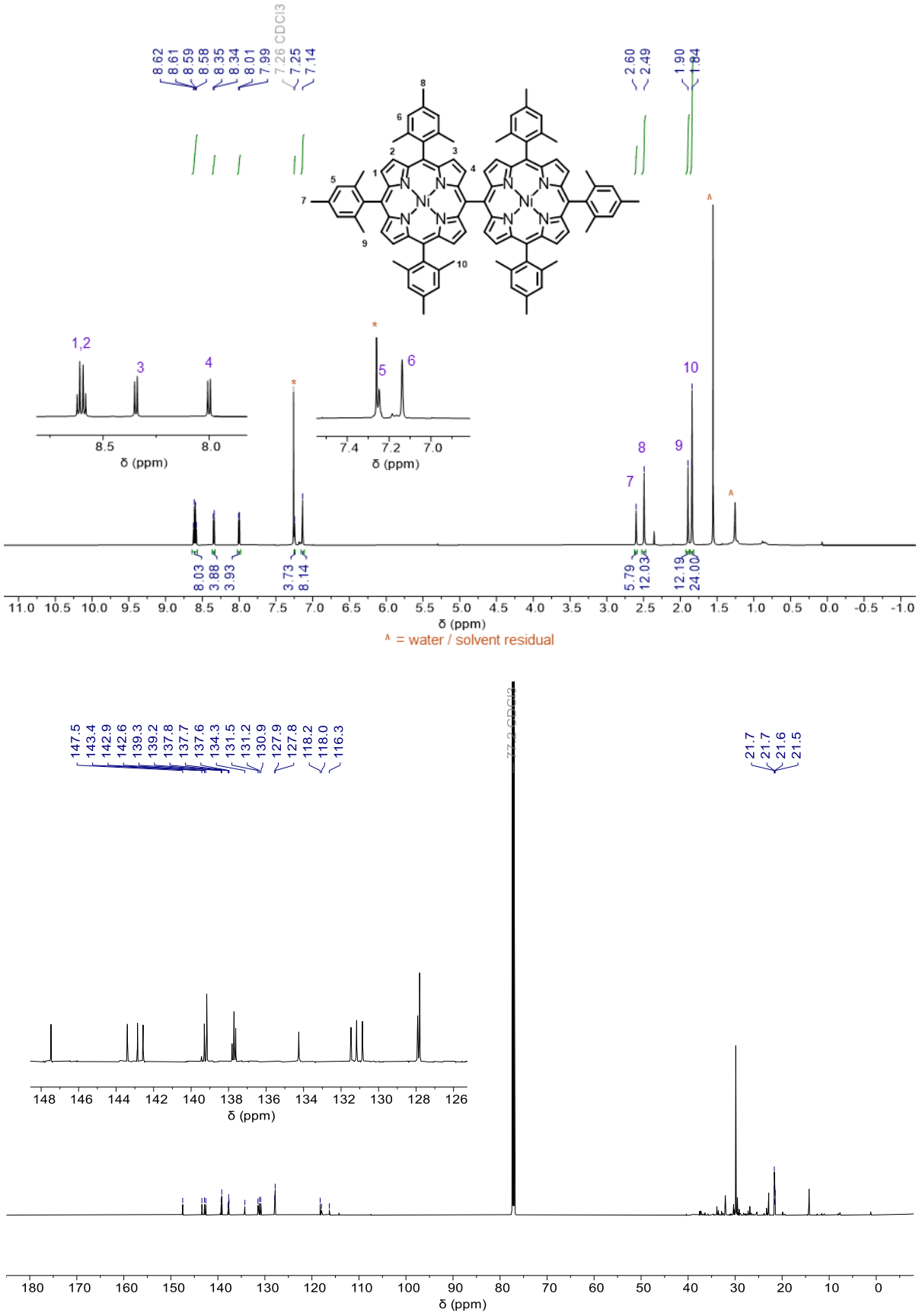


Figure S3.3: (top) ^{1}H NMR (400 MHz) and (bottom) ^{13}C NMR (151 MHz) spectra of porphyrin dimer ***s*-P2a** ($CDCl_3$, 298 K).

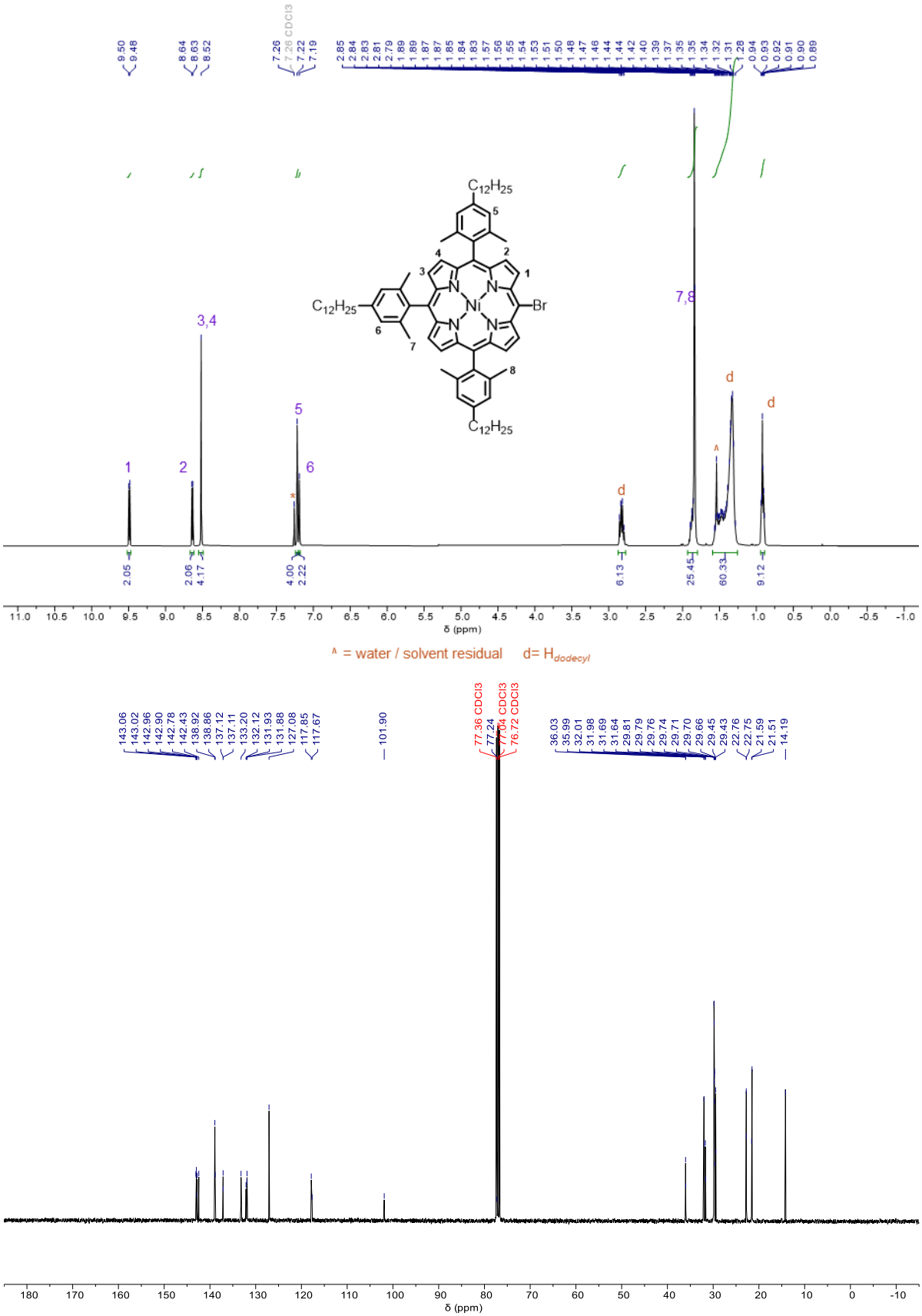


Figure S3.4: (top) ^{1}H NMR (400 MHz) and (bottom) ^{13}C NMR (151 MHz) spectra of porphyrin **3.4b** ($CDCl_3$, 298 K).

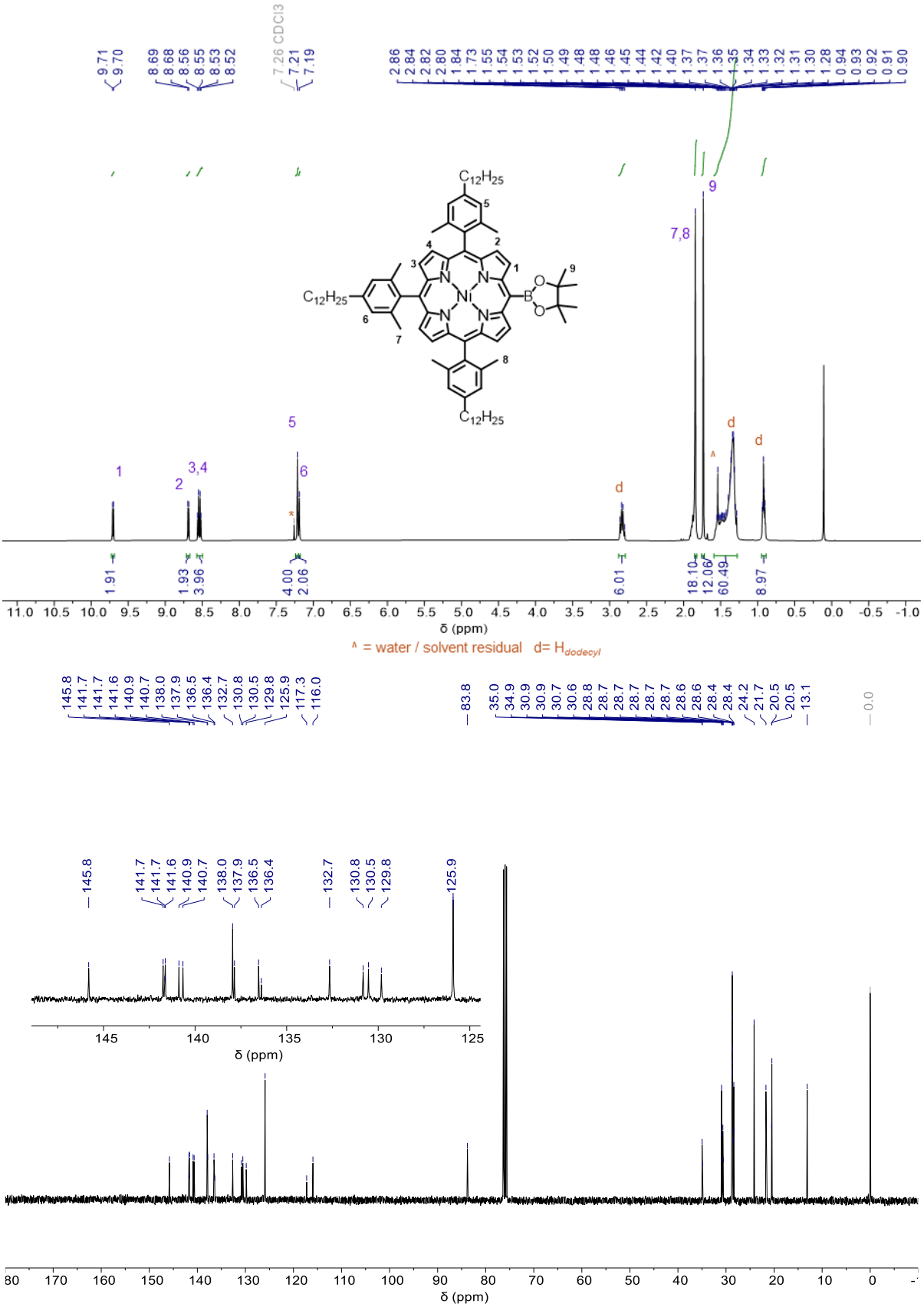


Figure S3.5: (top) ^{1}H NMR (400 MHz) and (bottom) ^{13}C NMR (101 MHz) spectra of porphyrin **3.4b** ($CDCl_3$, 298 K).

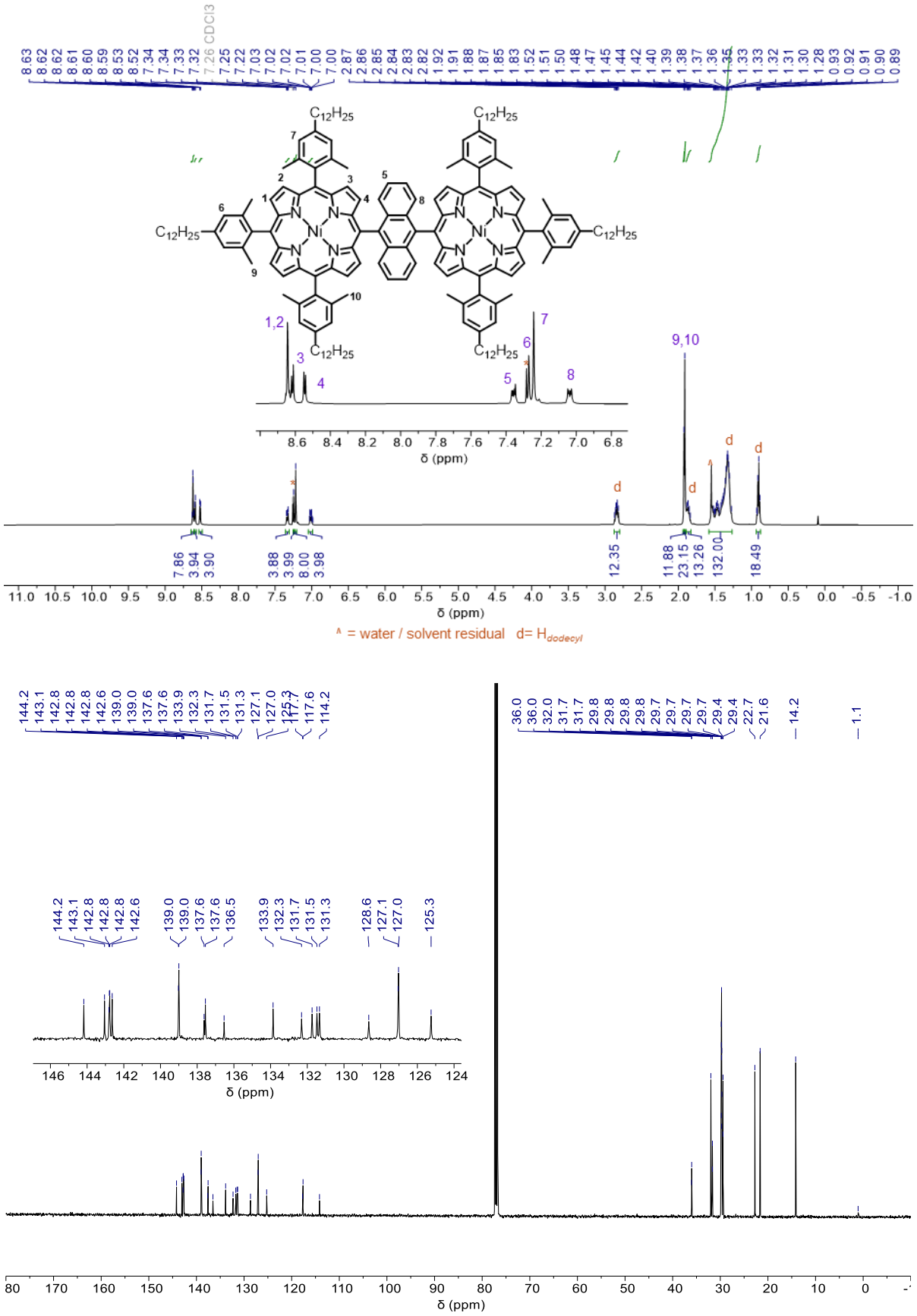


Figure S3.6: (top) ^{1}H NMR (500 MHz) and (bottom) ^{13}C NMR (126 MHz) spectra of porphyrin dimer **3.3b** ($CDCl_3$, 298 K).

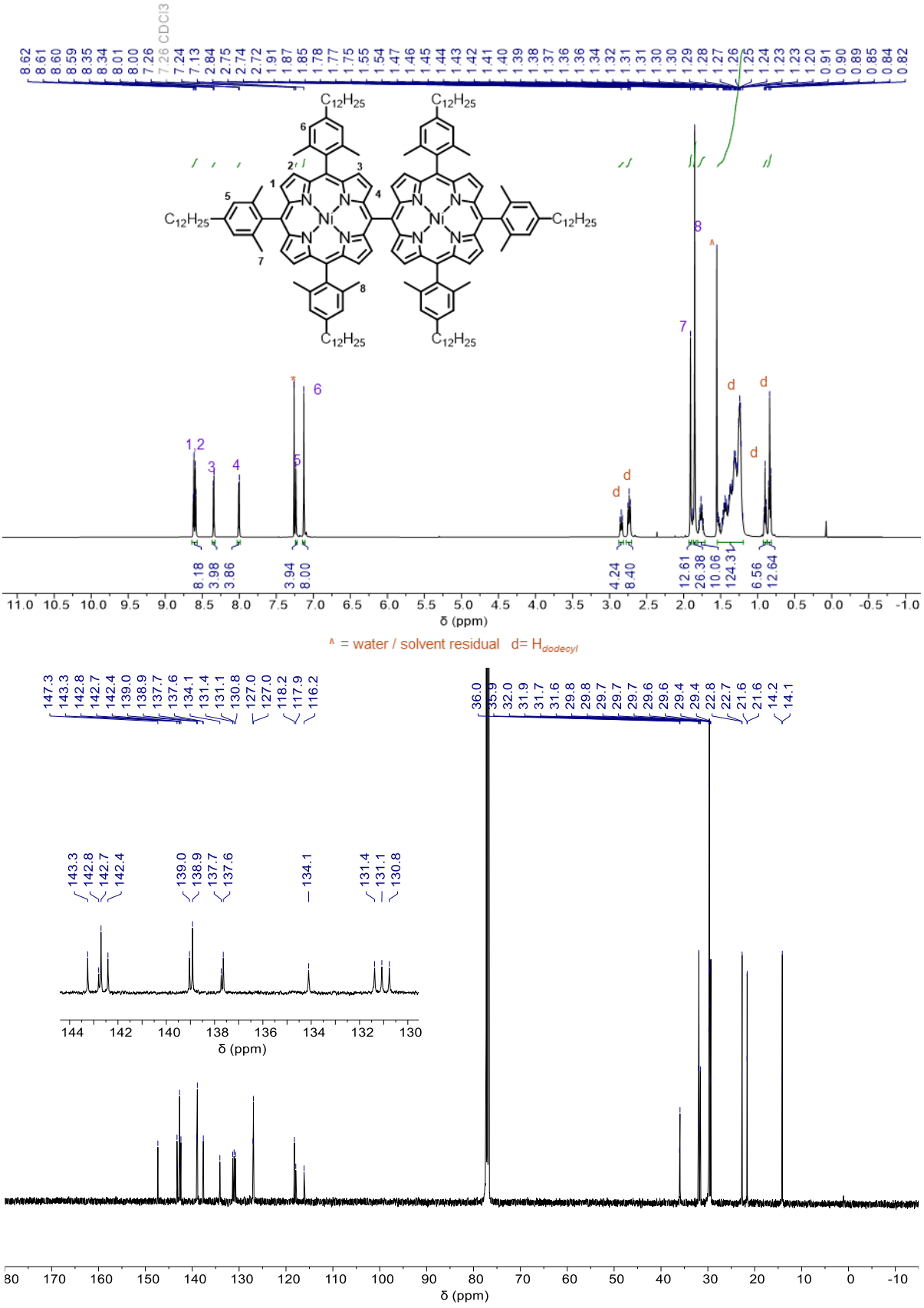


Figure S3.7: (top) ^{1}H NMR (500 MHz) and (bottom) ^{13}C NMR (126 MHz) spectra of porphyrin dimer ***s*-P2b** ($CDCl_3$, 298 K).

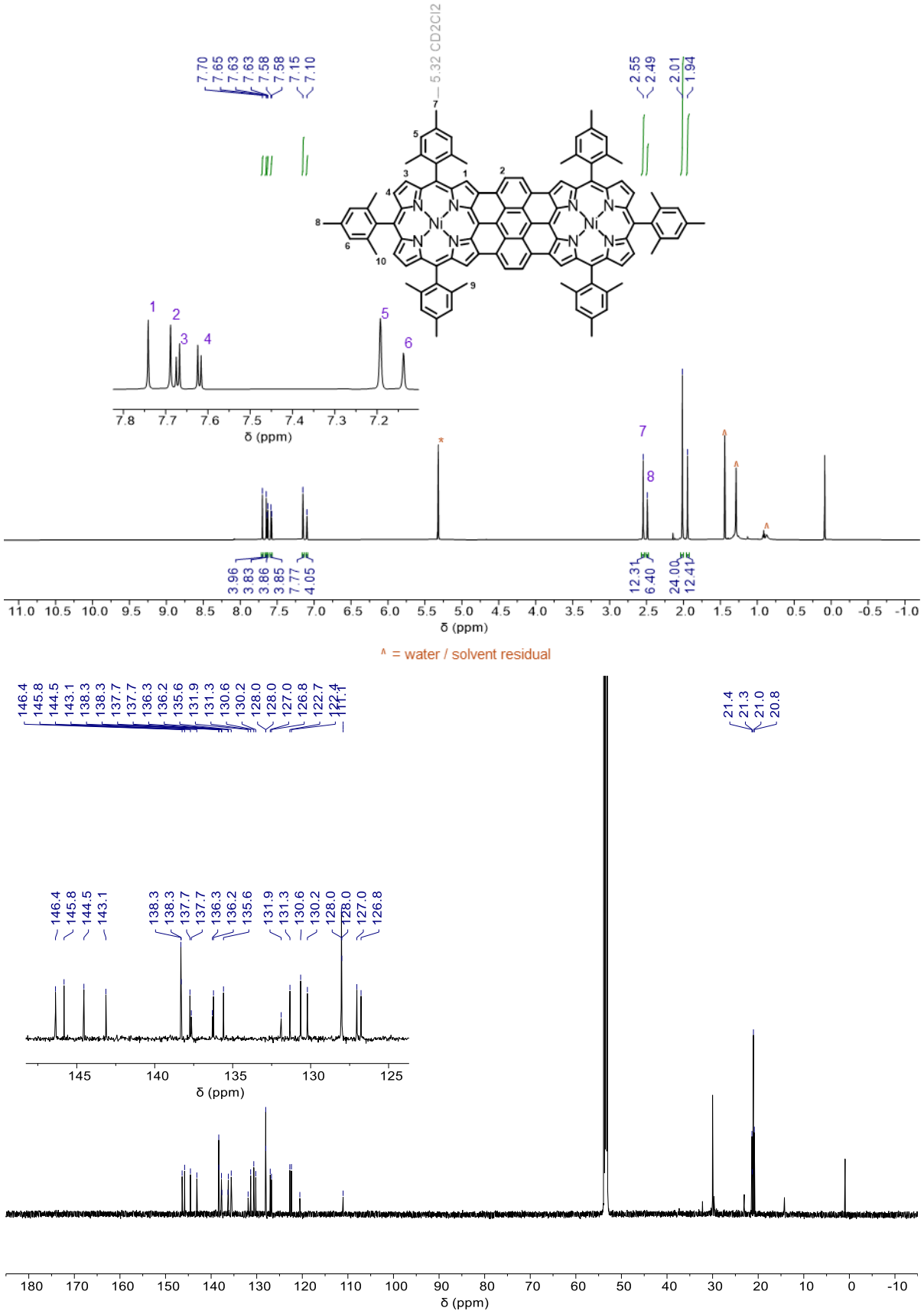


Figure S3.8: (top) ^{1}H NMR (600 MHz) and (bottom) ^{13}C NMR (151 MHz) spectra of fused porphyrin dimer **AP2a** (CD_2Cl_2/CS_2 (2:1, v/v), 298 K).

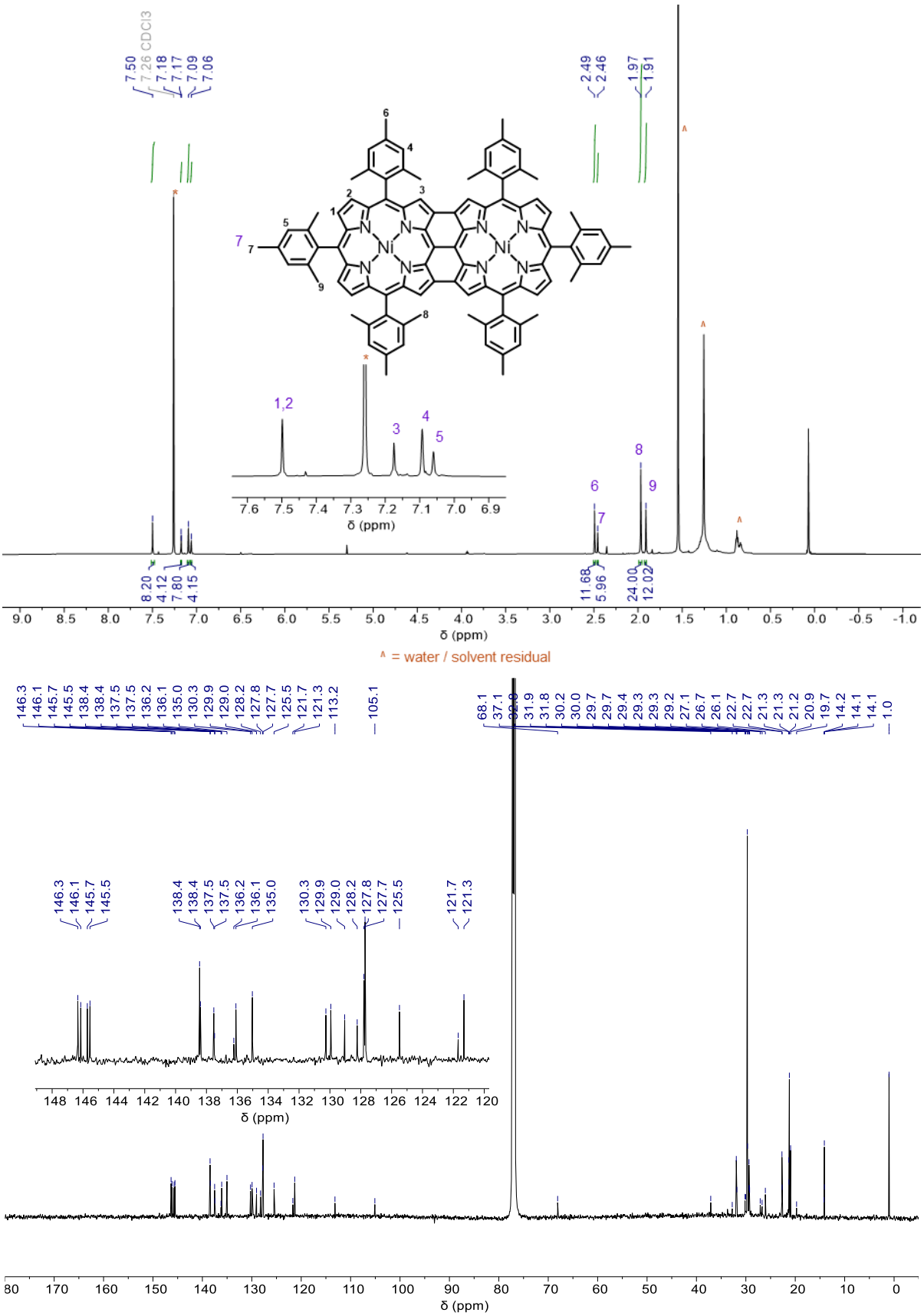


Figure S3.9: (top) ^{1}H NMR (400 MHz) and (bottom) ^{13}C NMR (151 MHz) spectra of fused porphyrin dimer **P2a** ($CDCl_3$, 298 K).

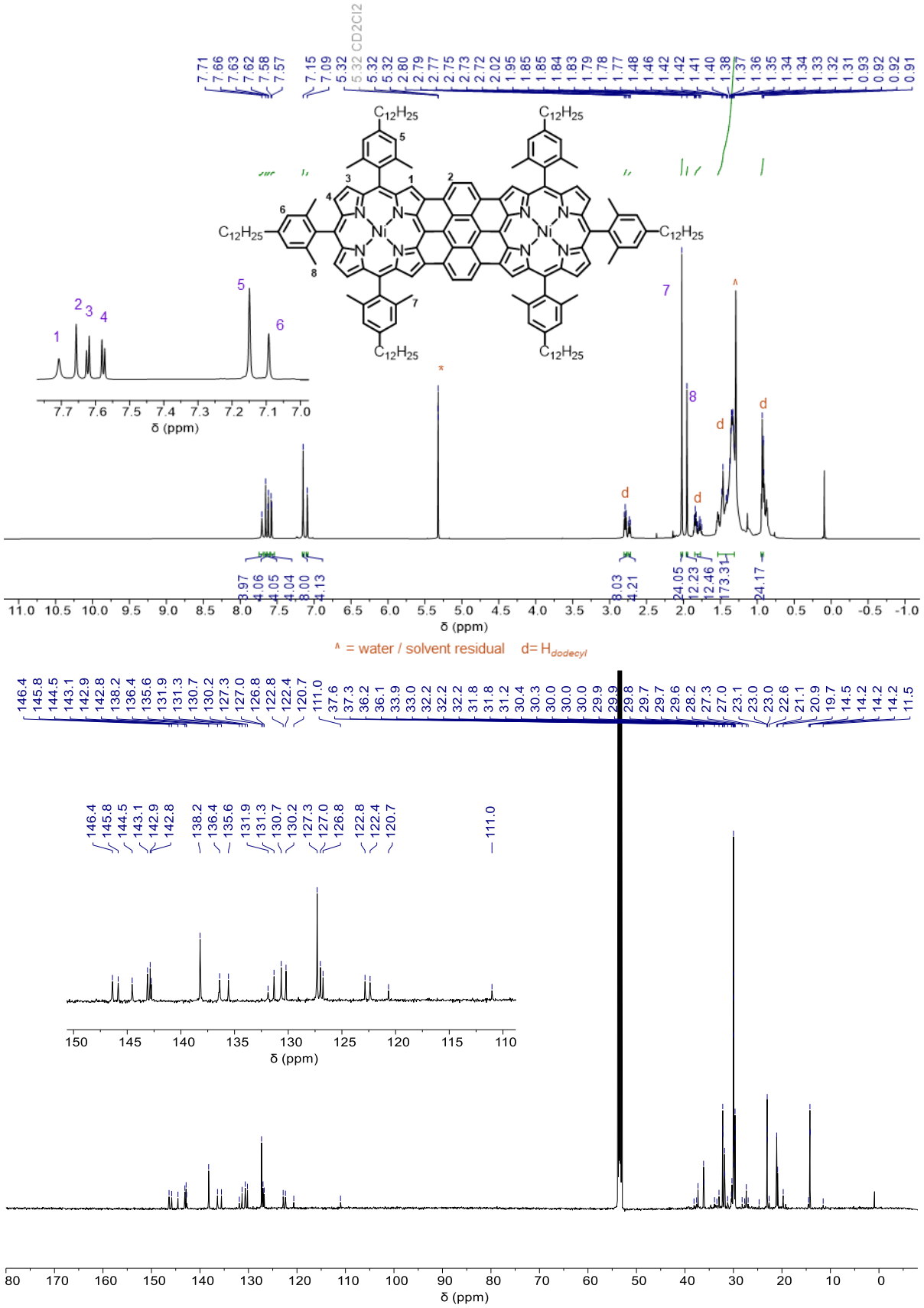


Figure S3.10: (top) ^{1}H NMR (600 MHz) and (bottom) ^{13}C NMR (151 MHz) spectra of fused porphyrin dimer (CD_2Cl_2/CS_2 (2:1, v/v), 298 K).

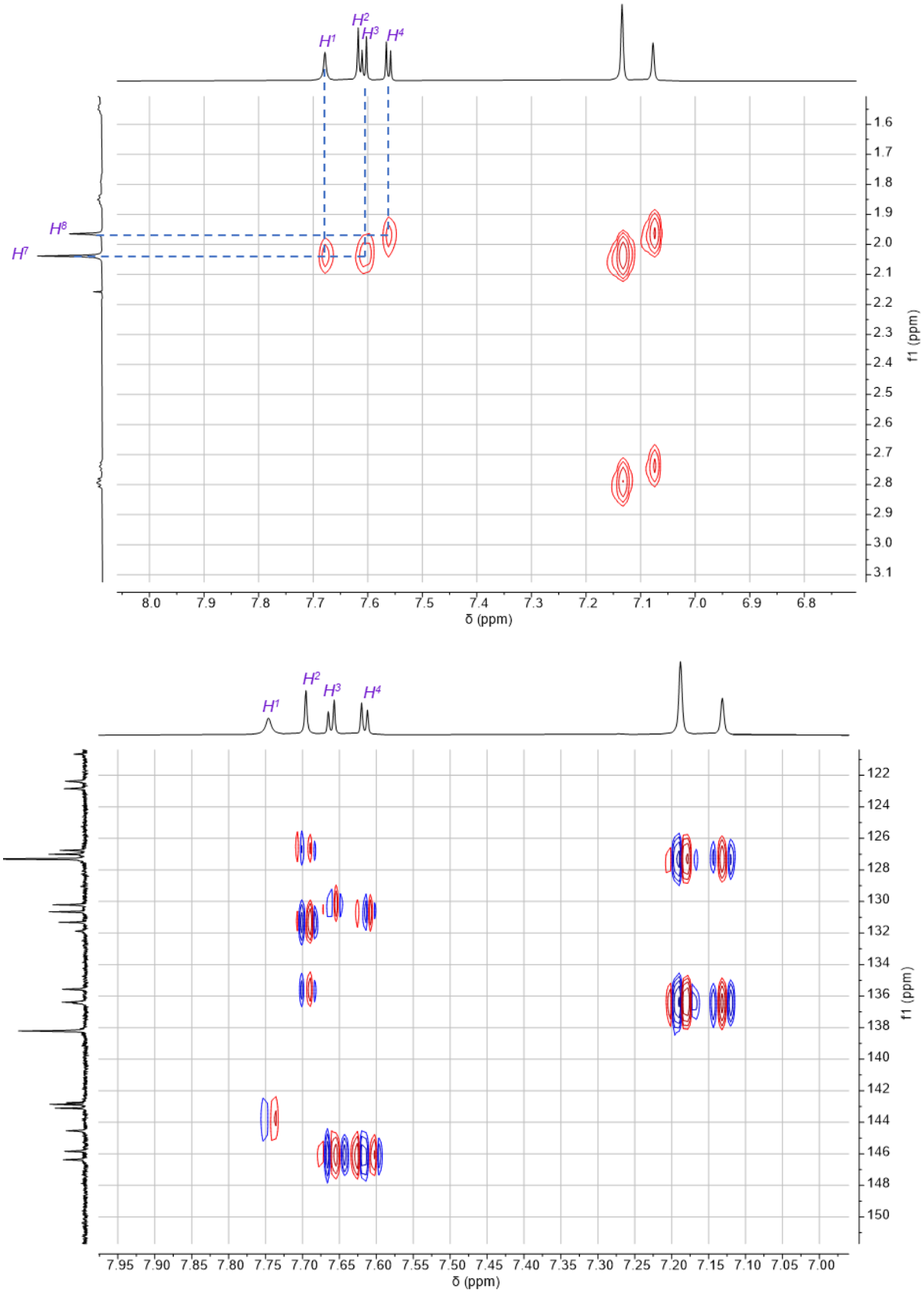


Figure S3.11: Aromatic regions of (top) $^{1}H–^{1}H$ NOESY spectrum and (bottom) $^{1}H–^{13}C$ high-resolution HMBC spectrum (CD_2Cl_2/CS_2 (2:1, v/v), 298 K at 600 MHz) of **AP2b**. (CD_2Cl_2/CS_2 (2:1, v/v), 298 K at 600 MHz)

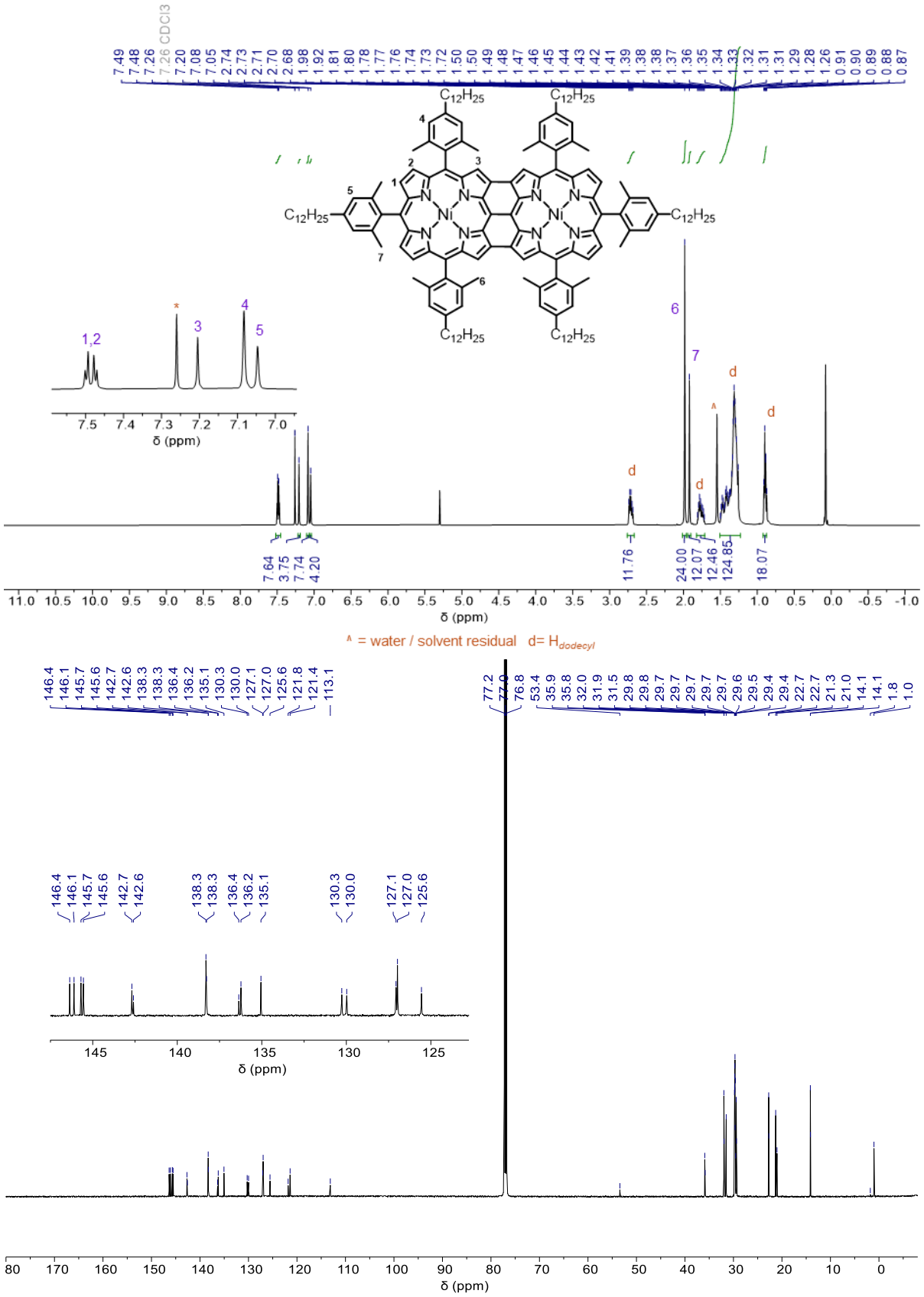


Figure S3.12: (top) ^{1}H NMR (400 MHz) and (bottom) ^{13}C NMR (126 MHz) spectra of fused porphyrin dimer **P2b** ($CDCl_3$, 298 K).

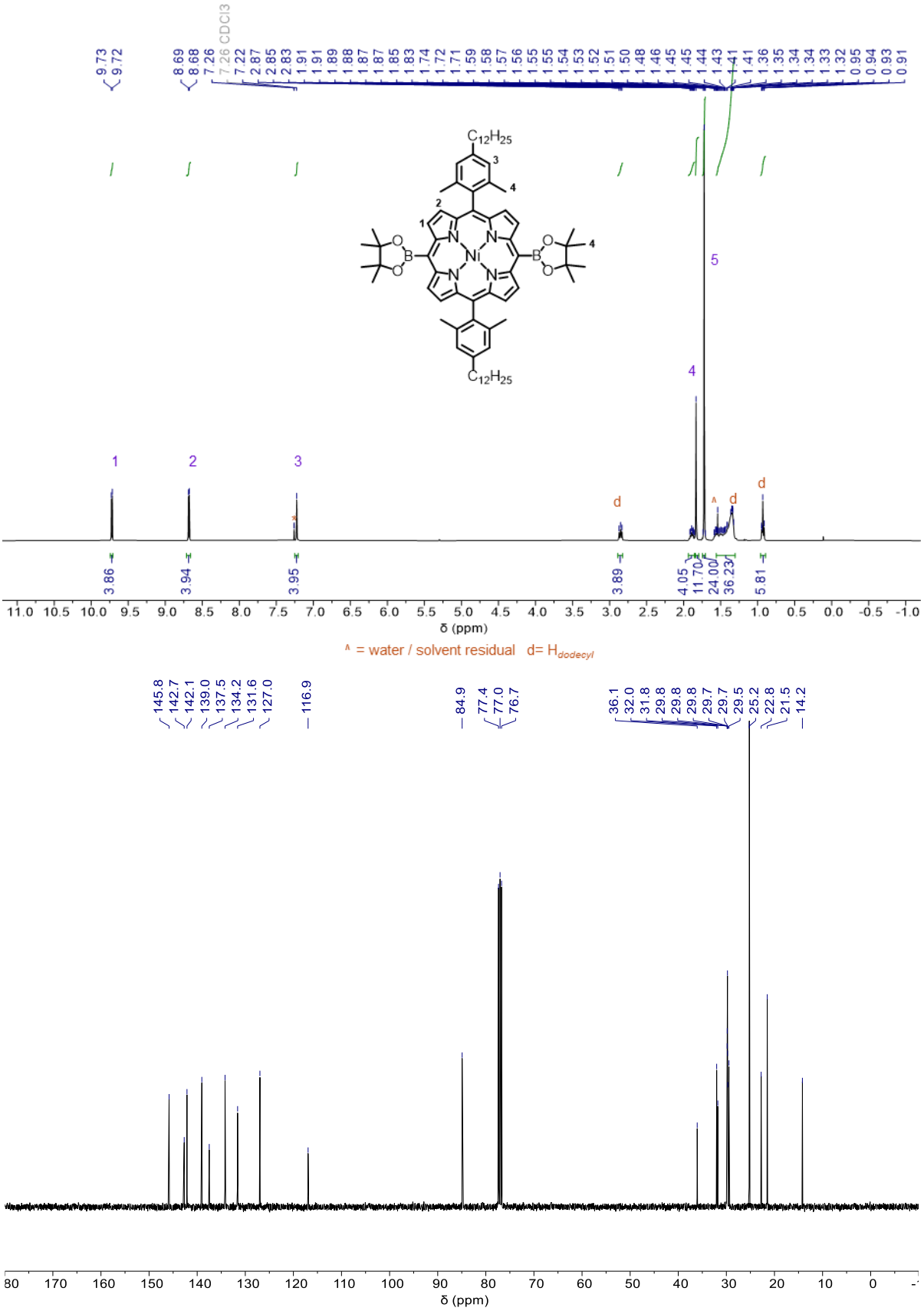


Figure S3.13: (top) ^{1}H NMR (400 MHz) and (bottom) ^{13}C NMR (101 MHz) spectra of porphyrin **3.7b** ($CDCl_3$, 298 K).

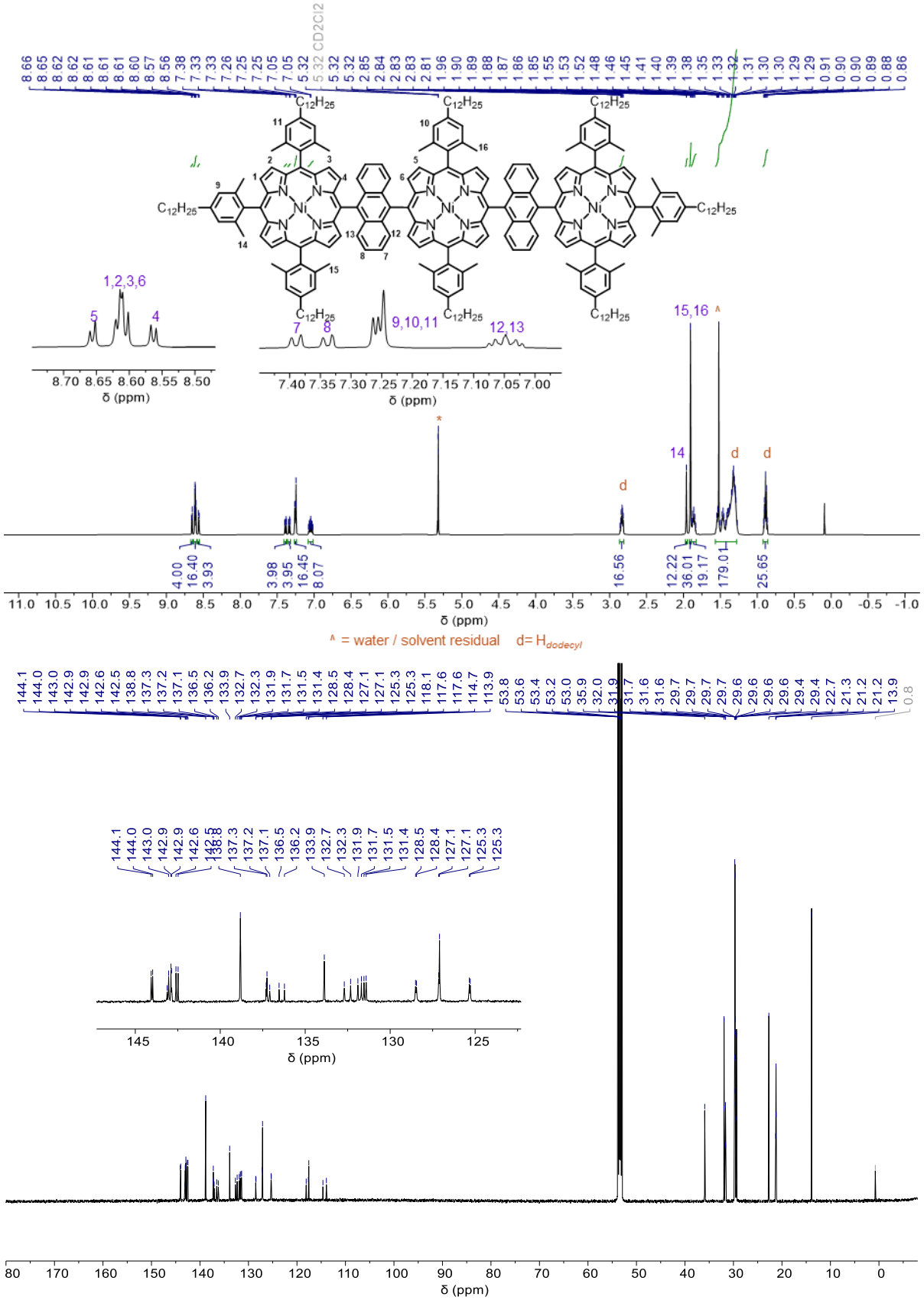


Figure S3.14: (top) ^{1}H NMR (600 MHz) and (bottom) ^{13}C NMR (151 MHz) spectra of porphyrin trimer **3.9b** (CD_2Cl_2, 298 K).

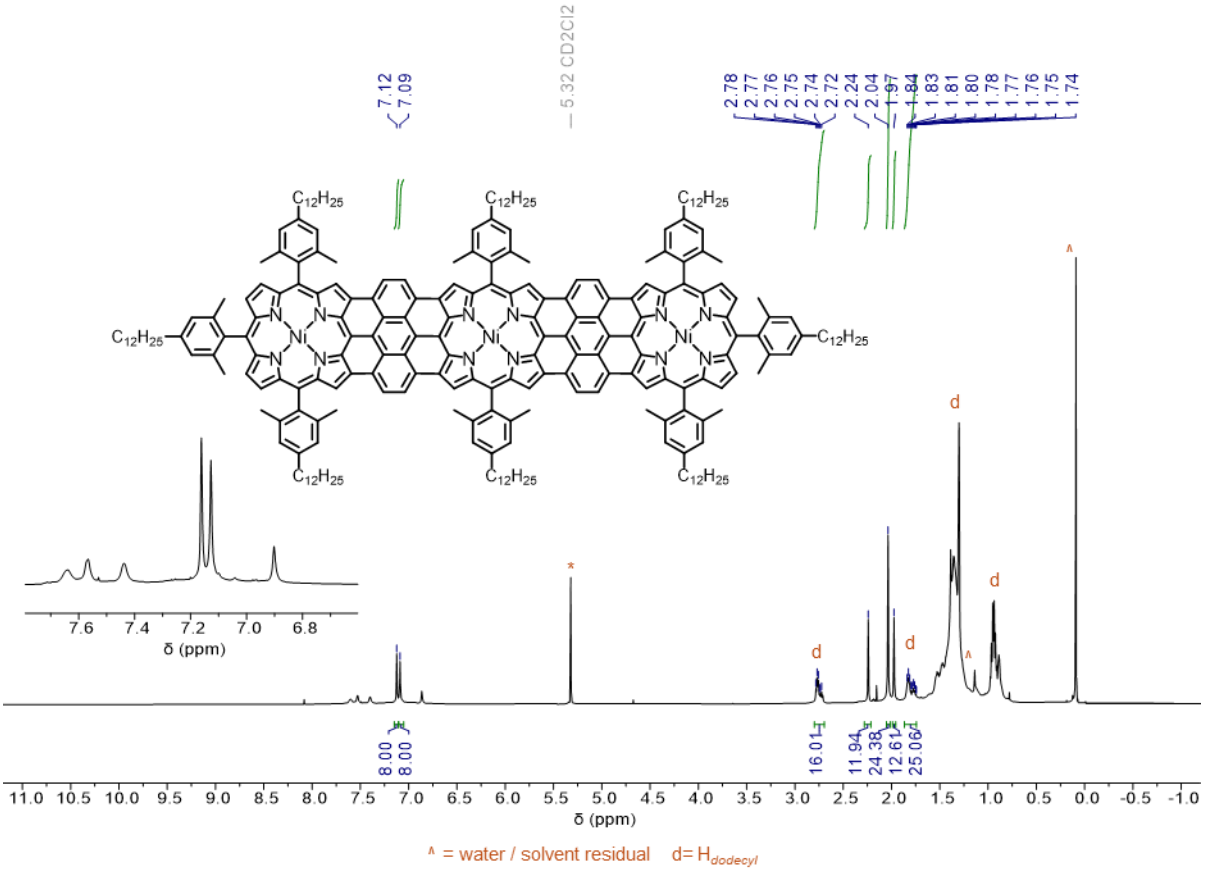


Figure S3.15: ^{1}H NMR (600 MHz) spectrum of fused porphyrin trimer **AP3b** (CD_2Cl_2/CS_2 (2:1, v/v), 298 K).

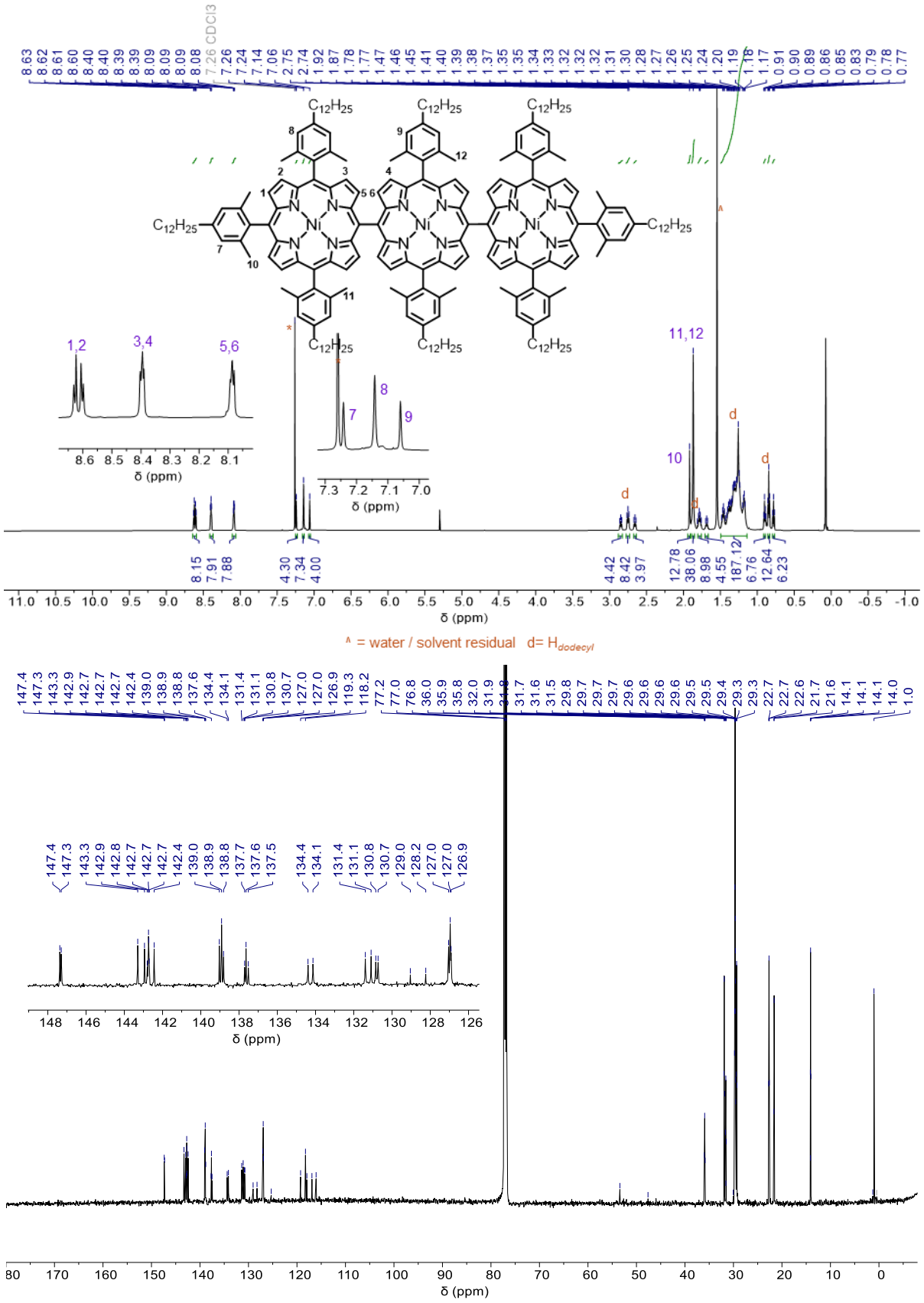


Figure S3.16: (top) ^{1}H NMR (400 MHz) and (bottom) ^{13}C NMR (151 MHz) spectra of porphyrin trimer ***s*-P3b** ($CDCl_3$, 298 K).

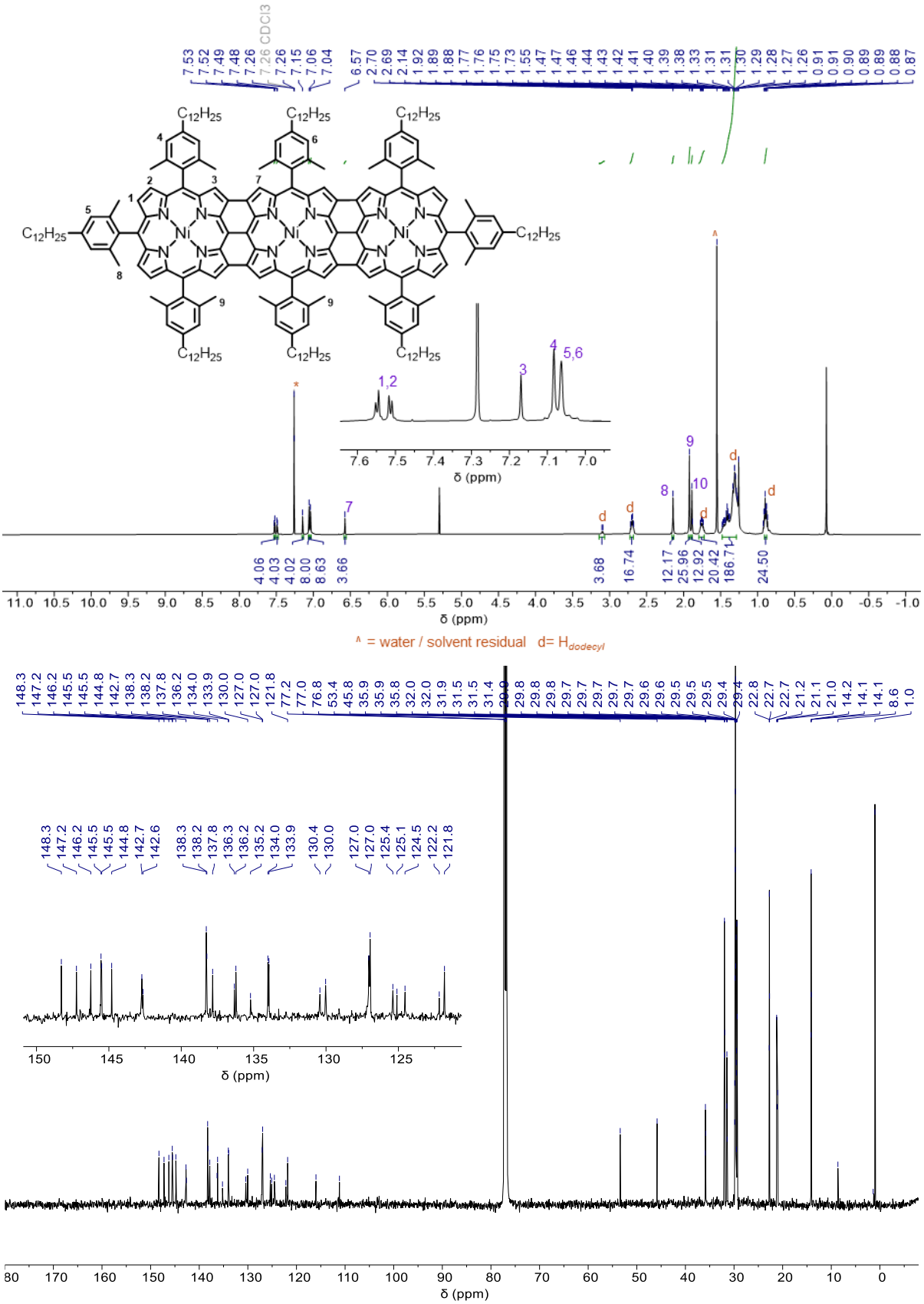


Figure S3.17: (top) ^{1}H NMR (400 MHz) and (bottom) ^{13}C NMR (151 MHz) spectra of fused porphyrin trimer **P3b** ($CDCl_3$, 298 K).

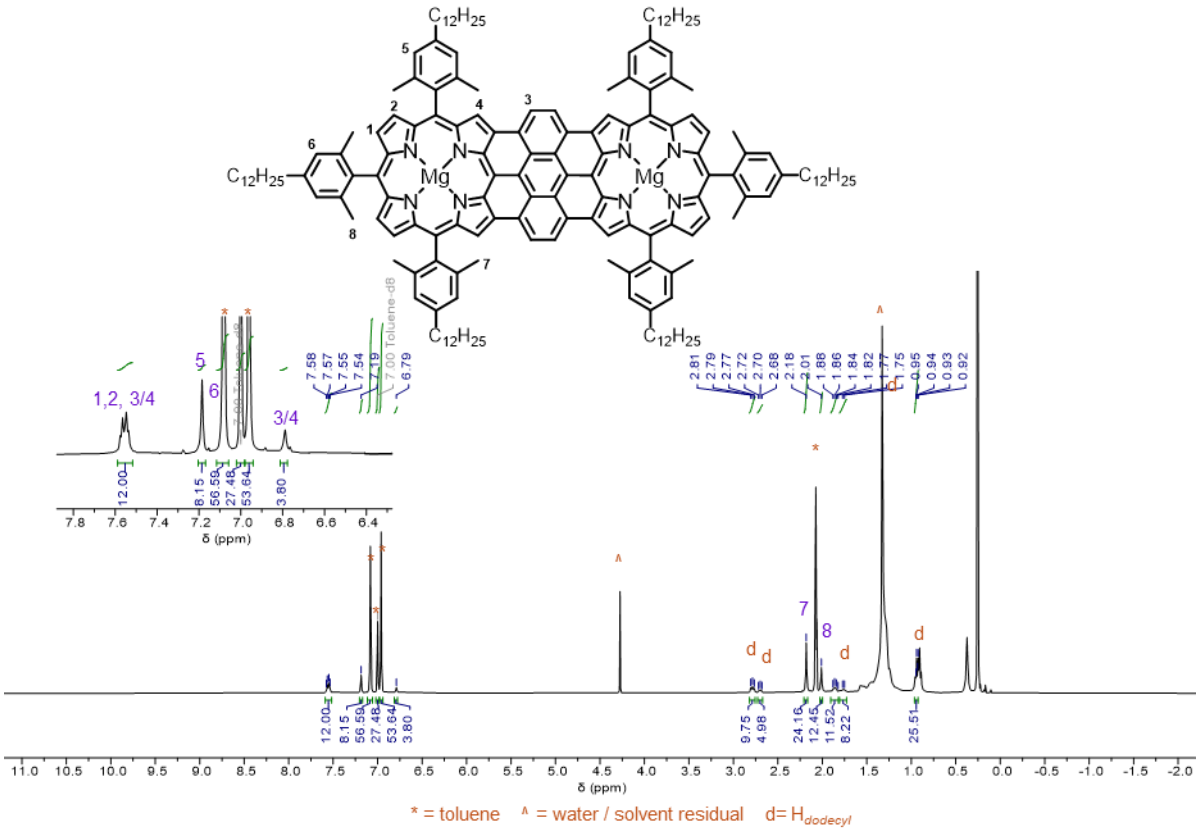


Figure S3.18: ^{1}H NMR (400 MHz) spectrum of fused porphyrin dimer **Mg-AP2b** (toluene-d_8, 298 K).

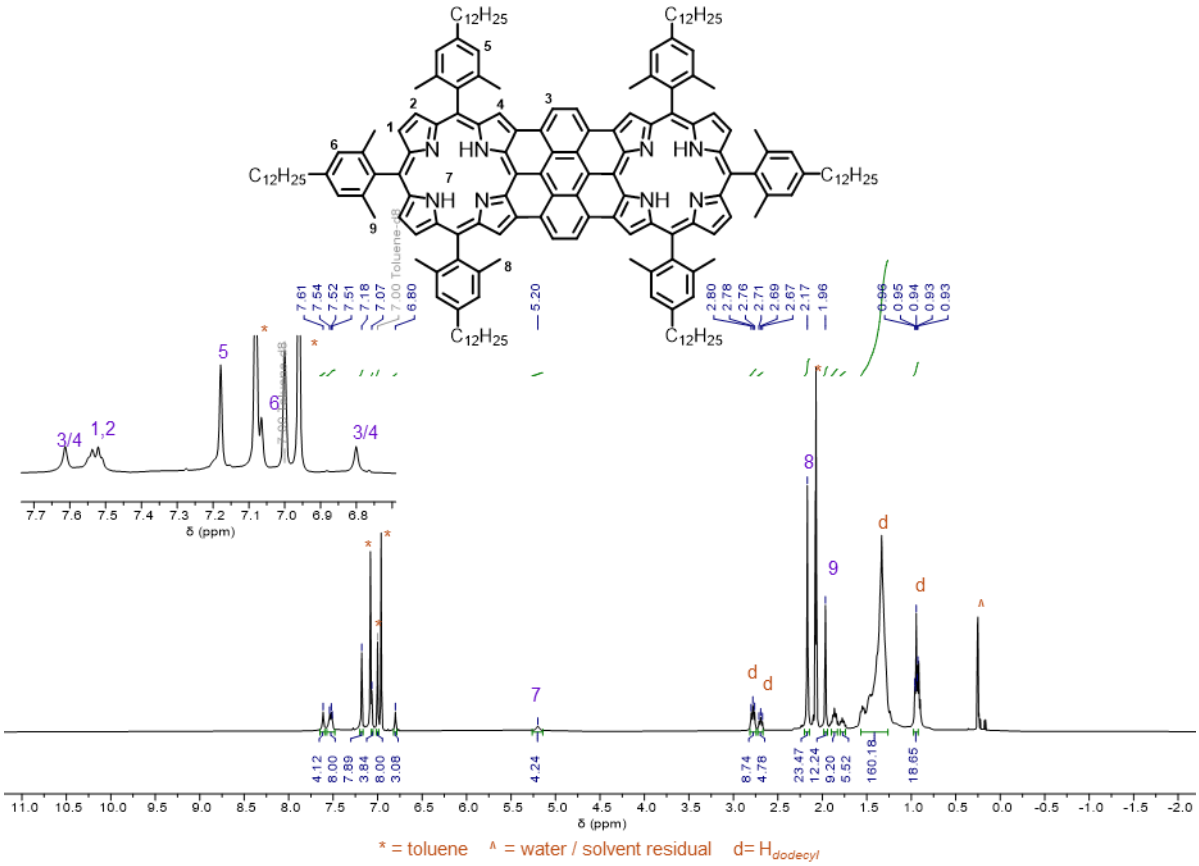


Figure S3.19: ^{1}H NMR (400 MHz) spectrum of fused porphyrin dimer **FB-AP2b** (toluene-d_8, 298 K).

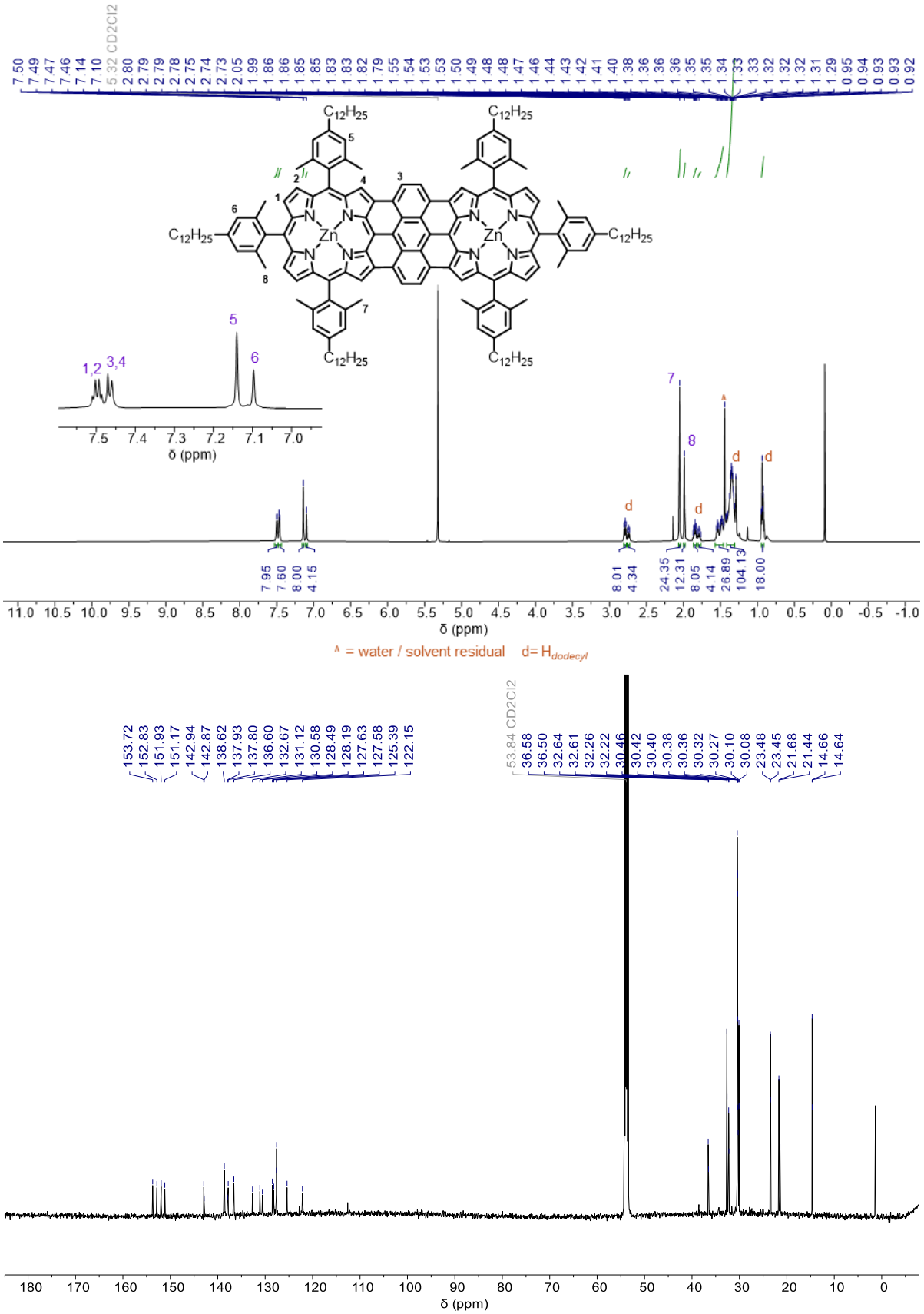


Figure S3.20: (top) ^{1}H NMR (600 MHz) and (bottom) ^{13}C NMR (151 MHz) spectra fused porphyrin dimer **Zn-AP2b** (CD_2Cl_2/CS_2 (2:1, v/v), 298 K).

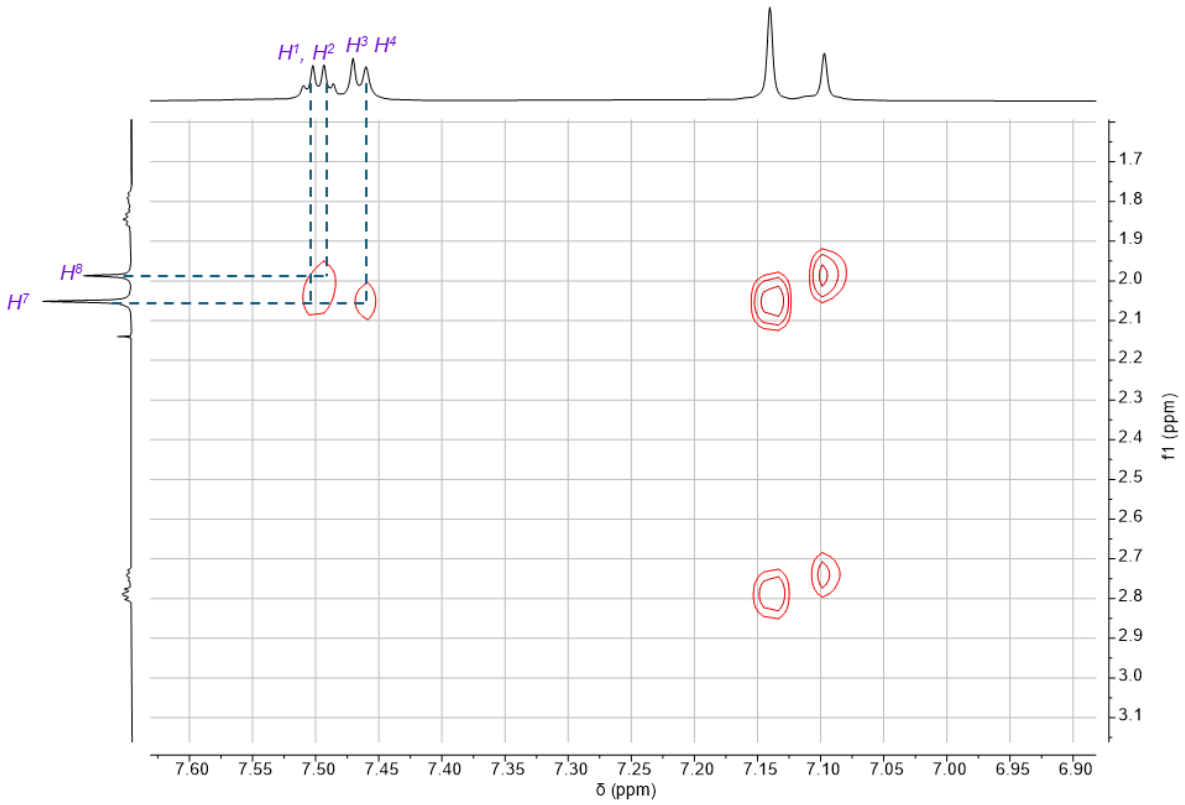


Figure S3.21: Aromatic regions of ^{1}H-^{1}H NOESY spectrum (CD_2Cl_2/CS_2 (2:1, v/v), 298 K at 600 MHz) of **Zn-AP2b**.

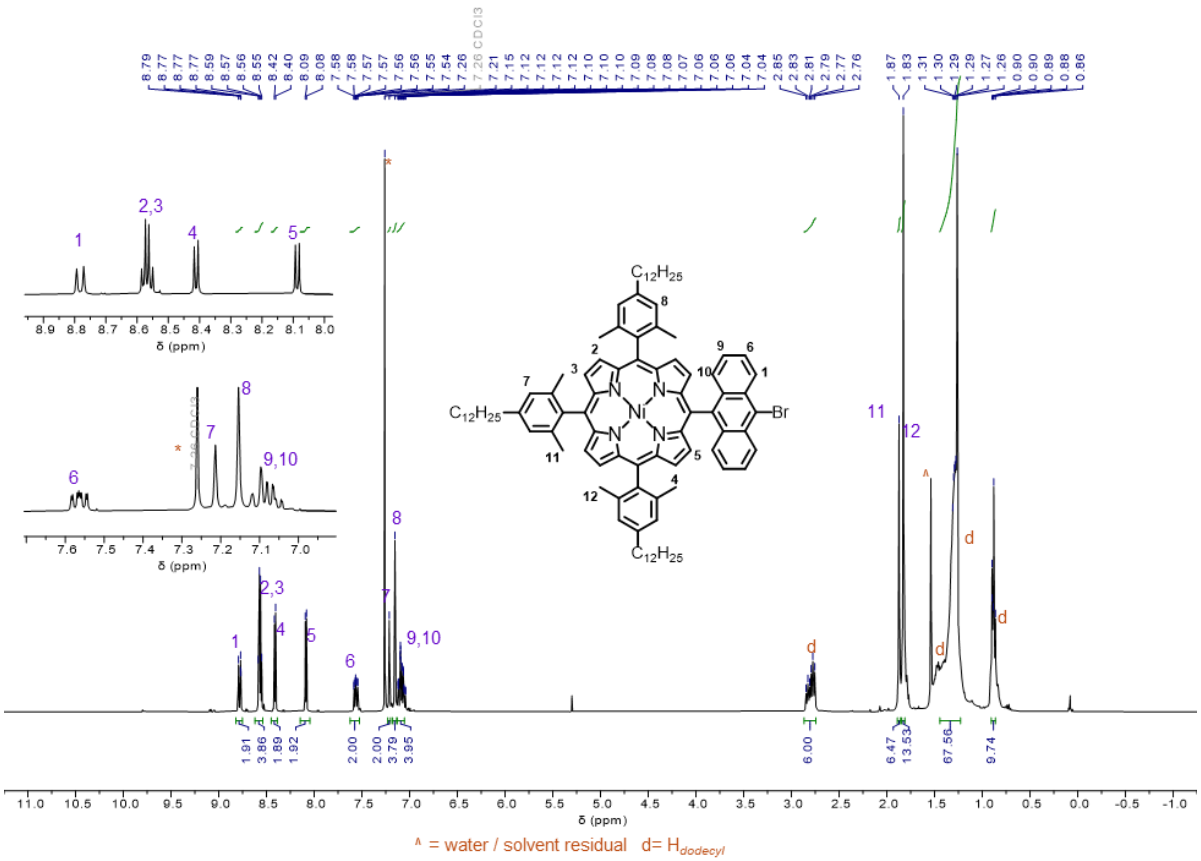


Figure S3.22: ^{1}H NMR (400 MHz) spectrum of porphyrin **3.10b** ($CDCl_3$, 298 K).

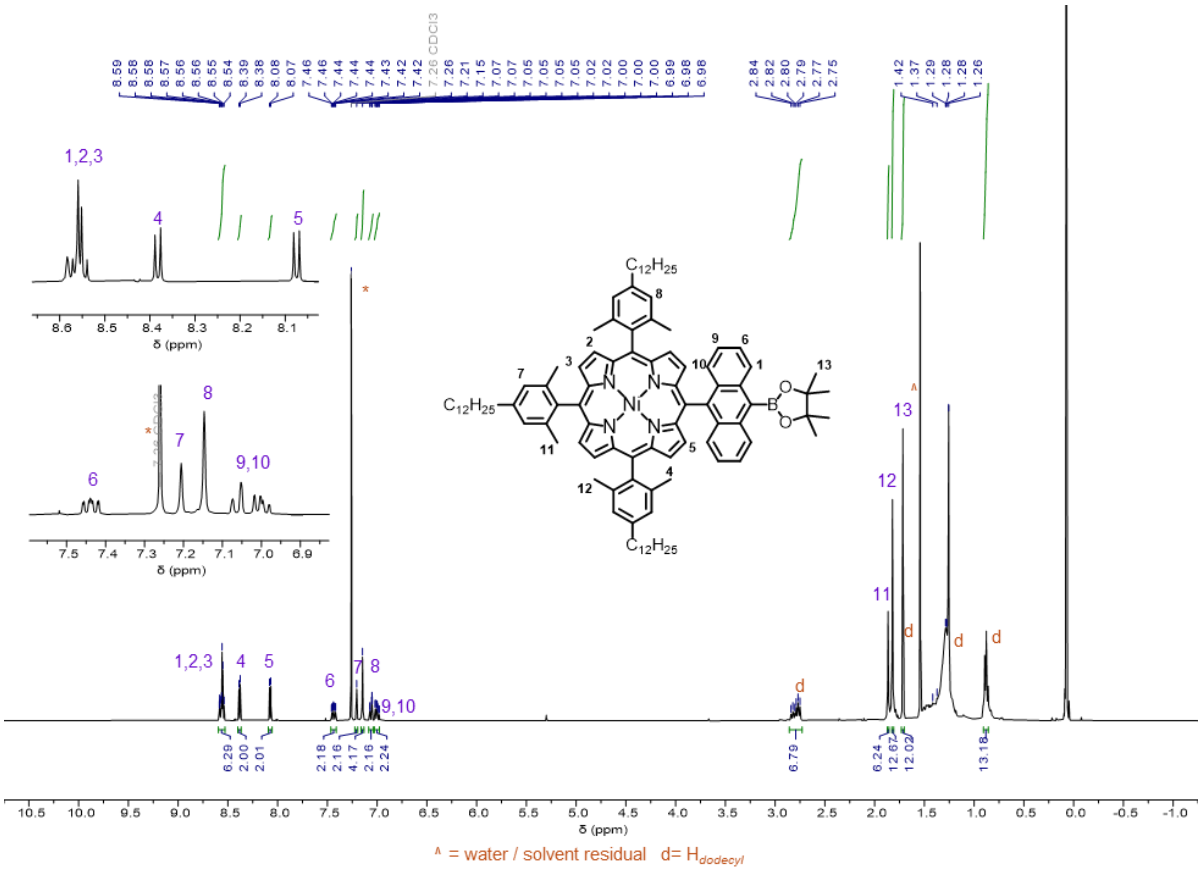


Figure S3.23: ^{1}H NMR (400 MHz) spectrum of porphyrin **3.11b** ($CDCl_3$, 298 K).

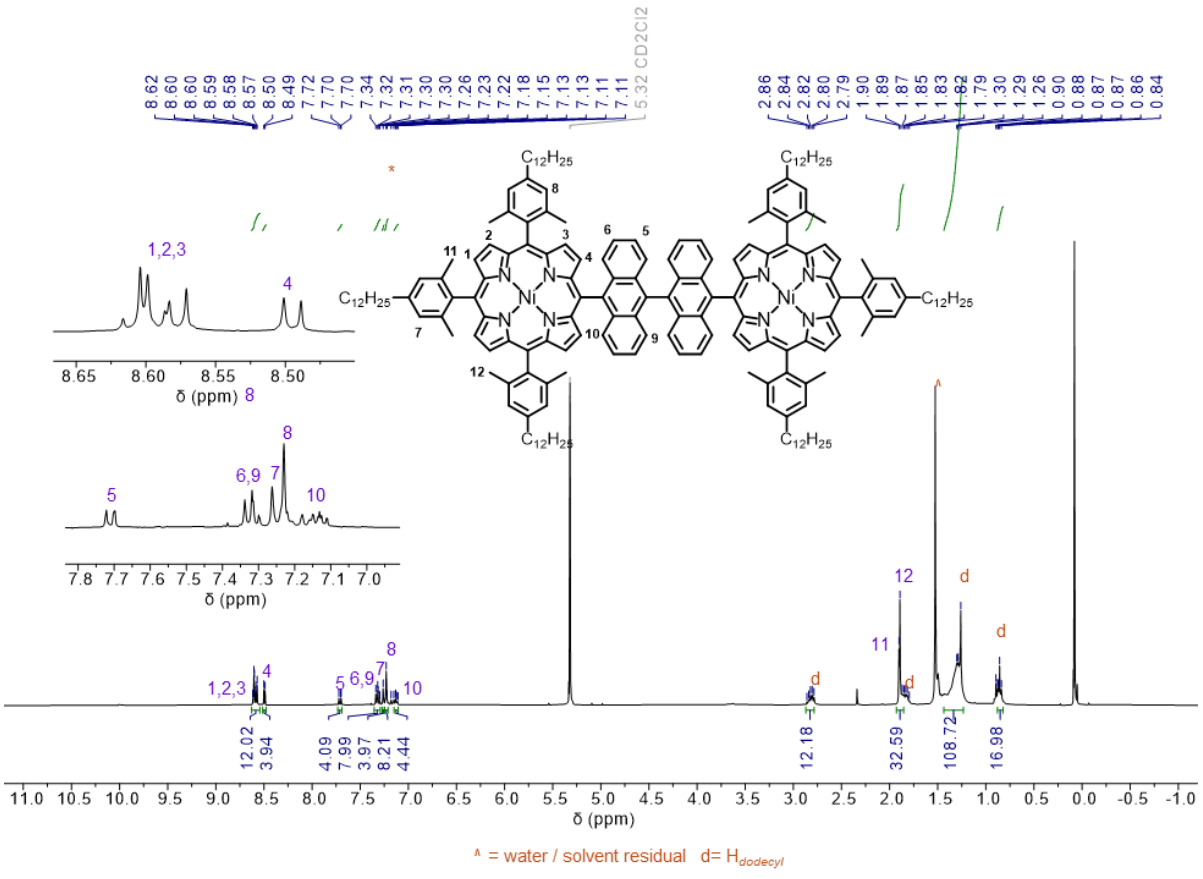


Figure S3.24: ^{1}H NMR (400 MHz) spectrum of porphyrin **3.12b** (CD_2Cl_2, 298 K).

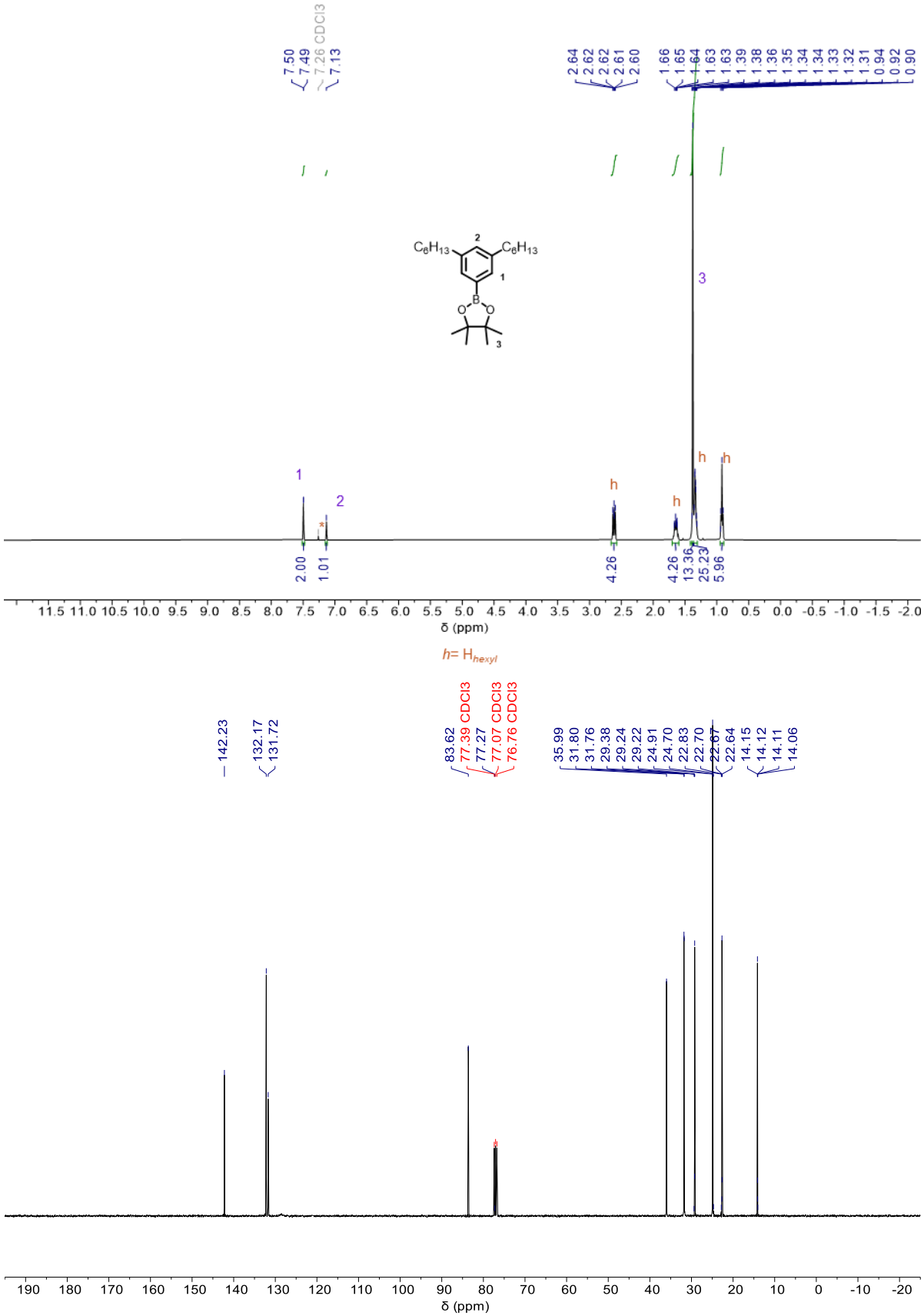


Figure S3.25: (top) ^{1}H NMR (400 MHz) and (bottom) ^{13}C NMR (101 MHz) spectra of 1-Bpin-3,5-dihexyl benzene **3.14d** ($CDCl_3$, 298 K).

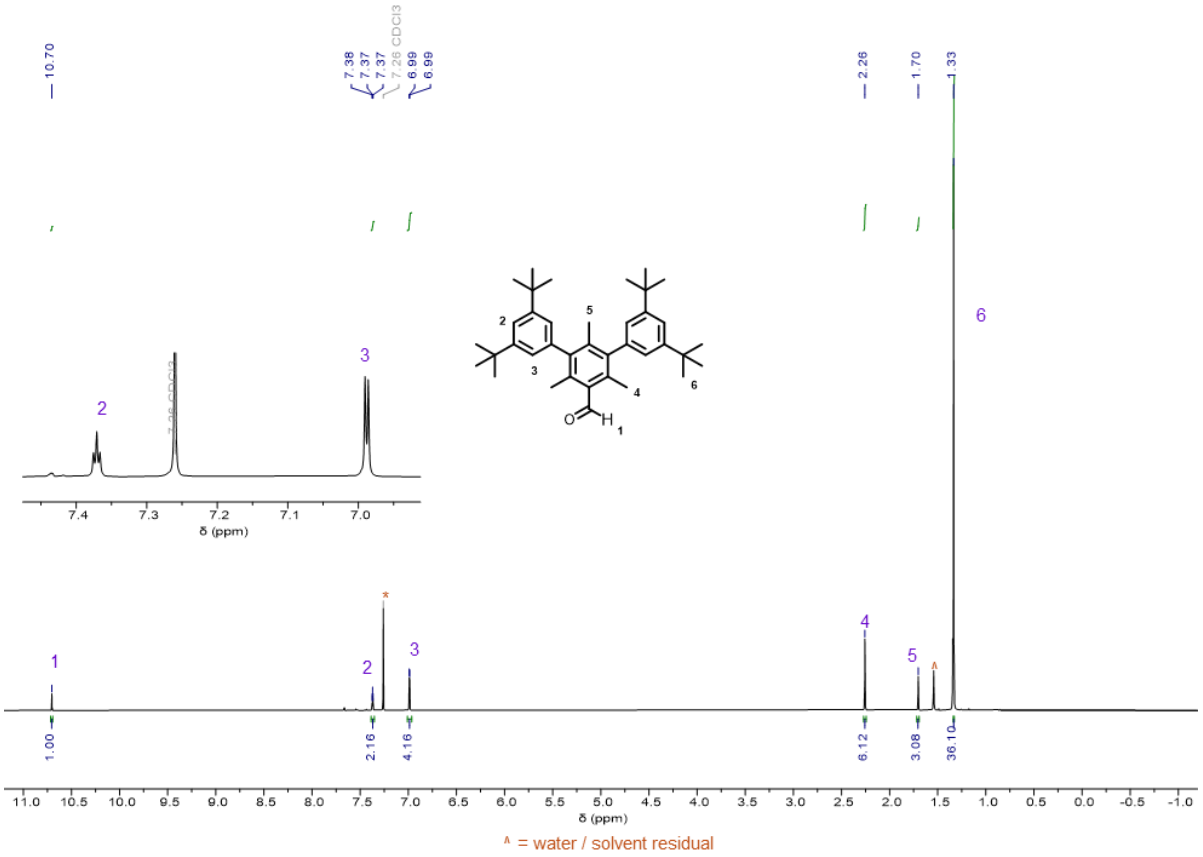


Figure S3.26: ^{1}H NMR (400 MHz) spectrum of tetra-*tert*-butyl aldehyde **3.15c** ($CDCl_3$, 298 K).

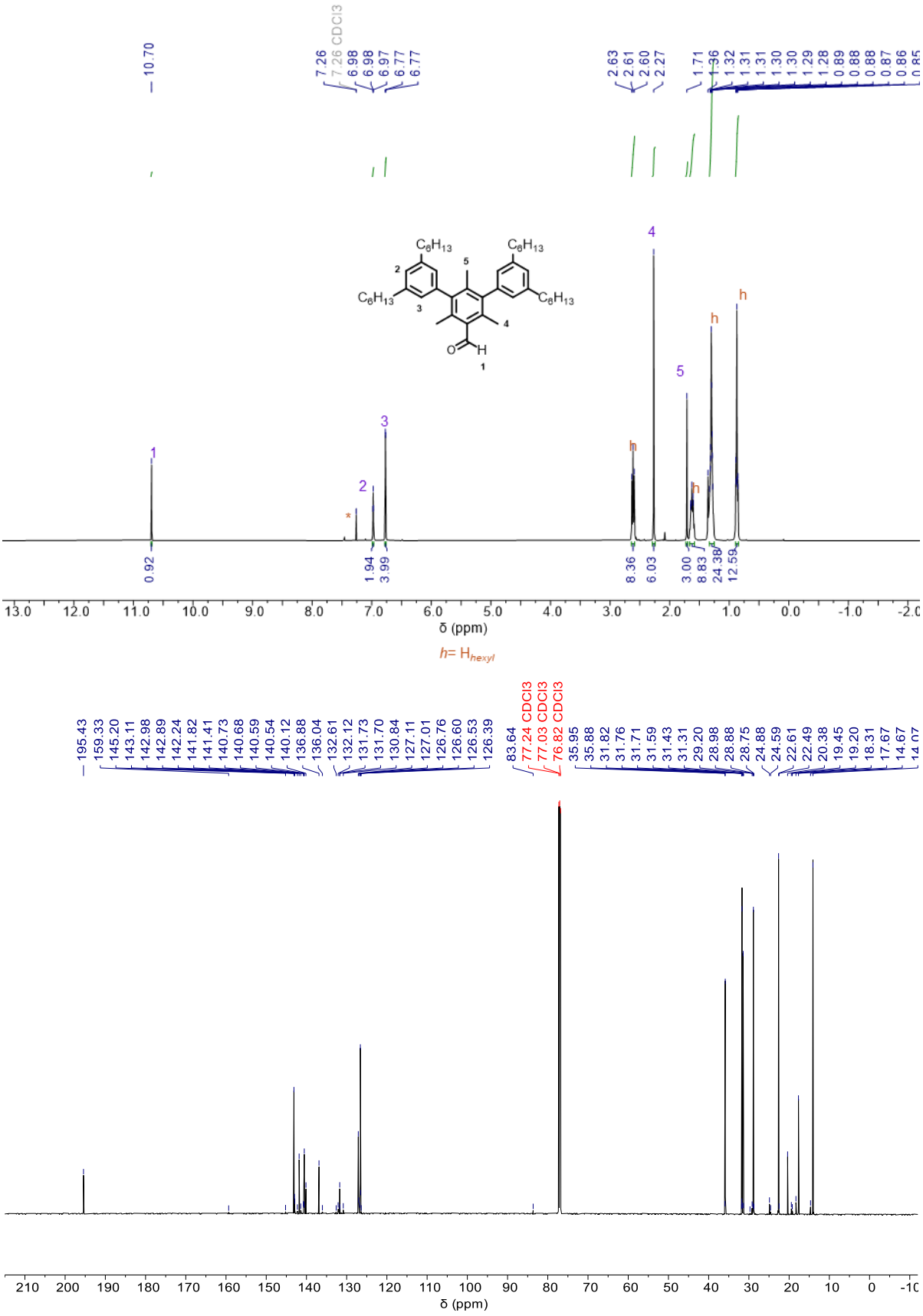


Figure S3.27: (top) ^{1}H NMR (400 MHz) and (bottom) ^{13}C NMR (101 MHz) spectra of tetra-hexyl aldehyde **3.15d** ($CDCl_3$, 298 K).

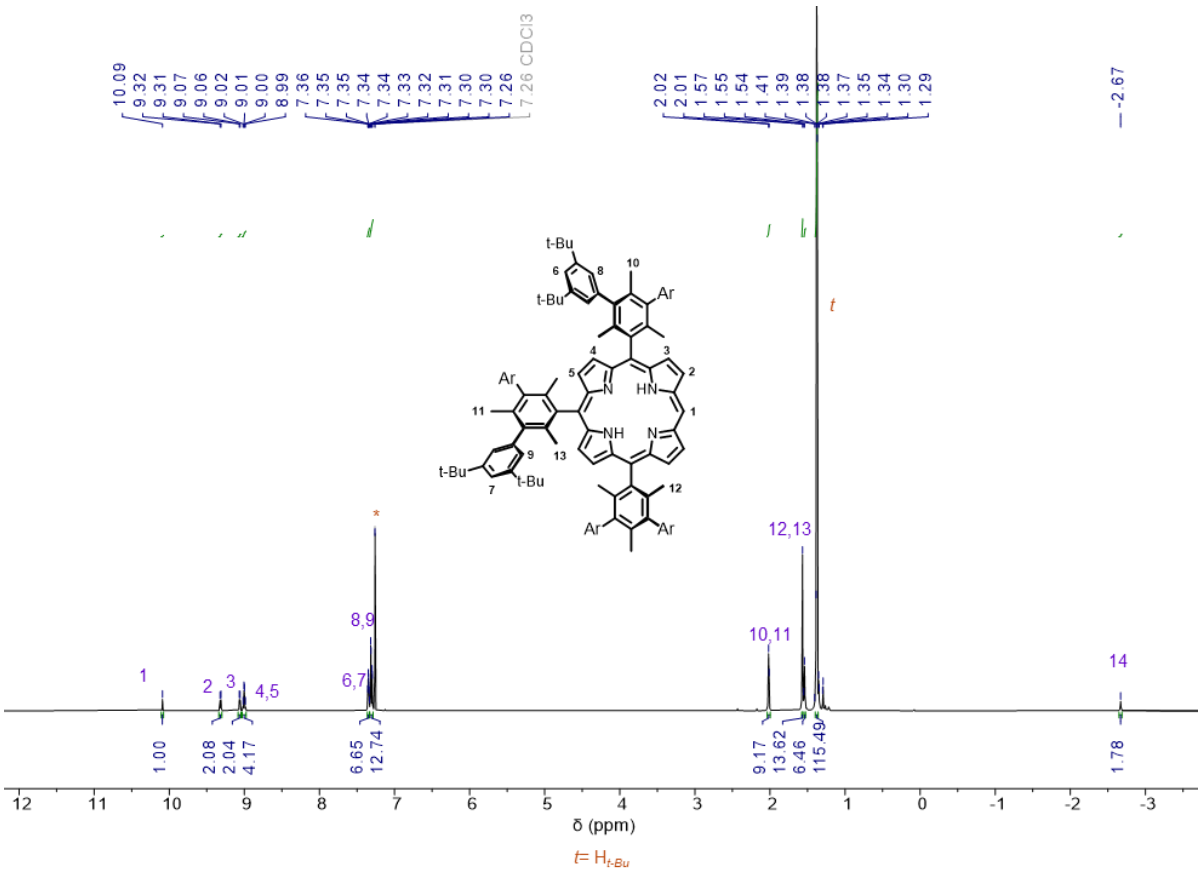


Figure S3.28: ^{1}H NMR (400 MHz) spectrum of 5,10,15-tri(tetra-*tert*-butylphenyl)-porphyrin **3.21c** ($CDCl_3$, 298 K).

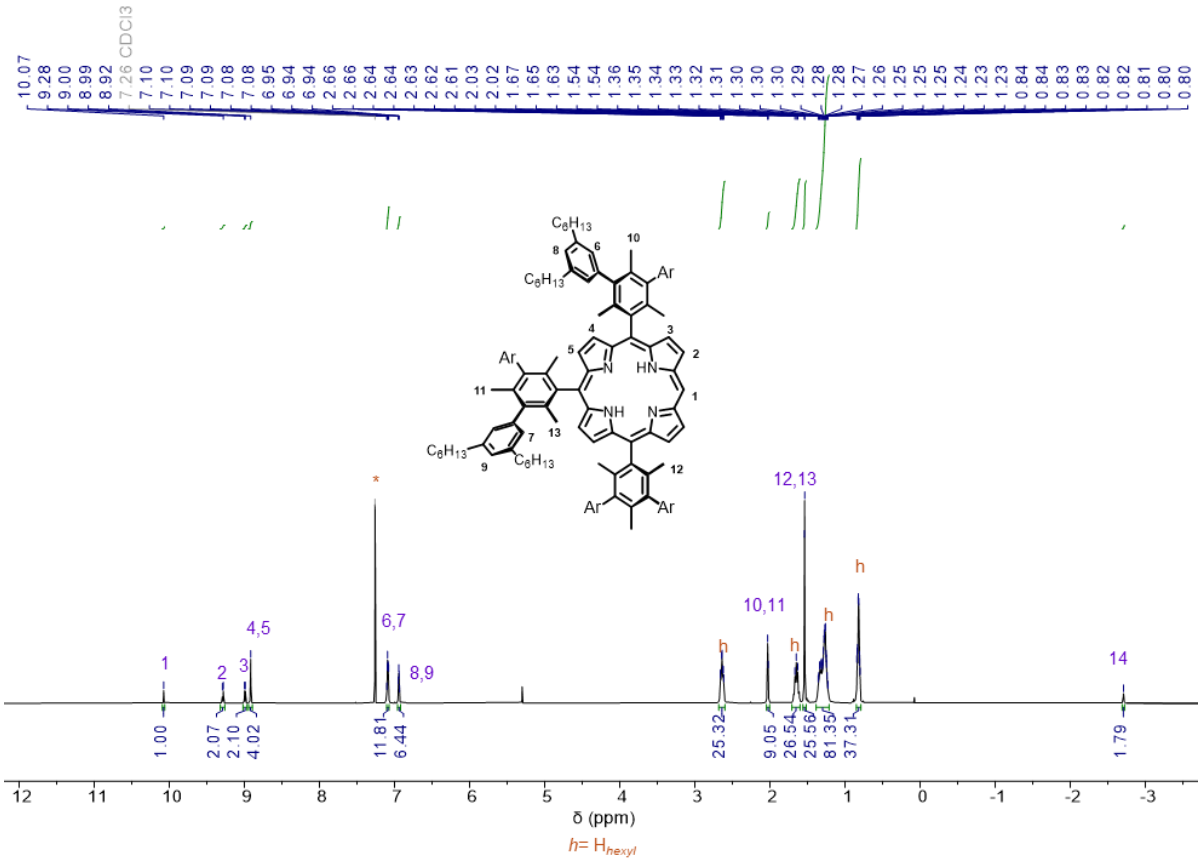


Figure S3.29: ^{1}H NMR (400 MHz) spectrum of 5,10,15-tri(tetra-hexylphenyl)-porphyrin **3.21d** ($CDCl_3$, 298 K).

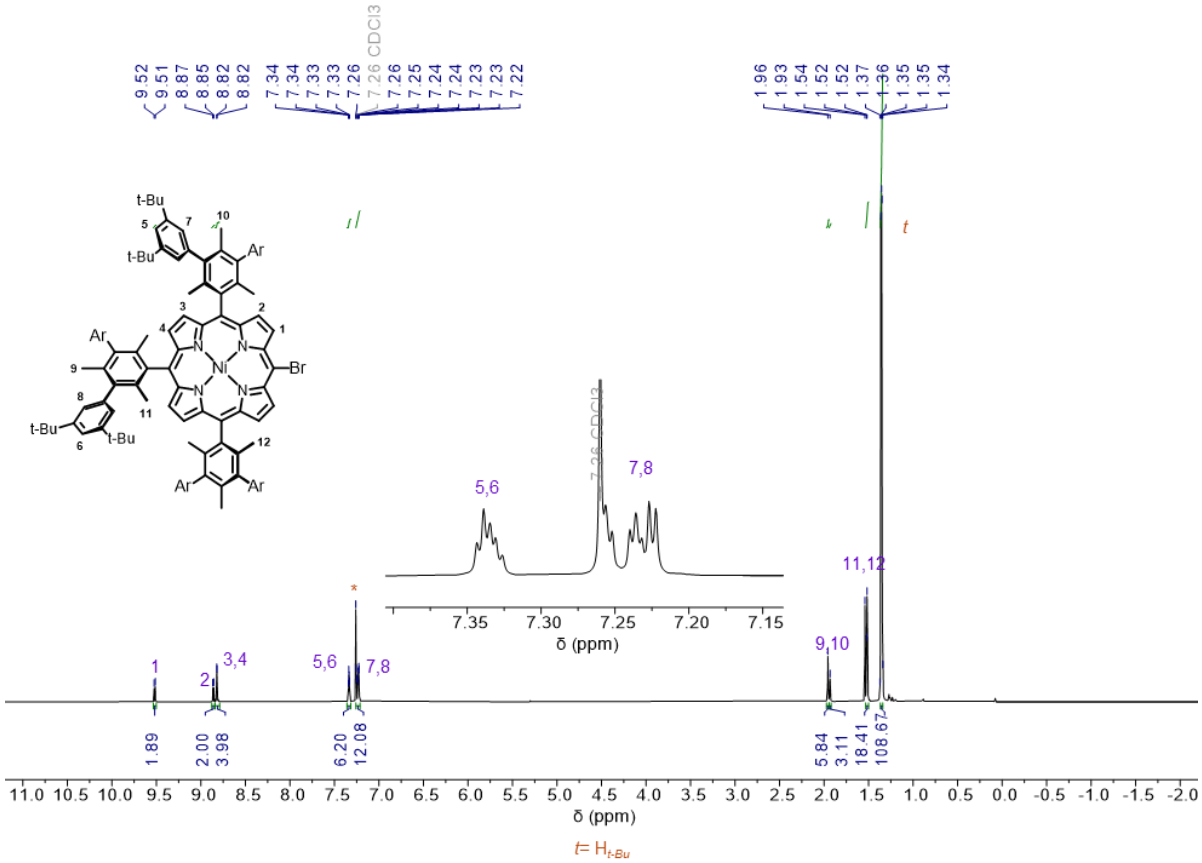


Figure S3.30: ^{1}H NMR (400 MHz) spectrum of Ni(II) 5-bromo-10,15,20-tri(tetra-*tert*-butyl)porphyrin **3.22c** ($CDCl_3$, 298 K).

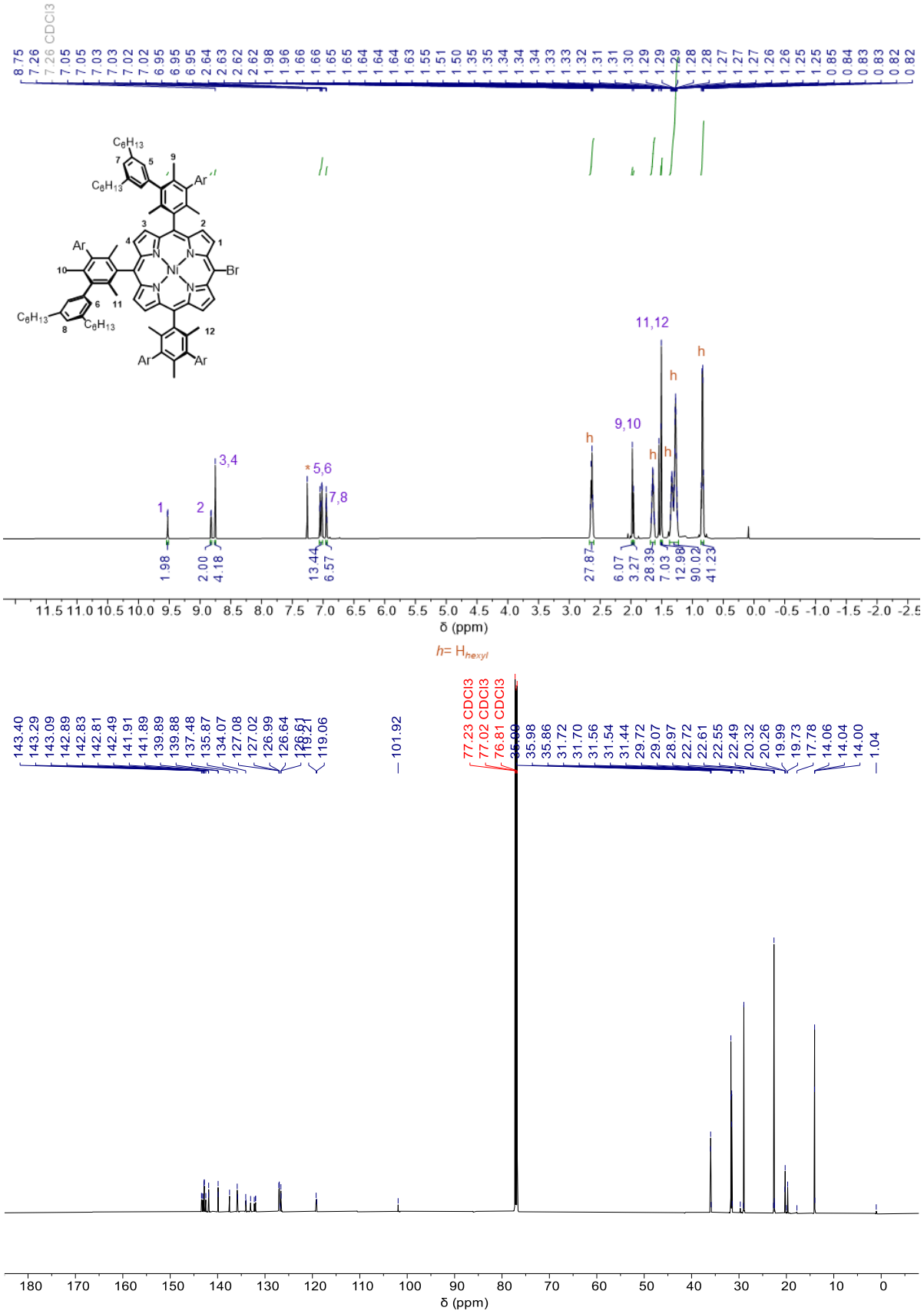


Figure S3.31: (top) ^{1}H NMR (400 MHz) and (bottom) ^{13}C NMR (101 MHz) spectra of Ni(II) 5-bromo-10,15,20-tri(tetra-hexyl)porphyrin **3.22d** ($CDCl_3$, 298 K).

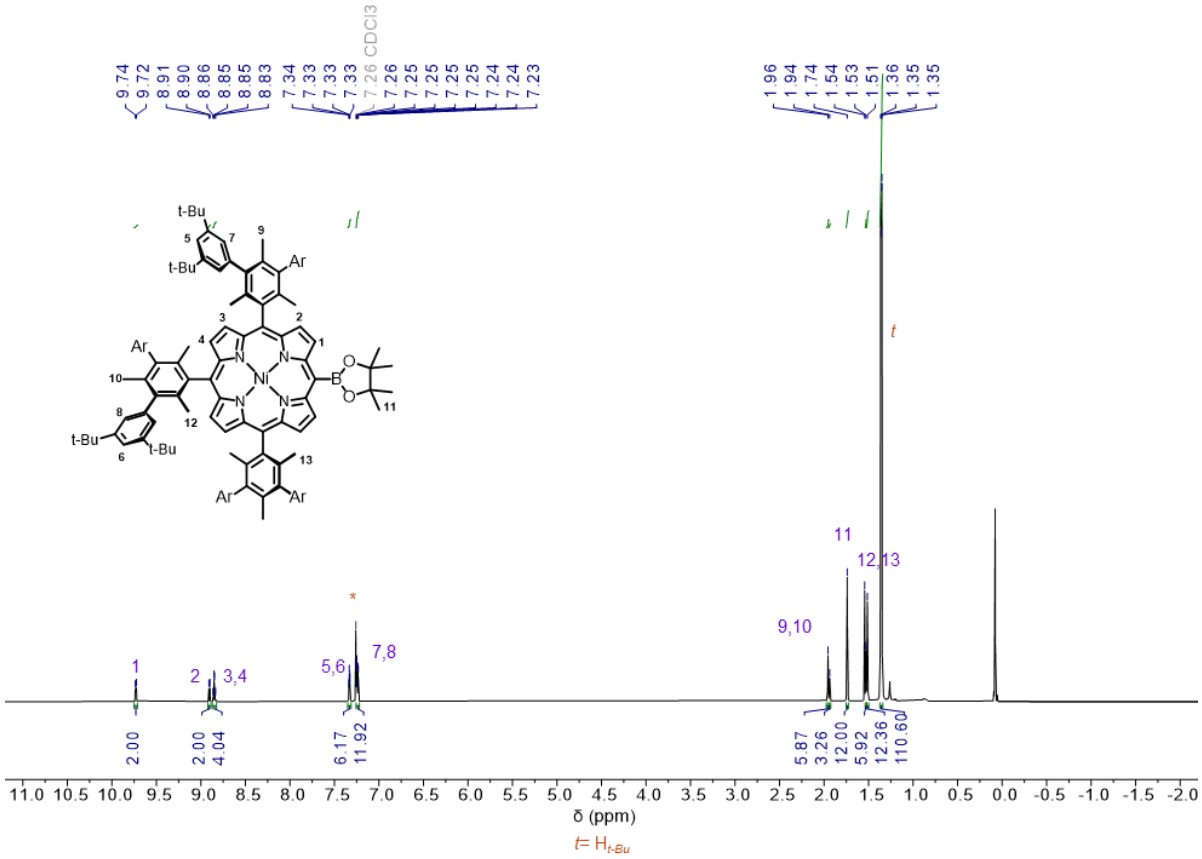


Figure S3.32: ^{1}H NMR (400 MHz) spectrum of Ni(II) 5-Bpin-10,15,20-tri(tetra-*tert*-butyl)porphyrin **3.23c** ($CDCl_3$, 298 K).

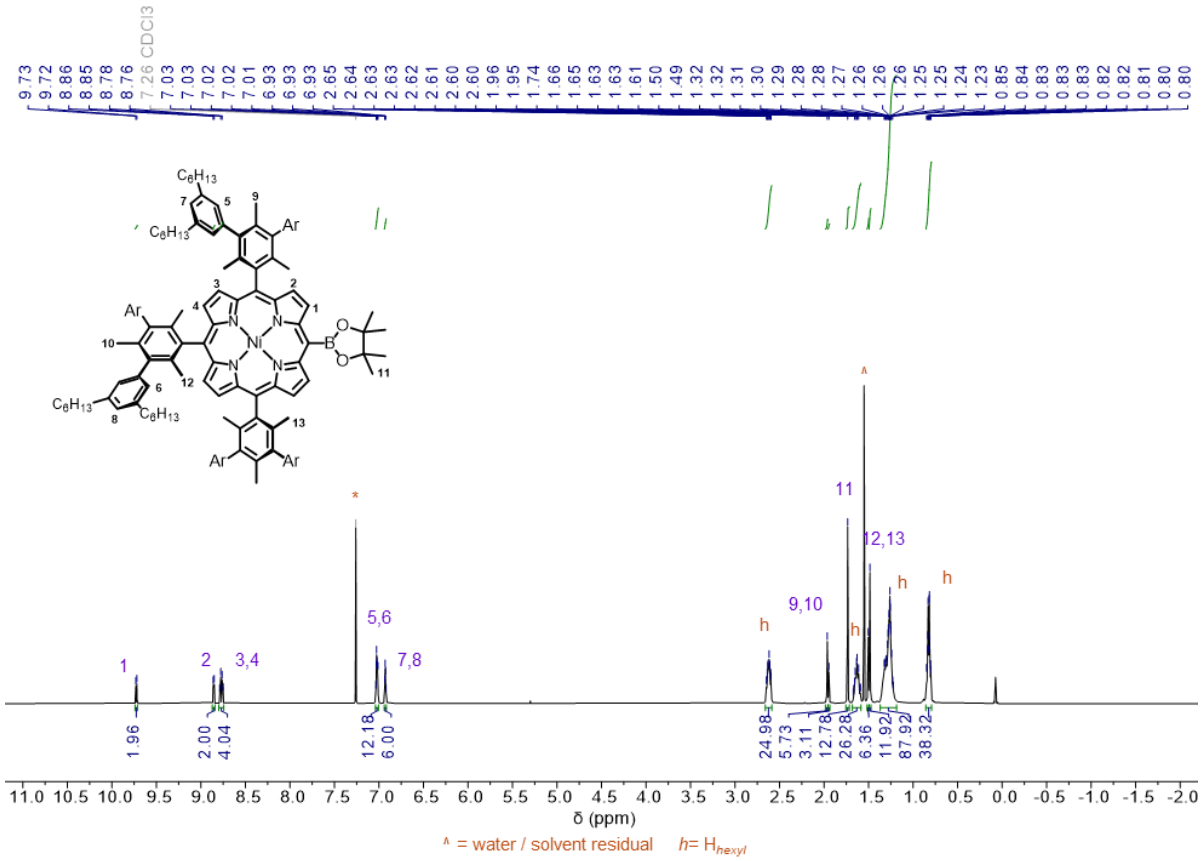


Figure S3.33: ^{1}H NMR (400 MHz) spectrum of Ni(II) 5-Bpin-10,15,20-tri(tetra-hexyl)porphyrin **3.23d** ($CDCl_3$, 298 K).

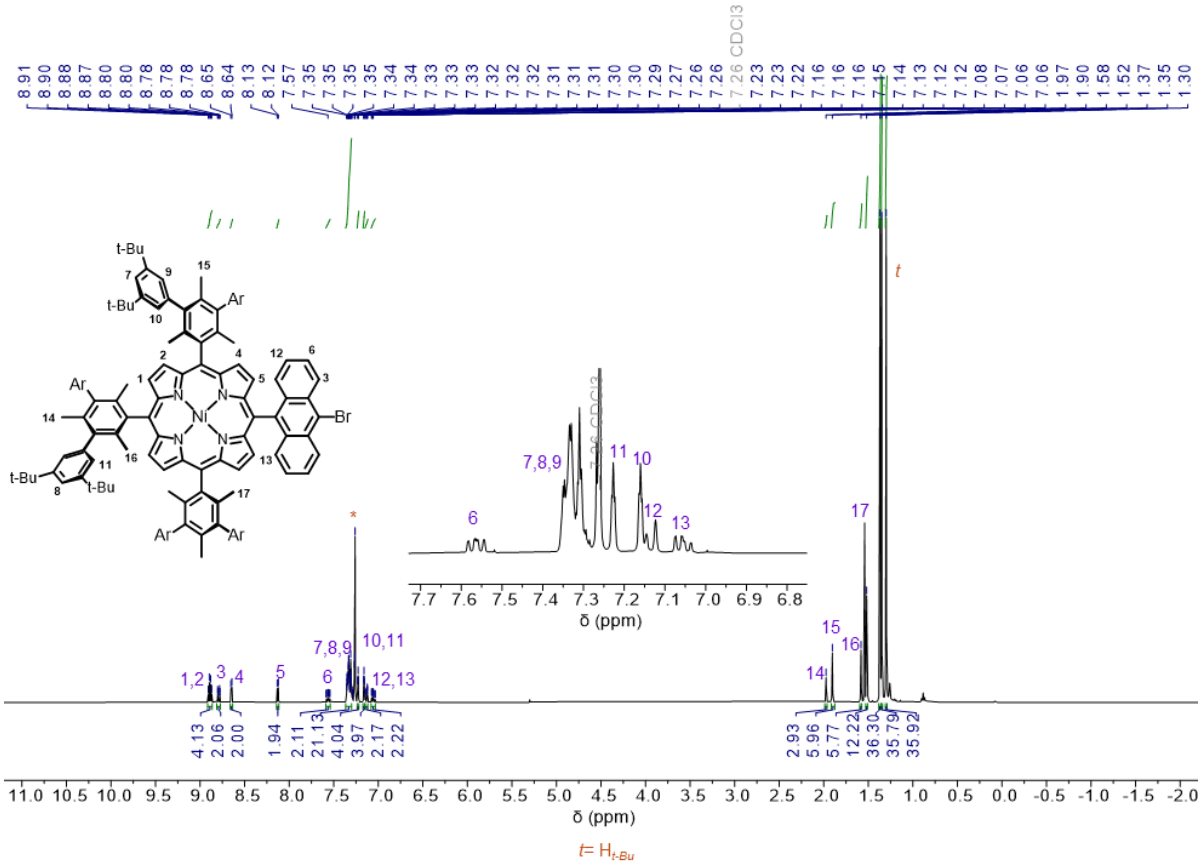


Figure S3.34: ^{1}H NMR (400 MHz) spectrum of bromo-functionalized monoanthracenyl-porphyrin **3.24c** ($CDCl_3$, 298 K).

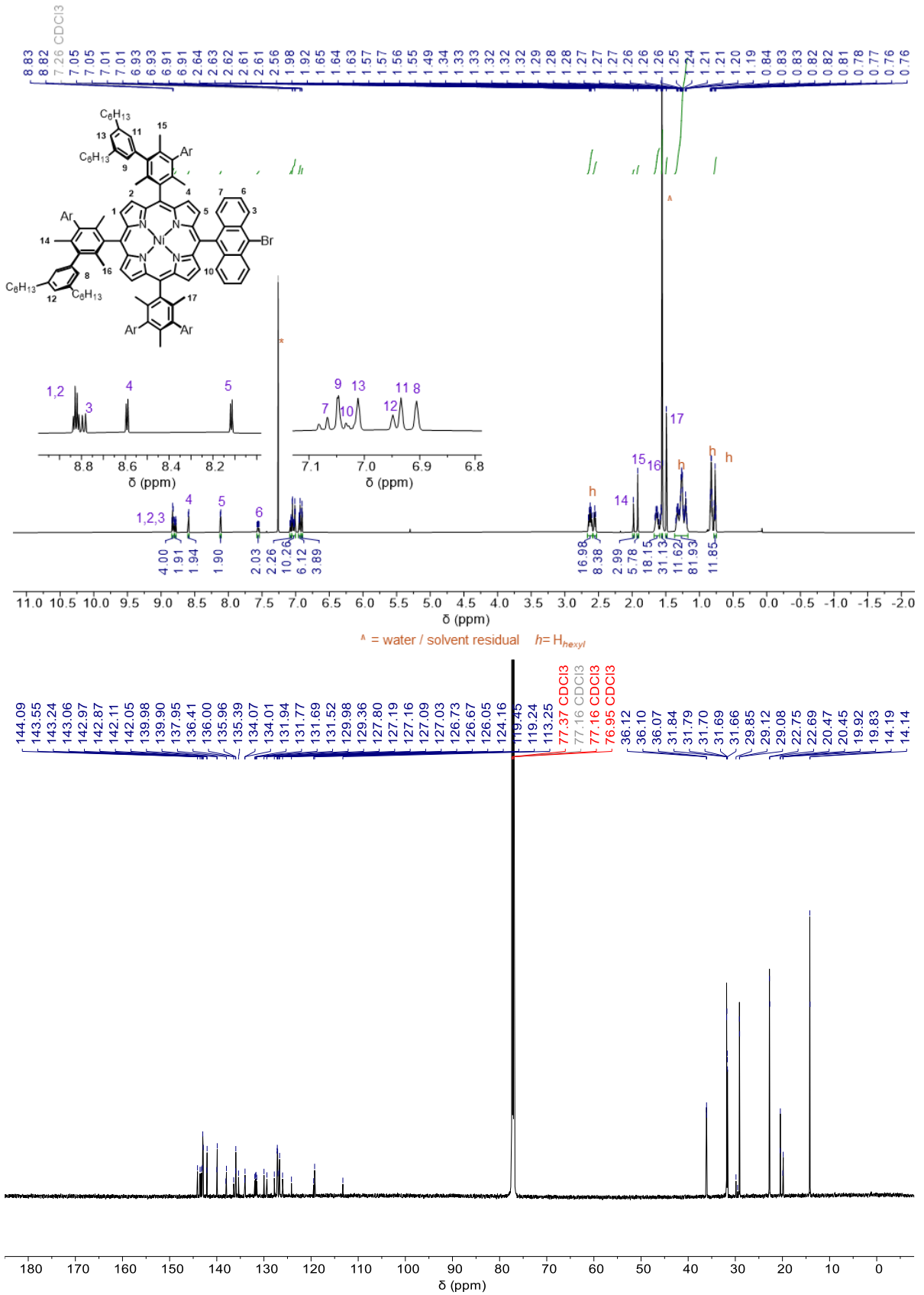


Figure S3.35: (top) ^{1}H NMR (400 MHz) and (bottom) ^{13}C NMR (101 MHz) spectra of bromo-functionalized monoanthracenyl-porphyrin **3.24d** ($CDCl_3$, 298 K).

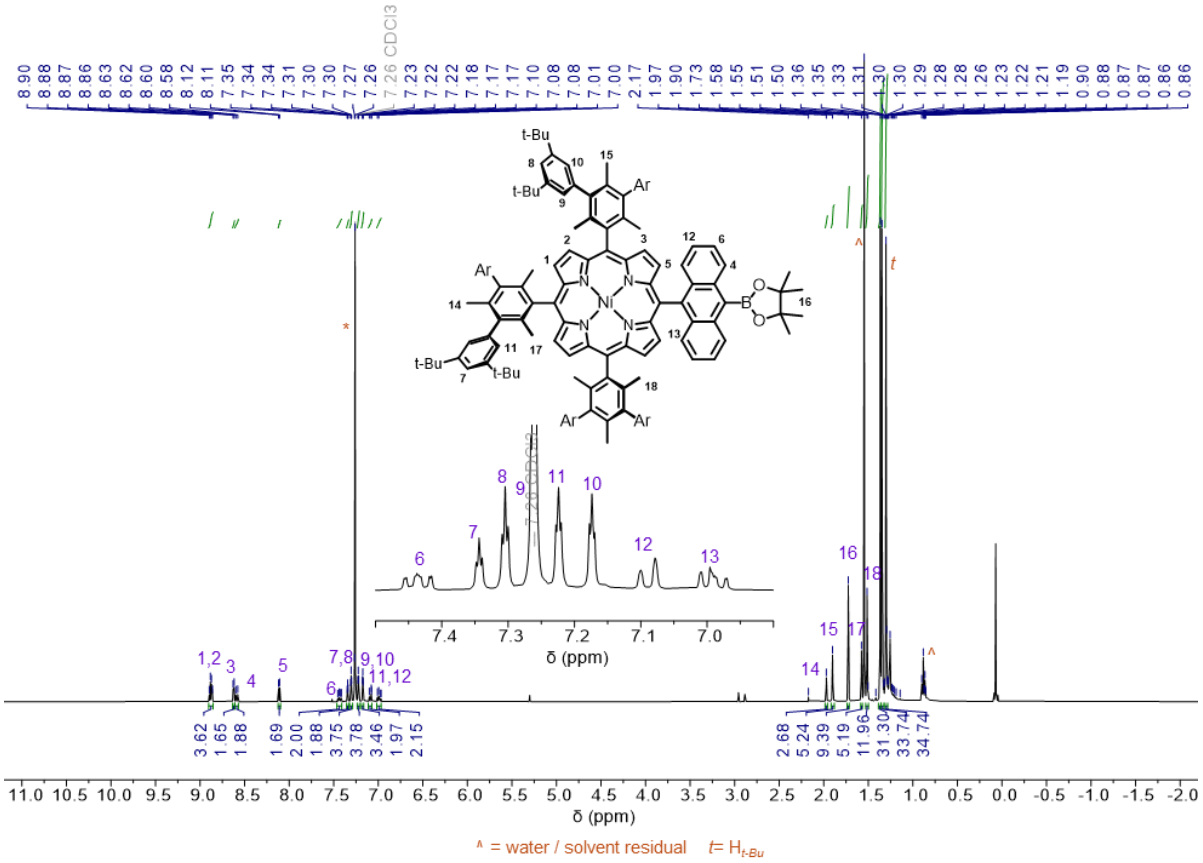


Figure S3.36: ^{1}H NMR (400 MHz) spectrum of boronate ester-functionalized monoanthracenyl-porphyrin **3.25c** ($CDCl_3$, 298 K).

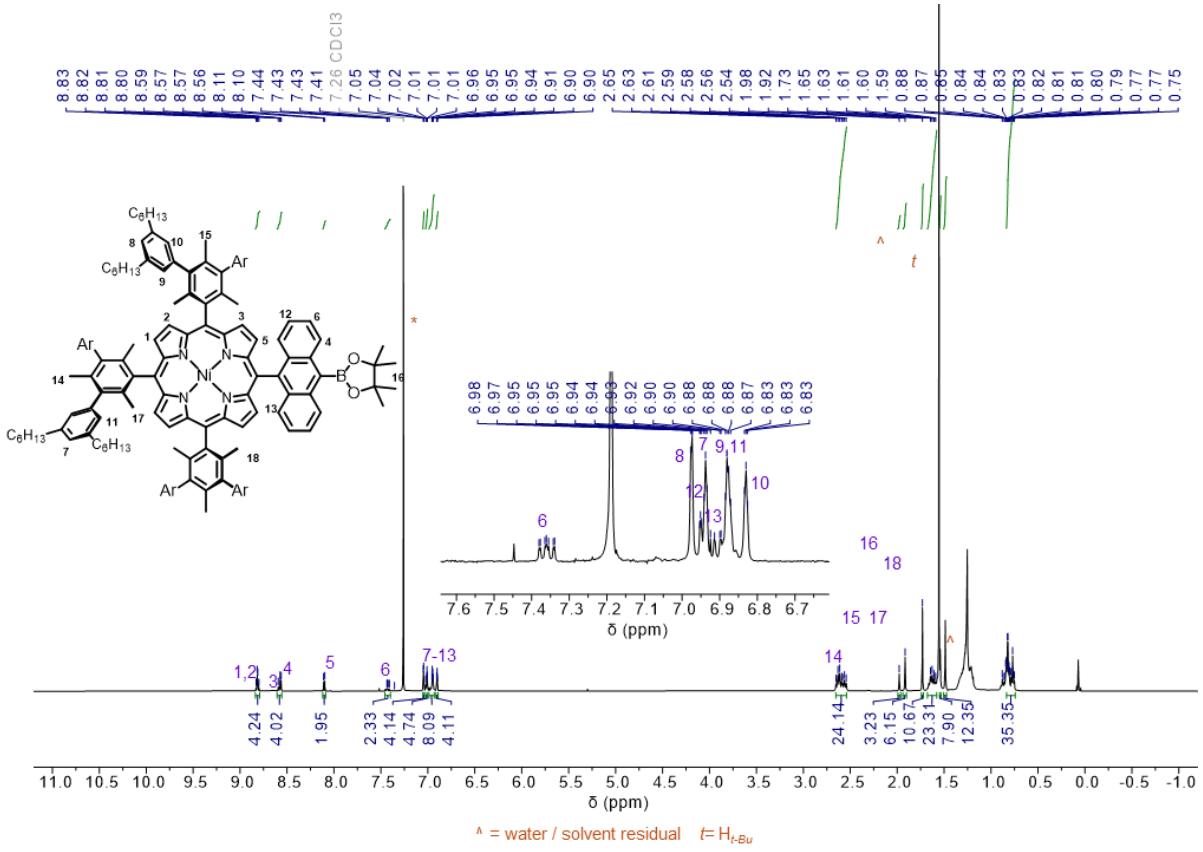


Figure S3.37: ^{1}H NMR (400 MHz) spectrum of boronate ester-functionalized monoanthracenyl-porphyrin **3.25d** ($CDCl_3$, 298 K).

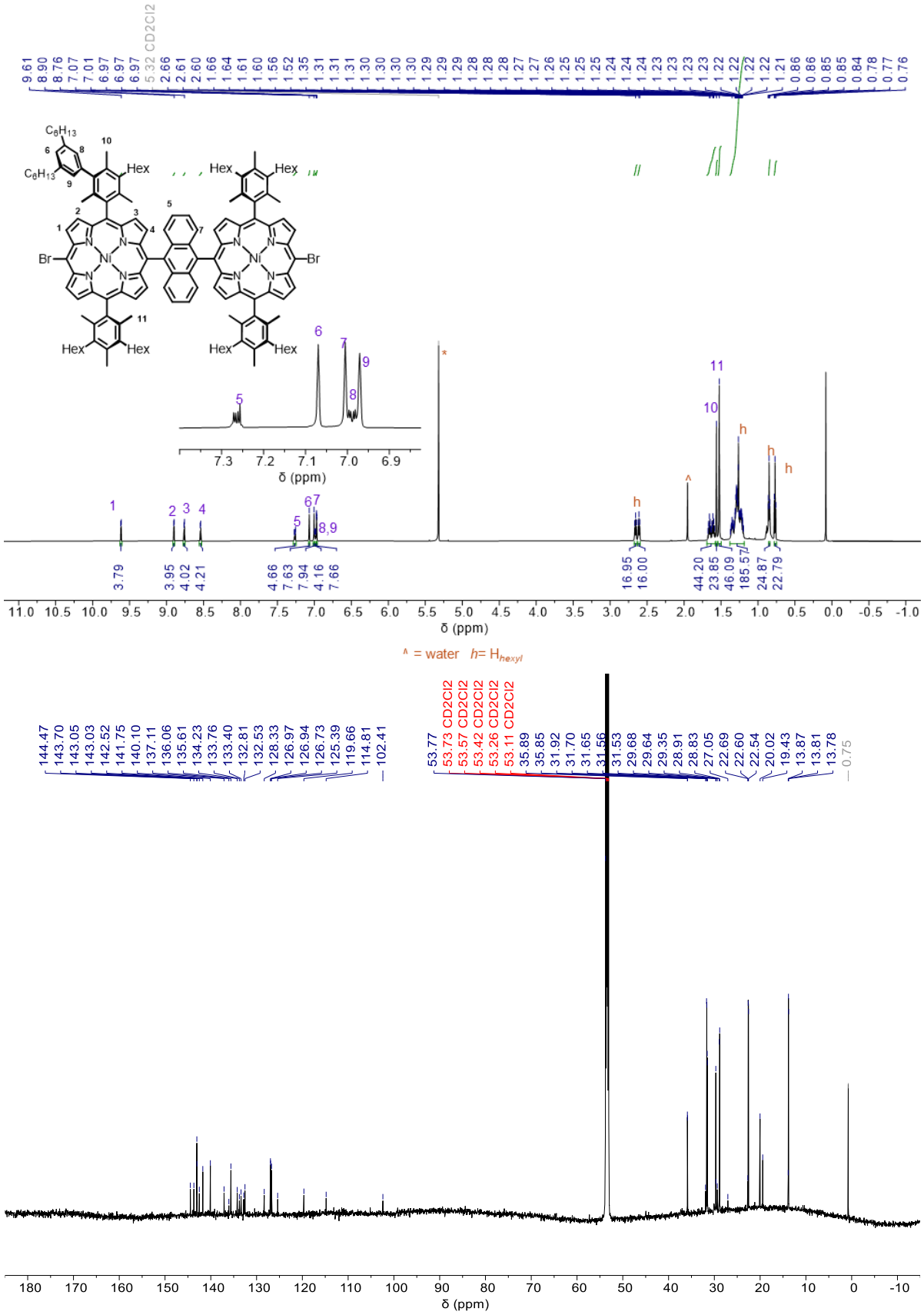


Figure S3.38: (top) ^{1}H NMR (700 MHz) and (bottom) ^{13}C NMR (176 MHz) spectra of singly-linked anthracenyl-dibromoporphyrin dimer **3.27d** (CD_2Cl_2, 298 K).

Selected UV–vis–NIR Absorption Spectra

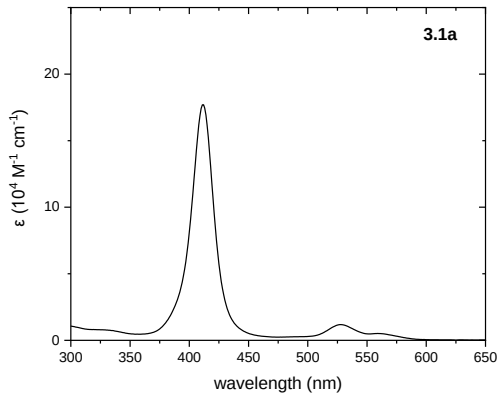


Figure S3.39: UV–vis absorption spectrum of **3.1a** in dichloromethane (298 K).

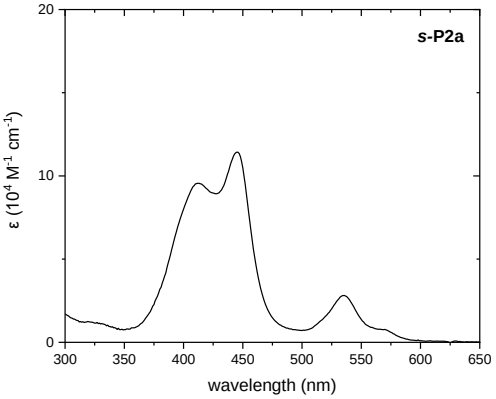


Figure S3.40: UV–vis absorption spectrum of ***s*-P2a** in dichloromethane (298 K).

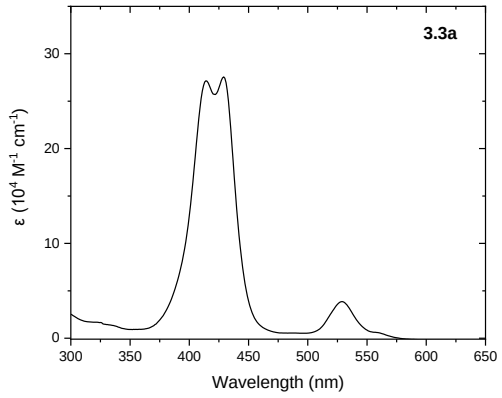


Figure S3.41: UV–vis absorption spectrum of **3.3a** in dichloromethane (298 K).

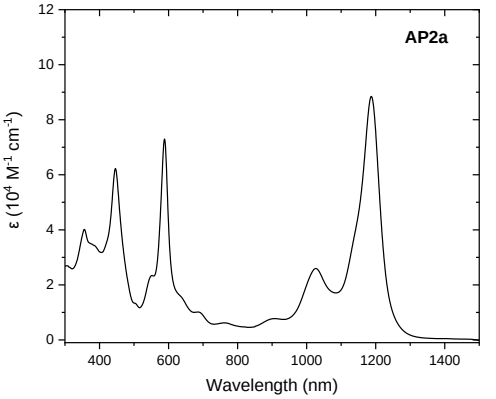


Figure S3.42: UV–vis–NIR absorption spectrum of **AP2a** in toluene-d_8 (298 K).

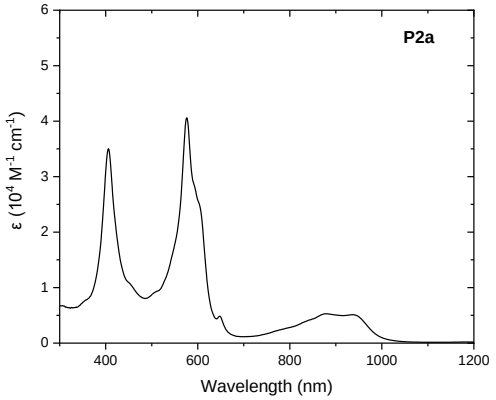


Figure S3.43: UV–vis–NIR absorption spectrum of **P2a** in toluene-d_8 (298 K).

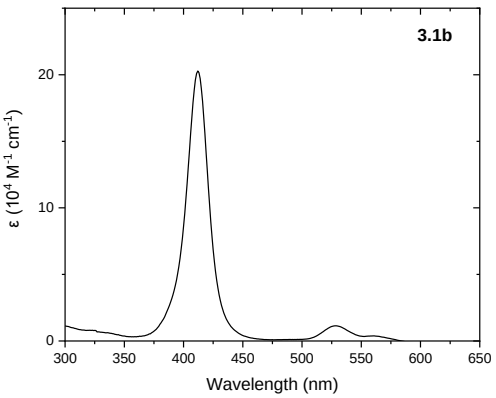


Figure S3.44: UV–vis absorption spectrum of **3.1b** in dichloromethane (298 K).

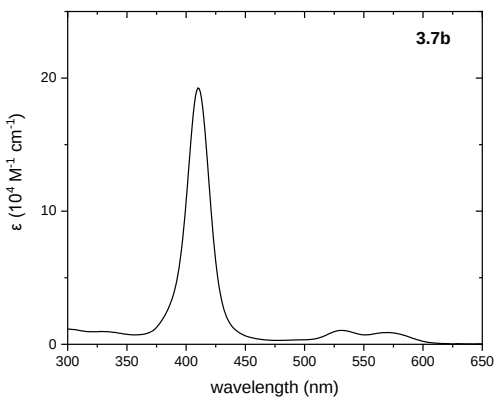


Figure S3.45: UV–vis absorption spectrum of **3.7b** in dichloromethane (298 K).

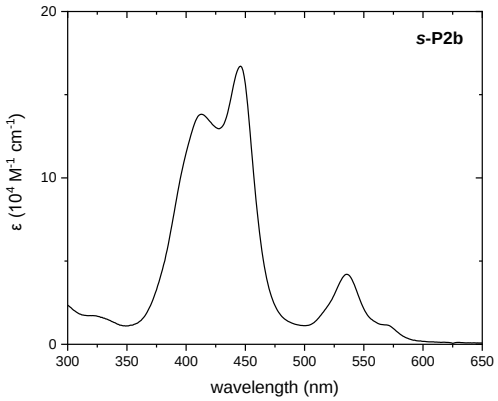


Figure S3.46: UV–vis absorption spectrum of ***s*-P2b** in dichloromethane (298 K).

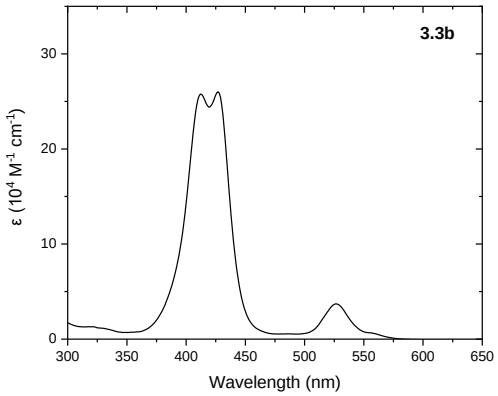


Figure S3.47: UV–vis absorption spectrum of **3.3b** in dichloromethane (298 K).

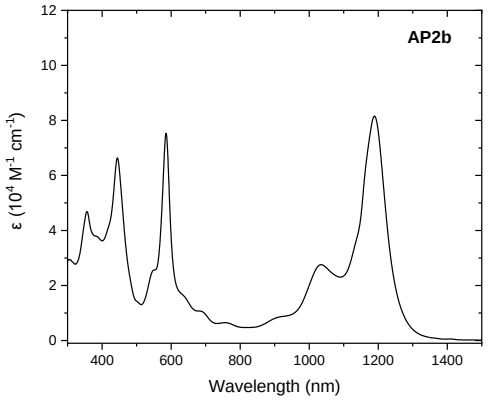


Figure S3.48: UV–vis–NIR absorption spectrum of **AP2b** in toluene-d_8 (298 K).

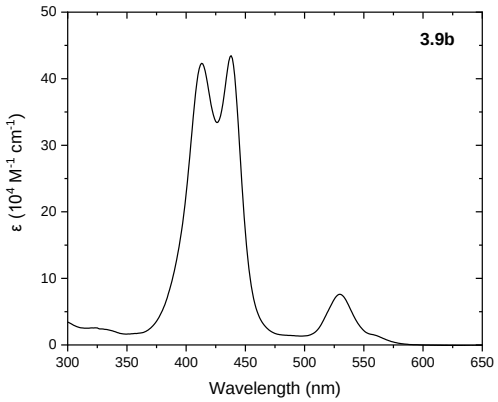


Figure S3.49: UV–vis absorption spectrum of **3.9b** in dichloromethane (298 K).

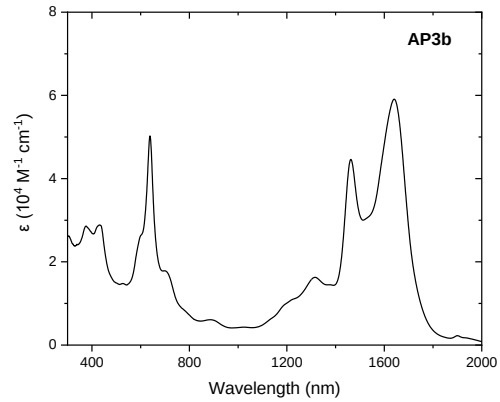


Figure S3.50: UV–vis–NIR absorption spectrum of **AP3b** in toluene-d_8 (298 K).

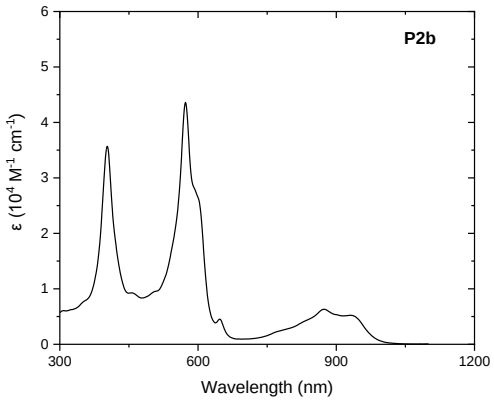


Figure S3.51: UV–vis–NIR absorption spectrum of **P2b** in toluene-d_8 (298 K).

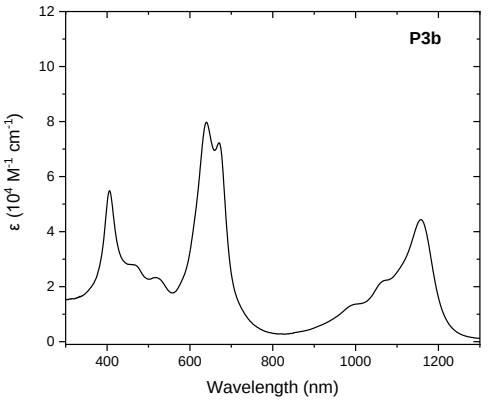


Figure S3.52: UV–vis–NIR absorption spectrum of **P3b** in toluene-d_8 (298 K).

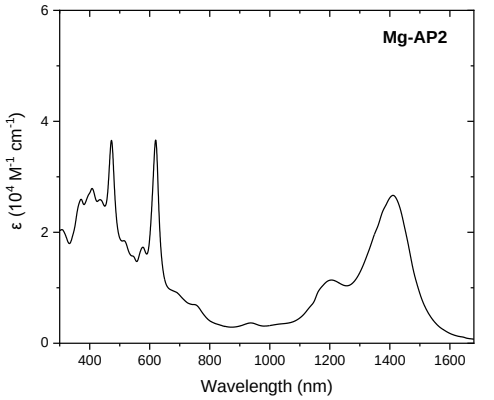


Figure S3.53: UV–vis–NIR absorption spectrum of **Mg-AP2b** in toluene-d_8 (298 K).

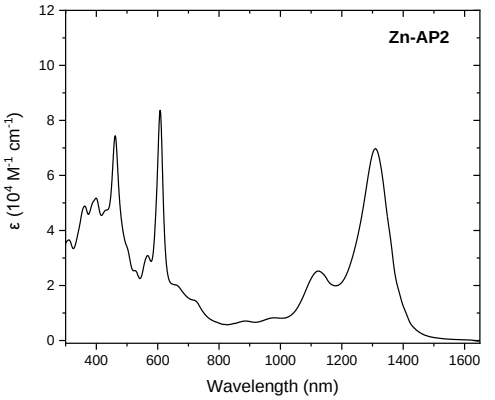
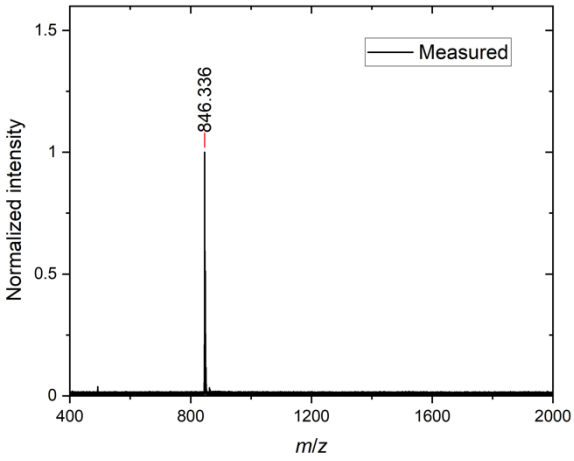
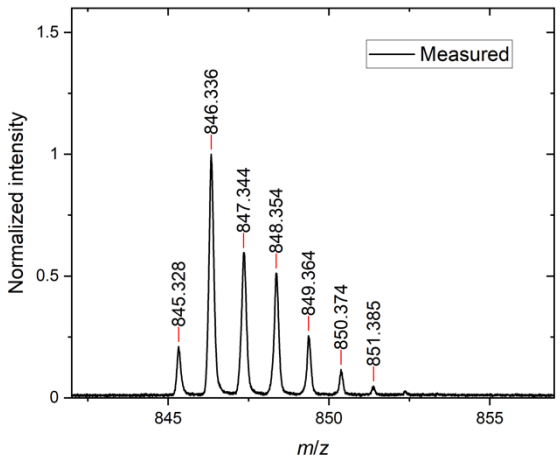


Figure S3.54: UV–vis–NIR absorption spectrum of **Zn-AP2b** in toluene-d_8 (298 K).

Selected Mass Spectra





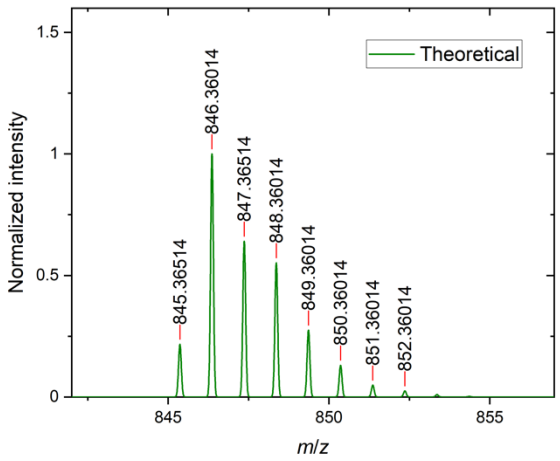
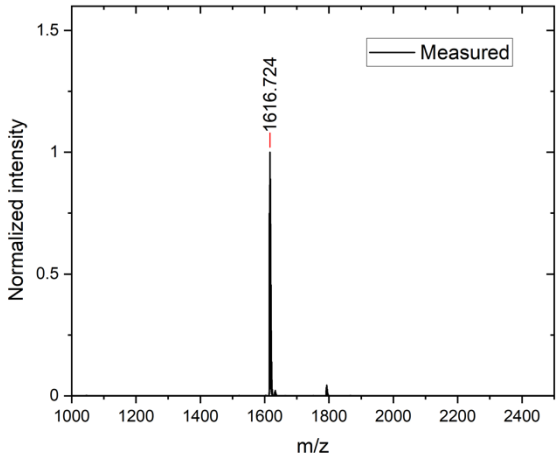
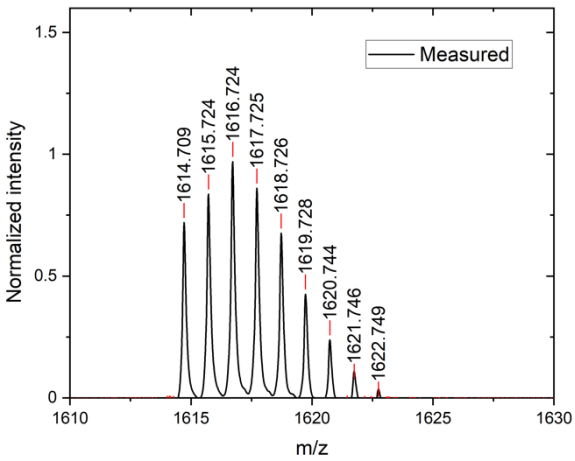


Figure S3.55: MALDI-TOF MS spectrum of **3.1a**.





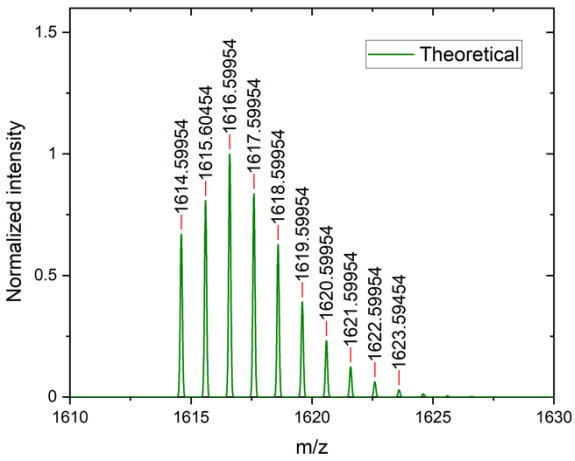
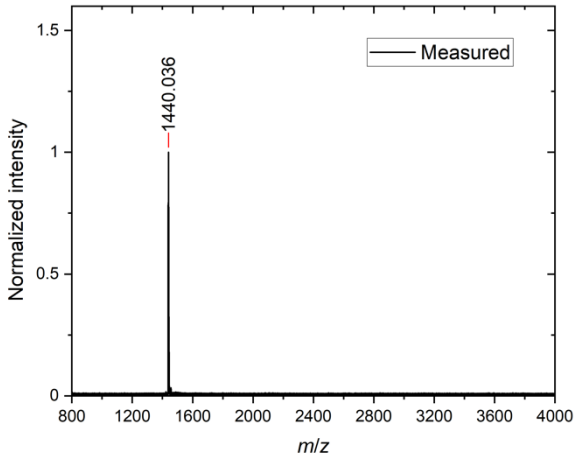
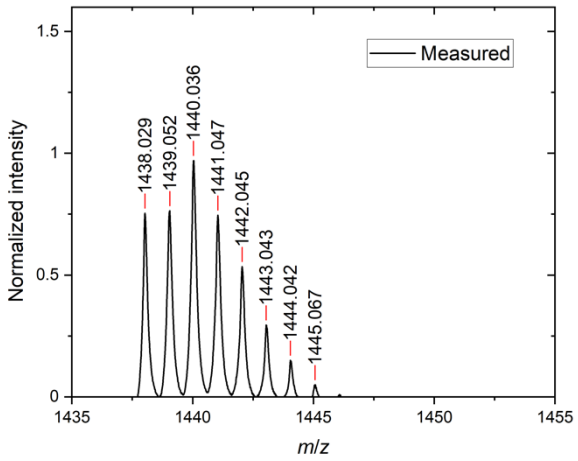


Figure S3.56: MALDI-TOF MS spectrum of **3.3a**.





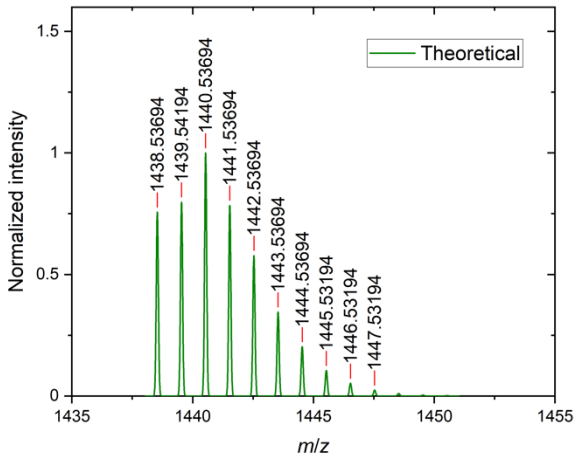
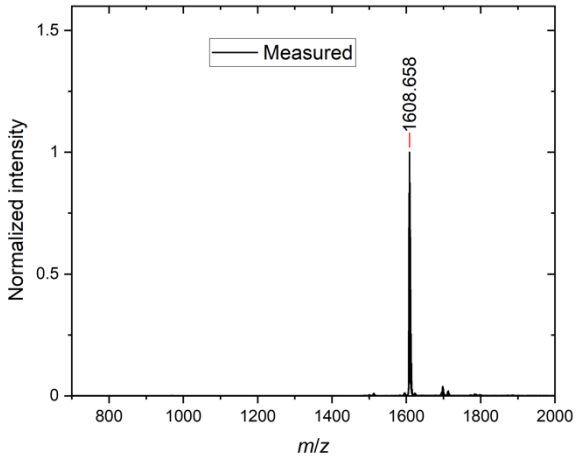
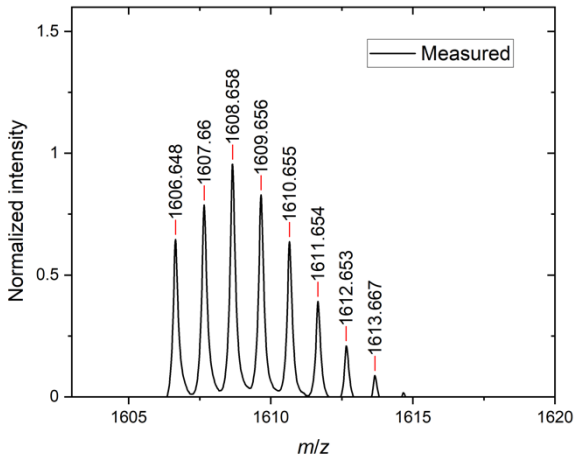


Figure S3.57: MALDI-TOF MS spectrum of ***s*-P2a**.





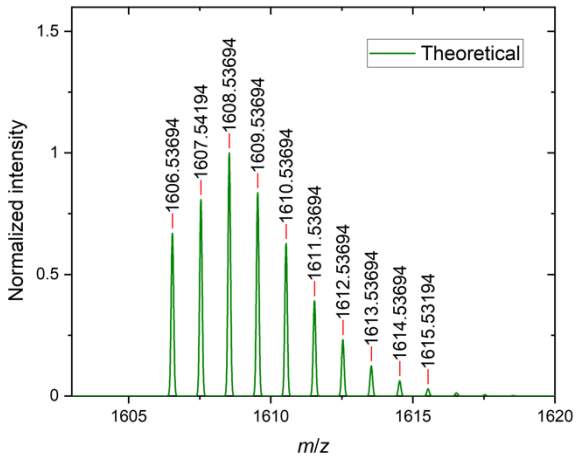


Figure S3.58: MALDI-TOF MS spectrum of **AP2a**.

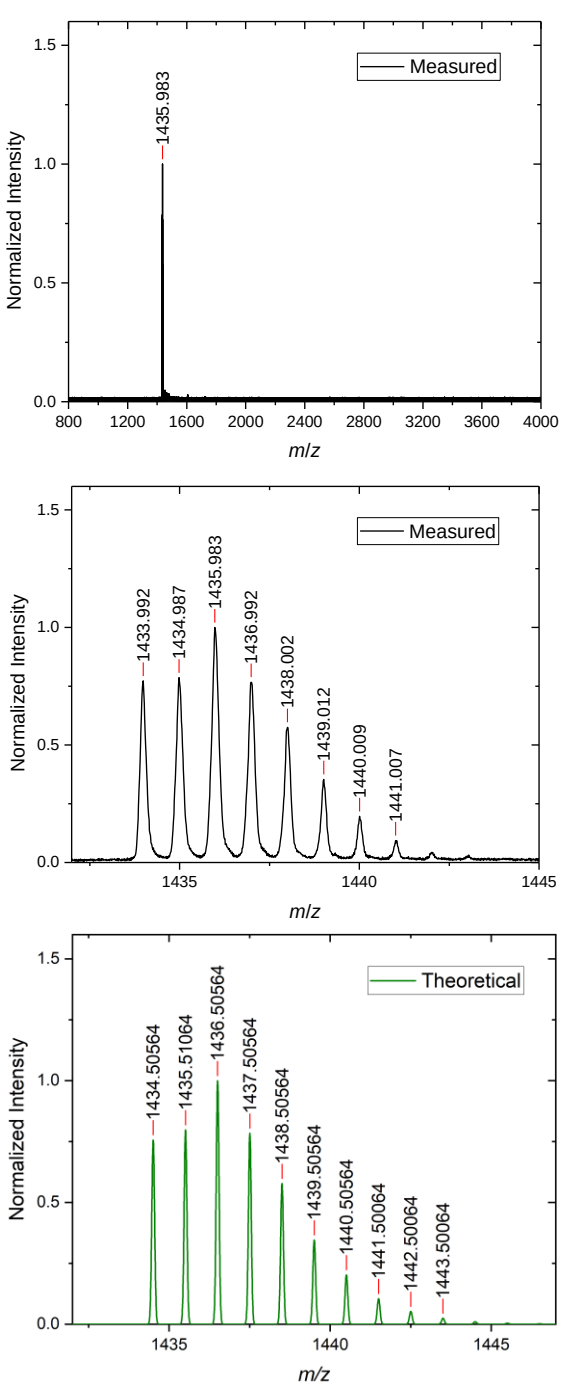


Figure S3.59: MALDI-TOF MS spectrum of **P2a**.

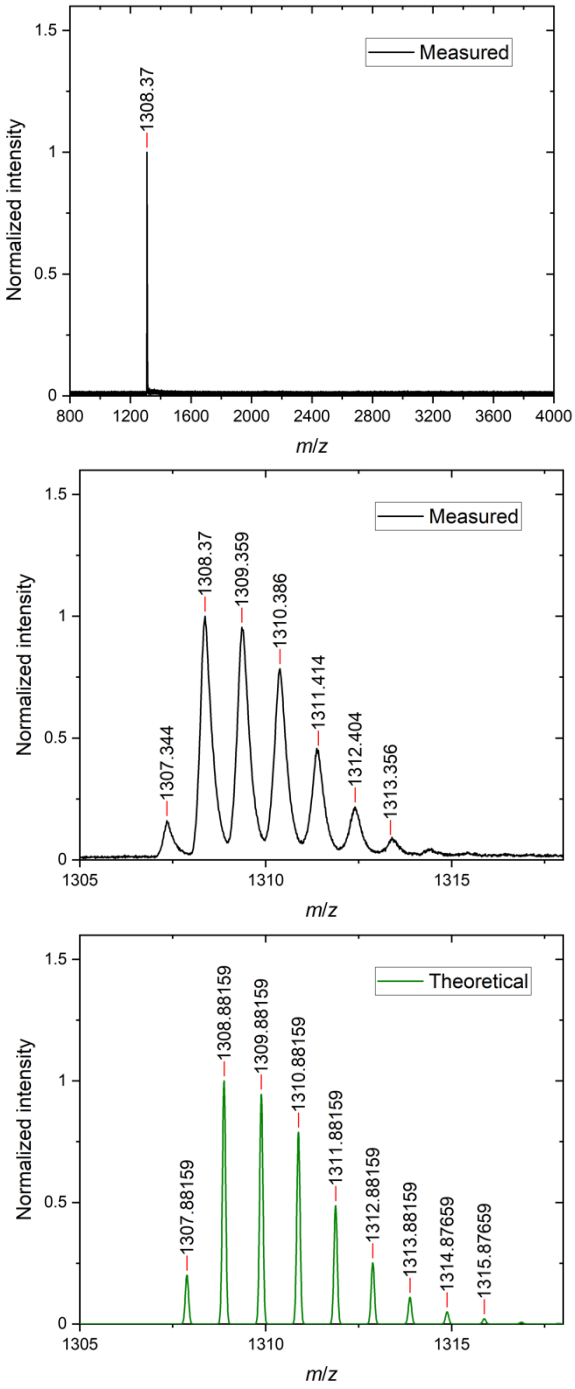


Figure S3.60: MALDI-TOF MS spectrum of **3.1b**.

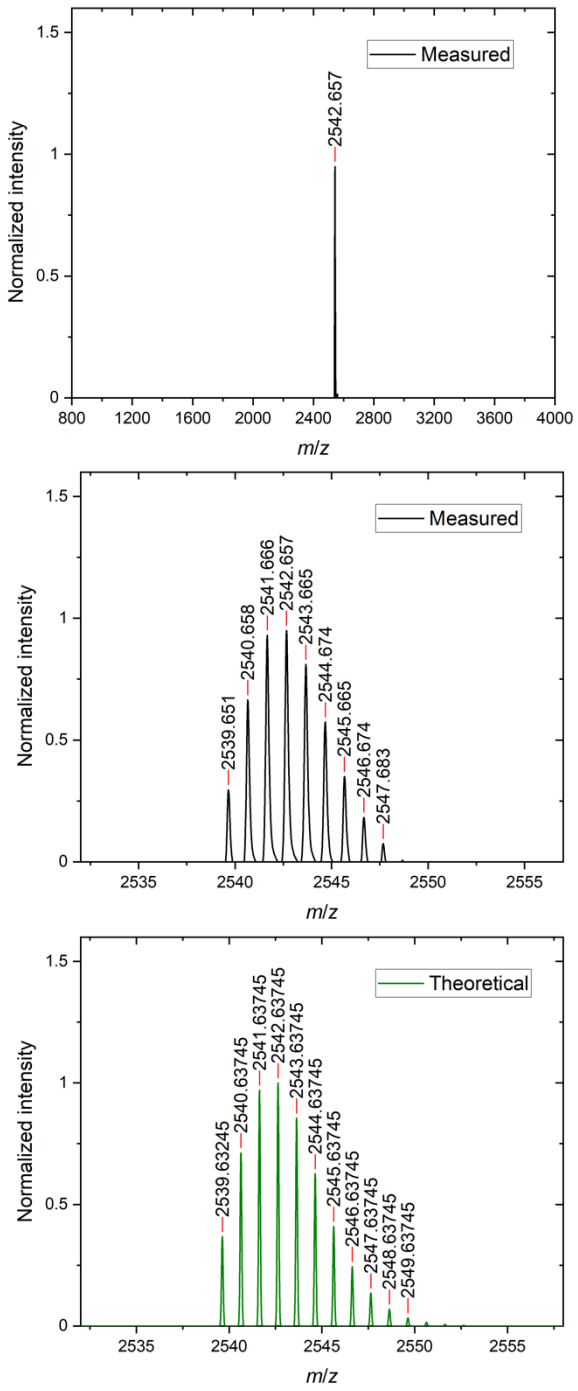


Figure S3.61: MALDI-TOF MS spectrum of **3.3b**.

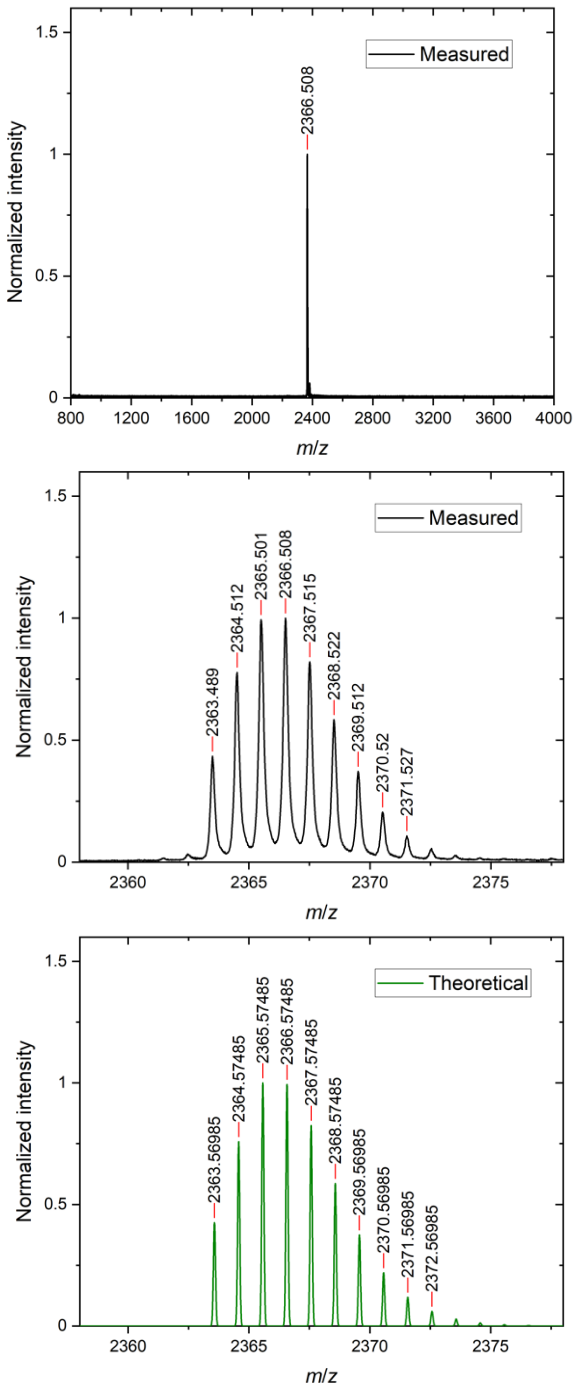
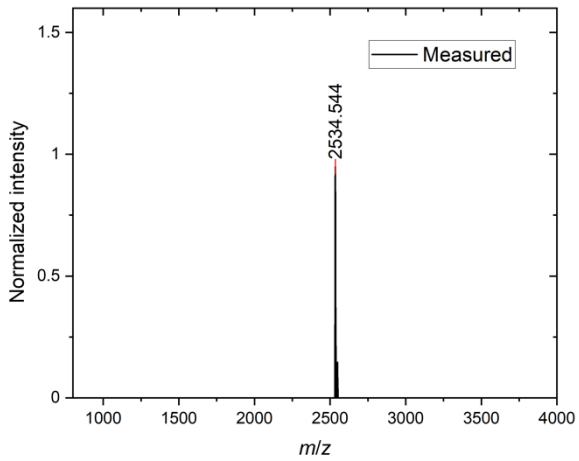
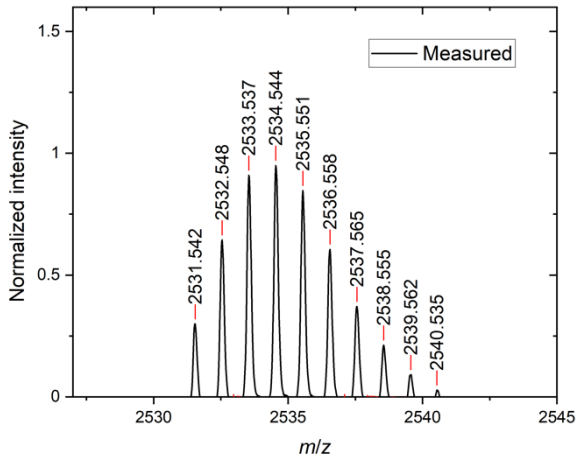


Figure S3.62: MALDI-TOF MS spectrum of ***s*-P2b**.





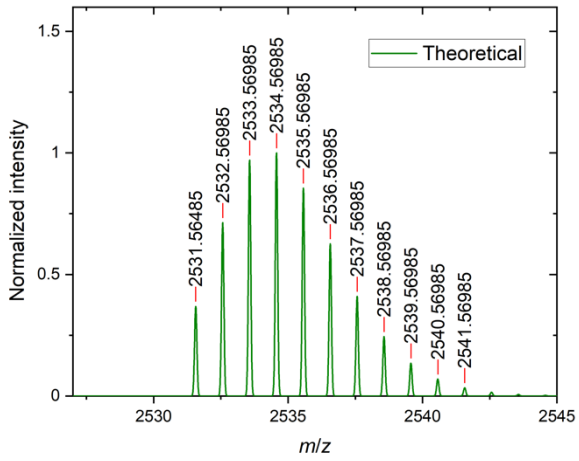
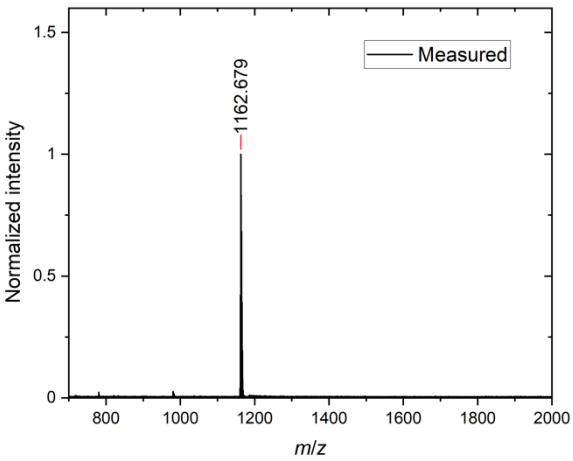
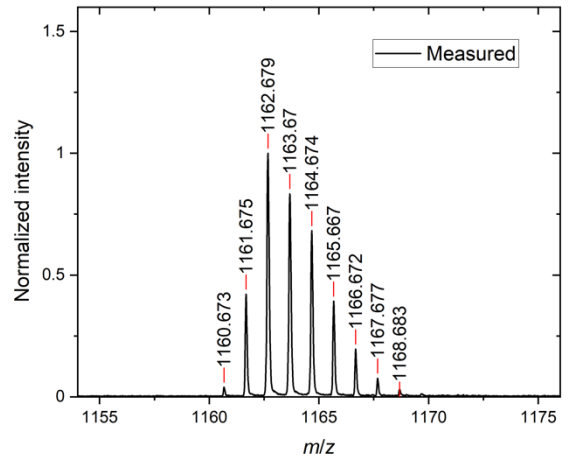


Figure S3.63: MALDI-TOF MS spectrum of **AP2b**.





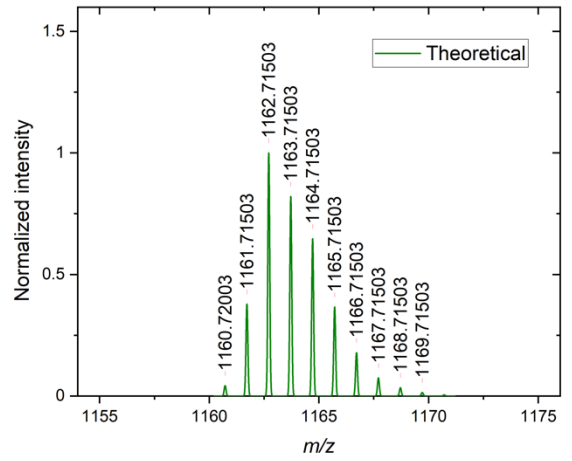


Figure S3.64: MALDI-TOF MS spectrum of **3.7b**.

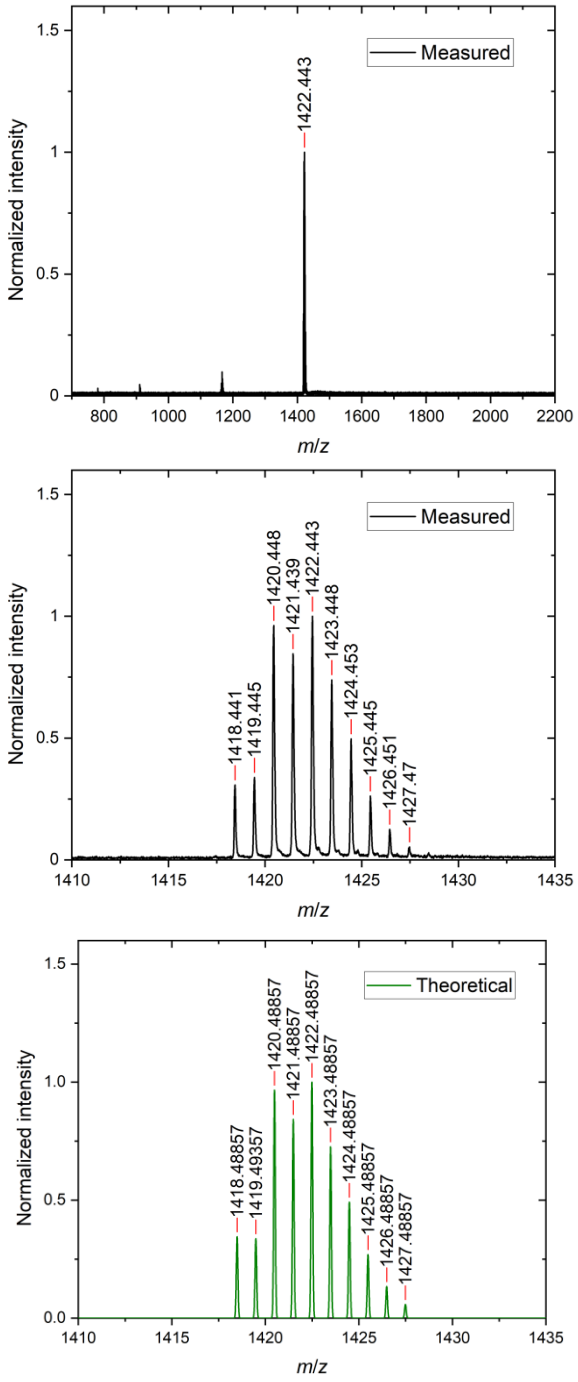


Figure S3.65: MALDI-TOF MS spectrum of **3.8b**.

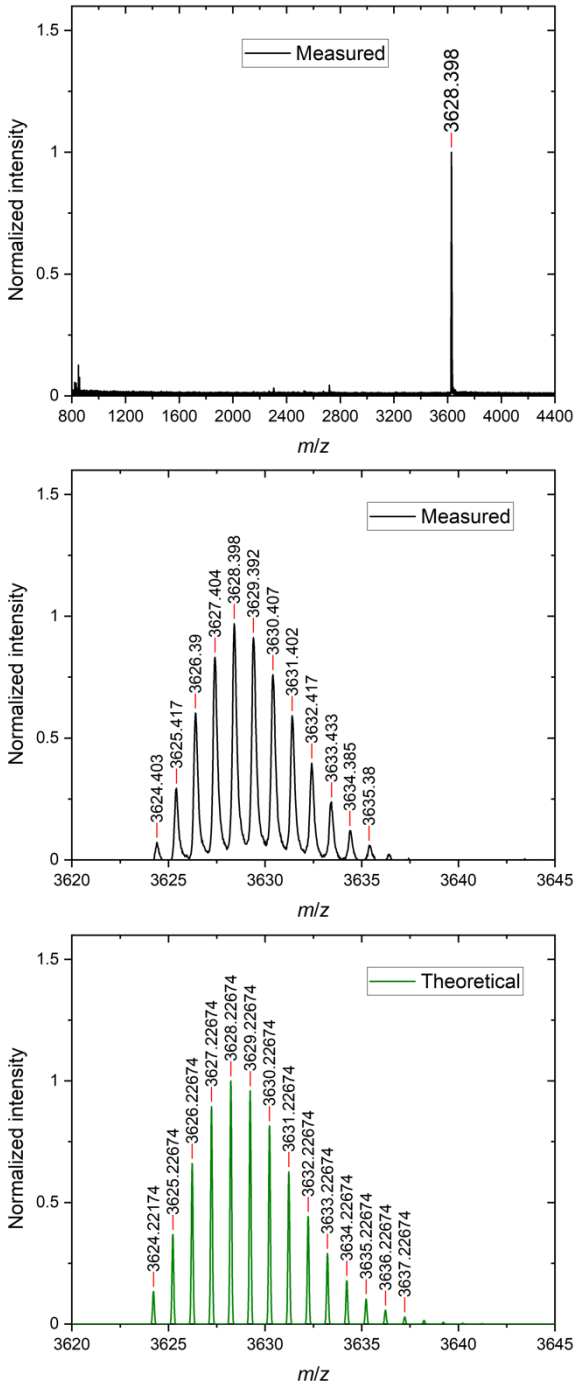


Figure S3.66: MALDI-TOF MS spectrum of **3.9b**.

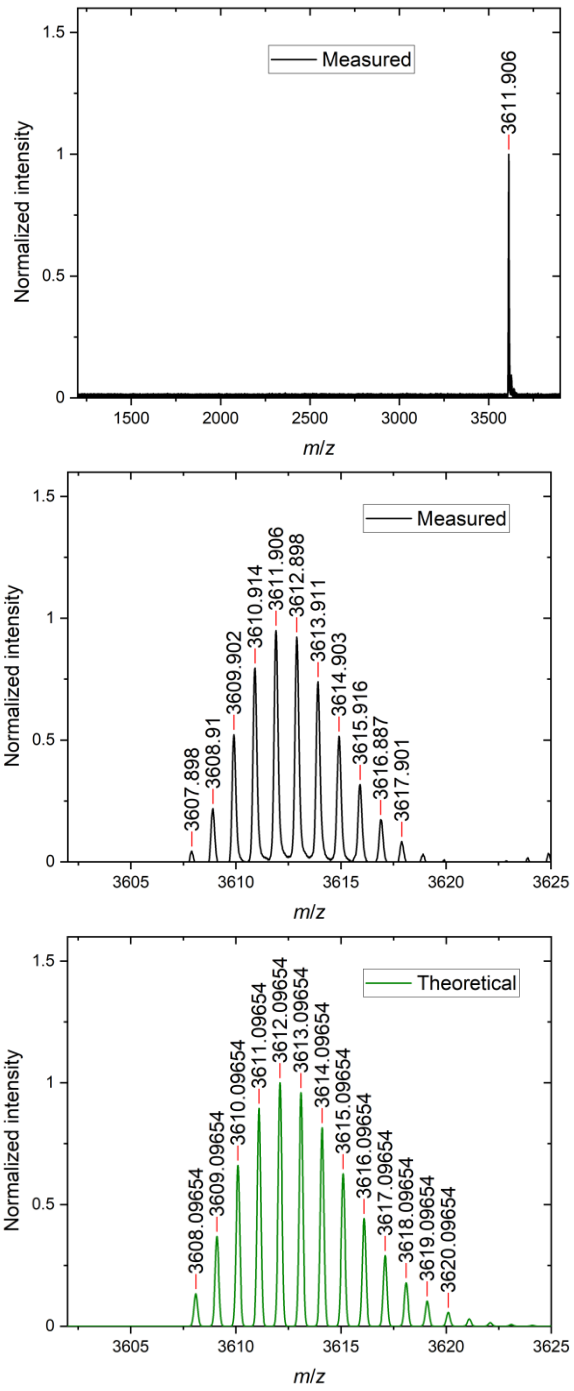


Figure S3.67: MALDI-TOF MS spectrum of **AP3b**.

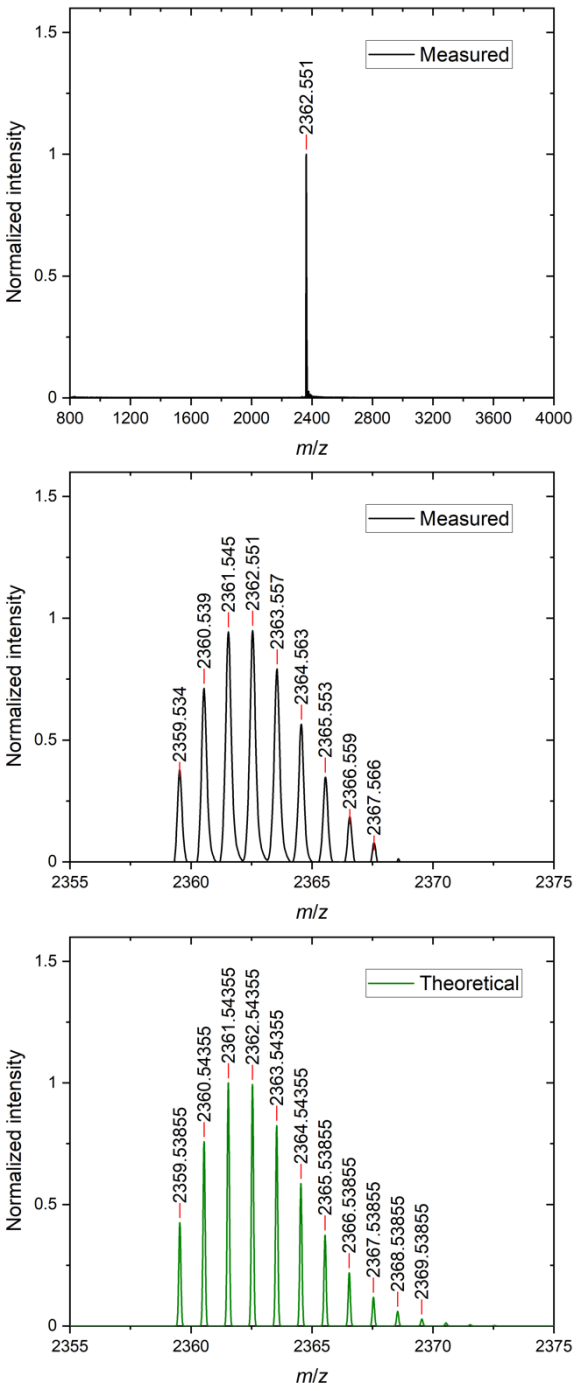


Figure S3.68: MALDI-TOF MS spectrum of **P2b**.

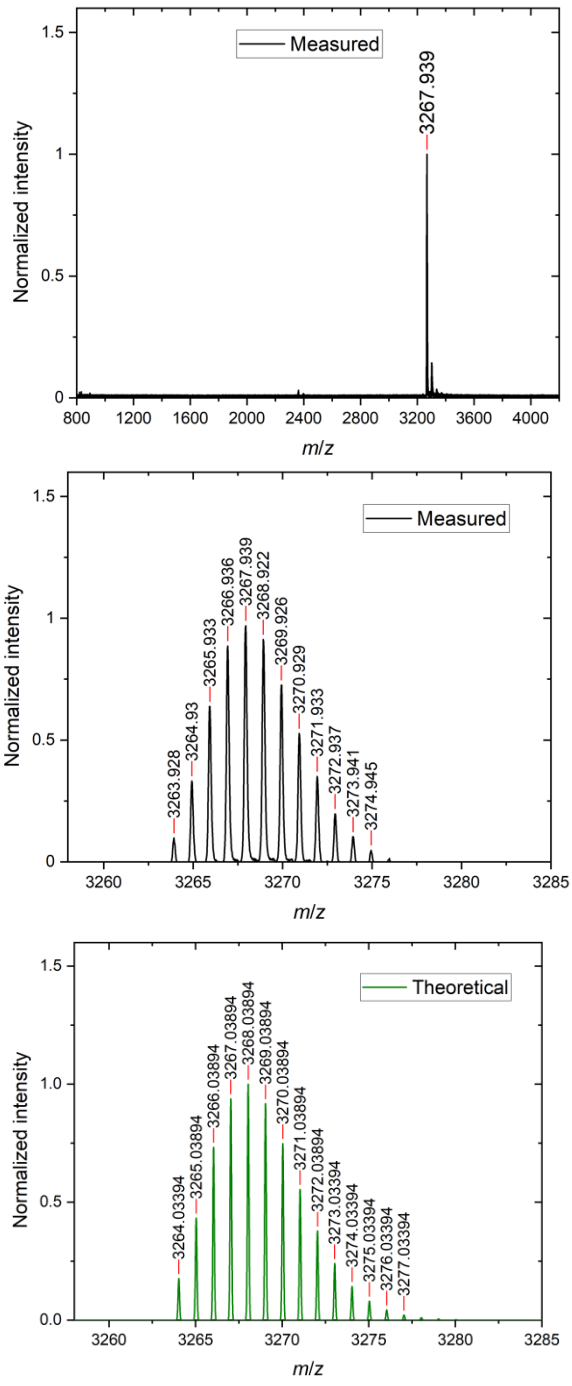


Figure S3.69: MALDI-TOF MS spectrum of **P3b**.

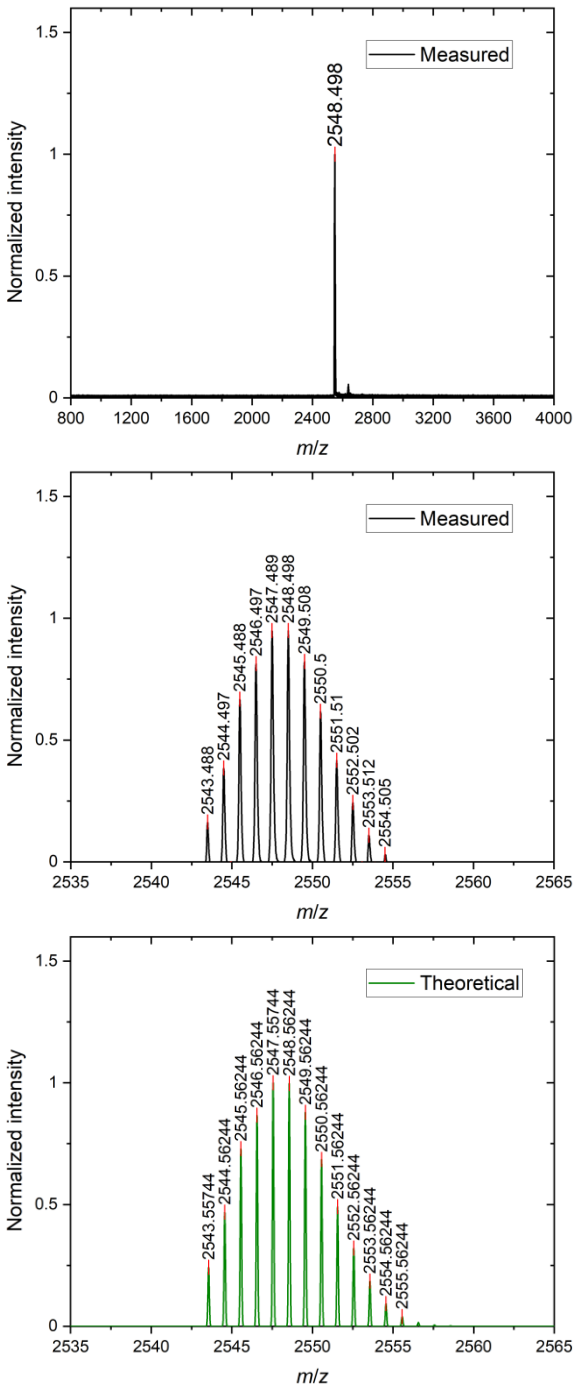
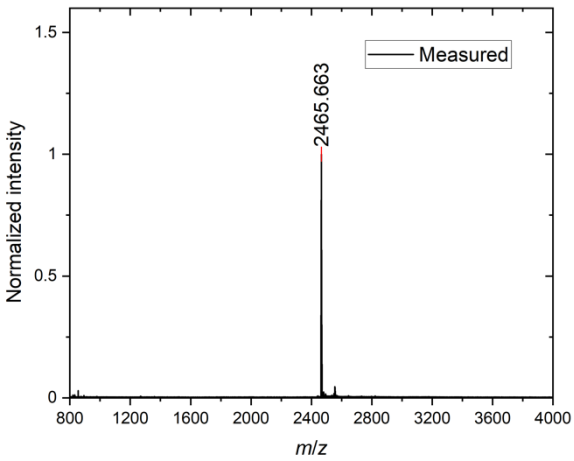
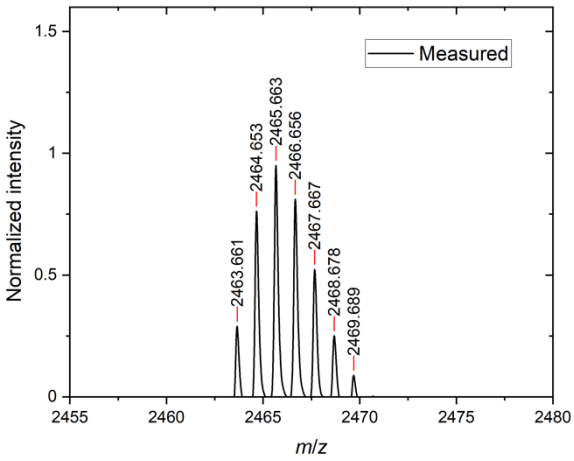


Figure S3.70: MALDI-TOF MS spectrum of **Zn-AP2b**.





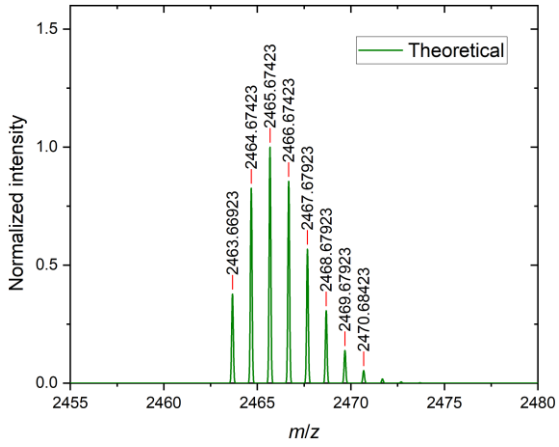
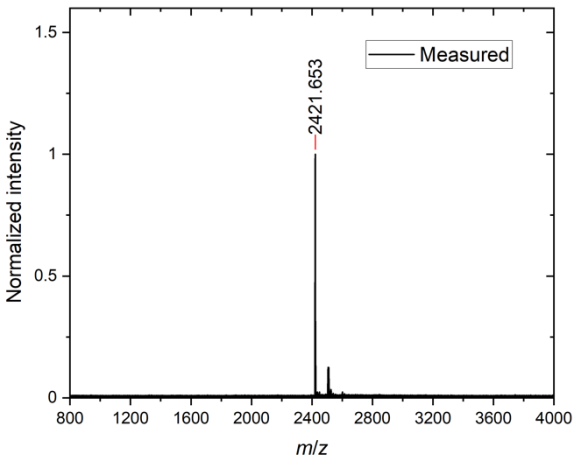
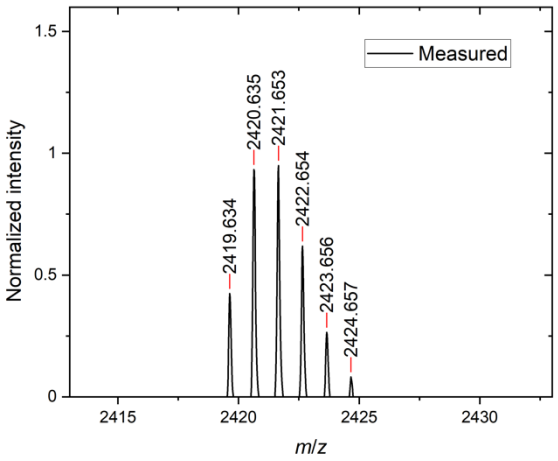


Figure S3.71: MALDI-TOF MS spectrum of **Mg-AP2b**.





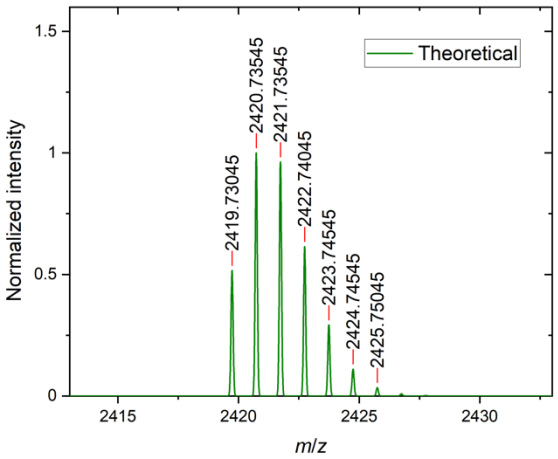


Figure S3.72: MALDI-TOF MS spectrum of **FB-AP2b**.

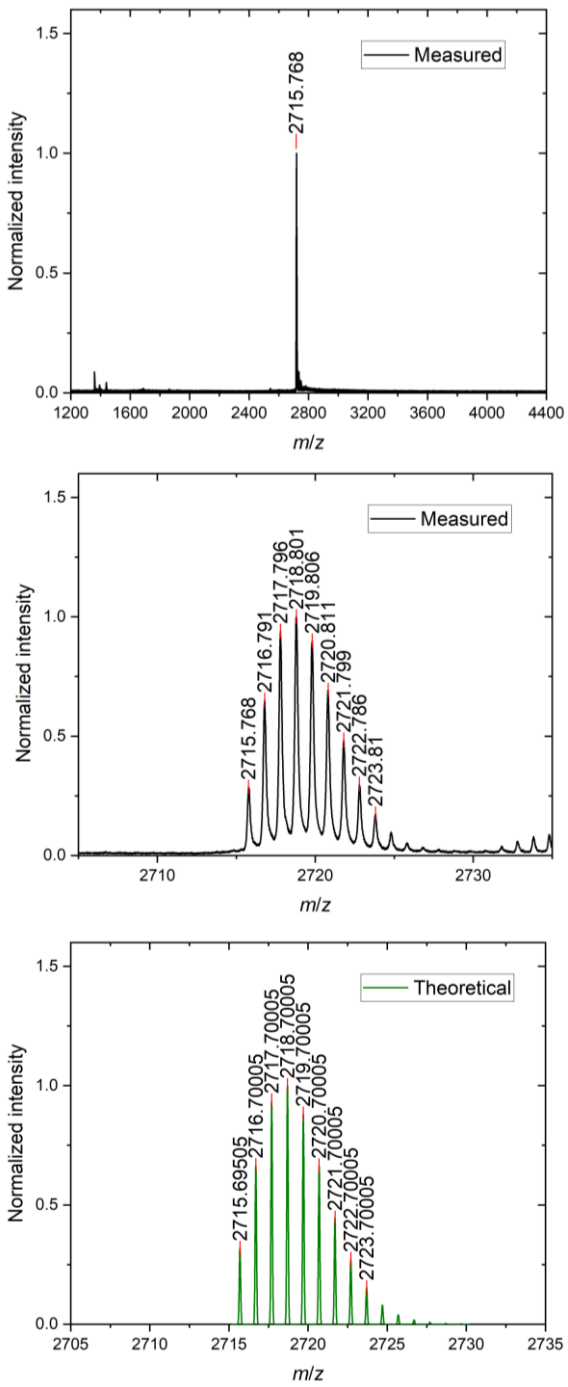


Figure S3.73: MALDI-TOF MS spectrum of **3.12b**.

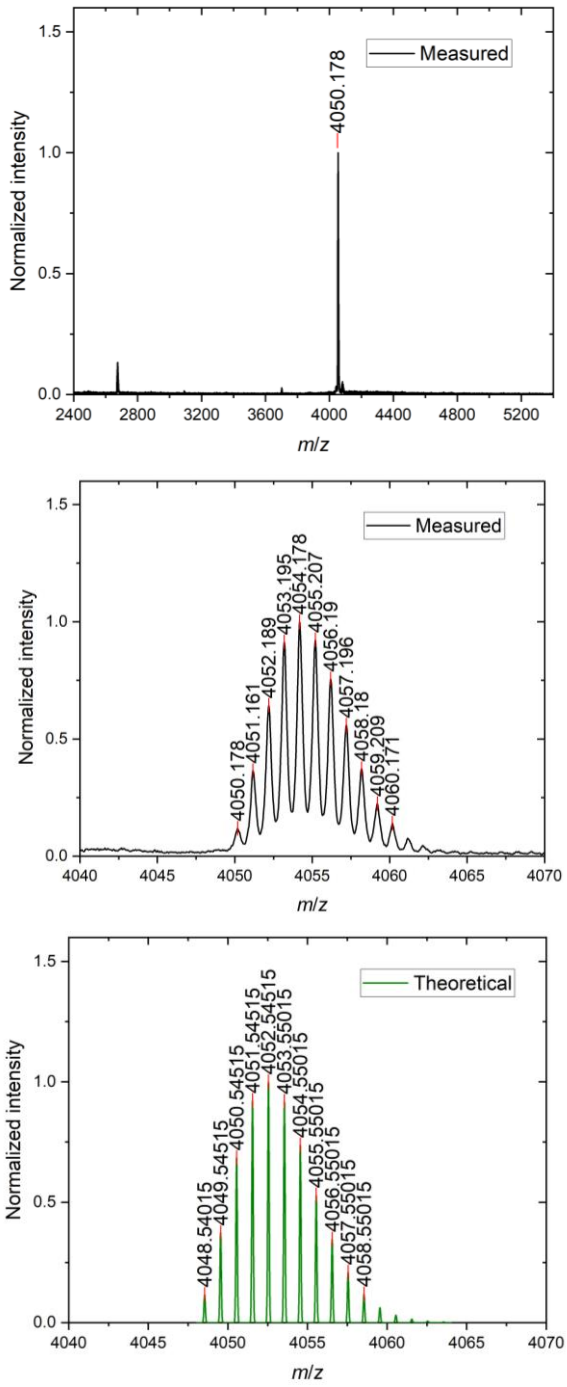


Figure S3.74: MALDI-TOF MS spectrum of **3.26c**.

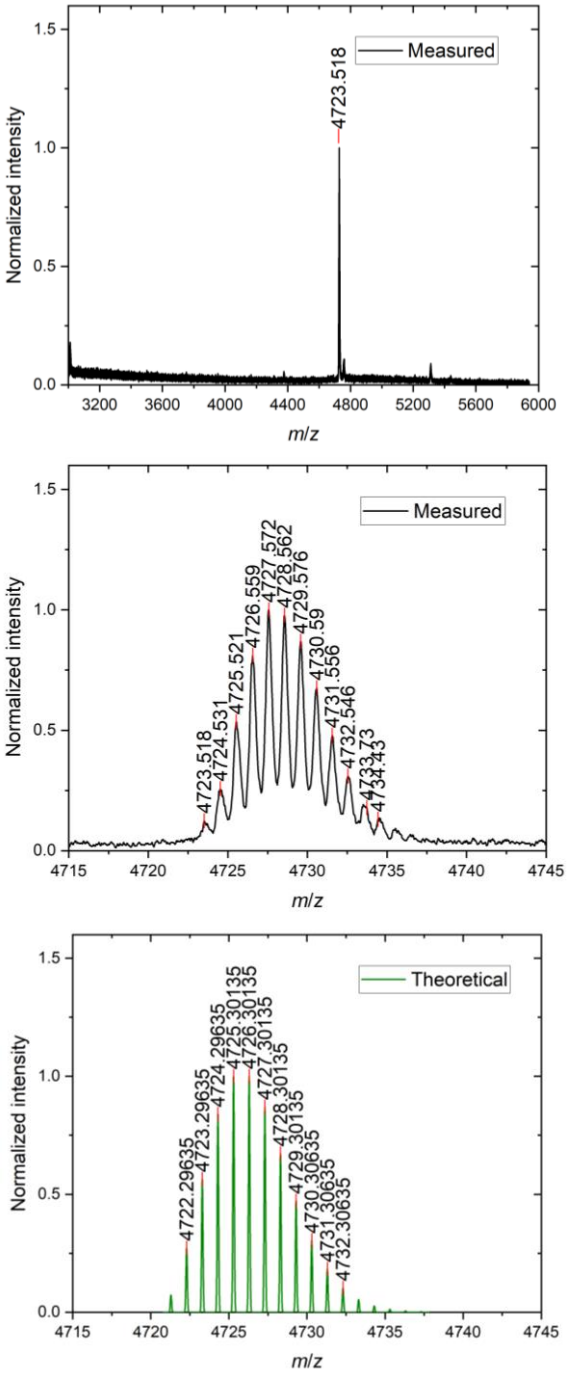


Figure S3.75: MALDI-TOF MS spectrum of **3.26d**.

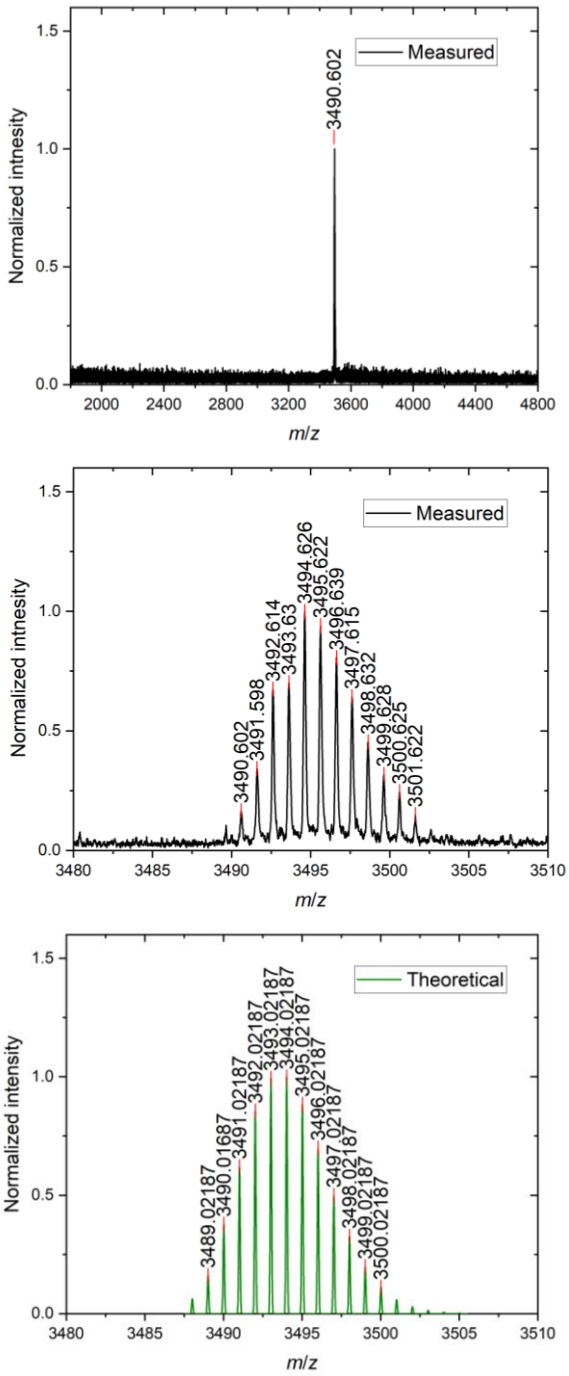


Figure S3.76: MALDI-TOF MS spectrum of **3.27d**.

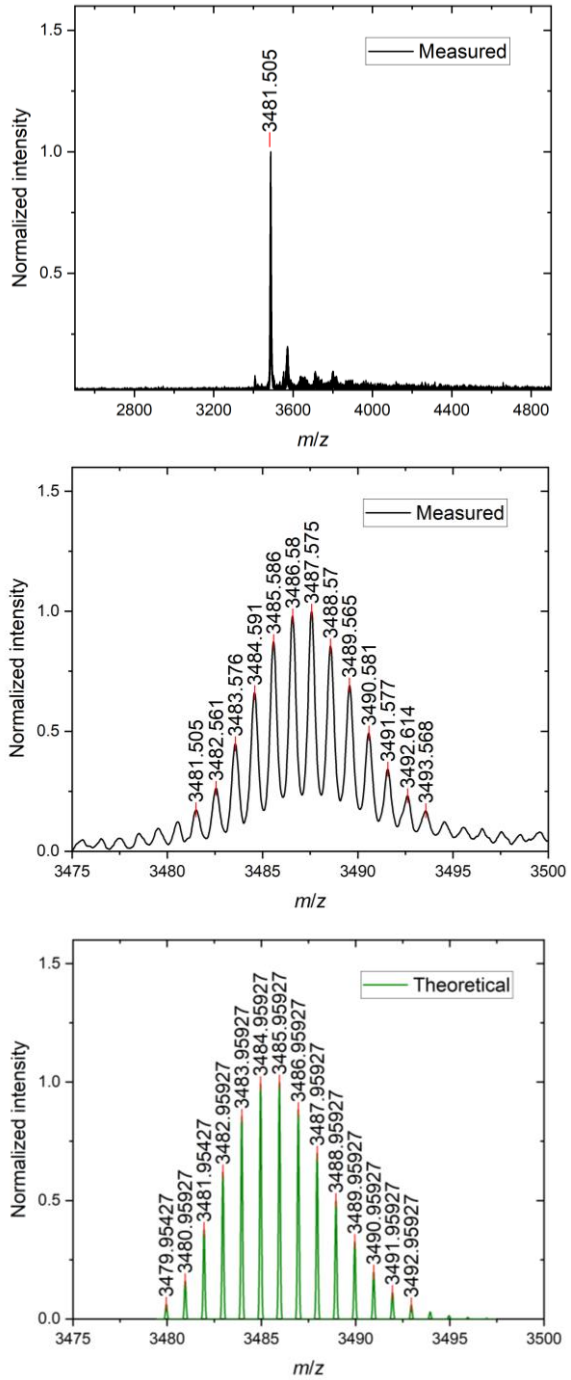


Figure S3.77: MALDI-TOF MS spectrum of **AP2d-Br$_2$**.

References

1 K. Hiroki and M. Kijima, *Chem. Lett.*, 2005, **34**, 942–943.

2 B. Vaz, R. Alvarez, M. Nieto, A. I. Paniello and A. R. de Lera, *Chem. Inform.*, 2002, **33**, 7409–7412.

3 Y. Matano, T. Shibano, H. Nakano and H. Imahori, *Chem. Eur. J.*, 2012, **18**, 6208–6216.

4 Q. Chen, L. Brambilla, L. Daukiya, K. S. Mali, S. De Feyter, M. Tommasini, K. Müllen and A. Narita, *Angew. Chem. Int. Ed.*, 2018, **57**, 11233–11237.

5 J. Rosenthal, E. R. Young and D. G. Nocera, *Inorg. Chem.*, 2007, **46**, 8668–8675.

6 D. Tatsumi, T. Tsukamoto, R. Honna, S. Hoshino, T. Shimada and S. Takagi, *Chem. Lett.*, 2017, **46**, 1311–1314.

7 Q. Chen, A. Lodi, H. Zhang, A. Gee, H. I. Wang, F. Kong, M. Clarke, M. Edmondson, J. Hart, J. N. O'Shea, W. Stawski, J. Baugh, A. Narita, A. Saywell, M. Bonn, K. Müllen, L. Bogani and H. L. Anderson, *Nat. Chem.*, 2024, DOI:10.1038/s41557-024-01477-1.

8 J. N. Moorthy, P. Mal, R. Natarajan and P. Venugopalan, *J. Org. Chem.*, 2001, **66**, 7013–7019.

9 J. Ranta, T. Kumpulainen, H. Lemmetyinen and A. Efimov, *J. Org. Chem.*, 2010, **75**, 5178–5194.

10 G. Kresse and J. Hafner, *Phys. Rev. B*, 1993, **47**, 558–561.

11 G. Kresse and J. Furthmüller, *Comput. Mater. Sci.*, 1996, **6**, 15–50.

12 G. Kresse and J. Furthmüller, *Phys. Rev. B, Condens. Matter*, 1996, **54**, 11169–11186.

13 G. K. H. Madsen, J. Carrete and M. J. Verstraete, *Comput. Phys. Commun.*, 2018, **231**, 140–145.

14 V. Wang, N. Xu, J. C. Liu, G. Tang and W. T. Geng, *Comput. Phys. Commun.*, 2021, **267**, 108033.

4

Synthesis of Polydisperse Porphyrin Nanoribbons

Contents

4.1 Introduction 226

4.1.1 Terahertz Time-Domain Spectroscopy 227

4.1.2 THz Response of Charge-Carriers 229

4.1.3 THz Properties of Carbon-Based Materials 232

4.1.4 Project Aim 235

4.2 Synthesis of Polydisperse Porphyrin Nanoribbons 236

4.2.1 Synthesis of Zn(II) Porphyrin Nanoribbons 237

4.2.2 Synthesis of Ni(II) Porphyrin Nanoribbons 241

4.2.3 Length Characterization of Porphyrin Nanoribbons 248

4.3 Photoconductivity of Ni(II) Porphyrin Nanoribbons from Terahertz Spectroscopy 251

4.4 Conclusions 253

4.5 References 255

4.6 Experimental 259

Chapter 4 - Synthesis of Polydisperse Porphyrin Nanoribbons

4.1 Introduction

Probing the conducting behavior of organic materials as electronic wires, through direct electrical conductance measurements, has emerged as a vibrant field of research, as highlighted in Chapter 1. Extending to broader applications, where organic materials serve as fundamental elements in high-tech fields, such as photovoltaic or optoelectronic devices, the performance of the devices critically relies on the intrinsic dynamics of charge carriers.[1,2] Therefore, characterizing the behavior of charge carriers within the material over varied time and length scales is important for device optimization.[3,4] The key quantity that characterizes this is the charge carrier mobility, μ, which describes the response of mobile charge carriers to an externally applied electric field. The applied electric field induces charge carriers to drift away from their average diffusion positions. When this response dominates the migration of charges in the material, the ratio between the drift velocity of charges, v_d, and the amplitude of the applied electric field, E, defines the value of μ in unit of $cm^2/V{\cdot}s$, as defined in Equation (4.1).[5]

$$\mu = v_d/E \tag{4.1}$$

In the case of organic semiconductors, free charge carriers in the material can either be doped, injected or photo-generated and their existing forms depend on factors such as morphology, temperature, and material properties such as the crystal structure and band gap.[1] Conventionally, the carrier mobility can be experimentally determined from direct-current experiments over macroscopic distances (~1 mm) in a static external electric field.[6–11] The obtained conductivity, σ, is primarily determined by the concentration of mobile charge carriers, N, and μ following Equation (4.2), in unit of S/m.

$$\sigma = N \cdot e \cdot \mu \tag{4.2}$$

More recently, much smaller distance-scale measurements can be achieved by using pulsed microwave (~1 ns duration) or terahertz (THz, ~1 ps duration) radiation to probe charge carriers without any influence of electrodes.[12–16] The pulsed nature of radiation restricts the probing of only small-domain motions of charge carriers (*e.g.*, <100 nm for THz measurements).[17] Therefore, the conductivity measured via these noninvasive and noncontact methods, where charge carriers can directly interact with the applied radiation, reflects transient

or short-lived phenomena involving charge carriers with high time-resolution. This chapter aims to explore the intrinsic photoconductivity of porphyrin nanoribbons with the utilization of THz time-domain spectroscopy techniques.

4.1.1 Terahertz Time-Domain Spectroscopy

THz radiation lies in the electromagnetic spectrum ranging between microwave and infrared radiation (Figure 4.1), spanning the regime of 0.1 – 10 THz (1 THz = 10^{12} Hz, 0.3 mm in wavelength, or 4.1 meV in energy). Such energies encompass various fundamental charge carrier activities, such as free charge conduction, intra-exciton excitations and carrier-phonon interactions.[18] Consequently, investigating their distinct response in the THz range makes it possible to probe and characterize the dynamics of carriers in detail. However, it has been a challenge historically to generate or detect THz radiation for a couple of reasons: 1) conventional electronic components lacked the ability to oscillate fast enough to generate substantial coherent sources beyond 300 GHz or detect such with reasonable sensitivity; and 2) THz photons possess energies comparable with, or below, the thermal energy at room temperature (1 THz corresponds to 48 K), resulting in low signal-to-noise ratios in THz waveforms that hinders data interpretation.[19] THz radiation remained the least explored region of the electromagnetic spectrum until the first demonstration of THz time-domain spectroscopy in late 1980s.[20,21]

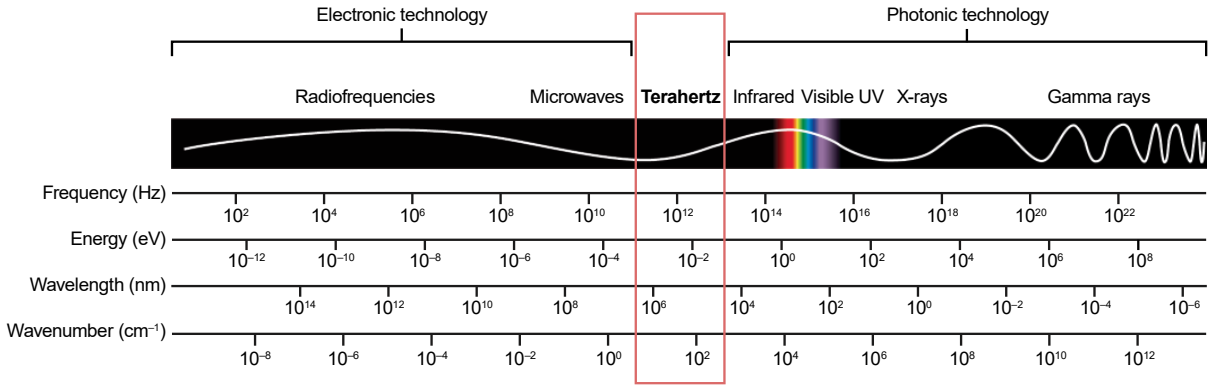


Figure 4.1: The electromagnetic spectrum highlighting the THz band. Names of the bands of each part of the spectrum (top) and various scales with different physical quantities that character the frequency of the radiation (bottom) as reference. Reproduced with permission.[19]

THz time-domain spectroscopy provides a platform to generate and coherently detect pulsed THz frequency radiation in a broad range, which can monitor the intrinsic transport behavior of nanomaterials through their distinctive spectral signals meanwhile avoiding interference from contact electrodes. A typical THz time-domain spectroscopy setup consists

of an optical pulsed laser, a THz-emitter, a THz-detector and optical elements for coupling and propagating THz radiation from the emitter to the detector (Figure 4.2).[22] The laser provides an ultrafast train of femtosecond optical pulses (normally in the IR regime, *e.g.*, 800 nm for Ti: sapphire amplified laser systems) that are divided into two paths through a beam splitter.[19] One of the pulses is used to excite a THz-emitter (a photoconductive emitter by a doped semiconductor "gap" or through optical rectification in nonlinear crystals) and in turn generates sub-picosecond THz pulses (E_{ref}) by frequency down-conversion.[23–25] These THz pulses then readily interact with charge carriers in the sample under study. Meanwhile, the other beam is directed towards the detector (a photoconductive switch or an electro-optic crystal), to determine the electric field of transmitted or reflected THz signals (E_{total}) from the photoinduced current.[26] In the time-domain method, the relative arrival time of the emitted THz pulse (from the THz-emitter) and resulting pulse (after sampling) can be altered by the incorporation of an optical delay line, allowing the electric field of the THz pulse to be recorded as a function of its arrival time. Moreover, the all-optical generation and detection of THz pulses allows an easy incorporation of an additional optical pulse into the system (known as optical-pump THz spectroscopy) to pump the sample out of equilibrium by photoexciting the carriers.[27,28] By recording the THz electric fields with a controlled pump-probe delay time, this approach allows probing of the time-dependent photoconductivity of materials and its ultrafast charge dynamics under non-equilibrium conditions.

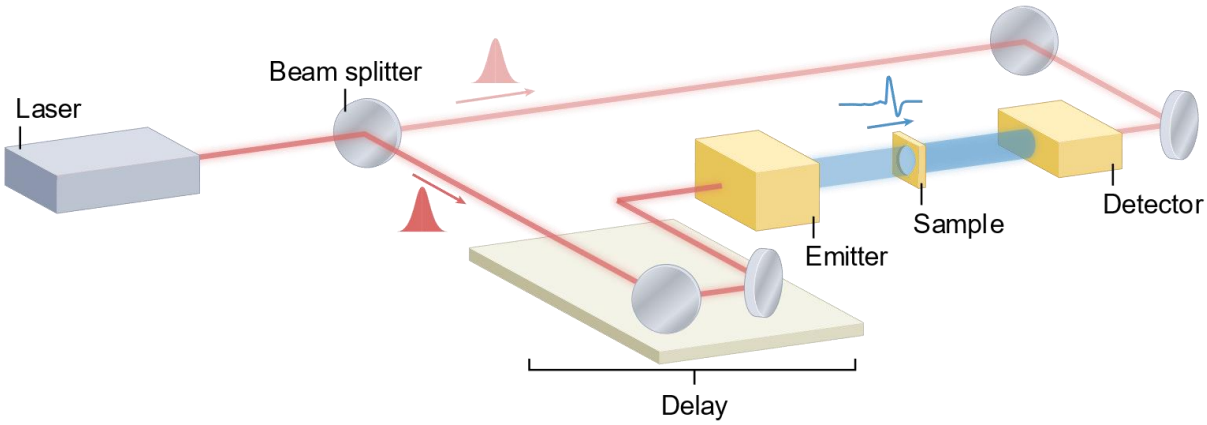


Figure 4.2: Schematic of THz time-domain spectrometer set-up. Reproduced with permission.[19]

In the aforementioned THz time-domain measurements, the interactions of charge carriers in the sample with applied THz pulses result in amplitude attenuation and phase shift of the THz waveforms ($\Delta E = E_{total} - E_{ref}$). Due to the coherent detection of THz pulses in the system, these alterations can be used to precisely extract individual components of the

conductivity from the frequency-resolved THz conductivity spectra, obtained via Fourier transform. The real part of THz conductivity is directly proportional to the relative attenuation of THz electric-field (describing the in-phase charge mobility), while the imaginary component of conductivity (*i.e.*, the polarizability induced by the sample) is reflected by the phase shift of the waveform. In the optical-pump THz spectroscopy experiment, the generation and recombination dynamics of photo-induced charge carriers can also be probed.

4.1.2 THz Response of Charge-Carriers

The free-carrier conduction in many bulk inorganic materials (*e.g.*, metals) can be well described by the Drude model proposed in 1900.[29,30] This model assumes that charge carriers behave like a free particle gas, which can move freely and undergo ballistic motion (*i.e.*, independent electron approximation). Only until randomly interrupted by impurities, phonons or defects, *etc.* through collision events the electrons then scatter. The ensemble charge scattering effect is represented by a mean scattering time, τ, (Figure 4.3a).

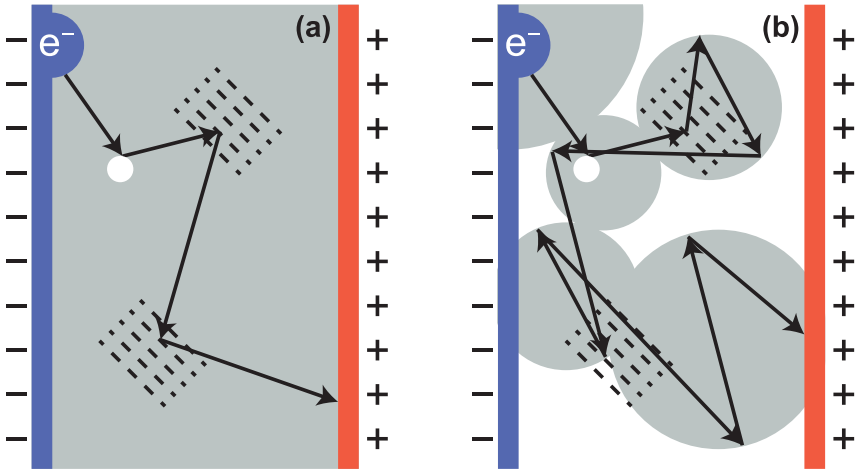


Figure 4.3: (a) In bulk Drude conductors, charge conduction occurs through charge carriers move ballistically between two scattering events, and now and then they are scattered by impurities (white dot), and lattice vibrations (or so-called phonons, sketched by parallel lines) *etc.* (b) The motion of charges in nanomaterials is generally more complex due to the presence of confining boundaries. Reproduced with permission.[2]

For a given material in the frame of the Drude model, in the presence of a time-varying electric field ($E(t)$ – here the electric field is provided by THz radiation), the preferential acceleration of carriers between collision induces the drift velocity $v_d(t)$ in carrier motion. The motion can be described by Newton's Law:

$$\frac{e}{m^*}E(t) = \frac{d}{dt}v_d(t) + \frac{1}{\tau}v_d(t) \tag{4.3}$$

where, e is the electronic charge, m^* is the effective charge of the charge carrier. The time-varying electric field can be represented in Equation (4.4):

$$E(t) = E_0 e^{-i\omega t} \tag{4.4}$$

where ω (= 2πν, ν is the frequency) is the oscillating angular frequency. As such, the equation for $v_{\mathrm{d}}(t)$ can be derived following Equation (4.5).

$$v_d(t) = \frac{e\tau}{m^*}\frac{1}{1-i\omega\tau}E_0 e^{-i\omega t} \tag{4.5}$$

Based on the definition of charge mobility from Equation (4.1), $\mu(\omega)$ can be obtained following Equation (4.6).

$$\mu(\omega) = \frac{v_{\mathrm{d}}(t)}{E(t)} = \frac{e\tau}{m^*}\frac{1}{1-i\omega\tau} \tag{4.6}$$

To describe the electrical properties of a material on the macroscopic scale, Equation (4.6) can be re-written in terms of the frequency-resolved Drude conductivity $\sigma_{\mathrm{Drude}}(\omega)$ using Equation (4.2):

$$\sigma_{\mathrm{Drude}}(\omega) = N\frac{e^2\tau}{m^*}\frac{1}{1-i\omega\tau} \tag{4.7}$$

In practice, Equation (4.7) is commonly re-written by introducing the plasma frequency, ω_p:

$$\omega_p = \sqrt{\frac{Ne^2}{\varepsilon_0 m^*}} \tag{4.8}$$

$$\sigma_{\mathrm{Drude}}(\omega) = \frac{{\omega_p}^2\varepsilon_0\tau}{1-i\omega\tau} \tag{4.9}$$

where ε_0 is the vacuum permittivity. ω_p represents the plasma oscillation resonance of charge carriers, which can be employed as a direct measure of the square root of the density of electrons in a solid. The Drude model only contains two free parameters, ω_p and τ, which can be extracted by fitting this equation to the measured frequency-resolved THz conductivity. The specific angular frequency corresponding to where the real and imaginary parts cross is related to the scattering time through $\omega_{\mathrm{cross}} = 1/\tau$ (Figure 4.4).

Although the Drude model has been applied in many instances where the frequency-dependent conductivity was determined, in the context of many nanomaterials with reduced size, the carrier mean free path is no longer solely inside individual nanoparticles. Additional factors, such as the spatial distribution of nanoparticles or the physical boundaries in confining

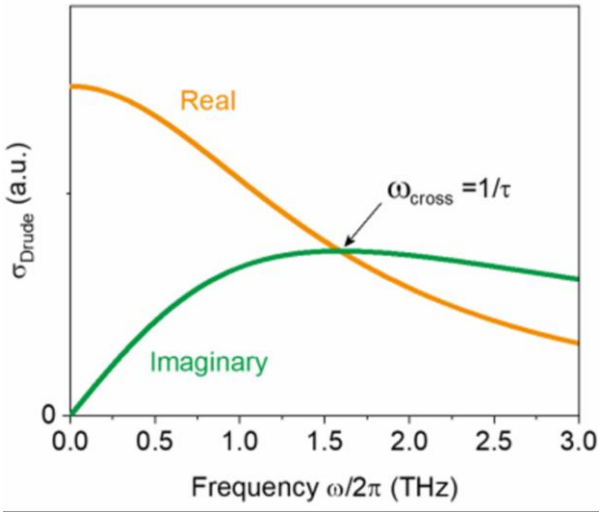


Figure 4.4: The THz conductivity spectrum in the Drude model. ω_{cross} represents the angular frequency where the real and imaginary conductivity cross each other.[32] Reproduced from ref. 32.

structures, start to impose dominant effects on the randomized scattering events (Figure 4.3b). Accordingly, these free carrier responses significantly deviate from the typical Drude model. To interpret the strong localization caused by such charge confinement, a modified version of the Drude model, the Drude-Smith (DS) model, has been extensively used to understand the charge transport under spatial confinement.[31] The model reads Equation (4.10):

$$\sigma_{DS}(\omega) = \frac{\omega_p^2 \varepsilon_0 \tau_{DS}}{1-i\omega\tau_{DS}}\left(1+\frac{c}{1-i\omega\tau_{DS}}\right) \tag{4.10}$$

where a localization parameter c ($-1 \leq c \leq 0$) is introduced to describe the extent of effective confinement that limits the long-range transport. The parameter c can be seen as a measure for the fraction of electrons backscattered at the boundary (*i.e.*, backscattering effect) and thus is an indicator for the degree of charge carrier localization.[33] The exemplified frequency-resolved THz conductivity with different c values are shown in Figure 4.5. Regardless of the nanoparticle

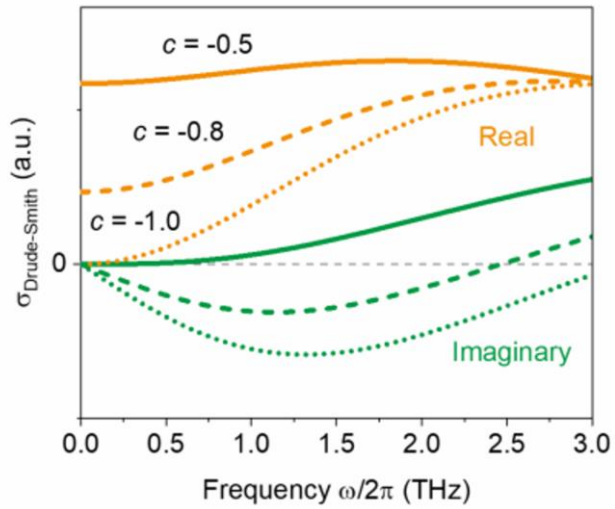


Figure 4.5: The THz conductivity spectrum in the Drude-Smith model. Three conditions with c = −0.5 (solid lines), c = −0.8 (dashed lines) and c = −1.0 (dotted lines) are plotted here as examples.[32] Reproduced from ref. 32.

shape, size and spatial distribution and orientation, many examples have successfully employed the Drude-Smith model as a basis for fitting the THz conductivity spectra.[34,35]

4.1.3 THz Properties of Carbon-Based Materials

In the past two decades, THz time-domain spectroscopy has been employed to explore the charge transport properties within individual nano-objects as well as over short distances among nanocrystals, owing to its high frequency and broadband characteristics. The following section centers on discussing how THz time-domain spectroscopy and optical-pump THz spectroscopy has been key in advancing the understanding of conductive response of carbon-based graphitic nanostructures.

Graphene is a single sheet of sp^2-hybridized carbon atoms forming a 2D hexagonal lattice, and it serves as the structural foundation from which all the other graphitic materials can be derived from.[36] The intrinsic electronic band structure of a graphene monolayer has been found to feature a completely filled valence band below zero energy (*i.e.*, Fermi level) and an empty conduction band above (Figure 4.6). These two bands meet each other at *K* and *K'* points (*i.e.*, the Dirac points), with an unusual linear energy-momentum dispersion. This unique band structure makes pristine graphene a gapless material, which contributes to graphene featuring, for example, wavelength-independent absorption over a wide range of optical frequencies and exceptionally high charge carrier mobilities reaching 2×10^5 cm^2/V·s.[36–38]

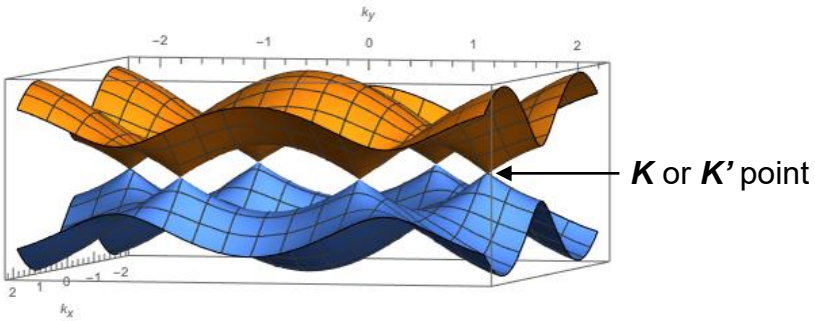


Figure 4.6: Electronic band structure of graphene.[39]

Graphene samples have been traditionally prepared through mechanical exfoliation from a piece of graphite, epitaxial growth on the surface of SiC substrate by thermal deposition and graphitization or chemical vapor deposition (CVD) on transition metal surfaces.[40–42] The production method would heavily alter their compositions, defects concentration and thereby the intrinsic charge carrier behavior and mobility. A variety of reports investigating exfoliated

graphite or epitaxial grown graphene confirm that the equilibrium conductivity of graphene is Drude-like in the low-frequency THz range, and dominated by intraband conductivity (*i.e.*, the conductivity arising from the charge carriers within a single band) with scattering times of 20 fs or shorter.[28,43,44] The optical-pump THz probe experiment performed by Winnerl *et al.* indicates that the conductivity of epitaxial grown graphene increases upon the photoexcitation as a result of increasing the free carrier density.[45] Comparable results well-described by the Drude model have been obtained with CVD-grown graphene.[46,47] For highly-doped graphene or graphene with high static carrier density, a decrease in conductivity was observed upon photoexcitation, which is related to an increased carrier scattering rate.[48,49] Recently, an optical-pump THz probe experiment performed with a gated CVD-grown single layer graphene by Tomadin *et al.* provided a comprehensive picture of ultrafast carrier dynamics and electron relaxation after optical photoexcitation (Figure 4.7).[50] With weak doping (E_F = 0.05 eV), the broadening of electron distribution after the photoexcitation involves electron transitions from valance to conduction bands (interband transitions, blue line). At high doping (E_F = 0.40 eV), intraband electronic transition, by promoting carriers from below E_F above, dominates the broadening (orange line).

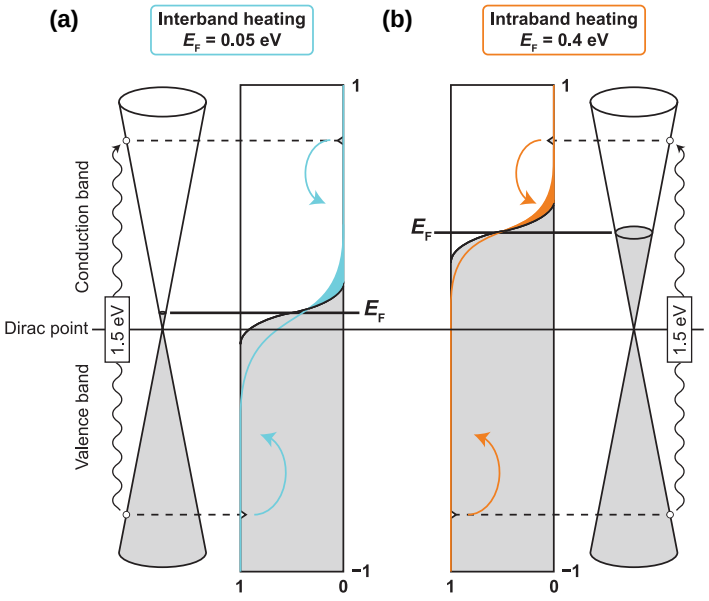


Figure 4.7: Scheme of the calculated Dirac cone and electron distribution as a function of energy level for the (a) weak doping with E_F = 0.05 eV and (b) strong doping with E_F = 0.40 eV. The gray level indicates occupation of states in equilibrium state (at t = 0 before photoexcitation) while the blue and orange lines and areas represent at t = 300 fs after the photoexcitation. From Tomadin *et al.*, *Sci. Adv.*, 2018, **4**, 1–11. Reprinted with permission from AAAS.[50]

Utilizing quantum confinement to induce a bandgap in graphene has led to the establishment of two types of one-dimensional graphene-based structures: carbon nanotubes (CNTs) and flat graphene nanoribbons (GNRs) with nanometer-scale widths (Figure 4.8). Both achieve carrier confinement in the lateral dimensions, where the movement of charge carriers within the other two dimensions is prohibited.

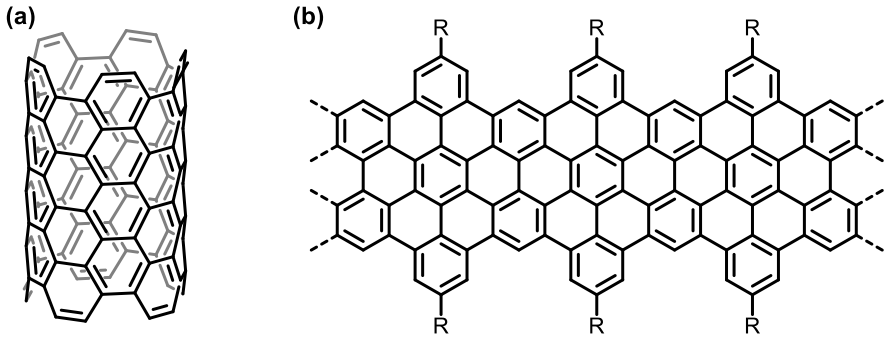


Figure 4.8: Exemplified chemical structures of representative one-dimensional carbon materials: (a) (5,5)-armchair single-wall carbon nanotube and (b) chemically precise graphene nanoribbons.[51,52]

Depending on the rolling directions, CNTs can either show metallic conductivity or be semiconducting with controlled band gap.[53] Although the charge transport behavior of CNTs have been investigated more extensively than for graphene, there is still no widely accepted conclusion about the THz response of CNTs. Experimental results have recorded that the CNTs have the charge carriers that can be simply described by the Drude model, or gave a very localized response, or showed typical Drude-Smith photoconductivity.[54–56] In reality, the current fabrication methods limit the exploration of the THz response of individual types of CNT, with signals often complicated by the variations in length, chirality, doping levels, orientations and alignment of the CNTs.

Regarding GNRs, the development of chemical "bottom-up" synthesis allows the fabrication of GNRs with bandgap energies corresponding to visible excitation wavelengths, as well as well-defined length, width, and edge structures (Figure 4.8b). The in-solution synthetic strategy has significant advantages in terms of scalability and processability. This method provides access to several GNRs with high dispersibility, facilitating the characterization of their charge carriers through THz spectroscopy.[52,56–59] Charges in GNRs are often mobilized through photoexcitation and THz spectroscopy assesses the photoconductivity and recombination dynamics of those photo-generated charge carriers. Examples of time- and frequency-resolved THz spectra of the complex photo-induced conductivity of GNR (Figure 4.8b) are shown in Figure 4.9.[52] Along with the pump-probe delay time, time-resolved THz conductivity normally

shows a trend where a fast rise after the photoexcitation (sub-ps) and a subsequent rapid decay within a characteristic lifetime in both real and imaginary parts, indicating the generation of free carriers and carrier trapping and/or exciton formation processes, respectively (Figure 4.9a).[58–61] The frequency-resolved complex photoconductivity commonly presents positive real and negative imaginary components, both of which increase in absolute value with frequency (Figure 4.9b). Such THz responses obtained from GNRs are commonly in strong agreement with the Drude-Smith model.

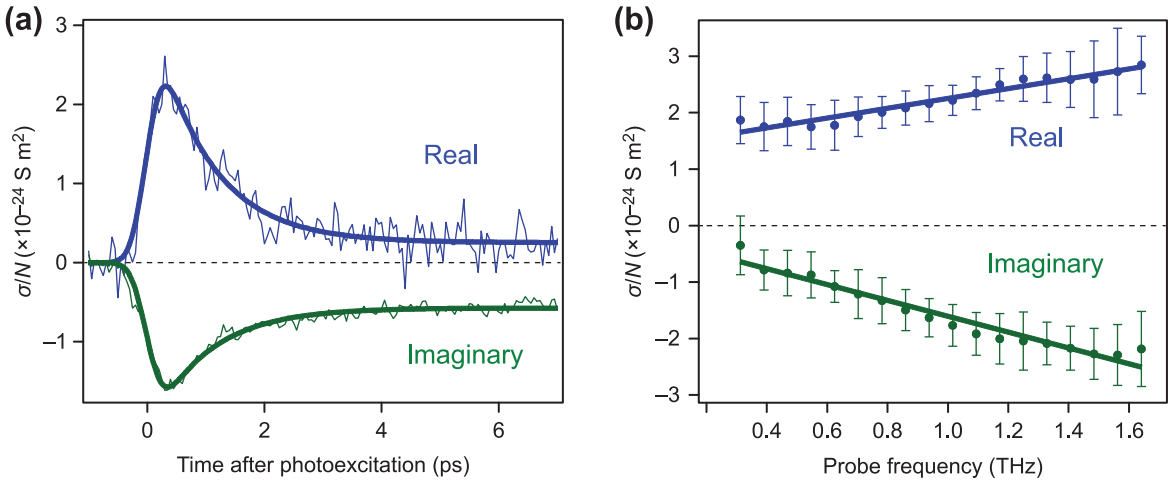


Figure 4.9: (a) Example of time-resolved real and imaginary components of complex photoconductivity dynamics of GNRs. (b) Example of frequency-resolved real and imaginary components of complex photoconductivity dynamics photoconductivity of GNRs. Reproduced with permission.[52]

4.1.4 Project Aim

Triply fused porphyrin oligomers (termed porphyrin nanoribbons in this chapter) have high structural similarity to GNR heterostructures. The strong electronic coupling between neighboring porphyrin units makes them highly conductive compared to *meso–meso* singly-linked porphyrin oligomers.[62–65] The steep narrowing in HOMO-LUMO gaps as the porphyrin oligomer length elongates also renders a unique length-independent conductance decay in their single-molecule conductance studies.[66,67] However, charge carrier properties of solely porphyrin-based materials in the THz frequency range have not yet been investigated. The closest nanostructure that has been studied so far is the solution-phase synthesized porphyrin-fused graphene hybrid nanoribbons (PGNRs) reported by the Anderson group recently (Figure 4.10).[68] For these PGNRs with average length of ~85 nm ($\overline{N}$ = 34), THz spectroscopy reveals that they exhibit a longer scattering time (~50 fs) compared to most pure carbon-based GNRs

(~30 fs) and a one of the highest intrinsic charge carrier mobilities (450 ± 60 $cm^2/V{\cdot}s$) among the reported GNRs characterized by THz spectroscopy.[52,56–59]

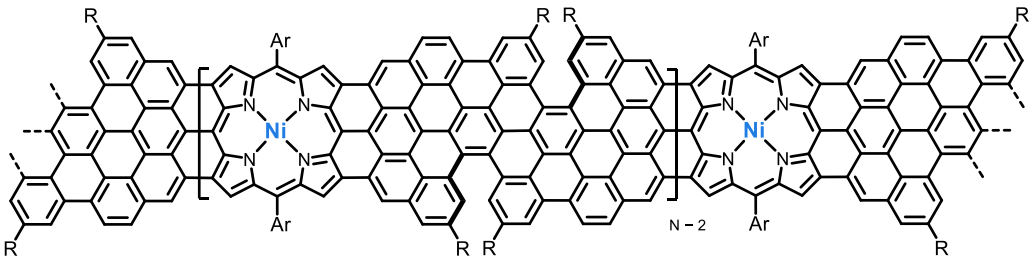


Figure 4.10: Porphyrin-fused graphene hybrid nanoribbon (PGNRs) of which the charge carrier mobility has been studied using THz spectroscopy.[68]

This project aims to assess the potential of porphyrin nanoribbons for optoelectronics by evaluating their charge carrier behavior from their THz photoconductivity. Two groups of triply fused porphyrin oligomers respectively possessing Zn(II) or Ni(II) ion metal centers (Figure 4.11) are selected. We decided to prepare polydisperse porphyrin materials for this study for the following reasons: 1) to simplify the material preparation process to a one-step oligomerization reaction from single initial material; and 2) to estimate the length of formed oligomers from the corresponding gel permeation chromatography (GPC) retention time. The latter allows the isolation of several batches of materials with different lengths from a one-pot synthesis and exploring whether their charge transport behavior displays any oligomer-length dependence. In this chapter, we explore the efficient oligomerization conditions to form long *meso–meso* singly-linked porphyrin oligomers (~20 nm, $\overline{N}$ ~ 25) and test a variety of the oxidation conditions required by porphyrins with different metal centers to achieve the complete fusion. After the synthesis, charge transport properties are examined by the contact-free, ultrafast optical-pump THz probe spectroscopy.

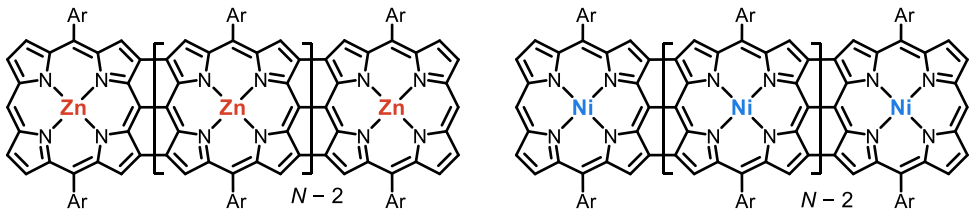


Figure 4.11: Structures of the targeted triply fused porphyrin oligomers.

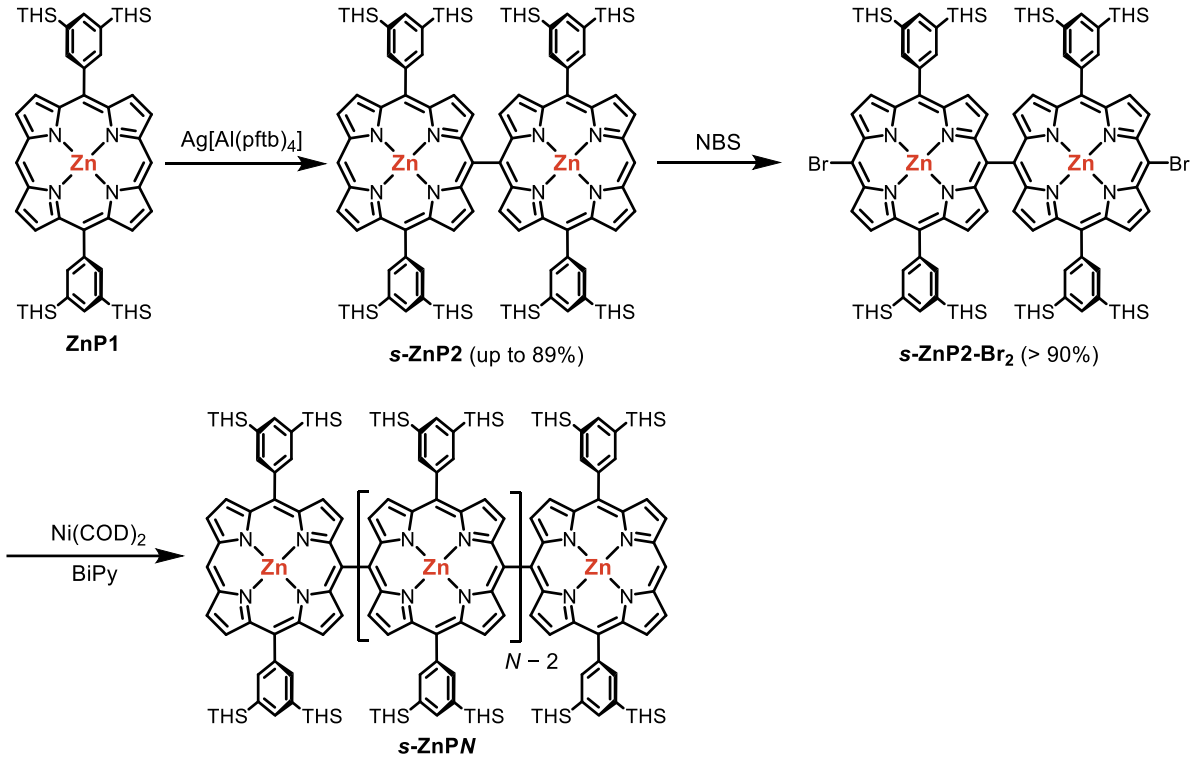
4.2 Synthesis of Polydisperse Porphyrin Nanoribbons

The extension of triply fused porphyrin structures is often limited by their instability, reduced solubility and an increased tendency to aggregate. Therefore, to address these factors, 3,5-

bis(trihexylsilyl)phenyl (termed THS group from this point forward) and the previously developed bulky **ArHex** group (Scheme 3.7 in Chapter 3) were chosen as solubilizing groups on Zn(II) and Ni(II) porphyrins, respectively. To obtain the long *meso-meso* singly-linked porphyrin oligomer precursors, the approach requires bulk preparation of initial building blocks with high yield and optimal conditions for efficient Yamamoto polymerization.

4.2.1 Synthesis of Zn(II) Porphyrin Nanoribbons

Zn(II) porphyrins have relatively low-oxidation potentials and they have been demonstrated to require milder fusion conditions than Ni(II) porphyrins.[69,70] Therefore, the THS group was selected to synthesize Zn(II) porphyrin oligomers ***s*-ZnP*N*** (Scheme 4.1), with the aim of addressing solubility and aggregation challenges.



Scheme 4.1: Synthetic route towards ***s*-ZnP*N***.

PIFA, $PhI(O_2CCF_3)_2$ can mediate the singly oxidative homocoupling of Zn(II) porphyrin monomers at *meso*-positions rather than yielding the triply fused product, by precisely controlling the relative quantities of reagents and temperature.[71] However, the trial reaction on **ZnP1** (Scheme 4.1) proved that PIFA failed to yield long oligomers when the side aryl groups of porphyrin are THS groups. This lack of reactivity can be explained by the steric bulkiness of THS side chains. A similar steric effect has also been noticed when applying $AgPF_6$

as the oxidant on **ZnP1**, where the oligomerization required longer reaction time to access ***s*-ZnP*N*** and only yielded products with $N < 10$.

$Ag[Al(pftb)_4]$(pftb = perfluoro-*tert*-butoxy, $OC(CF_3)_3$) has been found capable of selectively dimerizing **ZnP1** to ***s*-ZnP2** in over 80% yield under ambient conditions, instead of forming longer oligomers ($N > 4$).[72] Moreover, ***s*-ZnP2** can be brominated by *N*-bromosuccinimide to afford ***s*-ZnP2-Br$_2$**, ready to oligomerize through Ni-mediated Yamamoto coupling (Scheme 4.1). Such a selective dimerization facilitates the formation of ***s*-ZnP*N*** with a higher degree of polymerization by extending the building unit. The $Ag[Al(pftb)_4]$ salt was prepared through reported conditions.[73] The yielded ***s*-ZnP2** from the dimerization was isolated using recycling GPC on a gram scale. $Ni(COD)_2$ was utilized in the subsequent oligomerization reaction of ***s*-ZnP2-Br$_2$**. To optimize the efficiency of Yamamoto coupling, a set of conditions with a variation of solvents, quantities of $Ni(COD)_2$, and addition of extra ligands (2,2'-bipyridine, BiPy) were investigated (Table 4.1).[74]

Table 4.1: List of ***s*-ZnP2** oligomerization conditions and their respective outcomes.

Entry	Solvents	$Ni(COD)_2$	BiPy	Outcome
1	THF/DMF (1:1)	20 eq.	-	Low degree of oligomerization up to ***s*-ZnP8**
2	Tol/DMF (1:1)	20 eq.	-	***s*-ZnP2** (>90%), trace amount of ***s*-ZnP4**
3	THF	20 eq.	-	***s*-ZnP2** (>90%), trace amount of ***s*-ZnP4**
4	DMF	12 eq.	-	Moderate degree of oligomerization to ***s*-ZnP*N*** ($N_{max} \sim 12$)
5	DMF	15 eq.	-	High degree of oligomerization to ***s*-ZnP*N*** ($N_{max} > 20$)
6	DMF	20 eq.	-	High degree of oligomerization to ***s*-ZnP*N*** ($N_{max} > 20$)
7	DMF	20 eq.	20 eq.	High degree of oligomerization to ***s*-ZnP*N*** ($N_{max} > 40$)

N_{max} refers to the maximum number of repeating units in the oligomer according to MALDI-ToF MS analysis.

Regarding solvent selection, while both THF and toluene are good solvents for ***s*-ZnP2-Br$_2$** under ambient conditions, Yamamoto coupling appeared to progress poorly in

them (Table 4.1, entries **1**–**3**). Short oligomers were formed due to severe debromination (as indicated by MALDI-ToF MS analysis), causing the rapid termination of the oligomerization reaction. Running the reaction in neat DMF successfully afforded ***s*-ZnP*N*** with a moderate to high degree of oligomerization. The solubility of ***s*-ZnP2-Br$_2$** in DMF is poor at room temperature, but it improves after heating to 50 °C, with all reagents being fully dissolved after stirring for 10 min. As the reaction progressed, a color change from green to brown was noted. Upon cooling to room temperature, a brown-colored product precipitated out from the solution, which could then be redissolved by the addition of dichloromethane.

An investigation was also made into the effect of Ni(COD)$_2$ quantities on the oligomerization reaction. Analytical GPC was used to monitor the variation among reactions using 12, 15 and 20 equivalents of Ni(COD)$_2$. The results suggested that the impact from Ni(COD)$_2$ quantity on coupling efficiency appears to saturate at 15 equivalents. Beyond this threshold, further addition of Ni(COD)$_2$ had negligible effect on the extent of oligomerization (Table 4.1, entries **4**–**6**). In contrast, the addition of BiPy (entry **7**) was found to markedly enhance the oligomerization efficiency, yielded a batch of long ***s*-ZnP*N*** with oligomers reaching a maximum number of repeating units N_{max} over 40 (as indicated by the MALDI-ToF MS analysis).[74] The material obtained from this last batch was thus taken for further purification.

The crude sample was first subjected to recycling GPC to remove the short oligomers ($N < 10$). Then the longer oligomers were resubmitted to recycling GPC to separate them into three different length sets based on the relative retention time (Figure 4.12, isolated yields in ascending order of length: ***s*-ZnP*N*(1)** (12%), ***s*-ZnP*N*(2)** (5%) and ***s*-ZnP*N*(3)** (4%)). The terminal groups of all samples are free *meso*-protons (as indicated by MALDI-ToF MS analysis), which may intermolecularly cross-couple with other oligomers under the fusion conditions. In order to prevent this and represent the molecular weight distribution of the final fused product by using that of singly-linked oligomers, terminal capping groups are required. One straightforward method of capping is brominating the terminal *meso*-protons. The viability of the final fusion reaction was tested with ***s*-ZnP*N*(1)-Br$_2$**, which was obtained quantitatively from the shortest oligomer ***s*-ZnP*N*(1)** (Scheme 4.2). Either Sc(OTf)$_3$/DDQ or PIFA were chosen as the oxidants to mediate the fusion reaction, and the reaction progress was monitored by UV−vis−NIR spectroscopy.[69,70] However, surprisingly neither of the reaction products using

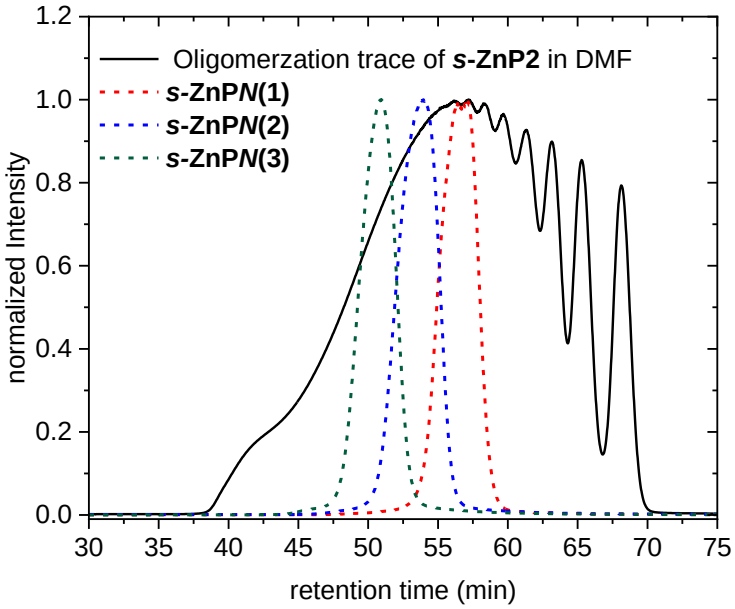
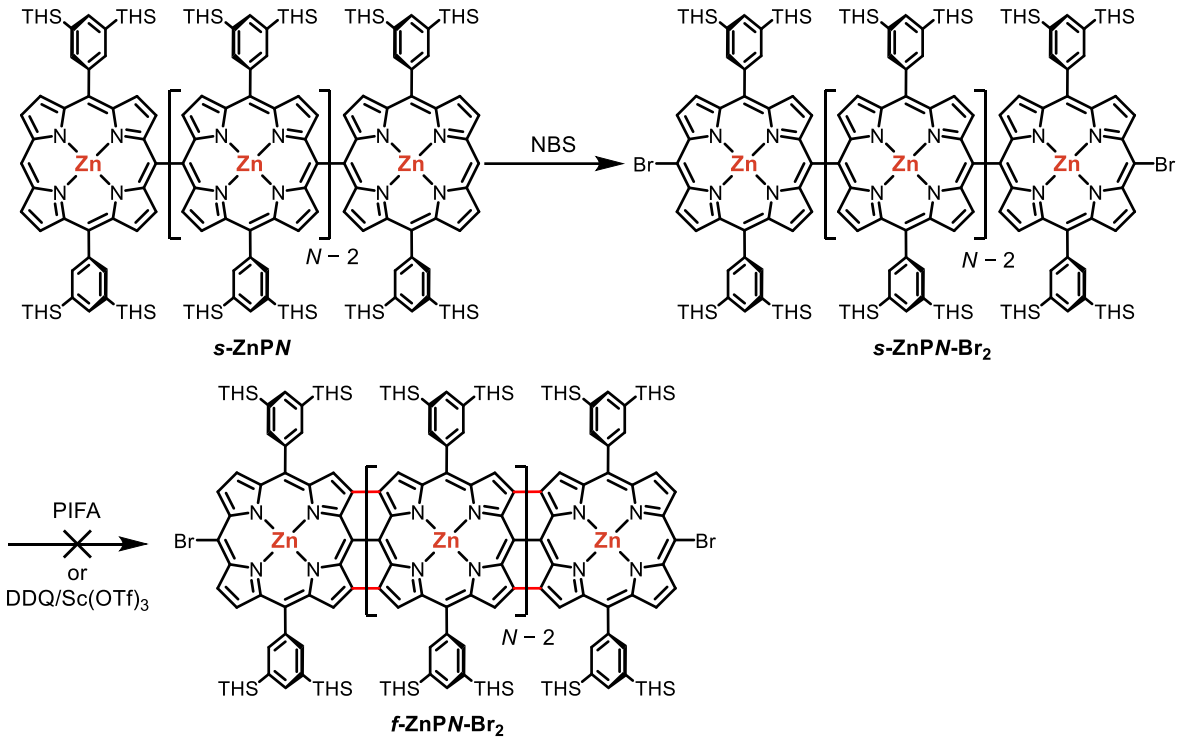


Figure 4.12: Recycling GPC traces of three batches of Zn(II) porphyrin oligomers (***s*-ZnP*N*(1)** (red), ***s*-ZnP*N*(2)** (blue) and ***s*-ZnP*N*(3)** (green)) compared with the crude reaction mixture.



Scheme 4.2: Synthetic route towards ***f*-ZnP*N*-Br$_2$**.

these oxidants displayed a second-Soret band absorption peak (Figure 4.13), as would be expected for the corresponding fully fused species (expected to occur around 800–1000 nm).[75] One explanation is that the terminal bromo-groups retain high reactivity, resulting in unidentified side-reactions with oxidants, rather than the formation of C–C bonds in between porphyrins at β-positions.[76]

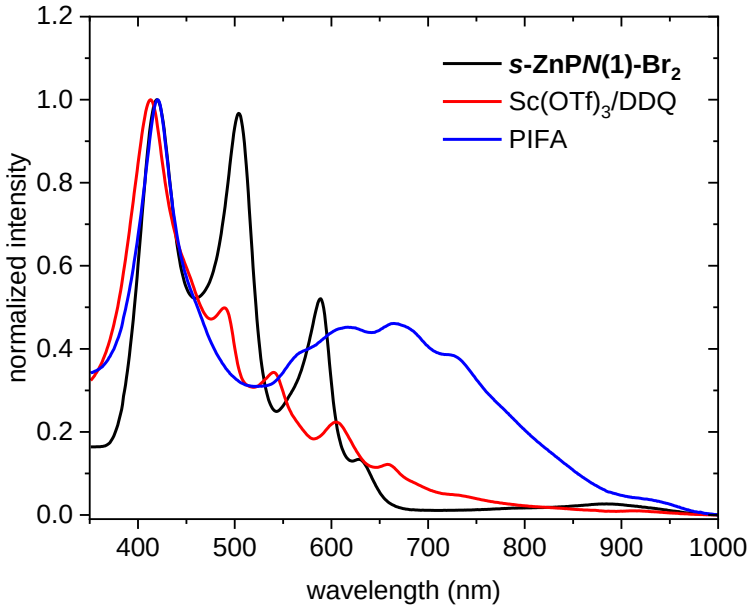


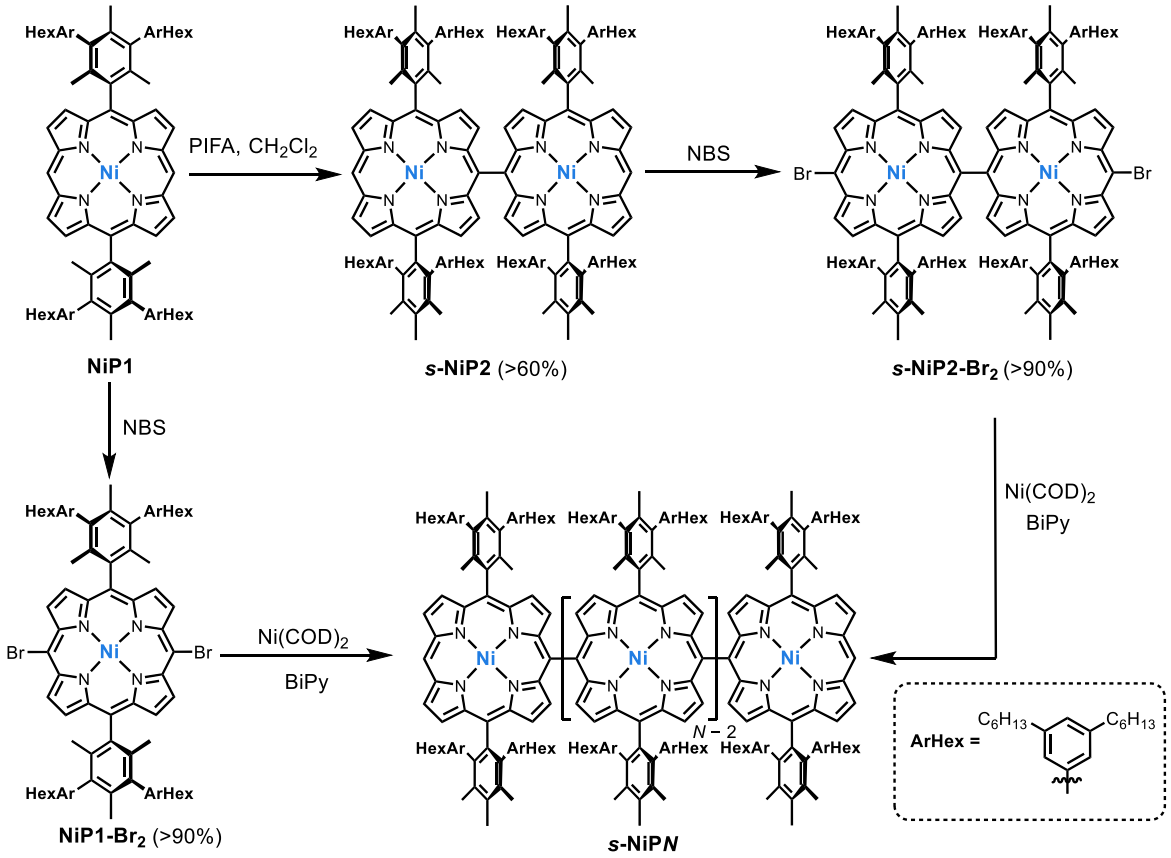
Figure 4.13: UV–vis–NIR absorption spectra of the ***s*-ZnP*N*(1)-Br$_2$**, compared with two spectra of resulted product obtained using either Sc(OTf)$_3$/DDQ (red) or PIFA (blue) as the oxidants, respectively.

Phenylating (by treating with phenyllithium, PhLi) the terminal *meso*-protons of the porphyrin oligomers was also investigated for ***s*-ZnP*N*(1)**. After the addition of a substantial excess of PhLi, central Zn(II) ions of porphyrins were mostly demetallated as expected, along with the desired terminal substitutions. Due to the high molecular weight and broad polydispersity of the oligomers, it proved challenging to determine the completion of phenylation and the process of Zn(II) ion reinsertion by MALDI-ToF MS. The peaks observed in the mass spectra became broader, indicating a complex mixture arising from the removal and reinsertion of varying numbers of Zn(II) ions in the porphyrin oligomers. Due to these unexpected problems encountered in both approaches, it was not possible to obtain long Zn(II) porphyrin nanoribbons on the timescale of this thesis.

4.2.2 Synthesis of Ni(II) Porphyrin Nanoribbons

Similar to the route towards **s-ZnP*N***, the synthesis of Ni(II) porphyrin oligomers ***s*-NiP*N*** was planned to start from ***s*-NiP2-Br$_2$** (Scheme 4.3). Owing to their electron deficiency, Ni(II) porphyrins have higher oxidation potential than Zn(II) porphyrins. This implies the need for more stringent oxidation conditions in the final fusion step. For this reason, the bulky and robust **ArHex** group was selected as the aryl groups for porphyrins (Scheme 4.3). The dimerization of Ni(II) porphyrin monomer **NiP1** was tested using Ag[Al(pftb)$_4$] salt or PIFA as the oxidant. With the former, unfortunately, the reaction returned predominantly starting

material, and only a trace amount of Ni(II) porphyrin dimer ***s*-NiP2**. In contrast, PIFA-mediated oxidative homocoupling, by treating **NiP1** with 0.5 equivalents of PIFA, ***s*-NiP2** was isolated in 30% yield after 2 h, with high recovery of unreacted monomers. Through a couple of iterations of resubmitting the recovered monomers to the same reaction conditions, the overall yield of ***s*-NiP2** could be improved to 60%. However, compared to the efficiency of the Ag-mediated dimerization of **ZnP1**, this yield remains relatively low. Considering this more intricate synthetic route towards ***s*-NiP2**, the oligomerization conditions were then optimized employing both Ni(II) porphyrin monomer and dimer (Scheme 4.3).



Scheme 4.3: Synthetic routes towards **s-NiP*N*** started from Ni(II) porphyrin monomer and dimer.

NiP1-Br$_2$ and ***s*-NiP2-Br$_2$** were afforded quantitatively from the corresponding starting material, ready for the following Ni-mediated Yamamoto coupling (Scheme 4.3). All the test reactions were carried out with 20 equivalents of Ni(COD)$_2$. Both **NiP1-Br$_2$** and ***s*-NiP2-Br$_2$** showed extremely low solubility in DMF, even after the reaction was heated up to 70 °C. The oligomerization solely returned starting materials after stirring overnight (Table 4.2, entries **1** and **2**). To address the solubility issue, the subsequent attempts used either THF or THF/DMF (1:3) mixture as the solvent for the coupling reactions, in which the starting materials displayed

Table 4.2: List of **NiP1** and ***s*-NiP2** oligomerization conditions and their respective outcomes.

Entry	Solvents	Precursor	BiPy	Outcome
1	DMF	**NiP1-Br$_2$**	-	No oligomerization
2	DMF	***s*-NiP2-Br$_2$**	-	No oligomerization
3	THF	**NiP1-Br$_2$**	-	Low degree of oligomerization to ***s*-NiP*N*** (N_{max} ~ 8)
4	THF	***s*-NiP2-Br$_2$**	-	Low degree of oligomerization to ***s*-NiP*N*** (N_{max} ~ 14)
5	THF/DMF (1:3)	**NiP1-Br$_2$**	-	Low degree of oligomerization to ***s*-NiP*N*** (N_{max} ~ 8)
6	THF/DMF (1:3)	***s*-NiP2-Br$_2$**	-	High degree of oligomerization to ***s*-NiP*N*** (N_{max} > 30)
7	THF/DMF (1:3)	**NiP1-Br$_2$**	20 eq.	High degree of oligomerization to ***s*-NiP*N*** (N_{max} > 20)
8	THF/DMF (1:3)	***s*-NiP2-Br$_2$**	20 eq.	High degree of oligomerization to ***s*-NiP*N*** (N_{max} > 40)

N_{max} refers to the maximum number of repeating units in the oligomer according to MALDI-ToF MS analysis.

improved solubility at room temperature. Similar to the results obtained from the oligomerization of Zn(II) porphyrins, reactions conducted in neat THF (entries **3** and **4**) could only yield short oligomers, regardless of whether starting from the porphyrin monomer or dimer. With the mixed solvent system, initially this condition did not appear promising, since for the reaction of **NiP1-Br$_2$** (entry **5**) returned a similar oligomer distribution as using THF. Surprisingly, ***s*-NiP2-Br$_2$** demonstrated a high oligomerization efficiency in such solvent environment (entry **6**) and Ni(II) porphyrin oligomers ***s*-NiP*N*** with N_{max} over 30 were yielded. In addition, similar to the formation of long ***s*-ZnP*N***, the presence of BiPy has played a crucial role in facilitating the oligomerization of Ni(II) porphyrins – the reaction starting from **NiP1-Br$_2$** (entry **7**) afforded ***s*-NiP*N*** with N_{max} over 20 and, and when started from ***s*-NiP2-Br$_2$** (entry **8**), ***s*-NiP*N*** with N_{max} over 40 could be obtained.

However, it should be noted that the reproducibility of these conditions heavily depends on the oxygen content in the reaction vessel and the quality of Ni(COD)$_2$. This can be seen in Figure 4.14, where *Reaction **1**, **2*** and ***3*** started under the same initial conditions (Table 4.2, entry **8**) but offered oligomers in three different length ranges. In this case, three batches of long Ni(II) porphyrin oligomers ***s*-NiP*N*(1)** (50%), ***s*-NiP*N*(2)** (67%) and ***s*-NiP*N*(3)** (68%) with

different lengths (in ascending order) were isolated from these three oligomerization reactions (Figure 4.15). To prevent the cross-coupling between oligomers in the next fusion step, three batches of ***s*-NiP*N*** were brominated to their corresponding ***s*-NiP*N*(1)-Br$_2$**, ***s*-NiP*N*(2)-Br$_2$** and ***s*-NiP*N*(3)-Br$_2$** (Scheme 4.4), which was identified by the disappearance of free *meso*-proton signals in the ^{1}H NMR spectra.

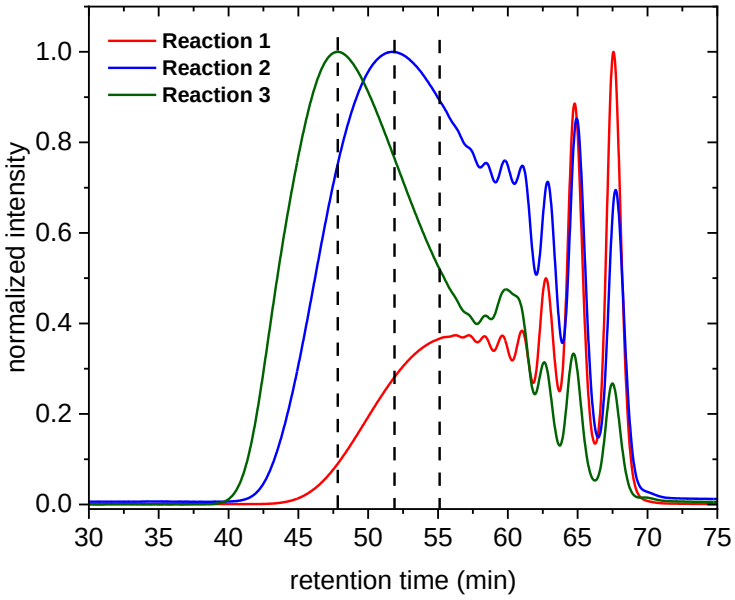


Figure 4.14: Recycling GPC traces of three oligomerization reactions started from ***s*-NiP2-Br$_2$** under the same reaction conditions (*Reaction **1*** (red), *Reaction **2*** (blue) and *Reaction **3*** (green)).

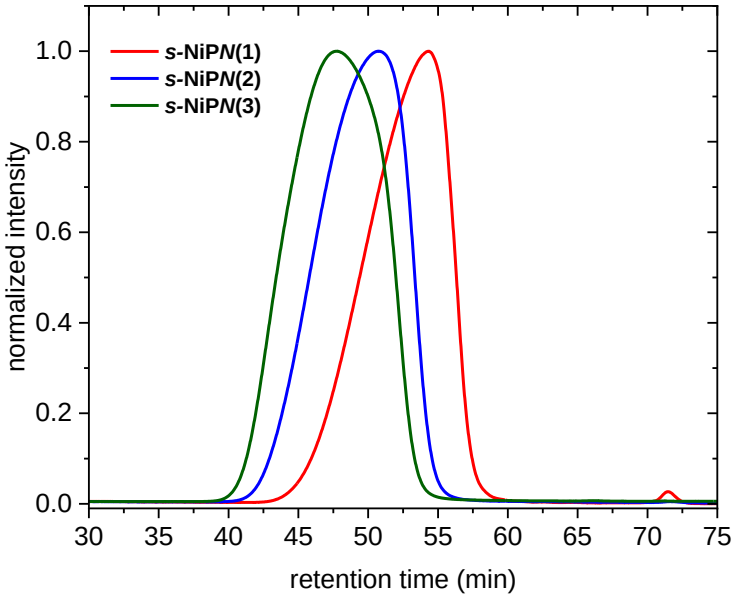
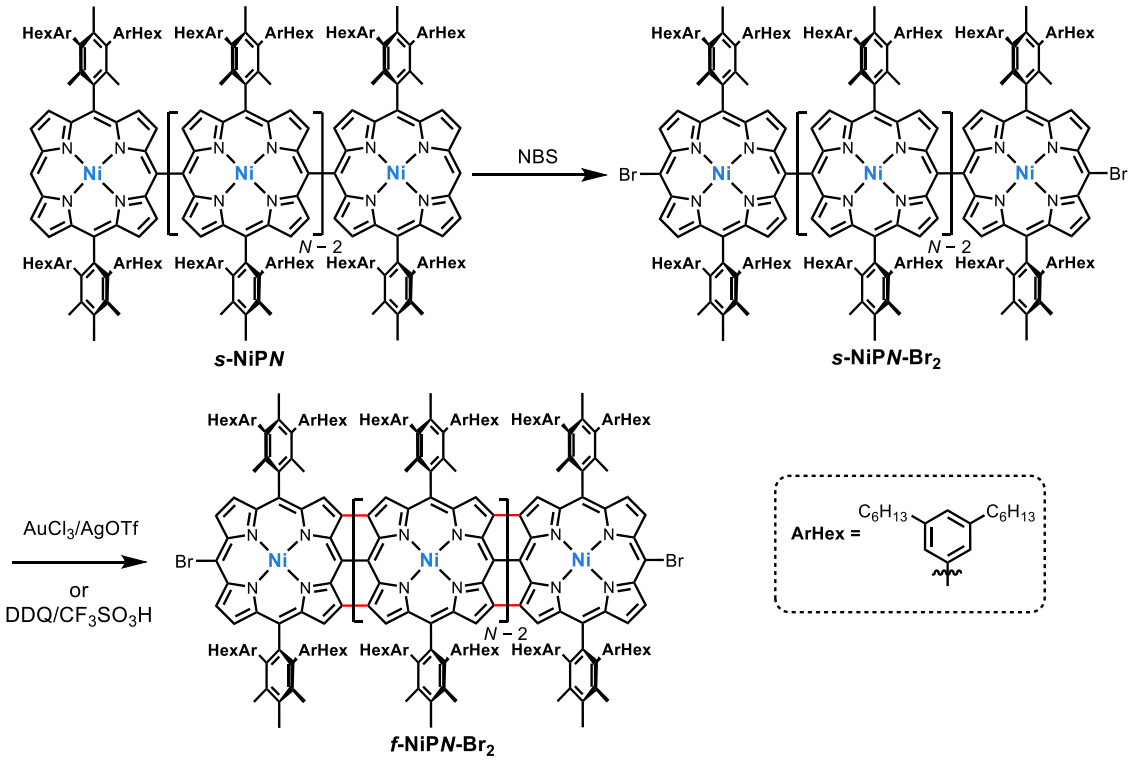


Figure 4.15: Recycling GPC traces of three individual batches of Ni(II) porphyrin oligomers isolated from *Reaction **1**, **2*** and ***3***, respectively. (***s*-NiP*N*(1)** (red), ***s*-NiP*N*(2)** (blue) and ***s*-NiP*N*(3)** (green)).



Scheme 4.4: Synthetic route towards ***f*-NiP*N*-Br$_2$**.

It was reported that when using $AuCl_3$/AgOTf as the oxidants, dibrominated *meso-meso* singly-linked Ni(II) porphyrin dimer, tetramer, hexamer and octamer can be readily converted to the corresponding fused products.[72,77] In Chapter 3, we have also demonstrated that Ni(II) porphyrin with **ArHex** side-aryl group can remain stable in harsh TfOH/DDQ fusion condition. Hence, here we adopted both conditions and compared their efficiency on synthesizing fused Ni(II) porphyrin oligomers ***f*-NiP*N*-Br$_2$** (Scheme 4.4). Firstly, fusion reactions of ***s*-NiP*N*-Br$_2$** using $AuCl_3$/AgOTf were attempted in dichloromethane under ambient conditions. The oxidant was added in small portions and the progress of the fusion reaction was monitored by UV–vis–NIR spectroscopy. As an example, Figure 4.16 presents the fusion progress of ***s*-NiP*N*(1)-Br$_2$**. As the reaction progressed, a significant change in spectral form and a bathochromic shift of maximum absorption peak were concurrently observed. When there was no significant change in spectral form between traces with further addition of oxidant (*e.g.*, the green trace and orange trace in Figure 4.16, recorded 5 min apart) the reaction was deemed complete. The resulting mixture was precipitated by the addition of methanol, and a dark solid was collected by filtration. The filtrate was washed with methanol and UV–vis–NIR absorption spectra were recorded after redissolving the sample in toluene (Figure 4.17). The

change in the signal intensity around 400 nm suggested the successful removal of residual impurities after washing.

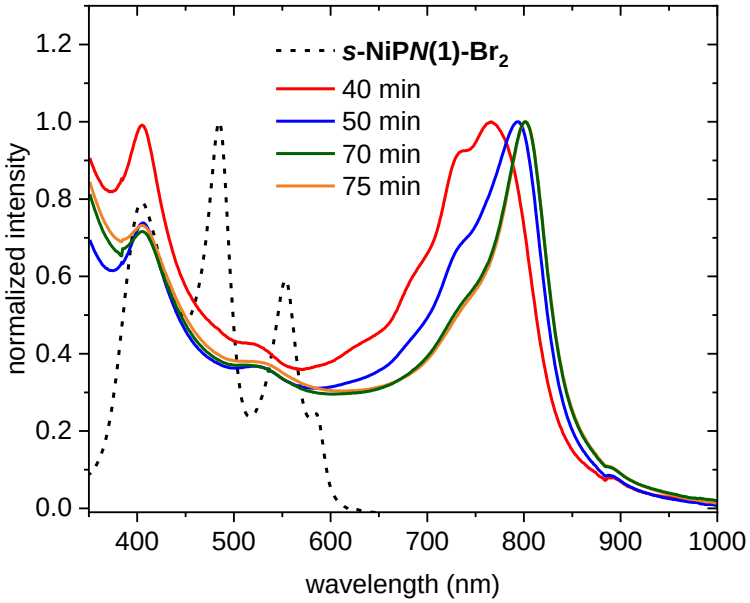


Figure 4.16: UV–vis–NIR absorption spectra in dichloromethane (1% triethylamine) monitoring the fusion of ***s*-NiP*N*(1)-Br$_2$**.

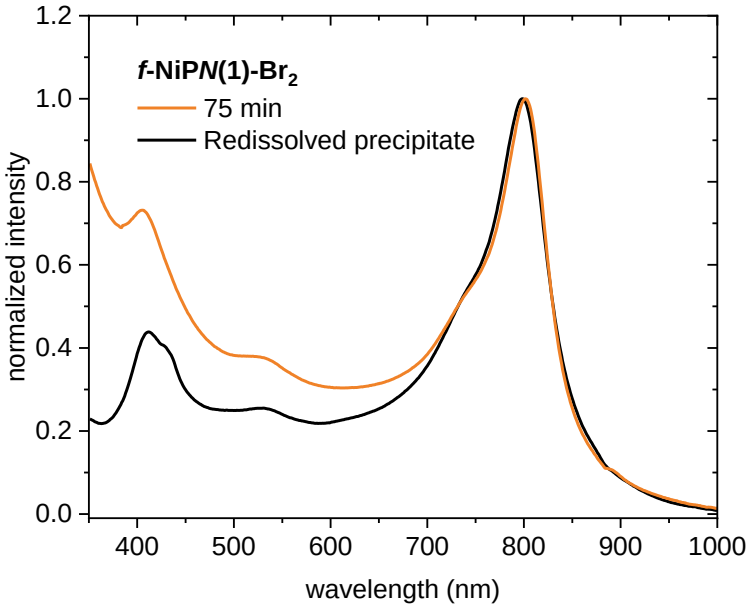


Figure 4.17: Comparison of the UV–vis–NIR absorption spectra of ***s*-NiP*N*(1)-Br$_2$** (in dichloromethane) before (orange) and after (black) washing the fused product with methanol.

By contrast, when subjecting ***s*-NiP*N*(1)-Br$_2$** to the TfOH/DDQ fusion conditions, UV–vis–NIR absorption spectra initially suggested that the fused product had formed. However, the reduced DDQ side-product and some unidentified impurities could not be removed by precipitation and washing (as evidenced by an unexpected absorption peak occurring at around 400 nm, Figure 4.18). Considering the low solubility of the fused product and the benefits of tracking the reaction process via UV–vis–NIR spectroscopy by using

$AuCl_3$/AgOTf, we opted for this system as the oxidant to prepare the longer ***f*-NiP*N*(2)-Br_2** and ***f*-NiP*N*(3)-Br_2** porphyrin nanoribbons.

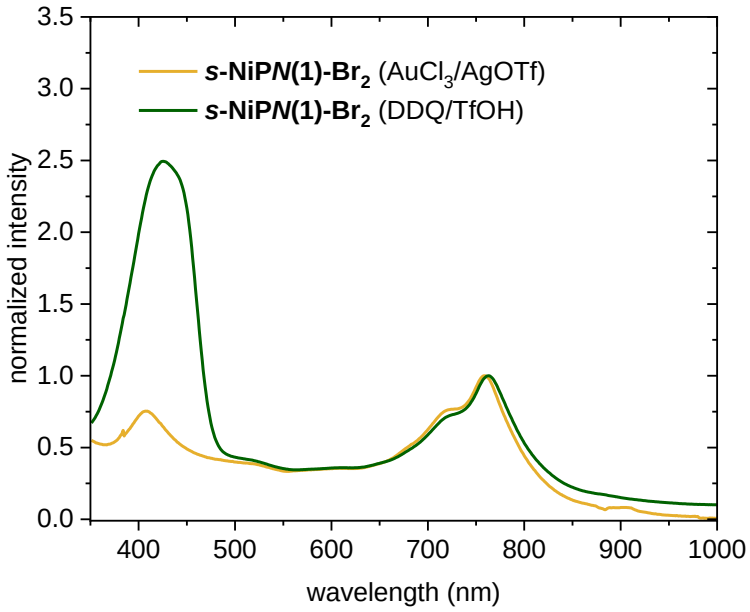


Figure 4.18: UV–vis–NIR absorption spectra of fusion products from ***s*-NiP*N*(1)-Br_2** (in dichloromethane) obtained using either $AuCl_3$/AgOTf (yellow) or DDQ/TfOH (green) as the corresponding oxidants.

In order to evaluate the reduction of the HOMO–LUMO gap caused by the extension of the fused porphyrin structure, the absorption spectra into the mid-infrared (MIR) range for all three samples were recorded. We initially attempted to measure the absorption spectra in solution (*e.g.*, in toluene-d_8, dichloromethane/CS_2 or 1,2-dichlorobenzene), but realized that an undesired distortion of the spectra was present. This was caused by the strong vibrational overtone of solvents in NIR region. Therefore, instead, we prepared drop-casting thin films on CaF_2 substrates using toluene solutions of the fused porphyrins and successfully recorded the UV–vis–NIR–MIR spectra using those samples (Figure 4.19). ***f*-NiP*N*(1)-Br_2**, ***f*-NiP*N*(2)-Br_2** and ***f*-NiP*N*(3)-Br_2** display an intense maximum absorption band at 2178, 2222 and 2276 nm, respectively. The spectra were normalized according to the intensity of this peak for each sample, and this presented a clearer comparison of the electronic structure change as the fused porphyrin structure getting longer. The observed red-shifting trend of the maximum absorption peak indicates the narrowing of HOMO–LUMO energy gap, anticipated with the extension of the conjugated fused structure.

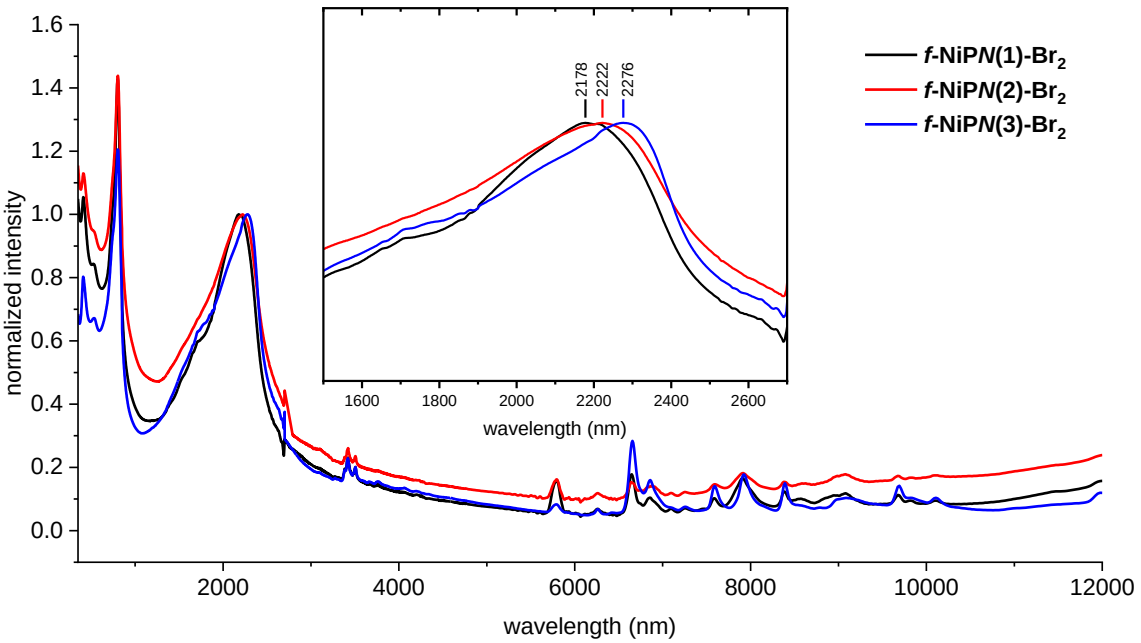


Figure 4.19: UV–vis–NIR–MIR absorption spectra of three Ni(II) porphyrin nanoribbons. (***f*-NiP*N*(1)-Br$_2$** (black), ***f*-NiP*N*(2)-Br$_2$** (red) and ***f*-NiP*N*(3)-Br$_2$** (blue)); Insert: Zoomed-in presentation of peaks around 2200 nm to compare the changes of the maximum absorption peak along with the elongation of the fused porphyrin structure.

4.2.3 Length Characterization of Porphyrin Nanoribbons

Since the terminals of singly-linked Ni(II) porphyrin oligomer precursors were protected by the bromo-group before the fusion reaction, the length of porphyrin nanoribbons could be represented by the length of ***s*-NiP*N***. The length and the distribution of average molecular weight for ***s*-NiP*N*** were estimated using GPC referenced to two types of standards: *Method 1*: polystyrene (narrow dispersity Đ < 1.10) or; *Method 2*: the corresponding discrete porphyrin oligomers (**NiP1**, ***s*-NiP2**, ***s*-NiP4**, ***s*-NiP6**, ***s*-NiP8**, ***s*-NiP10**, ***s*-NiP12** and ***s*-NiP16**). Using *Method 1*, the number-average (M_n) and weight-average (M_w) molecular weights of three samples were automatically calculated and are summarized in Figure 4.20. The M_n and polydispersity ($Đ$) were found to be 23.8 kDa (number-average repeating units $\overline{N}$ = 15, $Đ$ 1.08) for ***s*-NiP*N*(1)**, 42.2 kDa ($\overline{N}$ = 26, $Đ$ 1.21) for ***s*-NiP*N*(2)** and 57.7 kDa ($\overline{N}$ = 36, $Đ$ 1.39) for ***s*-NiP*N*(3)**, respectively.

With respect to the calibration using discrete porphyrin samples (*Method 2*), the linear fit of data points gave a reasonable estimation of the correlation between molecular weight and GPC retention time (R^2 = 0.99858, Figure 4.21). The M_n and $Đ$ determined from this method are 47.8 kDa ($\overline{N}$ =30, $Đ$ 1.22) for ***s*-NiP*N*(1)**, 76.7 kDa ($\overline{N}$ = 48, $Đ$ 1.2) for ***s*-NiP*N*(2)** and

100.5 kDa ($\bar{N}$ = 63, $Đ$ 1.19) for ***s*-NiP*N*(3)**, respectively. The length of ***s*-ZnP*N*(1)**, ***s*-ZnP*N*(2)** and ***s*-ZnP*N*(3)** were also characterized using this calibration with discrete Ni(II) porphyrin oligomers (summarized in Figure 4.22). The M_n and $Đ$ determined to be 24.1 kDa ($\bar{N}$ =14, $Đ$ 1.03) for ***s*-ZnP*N*(1)**, 38.0 kDa ($\bar{N}$ = 23, $Đ$ 1.04) for ***s*-ZnP*N*(2)** and 58.3 kDa ($\bar{N}$ = 35, $Đ$ 1.03) for ***s*-ZnP*N*(3)**, respectively.

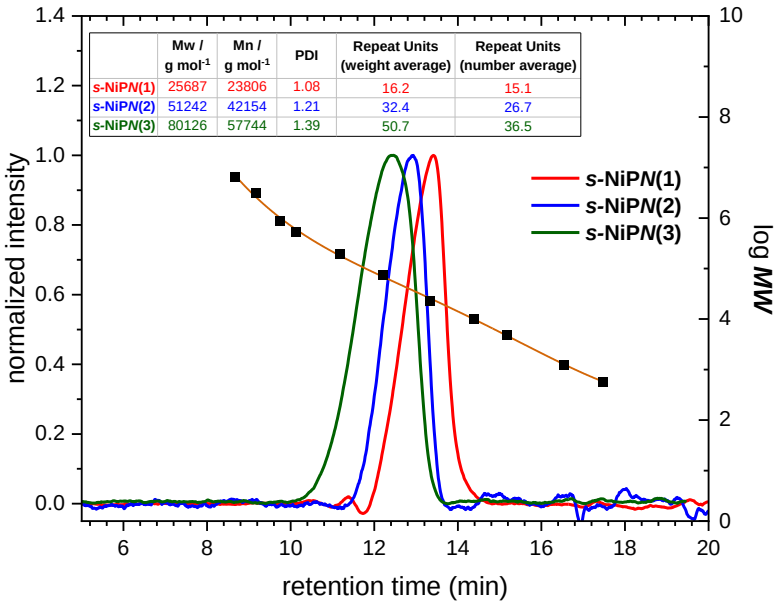


Figure 4.20: GPC traces of ***s*-NiP*N*(1)** (red), ***s*-NiP*N*(2)** (blue) and ***s*-NiP*N*(3)** (green) in chlorobenzene at 40 °C calibrated using low dispersity (<1.10) polystyrene standards (black squares; orange line shows the instrument calibration). Insert: summary of M_w, M_n, polydispersity (PDI) and the corresponding average number of repeating units in each sample.

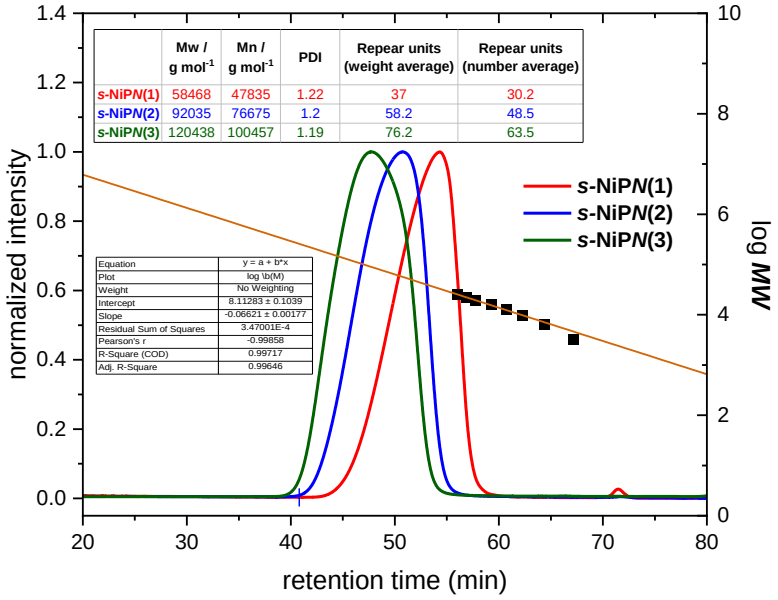


Figure 4.21: GPC traces of ***s*-NiP*N*(1)** (red), ***s*-NiP*N*(2)** (blue) and ***s*-NiP*N*(3)** (green) in toluene at 25 °C calibrated using discrete porphyrin oligomer standards (black squares; orange line shows the linear fit of the calibration). Insert: summary of M_w, M_n, polydispersity (PDI) and the corresponding average number of repeating units in each sample.

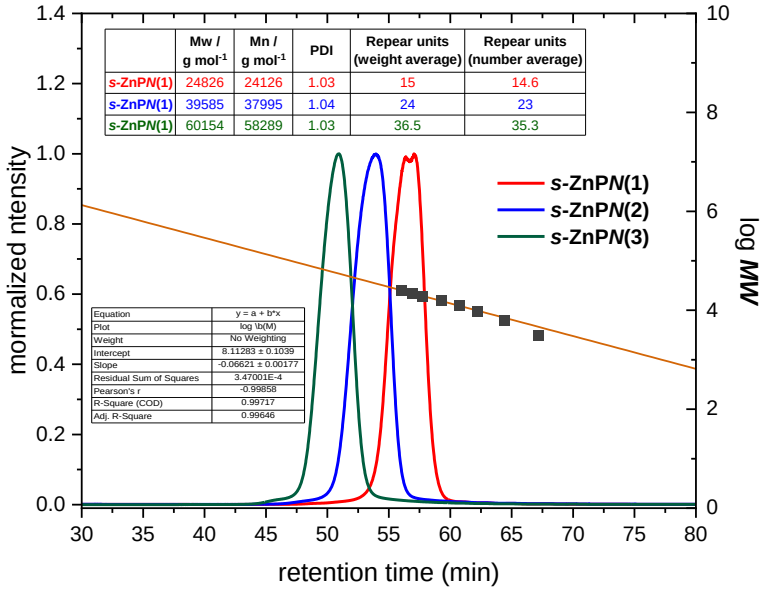
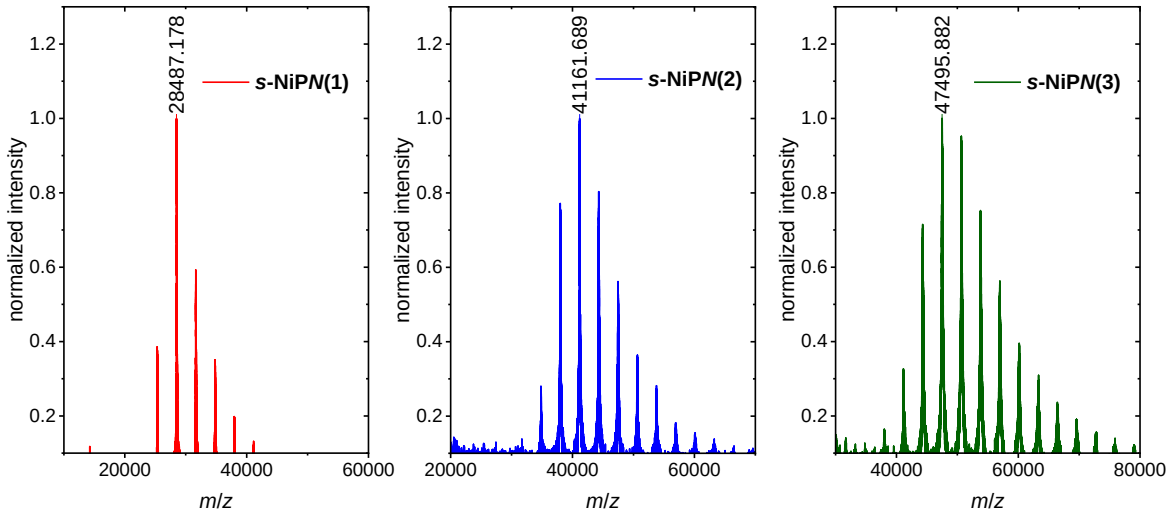


Figure 4.22: GPC traces of ***s*-ZnP*N*(1)** (red), ***s*-ZnP*N*(2)** (blue) and ***s*-ZnP*N*(3)** (green) in toluene at 25 °C calibrated using discrete porphyrin oligomer standards (black squares; orange line shows the linear fit of the calibration). Insert: summary of M_w, M_n, polydispersity (PDI) and the corresponding average number of repeating units in each sample.

MALDI-ToF MS data of each sample was also recorded. While it should be acknowledged that mass spectra would show reduced sensitivity to longer oligomers due to their larger molecular weights, it could still provide insight into the molecular weight distribution. For this reason, the M_w, M_n and $Đ$ based on obtained MALDI-ToF MS were calculated and summarized in Figure 4.23. The M_n and polydispersity ($Đ$) were found to be 30.9 kDa ($\bar{N}$ = 19, $Đ$ 1.02) for ***s*-NiP*N*(1)**, 45.1 kDa ($\bar{N}$ = 28, $Đ$ 1.02) for ***s*-NiP*N*(2)** and 53.1 kDa ($\bar{N}$ = 33, $Đ$ 1.02) for ***s*-NiP*N*(3)**, respectively. It is worth noting that the molecular weight distribution of ***s*-NiP*N*** obtained from *Method 1* and from MS data show reasonable comparability. Instead, in *Method 2*, the absence of larger porphyrin oligomer standards covering the desired molecular weight range necessitated an extrapolated calibration, resulting in inaccuracies in estimating molecular length.

We conclude by using polystyrenes as standards to describe the content in each oligomer mixture. Size estimation suggested that the average length of ***f*-NiP*N*(1)-Br$_2$** is ~12 nm, ***f*-NiP*N*(2)-Br$_2$** is ~20 nm and ***f*-NiP*N*(3)-Br$_2$** is ~28 nm. A difference of approximately 10 porphyrin units between each sample led to a length change of ~8 nm. This distribution should hopefully provide insights into the length dependence of the local charge transport of Ni(II) porphyrin nanoribbons in the THz range.



	Mw / g mol^{-1}	Mn / g mol^{-1}	PDI	Repear units (weight average)	Repear units (number average)
***s*-NiP*N*(1)**	31478	30902	1.02	19.9	19.6
***s*-NiP*N*(2)**	46165	45062	1.02	29.2	28.5
***s*-NiP*N*(3)**	54304	53106	1.02	34.4	33.6

Figure 4.23: MALDI-ToF mass spectra of three batches of singly-linked Ni(II) porphyrin oligomers (***s*-NiP*N*(1)** (red), ***s*-NiP*N*(2)** (blue) and ***s*-NiP*N*(3)** (green)). Table insert: summary of M_w, M_n, polydispersity (PDI) and the corresponding average number of repeating units in each sample.

4.3 Photoconductivity of Ni(II) Porphyrin Nanoribbons from Terahertz Spectroscopy

Optical-pump THz probe spectroscopy was used to study the charge carrier mobility of this series of Ni(II) porphyrin nanoribbons. We photogenerated charge carriers by above-bandgap excitations, using a short femtosecond optical pulse (400 nm). The THz pulse was generated by optical rectification and focused and transmitted through the photoexcited sample (thin films of ***f*-NiP*N*-Br$_2$** on fused silica substrate). The transmitted single-cycle THz waveform was then detected with a time-delayed pulse through electrooptic sampling. By varying the time delay t_p between the optical pump pulse and THz pulse, the time-resolved photoconductivity ***f*-NiP*N*-Br$_2$** can be individually obtained (Figure 4.24a). The photogenerated free electrons and holes rapidly (in less than 1 ps) combine to form electrically insulating excitons, in line with previously reported sub-10 ps exciton formation time in GNRs and PGNRs.[16,52,61,68] It is obvious that along with the increasing length of Ni(II) porphyrin nanoribbons, the photoconductivity remarkably increases, which indicates that the longitudinal confinement has strong impact on the THz conductivity for this series of molecules. The high polarizability of excitons is characterized by the persisting negative imaginary conductivity for long delay times.[61]

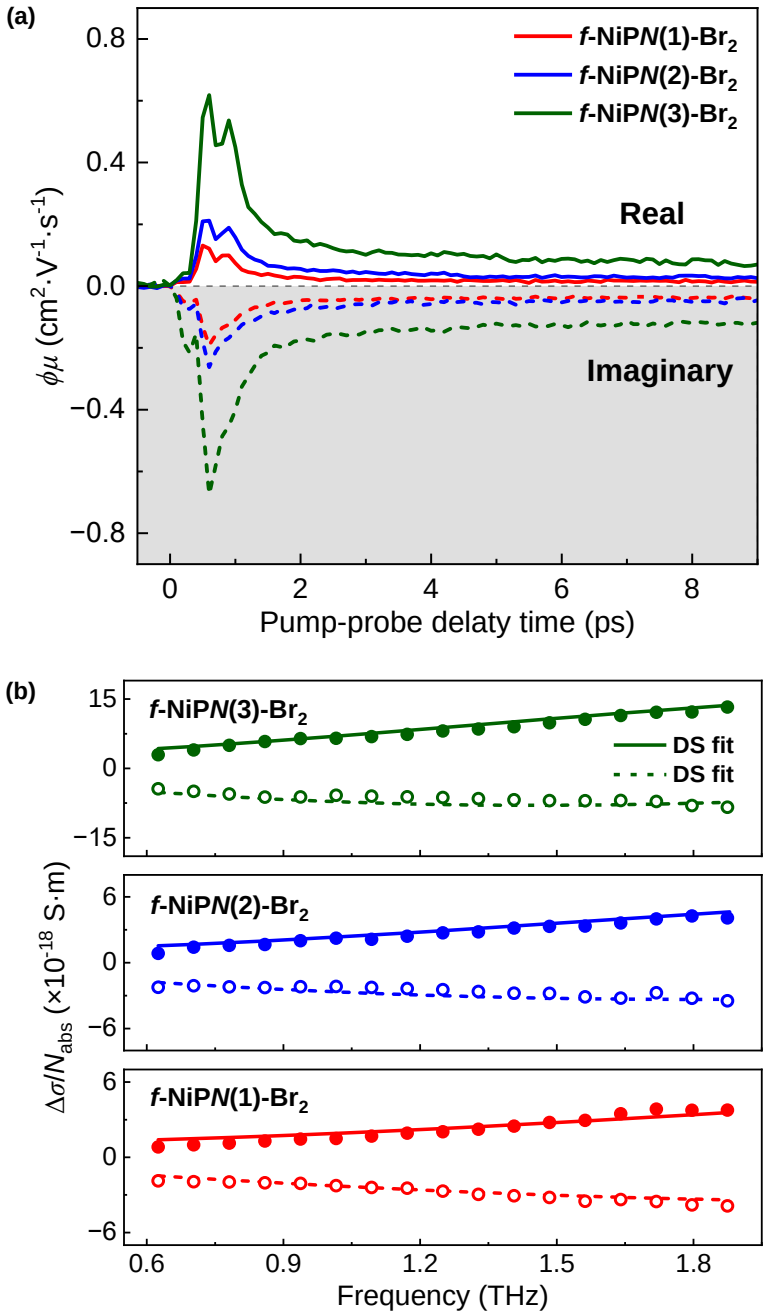


Figure 4.24: (a) Time-resolved complex photoconductivity measured for thin films of ***f*-NiP*N*(1)-Br$_2$**, ***f*-NiP*N*(2)-Br$_2$** and ***f*-NiP*N*(3)-Br$_2$**. (b) Frequency-resolved THz photoconductivity of ***f*-NiP*N*(1)-Br$_2$**, ***f*-NiP*N*(2)-Br$_2$** and ***f*-NiP*N*(3)-Br$_2$** measured at t_P = ~1.5 ps. The data are fitted by the Drude-Smith model.

The frequency-resolved complex photoconductivity for each sample recorded at t_P = ~1.5 ps after photo-injection of charge carriers are shown in Figure 4.24b. The THz conductivity of ***f*-NiP*N*-Br$_2$** is well described by the Drude-Smith model following Equation (4.10), with a negative imaginary part and a positive real part of which the absolute amplitude increasing with frequency. The results of these experiments are summarized in Table 4.3. The parameter c is found to be −0.93 and the corresponding scattering time for all three sample are determined: ***f*-NiP*N*(1)-Br$_2$**, τ_{DS} = 27 ± 3 fs, ***f*-NiP*N*(2)-Br$_2$**, τ_{DS} = 36 ± 2 fs and ***f*-NiP*N*(3)-Br$_2$**,

τ_{DS} = 44 ± 1 fs. The obtained τ_{DS} for Ni(II) porphyrin nanoribbons are within the reasonable range of reported GNRs (20 ~ 55 fs).[52,56–59] Using the effective mass m^* (0.02 m_0) obtained from the band structure calculation summarized in Chapter 3, the mobility of each sample in direct current-limit (dc-limit), μ_{dc} is obtained: ***f*-NiP*N*(1)-Br$_2$**, ~168 cm^2/V·s, ***f*-NiP*N*(2)-Br$_2$**, ~213 cm^2/V·s and ***f*-NiP*N*(3)-Br$_2$**, ~271 cm^2/V·s. We note that the inferred carrier mobility in the dc-limit is currently limited by the backscattering effects originated from the structural deformation or/and the ribbon length.[58] In extremely long and deformation-free ribbons, the intrinsic carrier mobility (taken the scattering time 44 fs from the longest ribbon) is expected to approach over 3000 cm^2/V·s. The extremely high intrinsic mobility is in line with a recent GNR field-effect device breakthrough in which a mobility over 1000 cm^2/V·s in atomically defined GNRs has been reported.[78] These values imply that Ni(II) porphyrin nanoribbons possess some of the highest mobilities among the known GNRs.

Table 4.3: Summary of parameter *c*, corresponding scattering time τ_{DS} and mobility in the dc-limit parameter μ_{dc} determined from the Drude-Smith model for each sample, all obtained from fitting of the THz spectra.

	Average Length (nm)	***c***	τ_{DS} (fs)	μ_{dc} (cm^2/V·s)
***f*-NiP*N*(1)-Br$_2$**	~12	−0.93	27 ± 3	~168
***f*-NiP*N*(2)-Br$_2$**	~20	−0.93	36 ± 2	~213
***f*-NiP*N*(3)-Br$_2$**	~28	−0.93	44 ± 1	~271

4.4 Conclusions

This chapter documents attempts towards building two series of polydisperse porphyrin nanoribbons with length over 10 nm. We have demonstrated the efficient Yamamoto coupling conditions for preparing both long singly-linked Zn(II) and Ni(II) porphyrin oligomers. By incorporating the extended **ArHex** side aryl group onto Ni(II) porphyrins, Ni(II) porphyrin nanoribbons at three distinct lengths were successfully isolated. The length of each sample was characterized by three different methods (GPC using both polystyrene standards or with known length porphyrin oligomers, and MALDI-TOF mass data). The complete fusion of Ni(II) oligomers was confirmed by UV−vis−NIR−MIR absorption spectra obtained from drop-casting thin film samples. Maximum absorption peaks (over 2000 nm) for all samples demonstrated their small optical energy gaps. The fusion of Zn(II) derivatives was proven challenging, where the synthesis may have been complicated by the sensitivity of coordinating

metal and reactive termini. Alternative capping methods and fusion conditions are likely required to overcome this.

In optical-pump THz probe experiments, we discovered that the photo-induced charge carriers in all three Ni(II) porphyrin nanoribbon samples show distinctive THz responses. This is the first time that charge carrier properties in THz range were accessed in solely porphyrin-based materials. The THz photoconductivity increases significantly with molecular length. Such a strong length-dependence indicates that the longitudinal confinement in porphyrin nanoribbon structures. Additionally, the THz measurements reveal that the highest charge carrier mobility of these samples reaching ~271 $cm^2/V{\cdot}s$, in dc-limit, which is also the highest mobilities among known GNRs. This unprecedented result strongly suggests the potential held by porphyrin nanoribbons in molecular electronics.

4.5 References

1 R. Ulbricht, E. Hendry, J. Shan, T. F. Heinz and M. Bonn, *Rev. Mod. Phys.*, 2011, **83**, 543–586.

2 P. Kužel and H. Němec, *Adv. Opt. Mater.*, 2020, **8**, 1–23.

3 D. M. Guldi, H. Nishihara and L. Venkataraman, *Chem. Soc. Rev.*, 2015, **44**, 842–844.

4 N. Karl, *Synth. Met.*, 2003, **133**–**134**, 649–657.

5 V. Coropceanu, J. Cornil, D. A. da Silva Filho, Y. Olivier, R. Silbey and J.-L. Brédas, *Chem. Rev.*, 2007, **107**, 926–952.

6 R. G. Kepler, *Phys. Rev.*, 1960, **119**, 1226–1229.

7 O. H. LeBlanc, *J. Chem. Phys.*, 1960, **33**, 626–626.

8 A. J. Campbell, D. D. C. Bradley and H. Antoniadis, *Appl. Phys. Lett.*, 2001, **79**, 2133–2135.

9 W. Warta, R. Stehle and N. Karl, *Appl. Phys. A*, 1985, **36**, 163–170.

10 G. Horowitz, R. Hajlaoui, H. Bouchriha, R. Bourguiga and M. Hajlaoui, *Adv. Mater.*, 1998, **10**, 923–927.

11 G. Horowitz, R. Hajlaoui, D. Fichou and A. El Kassmi, *J. Appl. Phys.*, 1999, **85**, 3202–3206.

12 F. C. Grozema and L. D. A. Siebbeles, *J. Phys. Chem. Lett.*, 2011, **2**, 2951–2958.

13 J. M. Warman, M. P. de Haas, G. Dicker, F. C. Grozema, J. Piris and M. G. Debije, *Chem. Mater.*, 2004, **16**, 4600–4609.

14 J. E. Kroeze, T. J. Savenije and J. M. Warman, *J. Am. Chem. Soc.*, 2004, **126**, 7608–7618.

15 H. Němec, P. Kužel and V. Sundström, *J. Photochem. Photobiol. A Chem.*, 2010, **215**, 123–139.

16 E. Hendry, J. M. Schins, L. P. Candeias, L. D. A. Siebbeles and M. Bonn, *Phys. Rev. Lett.*, 2004, **92**, 196601.

17 E. Hendry, M. Koeberg, J. M. Schins, L. D. A. Siebbeles and M. Bonn, *Chem. Phys. Lett.*, 2006, **432**, 441–445.

18 D. Mittleman, *Sensing with Terahertz Radiation*, Springer Berlin Heidelberg, 2003, vol. 85.

19 M. Koch, D. M. Mittleman, J. Ornik and E. Castro-Camus, *Nat. Rev. Methods Prim.*, 2023, **3**, 48.

20 P. R. Smith, D. H. Auston and M. C. Nuss, *IEEE J. Quantum Electron.*, 1988, **24**, 255–260.

21 C. Fattinger and D. Grischkowsky, *Appl. Phys. Lett.*, 1989, **54**, 490–492.

22 M. Hangyo, M. Tani and T. Nagashima, *Int. J. Infrared Milli.*, 2005, **26**, 1661–1690.

23 P. U. Jepsen, R. H. Jacobsen and S. R. Keiding, *J. Opt. Soc. Am. B*, 1996, **13**, 2424.

24 D. H. Auston, K. P. Cheung and P. R. Smith, *Appl. Phys. Lett.*, 1984, **45**, 284–286.

25 K. Reimann, *Reports Prog. Phys.*, 2007, **70**, 1597–1632.

26 Y. Cai, I. Brener, J. Lopata, J. Wynn, L. Pfeiffer, J. B. Stark, Q. Wu, X. C. Zhang and J. F. Federici, *Appl. Phys. Lett.*, 1998, **73**, 444–446.

27 P. a George, J. Strait, J. Dawlaty, S. Shivaraman, M. Chandrashekhar, F. Rana and M. G. Spencer, *Nano Lett.*, 2008, **8**, 4248–4251.

28 J. M. Dawlaty, S. Shivaraman, J. Strait, P. George, M. Chandrashekhar, F. Rana, M. G. Spencer, D. Veksler and Y. Chen, *Appl. Phys. Lett.*, 2008, **93**, 131905.

29 P. Drude, *Ann. Phys.*, 1900, **306**, 566–613.

30 P. Drude, *Ann. Phys.*, 1900, **308**, 369–402.

31 N. Smith, *Phys. Rev. B*, 2001, **64**, 155106.

32 H. Zhang, Max Planck Institute for Polymer Research, 2022.

33 D. G. Cooke, A. N. MacDonald, A. Hryciw, J. Wang, Q. Li, A. Meldrum and F. A. Hegmann, *Phys. Rev. B*, 2006, **73**, 193311.

34 N. V. Smith, *Phys. Lett. A*, 1968, **26**, 126–127.

35 T. L. Cocker, D. Baillie, M. Buruma, L. V. Titova, R. D. Sydora, F. Marsiglio and F. A. Hegmann, *Phys. Rev. B*, 2017, **96**, 205439.

36 A. H. Castro Neto, F. Guinea, N. M. R. Peres, K. S. Novoselov and A. K. Geim, *Rev. Mod. Phys.*, 2009, **81**, 109–162.

37 K. I. Bolotin, K. J. Sikes, Z. Jiang, M. Klima, G. Fudenberg, J. Hone, P. Kim and H. L. Stormer, *Solid State Commun.*, 2008, **146**, 351–355.

38 K. F. Mak, M. Y. Sfeir, Y. Wu, C. H. Lui, J. A. Misewich and T. F. Heinz, *Phys. Rev. Lett.*, 2008, **101**, 196405.

39 S. Chatterjee and S. Chatterjee, Band Structure of Graphene, http://demonstrations.wolfram.com/BandStructureOfGraphene/, (accessed 11 April 2024).

40 K. S. Novoselov, A. K. Geim, S. V. Morozov, D. Jiang, Y. Zhang, S. V. Dubonos, I. V. Grigorieva and A. A. Firsov, *Science*, 2004, **306**, 666–669.

41 J. Hass, F. Varchon, J. E. Millán-Otoya, M. Sprinkle, N. Sharma, W. A. De Heer, C. Berger, P. N. First, L. Magaud and E. H. Conrad, *Phys. Rev. Lett.*, 2008, **100**, 3–6.

42 K. S. Kim, Y. Zhao, H. Jang, S. Y. Lee, J. M. Kim, K. S. Kim, J.-H. Ahn, P. Kim, J.-Y. Choi and B. H. Hong, *Nature*, 2009, **457**, 706–710.

43 H. Choi, F. Borondics, D. A. Siegel, S. Y. Zhou, M. C. Martin, A. Lanzara and R. A. Kaindl, *Appl. Phys. Lett.*, 2009, **94**, 172102.

44 P. a George, J. Strait, J. Dawlaty, S. Shivaraman, M. Chandrashekhar, F. Rana and M. G. Spencer, *Nano Lett.*, 2008, **8**, 17–20.

45 S. Winnerl, M. Orlita, P. Plochocka, P. Kossacki, M. Potemski, T. Winzer, E. Malic, A. Knorr, M. Sprinkle, C. Berger, W. A. De Heer, H. Schneider and M. Helm, *Phys. Rev. Lett.*, 2011, **107**, 2–6.

46 C. Lee, J. Y. Kim, S. Bae, K. S. Kim, B. H. Hong and E. J. Choi, *Appl. Phys. Lett.*, 2011, **98**, 10–13.

47 J. Horng, C.-F. Chen, B. Geng, C. Girit, Y. Zhang, Z. Hao, H. A. Bechtel, M. Martin, A. Zettl, M. F. Crommie, Y. R. Shen and F. Wang, *Phys. Rev. B*, 2011, **83**, 165113.

48 G. Jnawali, Y. Rao, H. Yan and T. F. Heinz, *Nano Lett.*, 2013, **13**, 524–530.

49 A. J. Frenzel, C. H. Lui, W. Fang, N. L. Nair, P. K. Herring, P. Jarillo-Herrero, J. Kong and N. Gedik, *Appl. Phys. Lett.*, 2013, **102**, 113111.

50 A. Tomadin, S. M. Hornett, H. I. Wang, E. M. Alexeev, A. Candini, C. Coletti, D. Turchinovich, M. Kläui, M. Bonn, F. H. L. Koppens, E. Hendry, M. Polini and K.-J. Tielrooij, *Sci. Adv.*, 2018, **4**, 1–11.

51 S. Iijima and T. Ichihashi, *Nature*, 1993, **363**, 603–605.

52 A. Narita, X. Feng, Y. Hernandez, S. A. Jensen, M. Bonn, H. Yang, I. A. Verzhbitskiy, C. Casiraghi, M. R. Hansen, A. H. R. Koch, G. Fytas, O. Ivasenko, B. Li, K. S. Mali, T. Balandina, S. Mahesh, S. De Feyter and K. Müllen, *Nat. Chem.*, 2014, **6**, 126–132.

53 C. Liu and H.-M. Cheng, *J. Am. Chem. Soc.*, 2016, **138**, 6690–6698.

54 B. P. Gorshunov, E. S. Zhukova, J. S. Starovatykh, M. A. Belyanchikov, A. K. Grebenko, A. V. Bubis, V. I. Tsebro, A. A. Tonkikh, D. V. Rybkovskiy, A. G. Nasibulin, E. I. Kauppinen and E. D. Obraztsova, *Carbon N. Y.*, 2018, **126**, 544–551.

55 Q. Zhang, E. H. Hároz, Z. Jin, L. Ren, X. Wang, R. S. Arvidson, A. Lüttge and J. Kono, *Nano Lett.*, 2013, **13**, 5991–5996.

56 S. A. Jensen, R. Ulbricht, A. Narita, X. Feng, K. Müllen, T. Hertel, D. Turchinovich and M. Bonn, *Nano Lett.*, 2013, **13**, 5925–5930.

57 X. Wang, J. Ma, W. Zheng, S. Osella, N. Arisnabarreta, J. Droste, G. Serra, O. Ivasenko, A. Lucotti, D. Beljonne, M. Bonn, X. Liu, M. R. Hansen, M. Tommasini, S. De Feyter, J. Liu, H. I. Wang and X. Feng, *J. Am. Chem. Soc.*, 2022, **144**, 228–235.

58 I. Ivanov, Y. Hu, S. Osella, U. Beser, H. I. Wang, D. Beljonne, A. Narita, K. Müllen, D. Turchinovich and M. Bonn, *J. Am. Chem. Soc.*, 2017, **139**, 7982–7988.

59 X. Yao, H. Zhang, F. Kong, A. Hinaut, R. Pawlak, M. Okuno, R. Graf, P. N. Horton, S. J. Coles, E. Meyer, L. Bogani, M. Bonn, H. I. Wang, K. Müllen and A. Narita, *Angew. Chem. Int. Ed.*, 2023, **62**, e202312610.

60 G. Soavi, S. Dal Conte, C. Manzoni, D. Viola, A. Narita, Y. Hu, X. Feng, U. Hohenester, E. Molinari, D. Prezzi, K. Müllen and G. Cerullo, *Nat. Commun.*, 2016, **7**, 11010.

61 A. Tries, S. Osella, P. Zhang, F. Xu, C. Ramanan, M. Kläui, Y. Mai, D. Beljonne and H. I. Wang, *Nano Lett.*, 2020, **20**, 2993–3002.

62 H. S. Cho, D. H. Jeong, S. Cho, D. Kim, Y. Matsuzaki, K. Tanaka, A. Tsuda and A. Osuka, *J. Am. Chem. Soc.*, 2002, **124**, 14642–14654.

63 D. H. Yoon, S. B. Lee, K.-H. Yoo, J. Kim, J. K. Lim, N. Aratani, A. Tsuda, A. Osuka and D. Kim, *J. Am. Chem. Soc.*, 2003, **125**, 11062–11064.

64 B. K. Kang, N. Aratani, J. K. Lim, D. Kim, A. Osuka and K. H. Yoo, *Chem. Phys. Lett.*, 2005, **412**, 303–306.

65 B. K. Kang, N. Aratani, J. K. Lim, D. Kim, A. Osuka and K. H. Yoo, *Mater. Sci. Eng. C*, 2006, **26**, 1023–1027.

66 G. Sedghi, L. J. Esdaile, H. L. Anderson, S. Martin, D. Bethell, S. J. Higgins and R. J. Nichols, *Adv. Mater.*, 2012, **24**, 653–657.

67 E. Leary, B. Limburg, A. Alanazy, S. Sangtarash, I. Grace, K. Swada, L. J. Esdaile, M. Noori, M. T. González, G. Rubio-Bollinger, H. Sadeghi, A. Hodgson, N. Agraït, S. J. Higgins, C. J. Lambert, H. L. Anderson and R. J. Nichols, *J. Am. Chem. Soc.*, 2018, **140**, 12877–12883.

68 Q. Chen, A. Lodi, H. Zhang, A. Gee, H. I. Wang, F. Kong, M. Clarke, M. Edmondson, J. Hart, J. N. O'Shea, W. Stawski, J. Baugh, A. Narita, A. Saywell, M. Bonn, K. Müllen, L. Bogani and H. L. Anderson, *Nat. Chem.*, 2024, DOI:10.1038/s41557-024-01477-1.

69 M. Kamo, A. Tsuda, Y. Nakamura, N. Aratani, K. Furukawa, T. Kato and A. Osuka, *Org. Lett.*, 2003, **5**, 2079–2082.

70 Q. Ouyang, Y.-Z. Zhu, C.-H. Zhang, K.-Q. Yan, Y.-C. Li and J.-Y. Zheng, *Org. Lett.*, 2009, **11**, 5266–5269.

71 H. Gotfredsen, J. Deng, J. M. Van Raden, M. Righetto, J. Hergenhahn, M. Clarke, A. Bellamy-Carter, J. Hart, J. O'Shea, T. D. W. Claridge, F. Duarte, A. Saywell, L. M. Herz and H. L. Anderson, *Nat. Chem.*, 2022, **14**, 1436–1442.

72 J.-R. Deng, M. T. González, H. Zhu, H. L. Anderson and E. Leary, *J. Am. Chem. Soc.*, 2024, **146**, 3651–3659.

73 I. Krossing, *Chem. Eur. J.*, 2001, **7**, 490–502.

74 T. Yamamoto, S. Wakabayashi and K. Osakada, *J. Organomet. Chem.*, 1992, **428**, 223–237.

75 A. Tsuda and A. Osuka, *Science*, 2001, **293**, 79–82.

76 S. Richert, B. Limburg, H. L. Anderson and C. R. Timmel, *J. Am. Chem. Soc.*, 2017, **139**, 12003–12008.

77 A. K. Sahoo, Y. Nakamura, N. Aratani, K. S. Kim, S. B. Noh, H. Shinokubo, D. Kim and A. Osuka, *Org. Lett.*, 2006, **8**, 4141–4144.

78 B. Lyu, J. Chen, S. Wang, S. Lou, P. Shen, J. Xie, L. Qiu, I. Mitchell, C. Li, C. Hu, X. Zhou, K. Watanabe, T. Taniguchi, X. Wang, J. Jia, Q. Liang, G. Chen, T. Li, S. Wang, W. Ouyang, O. Hod, F. Ding, M. Urbakh and Z. Shi, *Nature*, 2024, **628**, 758–764.

4.6 Experimental

Contents

General Methods 260

Synthesis of Known Compounds 261

3,5-Bis(trihexylsilyl)benzaldehyde 261

5,15-Bis(3,5-bis(trihexylsilyl)phenyl)porphyrin 262

Zn(II) 5,15-bis(3,5-bis(trihexylsilyl)phenyl)porphyrin **ZnP1** 263

Ag[Al(pftb)$_4$] (pftb = OC(CF$_3$)$_3$) 263

Ag[Al(pftb)$_4$]-Mediated Dimerization of **ZnP1** to ***s*-ZnP2** 264

Dibrominated Singly-linked Zn(II) Porphyrin Dimer ***s*-ZnP2-Br$_2$** 265

Singly-linked Zn(II) Porphyrin Oligomers ***s*-ZnP*N*** 266

Synthesis of Novel Compounds 267

5,15-Bis(2,4,6-trimethyl-3,5-bis(ArHex))porphyrin 267

Ni(II) 5,15-bis(2,4,6-trimethyl-3,5-bis(ArHex))porphyrin **NiP1** 268

Dibrominated Ni(II) 5,15-bis(2,4,6-trimethyl-3,5-bis(ArHex))porphyrin **NiP1-Br$_2$** 268

PIFA-Mediated Dimerization of **NiP1** to ***s*-NiP2** 269

Dibrominated Singly-linked Ni(II) Porphyrin Dimer ***s*-NiP2-Br$_2$** 270

Singly-linked Ni(II) Porphyrin Oligomers ***s*-NiP*N*** (starting from ***s*-NiP2-Br$_2$**) 271

Dibrominated Singly-linked Ni(II) Porphyrin Oligomers ***s*-NiP*N*-Br$_2$** 273

Ni(II) Porphyrin Nanoribbons ***f*-NiP*N*-Br$_2$** 274

Selected NMR Spectra 276

UV–vis–NIR Absorption Comparison 283

References 284

General Methods

Commercially available reagents from Alfa Aesar, Fluorochem, Merck, Strem Chemicals and TCI were used as received. Anhydrous tetrahydrofuran (THF), dichloromethane, chloroform, toluene, dimethylformamide (DMF) 1,4-dioxane and triethylamine were purified by a MBraun MN-SPS-5 Bench-Top under nitrogen atmosphere (H_2O content < 20 ppm as determined by Karl-Fischer titration). All other solvents used for extraction or column chromatography (silica gel: SiO_2, 60 Å, 40–63 μm) were HPLC grade and dried over appropriate drying agents when required. Reactions, unless otherwise stated, proceeded in oven-dried glassware under argon atmosphere. Thin layer chromatography (TLC) was carried out on aluminum-backed silica gel 60 F_{254} plates (Merck) and visualized under UV irradiation either at 254 or 365 nm. Petroleum ether (pet. ether) boiling point range of 40-60 °C was used for column chromatography. Size exclusion chromatography (SEC) was carried out using Bio-Rad Bio-Beads S-X1 (1% cross linked, 40–80 μm bead size). Evaporation of solvents was performed at 20–50 °C and 5–1010 mbar. Reported yields refer to pure compounds dried under high vacuum (< 0.1 mbar).

^{1}H and ^{13}C nuclear magnetic resonance (NMR) spectra were recorded on Bruker AVIII HD 400 and AVIII HD 500 spectrometers at 400 MHz and 500 MHz (^{1}H) and 101 MHz and 126 MHz (^{13}C), respectively at 298 K unless otherwise stated. ^{1}H NMR chemical shifts were reported in ppm to the nearest 0.01 ppm relative to $SiMe_4$ ($\delta = 0$) and coupling constants (J) are in Hertz. Spectra were referenced internally to residual solvent protons in the deuterated solvent using the reported values ($\delta = 5.32$ for dichloromethane-d_2 and 7.26 for chloroform-d). Multiplicities are reported in accordance with the following: s = singlet; d = doublet; dd = doublet of doublet; t = triplet and m = multiplet. ^{13}C chemical shifts were reported in ppm to the nearest 0.1 ppm relative to $SiMe_4$ ($\delta = 0$) and were referenced internally with respect to residual carbons in the solvents ($\delta = 53.8$ for dichloromethane-d_2 and 77.2 for chloroform-d). ^{1}H assignments were made using 2D NMR methods (COSY, NOESY, HSQC, HMBC).

UV−vis−NIR spectra in solution were recorded with a Perkin-Elmer Lambda 20 or a Perkin-Elmer Lambda 25 spectrometer with temperature control by a PTP-1 Peltier unit or a JASCO V-770 spectrometer using Infrasil® Quartz 1 cm cuvettes at 298 K. UV−vis−NIR−MIR

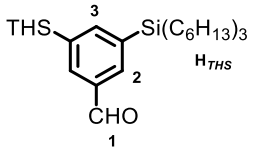
spectra using thin films were recorded with JASCO V-770 spectrometer or a VERTEX 80 spectrometer using CaF_2 polished window substrates with a pathlength of 1 cm at 298 K.

MALDI-ToF MS spectra was measured using Bruker MALDI Autoflex Speed spectrometer utilizing *trans*-2-[3-(4-tert-butylphenyl-2-methyl-2-propenylidene]-malononitrile (DCTB) as matrix.

GPC measurements (using polystyrene as calibration standards): Number-average (Mn) and weight-average (Mw) molecular weights were determined using an Agilent Technologies 1260 infinity GPC at 40 °C in chlorobenzene, using two PLgel 10 micrometer Mixed-B columns in series (300 × 7.5 mm), and calibrated against narrow dispersity (Đ <1.10) polystyrene standards.

Synthesis of Known Compounds

3,5-Bis(trihexylsilyl)benzaldehyde



1,3,5-Tribromobenzene (5.0 g, 16 mmol) in Et_2O (125 mL) were added into a 250-mL round-bottom flask and the suspension was degassed with argon and cooled to −20 °C. *n*-Butyl lithium (1.6 M in hexane, 21 mL, 33 mmol) was added dropwise. The mixture was stirred for 1.5 h, followed by the dropwise addition of trihexylsilylchloride (14 mL, 35 mmol). It was allowed to warm to room temperature and react for another 1.5 h. The resulting mixture was hydrolyzed by water (100 mL × 2), dried over $MgSO_4$ and the solution was concentrated under reduced pressure. The remaining mixture was then filtered through a silica plug (pure pet. ether). The solvent was evaporated to yield a yellow oil (9.2 g) which was dried under vacuum overnight. The obtained crude intermediate was directly put into the next step synthesis.

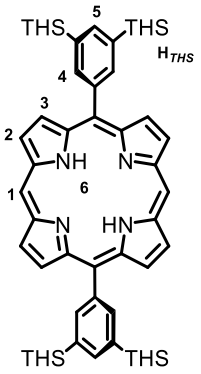
The yellow oil was dissolved in dry Et_2O (70 mL) in a 250 mL round-bottom flask and the solution was degassed with argon. *n*-Butyl lithium (1.6 M in hexane, 28 mL, 44 mmol) was

added dropwise at 0 °C. The reaction was stirred at this temperature for 30 min. The solution was allowed to warm to room temperature over a period of 1.5 h. Subsequently, DMF (5.0 mL, 70 mmol) was added, and the reaction was stirred for another 1 h. NH_4Cl aqueous saturated solution (100 mL) was added to quench the reaction. The aqueous phase was extracted by Et_2O (3 × 100 mL) and the combined organic extract was washed with $NaHCO_3$ solution (100 mL), followed by water (2 × 100 mL) and dried over Na_2SO_4. The solution was concentrated under reduced pressure. The crude material was purified by silica column chromatography (pet. ether/dichloromethane, v/v, gradient elution from 100:0 to 100:10) to yield 3,5-bis(trihexylsilyl)benzaldehyde (3.6 g, 30%) as a yellow oil.

^{1}**H NMR** (400 MHz, $CDCl_3$, 298 K) δ_H 10.03 (s, 1H, *H1*), 7.93 (d, *J* = 1.2 Hz, 2H, *H2*), 7.84 (t, *J* = 1.3 Hz, 1H, *H3*), 1.24 – 0.83 (m, 78H, H_{THS}).

Analytical data as in lit.[1]

5,15-Bis(3,5-bis(trihexylsilyl)phenyl)porphyrin

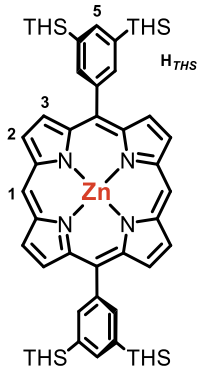


Dipyrromethane (0.56 g, 3.8 mmol, 2.0 equiv.) and 3,5-bis(trihexylsilyl)benzaldehyde (2.5 g, 3.8 mmol, 2.0 equiv.) were added into a 1 L round-bottom flask followed by the addition of dichloromethane (700 mL) and the solution was degassed with argon for 20 min. TFA (0.5 mL, 7.6 mmol, 4 equiv.) was added dropwise, and the reaction was stirred in the dark for 3 h. DDQ (1.5 g, 6.6 mmol, 3.6 equiv.) was added and the mixture was stirred for another 20 min. Subsequently, the reaction was quenched by the addition of triethylamine (3.8 mL). The solution was then concentrated under reduced pressure and purified by a short silica plug (pet. ether/dichloromethane, v/v, 10:1) to yield 5,15-bis(3,5-bis(trihexylsilyl)phenyl)porphyrin (1.9 g, 54%) as a red-purple solid.

^{1}**H NMR** (400 MHz, $CDCl_3$, 298 K) δ_H 10.58 (s, 2H, *H1*), 9.58 (d, *J* = 4.6 Hz, 4H, *H2*), 9.07 (d, *J* = 4.6 Hz, 4H, *H3*), 8.46 (d, *J* = 1.2 Hz, 4H, *H4*), 8.19 (t, *J* = 1.2 Hz, 2H, *H5*), 1.75 – 0.69 (m, 156H, H_{THS}), −3.10(s, 2H, *H6*).

Analytical data as in lit.[1]

Zn(II) 5,15-bis(3,5-bis(trihexylsilyl)phenyl)porphyrin ZnP1



5,15-Bis(3,5-bis(trihexylsilyl)phenyl)porphyrin (1.3 g, 0.80 mmol, 1.0 equiv.) was added into a 250 mL round-bottom flask followed by the addition of chloroform (70 mL). A solution of $Zn(OAc)_2{\cdot}2H_2O$ (0.92 g, 4.2 mmol, 5.0 equiv.) in methanol (10 mL) was added and the mixture was stirred at 40 °C for 1 h and the reaction was monitored by TLC (pet. ether/dichloromethane, v/v, 9:1). The resulting solution was concentrated under reduced pressure and purified through a short silica plug (pet. ether/dichloromethane, v/v, 4:1) to yield **ZnP1** (1.3 g, 87%) was yielded as a red-purple solid.

^{1}**H NMR** (400 MHz, $CDCl_3$, 298 K) δ_H 10.36 (s, 2H, *H1*), 9.44 (d, *J* = 4.5 Hz, 4H, *H2*), 9.14 (d, *J* = 4.5 Hz, 4H, *H3*), 8.35 (d, *J* = 1.1 Hz, 4H, *H4*), 8.01 (t, *J* = 1.2 Hz, 2H, *H5*), 1.33 – 1.07 (m, 156H, H_{THS}).

Analytical data as in lit.[1]

$Ag[Al(pftb)_4]$ (pftb = $OC(CF_3)_3$)

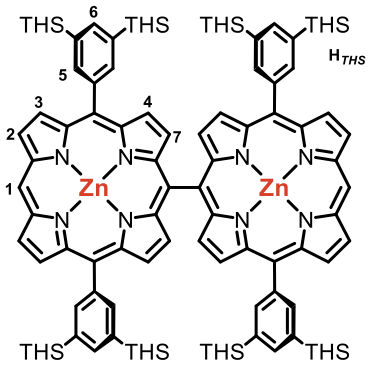
Under argon, $LiAlH_4$ solution (4.0 M in diethyl ether, 2.0 mL, 8.0 mmol, 1.0 equiv.) was added into a 250 mL two-necked flask and the solvent was removed by vacuum to give white $LiAlH_4$ powder. Dry toluene (70 mL) was added to suspend the $LiAlH_4$ powder and under argon, $HOC(CF_3)_3$ (4.9 mL, 33 mmol, 4.1 equiv.) was added dropwise to the suspension at 0 °C. The

mixture was stirred at 80 °C for 20 h. Subsequently, the solvent was removed under reduced pressure to yield crude Li[Al(pftb)$_4$] (7.5 g, 96%) as white powder, which was subjected to the next step without further purification.

Under argon, a mixture of Li[Al(pftb)$_4$] (7.5 g, 4.9 mmol, 1.0 equiv.), AgF (2.0 g, 7.7 mmol, 2.0 equiv.) and dry dichloromethane (90 mL) was sonicated for 1 h and then was kept stirring at 40 °C for 20 h. After the reaction, the resulting mixture was filtered by a celite column with dichloromethane as eluent. The solvent was removed under reduced pressure to yield the desired product Ag[Al(pftb)$_4$] (5.6 g, 68%) as brown solid. The product was preserved in a sealed container under argon in freezer to prevent the hydrolyzation of the compound.

Analytical data as in lit.[2]

Ag[Al(pftb)$_4$]-Mediated Dimerization of ZnP1 to *s*-ZnP2

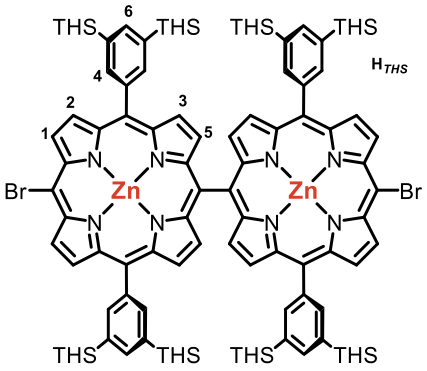


ZnP1 (0.26 g, 0.16 mmol, 1.0 equiv.) was added into a 50 mL Schlenk tube followed by the addition of dry $CHCl_3$ (23 mL) and *N*,*N*-dimethylacetamide (1.8 mL) under argon. Ag[Al(pftb)$_4$] (0.33 g, 0.31 mmol, 2.0 equiv.) in chloroform (11.5 mL) was added and the mixture was stirred at room temperature for 30 min. The resulting mixture was concentrated and passed through purified by silica column chromatography (pet. ether/dichloromethane, v/v, 10:1), followed by size-exclusion chromatography (Bio-Beads, S-X1) with toluene as eluent to give the *meso-meso* singly-linked Zn(II) porphyrin oligomers as a crude mixture. The crude mixture was further subjected to reversible recycling GPC to separate the desired dimer ***s*-ZnP2** (0.20 g, 77%).

^{1}H NMR (400 MHz, $CDCl_3$, 298 K) δ_H 10.28 (s, 2H, *H1*), 9.41 (d, *J* = 4.5 Hz, 4H, *H2*), 9.03 (d, *J* = 4.5 Hz, 4H, *H3*), 8.59 (d, *J* = 4.6 Hz, 4H, *H4*), 8.29 (d, *J* = 1.2 Hz, 8H, *H5*), 7.92 (t, *J* = 1.2 Hz, 4H, *H6*), 7.88 (s, 4H, *H7*), 1.44 – 0.69 (m, 312H, H_{THS}).

Analytical data as in lit.[3]

Dibrominated Singly-linked Zn(II) Porphyrin Dimer *s*-ZnP2-Br$_2$

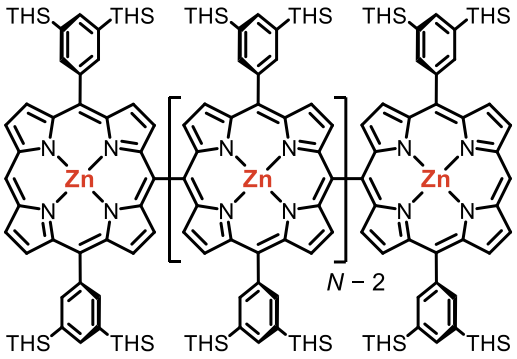


***s*-ZnP2** (0.25 g, 0.08 mmol, 1.0 equiv.) was added into a 150 mL round-bottom flask followed by the addition of chloroform (80 mL) with pyridine (0.8 mL). It was cooled down to 0 °C in an ice bath and to the stirred mixture, a solution of *N*-bromosuccinimide (28 mg, 0.16 mmol, 2.1 equiv.) in chloroform (16 mL) was added dropwise. The reaction was conducted at 0 °C for 15 min. Subsequently, acetone (5.0 mL) was added to quench the excess *N*-bromosuccinimide. The resulting mixture was concentrated under reduced pressure and purified by a silica plug (pet. ether/dichloromethane, v/v, 9:1) to yield ***s*-ZnP2-Br$_2$** (0.24 g, 93%).

^{1}H NMR (400 MHz, $CDCl_3$, 298 K) δ_H 9.85 (d, *J* = 4.8 Hz, 4H, *H1*), 9.00 (d, *J* = 4.8 Hz, 4H, *H2*), 8.61 (d, *J* = 4.7 Hz, 4H, *H3*), 8.26 (d, *J* = 1.1 Hz, 8H, *H4*), 8.05 (d, *J* = 4.8 Hz, 4H, *H5*), 7.91 (t, *J* = 1.1 Hz, 4H, *H6*), 1.44 – 0.67 (m, 312H, H_{THS}).

Analytical data as in lit.[3]

Singly-linked Zn(II) Porphyrin Oligomers *s*-ZnP*N*



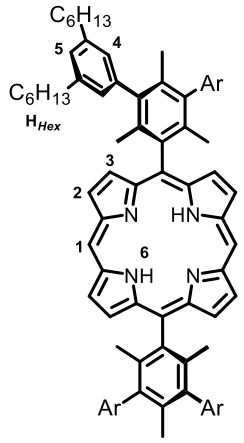
s*-ZnP2-Br$_2$** (0.22 g, 64 μmol, 1.0 equiv.), Ni(COD)$_2$ (0.35 g, 1.3 mmol, 20 equiv.) and 2,2'-bipyridine (0.20 g, 1.3 mmol, 20 equiv.) were added into a 25-mL Schlenk tube followed by the addition of dry DMF (5 mL) with pyridine (0.5 mL). It was degassed by three freeze-pump-thaw cycles and the mixture was stirred at 80 °C in dark for 6 h. The resulting mixture was diluted by water (50 mL) and washed by dichloromethane (50 mL × 3). The combined organic phase was concentrated under reduced pressure and passed through a silica plug (pet. ether/dichloromethane, v/v, 9:1), followed by size-exclusion chromatography with toluene as eluent to yield crude mixture of singly-linked Zn(II) porphyrin oligomers ***s*-ZnP*N. The mixture was further subjected to recycling GPC with toluene/pyridine (99:1) to separate them into three length sets based on the relative retention time (in ascending order of length, from short to long: ***s*-ZnP*N*(1)** (27 mg, 12%), ***s*-ZnP*N*(2)** (22 mg, 5%) and ***s*-ZnP*N*(3)** (18 mg, 4%))

Recycling GPC retention time: ***s*-ZnP*N*(1)** (57.0 min), ***s*-ZnP*N*(2)** (54.0 min), ***s*-ZnP*N*(3)** (50.9 min)

Analytical data as in lit.[4]

Synthesis of Novel Compounds

5,15-Bis(2,4,6-trimethyl-3,5-bis(ArHex))porphyrin

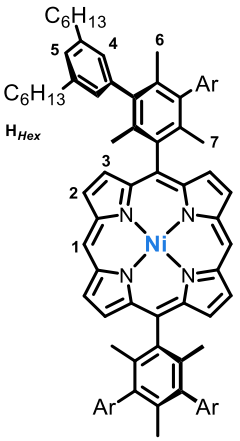


Dipyrromethane (0.44 g, 3.0 mmol, 2.0 equiv.) and 2,4,6-trimethyl-3,5-bis(ArHex)benzaldehyde (1.9 g, 3.0 mmol, 2.0 equiv.) were added into a 1 L round-bottom flask followed by the addition of chloroform (500 mL) and the solution was degassed with argon for 20 min. Boron trifluoride etherate (BF_3OEt_2, 0.25 mL, 7.6 mmol, 1.3 equiv.) was added dropwise, and the reaction was stirred in the dark for 3 h. DDQ (1.5 g, 6.6 mmol, 3.0 equiv.) was added and the mixture was stirred for another 20 min. Subsequently, the reaction was quenched by the addition of triethylamine (5.0 mL). The solution was then concentrated under reduced pressure and purified by a short silica plug (pet. ether/dichloromethane, v/v, gradient elution from 10:3 to 10:5) to yield 5,15-bis(2,4,6-trimethyl-3,5-bis(ArHex))porphyrin (0.65 g, 28%) as a red-purple solid.

^{1}H NMR (400 MHz, $CDCl_3$, 298 K) δ_H 10.30 (s, 2H, *H1*), 9.45 (d, *J* = 4.6 Hz, 4H, *H2*), 9.16 (d, *J* = 4.6 Hz, 4H, *H3*), 7.20 (d, *J* = 1.6 Hz, 8H, *H4*), 7.03 (t, *J* = 1.6 Hz, 4H, *H5*), 2.72 (t, *J* = 7.7 Hz, 17H, H_{Hex}), 2.13 (s, 6H, *H6*), 1.78 – 1.68 (m, 17H, H_{Hex}), 1.62 (s, 12H, *H7*, H_{Hex}), 0.94 – 0.86 (m, 24H, H_{Hex}), −2.90 (s, 2H, *H8*).

MALDI-ToF MS: *m*/*z* = 1523.253 ($C_{110}H_{146}N_4$, M^+ requires 1523.155)

Ni(II) 5,15-bis(2,4,6-trimethyl-3,5-bis(ArHex))porphyrin NiP1

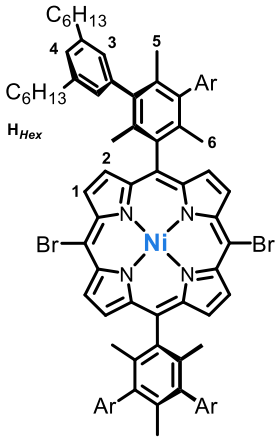


5,15-Bis(2,4,6-trimethyl-3,5-bis(ArHex))porphyrin (0.37 g, 0.24 mmol, 1.0 equiv.) and $Ni(OAc)_2{\cdot}4H_2O$ (0.45 g, 0.72 mmol, 3.0 equiv.) were added into a 100 mL round-bottom flask followed by the addition of DMF (20 mL) and *m*-xylene (20 mL). The mixture was stirred at 140 °C overnight and the reaction was monitored by TLC (pet. ether/dichloromethane, v/v, 4:1). The resulting solution was concentrated under reduced pressure and purified through a short silica plug (pet. ether/dichloromethane, v/v, 1:1) to yield **NiP1** (0.35 g, 91%) was yielded as a red-purple solid.

^{1}H NMR (400 MHz, $CDCl_3$, 298 K) δ_H 9.92 (s, 2H, *H1*), 9.19 (d, J = 4.7 Hz, 4H, *H2*), 8.98 (d, J = 4.7 Hz, 4H, *H3*), 7.06 (d, J = 1.6 Hz, 8H, *H4*), 6.94 (t, J = 1.6 Hz, 4H, *H5*), 2.64 (t, J = 7.7 Hz, 16H, H_{Hex}), 1.99 (s, 6H, *H6*), 1.69 – 1.57 (m, 16H, H_{Hex}), 1.47 (s, 12H, *H7*), 1.27 (pd, J = 9.2, 3.4 Hz, 47H, H_{Hex}), 0.83 (td, J = 5.9, 2.0 Hz, 24H, H_{Hex}).

MALDI-ToF MS: m/z = 1579.473 ($C_{110}H_{144}N_4Ni$, M^+ requires 1579.074)

Dibrominated Ni(II) 5,15-bis(2,4,6-trimethyl-3,5-bis(ArHex))porphyrin NiP1-Br$_2$

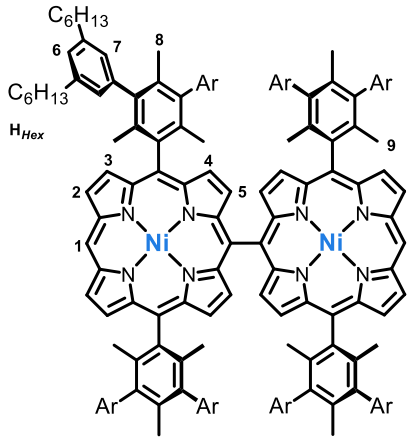


NiP1(0.12 g, 0.07 mmol, 1.0 equiv.) was added into a 100 mL round-bottom flask followed by the addition of dichloromethane (50 mL) with pyridine (0.5 mL). It was cooled down to 0 °C in an ice bath and to the stirred mixture, a solution of *N*-bromosuccinimide (29 mg, 0.16 mmol, 2.2 equiv.) in dichloromethane (10 mL) was added dropwise. The reaction was conducted at 0 °C for 15 min. Subsequently, acetone (1.0 mL) was added to quench the excess *N*-bromosuccinimide. The resulting mixture was concentrated under reduced pressure and purified by a silica plug (pet. Ether/dichloromethane, v/v, 1:1) to yield **NiP1-Br$_2$** (0.24 g, 93%).

^{1}H NMR (400 MHz, $CDCl_3$, 298 K) δ_H 9.54 (d, J = 4.9 Hz, 4H, *H1*), 8.84 (d, J = 5.0 Hz, 4H, *H2*), 7.08 (d, J = 1.6 Hz, 8H, *H3*), 7.00 (t, J = 1.6 Hz, 4H, *H4*), 2.68 (t, J = 7.7 Hz, 16H, H_{Hex}), 2.02 (s, 6H, *H5*), 1.74 – 1.64 (m, 16H, H_{Hex}), 1.53 (s, 12H, *H6*), 1.43 – 1.26 (m, 51H, H_{Hex}), 0.93 – 0.84 (m, 24H, H_{Hex}).

MALDI-ToF MS: m/z = 1735.266 ($C_{110}H_{142}Br_2N_4Ni$, M^+ requires 1734.895)

PIFA-Mediated Dimerization of NiP1 to *s*-NiP2



NiP1(0.17 g, 0.11 mmol, 1.0 equiv.) was added into a 50 mL Schlenk tube followed by the addition of dry dichloromethane (14 mL) and [bis(trifluoro-acetoxy)iodo]benzene (PIFA, 24 mg, 55 μmol, 0.5 equiv.). The progress of the coupling was monitored by TLC. After 1 h, a suspension of NaBH4 (42 mg, 1.1 mmol, 10 equiv.) in methanol (10 mL) was added and the reaction mixture was stirred at room temperature for 30 min. The resulting mixture was concentrated and passed through purified by silica column chromatography (pet. ether/dichloromethane, v/v, 1:1), followed by size-exclusion chromatography (Bio-Beads, S-X1) with toluene as eluent to separate the *meso-meso* singly-linked Ni(II) porphyrin dimer

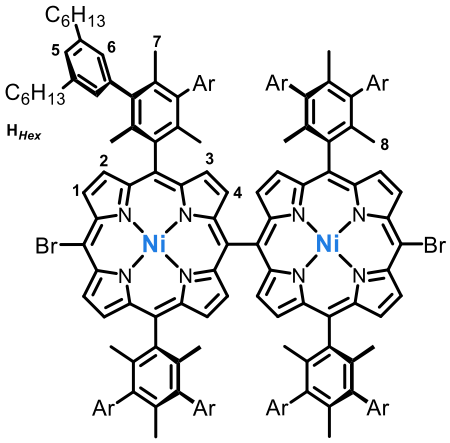
***s*-NiP2** and unreacted **NiP1** (96 mg). Recovered **NiP1** was resubmitted under the same reaction conditions and ***s*-NiP2** (in total 95 mg, 54%) was yielded as red-purple solid.

^{1}H NMR (400 MHz, $CDCl_3$, 298 K) δ_H 9.97 (s, 2H, *H1*), 9.25 (d, *J* = 4.7 Hz, 4H, *H2*), 8.99 (d, *J* = 4.7 Hz, 4H, *H3*), 8.60 (d, *J* = 4.9 Hz, 4H, *H4*), 8.08 (d, *J* = 4.9 Hz, 4H, *H5*), 7.04 (d, *J* = 1.6 Hz, 8H, *H6*), 6.89 (dt, *J* = 7.1, 1.7 Hz, 16H, *H7*), 2.63 (t, *J* = 7.7 Hz, 16H, H_{Hex}), 2.49 (t, *J* = 7.7 Hz, 16H, H_{Hex}), 1.89 (s, 12H, *H8*), 1.68 – 1.59 (m, 16H, H_{Hex}), 1.53 (s, 24H, *H9*), 1.53 – 1.44 (m, 16H, H_{Hex}) 1.38 – 1.23 (m, 57H, H_{Hex}), 1.23 – 1.07 (m, 52H, H_{Hex}), 0.87 – 0.82 (m, 24H, H_{Hex}), 0.72 – 0.65 (m, 24H, H_{Hex}).

^{13}C NMR (101 MHz, $CDCl_3$, 298 K) δ_C 147.1, 143.7, 143.1, 142.9, 142.0, 139.9, 137.8, 136.0, 134.1, 127.1, 126.6, 119.6, 77.4, 36.1, 35.9, 31.9, 31.7, 31.5, 29.1, 28.9, 22.7, 22.6, 20.5, 19.8, 14.2, 14.1.

MALDI-ToF MS: *m*/*z* = 3158.747 ($C_{220}H_{286}N_8Ni_2$, M^+ requires 3156.133)

Dibrominated Singly-linked Ni(II) Porphyrin Dimer *s*-NiP2-Br$_2$



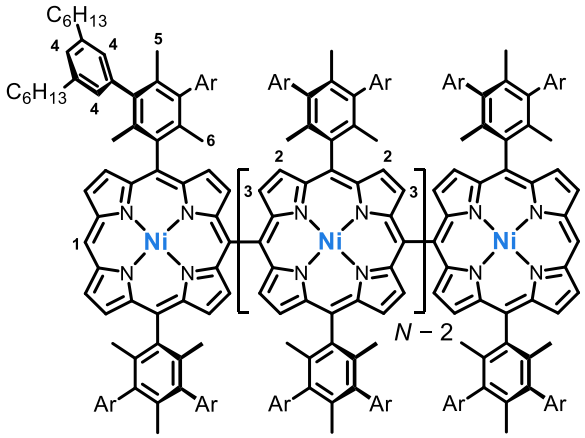
***s*-NiP2** (53 mg, 17 μmol, 1.0 equiv.) was added into a 50 mL round-bottom flask followed by the addition of dichloromethane (17 mL) with pyridine (0.17 mL). It was cooled down to 0 °C in an ice bath and to the stirred mixture, a solution of *N*-bromosuccinimide (6.6 mg, 37 μmol, 2.2 equiv.) in chloroform (3.5 mL) was added dropwise. The reaction was conducted at 0 °C for 15 min. Subsequently, acetone (1.0 mL) was added to quench the excess *N*-bromosuccinimide. The resulting mixture was concentrated under reduced pressure and purified by a silica plug (pet. Ether/dichloromethane, v/v, 1:1) to yield ***s*-NiP2-Br$_2$** (40 mg, 72%).

^{1}H NMR (400 MHz, $CDCl_3$, 298 K) δ_H 9.63 (d, J = 5.0 Hz, 4H, *H1*), 8.88 (d, J = 5.0 Hz, 4H, *H2*), 8.52 (d, J = 5.0 Hz, 4H, *H3*), 8.04 (d, J = 4.9 Hz, 4H, *H4*), 7.02 (d, J = 1.6 Hz, 8H, *H5*), 6.90 (t, J = 1.7 Hz, 8H, *H6*), 6.86 (t, J = 1.5 Hz, 8H, *H6*), 2.63 (t, J = 7.7 Hz, 16H, H_{Hex}), 2.50 (t, J = 7.6 Hz, 16H, H_{Hex}), 1.88 (s, 12H, *H7*), 1.64 (dq, J = 15.1, 7.0 Hz, 18H, H_{Hex}), 1.53 (s, 24H, *H8*), 1.49 (d, J = 7.5 Hz, 14H, H_{Hex}), 1.38 – 1.24 (m, 65H, H_{Hex}), 1.23 – 1.09 (m, 53H, H_{Hex}), 0.87 – 0.83 (m, 24H, H_{Hex}), 0.73 – 0.66 (m, 24H, H_{Hex}).

^{13}C NMR (101 MHz, $CDCl_3$, 298 K) δ_C 147.4, 144.2, 143.0, 142.9, 142.6, 141.9, 140.0, 137.4, 135.9, 134.3, 133.6, 127.1, 126.7, 120.5, 77.4, 36.1, 36.0, 31.9, 31.7, 31.7, 31.5, 29.9, 29.1, 28.9, 22.8, 22.6, 20.5, 19.8, 14.2, 14.1.

MALDI-ToF MS: m/z = 3310.562 ($C_{220}H_{284}Br_2N_8Ni_2$, M^+ requires 3311.954)

Singly-linked Ni(II) Porphyrin Oligomers *s*-NiP*N* (starting from *s*-NiP2-Br$_2$)



$Ni(COD)_2$ (37 mg, 0.13 mmol, 20 equiv.) and 2,2'-bipyridine (20 mg, 0.13 mmol, 20 equiv.) were added into a 25 mL Schlenk tube followed by the addition of dry DMF (4.9 mL) with pyridine (82 μL). The solution was degassed by three freeze-pump-thaw cycles and the mixture was stirred at 60 °C for 1 h until it turned into a dark-purple solution. ***s*-NiP2-Br$_2$** (22 mg, 6.6 μmol, 1.0 equiv.) was dissolved in THF (1.6 mL) and the solution was degassed by three freeze-pump-thaw cycles before mixing with the former. The mixture was stirred at 60 °C in dark for 24 h. The resulting mixture was diluted by water (20 mL) and washed by dichloromethane (20 mL × 3). The combined organic phase was concentrated under reduced pressure and passed through a silica plug (pet. ether/dichloromethane, v/v, 1:1), followed by size-exclusion chromatography with toluene as eluent to yield crude mixture of singly-linked Ni(II) porphyrin

oligomers. The mixture was further subjected to recycling GPC with toluene/pyridine (99:1) to separate out the short oligomers and long Ni(II) porphyrin oligomers ***s*-NiP*N*(3)** (15 mg, 68%) was yielded as a purple solid. The reproducibility of this reaction heavily depends on the oxygen content in the reaction vessel and the quality of $Ni(COD)_2$. The other two batches of long Ni(II) porphyrin oligomers ***s*-NiP*N*(1)** (8 mg, 50%) and ***s*-NiP*N*(2)** (12 mg, 67%) with different lengths were isolated from another two individual oligomerization reactions.

***s*-NiP*N*(1)**: **^{1}H NMR** (400 MHz, $CDCl_3$, 298 K) δ_H 9.93 (s, $H1_{meso}$),8.68 (s, 4H, $H2_{\beta}$), 8.25 (s, 4H, $H3_{\beta}$), 6.85 (2s, 12H, *H4*), 2.47 (s, 16H, H_{Hex}), 1.78 (s, 6H, *H5*), 1.64 (s, 12H, *H6*), 1.46 (m 30H, H_{Hex}), 1.13 (m, 45H, H_{Hex}), 0.66 (m, 24H, H_{Hex}).

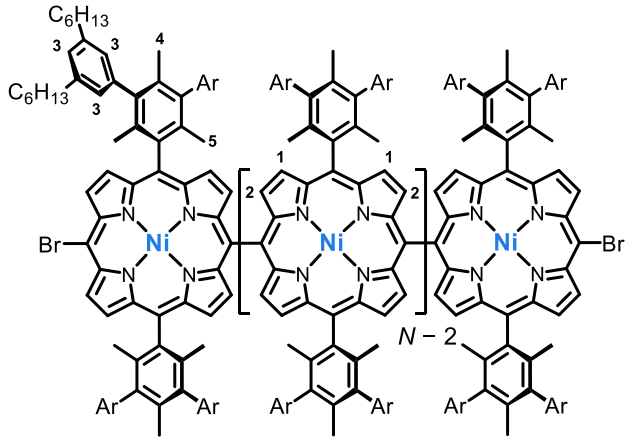
***s*-NiP*N*(2)**: **^{1}H NMR** (400 MHz, $CDCl_3$, 298 K) δ_H 10.00 (s, $H1_{meso}$), 8.75 (s, 4H, $H2_{\beta}$), 8.33 (s, 4H, $H3_{\beta}$), 6.92 (2s, 12H, *H4*), 2.54 (s, 16H, H_{Hex}), 1.86 (s, 6H, *H5*), 1.71 (m, 12H, *H6*), 1.20 (m, 43H, H_{Hex}), 0.74 (m, 24H, H_{Hex}).

***s*-NiP*N*(3)**: **^{1}H NMR** (400 MHz, $CDCl_3$, 298 K) δ_H 10.01 (s, $H1_{meso}$), 8.76 (s, 4H, $H2_{\beta}$), 8.33 (s, 4H, $H3_{\beta}$), 6.92 (2s, 12H, *H4*), 2.55 (s, 16H, H_{Hex}), 1.86 (s, 6H, *H5*), 1.72 (s, 12H, *H6*), 1.56 (m, 30H, H_{Hex}), 1.20 (m, 49H, H_{Hex}), 0.75 (m, 24H, H_{Hex}).

(The numbers of protons are corresponding to the relative ratios of protons in each position of porphyrins)

Recycling GPC retention time: ***s*-NiP*N*(1)** (54.6 min), ***s*-NiP*N*(2)** (50.9 min), ***s*-NiP*N*(3)** (47.8 min)

Dibrominated Singly-linked Ni(II) Porphyrin Oligomers *s*-NiP*N*-Br$_2$



***s*-NiP*N*(1)** (6.0 mg, 0.19 μmol, 1.0 equiv.) was added into a 10 mL round-bottom flask followed by the addition of dichloromethane (3.1 mL) with pyridine (31 μL). It was cooled down to 0 °C in an ice bath and to the stirred mixture, a solution of *N*-bromosuccinimide (74 μg, 0.42 μmol, 2.2 equiv.) in chloroform (0.6 mL) was added dropwise. The reaction was conducted at 0 °C for 15 min. Subsequently, acetone (1.0 mL) was added to quench the excess *N*-bromosuccinimide. The resulting mixture was concentrated under reduced pressure and purified by a silica plug (pet. Ether/dichloromethane, v/v, 1:4) to yield ***s*-NiP*N*(1)-Br$_2$** (4.5 mg, 75%).

^{1}H NMR (500 MHz, CD_2Cl_2, 298 K) δ_H 8.75 (s, 4H, *H1*$_\beta$), 8.34 (s, 4H, *H2*$_\beta$), 6.94 (s, 12H, *H3*), 2.56 (s, 16H, H_{Hex}), 1.85 (s, 6H, *H4*), 1.67 (s, 12H, *H5*), 1.62 – 1.48 (m, 32H, H_{Hex}), 1.24 – 1.09 (m, 46H, H_{Hex}), 0.78 – 0.62 (m, 24H, H_{Hex}).

***s*-NiP*N*(2)** (6.5 mg, 0.16 μmol, 1.0 equiv.) was added into a 10 mL round-bottom flask followed by the addition of dichloromethane (2.6 mL) with pyridine (26 μL). It was cooled down to 0 °C in an ice bath and to the stirred mixture, a solution of *N*-bromosuccinimide (62 μg, 0.35 μmol, 2.2 equiv.) in chloroform (0.5 mL) was added dropwise. The reaction was conducted at 0 °C for 15 min. Subsequently, acetone (1.0 mL) was added to quench the excess *N*-bromosuccinimide. The resulting mixture was concentrated under reduced pressure and purified by a silica plug (pet. Ether/dichloromethane, v/v, 1:4) to yield ***s*-NiP*N*(1)-Br$_2$** (4.2 mg, 64%).

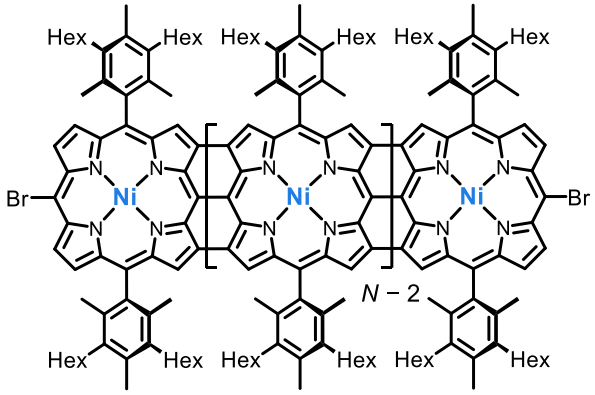
^{1}H NMR (500 MHz, CD_2Cl_2, 298 K) δ_H 8.76 (s, 4H, *H1*$_\beta$), 8.34 (s, 4H, *H2*$_\beta$), 6.94 (s, 12H, *H3*), 2.56 (s, 16H, H_{Hex}), 1.85 (s, 6H, *H4*), 1.68 (s, 12H, *H5*), 1.57 (m, 30H, H_{Hex}), 1.20 (m, 50H, H_{Hex}), 0.72 (m, 24H, H_{Hex}).

***s*-NiP*N*(3)** (8.0 mg, 0.16 μmol, 1.0 equiv.) was added into a 10 mL round-bottom flask followed by the addition of dichloromethane (2.6 mL) with pyridine (26 μL). It was cooled down to 0 °C in an ice bath and to the stirred mixture, a solution of *N*-bromosuccinimide (62 μg, 0.35 μmol, 2.2 equiv.) in chloroform (0.5 mL) was added dropwise. The reaction was conducted at 0 °C for 15 min. Subsequently, acetone (1.0 mL) was added to quench the excess *N*-bromosuccinimide. The resulting mixture was concentrated under reduced pressure and purified by a silica plug (pet. ether/dichloromethane, v/v, 1:4) to yield ***s*-NiP*N*(1)-Br$_2$** (6.2 mg, 77%).

^{1}H NMR (500 MHz, CD_2Cl_2, 298 K) δ_H 8.76 (s, 4H, *H1*$_\beta$), 8.34 (s, 4H, *H2*$_\beta$), 6.94 (s, 12H, *H3*), 2.56 (s, 16H, H_{Hex}), 1.85 (s, 6H, *H4*), 1.68 (s, 12H, *H5*), 1.63 – 1.40 (m, 38H, H_{Hex}), 1.18 (m, 42H, H_{Hex}), 0.73 (m, 24H, H_{Hex}).

(The numbers of protons are corresponding to the relative ratios of protons in each position of porphyrins)

Ni(II) Porphyrin Nanoribbons *f*-NiP*N*-Br$_2$



***s*-NiP*N*(1)-Br$_2$** (4.5 mg, 0.14 μmol, 1.0 equiv.) was added into a 25 mL Schlenk tube and the tube was evacuated and backfilled with argon for three times. Dry 1,2-dichloroethane (10 mL) and toluene (2.4 mL) were added to the tube under argon. Under vigorous stirring, the suspension of $AuCl_3$/AgOTf (1:5, 0.2 mM) in dry 1,2-dichloroethane (2 mL) was added to the tube dropwise and the reaction was monitored by UV–vis–NIR spectroscopy with toluene + 1% triethylamine as solvent. After completion, the reaction was quenched by the addition of triethylamine (1.0 mL) and the residue was precipitated by the addition of methanol. Ni(II) porphyrin nanoribbon ***f*-NiP*N*(1)-Br$_2$** (3.5 mg, 78%) was yielded as black solid.

***s*-NiP*N*(2)-Br$_2$** (4.2 mg, 0.10 μmol, 1.0 equiv.) was added into a 25 mL Schlenk tube and the tube was evacuated and backfilled with argon for three times. Dry 1,2-dichloroethane (6.5 mL) and toluene (1.7 mL) were added to the tube under argon. Under vigorous stirring, the suspension of $AuCl_3$/AgOTf (1:5, 0.2 mM) in dry 1,2-dichloroethane (2 mL) was added to the tube dropwise and the reaction was monitored by UV−vis−NIR spectroscopy with toluene + 1% triethylamine as solvent. After completion, the reaction was quenched by the addition of triethylamine (1.0 mL) and the residue was precipitated by the addition of methanol. Ni(II) porphyrin nanoribbon ***f*-NiP*N*(2)-Br$_2$** (3.5 mg, 76%) was yielded as black solid.

***s*-NiP*N*(3)-Br$_2$** (4.4 mg, 0.09 μmol, 1.0 equiv.) was added into a 25 mL Schlenk tube and the tube was evacuated and backfilled with argon for three times. Dry 1,2-dichloroethane (5.2 mL) and toluene (1.5 mL) were added to the tube under argon. Under vigorous stirring, the suspension of $AuCl_3$/AgOTf (1:5, 0.2 mM) in dry 1,2-dichloroethane (2 mL) was added to the tube dropwise and the reaction was monitored by UV−vis−NIR spectroscopy with toluene + 1% triethylamine as solvent. After completion, the reaction was quenched by the addition of triethylamine (1.0 mL) and the residue was precipitated by the addition of methanol. Ni(II) porphyrin nanoribbon ***f*-NiP*N*(3)-Br$_2$** (3.5 mg, 82%) was yielded as black solid.

Selected NMR Spectra

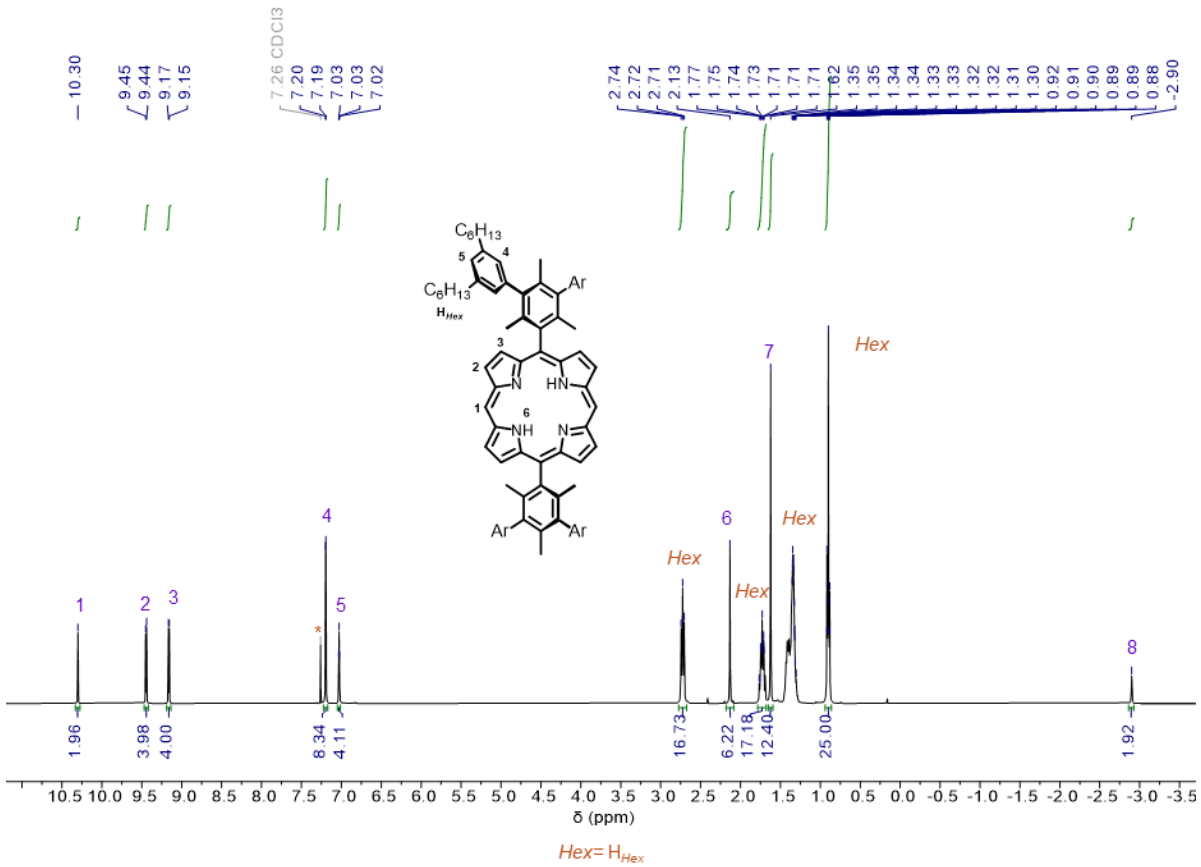


Figure S4.1: ^{1}H NMR (400 MHz) spectrum of 5,15-bis(2,4,6-trimethyl-3,5-bis(ArHex))porphyrin ($CDCl_3$, 298 K).

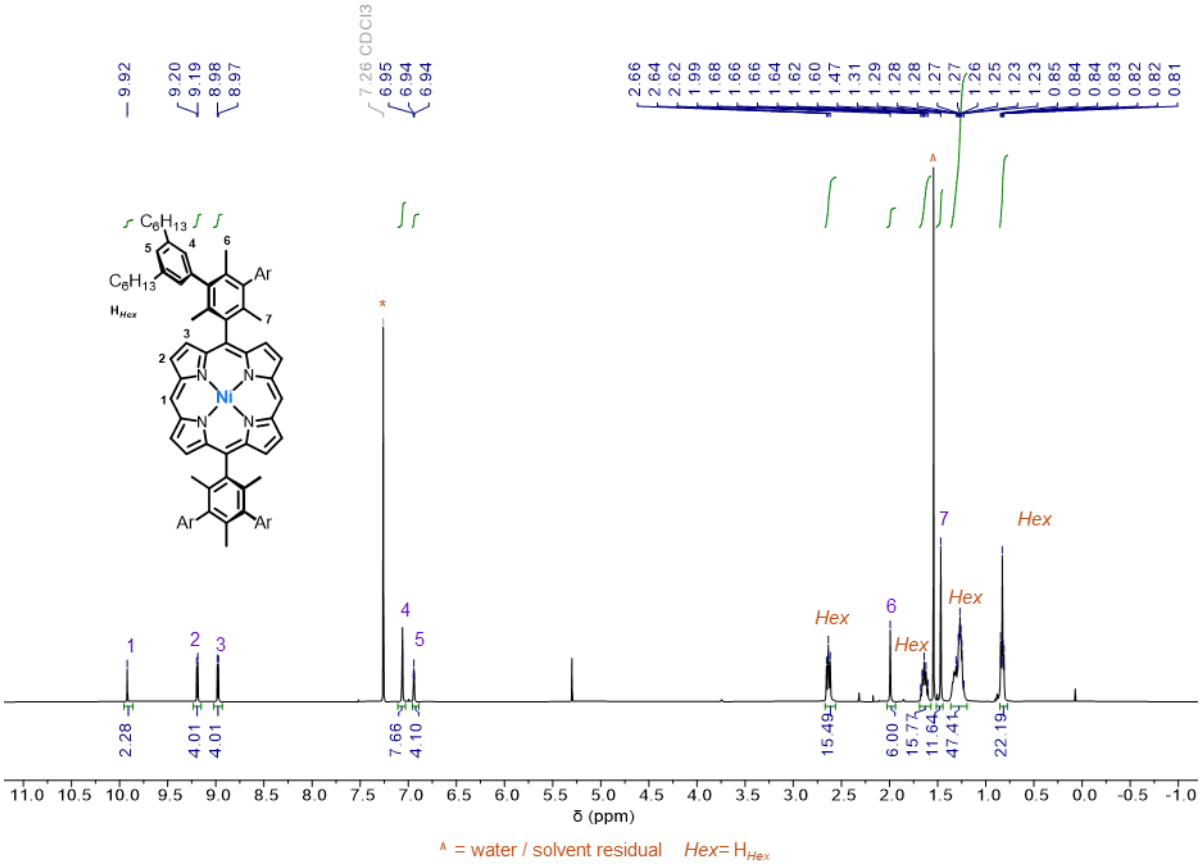


Figure S4.2: ^{1}H NMR (400 MHz) spectrum of **NiP1** ($CDCl_3$, 298 K).

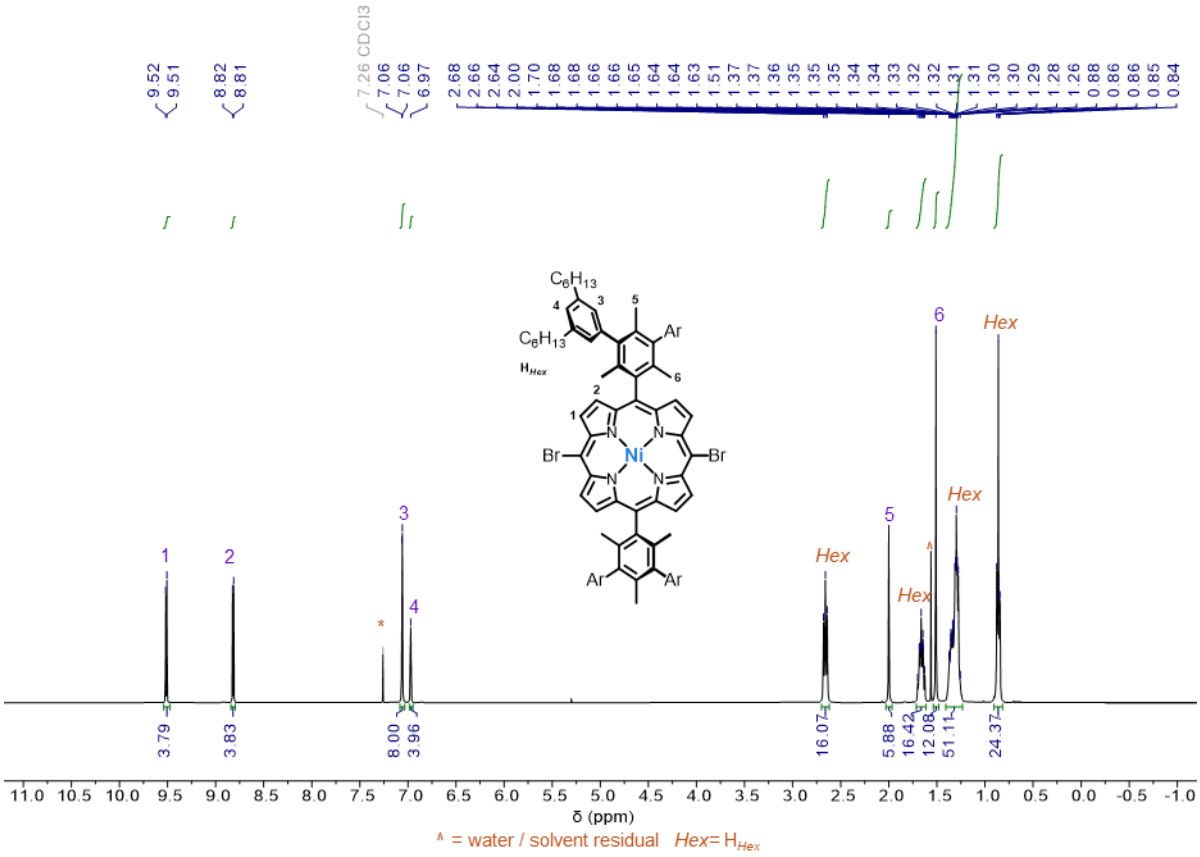


Figure S4.3: ^{1}H NMR (400 MHz) spectrum of **NiP1-Br$_2$** ($CDCl_3$, 298 K).

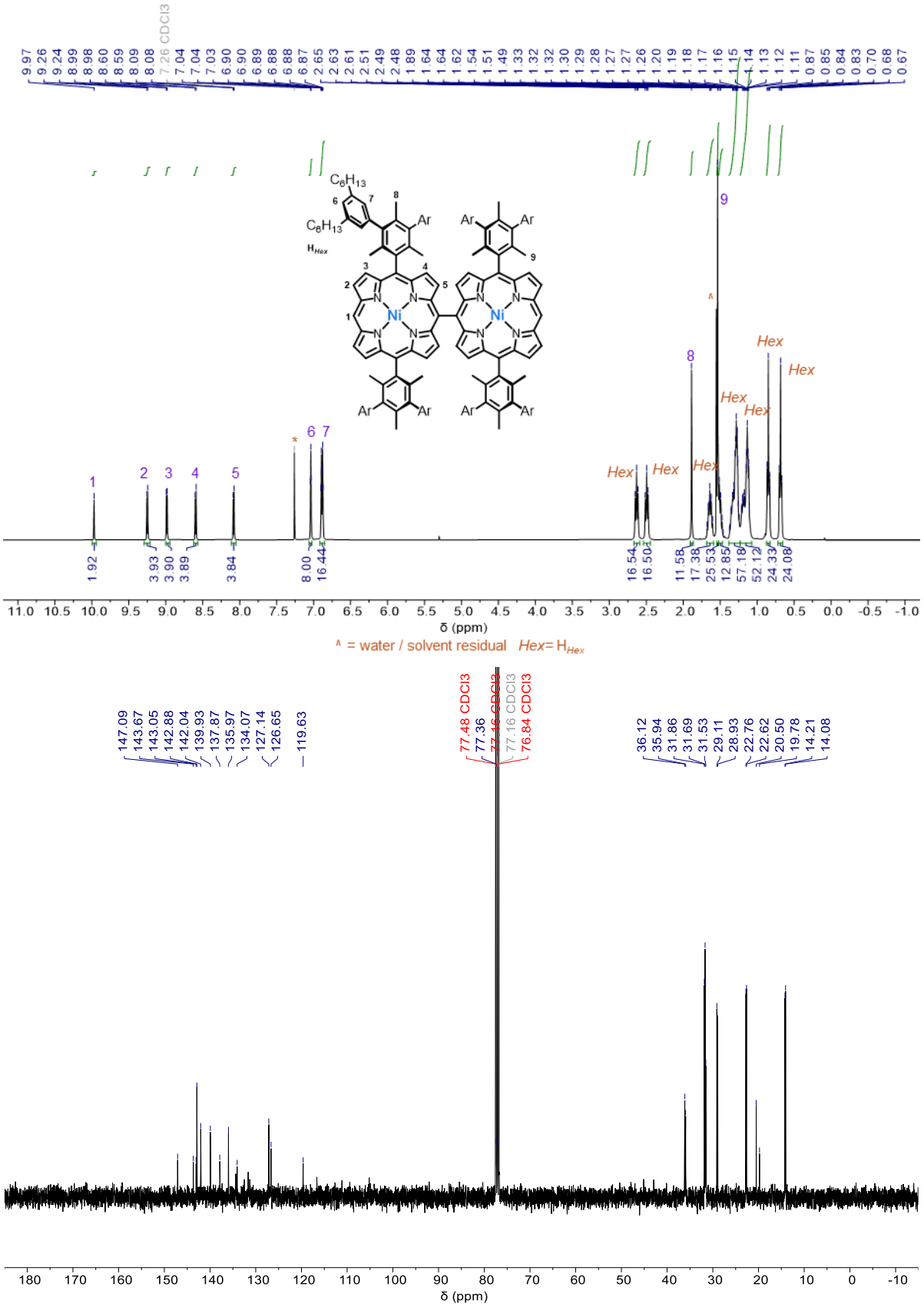


Figure S4.4: (top) ^{1}H NMR (400 MHz) and (bottom) ^{13}C NMR (101 MHz) spectra of ***s*-NiP2** ($CDCl_3$, 298 K).

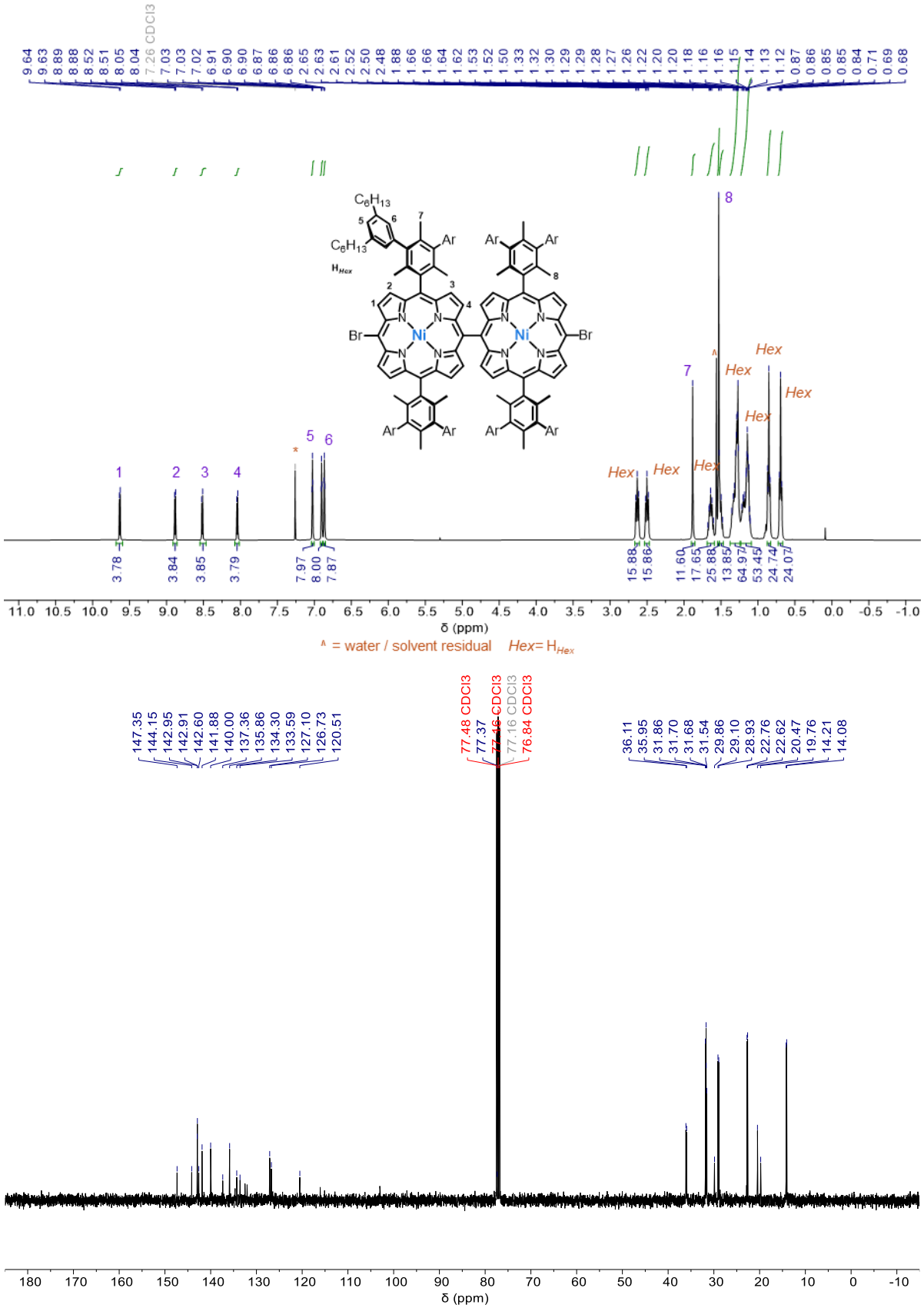


Figure S4.5: (top) ^{1}H NMR (400 MHz) and (bottom) ^{13}C NMR (101 MHz) spectra of ***s*-NiP2-Br$_2$** ($CDCl_3$, 298 K).

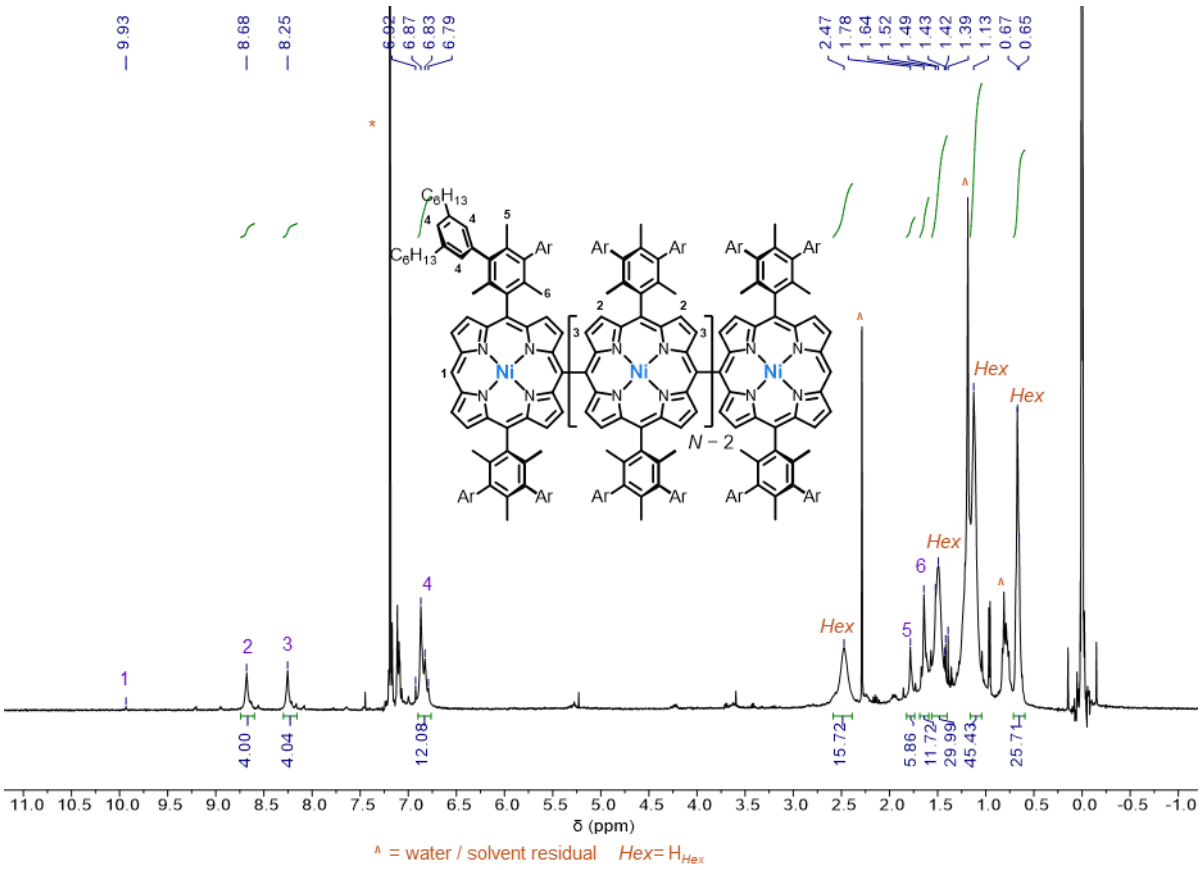


Figure S4.6: ^{1}H NMR (400 MHz) spectrum of ***s*-NiP*N*(1)** ($CDCl_3$, 298 K).

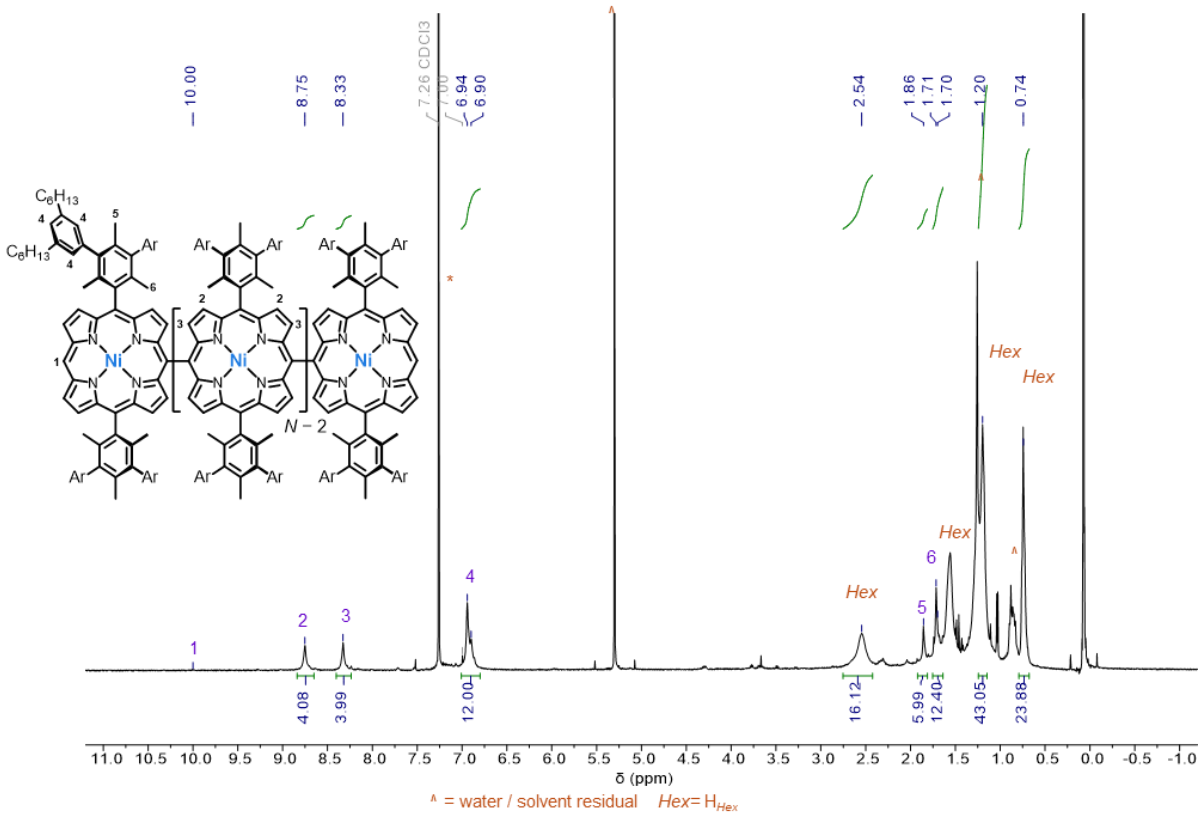


Figure S4.7: ^{1}H NMR (400 MHz) spectrum of ***s*-NiP*N*(2)** ($CDCl_3$, 298 K).

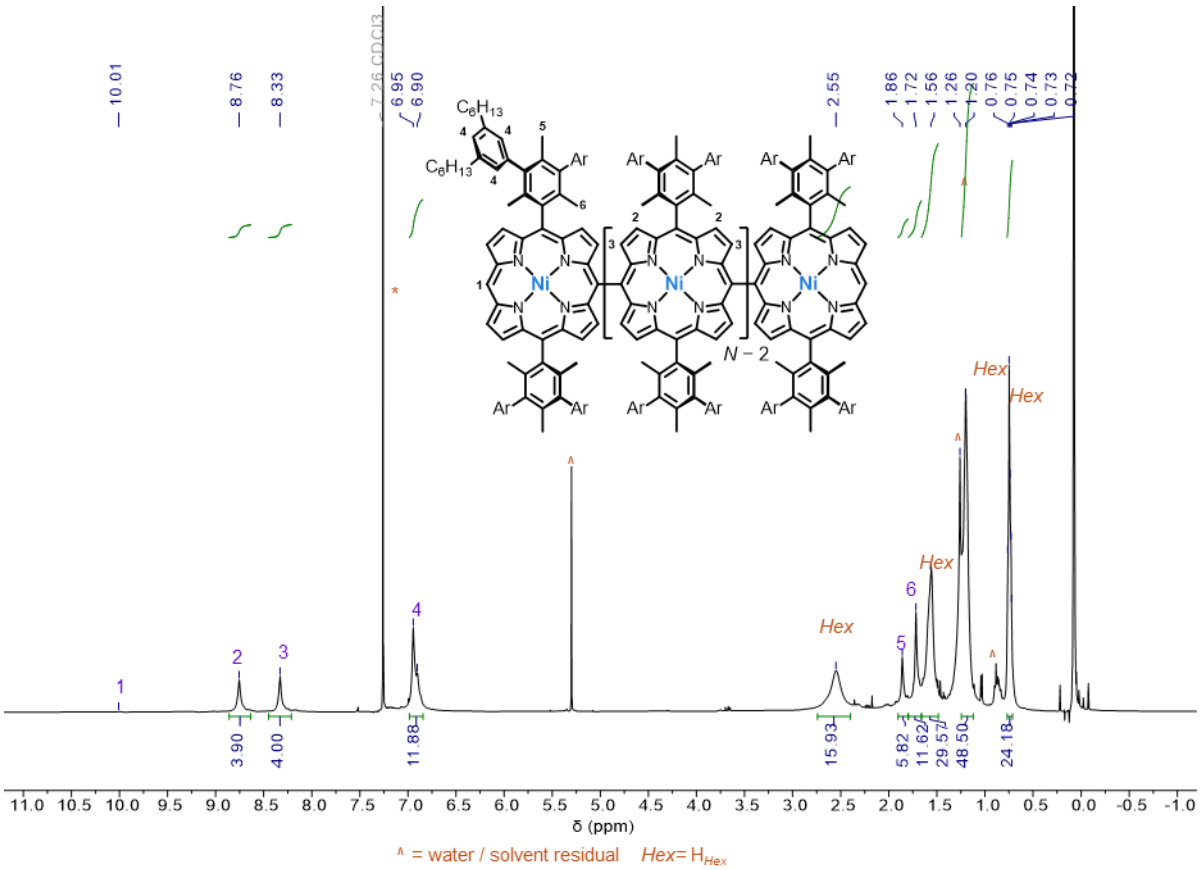


Figure S4.8: ^{1}H NMR (400 MHz) spectrum of ***s*-NiP*N*(3)** ($CDCl_3$, 298 K).

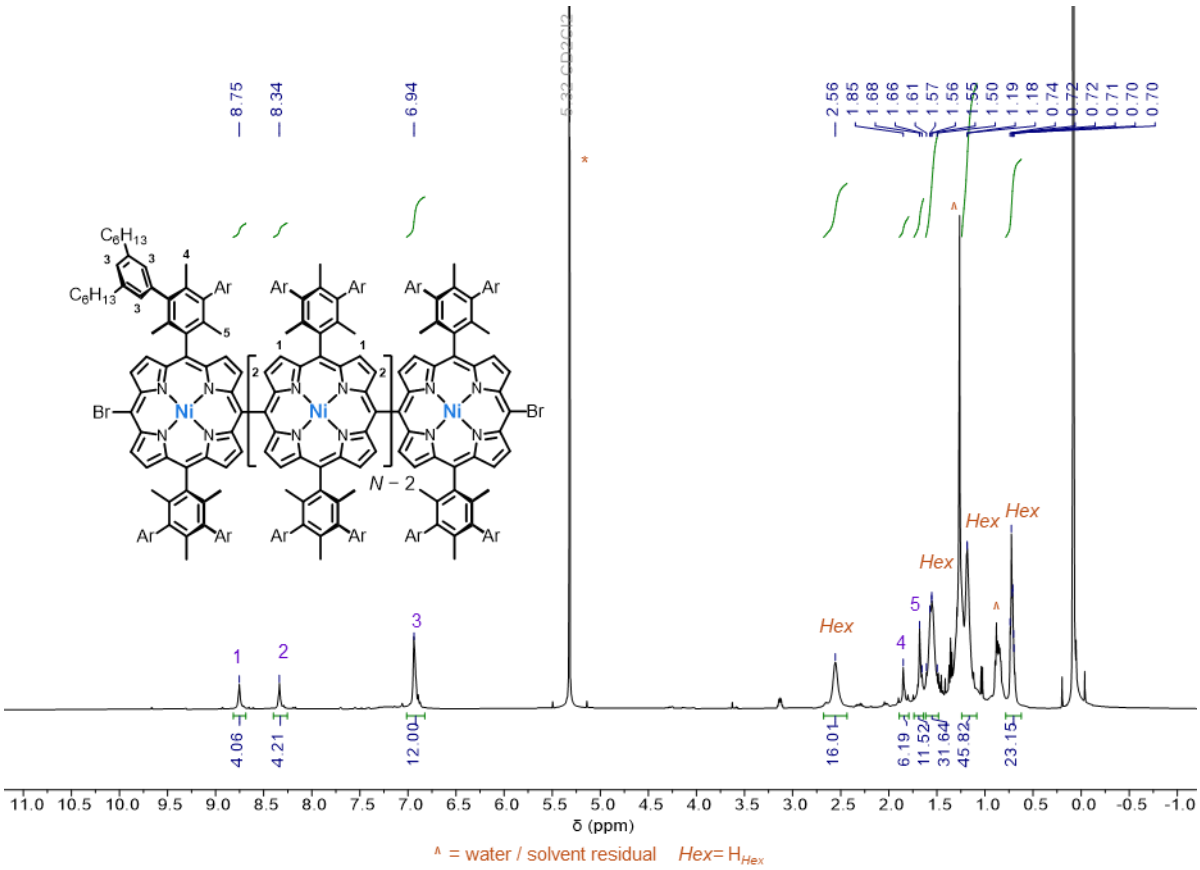


Figure S4.9: ^{1}H NMR (500 MHz) spectrum of ***s*-NiP*N*(1)-Br$_2$** (CD_2Cl_2, 298 K).

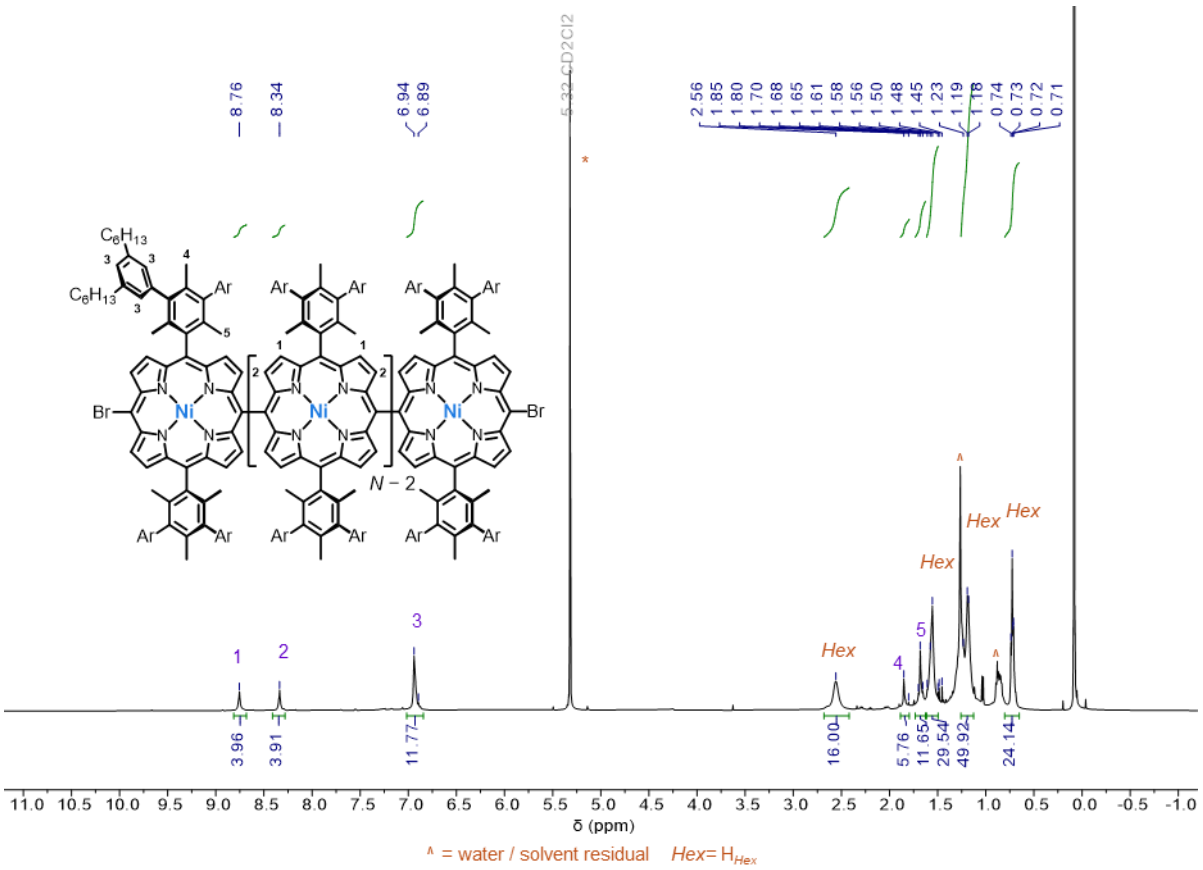


Figure S4.10: ^{1}H NMR (500 MHz) spectrum of ***s*-NiP*N*(2)-Br$_2$** (CD_2Cl_2, 298 K).

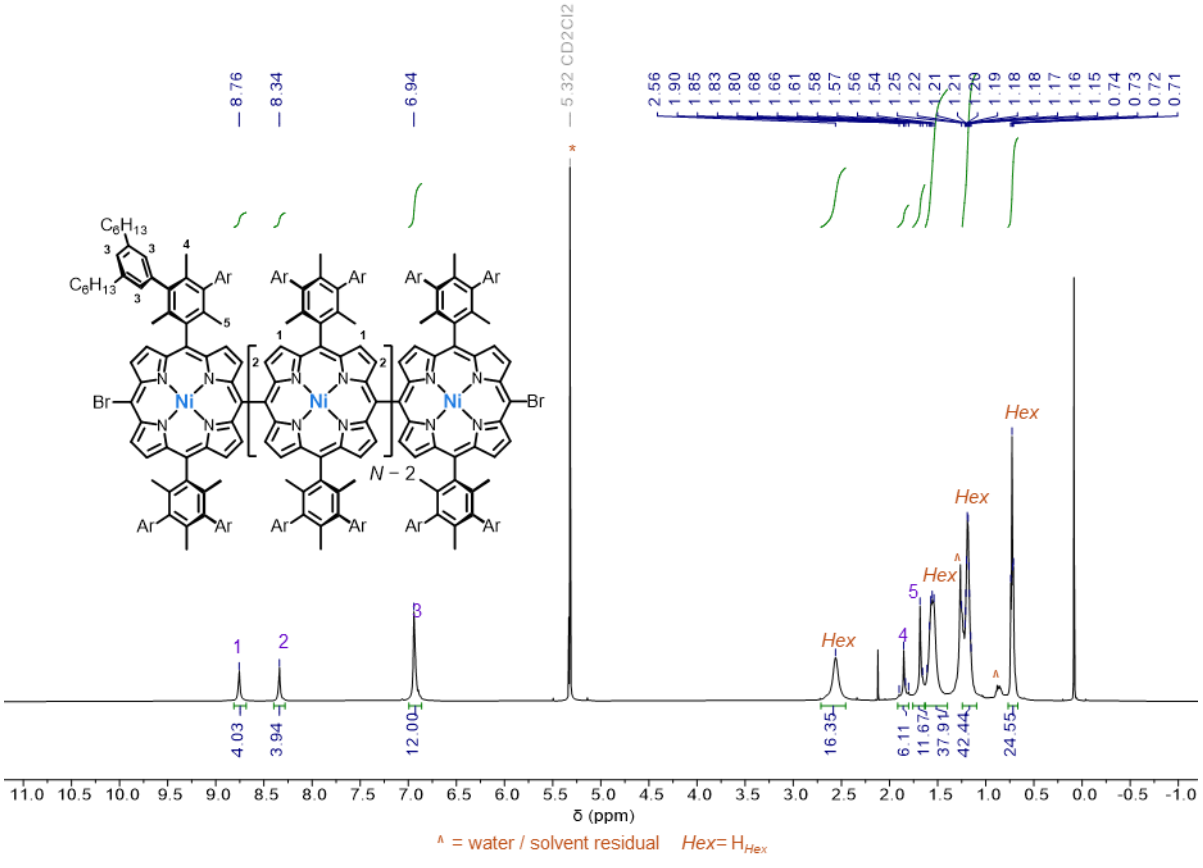


Figure S4.11: ^{1}H NMR (500 MHz) spectrum of ***s*-NiP*N*(3)-Br$_2$** (CD_2Cl_2, 298 K).

UV–vis–NIR Absorption Comparison

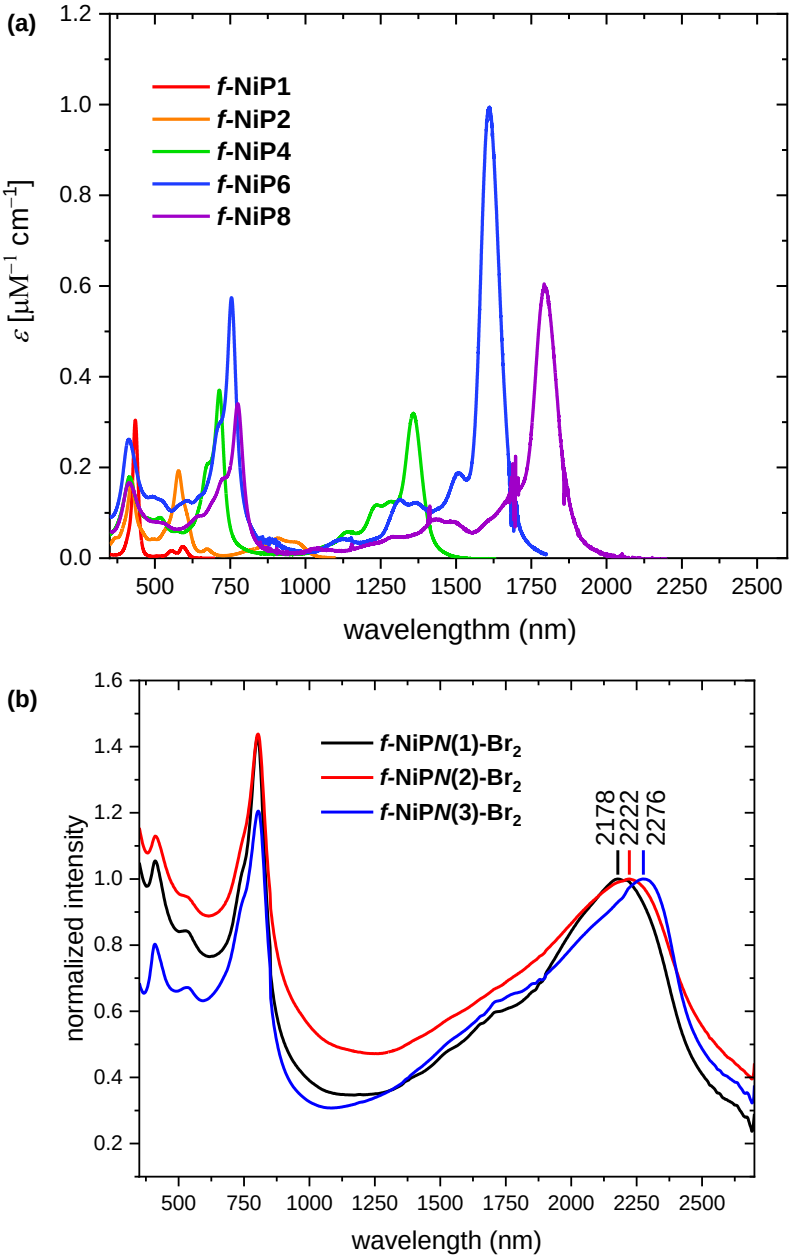


Figure S4.12: Comparison of (a) reported UV–vis–NIR absorption spectra for shorter triply fused Ni(II) porphyrin oligomers and (b) the zoomed-in absorption spectra obtained from this work.[4]

References

1 F. C. Grozema, C. Houarner-Rassin, P. Prins, L. D. A. Siebbeles and H. L. Anderson, *J. Am. Chem. Soc.*, 2007, **129**, 13370–13371.

2 I. Krossing, *Chemistry (Easton).*, 2001, **7**, 490–502.

3 S. Richert, B. Limburg, H. L. Anderson and C. R. Timmel, *J. Am. Chem. Soc.*, 2017, **139**, 12003–12008.

4 J.-R. Deng, M. T. González, H. Zhu, H. L. Anderson and E. Leary, *J. Am. Chem. Soc.*, 2024, **146**, 3651–3659.